STRESS DISTRIBUTIONS IN SILOS AND HOPPERS

JAMES CHRISTOPHER O'NEILL

A thesis submitted in partial fulfilment of the requirements of Teesside University for the degree of Doctor of Philosophy

July 2012

‘Stress Distributions in Silos and Hoppers’

Abstract

James O’Neill
Teesside University
July 2012

This thesis provides a report on the numerical analysis of stress distributions within granular materials held in silos and hoppers.

Stress distributions within granular materials stored in silos and hoppers have been the subject of research for over 100 years, work starting in this field in 1895 (Janssen). Knowledge of stress distributions within the granular materials contained is essential to allow structural design of the silo and hopper shell and attachments, and to allow estimation of likelihood and location of cohesive arch formation. National design codes for silos and hoppers (including BS EN 1993-4-1:2007 Eurocode 3 and DIN 1055-6:2005-03) are based on approximate techniques that assume vertical and horizontal directions of principal stresses, with constant horizontal stress across the silos. According to the knowledge of the author there are no industrial standards that allow calculation of loading on inserts within hoppers.

The objective of the research project is to develop algorithms to predict stresses in hoppers and silos using principal stress arc geometry methods, and implementation of these methods in various silo and hopper configurations including those with inserts for the purposes of aiding flow.

The research project algorithms are spreadsheet- and QB64 platform-based, and are able to produce stress distributions within silos and hoppers. This is achieved by extension of the principal stress arc method of analysis. The new algorithms allow prediction of common flow problems and provide new information on structural loading of silos and hoppers, including inserts used to promote flow. The research project models allow estimation of azimuthal stresses within three-dimensional case studies.

Acknowledgements

I would like to thank the following persons, who made this research project possible:

- Dr. Qiang Xu
- Mr. Alan Shaw
- Prof. Andy Matchett

'Stress Distributions in Silos and Hoppers'

Contents

14.0 Appendix Seven – Publications

14.1. Matchett, A.J., O'Neill, J.C., Shaw, A.P., 2007. Analytical solutions to stress distribution problems in wedge and conical hoppers. Proceedings of Enstimac 2007 Conference, Ecoles des Mines D’Albi, France.

14.2. Matchett, A.J., O'Neill, J.C., Shaw, A.P., 2008. Stress distributions in 2-dimensional, wedge hoppers with circular arc stress orientation — A co-ordinate-specific Lamé–Maxwell model. Powder Technology, **187** (3) pp. 298-306.

14.3. Matchett, A.J., O'Neill, J.C., Shaw, A.P., 2009. Stresses in bulk solids in wedge hoppers: A flexible formulation of the co-ordinate specific, Lamé–Maxwell equations for circular arc, principal stress systems. Powder Technology, **194** (3) pp. 166-180.

14.4. O’Neill, J.C., Matchett, A.J., Shaw, A.P., 2009. Stresses in bulk solids in cone hoppers: numerical solutions to the 3-dimensional stress distribution problem, using circular arc geometry. Proceedings of Flexible Automation and Intelligent Manufacturing 2009 Conference, Teesside University, UK.

‘Stress Distributions in Silos and Hoppers’

Notation

a	isostatic surface, Love (1927) notation	[-]
a_1	arc radius constant	[-]
a_2	arc thickness constant	[-]
$\alpha, \alpha_1, \alpha_2$	angle of hopper wall to vertical	[rad]
A	area	[m^2]
δA	incremental area	[m^2]
β, β_1, β_2	parameter in Janssen’s analysis / angle of arc to wall normal (calculated by equation 54) / isostatic surface	[rad]
$\beta_{ACTIVE}, \beta_{PASSIVE}$	limits for β	[rad]
b_{crit}	critical arching dimension, equation 12	[m]
c	cohesive stress	[Pa]
$CDEF$	points describing incremental element	[-]
$CD_1\ E_1F$	points describing incremental element	[-]
Δ	variations in wall stress data (calculated via $(\sigma_{W_{FINAL}} - \sigma) - (\sigma_{W_{INITIAL}} - \sigma))$	[Pa]
d	dimension in Walters’ analysis, Figure 9	[m]
$\bar{d}$	mean value of variations in wall stresses	[Pa]
d_{crit}	critical arching dimension, equation 13	[m]
D	dimension in Walters’ analysis, equation 7	[m]
D_{crit}	critical arching dimension, Table 2	[m]
ε	angular co-ordinate, angle between arc radius and vertical	[rad]
$\delta\varepsilon$	incremental element width	[rad]
ϵ	void fraction, used in equation 69	[-]
η, η_1, η_2	angle of precession of arc centre	[rad]
E	dimension in Walters’ analysis, equation 7	[m]
$E_{1,2}$	points on model geometry, Figure 34	[-]
f_α	component of acceleration normal to surface, Love (1927) notation	[m/s^2]
F	composite arc stress parameter: $F = \sigma_\varepsilon \left(\frac{\delta w}{\delta x}\right)$	[Pa]
F_α	body force normal to surface, Love (1927) notation	[Pa]

γ weight density ρg / angle formed by *r* and *y* dimensions, ref. Chapter 4.1 / isostatic surface, Love (1927) notation [rad]

g, g_θ acceleration due to gravity [m/s^2]

G point on principal stress arc, Figure 33 (also variable, equation 83) [-]

H value of x for upper boundary condition in σ_R [m]

H_2 value of x for lower boundary condition in σ_R [m]

J material ratio of effective stresses (calculated by equations 55 and 70) [-]

J_1 point on model geometry, Figures 73 and 75 [-]

$J_{ACTIVE}, J_{PASSIVE}$ limits for J [-]

k variable used in stress relationships equations 3 and 62 [-]

K variable used by Walters, Chapter 9.1.2 [-]

λ sum of α and β angles, equation 31 [-]

κ parameter in Jenike’s analysis, equations 9 and 10 [-]

μ coefficient of friction [-]

m parameter in Jenike’s analysis, equation 11 [-]

M variable used in Conical Yield function equation 68 [-]

n degrees of freedom of wall stress data sets [-]

O, O_1 arc centres [-]

O_x, O_z coordinates of arc centre [m]

$\delta O_x, \delta O_z$ incremental coordinates of arc centre [m]

δO incremental distance between arc centres [m]

$OMCD$ points within model geometry [-]

Ω variable used to simplify equation 77 and 78 [-]

OP overpressure [Pa]

π constant [-]

ϕ material angle of friction / angle of yield locus [rad]

ϕ_w angle of wall friction [rad]

ϕ_x variable in Jenike’s analysis, Figure 13 [-]

ϕ_e variable in Jenike’s analysis, Figure 13 [-]

ψ angle of principal stress trajectory [rad]

ψ^* angle from the *r*-direction of polar coordinates to the major principal stress direction, Radial Stress Field analysis [rad]

$\delta\psi, \delta\psi_1, \delta\psi_2$ incremental angle of principal stress trajectory [rad]

p	Radial Stress Field parameter, $p = \gamma r q$	[-]
P	point on principal stress arc, Figure 32	[Pa]
PT	theoretical hopper apex	[-]
q	Radial Stress Field parameter, $q = \rho/\gamma g$	[-]
Q_1	Point within model geometry, Figure 36	[-]
ρ_1, ρ_2	radii used in Lamé-Maxwell analysis, equations 16 and 17	[m]
ρ_{12}, ρ_{13}	principal radii of curvature, Love (1927) notation	[m]
ρ, ρ_b	bulk density	[kg/m^3]
ρ_s	solid density	[kg/m^3]
$\rho_{b_{crit}}$	critical bulk density, equations 12 and 13	[kg/m^3]
$\rho_{\theta\psi}, \rho_{\theta\varepsilon}, \rho_{\theta R}$	principal radii of curvature, equations A.51 and A.52	[m]
r	hypotenuse formed by x and z dimensions (also dimension in Jenike's analysis, Figure 13)	[m]
δr	incremental increase in r	[m]
$\bar{r}$	radius of rotation of incremental element	[m]
R	principal stress arc radius	[m]
R_2	radius of curvature upon which σ_ε acts, between points F and E_1, Figure 34	[m]
δR	incremental increase in R	[m]
σ	normal stress / normal stress at wall / surface stress / octahedral stress	[Pa]
σ_ε	arc stress	[Pa]
σ'_ε	equivalent arc stress	[Pa]
σ_n	contact forces / normal stress	[Pa]
σ_R	radial stress	[Pa]
σ'_R	equivalent arc stress	[Pa]
σ_θ	azimuthal stress	[Pa]
σ_{OCT}	octahedral stress, equivalent to $\frac{1}{3}(\sigma_\varepsilon + \sigma_R + \sigma_\theta)$	[Pa]
σ_v	vertical stress	[Pa]
σ_W	normal stress at wall	[Pa]
σ_x	stress in x-direction, equation 1	[Pa]

σ_z vertical stress in Walters' analysis, figure 9 [Pa]

$\bar{\sigma}_z$ averaged vertical stress in Walters' analysis, figure 9 [Pa]

$\sigma_c, \sigma_{c_{crit}}$ unconfined yield stress [Pa]

σ_1 maximum principal stress (also *P* in Lamé-Maxwell analysis) [Pa]

σ_1' stress required to support a cohesive arch, equation 11 [Pa]

σ_2 minimum principal stress (also *Q* in Lamé-Maxwell analysis) [Pa]

σ_3 intermediate principal stress (also *R* in Lamé-Maxwell analysis) [Pa]

s co-ordinate along a surface, Radial Stress Field analysis [m]

s_1, s_2, s_3 deviatoric stresses, equation 20, also stress trajectories in Lamé-Maxwell analysis, equations 16 and 17 [Pa]

S perimeter [m]

$SE(\bar{d})$ parameter used in equation C1, equal to $\frac{S_d}{\sqrt{n}}$ [-]

S_d standard deviation of wall stress data [-]

$\bar{S}_Z$ dimensionless average vertical stress, equation 8 [-]

soe second order effects [-]

τ shear stress or shear at wall (experimental data and equation 20) [Pa]

τ_W shear stress at wall [Pa]

θ rotational angle [rad]

Θ insert angle, Figure 73 (also hopper half angle in Jenike's analysis, Figure 13, and rat hole angle, Figure 75) [rad]

Θ' angle of Jenike's incremental element, Figure 13 [rad]

t *t* statistic found via equation C1, equal to $\frac{\bar{d}}{SE(\bar{d})}$ [-]

T Material tensile parameter [Pa]

V Point within model geometry [Pa]

δw incremental element thickness [m]

W Point within model geometry [Pa]

x vertical height [m]

δx incremental vertical distance [m]

X vertical coordinate [m]

$\delta\xi$ angle formed by $D_1E_1E_2$, Figure 34 [rad]

y	y-direction distance in equation 19 or distance between walls at point of principal stress arc contact, Figure 32	[m]
δz	incremental horizontal distance	[m]
z	horizontal distance	[m]
Z	horizontal coordinate	[m]
Z_0	horizontal coordinate	[m]

Chapter 1.0 - Introduction

Nedderman (1992) defines granular materials, or ‘bulk solids’, as any material composed of many individual solid particles, irrespective of particle size. Granular materials are used in a wide range of industries, including the medical, food, construction, chemical and manufacturing industries (McGlinchey 2005, Ajax Equipment 2012). To allow processing of materials, storage is required. Containers are often cylindrical, and can range in size from capacities measured in grams to thousands of tonnes (Nedderman 1992). At the base of the silo the container walls will converge to at least one small opening. This hopper section allows the flow of the granular material to be directed to the next stage of the process. Figure 1 shows an example of a silo and hopper in use in industry today.

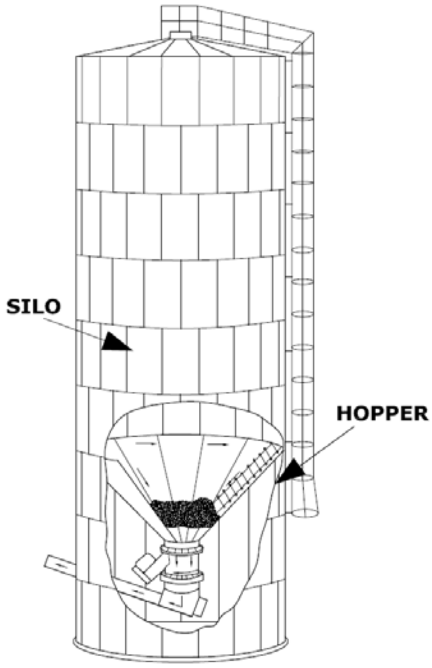

Figure 1. Conical Hopper below a Silo

Various terminologies are used for containers of granular materials. In this research project the section of the container with vertical walls is referred to as the silo and the section of container with sloping walls is referred to as the hopper.

Prior to the principal stress arc method, accurate two- and three-dimensional models were not available with exception of finite and discrete element analysis. A flexible, rigorous model was not available to assist designers of hoppers and silos. The research project improves accuracy in stress analysis in this area by extending the principal stress arc method. More simple previous methods included calculation of vertical stresses only and use of empirically calculated ratios to produce horizontal stresses. Force balance equations have been completed on 'slice' elements (Janssen 1895, Walker 1966, Walters 1973, Enstad 1975, Li 1994). Enstad and Li proposed curved surfaces in their models. First proposed by Matchett in 2004, a key feature of the principal stress arc model was the use of the principal stress direction such that it coincided with arc geometry, allowing calculation without shear stresses. The second key feature of the principal stress arc method is the use of incremental elements, allowing calculation of two- and three-dimensional stress distributions through the granular material, an improvement on previous methods that made use of averaged stresses.

The model published by Matchett in 2004 did not include rotational/azimuthal stresses. Matchett published two further papers (in 2006) including a proposal to calculate azimuthal stresses in silos. The latest version of the principal stress arc method is presented in this thesis with modifications after research into Lamé-Maxwell based equations (Coker et al 1957). The theory for the wedge hopper case, with 'Lamé-Maxwell' modification, was developed by Professor Matchett with assistance from the author during this research project. As part of this project the author extended the method to cover more complex geometries including three-dimensional silos, cones, and cones with conical inserts. Work on azimuthal stress relationships has been extended by the author, with alternative methods of calculation proposed. Extensive comparison to experimental data has been completed. Research carried out for this project has been subsequently published or is in preparation for publication.

The aims of the research project were as follows:

A. To develop algorithms to predict stresses in hoppers and silos using principal stress arc geometry methods.

B. To implement these methods in various hopper configurations including cones, wedges and hoppers with inserts.

C. To compare resultant data with experimental data from the literature.

D. To use the models to develop new methods of design for hopper systems.

The role of the thesis author during this research project:

Use of the principal stress arc method within spreadsheet-based algorithms to produce stress distributions for comparison to experimental data. This work covered the case studies of two-dimensional silos and wedge hoppers during 2005 to 2007.

Input to extension of the principal stress arc method to cover three-dimensional silos and cone hoppers, making use of rotational symmetry. Professor Matchett proposed the geometry for this case; the author of this thesis assisted with solution of force balance equations and produced spreadsheet- and QBasic-based algorithms. These algorithms were used for comparison to experimental data. A paper was co-authored which was included in the ENSTIMAC 2007 conference proceedings.

Research into the Lamé-Maxwell equations. During review of a co-authored paper, it was suggested by a reviewer that Lamé-Maxwell equations should be the subject of research. Subsequently Professor Matchett proposed a modified version of the principal stress arc method. The thesis author had input to the development and solution of the new force balance equations for the following case studies:

i. Two-dimensional silo
ii. Two-dimensional wedge hopper
iii. Three-dimensional silo
iv. Three-dimensional cone hopper

The thesis author developed spreadsheet- and QBasic-based algorithms for these case studies. Work on the two-dimensional wedge hopper case was published in two co-authored papers in 2008 and 2009. The three-dimensional cases allowed further work on azimuthal stress relationships, with comparison to experimental data of the various methods available. Professor Matchett proposed various relationships between principal stresses and the thesis author completed evaluations of these, including systematic validation of results. One relationship provided acceptable correlation to available experimental data. A paper was included in the FAIM 2009 conference proceedings (O'Neill et al 2009) and a further journal publication is in preparation covering this work.

Extension of the new method to cover the case studies of conical inserts and conical rat holes within cone hoppers. The thesis author proposed the geometry for this case, producing and solving force balance equations. The solutions to the force balance equations were used to provide stress distributions within spreadsheet- and QBasic-based algorithms, which were compared to experimental data from the literature.

1.1 Problems encountered prior to and during flow

Problems that can be encountered during storage and operation are shown in Figure 2.

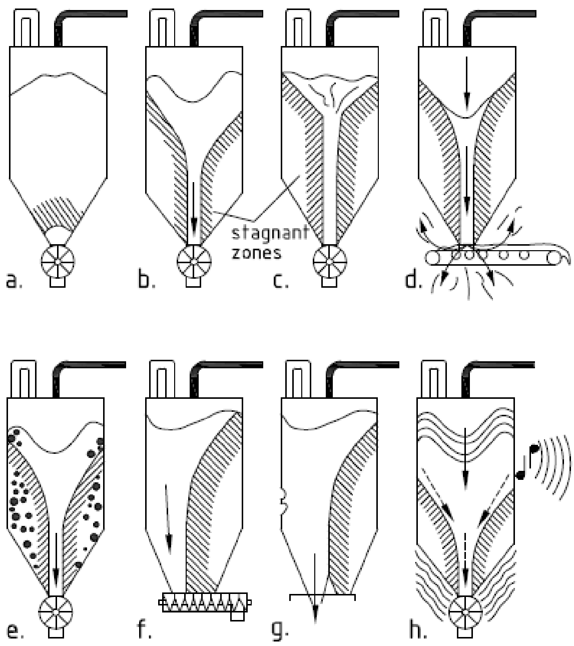

Figure 2. Possible problems with operation of silos and hoppers (Schulze 2008)

a. Arching. This problem can occur in two forms – cohesive arching and mechanical blockage. Cohesive arching occurs only with cohesive materials whereby an arch of material forms above the hopper opening, able to support both its own weight and the weight of material above (Berry 2000). Mechanical blockage occurs when the opening is small relative to particle size (To et al 2002). Mechanical blockage will normally occur when the outlet diameter is less than 6 to 8 times of the largest granular material particle (Marinelli and Carson 2001). Both modes of arching will prevent flow.

b. Funnel flow. This problem typically occurs with shallow hopper wall angles and/or wall materials of high friction (Jenike 1967). The ability of the material to flow along the hopper wall is reduced, allowing material directly above the hopper outlet to exit the hopper before material away from the silo centre-line. Funnel flow is particularly undesirable for industries where materials deteriorate with time, such as within the food industry.
c. Rat-holing. This problem can occur with funnel flow hoppers, where material within the stagnant zones shown in Figure 2 consolidates with time (Matchett 2006a). In extreme cases the centre section of the hopper (and silo) can empty completely, leaving a ‘rat-hole’ through the material remaining within the hopper.
d. Flooding. This problem occurs mainly with funnel flow silos, where easily fluidized granular material does not sufficiently deaerate. The material will then ‘flood’ out of the hopper outlet, acting like a fluid (Geldart and Williams 1985). Flooding is undesirable as control of flow rate is lost, and excess dust is created.
e. Segregation. Depending on particle size, granular materials can be subject to segregation (Johanson 2005). Angles of internal friction can vary within the granular material, producing segregation by angle of repose. Segregation can cause quality problems downstream (Ketterhagen et al 2007).
f. Non-uniform discharge with a screw feeder. This problem can occur with poorly designed hopper and feeder set-ups (Bates 2012). Stagnant zones are formed as the feeder is unable to remove sufficient material from the hopper outlet.
g. Eccentric flow. In addition to non-uniform discharge due to feeder design, eccentric flow can also be caused when multiple hopper outlets are present (Schulze 2008). Each outlet is subject to the problems described above, and

must be designed accordingly. If blockage occurs in one of the outlets, eccentric flow can be produced – creating eccentric loading on the silo structure. In extreme cases silos walls can be damaged (Carson 2000).

h. Vibrations. Silo quaking and/or silo noise can be caused by non-regular flow of material from the hopper outlet (Muite et al 2004).

1.2 Common flow regimes

Many of the problems encountered are caused by poor design of the silo and hopper set-up. This situation may be attributed to a lack of knowledge of stress distributions and flow/failure regimes prevalent within the granular material. If a hopper is designed so that mass flow is achieved, then funnel flow and its associated problems are not present (Schulze 2006a). Jenike (1967) compares funnel flow and mass flow in Figure 3.

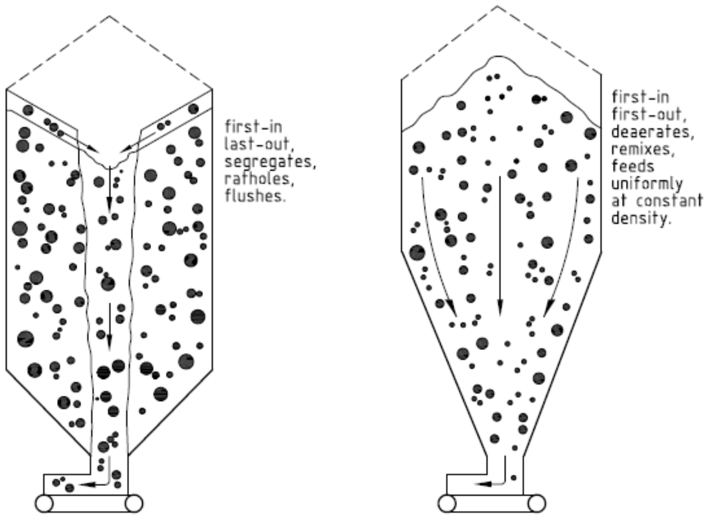

Figure 3. Funnel-flow (left) and mass-flow (right) (Jenike 1967)

Cohesive arching and mechanical blockage can occur during mass flow. These phenomena can be avoided by calculation of a minimum outlet size. The minimum outlet size for mechanical blockage can be estimated from particle diameter, as noted above. The minimum outlet diameter for avoidance of cohesive arching requires knowledge of empirical data, relevant to the granular material and the properties of the hopper (including wall friction data and hopper half-angle). Jenike (1961,1964,1967) has completed a large amount of work on design of hoppers to ensure mass flow, and calculation of critical outlet diameter for cohesive arching.

Jenike's work provided an empirical equation to determine this critical diameter, which has been successfully applied in industry (Jenike 1964, Schulze 2008). There has been suggestion that this equation is conservative, and successful attempts (Matchett 2004) have been made to induce flow in smaller diameters than dictated by Jenike's method.

1.3 Research into stress distributions

Knowledge of stress distributions within these granular materials is not only concerned with ensuring flow of material from hoppers: such knowledge is also required for mechanical design of vessel walls (Ooi et al 1996, Chen et al 1998, Song 2004, Zhao and Teng 2004). A lack of consideration of internal stresses can result in catastrophic failure (Carson 2000).

For a long period of time, stress distributions within granular materials stored in hoppers and silos have been the subject of research (Janssen 1895, Schulze 2008). During this time period of over 100 years, stress distribution research in this field has continually developed (Jenike 1964, Motzkus 1974, Enstad 1975, Matchett 2004, Matchett 2006a,2006b, Schulze 2008). The early mathematical models of Janssen, Jenike and Enstad were one-dimensional where stresses in one direction are calculated by rigorous solution, and other stresses approximated by empirically derived constants. Finite Element and Discrete Element computer simulation methods have become widely available (Cundall and Strack 1979, Li et al 2004, Schimdt and Wu 1989, Kamath and Puri 1999, Tejchman and Klisinski 2001, Wojcik et al 2003, Landry et al 2004). However these methods are still under development (Karlsson et al 1998, Landry et al 2004, Mio et al 2009). The number of particles that a DEM computer program can accurately represent falls short of current industrial requirements (Cleary and Sawley 2002, Li et al 2004, Kruggel-Emden et al 2010).

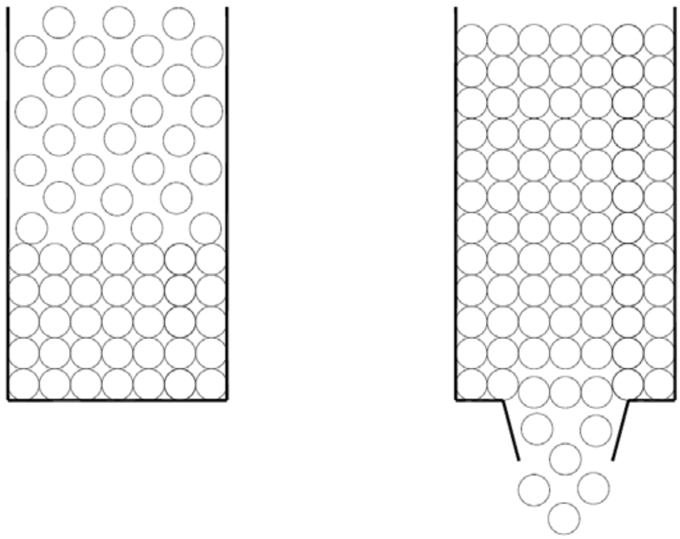

Figure 4. Discrete Element Simulation of silo filling and discharge (Li et al 2004)

It is apparent that problems (including those noted in Chapter 1.1) remain within the field of calculation of stress distributions within granular materials. Problems first documented decades ago remain current issues (Drescher 1995 et al, McGlinchey 2005, McGee 2008). Modern industrial practice imposes complex requirements and boundary conditions during the processing of granular materials.

1.4 Research project contributions

The project analyzed case studies by numerical solution to provide more accurate knowledge of the stress distribution in silos and hoppers. The methodology followed in the project is that a case specific geometry was proposed, from which force balance equations were developed and solved. The proposed equations were used to produce results, which were subject to validation exercises using data available from the literature and previous models. The calculated stress distributions were compared to experimental data.

The analytical equations were derived from the principal stress arc method initially proposed by Matchett (2004). Further improvement in accuracy was achieved by this research project and has subsequently been published. A further paper is planned for publication (O'Neill et al 2013 [in preparation]). The research project has improved early versions of the principal stress arc methods by use of modifications after Lamé-Maxwell equations and extension of the method to cover more complex shapes, including cone hoppers with conical inserts and conical rat holes. One of the primary reasons for selection of this project was the expertise of the research project team at that time.

Validation carried out in Chapters 4, 5 and 6 gave support to the principal stress arc method results. The stress distributions produced were compared to experimental data from the literature with partial success. Chapter 7 provides specific summaries of the case studies and model verification. The wall stress data comparisons completed as part of this research project may be used for structural design of silos and hoppers, allowing shell and insert loading to be more accurately determined. The critical outlet dimensions calculated via the principal stress arc method may also be used to improve current industrial practice. Prior methods have been proved to be conservative through work on this research project. The algorithms proposed allow new methods for design of hoppers systems to be achieved in that recommendations can be made to avoid cohesive arching or excessive stress loading by evaluating stress distributions for a given set of silo and hopper dimensions. If the models indicate excessive stresses or the presence of a cohesive arch is suspected, then the hopper parameters can be altered until more favourable conditions are produced. The alternative to review of stress distributions using the new algorithms (or other theoretical stress analysis methods such as FEA) would be to make of full scale experimental apparatus. This may not be feasible for large or even small scale items when time and cost are considered.

1.5 Research project structure

The structure of the research project follows Teesside University regulations and code of practice.

After the title page abstract, acknowledgements, contents, notation and an introduction to the thesis are provided. Specific information is then introduced, including a review of prior stress analysis methods and the underpinning knowledge necessary to complete the project. Subsequently research work on the six case studies is documented, with principal stress arc geometries, solution of resultant force balance equations and comparison of calculated stress distributions to theoretical and empirical data.

i. Two-dimensional silo
ii. Two-dimensional wedge hopper
iii. Three-dimensional silo
iv. Three-dimensional cone hopper
v. Three-dimensional cone hopper with conical insert
vi. Three-dimensional cone hopper with conical rat hole

Remaining sections of the thesis include project conclusions and recommendations for further work. Supporting appendices include references, derivations, user information for the spreadsheet and QBasic-based algorithms, statistical tests and published works.

Chapter 2.0 - Literature Review

2.1 Introduction

This chapter documents a literature review undertaken into stress distributions within granular material in hoppers and silos. Stress analysis can be completed via either treating the bulk solid as a continuous entity, known as continuum methods, or by consideration of individual particles, known as discrete element methods. The latter method of analysis is limited by computer processing power (Landry et al 2004, Tatemoto et al 2005, Ketterhagen et al 2008, Frenning 2008). Historically continuum methods have constituted the majority of works in this field of knowledge, with studies making use of discrete element simulation recently increasing in number.

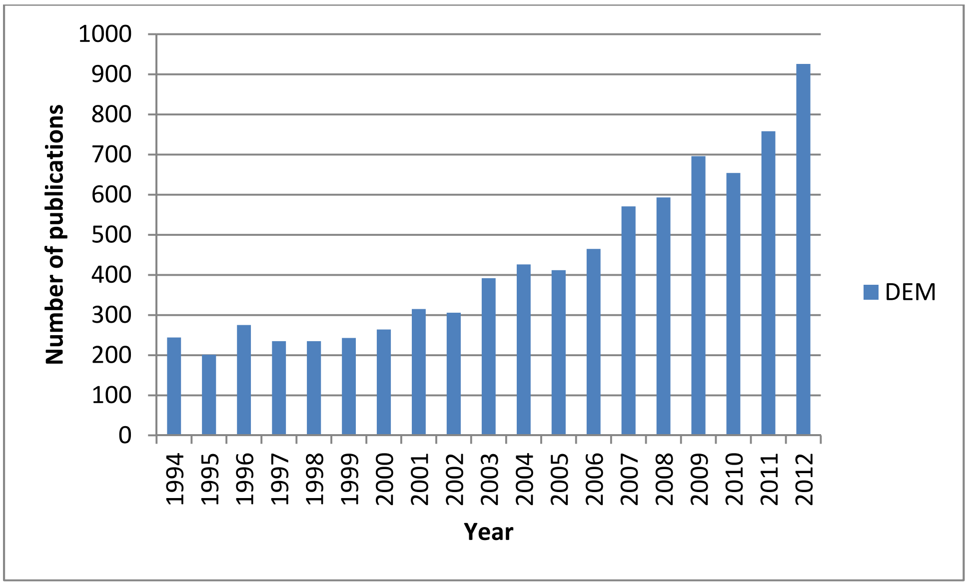

Figure 5. Number of publications related to discrete element simulation

Figure 5 shows a review of a popular online journal article database (Science Direct online database, February 2013), demonstrating the increasing number of publications with the key words ‘discrete element method’.

2.2 Continuum analysis

Continuum methods treat the granular material as a continuous entity. Uniform material properties are usually assumed. Early methods considered a vertical force balance upon a slice element of material within a vertical-sided silo (Janssen 1895, Nedderman 1992). More recent works considered an incremental element within a wedge hopper (Enstad 1975, Li 1994). The principal stress arc method proposed by Matchett (2004) and extended by this research project can be used to describe an incremental element within a three-dimensional silo and hopper shapes.

2.2.1 Method of Differential Slices

Janssen (1895) developed a method to analyze stresses within granular materials contained in parallel-sided vessels, which could be used to consider small elements of material, demonstrating stresses present at defined depths. The analysis is also known as the 'Method of Differential Slices' (Tardos 1999). Janssen considered a horizontal incremental slice element of material in a parallel-sided vessel, demonstrating stresses present at defined depths. Many attempts to improve the method have been made throughout the twentieth century (Walker 1966, Walters 1973, Motzkus 1974, Strusch and Schwedes 1994). These later works extended the theory to hoppers as opposed to parallel-sided vessels only.

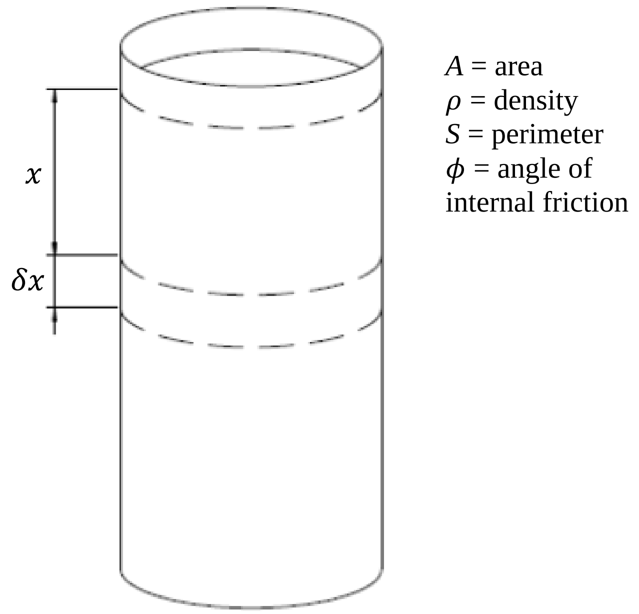

Figure 6. Incremental element in circular silo

In Figure 6, consider forces acting on a small element of width δx at depth x below surface. Forces acting are gravity g, normal contact forces σ_n, shear forces τ at wall and stress on area A, σ_x.

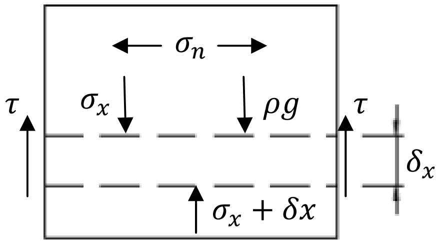

Figure 7. Force balance on incremental element

Force balance on element δx shown in Figure 7:

$$\begin{aligned} &\delta x A - (\sigma_x + \delta x)A - \tau \int \delta x + \rho g A \delta x = 0 \\ &\therefore \delta x - (\sigma_x + \delta x) - \frac{\tau}{A} \int \delta x + \rho g \delta x = 0 \end{aligned} \tag{1}$$

$$\therefore -\frac{d\sigma}{dx} - \frac{S}{A}\tau + \rho g = 0 \tag{2}$$

Assume $\tau = \mu\sigma_n$ (coefficient of friction μ multiplied by normal contact forces). If material is in a state of incipient failure (Rankine 1857, Nedderman 1992):

$$k_A = \frac{1 - \sin\phi}{1 + \sin\phi} \text{ or } k_P = \frac{1 + \sin\phi}{1 - \sin\phi} \tag{3}$$

The choice of k-value in equation 3 is dependent on the stress state within the material, k_A and k_P represent the ratio of horizontal and vertical stresses. If the vertical stress is the major principal stress then the material can be assumed to be in the 'active' case, or if the vertical stress is the minor principal stress then the material can be assumed to be in the 'passive' case (Rankine 1857, Nedderman 1992). Passive and active stress cases are explained in Chapter 3.2.2. For the active case k can be denoted as k_A, and for the passive case k_P. Ooi et al (1996) give discussion on the choice of k-values in the literature. It should be highlighted at this point that the assumptions in this method include those of horizontal and vertical stresses being principal stresses. There is evidence to suggest that this assumption is incorrect (Nedderman 1992, Matchett 2007).

$$\sigma = \frac{\rho g}{\beta}\left(1 - e^{-\beta x}\right) \tag{4}$$

Equation 4 above is the solution to Janssen's analysis (Janssen 1895, Walker 1966, Walters 1973, Nedderman 1992) for surface stress σ; full derivation can be found in Appendix Two. The solution can be used to prove that applying a load to the top surface of the granular material does not promote flow at large depths x. Shown in Appendix Two, Chapter 9.1.1, the equation can be modified to allow for a surcharge Q.

$$\sigma = \frac{\rho g}{\beta}\left(1 - e^{-\beta x}\right) + Qe^{-\beta x} \tag{5}$$

The new solution, equation 5, is represented graphically in Figure 8. Differing rates of exponential growth for surface stress σ are demonstrated, as depth x increases.

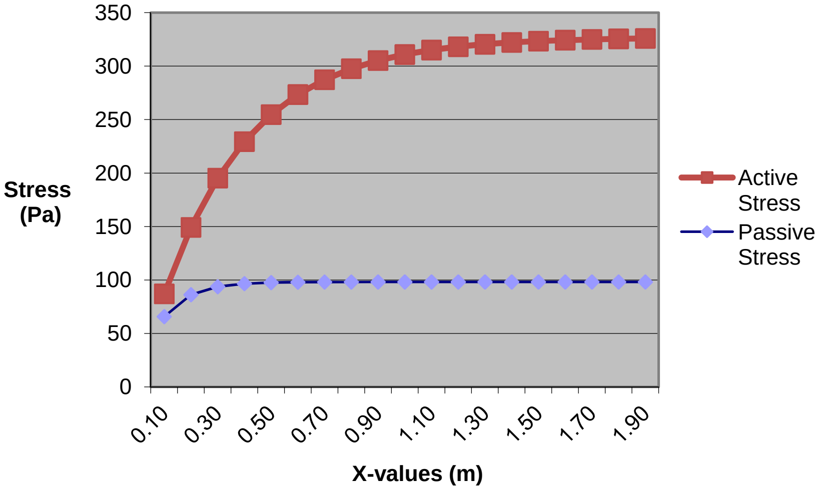

Figure 8. Janssen equation

The theory as it is shown above is only suitable for parallel-sided vessels and does not account for occurrences that can cause stress irregularities, such as switch stresses, imperfections and eccentric flow (Schulze 2006b). However Janssen's method provides a standard equation to which other methods can be compared. The method is used within industrial design standards, including British Standard EN 1991-4:2006, with empirically derived correction factors (Ooi et al 1996). BS EN 1991-4 contains a 'modification coefficient for lateral pressure ratio' a_K. A typical value is 1.5, unless this dimensionless coefficient can be reduced by testing.

As described above Janssen's method has been expanded upon by various authors (Schulze 2006b), notable works include those which extended the theory to hoppers as opposed to parallel-sided vessels only (Walker 1966, Walters 1973). Figure 9 shows a force balance on a slice element such as could be found within a hopper (Walters 1973).

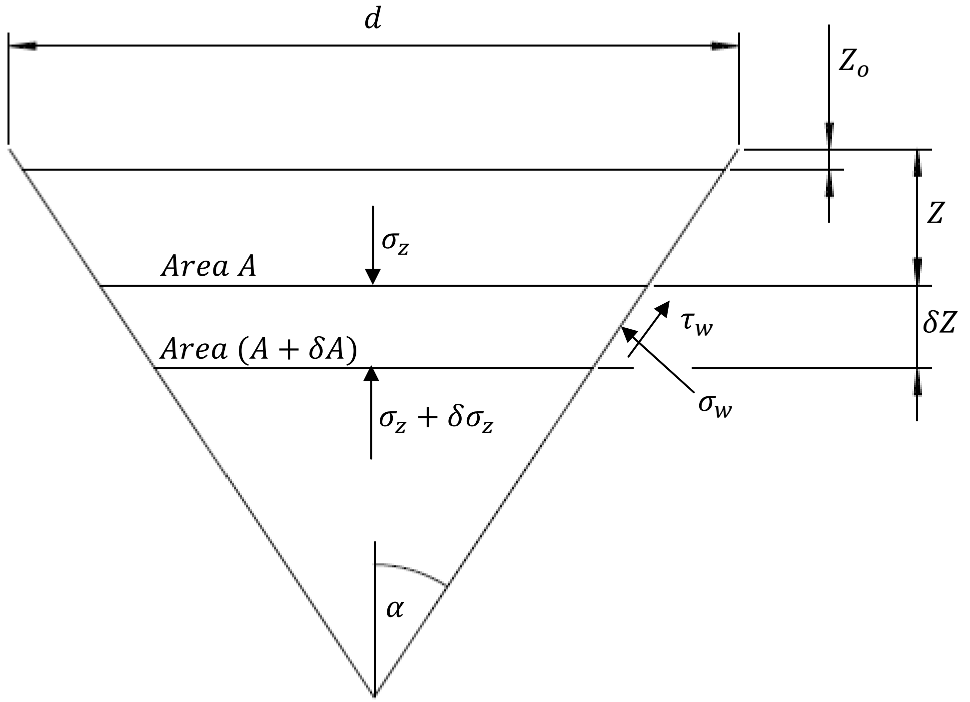

Figure 9. Walters' force balance

Equation 6 is the result of a vertical force balance on the horizontal element in Figure 9 with upwards direction taken as positive. Forces acting are gravity g, wall stress σ_w, wall shear stress τ_w and stress on area A, σ_z.

$$\frac{\delta\sigma_z}{\delta z} + \frac{1}{A}\frac{\delta A}{\delta z}\sigma_z + \frac{P}{A}\left(\tau_w + \sigma_w \tan\alpha\right) = \rho g \tag{6}$$

A full derivation is shown in Appendix Two. A similar method of force balance is used in this research project, although the method in the project includes use of circular arc geometry and more than one dimension is considered. In the method above it can be seen that vertical stress value is averaged over the horizontal slice. To relate vertical stresses to horizontal or wall stresses Walters used factor *D*, which was equivalent to Janssen's use of a *K*-value. The *D* factor is a function of ϕ and ϕ_w, determined by empirical means. Design standard DIN 1055-6:2005-03 previously used a *K*-value with a 1.2 safety factor to produce more conservative wall loading assumptions (Schulze 2008).

Walters (1973) gives a derivation of mean vertical stress $\bar{\sigma}_z$, using the force balance equation 6.

$$\frac{d\bar{\sigma}_z}{dz}+\frac{4\bar{\sigma}_z}{d-2z\tan\alpha}\left[ED+\tan\alpha(D-1)\right]=\rho g \tag{7}$$

This differential equation (7) is solved by integration between the limits of averaged vertical stress $\bar{S}_{z,0}$ at $Z=Z_0$ and $\bar{S}_z$ at Z. An extract from Walters' (1973) paper is given in Appendix Two, Chapter 9.1.2.

$$\bar{S}_Z=\frac{(1-2Z\tan\alpha)}{2\tan\alpha(K-1)}\left[1-\left(\frac{1-2Z\tan\alpha}{1-2Z_0\tan\alpha}\right)^{K-1}\right]+\bar{S}_{Z,0}\left(\frac{1-2Z\tan\alpha}{1-2Z_0\tan\alpha}\right)^{K} \tag{8}$$

Figure A.2 in Appendix Two, Chapter 9.1.2, shows a graph of mean vertical stress against depth for various values of variable *K*. Some differences from Janssen's method shown in Figure 8 are apparent, although for shallow depths a similar exponential increase is traced.

Strusch and Schwedes (1994) used a method proposed by Motzkus (1974) to predict stress distributions within a silo with an insert, during filling. The method was developed from that proposed by Janssen, Walters and subsequently Walker, and was employed by Strusch and Schwedes to calculate insert loads using a non-symmetrical incremental slice element as shown in Figure 10. Results were compared to experimental data with partial success.

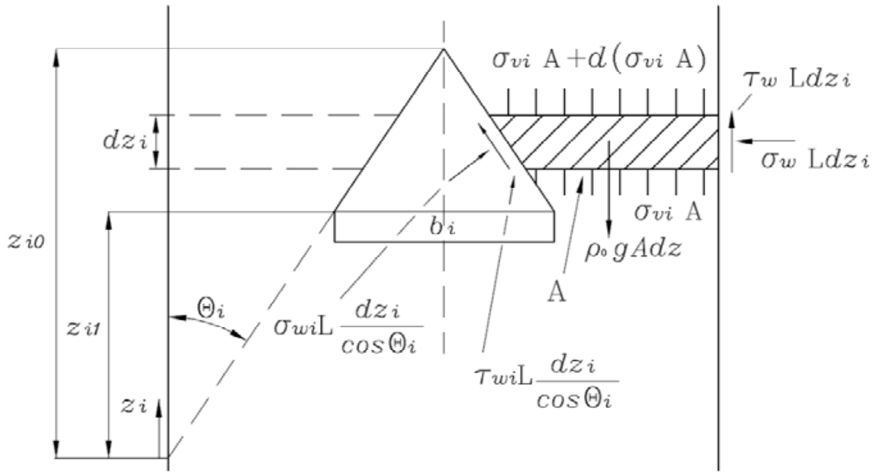

Figure 10. A non-symmetrical slice element constructed using Motzkus' method (Strusch and Schwedes 1994)

All of the incremental horizontal slice methods above make the assumption of horizontal and vertical principal stresses, and calculate vertical stresses only. Horizontal stresses are produced by a relationship to vertical values.

2.2.2 Method of Characteristics

Sokolovskii (1965) and Nedderman (1992) describe use of the Method of Characteristics or 'slip-line method' to solve partial differential equations. The method is typically applied to soil mechanics case studies. For example in Figure 11 a characteristic mesh is shown, depicting 'slip-lines' of soil foundations. The text goes on to determine the maximum stress state prior to loss of equilibrium and therefore failure of the foundations. The assumption of Mohr-Coulomb failure mode or other methods can be used with the Method of Characteristics.

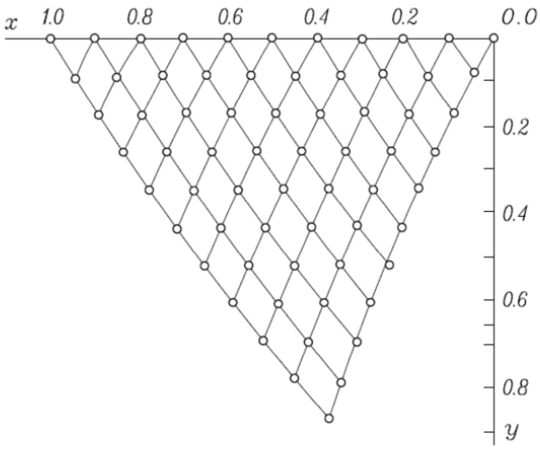

Figure 11. Network of characteristics (slip-lines) for the coordinates of nodal points (Sokolovskii 1965)

This technique is presented by Sokolovskii as a method suitable for solution of equations derived for an ideal Coulomb material. An ideal Coulomb material is a granular material whereby its yield locus follows a linear path with a rigid-plastic failure mode (Nedderman 1992). A Mohr-Coulomb criterion is employed in the principal stress arc method as a boundary condition relationship between principal stresses (Coulomb 1776, Mohr 1906, Nedderman 1992, Venkatramaiah 2006).

2.2.3 Radial stress field method

According to Jenike (1961,1964), during hopper emptying (passive stress state) the vertical stresses present within a bulk solid are approximately proportional to the distance from hopper apex – i.e. proportional to the diameter of the hopper at any one point; this relationship is assumed to be linear and is termed the Radial Stress Field, used by Jenike (1961).

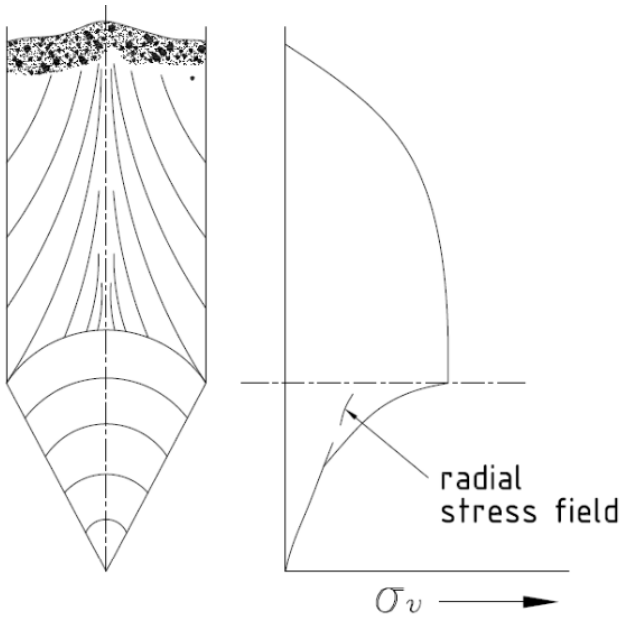

Figure 12. Radial stress field (Schulze 2006b)

Figure 12 shows major principal stress distribution after discharge of a small amount of material. The stress values follow a linear path within the hopper, up to a point some way below the transition between silo and hopper. Pitman (1986) proposed that the Radial Stress Field is valid only close to the hopper outlet. The stress values tend towards zero at the theoretical hopper apex.

This method of hopper design is based on the simple fact that a sufficiently large opening must be present in the hopper to allow flow, and also the observation that the flowing material continually forms and breaks arches above the opening. Tardos (1999) describes Jenike's method as reducing hopper design to the calculation of the minimum outlet dimension.

According to Berry et al (2000), Jenike's method is based on three key elements:

- Experimental data concerning bulk solid failure characteristics.
- Stress distribution analysis during mass flow of bulk solid, using radial stress field method.
- Critical arch failure model, an arch element which is free from the stresses transmitted from bulk solids above.

In his work Jenike assumed a circular arch. Berry goes on to experimentally determine arch shape – uneven surfaces were measured, although the averaged shape was approximately circular.

According to Schulze (2008), Jenike noted that the critical properties of bulk solids include bulk density, angle of internal friction ϕ, unconfined yield stress σ_c and angle of wall friction ϕ_w. Angle of wall friction is an important property for determination of mass flow, and unconfined yield stress is similarly important in calculation of critical outlet width. Using these critical properties, Jenike carried out force balances on an infinitesimal element in a bulk solid within a hopper, resulting in partial differential equations 9 and 10 (Nedderman 1992). The ratio between principal stresses was fixed by the angle of internal friction, or by the yield locus during flow.

$$\begin{aligned}&\left(1+\sin\phi\cos 2\psi^{*}\right)q+\sin\phi\cos 2\psi^{*}\frac{dq}{d\theta}+2q\sin\phi\cos 2\psi^{*}\frac{d\psi^{*}}{d\theta}\\&+q\sin\phi\left(3\cos 2\psi^{*}-\kappa+\sin 2\psi^{*}\cot\theta\right)+\cos\theta=0\end{aligned} \tag{9}$$

$$\begin{aligned}&q\sin\phi\cos 2\psi^{*}+\left(1-\sin\phi\cos 2\psi^{*}\right)\frac{dp}{d\theta}+2q\sin\phi\sin 2\psi^{*}\frac{d\psi^{*}}{d\theta}\\&+q\sin\phi\left(3\sin 2\psi^{*}-\cos\psi^{*}\cot\theta-\kappa\cot\theta\right)+\sin\theta=0\end{aligned} \tag{10}$$

where ψ^* is the angle from the *r*-direction in polar coordinates to the major principal stress direction, *q*, *p* and κ are parameters used in the Radial Stress field method.

Jenike assumed that the major principal stress in the lower section of the hopper was proportional to the distance *r* from the theoretical hopper apex – Figure 13.

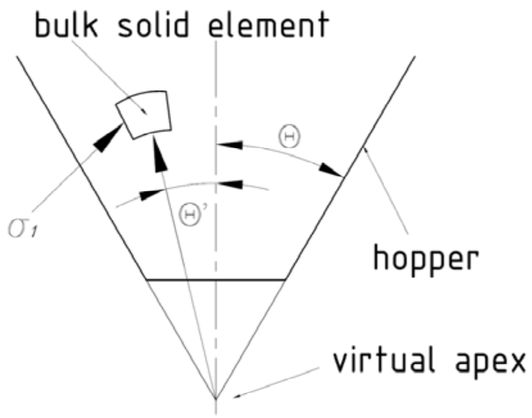

Figure 13. Polar coordinates in a hopper (Schulze 2008)

From equations 9 and 10, and Figure 13, $\sigma_1 = rg\rho_b s(\Theta', \Theta, \phi_x, \phi_e)(1+\sin\phi_e)$. Angle Θ' and radius *r* determine the position of the infinitesimal element in a polar coordinate system; Θ is the hopper half-angle; ϕ_x and ϕ_x are equivalent angles of friction; *s* is a co-ordinate along a surface. Solutions to the differential equations exist only for specific parameters (i.e. for mass flow only). Due to their complex nature solutions were presented in graphical form, although modifications were made by Jenike, based on practical experience.

In the Radial Stress Field method it is assumed that the major principal stress σ_1 acts as a consolidation stress, dictating bulk density ρ_b and unconfined yield stress σ_c. These are different for each consolidation stress. A cohesive arch is assumed to exist when σ_c is greater than σ_1' bearing stress. The relationship between consolidation stress and yield stress is known as the Flow Function *f* of the material (i.e. the normal stress at which the unconfined, consolidated material yields – Tardos 1999).

Stress in the hopper can be considered to determine critical outlet diameter for arching. For each major principal stress (i.e. consolidation stress), the unconfined yield stress can be measured. In Jenike’s work, this relationship is known the flow function. Figure 14 shows typical flow function curves.

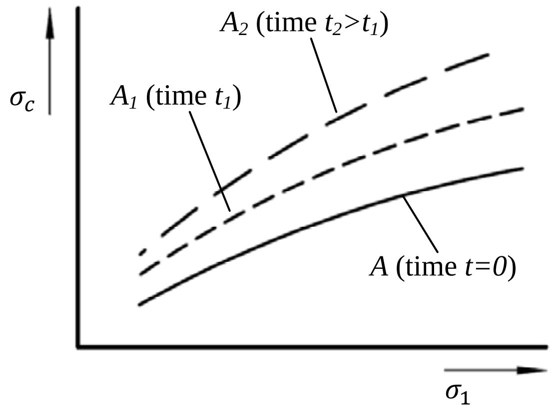

Figure 14. Flow function and time flow functions for two different storage times t_1 and $t_2 < t_1$ (Schulze 2006b)

If a cohesive arch is formed in the hopper, a force is transferred to the walls. This effect is represented by the stress required to support a stable arch (σ_1').

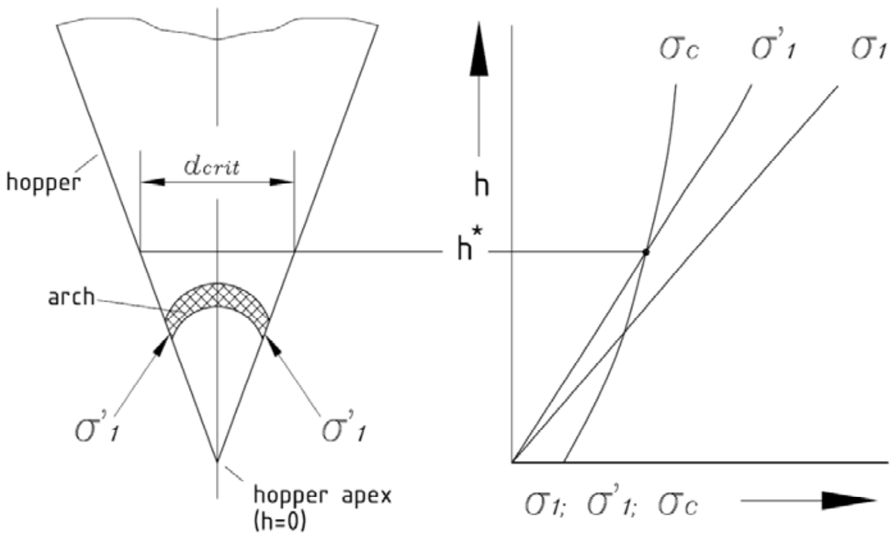

Figure 15. Stress conditions in the hopper, emptying (Schulze 2006a)

Jenike calculated σ_1' by assuming the arch had a smooth shape with a constant thickness in the vertical direction, and that the arch must carry its own weight. It should be noted that load from granular materials above is neglected. Figure 15 shows a stable arch and associated stress conditions in the hopper.

From Figures 13 and 15,

$$\sigma_1' = \frac{2r\sin\Theta g\rho_b}{1+m} \tag{11}$$

Parameter *m* describes hopper shape (*m* = 0 wedge shaped, *m* = 1 conical). Local hopper diameter, or local width for wedge shaped hoppers, is represented by $2r\sin\Theta$. Coordinate *r* measures the distance from the hopper apex to the support of the arch (i.e. true length along the hopper wall).

A stable arch occurs when σ_c is greater than σ_1'. The arch will only fail when the bearing stress is greater than the yield stress. From this the critical outlet diameter can be determined, by rearranging equation 11 (Schulze 2008):

For wedge hoppers $$b_{crit} = \frac{\sigma_{c,crit}}{g\rho_{b,crit}} \tag{12}$$

For conical hoppers $$d_{crit} = \frac{2\sigma_{c,crit}}{g\rho_{b,crit}} \tag{13}$$

An iterative process would be required to find correct values. Enstad (1975) and Matchett (2004) demonstrate that the above method produces conservative results. As pointed out by Jenike (Enstad 1975, Jenike 1987) and Kruyt (1993), Jenike's method does not take account of the weight of granular material above the cohesive arch.

Schulze goes on to note that the equations discussed above are valid during emptying of the bulk solid. Calculations are not valid for filling of an empty silo without discharge. Stress during filling can be higher than during discharge. Jenike's work has become a popular method of silo design throughout the world – no failures have been reported (Berry et al 2000), although this is thought to be due to conservative prediction of outlet dimensions (Drescher et al 1995, Matchett 2004, McCue and Hill 2005). As noted above, stress values predicted by this method are inaccurate near the transition between silo and hopper (Moreea and Nedderman 1996). Moreea and Nedderman go on to question the validity of the radial stress field method for all applications.

2.2.4 Principal stress arc method

Use of the stress analysis methods described above have challenges in their application: the axes in the differential slice method do not coincide with the directions of principal stress, which are not known. In the radial stress field theory, the orientation of principal stresses is a variable within the model – leading to great complexities. Enstad (1975) published a novel theory on stress analysis within hoppers, one important aspect of this work was the assumption that a principal stress direction followed a surface comprising a circular arc, whereas previously vertical stresses were assumed to be constant across any horizontal cross-section (Walker 1966, Nedderman 1992). Benefits of this assumption include the fact that Mohr's circle (Mohr 1906) is not required to determine stresses as stress orientation is known and therefore fixed, additionally equations are simplified as work with shear stresses does not need to be included. In Appendix Two, Chapter 9.1.3, an extract from Enstad's (1975) paper is included. Figures 16a and 16b show the geometry in this method.

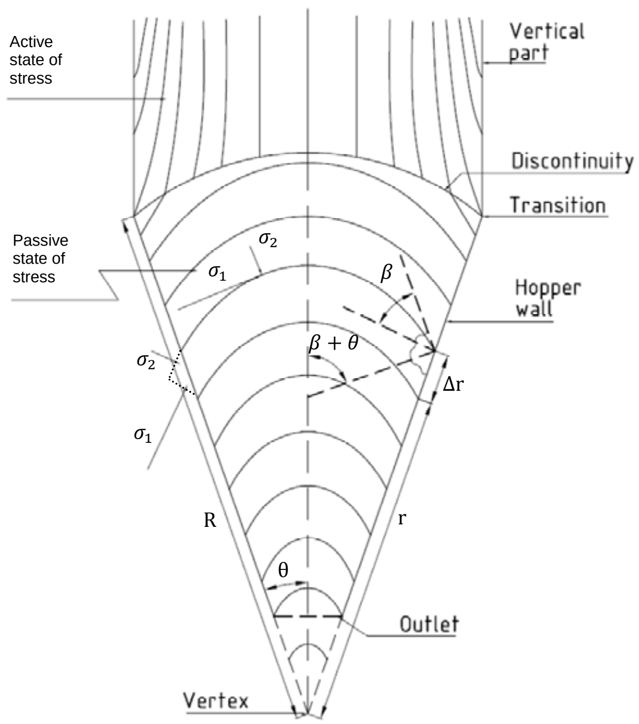

Figure 16a. Cross-section through a wedge shaped hopper with assumed directions of major principal stress (Enstad 1975)

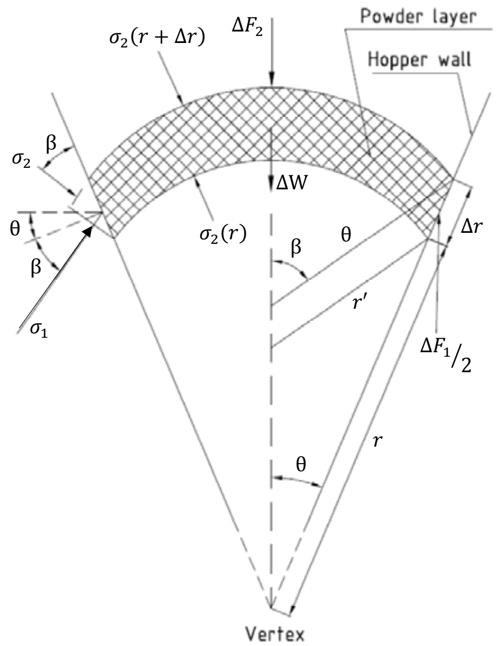

Figure 16b. Cross-section of the hopper with a powder layer (Enstad 1975)

A force balance is completed on the incremental arch and the following differential equation is produced.

$$r\frac{d\sigma}{dr} - X\sigma = -\gamma Yr \tag{14}$$

where r is the distance from the vertex along the hopper wall, σ is the mean stress, γ is density, X and Y are functions of frictional angles, hopper half angle and angle β between wall normal and the principal stress arc.

Equation 14 can be solved to give the solution below, equation 15.

$$\sigma(r) = \frac{\gamma Yr}{X-1} + \left(\sigma(R) - \frac{\gamma YR}{X-1}\right)\left(\frac{r}{R}\right)^X \tag{15}$$

where R is the distance from the vertex along the hopper wall to the transition.

As shown in Appendix Two, Chapter 9.1.3, in his paper Enstad takes account of the weight of the incremental arch, the interaction of the powder above and below the arch, and the reaction from the walls. Figure 17 demonstrates example results plotted from this equation. Enstad assumed a constant minor principal stress along the edge of the incremental slice. This has been demonstrated by Nedderman (1992) to be incorrect.

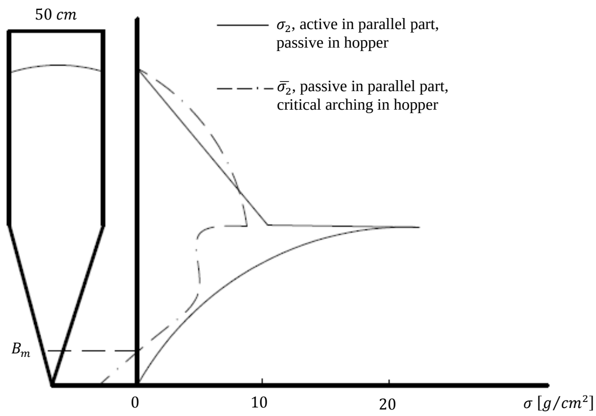

Figure 17. Minor principal stress during flow of a test powder (Enstad 1975)

After Enstad, Li (1994) used principal stress arc methods to model a curved slice element within a standpipe. Li's method made use of averaged minor principal stresses. Li's model is demonstrated in Figures 18a and 18b.

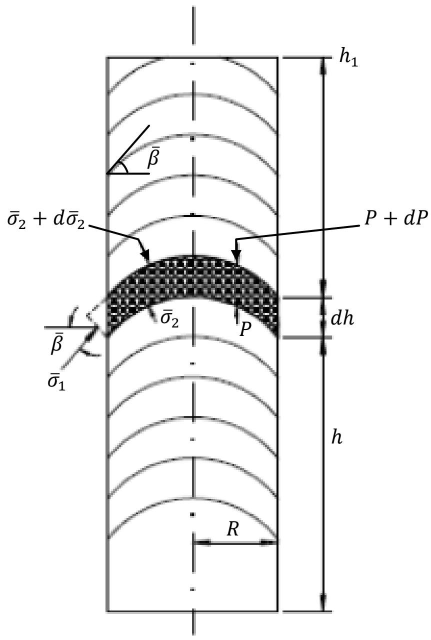

Figure 18a. Cross-section through a vertical wall tube with arched powder layers (Li 1994)

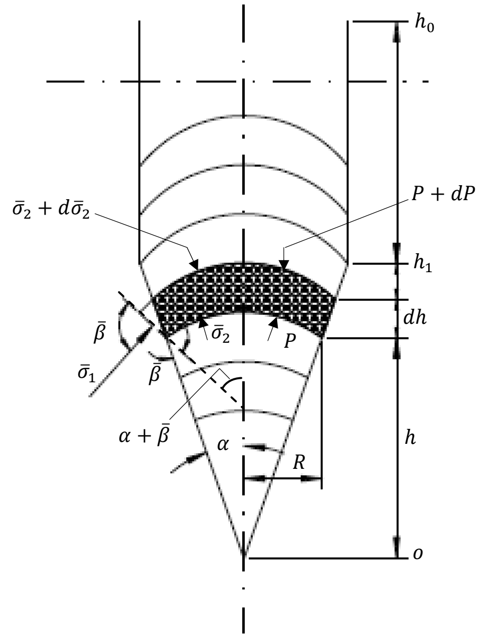

Figure 18b. Cross-section through a slanting wall tube with arched powder layers (Li 1994)

Matchett (2004) proposed a two-dimensional version of the principal stress arc method for the conical hopper case. The geometry proposed by Matchett can be considered to be an approximation of that shown in Figure 33, Chapter 4.1. The geometry of the method is similar to that proposed within this research project, including successive circular arc sections of constant radii making angle β with the wall normal and angle β being maintained by wall friction. In the 2004 proposal a vertical force balance was completed on an incremental arch considering radial stress acting in a direction normal to the principal stress arc and hoop stress acting tangentially. Matchett demonstrated theoretically that the application of vibration to conical hoppers can be used to induce flow under less conservative cases than previous analytical methods had suggested. This proposal has been proved by comparison to experimental data (Matsusaka et al 1995,1996 and Matchett et al 2000,2001) – indicating methods employed in current industrial practice may be conservative.

The geometry of the method proposed in 2004 was subsequently used by Matchett (2006a,2006b) to represent rotationally symmetric three-dimensional systems – silos with parallel-sided rat holes. Again the geometry proposed by Matchett can be considered to be an approximation of that shown in Figure 47, Chapter 5.1. Vertical and horizontal force balance equations were completed on an incremental annulus. Three stresses were now considered: radial stress acting in a direction normal to the principal stress arc, arc stress acting tangentially to the arc, and azimuthal stress acting in the direction normal to the page (see Figure 48). As with the model proposed in this research project Matchett considered three stresses in two differential equations; therefore a relationship was proposed for the third principal stress (Matchett 2006b). This relationship, equation 66, is used in Chapter 5.6.1 with the research project model where calculated results are compared to experimental data. In the second paper Matchett (2006b) explored the effect of variable and fixed incremental arc widths.

The work of Enstad (1975), Li (1994) and Matchett (2004,2006a,2006b) demonstrate that the principal stress arc method can tackle complex geometries with multiple boundaries. From the literature it is apparent that the potential exists to expand the method to cover more complex systems in two-dimensions, rotated three-dimensions and true three-dimensions; i.e. more complex hoppers shapes. However, even with this method of stress analysis, challenges are encountered – Matchett (2006b) discusses geometrical difficulties including incremental element dimensions. The current research project seeks to address these challenges by extending the principal stress arc method.

2.2.5 Finite element method

In recent times computer simulation is becoming commonly used in hopper design (Li et al 2004, Kruggel-Emden et al 2008) via the finite element and the discrete/distinct element methods. According to Kamath and Puri (1999), finite element methods have been used to model stress distributions for a considerable length of time – Haussler and Eibl (1984) are thought to be first to apply the method to granular materials. Since this time the finite element method has been developed by various authors; including Schmidt and Wu (1989), Karlsson et al (1998), Tejchman and Klisinski (2001), Wojcik et al (2003), Zhao and Teng (2004) and Goodey et al (2006).

Prior to the work of Kamath and Puri (1999), modelling using finite elements had been restricted to cohesionless materials. Their paper dealt with cohesive materials, and FEM results compared favourably with experimental tests. This work indicates that, although advanced, FEM is still under development – Karlsson et al (1998) note that for simplicity assumptions are made. As with other methods, the alternative is measurement of all parameters to validate FEM models. Langston et al (1995) comment as follows on ‘continuum’ and/or finite element methods;

> “Most of the bulk properties are assumed to be constant across the system and independent of particle properties such as shape, size and friction with the velocity and stress distributions within the flowing bulk being assumed to follow a certain functional form.”

FEM models require complex continuum properties to accurately replicate reality effectively – elastic movement at mesh nodes points are not sufficient, damping coefficients are also necessary (Kamath and Puri 1999). For the elastic and damping properties to be accurate then the models should be fully validated using stress distribution data within granular materials as opposed to at the vessel walls. This data is not available in sufficient quantity to verify Finite Element methods or other models (Malone and Xu 2008). These comments can be applied to the research project models.

A review of research articles utilising finite element methods for stress distributions within granular materials indicated that simple models use plane (two-dimensional) silos and hoppers (Karlsson et al 1998, Kamath and Puri 1999, Martinez et al 2002, Wojcik and Tejchman 2009, Yunming et al 2011). More complex publications make use of three-dimensional shell models to replicate stresses in the silo/hopper walls (Vidal et al 2008, Juan et al 2006, Zhao and Teng 2004, Sadowski and Rotter 2011, Gallego et al 2011). With these three-dimensional models the granular material is typically not represented by a dedicated FE mesh, instead wall loads are provided by other methods and applied to the shell mesh as boundary conditions. These other methods can include stresses calculated by methods based on Janssen’s equation (Juan et al 2006) and/or the assumption of a Coulomb material (Vidal et al 2008). An exception to this method is work by Goodey et al (2006), where the granular material was modelled by a mesh of 875 elements in a square section silo and pyramidal hopper. Wojcik and Tejchman (2008) and Ding et al (2008) modelled three-dimensional cone hoppers using two-dimensional FE meshes, by making use of axial symmetry. In Chapter 5 the FEA data provided by Wojcik and Tejchman and Ding et al was used to verify model results.

2.3 Discrete element method

The discrete element method or DEM is now used widely as increased computational power becomes available (Li et al 2004). This method uses individual particles as separate entities in the model (Langston et al 1995). Cleary and Sawley (2002) note that;

> "In the simulation of granular flows using the discrete element method (DEM) the trajectories, spins and orientations of all the particles are calculated, and their interaction with other particles and their environments are modelled."

DEM was first applied to granular materials by Cundall and Strack (1979), and is becoming increasingly popular as computational power increases; authors include Langston et al (1995, 2004), Cleary and Sawley (2002), To et al (2002), Landry et al (2004) and Li et al (2004). Li et al (2004) comment that most DEM applications consider spherical elements or, for two dimensions, discs. The paper goes on to demonstrate the use of non-spherical elements with DEM, with a point of interest in this work being the fact that element numbers are required to be limited to 200 to allow simulation time to be kept below five hours (on a PC).

Langston et al (2004) state that the main advantage of discrete element methods is that highly complex systems can be modelled without oversimplifying assumptions. However in the defence of other methods, Cleary and Sawley (2002) indicate that at the time of writing discrete element methods did not account for, among other things, cohesive materials and the effect of particle shape. In their paper concerning such matters, they note that for two-dimensional DEM substitution of circular particles do not suitably represent granular materials in reality, as they have a low shear and frictional resistance; this causes premature yielding via a rolling failure mode. In turn the premature failure will cause over-estimation of flow rates as real granular material flow is not imitated – the DEM model will show an "excessively fluid-like mass flow in the hopper". Goda and Ebert (2005) modelled three-dimensional square-sectioned silos and hoppers, with 40,000 cohesionless spherical particles of 6 mm diameter. Wu et al (2009) modelled a two-dimensional parallel-sided silo and wedge hopper with 4000 spherical particles, taking account of friction, damping and contact spring forces. The model (Wu et al) did not account for rolling resistance. Kruggel-Emden et al (2007) estimate that industrial silos may contain 10^9 particles per cubic meter for fine grained applications.

It can be seen that although the discrete element method is obviously a powerful and useful tool, it is not without limitations – progress is being made but limited by factors such as data input time and computational requirements. Zhu et al (2007,2008) offer an overview of the discrete element method development and propose areas for research to allow the method to be utilised in industry.

Recent developments in DEM are documented by Kruggel-Emden et al (2007,2008,2010) and Ketterhagen et al (2007,2008). Modelling of granular materials by discrete element method is advancing however can be seen to be limited by the inherent assumptions in the model. Particle size and shape is a key assumption within discrete element methods (Kruggel-Emden et al 2010). To accurately model particle shape increases computational time drastically, while oversimplification of the model can adversely affect results (Mio et al 2009).

A second key assumption within this method is particle interactions. Kruggel-Emden et al (2007) and Bierwisch et al (2009) introduced an assumption of a rolling resistance into their models of spherical particles, to avoid fluid-like behaviour. Snider (2007) proposes an alternative to 'spring-damper' particle interaction – Snider models collision forces using a computational particle fluid dynamic method. Results are compared to the available experimental data with favourable results. Anand et al (2009) and Ai et al (2011) offer insight into the particle interactions that should be present within a DEM model: contact spring and damping forces in normal and tangential directions, with more recent models incorporating rolling frictional torque and liquid 'bridges' between particles.

2.4 Experimental data collection and use

In the field of bulk solids handling collection of experimental data is required to allow quantitative and qualitative measurement of interesting physical phenomena, and to allow validation and calibration of mathematical models. It is very challenging to obtain meaningful experimental data for the granular materials involved. Khanam and Nanda (2004) list the variables relating to bulk solid characterization as: particle size, fines, unit surface, particle shape, angularity, hardness, roughness factor, actual density, bulk density, porosity, air permeability through the powder, electrostatic charge, humidity and cohesion factors. Smewing (2002) notes the following additions: size distribution, surface texture, particle interaction, stiffness, thermal properties, compression properties, vibration, container surface, container shape, outlet diameter and storage time. Assuming that a sample of the material in its correct state is available, data can be obtained through use of shear cells/boxes, tri-axial testers, (Puri and Ladipo 1997), automated tap density analysers (Abdullah and Geldart 1999), angle-of-repose or AOR testers (Geldart et al 2006), cohesion testers (Orband and Geldart 1997) and powder rheometers as shown in Figure 19 below.

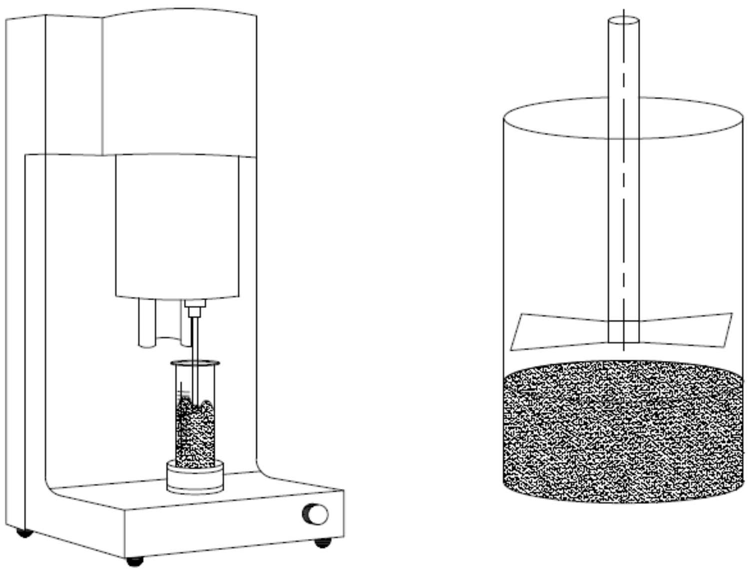

Figure 19. Powder rheometer (Freeman 2010)

Methods are available whereby tests can be conducted in-situ by use of tagged location devices placed within the material (Rotter et al 2005); the position with respect to time of these devices can be monitored, and this information can be used to form a picture of velocity distribution through the silo. However in this application (Rotter et al 2005) a purpose built test silo was used – in industrial applications the method may prove unsuitable for reasons of recovery of tagged devices for subsequent tests. Another method that may lend itself to gathering data ‘in-situ’ is use of x-ray technology to view velocity distributions (Nedderman 1992), although safety and cost considerations would obviously count against this method.

A large number of test silos have been built, however exact conditions are difficult to imitate. Test silos are usually much smaller than plant used in industry, and full scale testing with exactly matched conditions and materials is uncommon due to the time and expense required. It is apparent that the use of theoretical methods would be preferred to empirical ones, while experimentation is necessary to verify data. Schulze and Schwedes (1994) used a test silo to effectively compare various analytical methods to data obtained empirically for vertical and normal stresses during filling/before discharging in hoppers. They found that a reasonable degree of accuracy could be obtained using popular slice element methods. Accuracy could be increased with manipulation of various factors within the calculations to better suit prevailing conditions. However it was commented that these methods, including Walters (1973) and Motzkus (1974), did not take into account various conditions affecting the material. Factors such as compressibility and deformation of the bulk solid were not considered. Hence Schulze and Swedes suggested a new method to take account of such factors, and its use compared to the experimental data obtained. Many other works have been completed in the area of improving past methods, with differing levels of success apparent due to the wide range of materials and conditions that can occur in this discipline.

The experimental data obtained can be used in the design of hoppers and silos; one of the mechanical or ‘flow’ properties of primary importance is the bulk strength of the granular material. In order to reliably achieve flow, stresses within the material must reach yield. Schulze (2006a) discusses a method of obtaining a granular materials yield locus – the method used was the uniaxial compression test.

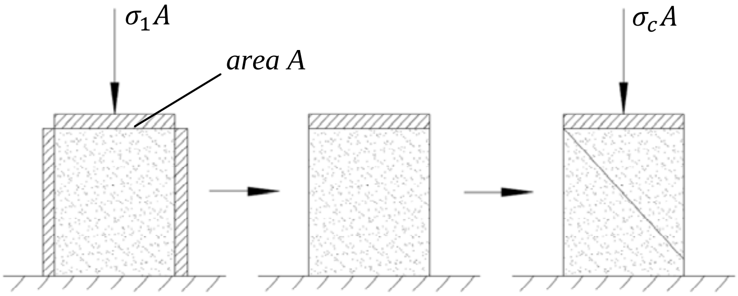

Figure 20. Uniaxial compression test (Schulze 2006a)

Figure 20 shows a hollow cylinder of cross-section A, filled with a cohesive granular material. A load is applied to the sample via stress σ_1, compressing and compacting the sample. The load and cylinder walls are then removed, leaving the granular material in the shape of the cylinder. The sample can now be loaded with increasing vertical stress – which eventually reaches the unconfined yield stress σ_C of the material, and it will yield.

Schulze (2006a) goes on to represent the uniaxial compression test on a σ, τ diagram in Figure 21. Shear stress τ is shown on the vertical axis.

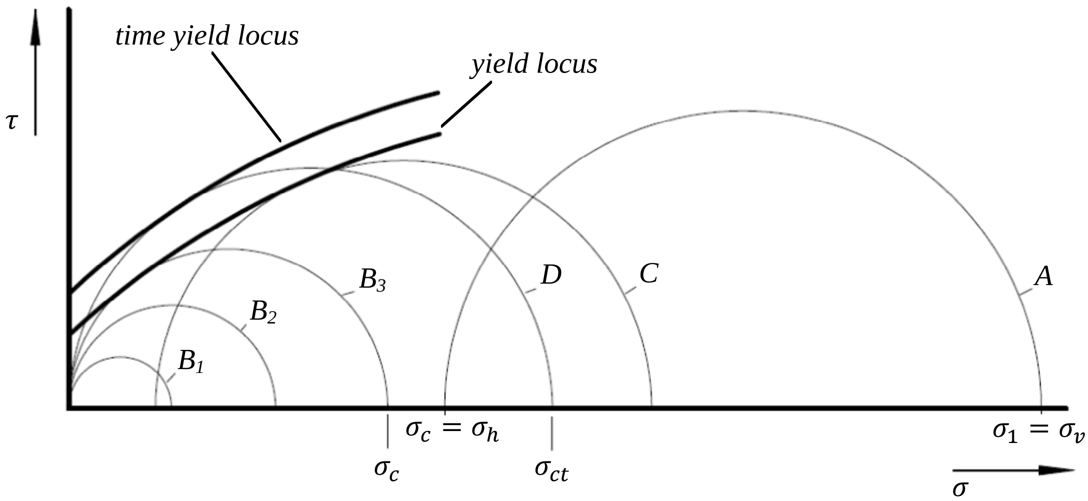

Figure 21. Measurement of the unconfined yield strength in a σ, τ diagram (Schulze 2006a)

Horizontal and vertical stresses within the sample are assumed to be principal stresses as all sides of the cylinder are assumed to be frictionless. The vertical stress applied to the granular material is the major principal stress represented by σ_1, and the horizontal stress is the minor stress represented by σ_2. The Mohr's stress circle used to represent the first stage of the test is shown on the diagram as circle A. In the second stage of the test the granular material is loaded with increasing vertical stress – since the horizontal stress is zero, this stage is represented by stress circles B1, B2 and B3. Note that B3 is tangential to the yield locus – Nedderman (1992) notes that yield loci can be approximated by drawing a locus tangential to the Mohr's circles created from data where the sample is known to have failed. Failure will occur at differing values of σ_C, depending on the value of horizontal stress present in the second part of the uniaxial compression test. Obviously since the cylinder walls have been removed this will have practical problems in application, therefore to accurately measure mechanical properties other methods have been developed using the principles of this test (Schulze 2006a). These include the test equipment noted in the first paragraph of this chapter.

Schulze (2006a) highlights the fact that the shape of the yield locus will depend on the compaction of the granular material. As compaction increases (i.e. as the stresses in the first part of the uniaxial compression test are increased) bulk density and unconfined yield stress increase, and similarly the τ and σ coordinates increase in value. Therefore for each compaction stress one yield locus can be found. It should be noted that some granular materials compact over time – therefore σ_C increases with increased storage time, even while the compaction stress remains the same. This means that more than one yield locus can be found for the same σ_1 value in the uniaxial compression test, depending on the length of time the compaction stress is applied for. The new loci are known as the time yield loci.

According to Bates, the second parameter of primary importance for gravity flow is wall friction measurement. This can be achieved by the simple test set up shown in Figure 22 (Bates, p. 25).

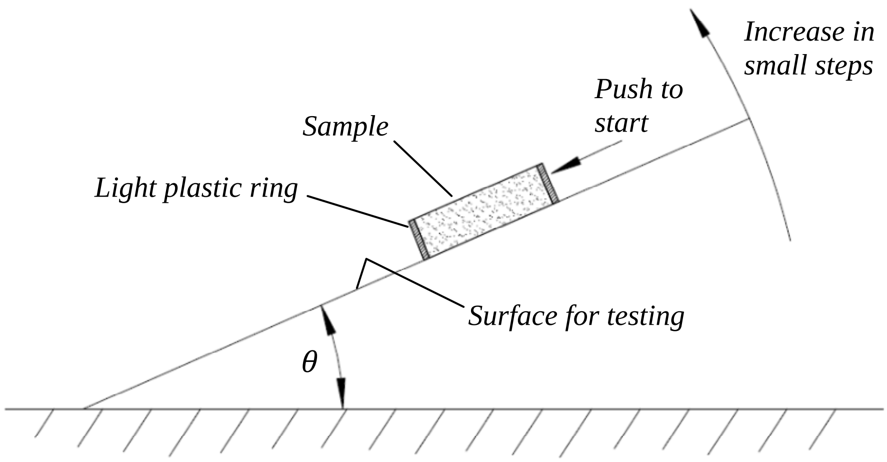

Figure 22. Checking wall slip by inclined plane (Bates)

However for more accurate data, or where surface adhesion is present, Bates recommends use of the set up shown in Figure 23.

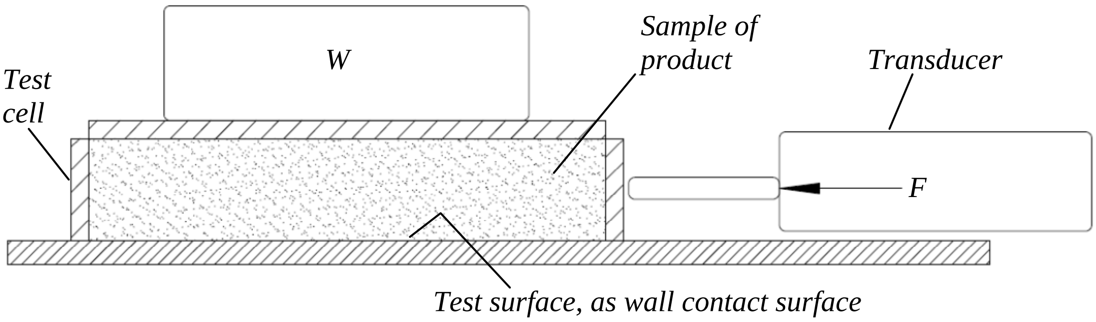

Figure 23. Wall friction tests with force measuring device (Bates)

Bates goes on to recommend various simple tests to be used for preliminary evaluation, and from this expands to further testing where thought necessary depending on initial test results.

In summary it seems that although collection of experimental data has progressed in this field, advances are still possible. Data obtained can be of limited use as experiments may not be conducted in identical conditions to that of actual usage of the granular material. Other problems are inherent with testing of such material – for example it has been proven that yielding of granular material can be time dependant, i.e. yield can occur at differing values of stress, depending on the time period of compaction (Nedderman 1992, Materials Today 2006). It has been found that a granular materials bulk density can change on flowing start and during compaction and expansion as a result of plastic deformation (Nedderman 1992). Testing methods are improving constantly: modern items of test equipment, including powder rheometers, are able to provide repeatability by conditioning samples of powder prior to testing (Freeman 2007). Complete examples of experimental data are not available for comparison to stress distributions produced by project models. Few sources exist of internal stress distributions within granular materials. In Chapter 4.6.1 data published by Walker and Blanchard (1967) are compared to calculated values of internal pressures within a coal hopper. In Chapters 4, 5 and 6 experimental data from the literature are compared to calculated wall stress values (Walker and Blanchard 1967, Rao and Ventaswarlu 1974, Tuzun and Nedderman 1985, Schulze and Swedes 1994, Berry et al 2000, Diniz and Nascimento 2006, Wojcik and Tejchman 2008).

2.5 Application in industry

An article by McGee (2008) indicates that flow problems within hoppers remains a common occurrence, despite years of research and various design codes. For design of hoppers and silos, many national and international standards (Nedderman 1992) make use of methods initially proposed by Janssen (1895) with empirical modifications. A commonly accepted method for determination of insert loading is not available (Schulze 2008). According to Schulze (2008), the following codes of practice do not include loads on inserts.

- DIN 1055-6:2005-03 Actions on structures – Part 6: Design loads for buildings and loads in silo bins.
- BS EN 1991-4:2006 Eurocode 1 – Actions on structures – Part 4: Silos and tanks
- BS EN 1993-4-1:2007 Eurocode 3 – Design of steel structures – Part 4-1: Silos

A great number of private enterprises are available within industry to offer advice on silo and hopper design. Jenike's methods (1961) have been widely employed in industry, yet as noted Enstad (1975) and Matchett (2004) demonstrated that these methods are conservative.

2.6 Areas of research relevant to research project

It should be noted that equations representing principal stresses on curved surfaces were developed prior to Enstad, and are known as the Lamé-Maxwell equations. Previous applications include the fields of Photoelasticity to model stresses within lacquer-coated test pieces and Geophysics to model tectonic stresses within the earth's crust (Maxwell 1853, Love 1927, Coker et al 1957, Frocht 1941, Durrance 1967, Zapletal 1970, Olsen 1982, Galybin and Mukhamediev 2004). The author is not aware of use of such equations for stress distributions within bulk solids. Features of the Lamé-Maxwell method were used in the force balance equations created for this research project.

Soil mechanics has areas of study associated with civil engineering and comparisons can be drawn with analysis of granular materials (Terzaghi 1925, Sokolovskii 1965, Nedderman 1992, Venkatramaiah 2006). Jenike's methods were influenced by soil mechanics (Nedderman 1992). According to Nedderman the discipline of soil mechanics is based on development from Coulomb's work (Coulomb 1776, Nedderman 1992). The intent of soil mechanics is to prevent deformation of the bulk material, whereas within use of granular materials hoppers and silos are designed to cause deformation of the bulk. Coulomb's Method of Wedges was developed to determine loading on retaining walls, and the Method of Characteristics (Sokolovskii 1965) can be used for similar applications. Lamé-Maxwell equations and areas of soil mechanics relevant to this project are further discussed in Chapters 3.1 and 3.2.

2.7 Summary

There is provision for development of analytical models in this field. A flexible, but rigorous approach is required using usual bulk solids properties. There are numerous models available for use: ranging from simple incremental methods to those working with multiple individual particles. These previous theories are not perfect in their application. Many require a number of simplifying assumptions to allow calculation, such as the number of dimensions used in the solutions, or the direction of principal axes.

As with other types of continuum analysis, finite element methods have not been fully verified by experimental data. Discrete element methods have made considerable development but are limited by available computing capabilities and assumptions of particle shape and size. Hence, continuum methods of stress analysis remain relevant to the current field of study. Enstad (1975) and Li (1994) made use of assumed a constant value of minor principal stress across their vessels in using an incremental slice. Matchett (2004) improved this method by using an incremental arch, proposing a principal stress arc method that allowed stresses to vary across the hopper under consideration. However this method, and further work with rotationally symmetric silos (Matchett 2006a,2006b) did not take account of curvature of the incremental element after Lamé-Maxwell and did not consider conical rat holes or conical inserts. Curvature of the incremental element is explained in more detail between Figures 35 and 36 in Chapter 4.1.

Much of current industrial practice is based on the conservative methods proposed in 1895 for silos and subsequently 1961 for hoppers, with numerous private enterprises providing advice based on empirical data. There can be no doubt that work based on empiricism is sound, but without a commonly accepted approach to design then results and recommendations will vary. Matchett (2004) reported that flow could be demonstrated through outlet diameters less than 1/20 of the size used in current industrial practice.

As noted detailed experimental data is not fully available for stress values within silos and hoppers. Loading, and therefore stresses, normal to vessel walls is available for a limited range of geometries (Walker and Blanchard 1967, Rao and Venkateswarlu 1974, Diniz and Nascimento 2006, Wojcik and Tejchman 2008). These data do not all provide shear stress data, which is necessary for verification of principal stresses. Stress distribution data away from vessel walls is limited to loading on inserts (Motzkus 1974, Strusch and Schwedes 1994). Stresses in the plane parallel to Jessop's (1949) 'z-direction' (or azimuthal stresses in the research project) do not have data for comparison available in the literature. It is therefore difficult to

verify results calculated via the principal stress arc method, or other methods, without use of comparison to proposed stress relationships. A common feature within a number of analyses is the Mohr-Coulomb yield criterion (Matchett 2004, 2006a,2006b). This relationship is used in the model created for the research project to provide an initial condition for σ_ε. Since stresses at the silo wall can be measured, it follows that the relationship derived from the Mohr-Coulomb yield criterion is used to allow comparison of available experimental data.
Nedderman (1992) gives support to the criterion;

> "The Coulomb yield criterion does seem to give an excellent prediction of the wall stresses for many materials but it does not follow that it is valid for all granular materials or for prediction of other phenomena in the materials for which it gives reliable stress distributions."

A second commonly used assumption is the Conical Yield function, used to describe three-dimensional cones (Jenike 1987, Nedderman 1992, Kruyt 1993). The Mohr-Coulomb and Conical Yield criterion can be used to evaluate stress distributions, including those produced for this research project. In Chapter 3.3 principal stress relationships are proposed and discussed.

This research project seeks to address the aims set out in Chapter 1.4 by calculation of stress distributions in two- and three-dimensions, subject to a range of assumptions, stress states and geometries. This approach can be described as a continuum model of intermediate complexity. Benefits include the ability to produce solutions from numerical and analytical methods, and to provide solutions for geometries of increased complexity over more simple theories. The basis for the model within this research project, circular principal stress arc geometry, was first used by Enstad (1975). The assumption of a circular principal stress arc has not been consistent in this field of research, with previous authors considering other shapes (Janssen 1895, Walker 1966, Benink 1989). Sufficient quantitative data was not available to verify the assumption of principal stress arc geometry. The limited evidence on this subject supports the assumption of a circular arc (Faure and Gendrin 1989, Sakaguchi et al 1993, Langston et al 1995, Kamath and Puri 1999, Berry et al 2000, McCue and Hill 2005, Matchett 2007), indicating that this geometry should allow development of models that imitate reality.

Chapter 3.0 - Underpinning Knowledge

The underpinning theory studied for completion of this research project is recorded below. The areas were applied to the subject of stress distributions within silos and hoppers.

- Stresses in two dimensions – plane stress.
- Stresses in three-dimensions – with and without rotational symmetry.
- Yield criteria – Mohr's circle and yield loci.
- Stresses on curved surfaces – Lamé-Maxwell equations.
- Numerical techniques for solution of partial differential equations.
- Use of computer programming languages to develop flexible algorithms.

The spreadsheet-based models were used for checking purposes and display results. QBasic was employed in the project for production of algorithms to demonstrate development of algorithms from first principles. Various platforms were considered for development of the research project models, including MathWorks Matlab, Wolfram Mathematica and Maplesoft Maple. The use of spreadsheet- and QB64-based algorithms during the project was dictated by the experience of the team at the outset of the project. A QB64 platform was selected to allow demonstration of algorithms created entirely by the thesis author.

The following sections present information on key areas of the research project. They are included for information and do not represent the author's own work.

3.1 Lamé-Maxwell equations

The Lamé-Maxwell equations are shown below and derived in Appendix Two, Chapter 9.8. Principal stresses σ_1 and σ_2 act over stress trajectories s_1 and s_2. The principal stress trajectories have radii ρ_1 and ρ_2.

$$\frac{\partial \sigma_1}{\partial s_1} + \frac{\sigma_1 - \sigma_2}{\rho_2} = 0 \quad (16)$$

$$\frac{\partial \sigma_2}{\partial s_2} + \frac{\sigma_1 - \sigma_2}{\rho_1} = 0 \quad (17)$$

Jessop (1949) extended the Lamé-Maxwell equations into three-dimensions for the purpose of photoelastic analysis of three-dimensional stress systems.

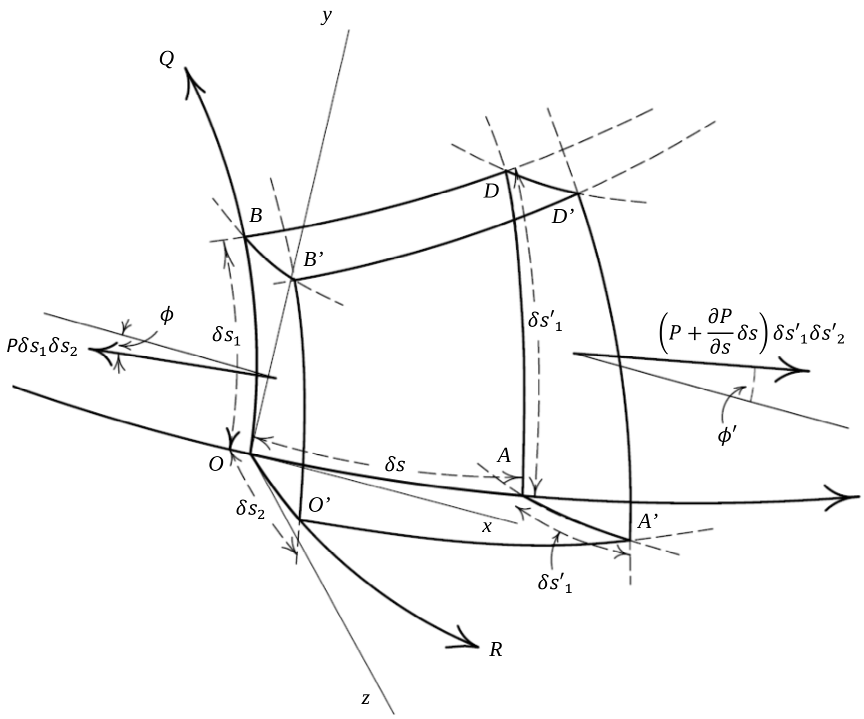

Figure 24. Geometry set up for solution by 3-D Lamé-Maxwell equations (Jessop 1949)

Jessop (1949) derived the following two differential equations from the geometry shown in Figure 24, where the notation *P*, *Q* and *R* represent the three principal stresses. Axes in Figure 24 are *x*-, *y*- and *z*-directions.

$$\frac{\partial P}{\partial s_1} + \frac{P - Q}{\rho_1} + \frac{R - P}{\rho_2} \cos x = 0 \text{ (in the } x\text{-direction)} \quad (18)$$

$$\frac{\partial Q}{\partial s_2}+\frac{P-Q}{\rho_1}+\frac{R-Q}{\rho_2}\cos y=0 \text{ (in the } y\text{-direction)} \qquad (19)$$

Jessop (1949) did not provide a differential equation for stresses in the third dimension or *z*-direction. It is supposed by the author that in the field of Photoelasticity this direction has limited application. In the analysis of stress distributions within hoppers and silos the third dimension is of interest to researchers and designers.

The application of the Lamé-Maxwell equations within this research project is explained in Figures 35 and 36, Chapter 4.1. It is demonstrated that early principal stress arc methods (Matchett 2004,2006a,2006b) did not take account of curvature in the direction normal to the principal stress arc.

3.2 Soil mechanics

Knowledge of soil mechanics has applications in many fields of Civil Engineering (Venkatramaiah 2006). These applications include foundations, underground/earth-retaining structures, pavement/road design and excavations/embankments/dams. According to Terzaghi (1925):

> "Soil Mechanics is the application of the laws of mechanics and hydraulics to engineering problems dealing with sediments and other unconsolidated accumulations of soil particles produced by the mechanical and chemical disintegration of rocks regardless of whether or not they contain an admixture of organic constituents."

3.2.1 Failure modes for aggregates

Sokolovskii (1965) and Nedderman (1992) give a detailed explanation on equilibrium and subsequent failure of granular materials. An understanding of these techniques is necessary for development of the research project models. Of particular interest is the ideal Coulomb material and Mohr-Coulomb failure analysis (Coulomb 1776, Mohr 1906, Nedderman 1992, Venkatramaiah 2007). According to Nedderman;

> "…the concept of the ideal Coulomb material forms the basis of a great many analyses of commercial importance and furthermore provides a firm foundation on which to develop important ideas of more general validity. The Coulomb material fulfils the same role in the study of granular materials as the Newtonian fluid does in viscous flow."

In Figure 25, a quantity of granular material is subject to a force. This force causes some small degree of deformation without failure. If the force reaches a value which causes materials yield stress to be exceeded, the material will fail as shown.

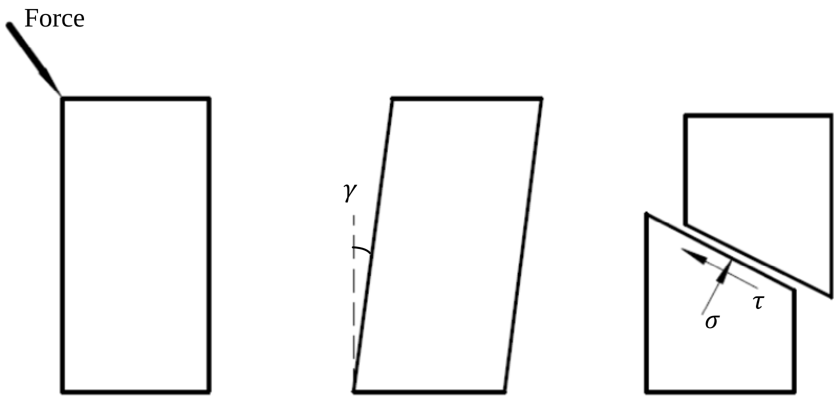

Figure 25. Distortion of an element due to the application of a force (Nedderman 1992)

If the elastic deformation is discounted, then this is termed a rigid-plastic failure mode. This type of failure is used in Figure 20 during a uniaxial compression test.

The shear stress τ on the slip plane is a function of on the normal stress σ acting on the plane. For ideal Coulomb materials this relationship is a linear one, and the Coulomb yield criterion for such materials is equation 20. The coefficient of internal friction ϕ and cohesion c are dictated by the material properties.

$$\tau = \sigma \tan \phi + c \tag{20}$$

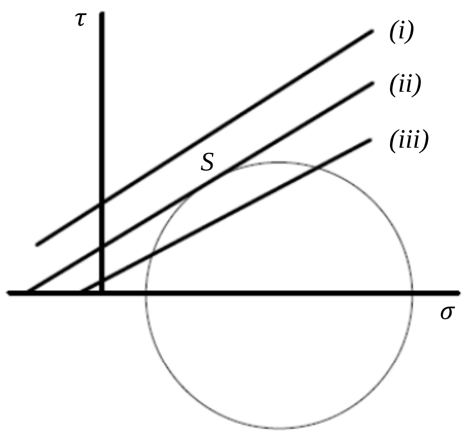

Figure 26. Mohr's circle and the Coulomb line (Nedderman 1992)

(i) The Coulomb line is entirely above Mohr's circle as shown by line (i). Therefore no slip plan is formed and the material is stable.

(ii) The Coulomb line is touching Mohr's circle. Therefore slip is about to occur at plane S. The material is at a state of incipient failure – any increase is stress will cause a slip plane to be formed. The models proposed in this research project assume a state of incipient failure.

(iii) The Coulomb line cutting the circle is not possible with an ideal Coulomb material.

Figure 26 demonstrates the combination of the Coulomb failure criterion with Mohr's circle to provide the Mohr-Coulomb failure analysis.

3.2.2 Areas of soil mechanics relevant to research project

Nedderman and Sokolovskii go on to discuss further soil mechanics topics in detail:

- The Rankine states. Rankine (1857) first used the terms 'Active' and 'Passive' stress states, which are shown in Figure 27. His methods can be used to provide theoretical limits for stresses within granular materials and the maximum compressive stress that can act along a free surface, known as the unconfined yield stress. Figure 27(a) illustrates how the active case is associated with granular materials. In this stress case the weight of the granular material pushes outwards on the restraining walls of the vessel. The discharging case, passive with negative wall shear, is also demonstrated in Figure 27(b). In this stress case frictional forces pull the restraining walls inwards as the material discharges. Nedderman refers to the active state as being characterised by the horizontal stress being lesser in magnitude than the vertical stress. In principal stress arc methods, at the centre of the system, the horizontal stress can be taken as σ_R and the vertical stress can be taken as σ_ε.

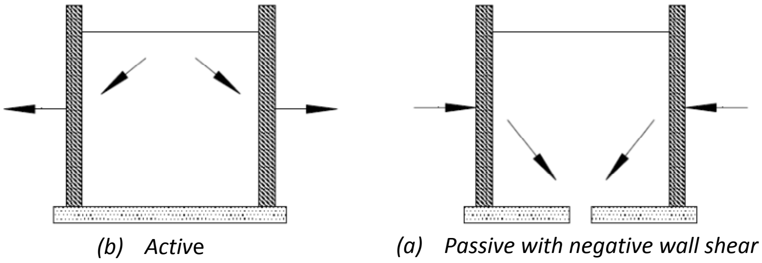

Figure 27. Two possible failure mechanisms for granular materials (Nedderman 1992)

- The angle of repose of cohesive and cohesionless materials. This material property is used with the research project analysis. The angle of repose of a cohesionless granular material typically equals its angle of internal friction. There is research to suggest that cohesive materials do not have identical angles of repose and internal friction (Tuzun and Nedderman 1989, Nedderman 1992, Gallego et al 2011).

- Wall failure criterion. Nedderman uses the Mohr-Coulomb failure analysis to represent slip along a boundary surface such as a retaining wall, with an ideal Coulomb material. In a related analysis Sokolovskii uses the Method of Characteristics to determine equilibrium of foundations.

- Coulomb's Method of Wedges. In Figure 28 a cohesionless granular material with a horizontal top surface causes a vertical retaining wall to fail. Coulomb's (1776) analysis is relevant to foundation design. Sokolovskii uses the Method of Characteristics to determine the load on a retaining wall with a surcharge.

(a) Before wall has broken

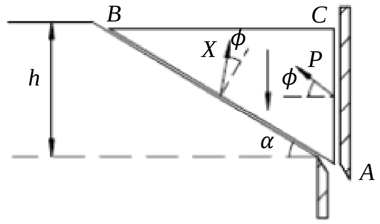

(b) After wall has broken

Figure 28. Failure of a retaining wall (Nedderman 1992)

3.3 Principal stress relationships

In the two-dimensional analyses within this research project, there are two unknown variables within two differential equations. Therefore the equations can be solved for these variables and a relationship is not required between principal stresses, with the exception of a boundary condition for arc stress from radial stress. This is achieved by use of the Mohr-Coulomb criterion.

In the three-dimensional analysis within this research project, there are three unknown variables within two differential equations. As noted by Matchett (2006a) in this situation a relationship is required between principal stresses to resolve variable values.

3.3.1 Mohr-Coulomb criterion

This criterion has been described above in Chapter 3.2.1. In the models used within the research project, equation 20 is used to derive equation A.35 in Appendix Two (Chapter 9.5). This equation provides an initial value for arc stress σ_ε from an assumed value of radial stress σ_R. If a model with zero overpressure on the top surface of the material is used, then σ_R is assumed to be equal to zero.

This criterion is applied in Appendix Three to check numerical solutions of the model are within the limits of static equilibrium (i.e. Coulomb line (i) or (ii) in Figure 26). Under certain conditions within the research project models, the presence of equilibrium may be taken as an indication of cohesive arching.

3.3.2 Azimuthal stress relationships

For the three-dimensional models, the analyses give two differential equations in three unknown stresses. Hence not all stresses are specified by solution of the equations and relationships between principal stresses are necessary. The following relationships between arc, radial and azimuthal stresses are used in later in this thesis for the three-dimensional models. For each relationship, correlation between calculated and available experimental data was reviewed and results shown in Appendix Six.

The Haar-von Karman hypothesis was used by Nedderman (1992) and Matchett (2006a,2006b) to provide a relationship between arc and azimuthal stresses. The relationship can be derived via force balance equations shown in this thesis. This derivation is shown in Appendix Two, Chapter 9.7.

The relationship proposed during this research project relates arc and radial stresses to azimuthal stresses. An empirical K-value is used. At zero ε (along the centre line of the silo/hopper) the proposed relationship is equal to the Haar-von Karman hypothesis. Use of K-values that tend towards zero produces stress distributions in line with use of the Haar-von Karman hypothesis.

The relationship proposed by Matchett (2006a) related radial and azimuthal stresses, including the material tensile parameter T. Matchett’s intention for this relationship was for failure to occur in the radial/azimuthal stress plane.

Love’s (1927) work related arc and radial stresses to azimuthal stress, with an empirical K-value.

The Conical Yield function was employed by Jenike (1987), Nedderman (1992) and Kruyt (1993) for analysis of cone hoppers. The criterion provided a relationship between arc, radial and azimuthal stresses. It was found by Jenike that the Coulomb model and assumptions did not give good location of the rathole walls in funnel flow, when used with the radial stress field method. The Conical Yield function works by measuring shear and normal stresses at some point within a material via octahedral stresses. Nedderman provided equations 21 and 22 below.

$$s_1{}^2 + s_2{}^2 + s_3{}^2 = 2M^2\sigma^2 \qquad (21)$$

also,

$$(\sigma_1 - \sigma_2)^2 + (\sigma_2 - \sigma_3)^2 + (\sigma_3 - \sigma_1)^2 = 6M^2\sigma^2 \qquad (22)$$

where s_1, s_2, s_3 are deviatoric stresses i.e. $s_1 = \sigma_1 - \sigma$, $s_2 = \sigma_2 - \sigma$, $s_3 = \sigma_3 - \sigma$; $\sigma = \sigma_{OCT} = \frac{1}{3}(\sigma_1 + \sigma_2 + \sigma_3)$; M can be taken as $\sin\phi$.

The Coulomb yield criterion assumes that shear stress is a linear function of normal stress. Nedderman found that stress distributions produced by use of the two methods did not vary significantly.

3.4 Modification of algorithm parameters

During comparison of experimental data to calculated stress distributions, the following parameters were modified in the spreadsheet- and QBasic-based models.

The tensile intercept, *T*. This parameter is explained in Appendix Two, Chapter 9.5, within the Mohr-Coulomb principal stress relationship. As demonstrated in Figure A.3 it is the value of tensile stress that a material can support prior to failure. A typical value of *T* for a cohesionless material is zero Pa.

The angle of principal stress arc to wall normal, β. This parameter can be determined from the system geometry and varies with wall friction angle ϕ_w. The dimension β for the wedge hopper geometry is shown later in this thesis.

The material ratio of effective stresses, *J*. This parameter is used in Appendix Two, Chapter 9.5, as a ratio between effective stresses. Values for *J* vary depending on angle of yield locus ϕ and the stress state of the material under consideration. The Rankine stress states are discussed in Chapter 3.2.2 above and provide limits for *J*-values.

3.5 Numerical methods

It is not possible to solve all differential equations by analytical methods. Reasons for this include slow convergence of the resulting series and multiple stages of differentiation (Stroud 1996). A further reason can be an excessive number of unknown variables for a given number of equations.

3.5.1 Numerical solution of differential equations

Where boundary conditions are known for a given differential equation, an approximate solution may frequently be found using numerical methods. Various methods exist, including but not limited to Euler, Euler-Cauchy, and Runge-Kutta (Stroud 1996), with varying degrees of complexity and resulting accuracy. The Euler method is based on Taylor's series and was selected as the method used in the research project.

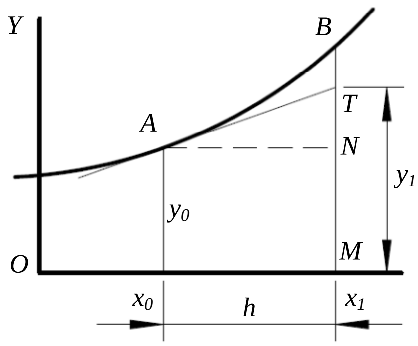

Figure 29. Graphical interpretation of Euler's method (Stroud 1996)

Figure 29 shows a graphical representation of the Euler method. The value of *Y* at the next point, y_1, is calculated by adding the slope differential multiplied by the step size to the previous value.

In the research project algorithms, equation 23 uses a backward step Euler method to calculate radial stress σ_R at each point down through the silos and hoppers using an incremental distance of δx in the x-direction.

$$(\sigma_R)_{x+\delta x} = (\sigma_R)_x - \left(\frac{\partial \sigma_R}{\partial x}\right)_x \delta x \tag{23}$$

An initial condition of zero (Pa) is used to signify a lack of overpressure at the surface of the silo. Non-zero values are selected to represent the overpressure that is assumed to occur at the top surface of the hopper, due to the weight of the granular material contained within the silo above. The application of equation 23 is explained in Appendix Three, Chapter 10.1. For the right-hand side of the model silos and hoppers, F is calculated via a forwards-step Euler numerical solution of the form shown below, moving across the vessel with incremental distance $\delta\varepsilon$ in the ε-direction.

$$(F)_{\varepsilon+\delta\varepsilon} = (F)_\varepsilon + \left(\frac{\partial F}{\partial \varepsilon}\right)_\varepsilon \delta\varepsilon \tag{24}$$

with initial condition,

$$F = \sigma_\varepsilon \left(\frac{\partial w}{\partial x}\right) \tag{25}$$

With correctly chosen parameters the Euler method can provide reasonable approximations to problems. It is the least accurate of the methods listed above. For step sizes small in relation to the area considered and without exact experimental data it is adequate for use in the research project, and has the added benefit of being simple in its application thereby reducing calculation time.

3.5.2 Finite difference techniques

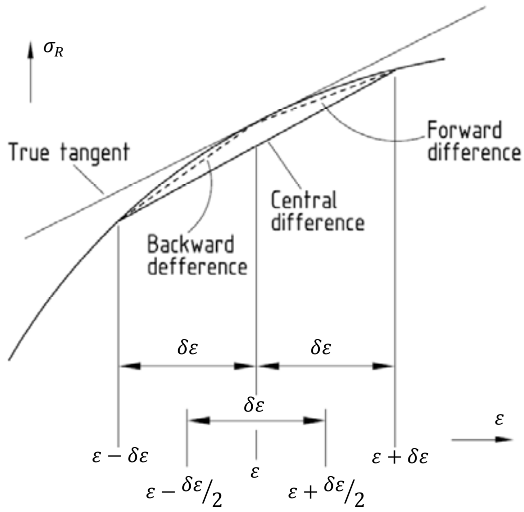

Figure 30. Diagrammatic definition of backward, forward, and central difference approximations (Eastop and McConkey 1993)

In Figure 30 the straight line approximation to an equations curve is demonstrated. It can be seen that the central difference technique provides a close approximation to the curves true tangent at the point under consideration. Equations 26 to 28 are finite differences techniques used to calculate $\frac{\partial \sigma_R}{\partial \varepsilon}$, a differential value used in the research project models.

$$\frac{\partial \sigma_R}{\partial \varepsilon}_{(\varepsilon)} = \frac{\sigma_{R(\varepsilon+\delta\varepsilon)} - \sigma_{R(\varepsilon)}}{\delta\varepsilon} \tag{26}$$

$$\frac{\partial \sigma_R}{\partial \varepsilon}_{(\varepsilon)} = \frac{\sigma_{R(\varepsilon+\delta\varepsilon)} - \sigma_{R(\varepsilon-\delta\varepsilon)}}{2\delta\varepsilon} \tag{27}$$

$$\frac{\partial \sigma_R}{\partial \varepsilon}_{(\varepsilon)} = \frac{\sigma_{R(\varepsilon)} - \sigma_{R(\varepsilon-\delta\varepsilon)}}{\delta\varepsilon} \tag{28}$$

The forward difference technique, equation 26, is used at the left-hand boundary of the model. The backward difference technique, equation 28, is used at the right-hand boundary. The remainder of the model uses the central difference equation 27.

There are various numerical methods available, of increased complexity – including but not limited to finite element and finite volume methods. Ooi et al (1996), Zhao and Teng (2004) and Vidal et al (2008) all made use of FEM software in their analysis of silos and hoppers. The finite difference technique is a simple one. It was chosen for the project as by use of central difference a high level of accuracy can be provided relative to the experimental data values, and the method is conditionally stable. A limitation of the finite difference method is at model boundaries (for example the vessel wall or at a free surface). In this case either forward or backward difference terms are needed, or a boundary condition where available.

3.5.3 Newton-Raphson method

Newton's method or the Newton-Raphson method is used for finding 'roots' i.e. zero values of an equation (Stroud 2003). For example consider a function y = *f*(x). Assume point *A* is the location where the function curve crosses the horizontal *x*-axis, here *f*(x) = 0. If a point *P* is chosen on the curve close to *A*, then the horizontal *x* coordinate for point *P* is an approximation of point *A* and therefore an approximation of *f*(x) = 0. If a tangent line to the curve y = *f*(x) is drawn at point *P*, then where this tangent point crosses the *x*-axis will be an improved approximation to the required root value. This process can be repeated on an iterative basis to converge on the required result.

3.6 Generalized Reduced Gradient nonlinear optimization

An optimization problem is one requiring the determination of an optimal value of a given function, subject to a set of restrictions placed on the variables concerned (Stroud 1996). A simple definition of a nonlinear system is one whose input is not directionally proportional to its output, and nonlinear programming is defined as the formulation and solution of constrained problems that are nonlinear (Baker 2005).

For nonlinear problems, Microsoft Excel makes use of the Generalized Reduced Gradient nonlinear optimization algorithm. The non-generalised form was first developed by Wolfe (1963). The GRG algorithm was developed from the reduced gradient method by Abadie and Carpentier (1969) to allow solution of problems with non-linear constraints. The method belongs to the family of techniques known as the Methods of Feasible Directions, where nonlinear programming problems are solved by moving from a feasible point to an improved feasible point (Bazaraa et al 1993). Figure 31 demonstrates this by approximating the contour of $f = -7.16$ via points x_2 and x_3. The algorithm makes use of $f = 0$ as a boundary condition, locating x_1.

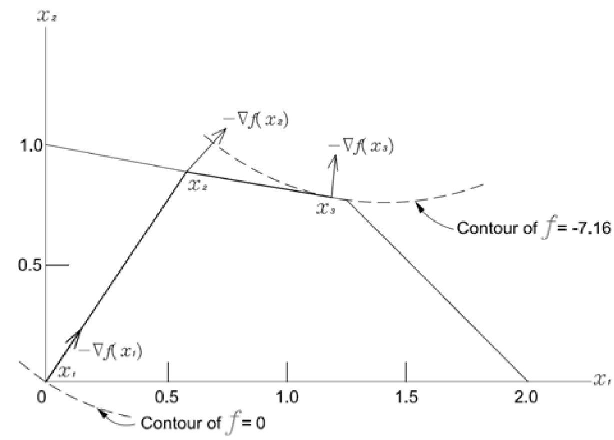

Figure 31. Illustration of reduced gradient method by Wolfe (Bazaraa et al 1993)

The use of a GRG algorithm within the Microsoft Excel software is further explained by Fylstra et al (1998) and Baker (2005). An example of the GRG method is given by Chen and Fan (2002) in their analysis of minimum zone straightness for measurement of manufactured parts. Chen and Fan use the GRG method to locate optimal parameter values for translation of the measured data into comparable values, while minimizing straightness error.

In Appendix Three application of the Solver software is explained. The Solver/GRG technique is combined with a least squares method (Gauss 1809, Stroud and Booth 2001) to determine optimum values for the research project models, in terms of matching calculated stress distributions to experimental data. The least squares technique is a simple and commonly used type of linear regression. Through use of statistical t-testing and comparison to experimental data, a least squares curve-fitting technique was proved to be suitable by the research team. Other methods are available, including M-estimation and least absolute estimation, although, like the least squares method, they can be considered ‘non-robust’ in the presence of outlying data, especially in the case of independent variables. Where outlying data points were identified, a least trimmed squares method (Rousseeuw 1984) was employed to ensure that the data was not adversely affected by a small number of outlying points. An example of this robust method is shown Chapter 5.6.4.

Baker (2005) cautions against the assumption that the Solver program will be reliable in finding an optimum or global solution to a nonlinear problem, without running the analysis from a variety of ‘starting solutions’. As was observed in the research project more than one solution may exist (‘local optima’), and the optimum solution was influenced by the initial condition of the model variables. Constraints used were taken from material properties and knowledge of the system. For example a range of bulk density or coefficients of internal friction values can be obtained from literature and radial stresses σ_R were assumed to be zero at the upper surface of the silos under consideration. Values for β and J were dictated by Mohr-Coulomb failure analysis and the assumption of Rankine states. Use of these boundary conditions and subsequent conformance to their prescribed limits, while theoretical, gave confidence that the algorithms produced were reliable, when combined with correlation to experimental data. Further confidence was provided by use of statistical tests, documented in Appendix Five, demonstrating improvement in correlation to experimental data with use of the GRG technique.

Chapter 4.0 – Two-dimensional parallel-sided silo and wedge hopper case studies

This chapter presents the development of an improved mathematical model for a two-dimensional problem idealised as vertical parallel walls and sloping wedge shaped walls. This development presents the advancement of considering the curvature of the incremental element in the direction normal to the principal stress arc. The modification makes use of Lamé-Maxwell theory (Maxwell 1853, Coker et al 1957) and represents an improvement in the accuracy in the assumption for the theoretical model. Consideration of the curvature of the incremental element is reported in section 4.1, Figures 35 and 36. The idea of curvature of the incremental element in the direction normal to the principal stress arc, and hence the Lamé-Maxwell equations, was suggested by an external expert. The new model geometry was proposed by Professor Andrew Matchett. The thesis author had input to the new model, including assistance with development of force balance equations, research into the 'Lamé-Maxwell' equations, checking of proposals and derivation of solutions (equations 50 and 51) for the force balance equations with guidance from Professor Matchett.

An early version of the principal stress arc method (Matchett 2004) did not take account of curvature of the incremental element in the direction normal to the principal stress arc. A key feature of Matchett's (2004) model was the assumption of the principal stress direction such that it coincided with arc geometry,
allowing calculation without shear stress calculation. The second key feature of the principal stress arc method is the use of incremental elements, allowing calculation of two- and three-dimensional stress distributions through the granular material, an improvement on previous methods where the minor principal stress was constant across the silo or hopper (Enstad 1975).

The models are spreadsheet- and QBasic programming language-based with graphical representation, displaying stresses in two dimensions within silos and hoppers with focus on material yield for the purpose of determining when arching will occur. Additional responsibilities of the author within the research project team included creation of new spreadsheet-based models and new QBasic algorithms, and use of these tools for comparison with data from the literature. Force balance equations have been completed in two directions, providing solutions in two dimensions. The analysis gives two differential equations in two unknown stresses. Hence all stresses are specified by solution of the equations via numerical methods described in Chapter 3.5. The numerical methods employed in the research project models include Euler, Newton-Raphson and finite difference techniques. Solution allows comparison of results with known stress relationships including Mohr-Coulomb criterion. Stress values in the third dimension are not calculated by the model proposed in this chapter. The resulting stress distributions are validated in Chapter 4.4 and applied to experimental data from the literature in Chapter 4.6.

In this research project, the Mohr-Coulomb criterion is used to relate radial stress to arc stress at one value of ε only. Therefore subsequent references to active and passive cases refer to the chosen value of ε. Other positions throughout the model may be in active or passive states, or at some stage between the two cases. Possible positions for the boundary condition are discussed in this chapter.

4.1 Model geometry, assumptions and resulting force balance equations

Figure 32 shows the principal stress arc geometry. The wedge hopper has half angle to the vertical α_1 and α_2 respectively; a circular arc cuts the right hand side wedge at a distance x above the apex with radius *R*.

Two-dimensional parallel-sided silo and wedge hopper

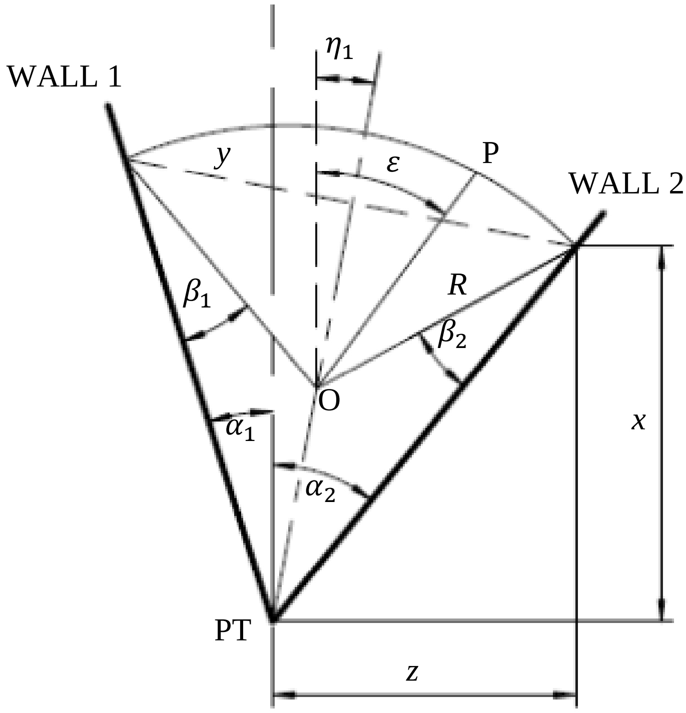

Figure 32. 2-D model geometry

The assumptions used in the model are listed below.

1. Stresses act over successive circular arc sections of radius *R*.

2. Each arc makes angle β with the wall normal and is held at that angle by wall friction. The value of β is chosen such that the model works in principal stress space, therefore shear stress terms are not present in the resulting equations.

3. At its extremity the radius makes angle $(\alpha + \beta)$ with the vertical.

4. The arc under consideration cuts the wall at vertical height *x* from the vertex, and intersects the wall at distance *r* from the vertex.

5. The incremental arc has a thickness of δ_w, which varies across the span of the arc with ε.

Two-dimensional parallel-sided silo and wedge hopper

6. In two-dimensional space there are two principal stresses acting: radial stress σ_R and arc stress σ_ε. These stresses are orientated along circular paths of radius R, within the vessel/hopper. Three-dimensional stresses in the direction normal to the page are not considered in the analysis. The wedge is assumed to be 'long', where frictional effects on the hopper sides in the plane of the page are not taken into account.

7. Positions within the vessel/hopper are located by the height at which the arc cuts the vessel wall x, and arc angle ε.

8. The angle of precession of arc centre to vertical is η.

9. The material is assumed to be in a state of incipient failure, therefore dynamic effects are not considered.

10. The principal stress arc is assumed to be circular in shape.

If an incremental element is considered cutting the right-hand side with vertical height δx, and at an angle of ε to the vertical with incremental angle $\delta\varepsilon$ - see Figure 33.

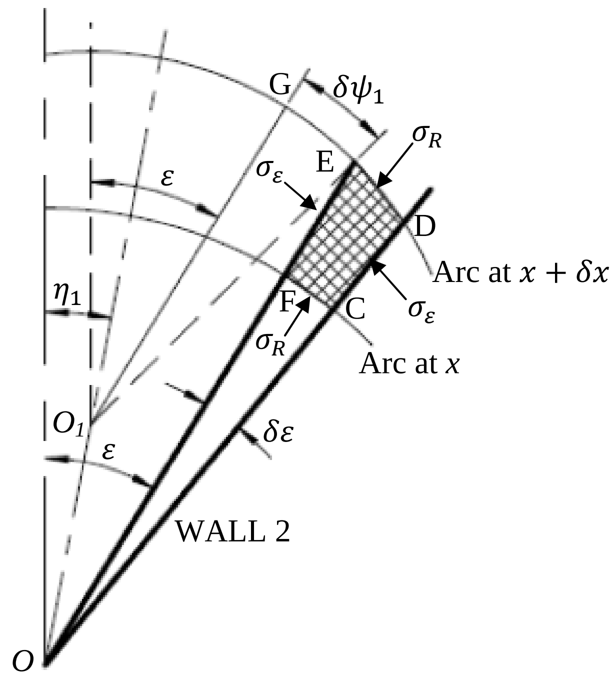

Figure 33. Circular arc incremental element

A detail of the incremental element is shown in Figure 34.

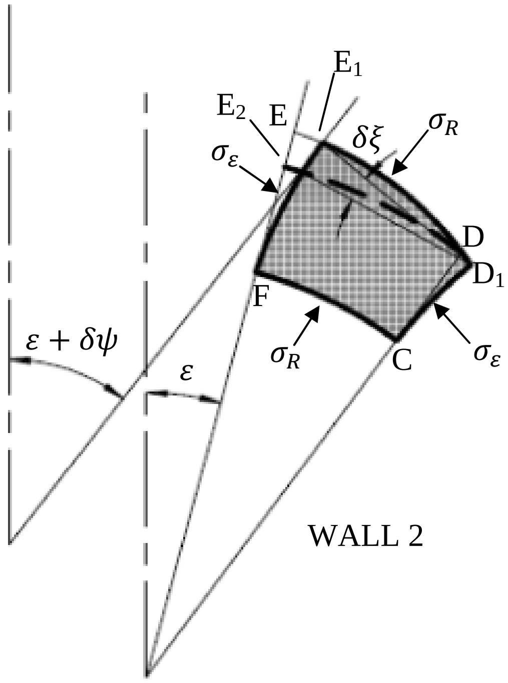

Figure 34. Incremental element detail

Using the circular arc geometry initially set out by Matchett (2004), a force balance on an incremental element can be completed. From the system geometry:

$$R = a_1 x \tag{29}$$

$$a_1 = \frac{\sin\gamma \sin(\alpha_1 + \alpha_2)}{\sin\lambda \cos\alpha_2 \sin(\gamma + \beta_1)} \tag{30}$$

$$\lambda = \alpha_1 + \alpha_2 + \beta_1 + \beta_2 \tag{31}$$

$$\gamma = \frac{\pi}{2} - \frac{\lambda}{2} \tag{32}$$

The arc centre, *O*, has coordinates *(O_x, O_z)* in *(X,Z)* space, where:

$$\begin{aligned} O_x &= x - R\cos(\alpha_2 + \beta_2) \\ O_z &= x\tan\alpha_2 - R\sin(\alpha_2 + \beta_2) \end{aligned} \tag{33}$$

Point *P* has coordinates in *(X,Z)* space of:

$$X = O_x + R\cos\varepsilon = x + R(\cos\varepsilon - \cos(\alpha_2 + \beta_2)) = x\{1 + a_1(\cos\varepsilon - \cos(\alpha_2 + \beta_2))\}$$
$$Z = O_z + R\sin\varepsilon = x\tan\alpha_2 + R(\sin\varepsilon - \sin(\alpha_2 + \beta_2)) = x\{\tan\alpha_2 + a_1(\sin\varepsilon - \sin(\alpha_2 + \beta_2))\}$$

(34)

The R-ε coordinate system is not orthogonal-curvilinear, as shown in Figures 35 and 36. The line of constant ε between the two arcs is *FG*. This must be considered when force balances are constructed. The centre point of the upper arc does not coincide with the centre point of the lower arc - the arc centre moves from point *O* to O_1, where:

$$OO_1 = \delta O \tag{35}$$

Figure 35 shows arc radii at angle ε for curves at *x* and $x + \delta x$. Lines O_1FE and *OMCD* are parallel, with distance *CD* equal to thickness δw. *M* is the normal projection from point O_1 onto line *OMCD*. This figure is superseded by Figure 36, which takes account of the arcs precession through the hopper. Figure 36 was used to incorporate findings after Lamé-Maxwell (Maxwell 1853, Coker et al 1957).

According to Figure 36, therefore:

$$OMCD = O_1FE + OM \tag{36}$$

OMC is the radius of the arc at $x = a_1 x$

$CD = \delta w$

O_1FE is the radius at $x + \delta x = a_1(x + \delta x)$

$$OM = \delta O\cos(\varepsilon - \eta_1) \tag{37}$$

$$\delta w = a_1\delta x + \delta O\cos(\varepsilon - \eta_1) \tag{38}$$

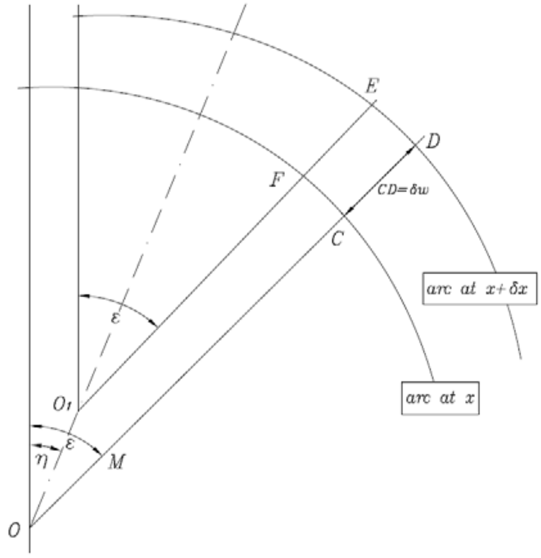

Figure 35. Arc radii for curves at x and $x+\delta x$ (prior to Lamé-Maxwell modification – Matchett 2004,2006a,2006b, Matchett et al 2007)

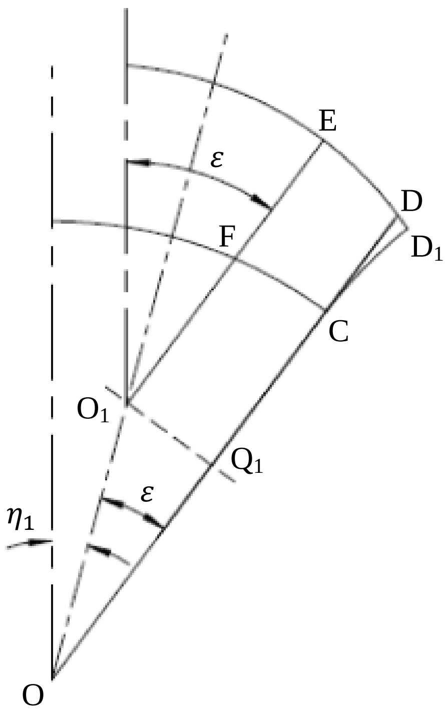

Figure 36. Arc radii for curves at x and $x + \delta x$ ('Lamé-Maxwell' version)

From equation 38,

$$\delta O_x = \{1 - a_1 \cos(\alpha_2 + \beta_2)\}\delta x$$
$$\delta O_z = \{\tan\alpha_2 - a_1 \sin(\alpha_2 + \beta_2)\}\delta x$$

$$\delta O = \sqrt{\left(\frac{\delta O_x}{\delta x}\right)^2 + \left(\frac{\delta O_z}{\delta x}\right)^2}\,\delta x \tag{39}$$

Hence:

$$\left(\frac{\partial w}{\partial x}\right) = a_1 + a_2 \cos(\varepsilon - \eta) \tag{40}$$

$$a_2 = \frac{\partial O}{\partial x} = \sqrt{\left(\frac{\delta O_x}{\delta x}\right)^2 + \left(\frac{\delta O_z}{\delta x}\right)^2}$$
$$\therefore a_2 = \sqrt{\{1 - a_1 \cos(\alpha_2 + \beta_2)\}^2 + \{\tan\alpha_2 - a_1 \sin(\alpha_2 + \beta_2)\}^2} \tag{41}$$

and:

$$\eta_1 = \arctan\left(\frac{\delta O_z}{\delta O_x}\right) = \arctan\left\{\frac{\tan\alpha_2 - a_1 \sin(\alpha_2 + \beta_2)}{1 - a_1 \cos(\alpha_2 + \beta_2)}\right\} \tag{42}$$

A benefit of the circular arch approach results from defining an incremental element that is co-incident with the directions of principal stresses. Calculation of shear stress is therefore not required in the analysis. In Figure 36, principal stress σ_R acts on surfaces *CF* and *DE*. While *CD* and *EF* are normal to line *CF*, they are not normal to line *DE*, due to precession of the arc centre from *O* to O_1. The radius from O_1 normal to *DE* is at angle $(\varepsilon + \delta\psi)$ to the vertical. Therefore the surfaces on which σ_ε acts as a principal stress must be curved, as shown in Figure 36, and the incremental element upon which the force balance is based will be CD_1E_1F. σ_ε can be defined as a major principal stress acting upon the curved surface between $(R(x),\varepsilon)$ and $(R(x+\delta x),(\varepsilon+\delta\psi))$.

As shown in Figure 36, surface CD_1 has radius R_2 and straight line CD_1 subtends an angle $\delta\psi/2$ with *CD*. Taking *CD* as δw, then:

$$\delta w \cos\left(\delta\psi/2\right) = R_2\delta\psi + soe \tag{43}$$

where *soe* are second order effect that vanish in the limit.

Therefore, in the limit as δx and $\delta\varepsilon$ tend to zero, $\delta\psi$ will also tend to zero, and:

$$R_2 = \frac{\partial w}{\partial x} \Big/ \frac{\partial \psi}{\partial x} \tag{44}$$

Similarly, point *E* and *E₁* will have approximately the same horizontal coordinate, in the limit as δx and $\delta\varepsilon$ tend to zero:

$$(R+\delta x)\sin\varepsilon = \delta O\sin\eta + (R+\delta R)\sin(\varepsilon+\delta\psi) + soe \tag{45}$$

In the limit, equation 45 gives:

$$\frac{\partial\psi}{\partial x} = \frac{a_2\{\cos(\varepsilon-\eta)\sin\varepsilon - \sin\eta\}}{a_1 x\cos\varepsilon} = \frac{a_2\{\cos(\varepsilon-\eta)\sin\varepsilon - \sin\eta\}}{R\cos\varepsilon} = \frac{a_2\sin(\varepsilon-\eta)}{R} \tag{46}$$

$$\therefore R_2 = \frac{R(a_1 + a_2\cos(\varepsilon-\eta_1))}{a_2\sin(\varepsilon-\eta_1)} \tag{47}$$

Force balance equations can now be found from the assumptions and equations set out about. Force balance equations are derived in Appendix Two, Chapter 9.4.

The two-dimensional wedge hopper can be represented by use of the circular arc geometry shown in Figure 32. The angles α_1 and α_2 take non-zero values. The assumptions used for this method are identical to those listed for the parallel-sided vessel case, and equations 38 to 41 are identical for both cases.

Two-dimensional horizontal and vertical force balances on the incremental element, shown in Figure 32, give:

$$-\frac{\partial}{\partial x}[R\sigma_R\cos\varepsilon] + \frac{\partial}{\partial\varepsilon}\left[\sigma_\varepsilon\left(\frac{\partial w}{\partial x}\right)\sin\varepsilon\right] - R\left(\frac{\partial w}{\partial x}\right)\rho g - \cos\varepsilon\left\{\sigma_R a_2\cos(\varepsilon-\eta) + R\frac{\partial\sigma_R}{\partial\varepsilon}\frac{\partial\psi}{\partial x}\right\}$$
$$+\sigma_R a_2\sin(\varepsilon-\eta)\sin\varepsilon = 0 \tag{48}$$

$$-\frac{\partial}{\partial x}\left[R\sigma_R \sin\varepsilon\right]-\frac{\partial}{\partial\varepsilon}\left[\sigma_\varepsilon\left(\frac{\partial w}{\partial x}\right)\cos\varepsilon\right]-\sin\varepsilon\left\{\sigma_R a_2\cos(\varepsilon-\eta)+R\frac{\partial\sigma_R}{\partial\varepsilon}\frac{\partial\psi}{\partial x}\right\}$$
$$-\sigma_R a_2\sin(\varepsilon-\eta)\cos\varepsilon=0 \tag{49}$$

4.2 Spreadsheet-based numerical solution

The particular solutions to the derivatives for the wedge hopper case can now be found using the force balance equations 48 and 49. Derivation of these equations can be found in Appendix Two, Chapter 9.4.

$$\frac{\partial\sigma_R}{\partial x}=\frac{F}{R}-\frac{\cos\varepsilon}{R\sin\varepsilon}\frac{\partial F}{\partial\varepsilon}-\frac{1}{R}\left\{\sigma_R a_2\cos(\varepsilon-\eta)+R\frac{\partial\sigma_R}{\partial\varepsilon}\frac{\partial\psi}{\partial x}\right\}-\frac{\sigma_R a_2\sin(\varepsilon-\eta)\cos\varepsilon}{R\sin\varepsilon}-\frac{a_1\sigma_R}{R} \tag{50}$$

$$\frac{\partial F}{\partial\varepsilon}=R\left(\frac{\partial w}{\partial x}\right)\rho g\sin\varepsilon-\sigma_R a_2\sin(\varepsilon-\eta) \tag{51}$$

For representation of the wedge hopper case *R* is a variable, and the entire form of equation 40 is required due to non-zero hopper half angles. Derivation is shown in Appendix Two, Chapter 9.3.

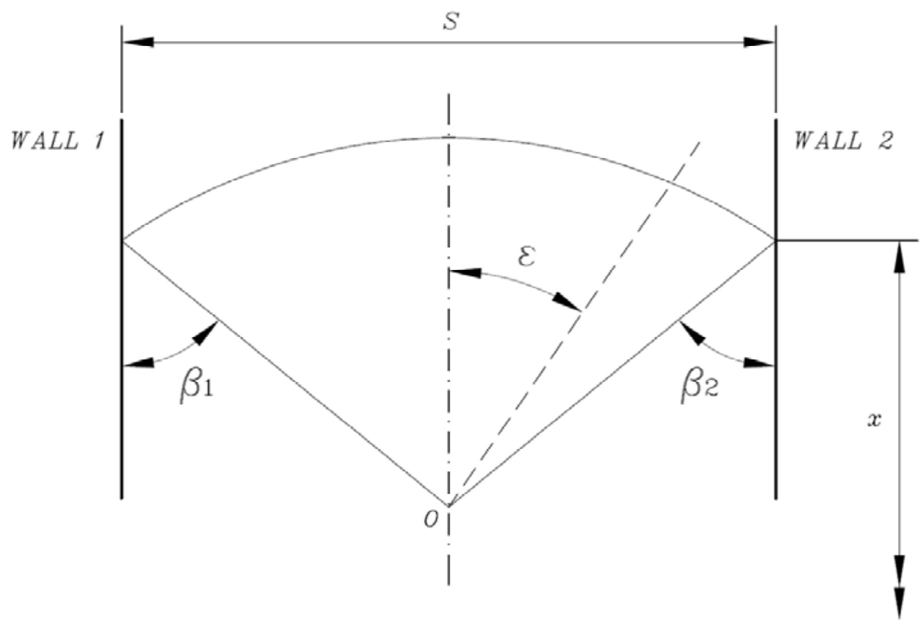

Figure 37. Model geometry for parallel-sided vessel

Two-dimensional parallel-sided silo and wedge hopper

The model geometry shown in Figure 32 can be used to represent the parallel-sided vessel case, by setting α_1 and α_2 to zero as in Figure 37.

In the parallel-sided case R is constant, with arc normal to the left-hand wall β_1 and arc normal to the right-hand wall β_2. The arch width is S, therefore:

$$R = \frac{S}{(\sin\beta_1 + \sin\beta_2)} \tag{52}$$

And from equation 40,

$$\frac{\partial w}{\partial x} = \cos\varepsilon \tag{53}$$

since a_1 is equal to zero and a_2 is equal to unity

The model presented in Chapter 4.1 has been set-up on spreadsheet software, and is made up of eight separate worksheets per case. Equations 50 and 51 have been used to form the basis of the model. An explanation of the spreadsheet-based models is given in Appendix Three, Chapters 10.1 and 10.2.

4.3 QBasic algorithm/programming

To improve flexibility of the model, QBasic programming language was used to produce an algorithm capable of an increased number of incremental elements. In Chapters 4.3.1 and 4.3.2, flow charts explain the QBasic algorithms for the cases of two-dimensional parallel-sided silo and wedge hopper. The QBasic algorithms are included in Appendix Four.

4.3.1 QBasic algorithm for two-dimensional parallel-sided silo case

Flow chart for QBasic two-dimensional parallel-sided silo algorithm:

Two-dimensional parallel-sided silo and wedge hopper

LINES 9 TO 34: USER INPUT OF MATERIAL PHYSICAL PROPERTIES. THESE DO NOT CHANGE THROUGHOUT PROGRAM.	CONSTANTS INPUT/CALCULATED: RHO, phi_w, phi, pi, T, Fc, Co
LINES 36 TO 122: USER INPUT OF SILO AND MODEL GEOMETRY DATA. THESE VARIABLES DO NOT CHANGE DURING PROGRAM ITERATIONS. ALPHA AND NU SET TO ZERO FOR SILO	CONSTANTS INPUT/CALCULATED: H, H2, ALPHA, BETA, LAMBDA, GAMMA, A1, A2, NU, J, DELTA_X_INC, DELTA_ETA_INC, DELTA_X, DELTA_ETA, ETA, X, PW_WRTX, R, PPSI_WRTX
LINES 124 TO 141: DIMENSIONING OF ARRAYS FOR VARIABLES THAT CHANGE DURING SUCCESSIVE ITERATIONS OF THE PROGRAM. INITIAL VALUES FOUND TO BE NECESSARY AND THEREFORE USED FOR SIG_R AND F: ACTUAL INITIAL VALUES BASED OF REVIEW OF EXCEL METHOD	ARRAYS DIMENSIONED: PF_WRTETA, PSIG_R_WRTETA, SIG_ETA, F, PSIG_R_WRTX, SIG_R
LINES 143 TO 151 (CLOSES ON LINE 344): NEWTON-RAPHSON TYPE METHOD EMPLOYED TO CREATE WHILE LOOP. WHILE DIFFERENCE BETWEEN SUCCESIVE ITERATIONS OF FINAL ROW OF SIG_R MATRIX IS GREATER THAN 0.1, THE PROGRAM WILL CONTINUE TO CYCLE.	WHILE LOOP CONDITIONS: Y# = 0, DIFF# = 1, Numberofiterations = 0, DIFF >= 0.1
LINES 153 TO 159: CALCULATE PF_WRTETA MATRIX USING ETA-DIRECTION FORCE BALANCE EQUATION (INITIAL CONDITION USED FOR SIG_R).	FUNCTION OF: SIG_R

Two-dimensional parallel-sided silo and wedge hopper

LINES 161 TO 175: CALCULATE PSIG_R_WRTETA MATRIX USING FINITE DIFFERENCE METHOD (LH WALL USES FORWARD DIFFERENCE, RH WALL BACKWARD DIFFERENCE, REMAINDER CENTRAL DIFFERENCE).	FUNCTION OF: SIG_R
LINES 177 TO 186: CALCULATE SIG_ETA MATRIX USING F/PW_WRTX WITH A CENTRAL BOUNDARY CONDITION OF MOHR-COULOMB CRITERION SIG_ETA=J*SIG_R+(J-1)*T.	FUNCTION OF: F, SIG_R
LINES 188 TO 202: CALCULATE F MATRIX USING FORWARD AND REVERSE EULER METHOD FROM CENTRAL BOUNDARY CONDITION OF PW_WRTX*SIG_ETA.	FUNCTION OF: SIG_ETA, PF_WRTETA
LINES 204 TO 210: CALCULATE PSIG_R_WRTX MATRIX USING R-DIRECTION FORCE BALANCE EQUATION.	FUNCTION OF: PF_WRTETA, SIG_R, PSIG_R_WRTETA, PPSI_WRTX
LINES 212 TO 222: CALCULATE SIG_R MATRIX USING REVERSE EULER METHOD FROM BOUNDARY CONDITION OF ZERO (AT MATERIAL SURFACE).	FUNCTION OF: PSIG_R_WRTX

LINES 224 TO 324: OUTPUT VARIABLES TO CSV FILES

LINES 326 TO 344: CLOSING STATEMENTS OF WHILE LOOP AND END PROGRAM, PRINT NUMBER OF ITERATIONS. NUMBER OF ITERATIONS LIMITED ON LINE 342.

The QBasic programming code for two-dimensional silo case is provided in Appendix Four, Chapter 11.1.

4.3.2 QBasic algorithm for two-dimensional wedge hopper case

Flow chart for QBasic two-dimensional wedge hopper algorithm:

LINES 9 TO 34: USER INPUT OF MATERIAL PHYSICAL PROPERTIES. THESE DO NOT CHANGE THROUGHOUT PROGRAM.	CONSTANTS INPUT/CALCULATED: RHO, phi_w, phi, pi, T, Fc, Co

LINES 36 TO 135: USER INPUT OF HOPPER AND MODEL GEOMETRY DATA. THESE VARIABLES DO NOT CHANGE DURING PROGRAM ITERATIONS	CONSTANTS INPUT/CALCULATED: H, H2, ALPHA1, ALPHA2, BETA1, BETA2, LAMBDA, GAMMA, A1, A2, NU, J, DELTA_X_INC, DELTA_ETA_INC, DELTA_X, DELTA_ETA, ETA, X, PW_WRTX, R, PPSI_WRTX

LINES 137 TO 154: DIMENSIONING OF ARRAYS FOR VARIABLES THAT CHANGE DURING SUCCESSIVE ITERATIONS OF THE PROGRAM. INITIAL VALUES FOUND TO BE NECESSARY AND THEREFORE USED FOR SIG_R AND F: ACTUAL INITIAL VALUES BASED OF REVIEW OF EXCEL METHOD	ARRAYS DIMENSIONED: PF_WRTETA, PSIG_R_WRTETA, SIG_ETA, F, PSIG_R_WRTX, SIG_R

LINES 156 TO 164 (CLOSES ON LINE 367): NEWTON-RAPHSON TYPE METHOD EMPLOYED TO CREATE WHILE LOOP. WHILE DIFFERENCE BETWEEN SUCCESIVE ITERATIONS OF FINAL ROW OF SIG_R MATRIX IS GREATER THAN 0.1, THE PROGRAM WILL CONTINUE TO CYCLE.	WHILE LOOP CONDITIONS: Y# = 0, DIFF# = 1, Numberofiterations = 0, DIFF >= 0.1
LINES 166 TO 172: CALCULATE PF_WRTETA MATRIX USING ETA-DIRECTION FORCE BALANCE EQUATION (INITIAL CONDITION USED FOR SIG_R).	FUNCTION OF: SIG_R
LINES 174 TO 188: CALCULATE PSIG_R_WRTETA MATRIX USING FINITE DIFFERENCE METHOD (LH WALL USES FORWARD DIFFERENCE, RH WALL BACKWARD DIFFERENCE, REMAINDER CENTRAL DIFFERENCE).	FUNCTION OF: SIG_R
LINES 190 TO 199: CALCULATE SIG_ETA MATRIX USING F/PW_WRTX WITH A CENTRAL BOUNDARY CONDITION OF MOHR-COULOMB CRITERION SIG_ETA=J*SIG_R+(J-1)*T.	FUNCTION OF: F, SIG_R
LINES 201 TO 215: CALCULATE F MATRIX USING FORWARD AND REVERSE EULER METHOD FROM CENTRAL BOUNDARY CONDITION OF PW_WRTX*SIG_ETA.	FUNCTION OF: SIG_ETA, PF_WRTETA
LINES 217 TO 223: CALCULATE PSIG_R_WRTX MATRIX USING R-DIRECTION FORCE BALANCE EQUATION.	FUNCTION OF: PF_WRTETA, SIG_R, PSIG_R_WRTETA, PPSI_WRTX

Two-dimensional parallel-sided silo and wedge hopper

LINES 225 TO 235: CALCULATE SIG_R MATRIX USING REVERSE EULER METHOD FROM BOUNDARY CONDITION OF ZERO (AT MATERIAL SURFACE).	FUNCTION OF: PSIG_R_WRTX

⇩

LINES 237 TO 347: OUTPUT VARIABLES TO CSV FILES

⇩

LINES 349 TO 367: CLOSING STATEMENTS OF WHILE LOOP AND END PROGRAM, PRINT NUMBER OF ITERATIONS. NUMBER OF ITERATIONS LIMITED ON LINE 365.

The QBasic programming code for two-dimensional wedge hopper case is shown in Appendix Four, Chapter 11.2.

4.4 Model validation

A comparison of stress distributions between old (Matchett 2004) and new models demonstrated the below characteristics when a two-dimensional wedge hopper is modelled. Hopper half-angle is 15 degrees and material surface height is 3.3 metres. Figure 38 considers the wedge hopper in its entirety. Figure 39 considers a section of the wedge hopper between depths 1.0 and 0.5 metres.

1. In Figure 38, values from current ‘Lamé-Maxwell’ models are indicated by curve C for stresses at the vessel walls and curve D for stresses along the vessel centreline. Values from previous models are indicated by curve A for wall stresses and curve B for stresses along the vessel centreline.
2. At shallow depths within the granular materials, stress distribution values were similar. This is indicated by all curves in Figure 38 for 3.3 to 3.1 metres depth.
3. With increasing depths, from 3.2 to 1.1 metres, curve C (Figure 38) showed a large variation in stress values when compared to A: at 1.1 metres 200%

variation. However curve B approximates the path of curve A. Hence for the previous models, there was not a large variation is stress values horizontally across the vessel (at 1.1 metres depth only 8% variation).

4. In Figure 39, experimental data values for wall stresses are shown by curve E, with experimental data values for centreline stresses are shown by curve F. For this small area of the wedge hopper, the new models show correlation with the experimental data at both the hopper wall and along the vessel centreline (only 5% average variation), while the previous models do not. In Figure 45 (Section 4.6.1), support is given to horizontal stress variation across vessels by close correlation between values predicted by the new models and experimental data taken from centreline of the pyramidal hopper. It can be seen in Figure 44 that stresses at the hopper wall are 7.9×10^3 Pa, while at the vessel centre stress are higher at 1.6×10^4 Pa. This can be seen in more detail in Walker and Blanchard's (1967) article.

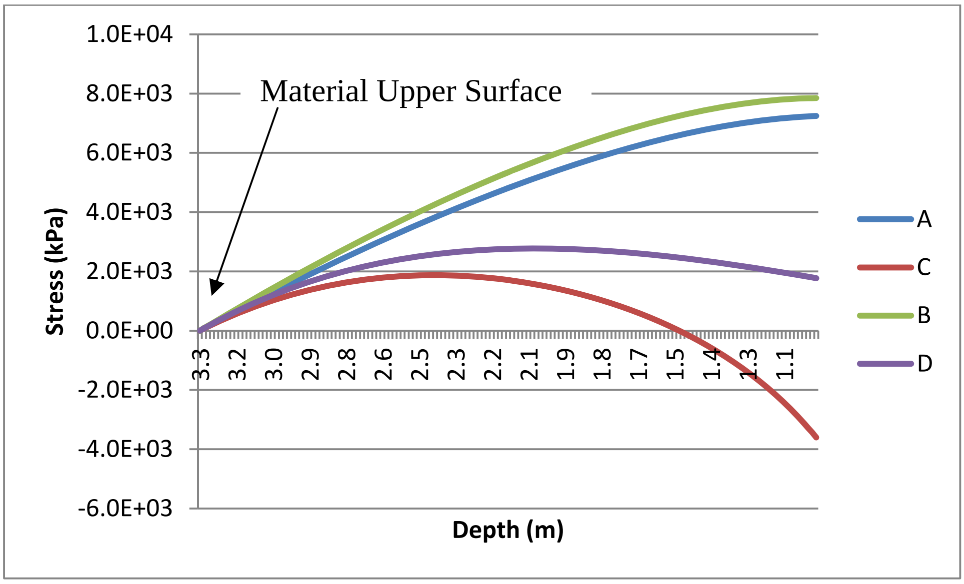

Figure 38. Comparison of current and previous versions of principal stress arc models

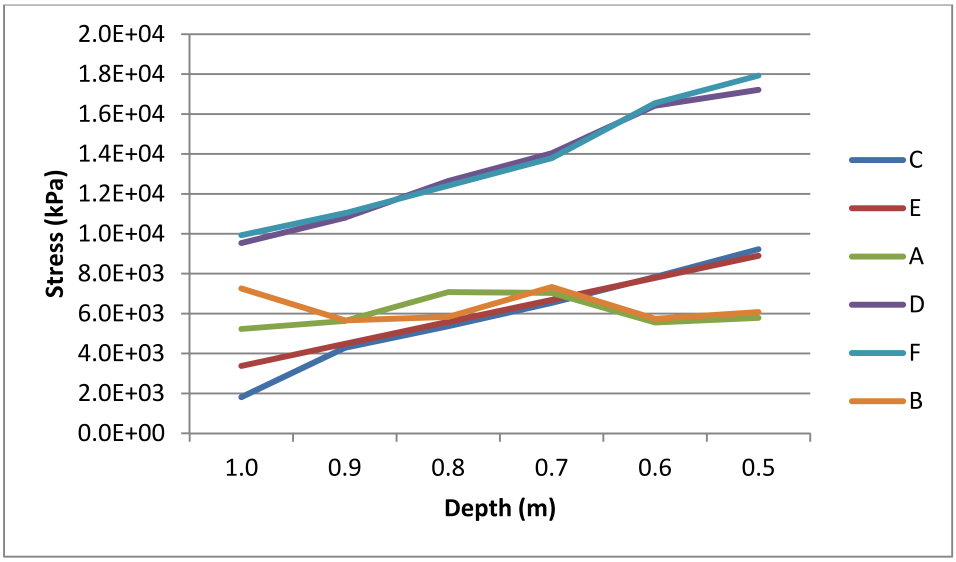

Figure 39. Comparison of current and previous versions at greater depth.

In order to further validate the new models, data from the literature was used to compare stress distributions from the new version of the principal stress arc method. Yunming et al (2011) provide data from a 'large-scale' wedge hopper finite element analysis model, as shown in Figure 40. The dimensions of the steep-sided hopper are expected to produce mass flow. The finite element analysis conducted by Yunming et al consisted of filling and discharging. The filling process is a discontinuous stress/displacement analysis and, within the finite element software Abaqus, the option of quasi-static analysis in Abaqus/Explicit was used to improve convergence. Loads were applied to the element nodes using the 'switch-on loading' of gravity.

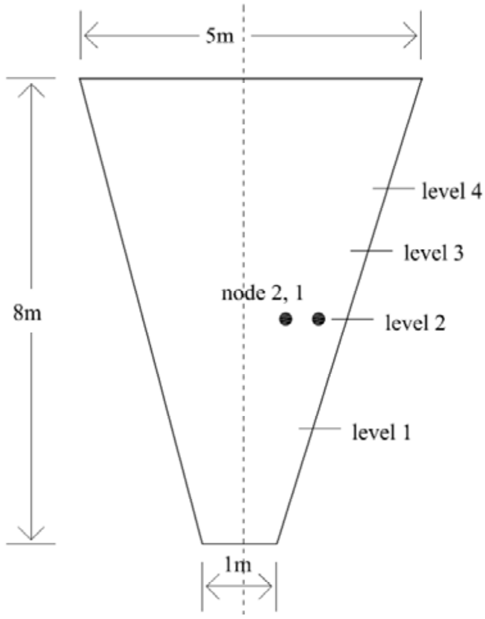

Figure 40. The geometry of the wedge hopper (Yunming et al 2011)

Two-dimensional parallel-sided silo and wedge hopper

A constant bulk density ρ_b of 1417 kg/m^3 was assumed for the granular material used. Angle of internal friction ϕ was given as 35 degrees and wall friction angle ϕ_W as 18 degrees.

A non-coaxial yield vertex FEA model was used, the granular material is modelled assuming elastic-perfectly plastic behaviour with a Drucker-Prager yield surface. The non-coaxiality is the non-coincidence between principal stresses and principal plastic strain rates (Yunming et al 2011). The Drucker-Prager yield surface follows similar boundaries to the Mohr-Coulomb failure surface (Drucker and Prager 1952). In the principal stress arc models, Mohr-Coulomb theory is used to provide an initial conditions for calculations. The Drucker-Prager method can be used for three-dimensional applications. The finite element mesh contained 10 increments or node points in the horizontal direction and 60 increments in the vertical direction; first-order 4-node quadrilateral elements were used. The research project models made use of at least 200 increments in the *x*-direction and 50 increments in the ε-direction.

The models produced by the current principal stress arc models do not take account of dynamic forces; therefore the static ‘end-of-filling’ values were used for comparison i.e. those without dynamic forces.

Figure 41 below provides a comparison of results calculated by two different stress analysis methods: the principal stress arc method and Yunming et al’s Finite Element model. This exercise was carried out for validation purposes. FEA results are indicated by ‘SIG FEA’ for wall normal stress data. Wall normal stress data calculated by the principal stress arc method is presented by ‘SIG W’.

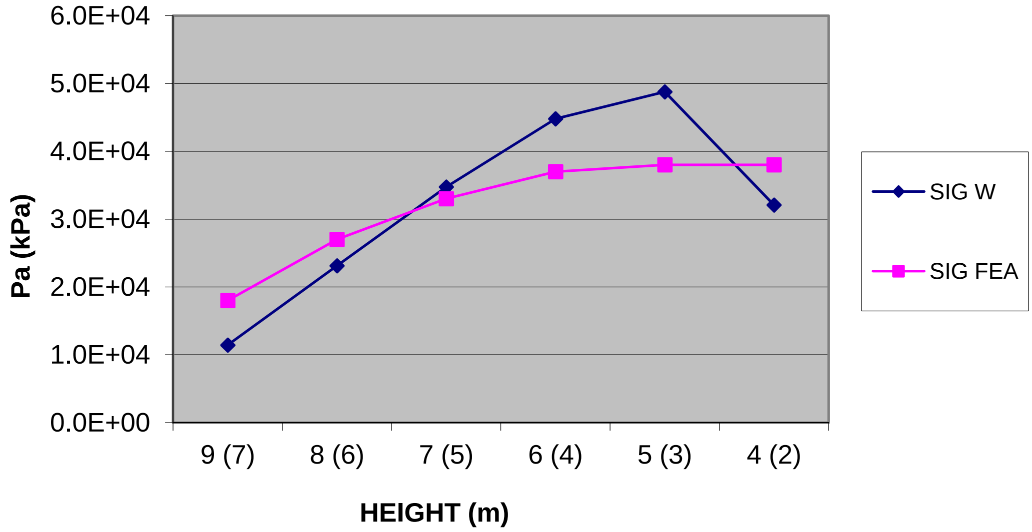

Figure 41. Comparison of Yunming hopper FEA data to calculated values: β = 0.21 rad, J = 0.35, T = 0 Pa, OP = 0 Pa

The validated two-dimensional wedge hopper algorithm was calibrated by use of data fitting, explained in Appendix Three (Chapter 10.1), and by use of material properties information sourced from the literature.

4.5 Experimental data sourced from the literature

In order to compare this newly developed method with experimental data, a complete literature survey was conducted and the most relevant experimental data have been gathered and used for comparison. They are:

1. Schulze and Schwedes 1994
2. Berry et al 2000
3. Walker and Blanchard 1967
4. Tuzun and Nedderman 1985
5. Drescher et al 1995

A preliminary comparison with experimental data listed above in 1 and 2 was published in Matchett et al’s paper (2009). Work by Schulze and Schwedes (1994) was used for comparison of stresses normal to the hopper wall. Data produced by

Berry et al (2000) was compared to critical outlet widths i.e. the hopper outlet width at which cohesive arching will begin to occur.

4.5.1 Walker and Blanchard experimental apparatus

Walker and Blanchard (1967) provided data from a pyramidal hopper shown in Figure 42. The hopper is described as pyramidal in shape however two of the sides were noted to be parallel to each other.

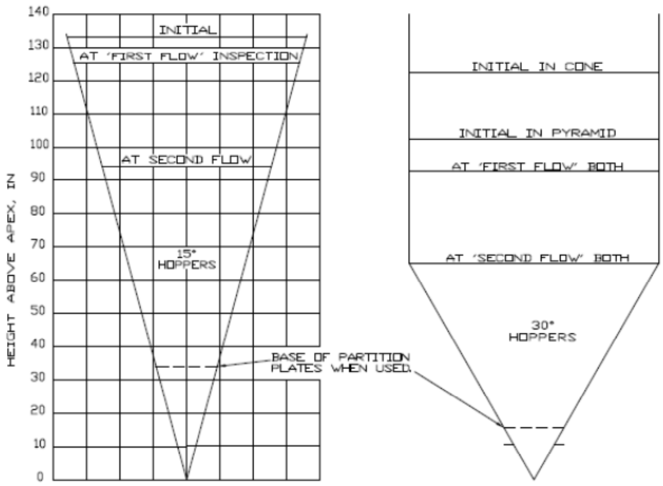

Figure 42. Fill heights of experimental hoppers (Walker and Blanchard 1967)

The granular material used was fine coal (International Dry Fines Rank 203), with a low moisture content of around 3%. The angle of internal friction ϕ was 41 degrees and the angle of wall friction ϕ_W 16 degrees.

Pressure cells were used to provide averaged wall pressures throughout the height of the hopper. The values under consideration were those produced shortly after filling. For initial modelling of the 15 degree hopper (Figure 42), the tensile intercept *T* was estimated to be equal to 2000 Pa as the presence of moisture can cause cohesion. Use of the *T*-value is explained in Appendix Two, Chapter 9.5. Bulk density ρ_b was stated in the literature to equal 812 kg/m^3.

J- and β-values were set to their active limits: equal to 0.21 and 0.36 respectively. Initial values for β and *J* were used with the intention of reproducing the active stress case, in accordance with equations 54 and 55 (Rankine 1857, Walker 1966, Nedderman 1992 and Matchett 2004).

$$\beta_{ACTIVE} = \frac{1}{2}\left(\phi_W - arcsin\left(\frac{sin\phi_W}{sin\phi}\right)\right) \tag{54a}$$

$$\beta_{PASSIVE} = \frac{1}{2}\left(\phi_W + arcsin\left(\frac{sin\phi_W}{sin\phi}\right)\right) \tag{54b}$$

$$J_{ACTIVE} = \frac{1-sin\phi}{1+sin\phi} \tag{55a}$$

$$J_{PASSIVE} = \frac{1+sin\phi}{1-sin\phi} \tag{55b}$$

Analysis of the active case was selected for the following reasons:

- Stresses in the active case are often found to be higher than within the passive case (Tardos 1999).
- The current force balance equations used for modelling of these systems do not include inertial terms.
- Several data sources were found in the literature detailing wall stress distributions from static/'end-of-filling' media (Wojcik and Tejchman 2008, Rao and Venkateswarlu 1974, Walker and Blanchard 1967, Diniz and Nascimento 2006).

The wedge hopper geometry force balance equations, 48 and 49, do not consider inertial terms therefore values at incipient flow were assumed. The flow regime of the pyramidal hopper was noted to be initially mass flow, with funnel flow occurring in the last stages of discharge. It is interesting to note that Walker and Blanchard (1967) indicate their experimental data shows active states stresses to be higher than the passive stress state. Tuzun and Nedderman (1985) indicate that some theoretical methods shown that actual stresses during discharging may be orders of magnitude higher than those at the end of filling. Testing by Hancock (1970) demonstrated higher stresses at the end of filling.

4.5.2 Tuzun and Nedderman experimental apparatus

Tuzun and Nedderman (1985) provided data from a parallel-sided silo shown in Figure 43.

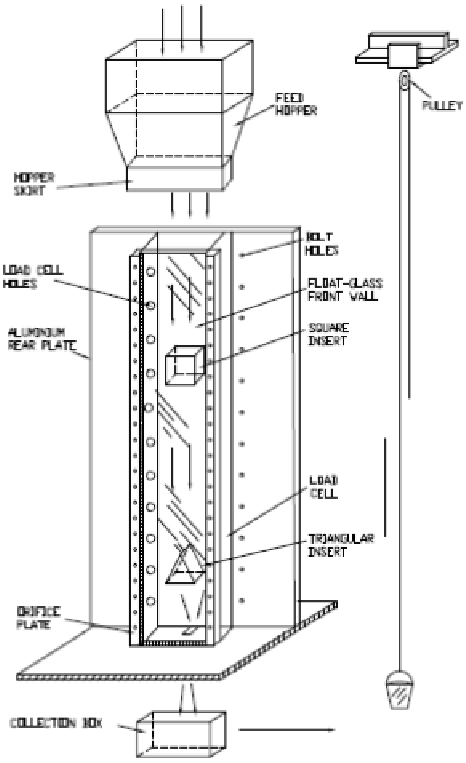

Figure 43. Experimental silo apparatus (Tuzun and Nedderman 1985)

The granular materials used for collection of experimental data were stated to be mustard seeds and polythene granules. For the mustard seeds, the angle of internal friction ϕ was 30 degrees and the angle of wall friction ϕ_W 8 degrees. For the polythene granules, the angle of internal friction ϕ was 40 degrees and the angle of wall friction ϕ_W 18 degrees.

Load cells were used to provide wall stresses throughout the height of the hopper. The values under consideration were those produced at the end of filling. For initial modelling of the silo (Figure 41), T was estimated to be equal to 0 Pa as the granular materials were not assumed to be cohesive. J- and β-values were set to their active limits. Bulk density ρ_b was stated in the literature to equal 750 kg/m^3 for the mustards seeds and 500 kg/m^3 for the polythene granules.

4.5.3 Drescher et al experimental apparatus

Drescher et al (1995) provided data from a plane wedge hopper of variable geometry. The hopper had adjustable side walls 0.6 metres long by 0.7 metres high. Side wall inclination to the vertical α could be varied from 10 to 40 degrees. Vertical walls were placed at each end of the hopper. A 1.0 metre high silo section was positioned above the hopper, to prevent spillage.

A number of granular material types were used, over a range of wall half-angles. The materials used for comparison to calculated data included limestone (water content 3.2%), coal and cement. The authors (Drescher et al) compared experimental data to critical outlet dimensions according to Jenike, Walker, Mroz and Szymanski, Arnold and McLean and Enstad. Non-linear and linear yield loci were used in calculation of theoretical values, as shown in Table 1.

Predicted outlet size for α_c=20°, (m)

Material	Hopper	Jenike [6]			Walker [4]			Mroz and Szymanski [10]			Arnold and McLean [11,12]			Enstad [4]
		Linear IYLs		Non-Lin IYLs	Linear IYLs		Non-Lin IYLs	Linear IYLs		Non-Lin IYLs	Linear IYLs		Non-Lin IYLs	
		Eq. (1)	Eq. (3)	Eq. (1)	Eq. (1)	Eq. (3)	Eq. (1)	Eq. (1)	Eq. (3)	Eq. (1)	Eq. (1)	Eq. (3)	Eq. (1)	Linear IYLs
Limestone	plane	0.34	0.36	0.36	1.35	Infinite	1.12	0.93	0.94	0.78	0.33	0.36	0.32	0.29
(w=5%)	conical	0.85	0.84	0.77	1.42	1.50	1.24	1.45	1.34	1.29	0.84	0.84	0.79	0.53
Limestone	plane	0.16	0.34	0.16	2.76	Infinite	2.76	0.70	0.60	0.70	0.17	0.34	0.17	0.22
(w=8.2%)	conical	0.35	0.70	0.37	0.59	0.70	0.59	0.58	0.83	0.58	0.35	0.71	0.42	0.54
Gypsum	plane	0.39	0.50	0.41	Infinite	Infinite	Infinite	2.23	Infinite	1.79	0.36	0.49	0.38	0.33
Coal	plane	0.31	0.81	0.24	0.84	0.89	0.60	0.63	1.03	0.44	0.32	0.81	0.21	0.72
	conical	0.75	1.72	0.51	0.79	1.50	0.54	0.78	1.76	0.53	0.69	1.71	0.47	1.48
Cement	plane	0.21	0.36	0.22	1.40	Infinite	1.03	0.71	0.66	0.61	0.21	0.36	0.22	0.27
	conical	0.47	0.77	0.48	0.84	0.85	0.75	0.85	0.98	0.79	0.48	0.78	0.49	0.56

Table 1. Predicted outlet size for α = 20 degrees (Drescher et al 1995)

4.6 Application of the method

4.6.1 Walker and Blanchard data

Comparison of calculated wall normal stress σ_W data with equivalent experimental σ values provided by Walker and Blanchard (1967) is shown below in Figure 44. As principal stress arc methods work in principal stress space, and experimental data is often reproduced as stress normal to the silo/hopper wall, Mohr's Circle theory (Mohr 1906, Hearn 2003) is required to align results. The relevant equations, 56 and 57, are shown below.

$$\sigma_W = \frac{1}{2}(\sigma_\varepsilon + \sigma_R) + \frac{1}{2}(\sigma_\varepsilon - \sigma_R)cos2\alpha \quad (56)$$

$$\tau_W = \frac{1}{2}(\sigma_\varepsilon - \sigma_R)sin2\alpha \quad (57)$$

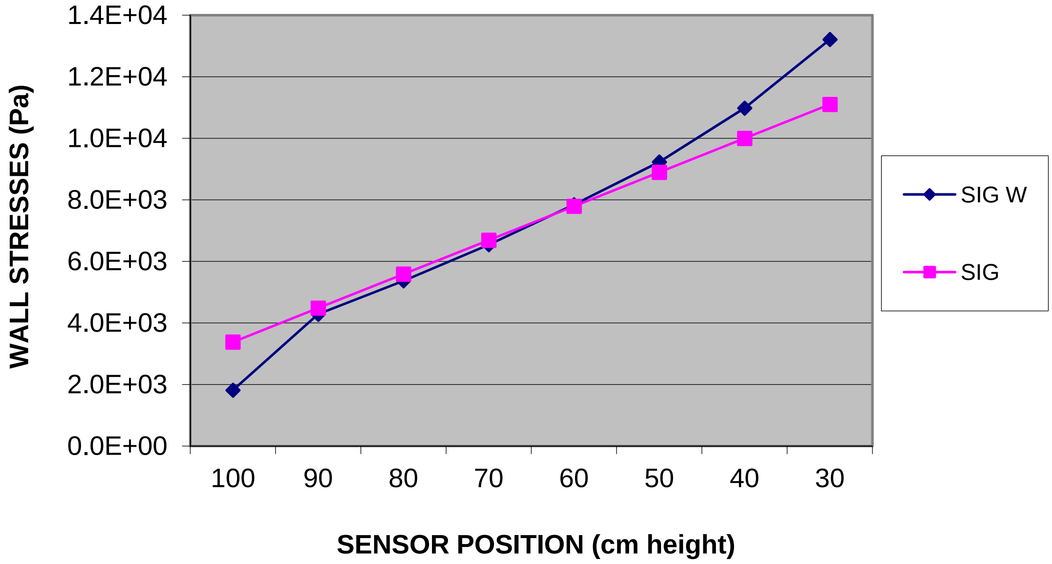

Figure 44. Comparison of Walker and Blanchard (1967) 15-degree hopper normal wall stress data to calculated values: β = 0.07 rad, J = 0.7, T = 500 Pa, OP = 0 Pa

The top surface of the material is at around 133 cm as shown in Figure 42. In the legend for Figure 44, 'SIG W' indicates σ_W-values and 'SIG' indicates σ-values. The model was fitted to the data using a least-squares approach. β, J, T and OP were selected as adjustable parameters. The Excel application 'Solver' was used to determine these values as described in Appendix Three, Chapter 10.1.

The results show reasonable agreement. A zero value of overpressure *OP* was used, as the authors (Walker and Blanchard) did not indicate any vertical silo section above the hopper. During experimental runs the top surface was noted to be raked flat. This surface profile does not coincide with the assumption of a circular principal stress arc. During test runs with the surface left ‘heaped’ (i.e. a dome shape) no significant differences in values were recorded. This gives support to the assumption of a principal stress arc at complex system boundaries where discontinuities are present.

The calculated values conformed to Mohr-Coulomb criterion limits. The central boundary condition at ε equal to zero used J equal to 0.7 i.e. approaching the active limit. This is in accordance with prior knowledge concerning filling of a hopper (Nedderman 1992). Walker and Blanchard compared their experimental data with theoretical values calculated by Walker’s method (1966), finding correlation between experimental scatter values and theoretical curves for the 15-degree hopper.

Walker and Blanchard (1967) also gave experimental data for pressures along the centre-line of the pyramidal hopper. This data is compared to the calculated values in Figure 45.

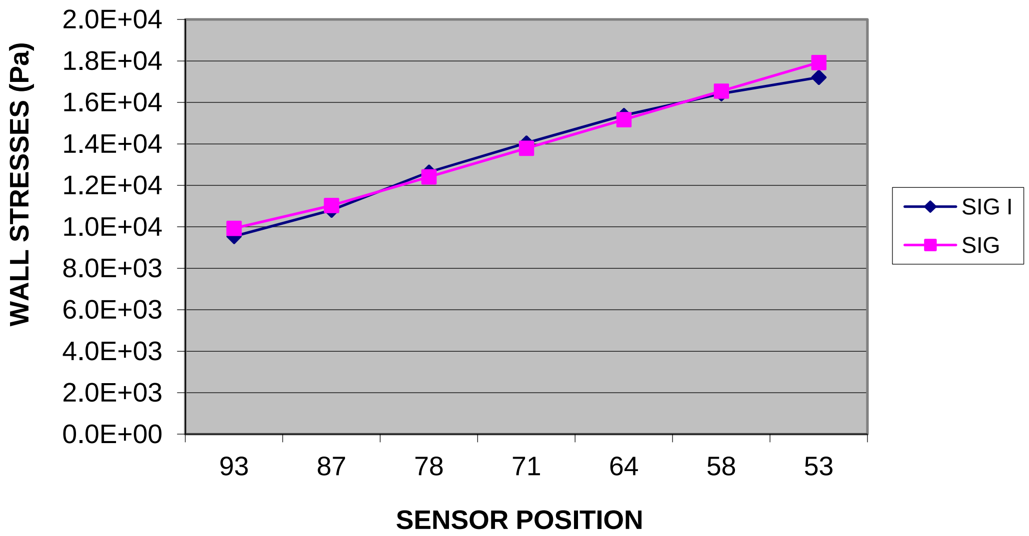

Figure 45. Comparison of Walker and Blanchard (1967) 15-degree hopper internal stress data to calculated values: β = 0.07 rad, J = 1.2, T = 500 Pa, OP = 0 Pa

The model was fitted to experimental data using a least-squares method. Similar values were used as those shown in Figure 42. The *J*-value was increased to 1.2 to provide the close correlation shown in Figure 45.

4.6.2 Tuzun and Nedderman data

Comparison of calculated wall normal stress data σ_w with results provided by Tuzun and Nedderman (1985) for mustard seeds is shown in Figure 46. The σ_a- and σ_b-values indicate upper and lower bounds for experimental data readings. In Figure 46 σ_w-values are indicated by 'SIG W', σ_a by 'SIG a' and σ_b by 'SIG b'. Tuzun and Nedderman indicated that their experimental data provided correlation to theoretical values in the active stress case during filling. Their theoretical values were calculated via the methods of Janssen (1895), Walker (1966) and Walters (1973).

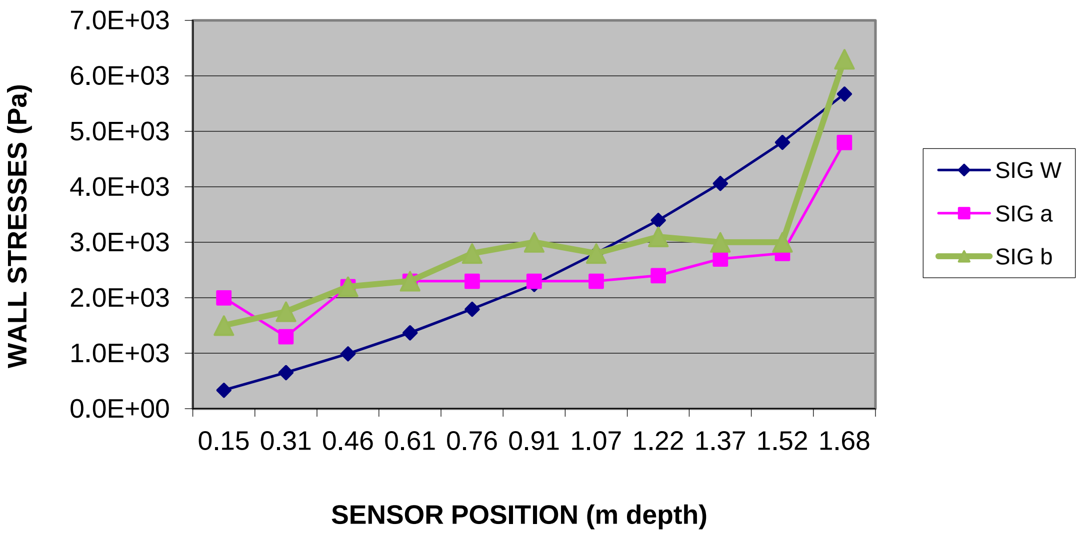

Figure 46. Comparison of Tuzun and Nedderman (1985) parallel-sided silo normal wall stress data to calculated values: β = 0.17 rad, *J* = 0.3, *T* = 0 Pa, *OP* = 0 Pa

The model was fitted to the data using a least-squares approach. β, *J*, *T* and *OP* were selected as adjustable parameters. The results did not show agreement with Mohr-Coulomb limits. Calculation of *J*-values from principal stresses using equation 70 in Chapter 5.6.6 is an indication of stability. Figure 46 shows calculated stress data that return *J*-values of 0.3. This is outside of the active limit of 0.33.

Overpressure was selected to be zero as correlation between calculated and experimental data did not improve with non-zero values. Figure 43 shows the experimental set up of the hopper. There is no indication of a silo above the hopper, hence the upper surface of the hopper is free with no overpressure from material weight above.

4.6.3 Drescher et al data

Comparison of calculated critical outlet dimensions with data provided by Drescher et al (1995) is shown in Table 2.

Material	β	J	ρ	D_{CRIT} (principal stress arc)	D_{CRIT} (experimental data)	Error
Limestone (w=3%)	0.28	1.9	1317	0.098 m	0.07 m to 0.1 m	-29 to +2%
Coal	0.26	1.5	612	0.092 m	0.13 m to 0.15 m	+41 to +63%
Cement	0.21	2	1473	0.085 m	0.05 m to 0.07 m	-41 to -18%

Table 2. Calculated outlet size for α = 20 degrees

The principal stress arc method approximated the location of a cohesive arch using the following procedure:

- Align model to experimental hopper dimensions and material properties.
- Adjust values within limits for stable results.
- Adjust J-value within limits until zero/negative σ_R–values are demonstrated across entire width of hopper.
- Read off position of first negative σ_R–values. This is the proposed location of the cohesive arch.

The calculated critical outlet dimension for limestone is 0.098 metres, cement 0.092 metres and coal 0.085 metres. The limestone material is within the dimensional range given by experimental data. The calculated critical outlet dimension for coal overestimates the experimental values. The calculated data for cement underestimates the experimental data.

Data calculated by the methods shown in Table 1 typically overestimate experimental data, in some cases by an order of magnitude. Values calculated by the Jenike (1964) method overestimate experimental data by an average of 125%. Values calculated by the Walker (1966) method overestimate experimental data by an average of 1490%. Values calculated by the Enstad (1975) method overestimate experimental data by an average of 195%.

4.7 Conclusions

To sum up: above, and within the literature (Matchett 2004), the principal stress arc method has been compared favourably to experimental data. In specific cases the proposed method improves on previous conservative methods that are in use within current industrial practice (Jenike 1964, Schulze 2008).

The two-dimensional cases are ideal ones, where stresses in the third dimension were not considered in the analysis. The silo and wedge hopper were assumed to be ‘long’ in that friction or stresses in the direction normal to the page (Figure 32 in Chapter 4.1) were not considered in the force balance equations. The principal stress arc method contains an increased number of increments in the ε- and x-directions. In Chapter 4.4 a validation exercise was successfully carried out using previous principal stress arc models and calculated data from a finite element analysis of a wedge hopper (Yunming et al 2011). The validation was feasible due to similarities in material model used: the Mohr-Coulomb criterion used in the principal stress arc method assumes a rigid-plastic failure mode with a linear yield locus (Nedderman 1992). In Chapter 4.6 calculated results from the method were compared to experimental data for wall normal stresses. In the two case studies correlation between calculated and experimental data was displayed.

As noted in Chapter 4.5, stresses calculated by the principal stress arc method were compared to Schulze and Schwedes (1994) and Berry et al (2000). The comparison showed that the principal stress arc method produced values that were in reasonable agreement with the experimental data. In some cases the principal stress arc method improved on conservative critical outlet diameter estimates made by use of prior methods. Jenike's method is frequently used in industry (Schulze 2008).

The data provided by Walker and Blanchard (1967) was compared to the principal stress arc two-dimensional wedge hopper case. The correlation shown in Figure 44 resulted from use of variables β equal to 0.07 rad, J equal to 0.7, T equal to 500 Pa and zero overpressure OP. The selected values are proposed as reasonable approximations to reality for the following reasons:

- The value of β used (0.07) is approximately at the limit of the passive stress state, given by equation 54b. Figure 27(b) demonstrates the relevant passive case.
- The Mohr-Coulomb yield function surface plot for this case shows that calculated J-values are within Mohr-Coulomb criterion limits. This is an indication that the material may form a stable, cohesive arch (Matchett 2008 et al). The value for J-input is set equal to 0.7. This value is above the active limit of 0.21, given by equation 55a. According to equation 55b the passive J-limit is equal to 4.81. An explanation of the Mohr-Coulomb yield function surface plot is given in Appendix Three, Chapter 10.1.
- T takes a non-zero value as the granular material used (coal) was indicated to contain 3% moisture, hence cohesion would be expected due surface tension of liquid 'bridges' between particles (Nedderman 1992).
- During the analysis the effect of overpressure OP was reviewed. The heaped or 'domed' surface was assumed to take the approximate shape of the principal stress arc. It is interesting to note that in their article Walker and Blanchard indicated that either a flat or domed shape of upper surface had a negligible effect on results. A zero value of overpressure was thought to be a reasonable assumption as the experimental set-up did not indicate a large vertical silo section above the hopper.

The data provided by Tuzun and Nedderman (1985) was compared to the principal stress arc two-dimensional parallel-sided silo hopper case. In their article the test materials used were mustard seeds and polyethylene granules. Figure 46 shows the resulting correlation between calculated and experimental data, for the mustard seed data. The correlation shown in Figure 46 resulted from use of variables β equal to 0.17 rad, J equal to 0.3, T equal to 0 Pa and zero overpressure OP. In summary:

- The value of β used (0.17) is approaching the limit of the active stress state, given by equation 54a. Figure 27(a) demonstrates the relevant active case.
- The Mohr-Coulomb yield function surface plot for this case shows that calculated J-values are outside of Mohr-Coulomb criterion limits. This is an indication that the material is not stable, hence the material may not be at incipient failure. The value for J-input is set at 0.3. This value is below the active limit of 0.33 by a relatively small amount. The passive J-limit for this case is equal to 3.
- T takes a zero value as the granular material used (mustard seeds) was expected to be cohesionless. It should be noted that cohesion within fine-grained materials may be attributed to Van der Waals attraction forces between particles (Nedderman 1992). Correlation to experimental data did not improve with non-zero T-values.
- A zero value of overpressure OP was used as this was dictated by the experimental set-up dictated.

Table 2, Chapter 4.6.3, compares critical outlet widths using data provided by Drescher et al (1995). Critical outlet widths calculated by the principal stress arc method were in most cases less conservative than prior methods shown in Table 1, including a method commonly used in industry (Jenike 1964, Schulze 2008) The three granular materials reviewed are listed below. Zero overpressure OP was used for all three materials, as dictated by the experimental set-up.

- Limestone with 3.2% moisture content: β set equal to 0.28 rad and J equal to 1.9. The values used were both within limits of 0.15 (passive) to 0.75 for β and 0.17 (active) to 5.97 for J. A T-value of 950 Pa was used as the material was expected to be cohesive.
- Coal: β set equal to 0.26 rad and J equal to 1.5. The values used were both within limits of 0.09 (passive) to 0.55 for β and 0.14 (active) to 7.04 for J. A zero T-value was used as the material was not expected to be cohesive.

- Cement: β set equal to 0.21 rad and J equal to 2.0. The values used were both within limits of 0.10 (passive) to 0.71 for β and 0.12 (active) to 8.34 for J. A T-value of 500 Pa was used as the material was expected to be cohesive.

In Chapter 4.6.1 experimental data from a granular material along a hopper centre-line (Walker and Blanchard 1967) is compared to results calculated by the principal stress arc method. Correlation between data sets is shown in Figure 45. The values used for this case included β equal to 0.07 rad, J equal to 1.2, T equal to 500 Pa, and a zero value of overpressure. These values are similar to those used in analysis of Walker and Blanchard wall stress data, with the exception of the increased J-value. This was increased to improve correlation, and is assumed to be reasonable as the J-value is within limits of 0.21 and 4.81. The selected value moves away from the passive limit. Very few examples of internal stress data are available within the literature.

Chapter 5.0 – Axially symmetric three-dimensional parallel-sided silo and cone hopper case studies

In this chapter the two-dimensional model presented in Chapter 4.1 is extended to cover the cases of circular, parallel-sided silos and cone hoppers. The rotational symmetry provided by these shapes is used to provide new force balance equations. The new model allows calculation of stresses including those in the third dimension – azimuthal stress σ_θ. Three-dimensional force balance equations have been derived. The analysis gives two differential equations in three unknown stresses. Hence not all stresses are specified by solution of the equations, therefore relationships between principal stresses are proposed and investigated. A relationship is proposed to provide azimuthal stress values (equation 62). Stress distributions are specified via numerical methods described in Chapter 3.5.

As with the two-dimensional case, the new model geometry was developed by Professor Andrew Matchett and was based on Matchett (2004,2006a,2006b). Modifications after Lamé-Maxwell equations (Maxwell 1853, Coker et al 1957) were completed to improve accuracy. In Chapter 4.1, Figures 35 and 36 explain this modification. Figure 35 does not take account of curvature of the incremental element in the direction normal to the principal stress arc. The three-dimensional model is documented below and was completed as part of this research project. The author of this thesis had input to the model, including assistance with development of new force balance equations, derivation of solutions for the new force balance equations with guidance from Professor Matchett and checking of proposals. The work has been subsequently presented in conference proceedings (O'Neill et al 2009).

The models are spreadsheet- and QBasic programming language-based with graphical representation, displaying stresses in three dimensions. The algorithms were developed and used for comparison with experimental data. Validation of the models was completed and reported. Seven case studies were conducted and reported, demonstrating application of the new models.

Axially symmetric three-dimensional parallel-sided silo and cone hopper

5.1 Model geometry, assumptions and resulting force balance equations

Model geometry is shown in Figures 47 and 48, demonstrating rotation of the incremental element to form an annulus with radius $\bar{r}$ around the silo centre line. The assumptions used in the new model are listed below, which are in addition to the 2-D silo and wedge hopper cases detailed in the previous chapter.

1. In three-dimensional space there are three principal stresses acting: radial stress σ_R, arc stress σ_ε and azimuthal stress σ_θ. Azimuthal stresses act on the incremental element shown, and are orientated normal to the page. This assumption replaces assumption number 6 of the previous model.

2. Azimuthal stresses act rotationally about the cone centre line.

3. The incremental element has radius of rotation $\bar{r}$ about the cone centre-line.

4. Rotational symmetry is assumed through azimuthal angle θ.

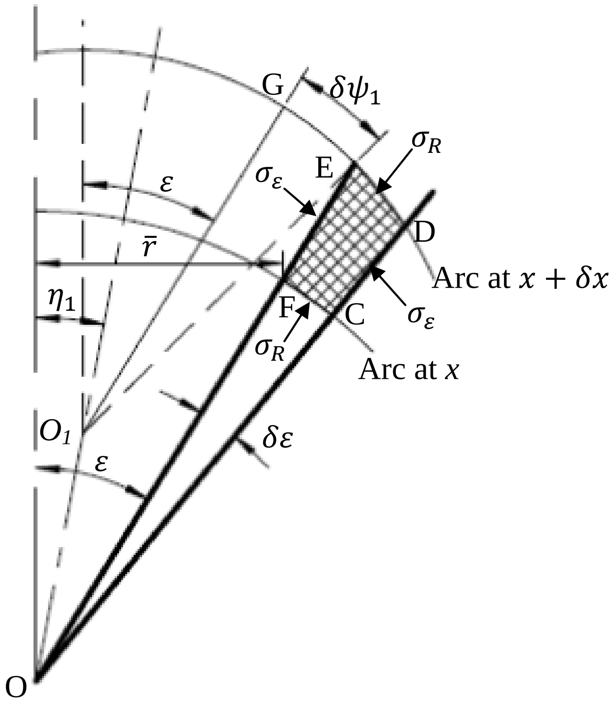

Figure 47. The three-dimensional incremental element

<u>**Axially symmetric three-dimensional parallel-sided silo and cone hopper**</u>

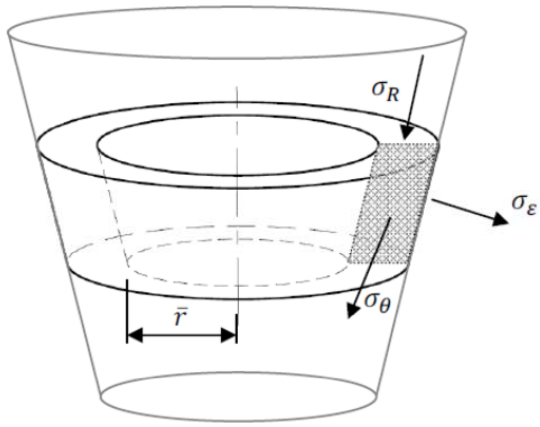

Figure 48. Stresses acting on the rotated incremental element

A detail of the incremental element is shown in Figure 48. Using the circular arc geometry initially set out by Matchett (2004), a force balance on an incremental element can be completed. Derivation is provided in Appendix Two, Chapter 9.6. Note that equations 29, 40 and 47 can be used for the cone hopper case without modification.

$$\frac{\partial}{\partial x}\left[R^2\sigma_R \cos\varepsilon \sin\varepsilon\right] = \frac{\partial}{\partial \varepsilon}\left[RF \sin^2\varepsilon\right] - \cos\varepsilon \sin\varepsilon\left(R\sigma_R a_2 \cos(\varepsilon-\eta) + R^2 \frac{\partial \sigma_R}{\partial \varepsilon}\frac{\partial \psi}{\partial x}\right)$$
$$- Ra_2\sigma_R \sin(\varepsilon-\eta)\cos 2\varepsilon - R^2\left(\frac{\partial w}{\partial x}\right)\rho g \sin\varepsilon \tag{58}$$

$$\frac{\partial}{\partial x}\left[R^2\sigma_R \sin^2\varepsilon\right] = -\frac{\partial}{\partial \varepsilon}\left[RF \cos\varepsilon \sin\varepsilon\right] - \sin^2\varepsilon\left(R\sigma_R a_2 \cos(\varepsilon-\eta) + R^2 \frac{\partial \sigma_R}{\partial \varepsilon}\frac{\partial \psi}{\partial x}\right)$$
$$- R\sigma_R a_2 \sin(\varepsilon-\eta)\sin 2\varepsilon + R\left(\frac{\partial w}{\partial x}\right)\sigma_\theta \tag{59}$$

As not all stresses are specified by solution of the equations, a relationship between principal stresses is required. There is little data in the literature - azimuthal stresses can be found via use of the Haar-von Karman hypothesis (Haar and von Karman 1909), Conical Yield function (Nedderman 1992), or by relationships derived from equation 59. It is shown in Appendix Two, Chapter 9.7, that when ε is equal to zero, azimuthal stress is equal to radial stress. In Chapter 5.6 alternative relationships are compared to experimental data from the literature.

5.2 Spreadsheet based numerical solution

The particular solutions to the force balance equations for this case can now be found using the equations 29 and 40. Derivation of equations 60 and 61 can be found in Appendix Two, Chapter 9.6.

$$\frac{\partial F}{\partial \varepsilon} = \left(\frac{\left(\frac{\partial w}{\partial x}\right)\sigma_\theta - F}{\tan \varepsilon} \right) - \sigma_R a_2 \sin \varepsilon + R\left(\frac{\partial w}{\partial x}\right)\rho g \sin \varepsilon \tag{60}$$

$$\frac{\partial}{\partial x}\left[R^2 \sigma_R\right] = RF - R^2\left(\frac{\partial w}{\partial x}\right)\rho g \cos \varepsilon - 2R\sigma_R a_2 \cos \varepsilon - Ra_2 \sin \varepsilon \frac{\partial \sigma_R}{\partial \varepsilon} + R\left(\frac{\partial w}{\partial x}\right)\sigma_\theta \tag{61}$$

σ_θ -values can be found by selecting a relationship to the other principal stresses. In the current model σ_θ can be set equal to σ_ε (the Haar-von Karman hypothesis), or to the following relationship;

$$\sigma_\theta = \sigma_\varepsilon + k\sigma_R \tag{62}$$

As with the Haar-von Karman hypothesis, equation 62, this relationship gives $\sigma_\theta = \sigma_\varepsilon$ when $\varepsilon = 0$. This derivation is shown in Appendix Two, Chapter 9.7.

Values for $\frac{\partial \sigma_R}{\partial \varepsilon}$ can be calculated via equation 63, which is a forward step finite difference method. Calculation of $\frac{\partial \sigma_R}{\partial \varepsilon}$ was not required in the two-dimensional model presented in Chapter 4.1. The parameter represents the rate of change of σ_R in the ε-direction across the silo.

$$\left[\frac{\partial \sigma_R}{\partial \varepsilon}\right]_\varepsilon \approx \frac{\left[\sigma_R\right]_{\varepsilon+\delta\varepsilon} - \left[\sigma_R\right]_\varepsilon}{\delta \varepsilon} \tag{63}$$

<u>Axially symmetric three-dimensional parallel-sided silo and cone hopper</u>

Note an initial condition is needed, unless a backward step finite difference method is used at the right hand wall of the wedge as below.

$$\left[\frac{\partial \sigma_R}{\partial \varepsilon}\right]_{\varepsilon} \approx \frac{[\sigma_R]_{\varepsilon} - [\sigma_R]_{\varepsilon-\delta\varepsilon}}{\delta\varepsilon} \tag{64}$$

The Mohr-Coulomb criterion is used to relate radial stress to arc stress at one value of ε only, as with the 2-D model.

The model presented in Chapter 5.1 has been set-up on spreadsheet software. Equations 60 and 61 have been used to form the basis of the model. An explanation of the spreadsheet-based models is given in Appendix Three.

5.3 QBasic algorithm/programming

In Chapters 5.3.1 and 5.3.2, flow charts explain the QBasic algorithms for the cases of three-dimensional parallel-sided silo and cone hopper. The QBasic algorithms are included in Appendix Four.

5.3.1 QBasic algorithm for three-dimensional parallel-sided silo case

Flow chart for QBasic three-dimensional parallel-sided silo algorithm:

LINES 9 TO 34: USER INPUT OF MATERIAL PHYSICAL PROPERTIES. THESE DO NOT CHANGE THROUGHOUT PROGRAM.	CONSTANTS INPUT/CALCULATED: RHO, phi_w, phi, pi, T, Fc, Co

Axially symmetric three-dimensional parallel-sided silo and cone hopper

LINES 36 TO 122: USER INPUT OF SILO AND MODEL GEOMETRY DATA. THESE VARIABLES DO NOT CHANGE DURING PROGRAM ITERATIONS. ALPHA AND NU SET TO ZERO FOR SILOS	CONSTANTS INPUT/CALCULATED: H, H2, S, ALPHA, BETA, R, LAMBDA, GAMMA, A1, A2, NU, J, DELTA_X_INC, DELTA_ETA_INC, DELTA_X, DELTA_ETA, ETA, X, PW_WRTX, R, PPSI_WRTX
LINES 124 TO 147: DIMENSIONING OF ARRAYS FOR VARIABLES THAT CHANGE DURING SUCCESSIVE ITERATIONS OF THE PROGRAM. INITIAL VALUES FOUND TO BE NECESSARY AND THEREFORE USED FOR SIG_R, SIG_THETA AND F.	ARRAYS DIMENSIONED: PF_WRTETA, PSIG_R_WRTETA, SIG_ETA, F, PSIG_R_WRTX, SIG_R, SIG_THETA
LINES 149 TO 157 (CLOSES ON LINE 368): NEWTON-RAPHSON TYPE METHOD EMPLOYED TO CREATE WHILE LOOP. WHILE DIFFERENCE BETWEEN SUCCESIVE ITERATIONS OF FINAL ROW OF SIG_R MATRIX IS GREATER THAN 1, THE PROGRAM WILL CONTINUE TO CYCLE.	WHILE LOOP CONDITIONS: Y# = 0, DIFF# = 2, Numberofiterations = 0, DIFF >=1
LINES 159 TO 165: CALCULATE PF_WRTETA MATRIX USING ETA-DIRECTION FORCE BALANCE EQUATION (INITIAL CONDITION USED FOR SIG_R, F and SIG_THETA).	FUNCTION OF: SIG_R, SIG_THETA, F
LINES 167 TO 181: CALCULATE PSIG_R_WRTETA MATRIX USING FINITE DIFFERENCE METHOD (LH WALL USES FORWARD DIFFERENCE, RH WALL BACKWARD DIFFERENCE, REMAINDER CENTRAL DIFFERENCE).	FUNCTION OF: SIG_R

LINES 183 TO 192: CALCULATE SIG_ETA MATRIX USING F/PW_WRTX WITH A CENTRAL BOUNDARY CONDITION OF MOHR-COULOMB CRITERION SIG_ETA=J*SIG_R+(J-1)*T.	FUNCTION OF: F, SIG_R
LINES 194 TO 208: CALCULATE F MATRIX USING FORWARD AND REVERSE EULER METHOD FROM CENTRAL BOUNDARY CONDITION OF PW_WRTX*SIG_ETA.	FUNCTION OF: SIG_ETA, PF_WRTETA
LINES 210 TO 216: CALCULATE SIG_THETA MATRIX USING SIG_THETA=SIG_ETA+k*ETA*SIG_R RELATIONSHIP	FUNCTION OF: SIG_ETA, SIG_R
LINES 218 TO 224: CALCULATE PSIG_R_WRTX MATRIX USING R-DIRECTION FORCE BALANCE EQUATION.	FUNCTION OF: PF_WRTETA, SIG_R, PSIG_R_WRTETA, PPSI_WTRX, SIG THETA
LINES 226 TO 236: CALCULATE SIG_R MATRIX USING REVERSE EULER METHOD FROM BOUNDARY CONDITION OF ZERO (AT MATERIAL SURFACE).	FUNCTION OF: PSIG_R_WRTX

LINES 238 TO 348: OUTPUT VARIABLES TO CSV FILES

LINES 350 TO 368: CLOSING STATEMENTS OF WHILE LOOP AND END PROGRAM, PRINT NUMBER OF ITERATIONS. NUMBER OF ITERATIONS LIMITED ON LINE 366.

The QBasic programming code for three-dimensional silo case is provided in Appendix Four, Chapter 11.3.

5.3.2 QBasic algorithm for three-dimensional cone hopper case

Flow chart for QBasic three-dimensional cone hopper algorithm:

LINES 9 TO 34: USER INPUT OF MATERIAL PHYSICAL PROPERTIES. THESE DO NOT CHANGE THROUGHOUT PROGRAM.	CONSTANTS INPUT/CALCULATED: RHO, phi_w, phi, pi, T, Fc, Co
LINES 36 TO 127: USER INPUT OF HOPPER AND MODEL GEOMETRY DATA. THESE VARIABLES DO NOT CHANGE DURING PROGRAM ITERATIONS. NU SET TO ZERO FOR EQUAL ANGLE HOPPER	CONSTANTS INPUT/CALCULATED: H, H2, ALPHA, BETA, R, LAMBDA, GAMMA, A1, A2, NU, J, DELTA_X_INC, DELTA_ETA_INC, DELTA_X, DELTA_ETA, ETA, X, PW_WRTX, R, PPSI_WRTX
LINES 129 TO 152: DIMENSIONING OF ARRAYS FOR VARIABLES THAT CHANGE DURING SUCCESSIVE ITERATIONS OF THE PROGRAM. INITIAL VALUES FOUND TO BE NECESSARY AND THEREFORE USED FOR SIG_R, SIG_THETA AND F: ACTUAL INITIAL VALUES BASED OF REVIEW OF EXCEL	ARRAYS DIMENSIONED: PF_WRTETA, PSIG_R_WRTETA, SIG_ETA, F, PSIG_R_WRTX, SIG_R, SIG_THETA
LINES 154 TO 162 (CLOSES ON LINE 383): NEWTON-RAPHSON TYPE METHOD EMPLOYED TO CREATE WHILE LOOP. WHILE DIFFERENCE BETWEEN SUCCESIVE ITERATIONS OF FINAL ROW OF SIG_R MATRIX IS GREATER THAN 1, THE PROGRAM WILL CONTINUE TO CYCLE.	WHILE LOOP CONDITIONS: Y# = 0, DIFF# = 2, Numberofiterations = 0, DIFF >=1

Axially symmetric three-dimensional parallel-sided silo and cone hopper

LINES 164 TO 170: CALCULATE PF_WRTETA MATRIX USING ETA-DIRECTION FORCE BALANCE EQUATION (INITIAL CONDITION USED FOR SIG_R, F and SIG_THETA).	FUNCTION OF: SIG_R, SIG_THETA, F
LINES 172 TO 186: CALCULATE PSIG_R_WRTETA MATRIX USING FINITE DIFFERENCE METHOD (LH WALL USES FORWARD DIFFERENCE, RH WALL BACKWARD DIFFERENCE, REMAINDER CENTRAL DIFFERENCE).	FUNCTION OF: SIG_R
LINES 188 TO 197: CALCULATE SIG_ETA MATRIX USING F/PW_WRTX WITH A CENTRAL BOUNDARY CONDITION OF MOHR-COULOMB CRITERION SIG_ETA=J*SIG_R+(J-1)*T.	FUNCTION OF: F, SIG_R
LINES 199 TO 213: CALCULATE F MATRIX USING FORWARD AND REVERSE EULER METHOD FROM CENTRAL BOUNDARY CONDITION OF PW_WRTX*SIG_ETA.	FUNCTION OF: SIG_ETA, PF_WRTETA
LINES 215 TO 221: CALCULATE SIG_THETA MATRIX USING SIG_THETA=SIG_ETA+k*SIN(ETA)*SIG_R RELATIONSHIP	FUNCTION OF: SIG_ETA, SIG_R
LINES 223 TO 229: CALCULATE PSIG_R_WRTX MATRIX USING R-DIRECTION FORCE BALANCE EQUATION.	FUNCTION OF: PF_WRTETA, SIG_R, PSIG_R_WRTETA, PPSI_WTRX, SIG_THETA

Axially symmetric three-dimensional parallel-sided silo and cone hopper

LINES 231 TO 241: CALCULATE SIG_R MATRIX USING REVERSE EULER METHOD FROM BOUNDARY CONDITION OF ZERO (AT MATERIAL SURFACE).	FUNCTION OF: PSIG_R_WRTX

LINES 243 TO 363: OUTPUT VARIABLES TO CSV FILES

LINES 365 TO 383: CLOSING STATEMENTS OF WHILE LOOP AND END PROGRAM, PRINT NUMBER OF ITERATIONS. NUMBER OF ITERATIONS LIMITED ON LINE 381.

The QBasic programming code for three-dimensional cone hopper case is provided in Appendix Four, Chapter 11.4.

5.4 Model validation

A comparison of stress distributions between old (Matchett 2004) and new models demonstrated similar characteristics to the two-dimensional models presented in Chapter 4.1:

- At shallow depths within the granular materials, stress distribution values produced by current and previous models were similar.
- Increase of stress distribution variation with increasing depths for the current models only.

Further validation was completed by comparison of the current models to data from the literature. This validation is reported in Chapters 5.4.1 and 5.4.2.

5.4.1 Three-dimensional parallel-sided silo case

Figure 49 below provides a comparison of results calculated by two different stress analysis methods: the principal stress arc method and a Finite Element model. This exercise was carried out for validation purposes. The case is a three-dimensional silo as shown in Figures 48 and 52. Results are produced from the finite element analysis (Wojcik and Tejchman 2008) by making use of a ‘hypoplastic’ material model. The finite element mesh contained 26 increments horizontal direction and 115 increments in the vertical direction; 4-node quadrilateral elements were used. A principal stress arc algorithm was created using identical material properties to Wojcik and Tejchman’s FE model. The research project model used 200 increments in the x-direction and 50 increments in the ε-direction. Kolymbas (2000) explains hypoplastic materials models:

> “Hypoplasticity aims to describe the aforementioned anelastic phenomena [irreversible deformation] without using the additional notions introduced by elastoplasticity (such as yield surface, plastic potential, etc.). Hypoplasticity recognizes that anelastic deformations may set on from the very beginning of the loading process. It does not *a priori* distinguish between elastic and plastic deformations. The outstanding feature of hypoplasticity is its simplicity: not only it avoids the aforementioned additional notions but also uses a unique equation (contrary to elastoplasticity) which holds equally for loading and unloading. The distinction between loading and unloading is automatically accomplished by the equation itself. Besides the indispensible quantities “stress” and “strain” (and their time rates) only some material constants appear in the hypoplastic equation...The hypoplastic constitutive equation expresses the stress increment as a function of a given strain element and of the actual stress and void ratio.”

Kolymbas notes that there is no way to measure the success or utility of a constitutive equation, however the method has advantages including simplicity of implementation into numerical algorithms. Rombach et al (2005) provide a comparison of results produced from finite element analyses using elastic-plastic and hypoplastic materials models. Correlation is demonstrated between the two methods. Wojcik and Tejchman’s (2008) hypoplastic model makes the assumption of Coulomb friction between the granular material and vessel walls. The value of wall friction ϕ_w used was 22 degrees. The principal stress arc method makes use of this assumption within equation 54.

In Figure 49, FEA results are indicated by ‘SIG FEA’ for wall normal stress data and ‘TAU FEA’ for shear stress data. Wall normal stress data calculated by the principal stress arc method is presented by ‘SIG W’ and shear stress data by ‘TAU W’.

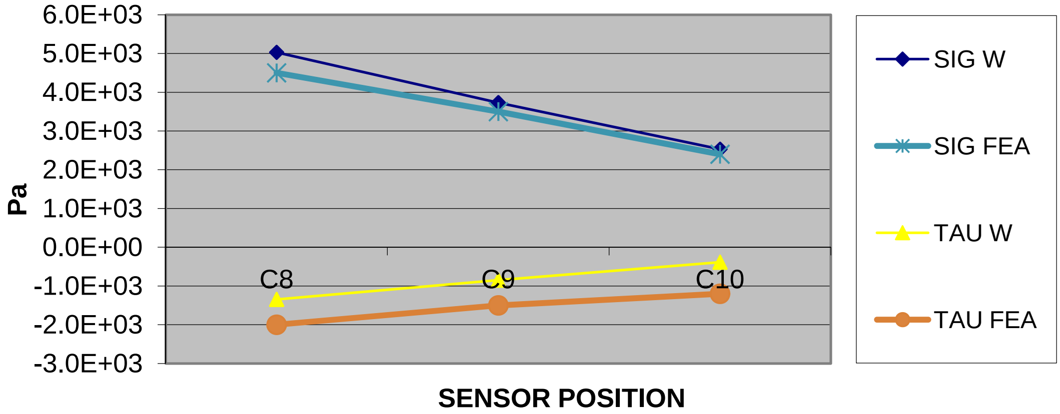

Figure 49. Comparison of Wojcik and Tejchman silo FEA data to calculated values: β = 0.15 rad, J =0.26, T = 200 Pa, OP = 0 Pa

The validated three-dimensional silo algorithm was calibrated by use of data fitting, explained in Appendix Three (Chapter 10.1), and by use of material properties information sourced from the literature.

5.4.2 Three-dimensional cone hopper case

Figure 50 below provides a comparison of results calculated by the principal stress arc method and Wojcik and Tejchman’s (2008) Finite Element model, for the three-dimensional cone hopper case (reference Figure 52). This exercise was carried out for validation purposes. Correlation between FEA data and results calculated by the principal stress arc method is poor at sensor locations C1 and C2. If sensor location C1 is discounted, average correlation improves.

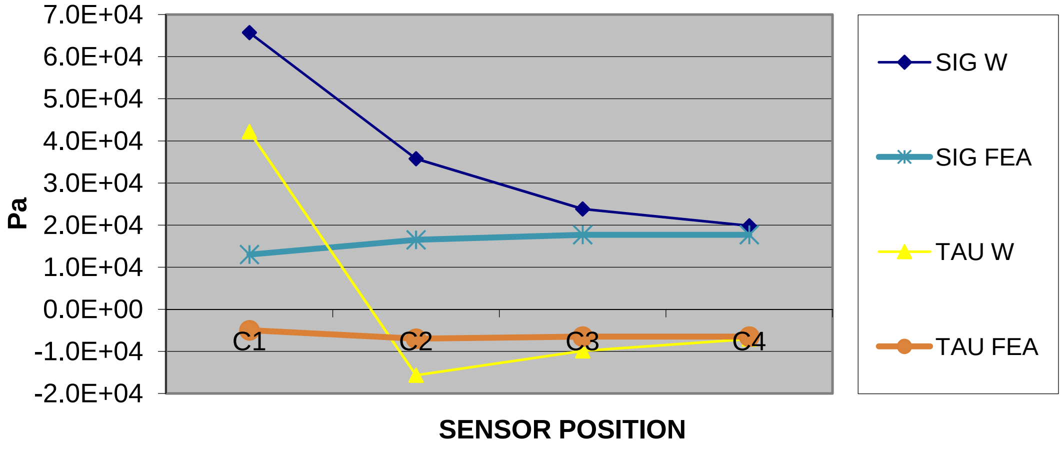

Figure 50. Comparison of Wojcik and Tejchman hopper FEA data to calculated values: β = 0.2 rad, J =0.2, T = 0 Pa, OP = non-zero values (22.0 kPa to 23.5 kPa)

Figure 50 indicates that correlation to finite element analysis results reduced as the sensor location approached the hopper apex. An additional validation exercise was carried out using data from Ding et al (2011). Ding et al provided wall normal stress data produced using an 'ideal Drucker–Prager elastic–plastic' FEA material model. The current case was an axi-symmetrical cone hopper of dimensions 4.8 metres in diameter and 3.232 metres material fill height, with a hopper half-angle of 23 degrees. Granular material properties used including ϕ equal to 23 degrees, ϕ_W equal to 26.6 degrees and density ρ equal to 1000 kg/m^3. Data on cohesion c was not provided therefore the tensile parameter T was estimated to be 2000 Pa. The Drucker-Prager material model was discussed in Chapter 4.4. The finite element model used continuum axi-symmetric elements in six layers. No overpressure was applied to the top surface of the granular material, a gravitational load only was applied throughout the FE mesh.

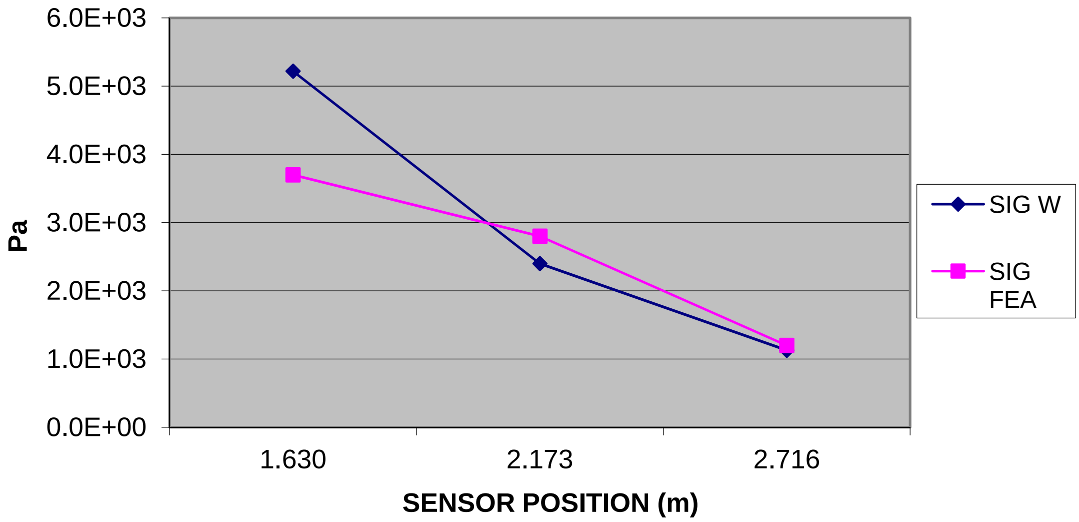

Figure 51. Comparison of Ding et al hopper data to calculated values: β = 0.01 rad, J =0.01, T = 2000 Pa, OP = 1000 Pa

In Figure 51 comparison is shown between results calculated by the principal stress arc method and those produced by Ding et al's finite element analysis. Correlation is demonstrated at these sensor locations with an average accuracy of 7%. Correlation reduces towards the hopper apex. It should be noted that while the β-value used is within limits dictated by equation 55, the J-value used is outside of limits. This occurrence would normally be a possible indicator of instability (i.e. flow) within the granular material, however the case reviewed was that of staged filling. A non-zero value of surcharge was used in order to replicate the heaped surface of the hopper, which was highlighted in the literature. The validated three-dimensional cone hopper algorithm was calibrated by use of data fitting described in Chapter 5.6.2, and by use of material properties information sourced from the literature.

5.5 Experimental data sourced from the literature

Sources of experimental data used for validation include:

- Wojcik and Tejchman 2008
- Rao and Ventaswarlu 1974
- Walker and Blanchard 1967
- Diniz and Nascimento 2006

Axially symmetric three-dimensional parallel-sided silo and cone hopper

There is not a large amount of detailed experimental data available in the literature pertaining to stress distributions within silos and silos. The sources above do not contain all information required to fully validate principal stress arc models, for example data is frequently limited to normal stresses or ’pressures’. None of the above sources give data for azimuthal stresses – in the author’s opinion none are available. The data that is provided is sufficiently detailed to allow comparison with calculated results.

Wojcik and Tejchman (2008) provide experimental data from a ‘large-scale’ hopper and silo arrangement, as shown in Figure 52.

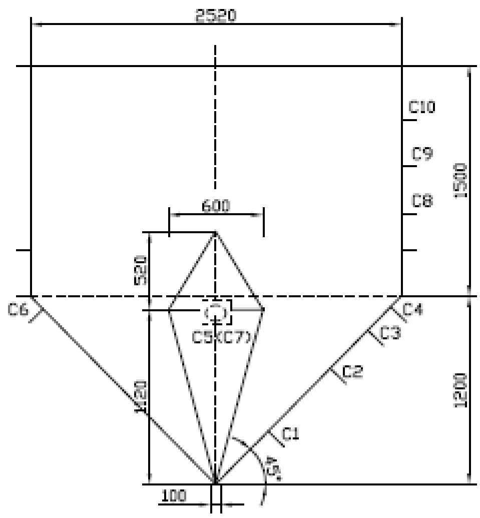

Figure 52. The geometry of the silo with insert and location of wall pressure cells C1-C10 (Wojcik and Tejchman 2008)

The granular material used was stated to be loose dry sand, with a bulk density ρ_b of 1428 kg/m^3. Angle of internal friction ϕ was given as 36 degrees and wall friction angle ϕ_W as 22 degrees.

Pressure cells were used at positions C1 to C10, providing experimental data for normal and shear pressures at the wall. Values were given at the end of the filling process and at the beginning of discharge, and also with and without a double-cone insert. The models produced by the current principal stress arc models do not take account of dynamic forces; therefore the static ‘end-of-filling’ values, without insert, were used for comparison.

Axially symmetric three-dimensional parallel-sided silo and cone hopper

Rao and Venkateswarlu (1974) provide experimental data from a relatively small scale hopper and silo arrangement. Hopper dimensions are designed to provide mass-flow (after Jenike 1964), and due to the use of a non-cohesive media then it can be assumed that funnel-flow was avoided. Bulk density for the glass beads was not stated; after Li et al (1998) and Wong (2000) this was assumed to be 1575 kg/m3. A value for *T* was also not provided and was therefore assumed to be zero. The experimental rig is shown in Figure 53.

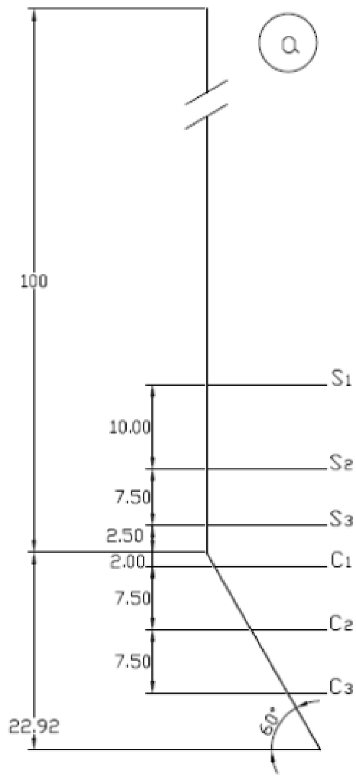

Figure 53. Positions for wall pressure measurement in a 30-degree hopper (Rao and Venkateswarlu 1974)

Pressure cells were used at S1 to S3 and C1 to C3 positions, providing static wall pressure measurements σ for comparison to calculated data σ_W. For the silo section shown in Figure 53, initial values were selected using active cases of equations 54 and 55. Note shear values were not available.

Walker and Blanchard (1967) provide experimental data for large scale hoppers and silos, with typical arrangements shown in Figure 54.

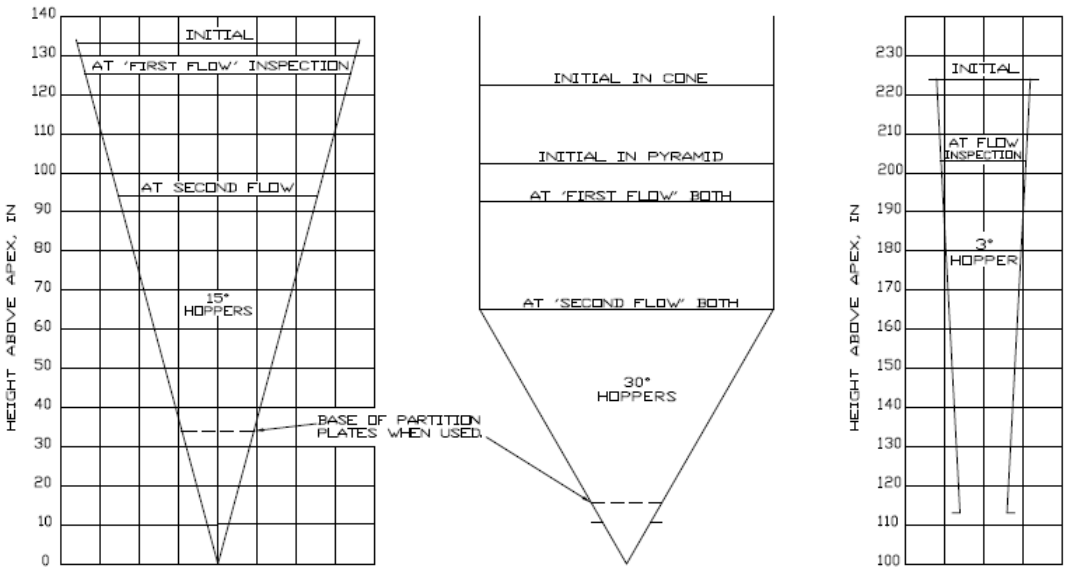

Figure 54. Fill heights of experimental hoppers (Walker and Blanchard 1967)

The granular material used was fine coal (International Dry Fines Rank 203), with a low moisture content of around 3%. The angle of internal friction ϕ was 41 degrees and the angle of wall friction ϕ_W 16 degrees. Pressure cells were used to provide averaged wall pressures throughout the height of the receptacles. The values under consideration were those produced shortly after filling.

For initial modelling of the silo above the 30-degree hopper, T was estimated to be equal to 2000 Pa as the presence of moisture can cause cohesion. J- and β-values were set to their active limits using equations 54 and 55: equal to 0.21 and 0.36 respectively. Bulk density ρ_b was stated in the literature to equal 817 kg/m^3.

Walker and Blanchard provided wall pressure data obtained by full-scale experimental testing using a 15-degree hopper, of dimensions shown in Figure 54 Again, the medium used is fine coal. The hopper is stated to be mass-flow type.

Diniz and Nascimento (2006) provide experimental data for sand with a silo constructed of masonry. Dimensions are shown in Figure 55. Data is provided from pressure cells at positions 1, 2 and 5.

Axially symmetric three-dimensional parallel-sided silo and cone hopper

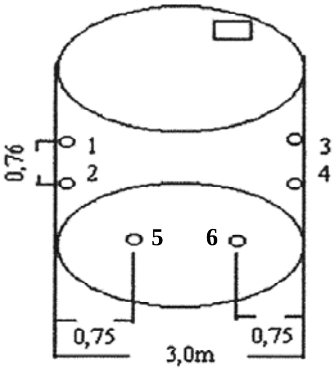

Figure 55. Position of [pressure] cells within the silo (Diniz and Nascimento 2006)

Material properties include ρ_b equal to 1632 kg/m^3, ϕ_W equal to 27 degrees and ϕ equal to 36 degrees. It was initially assumed that *T* was equal zero; this value was used with active values β equal to 0.68 and *J* equal to 0.26.

5.6 Application of the method

5.6.1 Application Case 1: Wojcik and Tejchman silo data

Wojcik and Tejchman (2008) provide experimental data for the silo case produced from a test silo. Table 3 and Figure 56 compare experimental data σ and τ to calculated data σ_W and τ_W, for the silo section of the arrangement. The three principal stresses, σ_R, σ_ε and σ_θ, are produced by the principal stress arc model for this case. Calculated wall normal and shear stress values σ_W and τ_W, are produced by use of equations 56 and 57.

Sensor	σ_ε	σ_R	σ_θ	$\boldsymbol{\sigma_W}$	$\boldsymbol{\sigma}$	$\boldsymbol{\tau_W}$	$\boldsymbol{\tau}$
C8	8.5E+03	3.9E+03	8.5E+03	**7.3E+03**	**5.0E+03**	**2.1E+03**	**-2.0E+03**
C9	7.0E+03	3.6E+03	7.0E+03	**6.1E+03**	**4.3E+03**	**1.5E+03**	**-1.6E+03**
C10	5.8E+03	2.4E+03	5.8E+03	**4.9E+03**	**1.8E+03**	**1.5E+03**	**0.0E+00**

Table 3. Comparison of Wojcik and Tejchman silo data to calculated values: β = 0.54 rad, *J* = 0.26, *T*= 500 Pa, *OP* = 0 Pa

A zero value of overpressure *OP* was used as the experimental apparatus did not indicate material above the silo. In Table 3, theoretical wall stresses σ_W overestimated experimental wall stress σ-values by an average of 87%. With the exception of cell C10, theoretical wall shear stresses τ_W were similar (within 5%) to experimental wall shear stress τ-values in magnitude but opposite in direction.

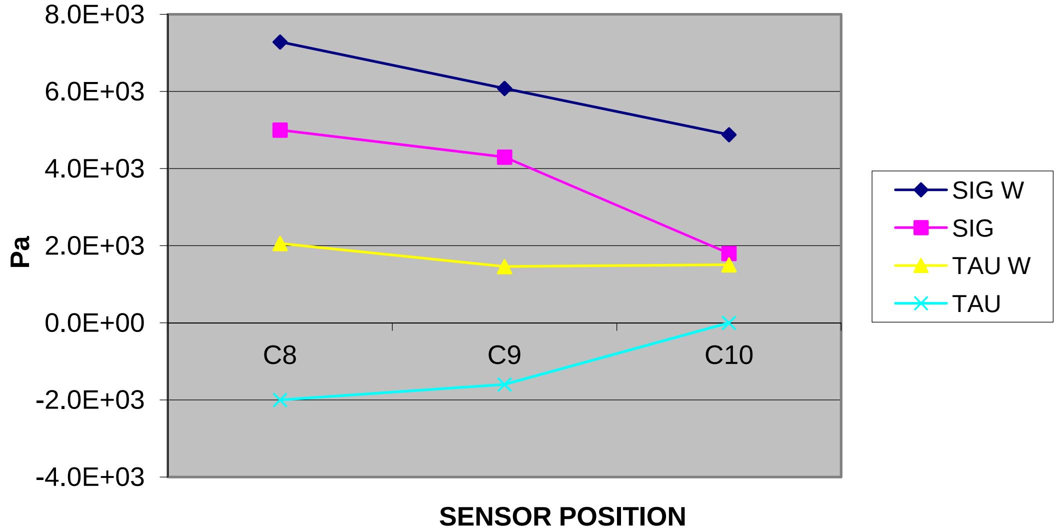

Figure 56. Comparison of Wojcik and Tejchman silo data to calculated values: β = 0.54 rad, J =0.26, T = 500 Pa, OP = 0 Pa

A least squares method (Gauss 1809, Stroud and Booth 2001) and the Microsoft Excel Solver application (Fylstra et al 1998) were used to improve correlation between experimental data and calculated results. The Solver software makes use of a Generalized Reduced Gradient nonlinear optimization code (Baker 2005). Use of statistical hypothesis testing is employed to control apparent improvements in correlation in Appendix Five.

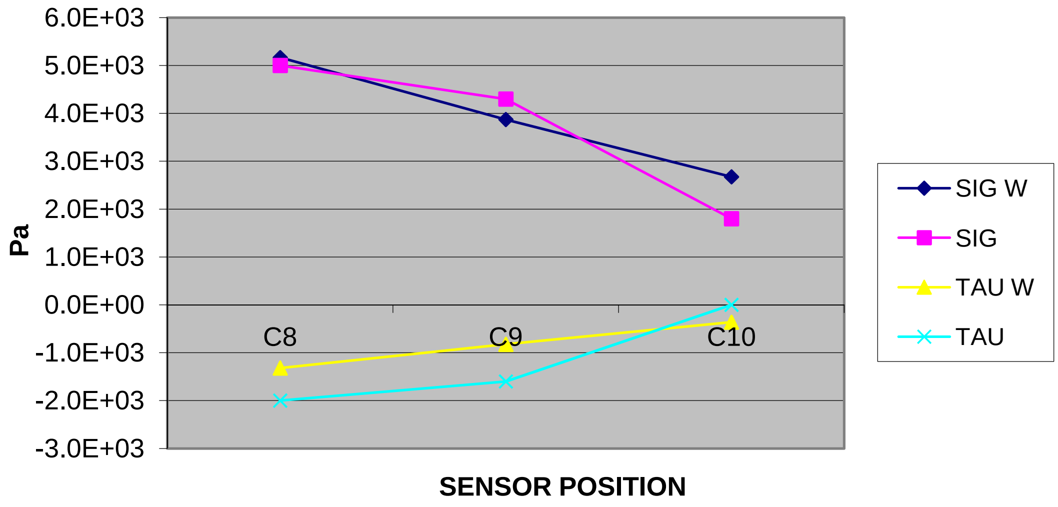

Figure 57. Comparison of Wojcik and Tejchman silo data to calculated values: β = 0.15 rad, J =0.26, T = 200 Pa, OP = 200 Pa

Values of β and J were varied from initial values, until results converged on an acceptable solution shown in Figure 57. The Microsoft Excel Solver application performed convergence checks with a limit of $1\text{x}10^{-6}$ Pa. Tensile parameter T was allowed to vary, and acceptable correlation was produced from a T- value of 200 Pa. Selection of this value is reasonable as the granular material used in the experiment was dry sand, which can exhibit limited or zero cohesion. It should be noted that dry, fine-grained media can demonstrate cohesion due to electrostatic forces (Schulze 2008). Table 4 compares FEA and principal stress arc results to experimental data, shown as percentage error. Values for location C10 are shown as 'not applicable' due to a zero value for experimental data. Absolute errors at this sensor location are -0.39 kPa and -1.2 kPa for principal stress arc and finite element methods respectively. For normal wall stress data the principal stress arc method results showed improved correlation when compared to FEA results. For shear stress values FEA data provided improved correlation over principal stress arc method calculations. The presence of a zero value at sensor location C10 creates an artificially low average error value, at this location the principal stress arc method matches experimental data more closely than FEA data.

Axially symmetric three-dimensional parallel-sided silo and cone hopper

	% SIG		% TAU	
Sensor	**PSA**	**FEA**	**PSA**	**FEA**
C8	100.6%	90.0%	67.3%	100.0%
C9	86.8%	81.4%	53.0%	93.8%
C10	140.6%	133.3%	N/A	N/A
Average %	109.3%	101.6%	60.2%	96.9%

Table 4. Comparison of Wojcik and Tejchman experimental and FEA silo data to calculated values, showing correlation to experimental data as a percentage

Equation 62 is proposed for calculation of azimuthal stresses. The value for k was also allowed to vary in the early stages of this analysis. Four alternative azimuthal stress relationships are shown below.

$$\sigma_\theta = \sigma_\varepsilon, \text{ (Haar and von Karman 1909)} \quad (65)$$

$$\sigma_\theta = \frac{\sigma_R + T}{J} - T, \text{ (Matchett 2006a)} \quad (66)$$

$$\sigma_\theta = \sigma_R\left(\frac{1}{1-k}\right) - \sigma_\varepsilon\left(\frac{k}{1-k}\right), \text{ (Love 1927)} \quad (67)$$

$$(\sigma_R - \sigma_\theta)^2 + (\sigma_\theta - \sigma_\varepsilon)^2 + (\sigma_\varepsilon - \sigma_R)^2 = 6M^2\sigma_{OCT}, \text{ (Jenike 1987)} \quad (68)$$

Repeated trials found equation 62 to provide a higher level of correlation than other functions of the three principal stresses. The procedure employed to select a relationship is recorded in Appendix Six, Chapter 13. During comparison of experimental data it was found that correlation to results improved when a small k-value was used. The k-value selected was of a magnitude that imposed an azimuthal stress relationship that tended towards Haar-von Karman results (i.e. σ_θ took on the value of σ_ε, Haar and von Karman 1909, Nedderman 1992). This is thought to be reasonable: the Haar-von Karman criterion can be derived from one of the force balance equations used in the principal stress arc method. Derivation of equation 65 is shown in Appendix Two, Chapter 9.7, and was noted in O'Neill et al 2009. Derivation of equation 67 is shown in Appendix Two, Chapter 9.8.2.

The Conical Yield function (equation 68, Jenike 1987, Kruyt 1993) was the subject of some investigation through comparison of results in Chapters 5.6.6 and 5.6.7. The Conical Yield function results indicated that *M* may not take a constant value throughout the model.

5.6.2 Application Case 2: Wojcik and Tejchman hopper data

Wojcik and Tejchman (2008) provide experimental data for the cone hopper case produced from the test rig shown in Figure 52. The initial values from the cone hopper model are shown in Table 5. Values for comparison are shown in bold text. In Table 5, theoretical wall stresses σ_W were negative while experimental wall stress σ-values were positive. Theoretical wall shear stresses τ_W returned positive values while experimental wall shear stress τ-values were negative. Wall normal or shear stress theoretical values did not demonstrate correlation in magnitude to experimental data.

Sensor	σ_ε	σ_R	σ_θ	$\boldsymbol{\sigma_W}$	$\boldsymbol{\sigma}$	$\boldsymbol{\tau_W}$	$\boldsymbol{\tau}$
C1	-4.2E+08	-3.2E+10	-4.6E+08	**-1.6E+10**	**6.8E+03**	**1.6E+10**	**-1.2E+03**
C2	1.2E+05	-2.1E+05	1.2E+05	**-4.5E+04**	**1.0E+04**	**1.6E+05**	**-4.2E+03**
C3	4.1E+04	-4.6E+04	4.1E+04	**-2.7E+03**	**1.5E+03**	**4.4E+04**	**-4.3E+03**
C4	2.8E+04	-1.7E+04	2.8E+04	**5.7E+03**	**1.5E+04**	**2.3E+04**	**-4.2E+03**

Table 5. Comparison of Wojcik and Tejchman hopper data to calculated values: β = 0.54 rad, *J* = 0.26, T= 500 Pa, *OP* = non-zero values (22.0 kPa to 23.5 kPa)

Subsequent use of the Microsoft Excel Solver application failed to converge on a solution. Poor correlation was apparent despite analysis of various combinations of β and *J*. An overpressure *OP* was applied in an attempt to replicate the experimental rig used by Wojcik and Tejchman, σ_R-values from the base of the silo model were used at the top of the cone hopper model (as opposed to the value of zero). Due to the sloping hopper walls a discontinuity is created, as shown in Figure 58. By inspection of the model geometry it can be seen that for the two models to have identical principal arc radii, the silo model would require a β-value equal to the cone hopper models α- and β-values combined (i.e. $\beta_{SILO} = \alpha_{HOPPER} + \beta_{HOPPER}$). This contravenes limits set out by equation 54. Instead, β-values within limits were initially used with both models. A proposal to avoid this discontinuity would be to use averaged values of σ_R stress from the base of the silo model, at the top surface of the cone hopper model.

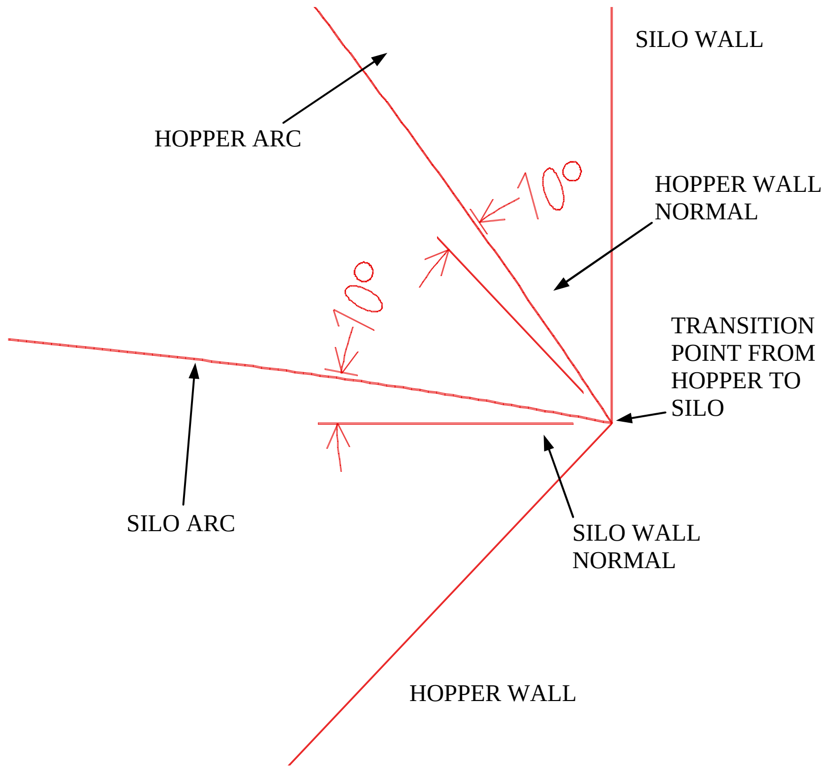

Figure 58. Demonstration of discontinuity between silo and hopper models due to wall angle

It can be seen from Figure 58 that if a negative β-value is used within the hopper section of the model, the silo and hopper principal stress arcs could coincide. This is investigated in Chapter 5.6.6, where experimental and calculated data did not provide correlation within β-limits.

With an overpressure applied to the model, correlation with experimental data improved to a point where a pattern of results could be discerned. Partial correlation is demonstrated in Figure 59.

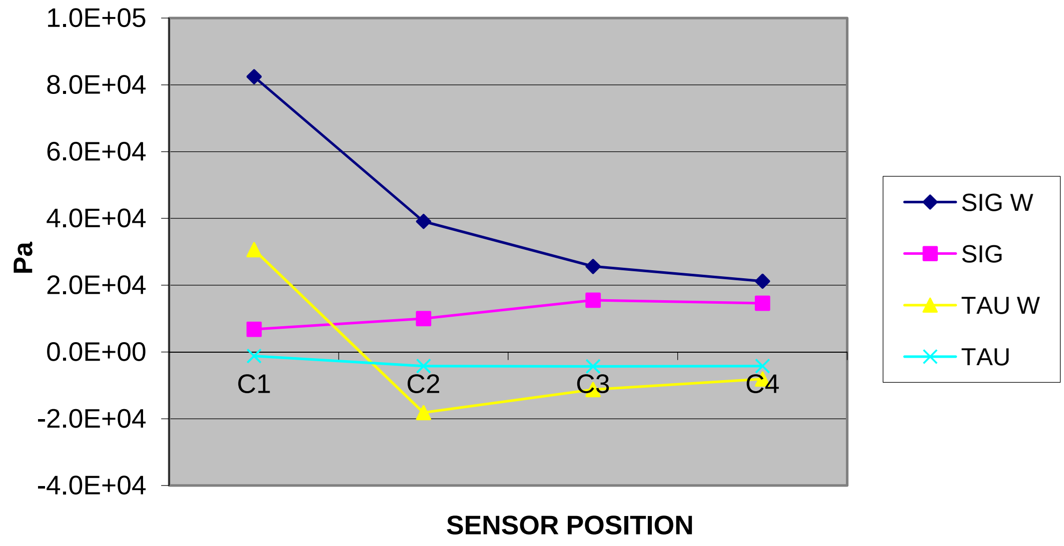

Figure 59. Comparison of Wojcik and Tejchman hopper data to calculated values: β = 0.2 rad, J =0.2, T = 200 Pa, OP = non-zero values (22.0 kPa to 23.5 kPa)

	% SIG		% TAU	
Sensor	**PSA**	**FEA**	**PSA**	**FEA**
C1	966.6%	191.2%	-3516.0%	416.7%
C2	357.7%	165.0%	373.3%	166.7%
C3	153.7%	114.2%	229.6%	151.2%
C4	135.9%	121.2%	168.3%	154.8%
Average %	**403.5%**	**147.9%**	**-686.2%**	**222.3%**

Table 6. Comparison of Wojcik and Tejchman experimental and FEA hopper data to calculated values, showing correlation to experimental data as a percentage

Table 6 compares experimental data and calculated results. Average correlation between experimental data and results calculated by the principal stress arc method is poor. If sensor location C1 is discounted, average correlation improves to 215.8% for wall normal stresses and 257.1% for shear stresses for the principal stress arc method results. Results calculated by FEA also improve if data from the same sensor location (C1) is not used to estimate correlation. In Chapter 5.7 an explanation for poor correlation is discussed.

A diagram of the cone and hopper are shown in Figure 60, demonstrating variables for each section of the model that provide highest level of correlation to experimental data.

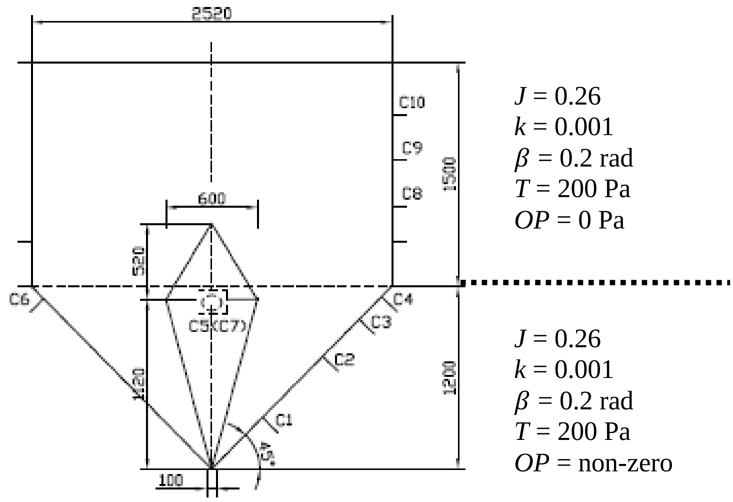

Figure 60. Diagram of model variables that provide highest level of correlation (Wojcik and Tejchman 2008)

In the hopper section the value of J (0.2) contravenes Mohr-Coulomb limits set out by equation 55. Correlation reduces if J is set equal to the lower limit of 0.26. An explanation of the reduced correlation of the hopper experimental data may be the presence of funnel flow. Wojcik and Tejchman state that mass flow was not achieved during their experiments.

5.6.3 Application Case 3: Rao and Venkateswarlu data

Table 7 compares Rao and Venkateswarlu's (1974) experimental data σ to calculated data σ_W, for their silo data (reference Figure 53). A zero value of overpressure was used. Poor correlation is apparent. Theoretical wall stress σ_W-values at positions S2 and S3 were negative while experimental data provided positive values for wall normal stress σ. At position S1, σ_W overestimated experimental data σ by an order of magnitude. The Solver application was subsequently used in Excel to vary β, T and J without imposed limits. The greatest error magnitude being 36% underestimation at position S3, with β equal to 0.11, T equal to 0 and J equal to 0.01.

Axially symmetric three-dimensional parallel-sided silo and cone hopper

Sensor	σ_ε	σ_R	σ_θ	$\boldsymbol{\sigma_W}$	$\boldsymbol{\sigma}$
S1	8.3E+03	1.7E+04	8.3E+03	**8.7E+03**	**3.7E+02**
S2	1.0E+04	-2.8E+05	1.0E+04	**-3.6E+03**	**4.7E+02**
S3	-1.5E+04	-3.5E+07	-7.6E+03	**-1.7E+06**	**9.4E+02**

Table 7. Comparison of Rao and Venkateswarlu silo data to calculated values: β = 0.22 rad, J = 0.24, T= 0 Pa, OP = 0 Pa

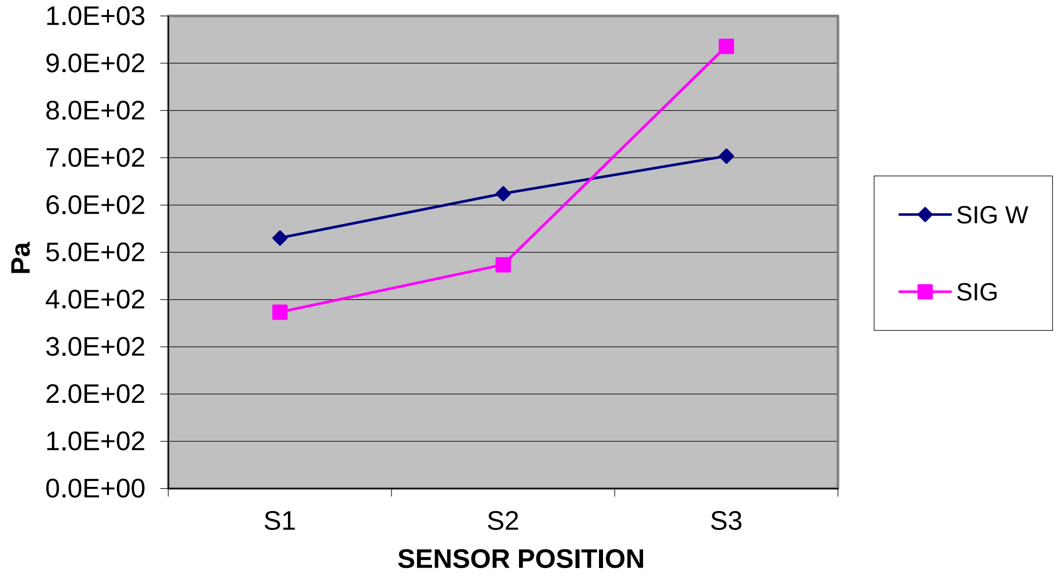

Figure 61. Comparison of Rao and Venkateswarlu silo data to calculated values: β = 0.11 rad, J =0.01, T = 0 Pa, OP = 0 Pa

The low value of J contravenes limits dictated by use of equation 55. Increasing J to the lower (active) limit of 0.44 significantly reduces correlation, with overestimates of more than two orders of magnitude. Re-running the Solver application gave results shown in Figure 62. Limits included 0.44 and 2.28 for J (from equation 55), and 0.1 and 0.22 rad for β (from equation 54).

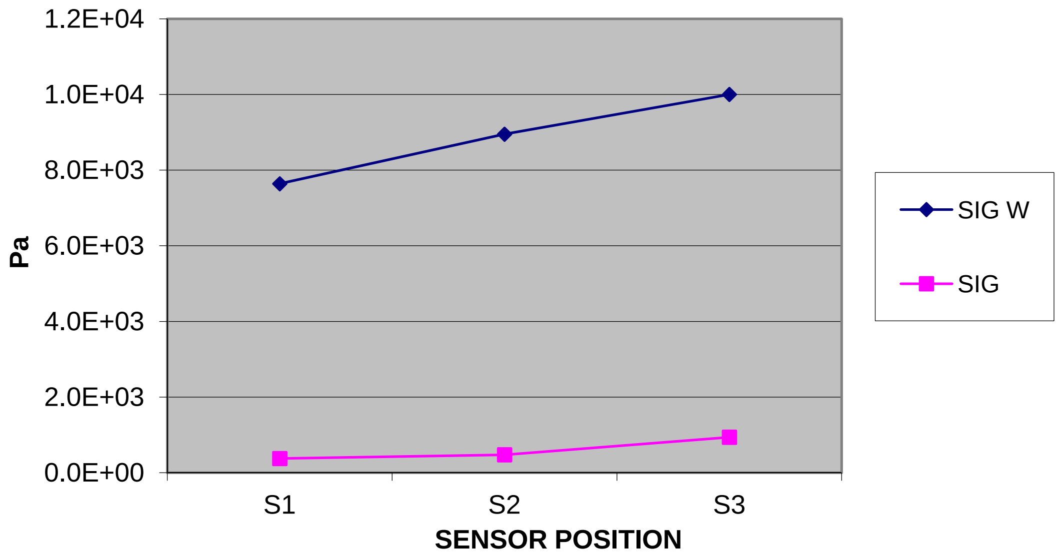

Figure 62. Graphical comparison of Rao and Venkateswarlu silo data to calculated values: β = 0.10 rad, J =0.44, T = 0 Pa, OP = 0 Pa

Sensor	σ_ε	σ_R	σ_θ	$\boldsymbol{\sigma_W}$	$\boldsymbol{\sigma}$
S1	7.6E+03	1.6E+04	7.6E+03	**7.6E+03**	**3.7E+02**
S2	8.9E+03	1.9E+04	8.8E+03	**9.0E+03**	**4.7E+02**
S3	9.9E+03	2.1E+04	9.9E+03	**1.0E+04**	**9.4E+02**

Table 8. Tabular comparison of Rao and Venkateswarlu silo data to calculated values: β = 0.10 rad, J =0.44, T = 0 Pa, OP = 0 Pa

It can be seen from Figure 62 and corresponding Table 8 that correlation between experimental data and calculated results is poor. Theoretical wall normal stress σ_W-values overestimate experimental data σ-values by an average of approximately 1600%. Variables are now adjusted to equal their limits, therefore no further improvement to correlation can be reasonably made using β, J or T. Further analysis indicates that variation of the assumed bulk density improves correlation. If ρ_b is reduced to the value of 110 kg/m^3: maximum error is reduced to around 40% overestimation at S1 and S2 positions, and 25% underestimation at S3. Such a low value for ρ_b is unlikely for a medium such as glass beads.

The initial values for Rao and Venkateswarlu's cone hopper model are shown in Table 9 (reference Figure 53). Non-zero values for overpressure are used. The actual values used are averaged data from the silo section above. Poor correlation is demonstrated, with theoretical values σ_W overestimating experimental data σ by several orders of magnitude.

Sensor	σ_ε	σ_R	σ_θ	$\boldsymbol{\sigma_W}$	$\boldsymbol{\sigma}$
C1	2.2E+03	2.7E+04	2.2E+03	**8.3E+03**	**1.3E+03**
C2	9.2E+03	4.1E+04	9.3E+03	**1.7E+04**	**1.4E+03**
C3	-4.3E+12	-5.8E+14	-4.9E+12	**-1.5E+14**	**1.0E+03**

Table 9. Comparison of Rao and Venkateswarlu hopper data to calculated values: β = 0.54 rad, J =0.26, T = 0 Pa, OP = non-zero values (20 kPa to 22.4 kPa)

Initial values for variables were β equal to 0.54, T equal to zero, J equal to 0.26 and ρ_b equal to 1575. Maximum values calculated were several orders of magnitude greater than experimental data values. The Solver application was used to vary β and J within limits of 0.15 to 0.54 and 0.26 to 3.85 respectively. The resulting values of J equal to 0.9 and β equal to 0.15 gave the correlation shown in Figure 63.

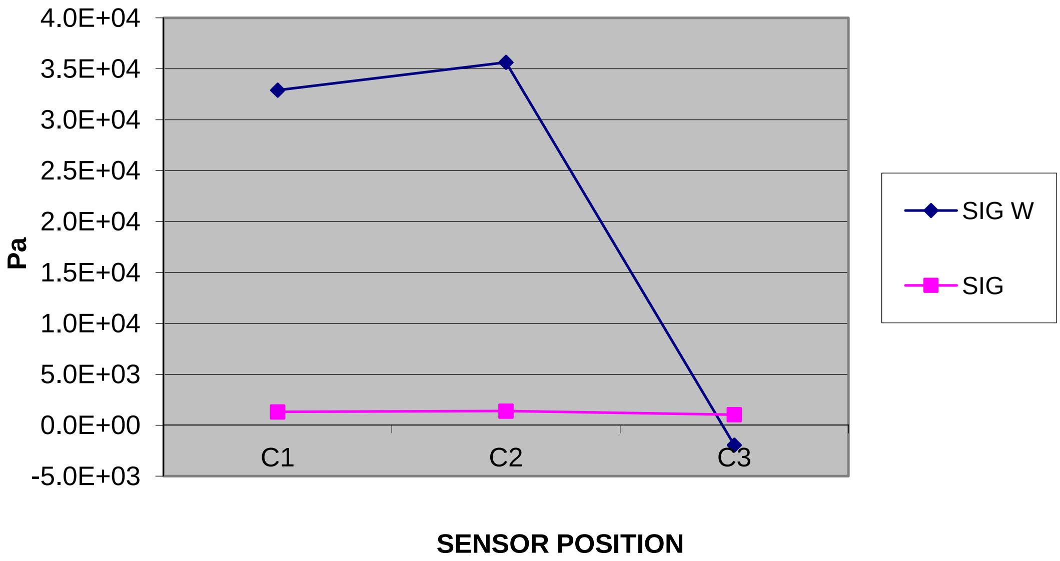

Figure 63. Comparison of Rao and Venkateswarlu hopper data to calculated values: β = 0.15 rad, J =0.9, T = 0 Pa, OP = non-zero values (20 kPa to 22.4 kPa)

The calculated values are clearly erroneous, while variables are not able to be adjusted within their limits to improve correlation. Again if bulk density is reduced to an unrealistic level then maximum errors of approximately 10% overestimation can be achieved, as shown in Figure 64.

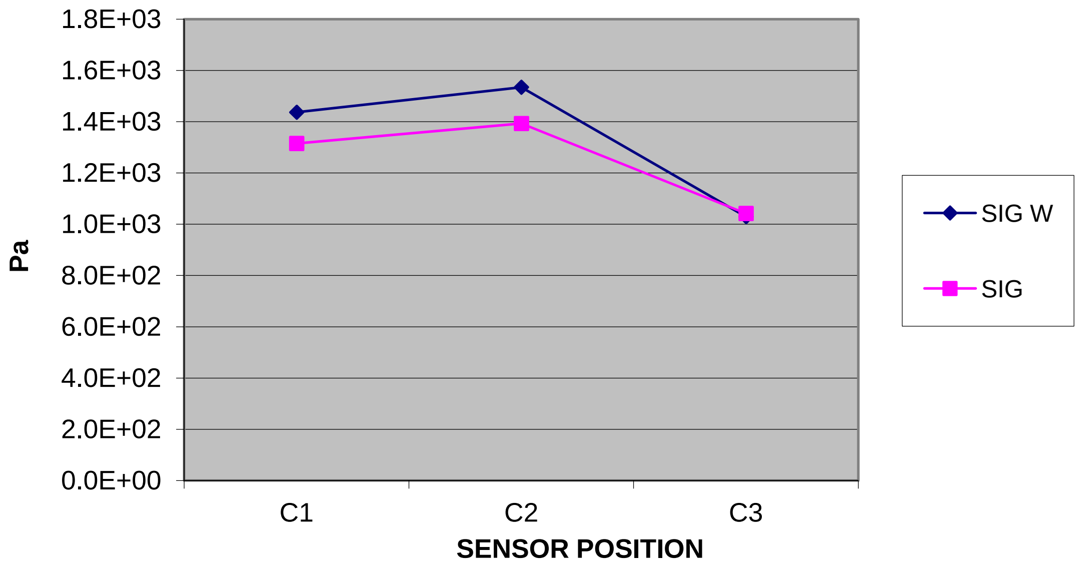

Figure 64. Comparison of Rao and Venkateswarlu hopper data to calculated values: β = 0.12 rad, J =0.9, T = 0 Pa, OP = non-zero values (20 kPa to 22.4 kPa)

5.6.4 Application Case 4: Walker and Blanchard data

Table 10 compares Walker and Blanchard's (1967) experimental data σ to calculated data σ_W, for the silo section of the arrangement located above the 30-degree hopper (reference Figure 54). A zero value of overpressure was used as the experimental apparatus did not indicate otherwise. Figure 65 contains identical data to Table 10.

Height (m)	σ_ε	σ_R	σ_θ	$\boldsymbol{\sigma_W}$	$\boldsymbol{\sigma}$
0.55	-3.6E+02	0.0E+00	-3.6E+02	**-3.2E+02**	**0.0E+00**
0.47	-2.4E+02	5.9E+02	-2.4E+02	**-1.3E+02**	**6.9E+02**
0.37	-7.3E+01	1.3E+03	-7.4E+01	**1.0E+02**	**6.9E+02**
0.27	1.1E+02	2.1E+03	1.1E+02	**3.6E+02**	**1.4E+03**
0.17	2.9E+02	3.0E+03	2.9E+02	**6.2E+02**	**1.4E+03**
0.07	5.0E+02	3.8E+03	5.0E+02	**9.1E+02**	**2.1E+03**
0	6.1E+02	4.3E+03	6.1E+02	**1.1E+03**	**8.3E+03**

Table 10. Tabular comparison of Walker and Blanchard silo data to calculated values: β = 0.36 rad, J =0.21, T = 2000 Pa, OP = 0 Pa

With the exception of the final value, calculated results show consistent underestimation of experimental data in Figure 65. A least trimmed squares (Rousseeuw 1984) was used due to the outlying data point at zero depth.

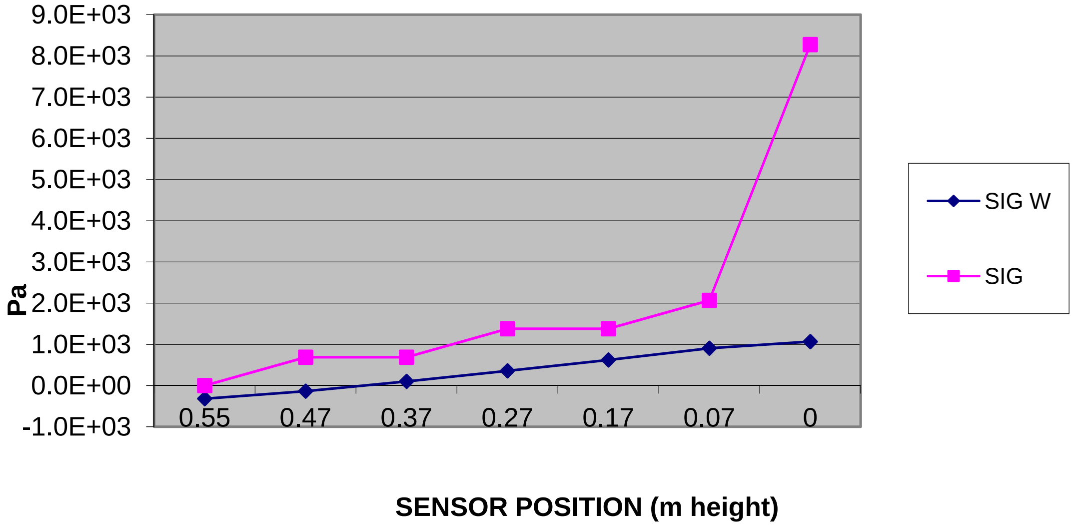

Figure 65. Comparison of Walker and Blanchard silo data to calculated values: β = 0.21 rad, J =0.36, T = 2000 Pa, OP = 0 Pa

Correlation can be improved by reduction of T-value to 1200. Adjusting β and J to 0.22 and 0.3 respectively provides calculated values that consistently underestimate experimental data, as shown in Table 11. With the variable set at their new values, the final value of σ remains underestimated by σ_W. This may be due to peak stresses close to the transition between silo and hopper – in this application the silo has been modelled independently of the hopper underneath. Values in the mid-section of the silo, from 0.37 to 0.07 metres, provided theoretical σ_W-values that were within 60% of experimental σ-values.

Height (m)	σ_ε	σ_R	σ_θ	$\boldsymbol{\sigma_W}$	$\boldsymbol{\sigma}$
0.55	-7.4E+01	0.0E+00	-7.4E+01	**-7.0E+01**	**0.0E+00**
0.47	1.2E+02	6.2E+02	1.2E+02	**1.4E+02**	**6.9E+02**
0.37	3.7E+02	1.4E+03	3.7E+02	**4.2E+02**	**6.9E+02**
0.27	6.3E+02	2.2E+03	6.3E+02	**7.1E+02**	**1.4E+03**
0.17	9.0E+02	3.1E+03	8.9E+02	**10.0E+02**	**1.4E+03**
0.07	1.2E+03	4.0E+03	1.2E+03	**1.3E+03**	**2.1E+03**
0	1.3E+03	4.4E+03	1.3E+03	**1.5E+03**	**8.3E+03**

Table 11. Comparison of Walker and Blanchard silo data to calculated values: β = 0.22 rad, *J* =0.3, *T* = 1200, Pa, *OP* = 0 Pa

Initial values for the Walker and Blanchard 30-degree cone hopper positioned below the silo (reference Figure 54) are shown in Table 12. *T* is set to 1200, *J* and β are set to their active limit values 0.21 and 0.36 respectively. Non-zero values for overpressure *OP* were used. Theoretical wall stress values were on average 53% of experimental values. The value of σ_W at 0.2 metres demonstrated the highest level of correlation and was within 7% of the equivalent σ-value.

Height (m)	σ_ε	σ_R	σ_θ	$\boldsymbol{\sigma_W}$	$\boldsymbol{\sigma}$
0.6	1.1E+03	4.9E+03	1.1E+03	**2.0E+03**	**8.3E+03**
0.5	1.8E+03	7.0E+03	1.8E+03	**3.1E+03**	**9.7E+03**
0.4	3.7E+03	8.5E+03	3.8E+03	**4.9E+03**	**1.1E+04**
0.3	1.1E+04	1.2E+03	1.1E+04	**8.3E+03**	**1.2E+04**
0.2	4.4E+04	-8.2E+04	4.4E+04	**1.3E+04**	**1.4E+04**

Table 12. Comparison of Walker and Blanchard 30-degree hopper data to calculated values: β = 0.36 rad, *J* = 0.21, *T* = 1200 Pa, *OP* = non-zero values (4000 Pa to 5500 Pa)

Adjusting β and *J* to 0.22 and 0.3 respectively provides calculated values that consistently underestimate experimental data values, as shown in Figure 66.

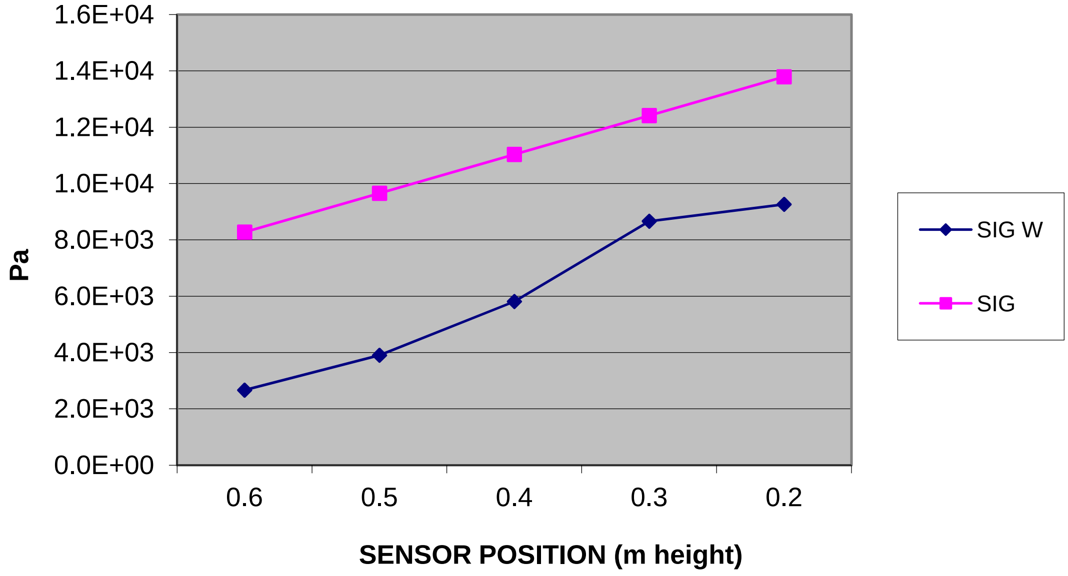

Figure 66. Comparison of Walker and Blanchard 30-degree hopper data to calculated values: β = 0.22 rad, J = 0.3, T = 1200 Pa, OP = non-zero values (4000 Pa to 5500 Pa)

Initial values for the Walker and Blanchard 15-degree cone hopper (reference Figure 54) included β set equal to 0.36 and J equal to 0.21. The Solver application provided results demonstrating correlation to experimental data, which are shown in Figure 67. Zero overpressure OP was applied.

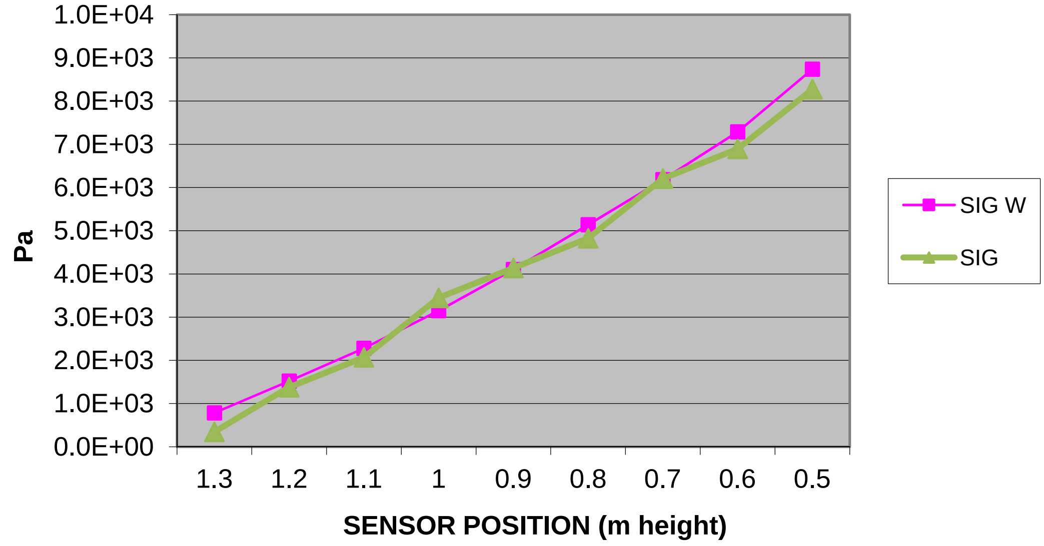

Figure 67. Comparison of Walker and Blanchard 15-degree hopper data to calculated values: β = 0.31 rad, J =0.8, T = 1200 Pa, OP = 0 Pa

Typical error magnitude was of less than 10% overestimation, after the Solver algorithm set β at 0.31 radians and J at 0.8.

5.6.5 Application Case 5: Diniz and Nascimento data

Table 13 compares Diniz and Nascimento's (2006) experimental data σ to calculated data σ_W, for the silo shown in Figure 55. A zero value of overpressure was used. At sensor location 1, theoretical values overestimate experimental data by 143%. At sensor locations 2 and 5, theoretical values underestimate experimental data by a large margin. Use of the Solver application adjusted the variables to β equal to 0.6 and T equal to 3000, thus improving correlation. Figure 68 compares experimental data σ to calculated data σ_W.

Sensor	σ_ε	σ_R	σ_θ	$\boldsymbol{\sigma_W}$	$\boldsymbol{\sigma}$
1	1.5E+04	-3.7E+03	1.5E+04	**7.3E+03**	**3.0E+03**
2	2.9E+04	-3.7E+04	2.9E+04	**2.7E+03**	**8.3E+03**
5	3.7E+04	-4.8E+04	3.7E+04	**3.0E+03**	**2.9E+04**

Table 13. Comparison of Diniz and Nascimento silo data to calculated values: β = 0.68 rad, J = 0.26, T = 0 Pa, OP = 0 Pa

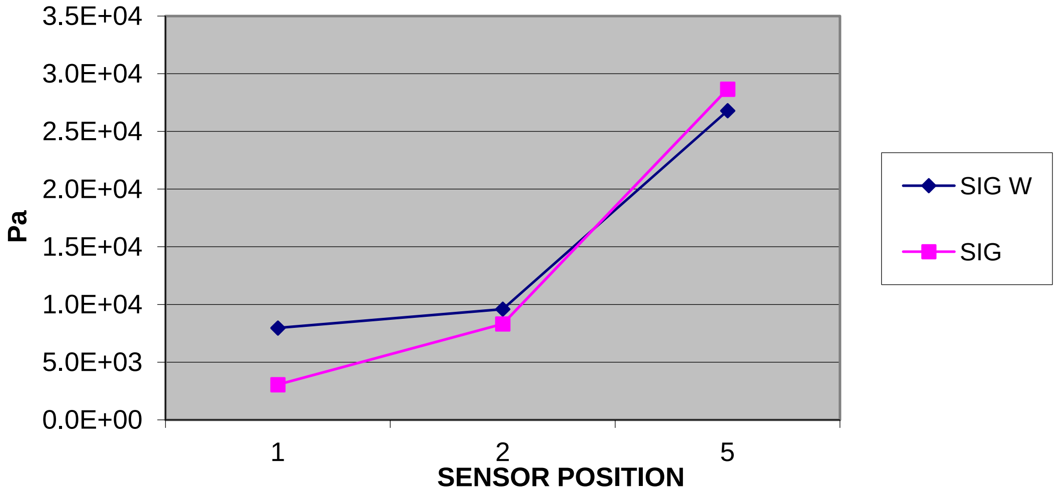

Figure 68. Comparison of Diniz and Nascimento silo data to calculated values: β = 0.6 rad, J =0.26, T = 3000 Pa, OP = 0 Pa

Axially symmetric three-dimensional parallel-sided silo and cone hopper

The collected experimental data sources above do not provide complete stress distributions for granular materials, however they provide values that can be utilised in model validation. Not all cases provided a high level of correlation to the literature. Silo results tended to show higher levels of correlation than hoppers. Walter and Blanchard's 15-degree hopper displayed a high level of correlation. A possible reason for this trend would be the influence of mass-flow design: funnel-flow hoppers may affect the formation of the principal stress arcs as material at incipient flow is not adjacent to the hopper wall. Hence effect of wall friction is negated.

The analysis of the silo and cone hopper experimental data allowed limited testing of results with azimuthal stress relationships, including the Conical Yield function (Nedderman 1992, Kruyt 1993). Analysis indicated that the variables (e.g. M-value) used in these relationships may not take a constant value throughout the granular material. Correlation between calculated values and experimental data may be improved with variable principal stress relationships, or by allowing azimuthal stresses to be dictated by the Conical Yield function.

A second route of investigation would be to produce a model that allowed bulk density to vary in accordance with stress distributions. Schulze (2008) and Nedderman (1992) indicate that bulk density will follow a function of consolidating stresses.

$$\rho_b = (1 - \epsilon)\rho_s \tag{69}$$

The equation above (Nedderman 1992), implies that bulk density will increase as void fraction ϵ is reduced. Void fraction is the amount of granular material occupied by an interstitial medium such as air. At comparatively low stresses, produced by handling and flow, granular materials are compressible as voids between grains can be reduced with increased pressure (Einav 2007). With increased stresses voids will be filled and compressibility is reduced. With further increase in stresses, to levels associated with pulverisation, grains will be crushed (McDowell et al 1996). Hence for the range of stresses normally considered by the silo designer, it can be assumed that a range of bulk densities is prevalent for each material – from a relatively low value after the silo or hopper is filled, to higher values where the material is subject to increased stresses and is therefore compacted, as described by Nedderman (1992). Reimbert and Reimbert (1976) and Schulze (2008) give ranges for granular materials bulk densities.

- ‘Limestone powder’ bulk density recorded as 650 to 1100 kg/m^3 in the stress range 60 Pa to 15 kPa (Schulze 2008). Values were reproduced from yield locus test performed with ring shear testers.
- ‘Moist coal’ bulk density recorded as 810 to 980 kg/m^3 in the stress range 5 kPa to 100 kPa (Schulze 2008). Values were reproduced from yield locus test performed with ring shear testers.

Materials with large, hard grains have small ranges in bulk density values (Schulze 2008). The coal produced a smaller range of bulk density with a larger range of stresses, when compared to the limestone sample.

Figures 59, 62, 63, 66 and Table 8 show comparison of stress distribution values where the model variables cannot be adjusted further to improve correlation, *within reasonable limits*. The highest level of correlation is demonstrated in Figure 67 – representing the Walker and Blanchard 15-degree hopper. The lowest level of correlation is demonstrated in Figure 66 – representing the Walker and Blanchard 30-degree hopper. A notable distinction between the two cases is mass-flow design according to Jenike (1964) and Schulze (2008) for the 15-degree hopper. These two extreme cases were the subject of further sensitivity analyses. It is recommended (Baker 2005) that care is taken with use of the Excel Solver-type algorithms: for example the GRG method is greatly affected by initial values. Initial values in the analyses detailed within this section were selected to represent the active case. Baker (2005) also recommends that variables are altered individually to demonstrate how results are affected. This was carried out for Walker and Blanchard’s 15 and 30-degree hoppers, as these two cases provided best and worst case correlation.

5.6.6 Application Case 6: Further analysis for 30-degree hopper with silo

The sensitivity testing was completed in the following sequence:

- Adjusting variables within, and outside of, their limits.
- Checking conformity to Mohr-Coulomb criterion.
- Review of azimuthal stress relationships.

The β-limits for this case (Walker and Blanchard 1967) are 0.08 to 0.36, with 0.36 as the active limit. J-limits for this case are 0.21 to 4.81, with 0.21 as the active limit. Initial values selected for further analysis were β = 0.22, J = 0.3, T = 1200, after Figure 64.

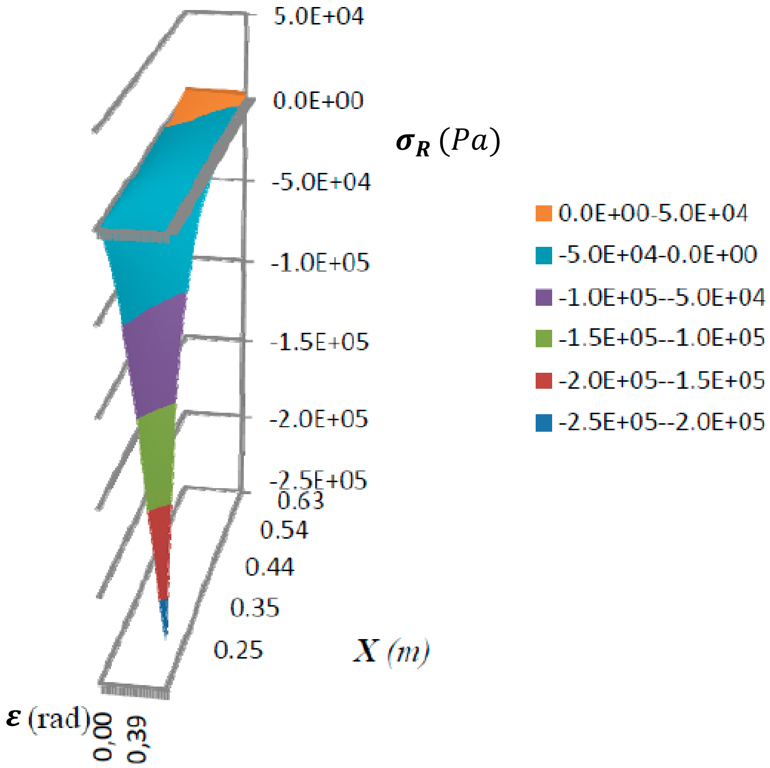

Figure 69. Surface plot showing modelled data with J increase towards passive limit: β = 0.22 rad, J = 4.0, T = 3000 Pa, OP = non-zero values

Reduction of J to its active limit changes shape of σ_W results, reducing correlation. Increasing J to its passive limit causes large negative σ_W-values as the hopper apex is approached. These negative σ_W results are dictated by relatively large negative σ_R results, indicating the material is capable of supporting tensile stresses. Figure 69 shows the distribution of σ_R results, modelled across one half of the cone hopper. Zero radial stress and/or the ability to support tension have been interpreted in previous models (Walker 1966, Enstad 1975, Matchett 2004) as an indication of cohesive arch formation. The material in these analyses are assumed to be stationary, although may be viewed as being at incipient flow. Incipient flow can be defined as where applied stresses have increased to, but not beyond, a materials yield locus. Arc stress (and therefore azimuthal stress) increase towards the hopper apex with use of *J*-values equal to approximately 0.8 and below; above this value a decrease in σ_ε and σ_θ can be observed. Agreement of results to the Mohr-Coulomb yield function can be checked using equation 70. Conformity to the function is not present throughout the system between *J* active and passive limits, although lower values of *J* (i.e. *J*-values tending towards active stress case) demonstrate increased conformity to the criterion.

$$J_{CALCULATED} = \frac{\sigma_R + T}{\sigma_\varepsilon + T} \tag{70}$$

Increase of β to its active limit does not instigate large changes in σ_W results. Reducing β towards passive limits reduces correlation of experimental to calculated data, by altering shape of σ_W results distribution. As β decreases towards 0.08 rad, σ_R increases in the positive direction. With β equal to 0.1 and below, negative arc stresses are present at the hopper walls. This is as expected as β is a function of wall friction, and the model is representing an increased angle of principal stress arc to wall normal – the material is able to support shear stresses of larger magnitudes. Results demonstrated complete conformity to the Mohr-Coulomb yield criterion with $\beta < 0.1$, and only small areas outside of Mohr-Coulomb limits in the range $0.1 < \beta < 0.36$.

Changes in *T* reduced correlation as the selected value moved away from the 'best-fit' target of 1200. Increasing *T* increased the presence of negative σ_R-values. A high *T*-value can be used to indicate high cohesion - this feature of the model demonstrates the granular material being able to support tension.

Axially symmetric three-dimensional parallel-sided silo and cone hopper

Increase of the *k*-value (within equation 62) towards unity caused reduced correlation. Further increase in *k*-value caused instability of results. It was observed that σ_R-values were commonly of an order of magnitude larger than σ_ε-values, within many of the analyses carried out by the author. With use of equation 62, it can be seen that values of k above unity would produce σ_θ results that were dictated mainly by σ_R stress distributions (with only small influence from σ_ε). This is not desired as equation 62 constrains σ_θ equal to σ_ε at zero ε i.e. along the centre line of the hopper. Therefore a discontinuity would be created as σ_θ-values adjacent to the hopper centre line do not equal, or tend towards, σ_ε.

A number of alternative relationships have been used to relate principal stresses – equations 65, 66, 67 and 68.

Equation 65: use of the Haar-von Karman relationship did not improve correlation between experimental and calculated values. As stated above use of relatively small *k*-values with equation 62 dictated results that tended towards Haar-von Karman distribution.

Equation 66: Matchett's (2006a) relationship did not provide stable results within β, T and J variable limits. If J was set equal to unity, selection of an unfeasibly small β-value allowed production of calculated results that underestimated experimental data in a consistent manner. It can be seen that use of such a *J*-value would render σ_θ equal to σ_R. Correlation could not be improved past that produced by use of equation 62. Matchett indicated that this relationship would be may be used to relate radial stress to azimuthal stress i.e. a σ_R-σ_θ failure plane as opposed to σ_R-σ_ε.

Equation 67: using relatively small *k*-values, the relationship derived from Love's (1927) work did not provide correlation to experimental data. Results did not conform to the Mohr-Coulomb criterion. Model variables were adjusted both inside and outside of active and passive limits in an attempt to produce correlation, without success. Use of large *k*-values (in the order of $1\text{x}10^{20}$) produced results that approximated Haar-von Karman distributions: it is a characteristic of this relationship at high *k*-values the σ_R term is nullified and σ_θ tends towards σ_ε.

Equation 68: if the Conical Yield function (Jenike 1987, Nedderman 1992, Kruyt 1993) is rearranged for parameter M, and a line graph is created using calculated principal stress values from the 30-degree hopper model, it can be shown that M would need to take a variable value as opposed to a constant; Nedderman (1992) states that M can be taken as $sin\ \phi$ for certain conditions. Therefore for models results that conform to the Conical Yield function, a relationship may be required to relate to third principal stress to σ_R and σ_ε. A model capable of this would require a dedicated algorithm: for example a program written in Matlab.

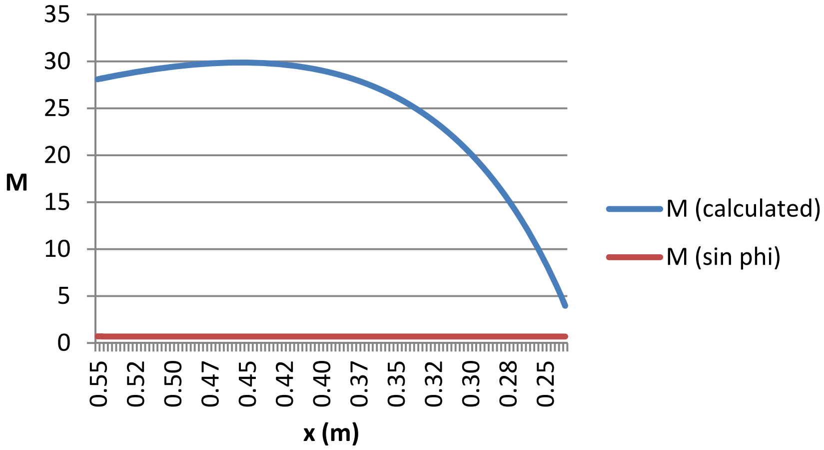

Figure 70. Comparison of calculated *M*-values for CYF (30-degree hopper)

Figure 70 demonstrates non-conformity to the Conical Yield function. It represents a sample section of the 30-degree cone hopper model. After Nedderman, *M* should take a constant value. With development in Matlab, making use of variable *k*-values may improve correlation. An alternative approach would be to allow the Conical Yield function to fix the intermediate principal stress, using the calculated minimum and maximum principal stresses. Values for azimuthal stress distribution were not available in the literature. The author has made use of data available – including normal and shear stress values, for example data given by Wojcik & Tejchman 2008, and theoretical criteria including equations 62, 70 and A.35.

5.6.7 Application Case 7: Further analysis for 15-degree cone hopper

The β-limits for this case (Walker and Blanchard 1967) are 0.08 to 0.36, with 0.36 as the active limit. *J*-limits for this case 0.21 to 4.81, with 0.21 as the active limit. Initial values selected were β = 0.31, J = 0.8, T = 1200, after Figure 67. Reduction of J to its active limit reduces correlation of results between σ_W and σ: calculated stress values take on an exponential curve shape, as opposed to a linear distribution. Increasing J to its passive limit reduces correlation, causing negative σ_W stress values towards the hopper apex. In a similar manner to that observed for the 30-degree hopper stress distributions, changes in σ_W-values are driven by negative σ_R results. Negative σ_R results indicate that the material is capable of supporting tensile stresses. σ_ε and σ_θ increase towards the hopper apex at J-values up to approximately 1.5; after this point a decrease in arc and azimuthal stress can be observed. Conformity of results to the Mohr-Coulomb criterion is poor throughout selected J-values between limits. Conformity is improved towards the J active limit.

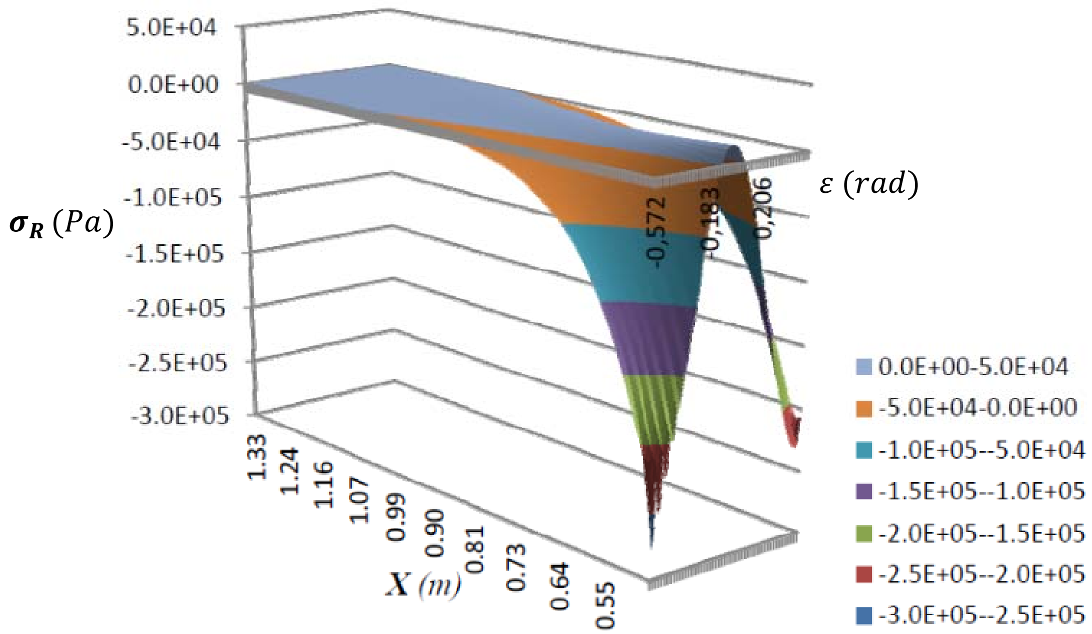

Figure 71. Surface plot showing modelled data with β increase towards passive limit: β = 0.3 rad, J = 0.8, T = 1200 Pa, OP = 0 Pa

Increase in β to its active limit causes a reduction in correlation to experimental data towards the hopper apex. Reduction of β to its passive limit does not produce significant reductions in correlation between σ_W and σ. Reduction of J-value causes a general increase in principal stress magnitudes in a positive direction. At approximately β = 0.3, σ_R results tend towards zero along the hopper centreline – Figure 71. Stresses close to the hopper apex have not been included in the plot, as a number of unstable results were in occurrence. Large negative values are present at the walls near the hopper apex, indicating the material is able to support tensile stresses. Conformity to the Mohr-Coulomb criterion is poor across the model at lower values of β, until β passive is reached – results at this point demonstrate a high level of agreement with the yield function.

A wide range of *T*-values provide acceptable correlation between calculated and experimental results. *T*-values approaching zero, and values above approximately 2000, reduced correlation. Stress distributions for the three principal stresses did not vary by large amounts throughout the selected *T* range. At extreme values of *T* (5000+) stresses began to increase. High *T*-values indicate strong cohesion within a granular material, providing the ability to support stresses of increased magnitude. Conformity to the Mohr-Coulomb yield criterion remained poor throughout use of various *T*-values.

Increase in *k*-value towards unity reduced correlation. Large *k*-values produced unstable results.

In a similar manner to the 30-degree hopper analysis, several functions relating principal stresses have been implemented within the 15-degree hopper model. Findings are listed below.

Equation 65: use of the Haar-von Karman relationship provided similar stress distributions to those for equation 62. Correlation between experimental data and calculated data was improved by a small amount with use of equation 62.

Equation 66: results provided by Matchett's (2006a) relationship were unstable for this system, until *J* was set to unity (therefore $\sigma_\theta = \sigma_R$). However correlation could not be improved past that provided by Matchett et al's (2008) relationship, even when variable were adjusted to values outside of *J* and β limits. With *J* set equal to one, the Mohr-Coulomb yield criterion was satisfied.

Equation 67: use of Love's (1927) relationship did not provide results with correlation between calculated and experimental data, unless a *k*-value was selected that was many orders of magnitude larger than expected principal stress values. For example a *k*-value of $1x10^{20}$ provided calculated results that tended towards Haar-von Karman distributions.

Equation 68: as with the 30-degree cone hopper, the Conical Yield function was rearranged for *M* and compared to calculated results from the model.

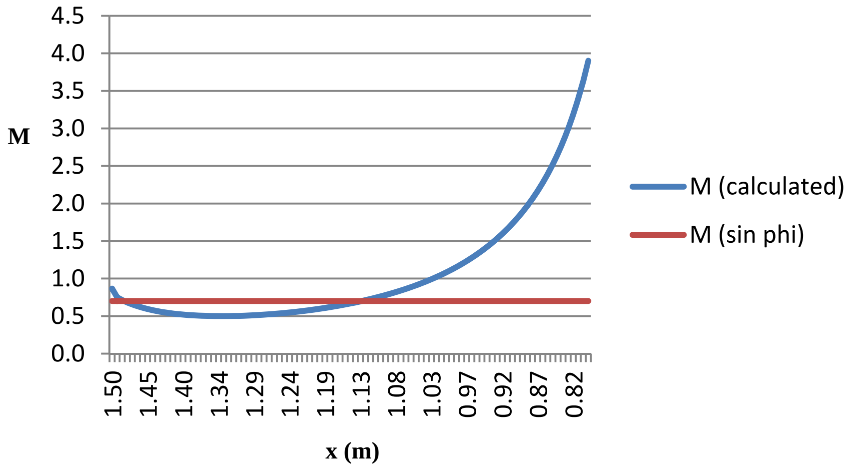

Figure 72. Comparison of calculated M-values for CYF (15-degree hopper)

Figure 72 demonstrates non-conformity to the Conical Yield function. It represents a sample section of the 15-degree cone hopper model

Equation 62 forms part of a novel method for determining stress distributions within granular materials. The method has been applied and used to compare experimental data. Not all analysed cases demonstrated high levels of correlation, however progress has been made in in the area of model validation. For the chosen examples of silos and mass-flow cone hoppers, the models demonstrated satisfactory levels of correlation. Experimental data were not available in the literature for azimuthal stress distributions. For two case studies, statistical hypothesis testing was successfully used to provide confidence with interpretations of data correlation.

Further analysis on two hopper cases failed to provide significant improvements in correlation, even when azimuthal stress relationships were varied. Insight was given into model behaviour, for example the effect of increased friction and the ability of the material to support tensile loading where cohesive arching may be expected. Areas for further research have been identified and include development of a specific algorithm within a popular computer programming language. Effects of bulk density

ρ_b and azimuthal stress relationship variable *k* have been investigated. Current theory utilizes constant values for ρ_b and *k* across silo and cone hopper models. There is limited evidence to suggest that correlation between calculated and experimental data may be improved with variation of these two parameters. In addition, it is hoped that a dedicated algorithm may be used to provide σ_θ-values that confirm to the Conical Yield function, in the absence of other methods of validation.

Throughout the various model alternatives, common features were apparent. Such features included low stress variation across the hopper with use of the Haar-von Karman hypothesis (Haar and von Karman 1909, Nedderman 1992) for σ_θ results. Careful selection of δx and *H* was required to for all model variations as, with the surface boundary condition model, large δx and small *H*-values would cause instability. Use of small δx and large *H*-values tended to produce linear values on surface plots. With the cohesive arch boundary condition model the reverse was true: small δx and large *H*-values produced unstable results. When the $\sigma_\varepsilon + f(\sigma_R, \varepsilon)$ relationship for σ_θ-values was used, an apparent insensitivity to use of sin or tan terms in the equation was demonstrated. This was assumed to be due to small σ_R-values relative to σ_ε results. Use of large *k*-values did not have a large effect on stress distributions: magnitudes of stresses were increased, but patterns of surface plots were rarely affected.

In the above sensitivity analysis reference is made to the MCYF via equation 70. In addition to comparison to the Mohr-Coulomb criterion, all variations of the model were compared to equation 68 – the Conical Yield function. However the results produced did not always fit with the Conical Yield relationship: a range of values for *M* (a constant parameter within the equation) was often required to provide a viable solution. The lack of correlation to the Conical Yield function can be explained as the model created here uses equations based on the Mohr-Coulomb criterion. With little experimental information to verify data, a correlation to a known relationship supports the feasibility of the model.

The findings above are difficult to interpret in their current form. If the model is set up so a silo and hopper are modelled simultaneously, cohesive arch location can be estimated. Instead of using zero for σ_R at the material surface within the hopper section of the model, the final values of the silo model are used (i.e. an overpressure within the surface boundary condition model). This set up is able to produce results with similarities to those shown by Enstad (1975). The location of the arch is indicated by zero or negative σ_R results in the hopper section of the model, shown on the attached three-dimensional surface plot.

5.7 Conclusions

To sum up: stress distributions calculated by the principal stress arc method were compared to theoretical and experimental data from the literature (Wojcik and Tejchman 2008, Rao and Ventaswarlu 1974, Walker and Blanchard 1967, Diniz and Nascimento 2006). Validation exercises were successfully carried out using Wojcik and Tejchman (2008) and Ding et al (2011) finite element model data. Wojcik and Tejchman made use of a hypoplastic material model rather than the rigid-plastic assumption of the principal stress arc method. Ding et al used a Drucker-Prager material model, which provided a yield surface not unlike the Mohr-Coulomb equivalent. The validation exercise demonstrated correlation with both material models.

This work, using three-dimensional silo and cone hopper principal stress arc algorithms, will be published (O'Neill et al 2012 [in preparation]). Matchett (2006a,2006b) considered silos with parallel-sided rat holes. Subsequent to work on this research project Matchett et al (2007) analysed the cone hopper case. In these early versions of the principal stress arc method, the modifications after Lamé-Maxwell were not included and as such can be considered approximations to the current method. The case study accounting for precession of arc centres was published after work as part of this research project.

The rotational symmetry provided by the silo and cone hopper is used to produce a model which allows calculation of stresses including those in the third dimension – azimuthal stress σ_θ . A three-dimensional force balance was completed. The analysis gives two differential equations in three unknown stresses. Hence not all stresses are specified by solution of the equations. As noted above experimental data is not available to verify all results provided by the model. There are no data available for azimuthal stress for example. Prior to the current principal stress arc method few authors have been in a position to comment on stresses in the third dimension although its presence has been acknowledged (Nedderman 1992, Johanson 1995, Johanson 2004, Matchett 2006a,2006b). Johanson used the term hoop stress. Various relationships for azimuthal stresses to the other principal stresses have been proposed and are investigated in Chapter 5.6, by comparison to data available from the literature. To the author's knowledge this research project constitutes the most substantial comparison to experimental data in the field of azimuthal stress relationships. There are few data available for other principal stresses within the granular material. To support the correlation shown in the research project analyses, statistical *t*-tests were carried out on the resultant data in Appendix Five.

The experimental data provided by Wojcik and Tejchman (2008) demonstrated the correlation between experimental and calculated data shown in Figure 57. This case was a three-dimensional silo (as shown in Figure 52), using a granular material of loose, dry sand. The correlation shown in Figure 57 resulted from use of variables β equal to 0.15 rad, J equal to 0.26, T equal to 200 Pa and zero overpressure OP. The selected values are proposed as reasonable approximations to reality for the following reasons:

- The value of β used (0.15) is equal to the passive stress state limit, given by equation 54b. Figure 27(b) demonstrates the passive case.
- The Mohr-Coulomb yield function surface plot for this case shows that calculated J-values are within Mohr-Coulomb criterion limits. This is an indication that the material is stable. The value for J-input is set equal to 0.26, which is equal to the active limit. According to equation 55b the passive J-limit is equal to 3.85.
- T takes a low value as the granular material used (loose, dry sand) was assumed to have limited cohesion.
- A zero value of overpressure OP was thought to be a reasonable assumption due to the experimental set-up.

Axially symmetric three-dimensional parallel-sided silo and cone hopper

- The validation exercise, with results shown in Figure 49, demonstrated correlation to finite element model stress distributions.

Equation 62 provided results that displayed correlation to experimental data. Equation 62 corresponds to a known stress relationship, Equation 65, at certain locations within the principal stress arc models. This is demonstrated in Appendix Two, Chapter 9.7. Azimuthal stress relationships require further, more detailed, experimental analysis when appropriate empirical data is available. Within the limits of this research project, a relationship was proposed that provided correlation between available data and could be derived from a known stress relationship. Therefore the work carried out as part of this project has furthered the level of knowledge in this area.

The Wojcik and Tejchman (2008) cone hopper data was compared to calculated values in Figure 59. The correlation was poor within specified limits of β and *J*, so values were adjusted outside of limits to improve correlation to experimental data. In summary:

- The value of β used (0.2) is within the passive stress state limit of 0.15. The active limit is 0.54.
- The Mohr-Coulomb yield function surface plot for this case shows that calculated *J*-values are also outside of Mohr-Coulomb criterion limits. The value for *J*-input is set equal to 0.2, which is below the active limit of 0.26. The passive *J*-limit is equal to 3.85.
- *T* takes a non-zero value, consistent with the silo analysis.
- A non-zero value of overpressure *OP* was used as the experimental set-up included a silo section above the hopper under consideration. Although a discontinuity was therefore present due to differing β angles, averaged stresses were used to approximate the load present at the top surface of the hopper caused by the granular material within the silo above. The discontinuity between silo and hopper geometries is demonstrated in Figure 58.

Axially symmetric three-dimensional parallel-sided silo and cone hopper

- The validation exercise, with results shown in Figure 51, demonstrated correlation to finite element model data (Ding et al 2011). Correlation reduced towards the hopper apex.

A possible explanation for the lack of correlation is that the hopper geometry, without use of an insert, dictated that funnel flow would be produced (according to Jenike 1964, Schulze 2008). With an angle of internal friction ϕ of 36 degrees and wall friction angle ϕ_W of 22 degrees, Wojcik and Tejchman's cone hopper would need a half-angle α of less than 10 degrees to approach mass-flow. The half-angle is given as 45 degrees in Figure 52, which implies funnel flow for the given granular material within a cone hopper according to Jenike's design procedure.

The data provided by Rao and Ventaswarlu (1974) demonstrated the correlation between experimental and calculated data shown in Figure 61. This case was a three-dimensional silo (as shown in Figure 53), using a granular material of glass beads. The correlation shown in Figure 61 resulted from use of variables β equal to 0.11 rad, *J* equal to 0.01, *T* equal to 0 Pa and zero overpressure *OP*. In summary:

- The value of β used (0.11) is above the passive stress state limit, given by equation 54b. The active limit for β is 0.22 rad.
- The Mohr-Coulomb yield function surface plot for this case shows that calculated *J*-values are outside of Mohr-Coulomb criterion limits. The value for *J*-input is set equal to 0.01, which is outside of *J*-value limits. According to equation 55a and 55b the active *J*-limit is equal to 0.44 and the passive limit 2.28. The model did not provide correlation when *J*-values within these limits were used.
- *T* takes a zero value as the granular material used was assumed to be cohesionless.
- A zero value of overpressure *OP* was thought to be a reasonable assumption due to the experimental set-up.

Equation 62 was used for the relationship to azimuthal stresses. This relationship improved correlation when compared to the alternative methods, although as noted above correlation was poor when *J*-values were used within passive and active limits.

Axially symmetric three-dimensional parallel-sided silo and cone hopper

The Rao and Ventaswarlu (1974) cone hopper data was compared to calculated values in Figure 63. The correlation was poor within specified limits of bulk density ρ. In summary:

- The value of β used (0.12) is outside of the passive stress state limit of 0.15. The active limit is 0.54.
- The Mohr-Coulomb yield function surface plot for this case shows that calculated *J*-values are also outside of Mohr-Coulomb criterion limits. The value for *J*-input is set equal to 0.9, which is below the active limit of 0.26. The passive *J*-limit is equal to 3.85.
- *T* takes a zero value as the granular material used was assumed to be cohesionless.
- A non-zero value of overpressure *OP* was used as the experimental set-up included a silo section above the hopper under consideration. As with the Wojcik and Tejchman case, averaged stresses were used to approximate the load present at the top surface of the hopper.
- Bulk density ρ at 1575 kg/m^3 gave poor correlation. Various values were investigated using the Microsoft Excel Solver application, demonstrating that this parameter had an effect on correlation. The possibility of an algorithm allowing variable bulk density is discussed in Chapter 7.3.

The data provided by Walker and Blanchard (1967) demonstrated the correlation between experimental and calculated data shown in Figures 65, 66 and 67. The three-dimensional cases considered were parallel-sided silo, a 30-degree cone hopper and a 15-degree cone hopper (as shown in Figure 54). The granular material used was coal with a moisture content of 3%. In summary:

- For the silo case, the correlation shown in Figure 65 resulted from use of variables β equal to 0.21 rad, *J* equal to 0.36, *T* equal to 2000 Pa and zero overpressure *OP*. The β active limit for this case is 0.36, and the *J* active limit is 0.21. Therefore β- and *J*-values were within limits and approach the active state, as the β passive limit is 0.08 and the *J* passive limit is 4.81. The analysis showed that reduction of *T* to 1200 Pa improved correlation with experimental data. This value of *T* was reasonable as the material was assumed to be cohesive. A zero value of *OP* was used due to the experimental set-up. The parallel-sided silo case demonstrated poor correlation towards the base of the silo. This was assumed to be due to possible ‘switch’ stresses (Schulze 2008) approaching the transition between silo to hopper. Values away from the transition demonstrated improved correlation.

- For the 30-degree cone hopper case, the correlation shown in Figure 66 resulted from use of variables β equal to 0.22 rad, *J* equal to 0.3, *T* equal to 1200 Pa. A non-zero value of overpressure *OP* was used to represent the material within the silo above the hopper. The β- and *J*-values used were within active and passive limits given above. The algorithm used overestimated experimental data values by an average value of 50%.
- For the 15-degree cone hopper case, the correlation shown in Figure 67 resulted from use of variables β equal to 0.31 rad, *J* equal to 0.8, *T* equal to 1200 Pa. A non-zero value of overpressure *OP* was used to represent the material within the silo above the hopper. The β- and *J*-values used were within active and passive limits given above. The algorithm used provided correlation to within 5% of experimental values.

In Chapters 5.6.6 and 5.6.7 further analysis was completed on the 30-degree and 15-degree cone hoppers. These cases were selected as they provided the two extremes of correlation – the former to within 5% and the latter overestimation of more than 50%. The additional analyses demonstrate the effects of adjustment of variables, allowing review of the Mohr-Coulomb criterion (represented by equation 70), Conical Yield function (equation 68) and azimuthal stress relationships equations 62, 65, 66 and 67. The models indicated that correlation could not be improved by use of azimuthal stress relationships other than equation 62. Calculated results did not conform to the Conical Yield function – it is proposed that the constant *M* within this function may take a variable form, as shown in Figures 70 and 72. Previous methods have employed the Conical Yield function and used a constant value of *M*.

The data provided by Diniz and Nascimento (2006) demonstrated the correlation between experimental and calculated data shown in Figure 68. This case was a three-dimensional silo (as shown in Figure 55), using a granular material of sand. The correlation shown in Figure 68 resulted from use of variables β equal to 0.6 rad, *J* equal to 0.26, *T* equal to 3000 Pa and zero overpressure *OP*. In summary:

- The value of β used (0.6) is below the active stress state limit of 0.68, given by equation 54a. The passive limit for β is 0.21 rad.
- The Mohr-Coulomb yield function surface plot for this case shows that calculated *J*-values are within Mohr-Coulomb criterion limits. The value for *J*-input is set equal to 0.26, which is equal to the *J* active limit. The passive *J*-limit is 3.85.
- *T* takes a non-zero value as the granular material used was assumed to be cohesive. Moisture content of the sand was not indicated.
- A zero value of overpressure *OP* was used due to the experimental set-up.

Chapter 6.0 – Axially symmetric three-dimensional cone hopper with conical insert and rat hole case studies

In this chapter the three-dimensional model presented in Chapter 5.1 is extended to cover the cases of cone hoppers with conical inserts and with conical rat holes. These shapes are rotationally symmetric. The model was based on work by Johanson (2004) and Matchett (2006a,2006b), with improvements after Lamé-Maxwell (Maxwell 1853, Coker et al 1957) to improve accuracy and extended to cover more complex geometries. Matchett's work considered silos with parallel-sided rat holes only. A new three-dimensional force balance has been completed to allow calculation of the three principal stresses. As with the previous model, the analysis gives two differential equations in three unknown stresses. The resulting equations are solved by use of numerical methods. The models take the form of spreadsheet and QBasic programming language algorithms.

6.1 Model geometry, assumptions and resulting force balance equations

6.1.1 Conical insert model

The assumptions used in the conical insert model are listed below, assuming incipient failure.

1. Stresses act over successive sections circular arc sections of radius *R*.

2. Each arc makes angle β with the wall normal and is held at that angle by wall friction (Matchett 2004). The value of β is chosen such that the model works in principal stress space, therefore shear stress terms are not present in the resulting equations.

3. The radius subtends an angle of $(\alpha + \beta)$ at *O*.

4. The arc under consideration cuts the wall at vertical height *x* from the vertex, and intersects the wall at distance *r* from the vertex.

5. The incremental arc has a thickness of δ_w, which varies across the span of the arc with ε.

6. Positions within the hopper are located by height at which the arc cuts the hopper wall *x*, and arc angle ε.

7. There are three principal stresses acting: radial stress σ_R, arc stress σ_ε and azimuthal stress σ_θ. Azimuthal stresses act on the incremental element and are orientated normal to the page.

8. Azimuthal stresses act rotationally about the cone centre line.

9. The incremental element has radius of rotation $\bar{r}$ about the cone centre-line.

10. Rotational symmetry is assumed through azimuthal angle θ.

12. Angle Θ is used to orientate the model through the cone hopper.

13. Limits for ε: $(\alpha+\beta) \leq \varepsilon \leq (\alpha+\beta)$

14. Limits for *x*: $H_1 \leq x \leq H_2$

15. The angle Θ and angle of insert wall (at $\Theta-\alpha$) are both coincident with the theoretical hopper apex.

Three-dimensional cone hopper with conical insert and rat hole

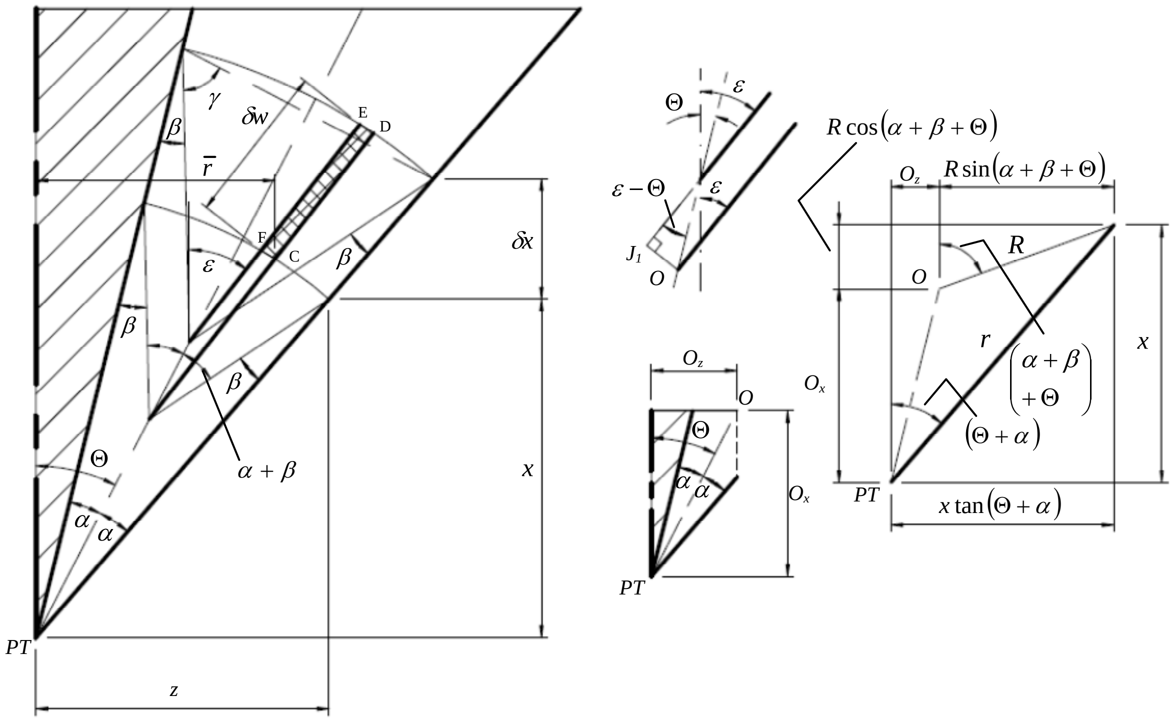

Figure 73. Model geometry

Figure 73 shows the principal stress arc geometry. The annulus between hopper wall and insert has half angle α respectively; a circular arc cuts the hopper right-hand side at a distance x above the apex with radius *R*. Angle Θ aligns the model with the inclined wall of the cone insert. As in Figure 48, Chapter 5.1, the incremental element is rotated about the hopper centre line with radius $\bar{r}$ to form an annulus.

Using the circular arc geometry, a force balance on an incremental element shown in Figure 73 can be completed. From the system geometry:

Since $\dfrac{y}{\sin(\alpha+\alpha)} = \dfrac{r}{\sin(\beta+\gamma)}$ and $\dfrac{y}{\sin(\alpha+\alpha+\beta+\beta)} = \dfrac{R}{\sin\gamma}$,

where $\gamma = 180 - \dfrac{\pi}{2} - \dfrac{\alpha+\alpha+\beta+\beta}{2}$

$$\therefore R = y\frac{\sin\gamma}{\sin(\alpha+\alpha+\beta+\beta)}$$
$$= \frac{r\sin(\alpha+\alpha)\sin\gamma}{\sin(\alpha+\alpha+\beta+\beta)\sin(\beta+\gamma)}$$

where $r = \frac{x}{\cos(\Theta+\alpha)}$

$$\therefore R = \frac{x\sin(\alpha+\alpha)\sin\gamma}{\cos(\Theta+\alpha)\sin(\alpha+\alpha+\beta+\beta)\sin(\beta+\gamma)} \tag{71}$$

Let $\lambda = \alpha+\alpha+\beta+\beta$

$$\therefore R = x\frac{\sin(\alpha+\alpha)\sin\gamma}{\cos(\Theta+\alpha)\sin\lambda\sin(\beta+\gamma)}$$
$$a_1 = \frac{\sin\gamma\sin(\alpha+\alpha)}{\sin\lambda\cos(\Theta+\alpha)\sin(\gamma+\beta)}$$
$$R = a_1 x$$

In Figure 73, an incremental element cuts the right-hand side of the model geometry with vertical height δx, and at angle ε to the vertical with incremental angle $\delta\varepsilon$:

$$O_z = x\tan(\Theta+\alpha) - R\sin(\Theta+\alpha+\beta)$$
$$O_x = x - R\cos(\Theta+\alpha+\beta) \tag{72}$$
$$\therefore \Theta = \tan^{-1}\frac{x\tan(\Theta+\alpha) - R\sin(\Theta+\alpha+\beta)}{x - R\cos(\Theta+\alpha+\beta)}$$

since $R = a_1 x$, $\therefore \Theta = \tan^{-1}\frac{\tan(\Theta+\alpha) - a_1\sin(\Theta+\alpha+\beta)}{1 - a_1\cos(\Theta+\alpha+\beta)}$ (73)

$$OCD = O_1FE + O_1J_1$$
$$\therefore R(x) + \delta w = R(x+\delta x) + \delta O\cos(\varepsilon-\Theta)$$
$$a_1 x + \delta w = a_1(x+\delta x) + \delta O\cos(\varepsilon-\Theta)$$
$$\delta w = a_1\delta x + \delta O\cos(\varepsilon-\Theta)$$

$$\frac{\delta O}{\delta x} = \frac{a_1 \sin\beta}{\sin\alpha}$$

$$\therefore \delta w = \left(a_1 + \frac{\delta O}{\delta x}\cos(\varepsilon - \Theta) \right)\delta x \tag{74}$$

Using equation 44 in Chapter 4.1:

$$(R + \delta x)\sin\varepsilon = \delta O \sin\Theta + (R + \delta R)\sin(\varepsilon + \delta\psi) + soe \tag{75}$$

$$\therefore \frac{\partial\psi}{\partial x} = \frac{a_2(\cos(\varepsilon - \Theta)\sin\varepsilon - \sin\Theta)}{a_1 x \cos\varepsilon} \tag{76}$$

Full derivations of the above equations are shown in Appendix Two. Force balance equations can be derived from the assumptions and equations set out in the preceding chapters. The cone hopper with insert case is fully derived in Appendix Two, Chapter 9.9. Force balance in vertical direction:

$$\begin{aligned}
&\frac{\partial}{\partial x}\left[R^2(\Omega + \sin\varepsilon)\sigma_R \cos\varepsilon\right] = \frac{\partial}{\partial\varepsilon}\left[F\sin\varepsilon(O_Z + R\sin\varepsilon)\right] + \\
&R\sigma_R a_2 \sin(\varepsilon - \Theta)(\Omega\sin\varepsilon - \cos\varepsilon - \cos 2\varepsilon) - R\left(\frac{\partial w}{\partial x}\right)\rho g(O_Z + R\sin\varepsilon) \\
&- \cos\varepsilon\left(R\sigma_R a_2(\Omega + \sin\varepsilon)\cos(\varepsilon - \Theta) - R^2 \sin\varepsilon \frac{\partial\psi}{\partial x}\frac{\partial\sigma_R}{\partial\varepsilon} \right)
\end{aligned} \tag{77}$$

Force balance in horizontal direction:

$$\begin{aligned}
&\frac{\partial}{\partial x}\left[\sigma_R R^2(\Omega + \sin\varepsilon)\sin\varepsilon\right] = -\frac{\partial}{\partial\varepsilon}\left[RF(\Omega + \sin\varepsilon)\cos\varepsilon\right] - \\
&R\sigma_R a_2 \sin(\varepsilon - \Theta)(\sin\varepsilon + 2\cos\varepsilon\sin\varepsilon + \Omega\cos\varepsilon) - R^2\sin^2\varepsilon\frac{\partial\sigma_R}{\partial\varepsilon}\frac{\partial\psi}{\partial x} - \\
&(\Omega + \sin\varepsilon)R\sigma_R a_2 \cos(\varepsilon - \Theta)\sin\varepsilon + R\left(\frac{\partial w}{\partial x}\right)\sigma_\theta
\end{aligned} \tag{78}$$

6.1.2 Conical rat hole model

The model described above can be modified to allow use with cone hoppers with conical rat holes. The assumptions are identical to the cone insert model with the following exception; the left hand wall is considered to be the boundary between static medium and rat hole void, there the angle of friction is assumed to be zero.

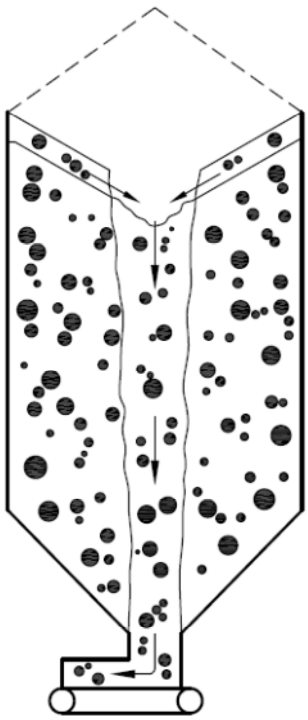

Figure 74. A rat hole in granular material (Jenike 1967)

Figure 74 shows a rat hole in a granular material. The rat hole appears to be conical in shape, for at least part of its height. A photograph of a rat hole in McGee (2008) shows a similar shape.

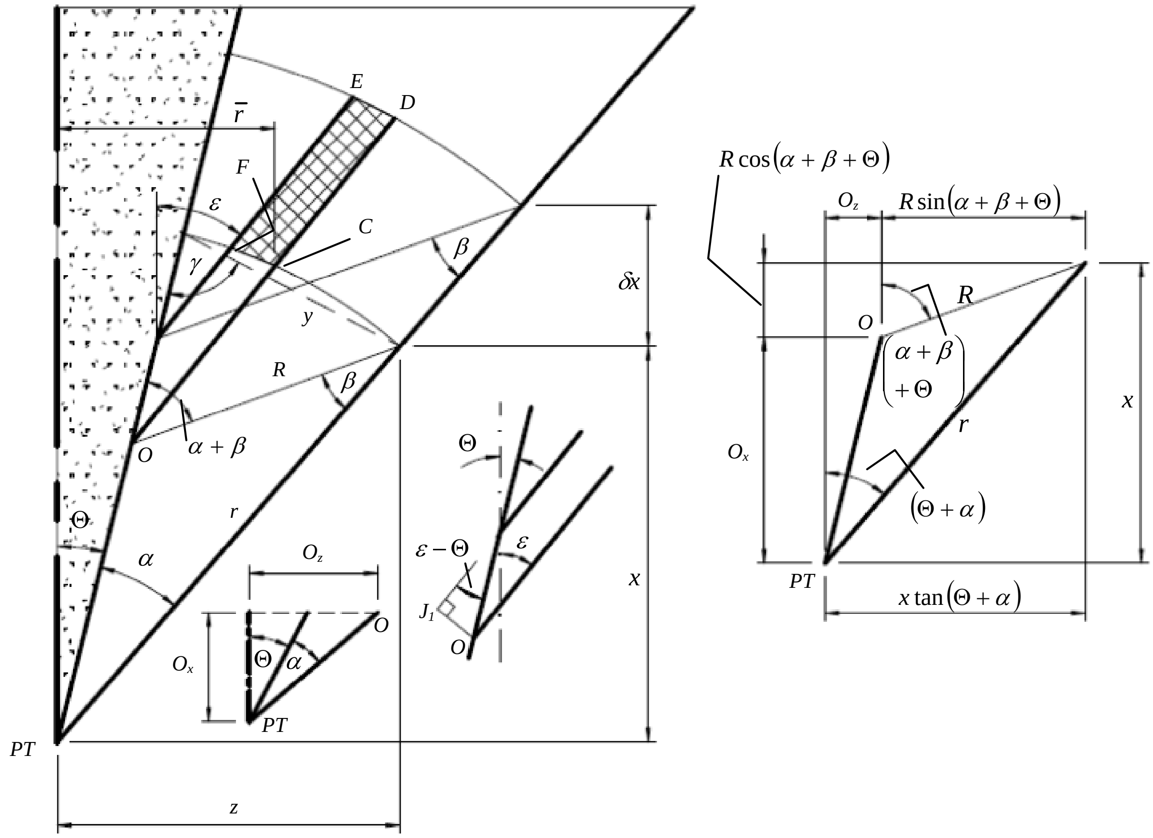

Figure 75. Model geometry

Figure 75 shows the principal stress arc geometry. The annulus between hopper wall and insert has angle α ; a circular arc cuts the hopper right-hand side at a distance x above the apex with radius R. Angle Θ defines the boundary of the static medium. In this model there is only a single value for β, as wall friction at the left wall of the static medium is assumed to be zero (Matchett 2006a). As in Figure 48, Chapter 5.1, the incremental element is rotated about the hopper centre line with radius $\bar{r}$ to form an annulus. From the system geometry:

$$R = \frac{x\sin\alpha}{\cos(\Theta + \alpha)\sin(\alpha + \beta_2)} \tag{79}$$

$$R = a_1 x$$

In Figure 75 an incremental element cuts the right-hand side of the model geometry with vertical height δx, and at angle ε to the vertical with incremental angle $\delta\varepsilon$.

$$\frac{PTO}{\sin\beta} = \frac{R(x)}{\sin\alpha}$$
$$\therefore \delta O = \frac{R(x+\delta x)\sin\beta_2}{\sin\alpha} - \frac{R(x)\sin\beta_2}{\sin\alpha} = \frac{R(\delta x)\sin\beta_2}{\sin\alpha} = \frac{a_1\delta x\sin\beta_2}{\sin\alpha}$$

where Θ can be specified or found using *Ox* and *Oz*;

$$O_z = x\tan(\Theta+\alpha) - R\sin(\Theta+\alpha+\beta_2)$$
$$O_x = x - R\cos(\Theta+\alpha+\beta_2)$$
$$\therefore \Theta = \tan^{-1}\frac{x\tan(\Theta+\alpha) - R\sin(\Theta+\alpha+\beta_2)}{x - R\cos(\Theta+\alpha+\beta_2)}$$

since $R = a_1 x$, $\therefore \Theta = \tan^{-1}\dfrac{\tan(\Theta+\alpha) - a_1\sin(\Theta+\alpha+\beta_2)}{1 - a_1\cos(\Theta+\alpha+\beta_2)}$

$$\frac{\delta O}{\delta x} = \frac{a_1\sin\beta}{\sin\alpha}$$
$$\therefore \delta w = \left(a_1 + \frac{\delta O}{\delta x}\cos(\varepsilon-\Theta)\right)\delta x \qquad (80)$$

The force balance equations, 77 and 78, are applicable for both the conical insert and conical rat hole models. Derivation of the above equations are shown in Appendix Two, Chapter 9.9.

6.2 Spreadsheet based numerical solution

The particular solutions to the force balance equations for this case can now be found using the equations 77 and 78. Derivation of these equations can be found in Appendix Two, Chapters 9.9 and 9.10

$$\therefore \frac{\partial F}{\partial \varepsilon} = \left[\begin{array}{l} -F\left(\frac{\cos 2\varepsilon}{\cos^2 \varepsilon} - \Omega \frac{\sin \varepsilon}{\cos^2 \varepsilon} + \frac{\cos 2\varepsilon}{\sin \varepsilon} - \Omega\right) - \\ \sigma_R a_2 \sin(\varepsilon - \Theta)\left(\Omega \frac{\sin \varepsilon}{\cos \varepsilon} - \frac{\cos 2\varepsilon}{\cos \varepsilon} + 2\cos \varepsilon + \Omega \frac{\cos \varepsilon}{\sin \varepsilon}\right) + \\ \frac{R(\Omega + \sin \varepsilon)}{\cos \varepsilon}\left(\frac{\partial w}{\partial x}\right)\rho g + \frac{1}{\sin \varepsilon}\left(\frac{\partial w}{\partial x}\right)\sigma_\theta \end{array} \right] \Bigg/ \left(\Omega + F\frac{\sin 2\varepsilon}{2\cos \varepsilon} + \Omega \frac{\cos \varepsilon}{\sin \varepsilon} + \frac{\sin 2\varepsilon}{2\sin \varepsilon}\right) \tag{81}$$

and

$$\begin{aligned} \frac{\partial}{\partial x}\left[\sigma_R R^2\right] = -G\left(\Omega \frac{\cos \varepsilon}{\sin \varepsilon} + \frac{\sin 2\varepsilon}{2\sin \varepsilon}\right) - \frac{RF}{\Omega + \sin \varepsilon}\left(\frac{\cos 2\varepsilon}{\sin \varepsilon} - \Omega\right) - \\ \frac{R}{(\Omega + \sin \varepsilon)\sin \varepsilon}\sigma_R a_2 \sin(\varepsilon - \Theta)(\sin \varepsilon + 2\cos \varepsilon \sin \varepsilon + \Omega \cos \varepsilon) - \\ \frac{R^2 \sin \varepsilon}{\Omega + \sin \varepsilon}\frac{\partial \sigma_R}{\partial \varepsilon}\frac{\partial \psi}{\partial x} - R\sigma_R a_2 \cos(\varepsilon - \Theta) + \frac{R}{(\Omega + \sin \varepsilon)\sin \varepsilon}\left(\frac{\partial w}{\partial x}\right)\sigma_\theta \end{aligned} \tag{82}$$

Where $G = R \dfrac{\left[\begin{array}{l} -F\left(\frac{\cos 2\varepsilon}{\cos^2 \varepsilon} - \Omega \frac{\sin \varepsilon}{\cos^2 \varepsilon} + \frac{\cos 2\varepsilon}{\sin \varepsilon} - \Omega\right) - \\ \sigma_R a_2 \sin(\varepsilon - \Theta)\left(\Omega \frac{\sin \varepsilon}{\cos \varepsilon} - \frac{\cos 2\varepsilon}{\cos \varepsilon} + 2\cos \varepsilon + \Omega \frac{\cos \varepsilon}{\sin \varepsilon}\right) + \\ \frac{R(\Omega + \sin \varepsilon)}{\cos \varepsilon}\left(\frac{\partial w}{\partial x}\right)\rho g + \frac{1}{\sin \varepsilon}\left(\frac{\partial w}{\partial x}\right)\sigma_\theta \end{array} \right]}{\left(\Omega + F\frac{\sin 2\varepsilon}{2\cos \varepsilon} + \Omega \frac{\cos \varepsilon}{\sin \varepsilon} + \frac{\sin 2\varepsilon}{2\sin \varepsilon}\right)(\Omega + \sin \varepsilon)}$ (83)

Force balance equations 77 and 78 apply to both the conical insert case and conical rat hole case. The models presented in Chapter 6.1.1 and 6.1.2 have been set-up on spreadsheet software. Solution equations 81 and 82 have been used to form the basis of these models. An explanation of the spreadsheet-based models is given in Appendix Three.

6.3 QBasic algorithm/programming

In Chapters 6.3.1 and 6.3.2, flow charts explain the QBasic algorithms for the cases of three-dimensional cone hopper with conical inserts and conical rat holes. The QBasic algorithms are included in Appendix Four.

6.3.1 QBasic algorithm for three-dimensional conical insert case

Flow chart for QBasic three-dimensional cone hopper with insert algorithm:

LINES 9 TO 34: USER INPUT OF MATERIAL PHYSICAL PROPERTIES. THESE DO NOT CHANGE THROUGHOUT PROGRAM.	CONSTANTS INPUT/CALCULATED: RHO, phi_w, phi, pi, T, Fc, Co

⇩

LINES 36 TO 131: USER INPUT OF HOPPER AND MODEL GEOMETRY DATA. THESE VARIABLES DO NOT CHANGE DURING PROGRAM ITERATIONS. NU SET TO ZERO FOR EQUAL ANGLE HOPPER	CONSTANTS INPUT/CALCULATED: H, H2, ALPHA, BETA, THETA, R, LAMBDA, GAMMA, A1, A2, NU, J, DELTA_X_INC, DELTA_ETA_INC, DELTA_X, DELTA_ETA, ETA, X, PW_WRTX, R, PPSI_WRTX

⇩

LINES 133 TO 156: DIMENSIONING OF ARRAYS FOR VARIABLES THAT CHANGE DURING SUCCESSIVE ITERATIONS OF THE PROGRAM. INITIAL VALUES FOUND TO BE NECESSARY AND THEREFORE USED FOR SIG_R, SIG_THETA AND F: ACTUAL INITIAL VALUES BASED OF REVIEW OF EXCEL METHOD	ARRAYS DIMENSIONED: PF_WRTETA, PSIG_R_WRTETA, SIG_ETA, F, PSIG_R_WRTX, SIG_R, SIG_THETA

⇩

Three-dimensional cone hopper with conical insert and rat hole

LINES 156 TO 166 (CLOSES ON LINE 387): NEWTON-RAPHSON TYPE METHOD EMPLOYED TO CREATE WHILE LOOP. WHILE DIFFERENCE BETWEEN SUCCESIVE ITERATIONS OF FINAL ROW OF SIG_R MATRIX IS GREATER THAN 1, THE PROGRAM WILL CONTINUE TO CYCLE.	WHILE LOOP CONDITIONS: Y# = 0, DIFF# = 2, Numberofiterations = 0, DIFF >=1
LINES 168 TO 174: CALCULATE PF_WRTETA MATRIX USING ETA-DIRECTION FORCE BALANCE EQUATION (INITIAL CONDITION USED FOR SIG_R, F & SIG_THETA).	FUNCTION OF: SIG_R, SIG_THETA, F
LINES 176 TO 190: CALCULATE PSIG_R_WRTETA MATRIX USING FINITE DIFFERENCE METHOD (LH WALL USES FORWARD DIFFERENCE, RH WALL BACKWARD DIFFERENCE, REMAINDER CENTRAL DIFFERENCE).	FUNCTION OF: SIG_R
LINES 192 TO 201: CALCULATE SIG_ETA MATRIX USING F/PW_WRTX WITH A CENTRAL BOUNDARY CONDITION OF MOHR-COULOMB CRITERION SIG_ETA=J*SIG_R+(J-1)*T.	FUNCTION OF: F, SIG_R
LINES 203 TO 217: CALCULATE F MATRIX USING FORWARD AND REVERSE EULER METHOD FROM CENTRAL BOUNDARY CONDITION OF PW_WRTX*SIG_ETA.	FUNCTION OF: SIG_ETA, PF_WRTETA
LINES 219 TO 225: CALCULATE SIG_THETA MATRIX USING SIG_THETA=SIG_ETA+k*SIN(ETA)*SIG_R RELATIONSHIP	FUNCTION OF: SIG_ETA, SIG_R

<u>Three-dimensional cone hopper with conical insert and rat hole</u>

LINES 227 TO 233: CALCULATE PSIG_R_WRTX MATRIX USING R-DIRECTION FORCE BALANCE EQUATION.	FUNCTION OF: PF_WRTETA, SIG_R, PSIG_R_WRTETA, PPSI_WTRX, SIG THETA

LINES 235 TO 245: CALCULATE SIG_R MATRIX USING REVERSE EULER METHOD FROM BOUNDARY CONDITION OF ZERO (AT MATERIAL SURFACE).	FUNCTION OF: PSIG_R_WRTX

LINES 247 TO 367: OUTPUT VARIABLES TO CSV FILES

LINES 369 TO 387: CLOSING STATEMENTS OF WHILE LOOP AND END PROGRAM, PRINT NUMBER OF ITERATIONS. NUMBER OF ITERATIONS LIMITED ON LINE 385.

The QBasic programming code for the three-dimensional cone hopper with conical inert case is provided in Appendix Four, Chapter 11.5.

6.3.2 QBasic algorithm for three-dimensional cone hopper with conical rat hole case

Flow chart for QBasic three-dimensional cone hopper with conical rat hole algorithm:

LINES 9 TO 34: USER INPUT OF MATERIAL PHYSICAL PROPERTIES. THESE DO NOT CHANGE THROUGHOUT PROGRAM.	CONSTANTS INPUT/CALCULATED: RHO, phi_w, phi, pi, T, Fc, Co

Three-dimensional cone hopper with conical insert and rat hole

LINES 36 TO 131: USER INPUT OF HOPPER AND MODEL GEOMETRY DATA. THESE VARIABLES DO NOT CHANGE DURING PROGRAM ITERATIONS. NU SET TO ZERO FOR EQUAL ANGLE HOPPER	CONSTANTS INPUT/CALCULATED: H, H2, ALPHA2, BETA2, THETA, R, LAMBDA, GAMMA, A1, A2, NU, J, DELTA_X_INC, DELTA_ETA_INC, DELTA_X, DELTA_ETA, ETA, X, PW_WRTX, R, PPSI_WRTX
LINES 133 TO 156: DIMENSIONING OF ARRAYS FOR VARIABLES THAT CHANGE DURING SUCCESSIVE ITERATIONS OF THE PROGRAM. INITIAL VALUES FOUND TO BE NECESSARY AND THEREFORE USED FOR SIG_R, SIG_THETA AND F: ACTUAL INITIAL VALUES BASED OF REVIEW OF EXCEL METHOD	ARRAYS DIMENSIONED: PF_WRTETA, PSIG_R_WRTETA, SIG_ETA, F, PSIG_R_WRTX, SIG_R, SIG_THETA
LINES 158 TO 166 (CLOSES ON LINE 387): NEWTON-RAPHSON TYPE METHOD EMPLOYED TO CREATE WHILE LOOP. WHILE DIFFERENCE BETWEEN SUCCESIVE ITERATIONS OF FINAL ROW OF SIG_R MATRIX IS GREATER THAN 1, THE PROGRAM WILL CONTINUE TO CYCLE.	WHILE LOOP CONDITIONS: Y# = 0, DIFF# = 2, Numberofiterations = 0, DIFF >=1
LINES 168 TO 174: CALCULATE PF_WRTETA MATRIX USING ETA-DIRECTION FORCE BALANCE EQUATION (INITIAL CONDITION USED FOR SIG_R, F & SIG_THETA).	FUNCTION OF: SIG_R, SIG_THETA, F

Three-dimensional cone hopper with conical insert and rat hole

LINES 176 TO 190: CALCULATE PSIG_R_WRTETA MATRIX USING FINITE DIFFERENCE METHOD (LH WALL USES FORWARD DIFFERENCE, RH WALL BACKWARD DIFFERENCE, REMAINDER CENTRAL DIFFERENCE).	FUNCTION OF: SIG_R
LINES 192 TO 201: CALCULATE SIG_ETA MATRIX USING F/PW_WRTX WITH A CENTRAL BOUNDARY CONDITION OF MOHR-COULOMB CRITERION SIG_ETA=J*SIG_R+(J-1)*T.	FUNCTION OF: F, SIG_R
LINES 203 TO 217: CALCULATE F MATRIX USING FORWARD AND REVERSE EULER METHOD FROM CENTRAL BOUNDARY CONDITION OF PW_WRTX*SIG_ETA.	FUNCTION OF: SIG_ETA, PF_WRTETA
LINES 219 TO 225: CALCULATE SIG_THETA MATRIX USING SIG_THETA=SIG_ETA+k*SIN(ETA)*SIG_R RELATIONSHIP	FUNCTION OF: SIG_ETA, SIG_R
LINES 227 TO 233: CALCULATE PSIG_R_WRTX MATRIX USING R-DIRECTION FORCE BALANCE EQUATION.	FUNCTION OF: PF_WRTETA, SIG_R, PSIG_R_WRTETA, PPSI_WTRX, SIG THETA
LINES 235 TO 245: CALCULATE SIG_R MATRIX USING REVERSE EULER METHOD FROM BOUNDARY CONDITION OF ZERO (AT MATERIAL SURFACE).	FUNCTION OF: PSIG_R_WRTX

Three-dimensional cone hopper with conical insert and rat hole

LINES 247 TO 367: OUTPUT VARIABLES TO CSV FILES

↓

LINES 369 TO 387: CLOSING STATEMENTS OF WHILE LOOP AND END PROGRAM, PRINT NUMBER OF ITERATIONS. NUMBER OF ITERATIONS LIMITED ON LINE 385.

The QBasic programming code for the three-dimensional cone hopper with conical rat hole case is provided in Appendix Four, Chapter 11.6.

6.4 Model validation

Figure 76 below provides a comparison of results calculated by the principal stress arc method and data produced by Wojcik and Tejchman's (2008) Finite Element model. The model used by Wojcik and Tejchman for this case was introduced in Chapter 5.4: a hypoplastic material model. The finite element mesh contained 26 increments horizontal direction and 115 increments in the vertical direction; 4-node quadrilateral elements were used. A principal stress arc algorithm was created using identical material properties to Wojcik and Tejchman's FE model. In Figure 76, FEA results are indicated by 'SIG FEA' for wall normal stress data and 'TAU FEA' for shear stress data. The case is a three-dimensional hopper with conical insert as shown in Figure 52.

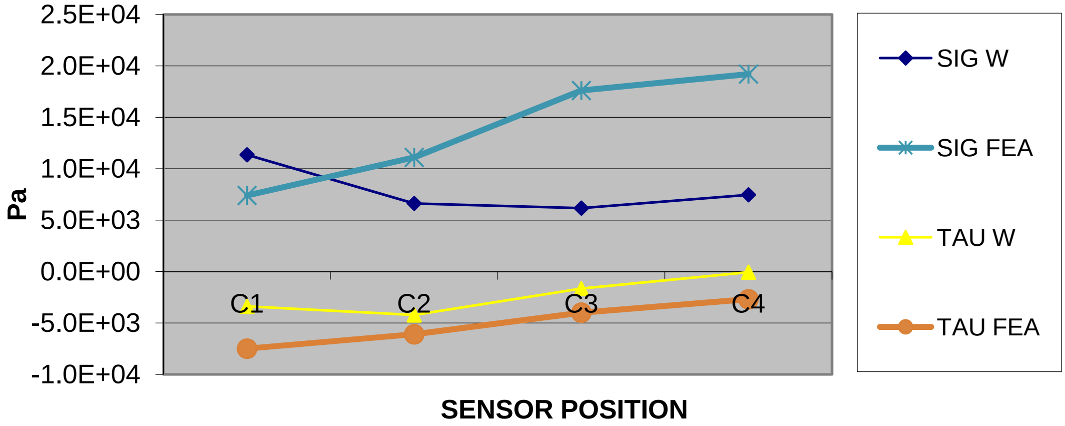

Figure 76. Comparison with Wojcik and Tejchman cone hopper with conical insert FEA data to calculated values, with J = 1.3, β = 0.41 rad, T = 900 Pa, OP = 9000 Pa.

While shear stress values demonstrated correlation, wall stress values calculated by the principal stress arc method overestimated FEA derived data. The validated three-dimensional cone hopper with conical insert algorithm was calibrated by use of data fitting, as noted in Chapter 6.6, and by use of material properties information sourced from the literature.

6.5 Experimental data sourced from the literature

Few examples of experimental data were available to compare with the geometry proposed in Chapter 6.1. Data from provided by Wojcik and Tejchman (2008) was used in Chapter 5.6.1 for comparison to cone hopper values without an insert. The experimental silo and cone hopper arrangement shown in Figure 52 do not match the assumptions set out above in Chapter 6.1 in their entirety, in that the apex of the insert does not match the theoretical hopper apex. However the following comparison has been carried out for the purpose of demonstrating application of the method.

The granular material was loose dry sand, with a bulk density ρ_b of 1428 kg/m^3. Angle of internal friction ϕ was 36 degrees and wall friction angle ϕ_W 22 degrees.

6.6 Application of method

This case was created for the purpose of demonstrating extension of the principal stress arc method. It is a specific case constrained by the geometry shown in Figures 73 and 75, hence the lack of comparable experimental data. The models proposed in Chapters 6.1.1 and 6.1.2 demonstrated the possibility of extending the principal stress arc method. The equations derived for this method, shown in Appendix Two, were complex and therefore increased the possibility of error within the algorithms created.

Figure 77 indicates that the cone insert model is a realistic case for the conical annulus formed between the hopper and insert walls. The cone model proposed in Chapter 5.1 can be used to evaluate stress distributions internal to the insert. Figure 74 (in Chapter 6.1.2) and McGee (2008) indicate that a conical rat hole assumption may be a viable one, if an averaged rat hole profile is taken.

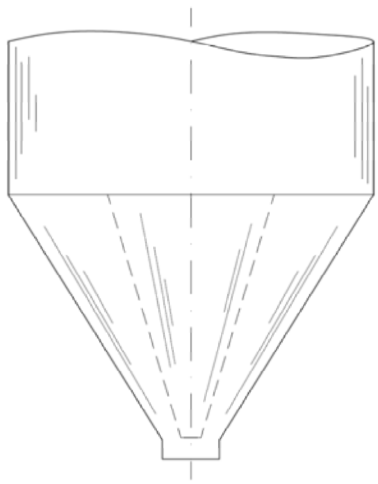

Figure 77. Cone-in-cone insert (McGee 2008)

As within previous silo, wedge and cone case studies in preceding chapters, the model was fitted to the data using a least-squares approach via the Solver application. Angle of arc to wall normal β, material ratio of effective stresses J, tensile parameter T and overpressure OP were selected as adjustable parameters.

Three-dimensional cone hopper with conical insert and rat hole

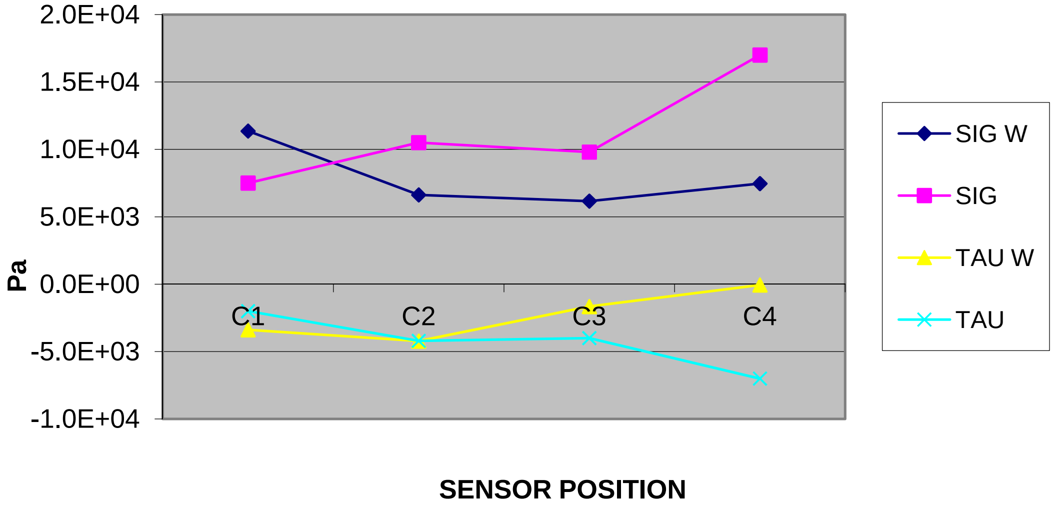

Figure 78. Comparison with Wojcik and Tejchman cone hopper with conical insert experimental data, with J = 1.3, β = 0.41 rad, T = 900 Pa, OP = 9000 Pa.

Figure 78 shows that the principal stress arc method underestimates the magnitude of experimental data for wall normal and shear stresses. Equation 62 was used to provide a relationship for the azimuthal stress σ_θ for other principal stress σ_R and σ_ε. The correlation between calculated and values from the literature reduces with increasing height within the hopper. At sensor location C2, theoretical value τ_W overestimates experimental data τ by less than 1% in magnitude. At sensor location C4, theoretical value σ_W underestimates experimental data σ by an order of magnitude. Table 14 provides average correlation between experimental data and calculated results.

	% SIG		% TAU	
Sensor	**PSA**	**FEA**	**PSA**	**FEA**
C1	151.4%	98.7%	169.1%	375.0%
C2	63.1%	105.7%	100.5%	145.2%
C3	62.9%	179.6%	41.4%	100.0%
C4	43.9%	112.9%	0.9%	38.6%
Average error	**80.3%**	**124.2%**	**78.0%**	**164.7%**

Table 14. Comparison with Wojcik and Tejchman cone hopper with conical insert FEA data to calculated values, showing correlation to experimental data as a percentage

6.7 Conclusions

A relatively high overpressure *OP* was required to improve correlation. This is in accordance with the experimental set up as the large-scale silo is situated above the hopper. Correlation reduced when the calculated values in Figure 78 were compared to experimental data given for a cone hopper without an insert (Wojcik and Tejchman 2008).

The conical insert and conical rat hole models were developed from the three-dimensional cone hopper model. This case has not been published prior to this research project. Matchett's (2006a,2006b) work covered parallel-sided silos with parallel-sided rat holes, without Lamé-Maxwell modifications. The insert model proposed for this research project is limited by geometry as the insert wall coincides with the hopper wall at the theoretical hopper apex. A model validation exercise was carried out in Chapter 6.4 with partial success using data produced via finite element analysis (Wojcik and Tejchman 2008), for the conical insert case. Different material models were used in the two analyses: the assumptions of a Mohr-Coulomb yield surface and a model described by a hypoplastic constitutive equation. As noted in Chapter 5.4.1, Rombach et al (2005) provide a comparison of results produced from finite element analyses using elastic-plastic and hypoplastic materials models. Correlation is demonstrated between the two methods.

Experimental data was available to allow comparison (Wojcik and Tejchman 2008), and in Chapter 6.5 was used for comparison between calculated stress values and data from the literature. No data was available for comparison of the rat hole model. Nedderman (1992) noted that the Coulomb model, used with the assumption of the Radial Stress Field, does not reliably predict the location of the rat hole in (dynamic) core flow. The model proposed by this research project assumes that static material forms an annulus around the central void of the conical rat hole, therefore wall friction at the void boundary is zero. Non-zero values of wall friction were assumed by Johanson (1995) in his work on vertical rat holes. Zero wall friction at this location was assumed by Matchett (2006a), in his work on the same geometry. Matchett considered the static case, while Johanson studied the dynamic case.

Three-dimensional cone hopper with conical insert and rat hole

The data provided Wojcik and Tejchman (2008) demonstrated the correlation between experimental and calculated data shown in Figure 78. Validation was provided by comparison to data provided by a finite element analysis. The granular material used was loose, dry sand with use of variables β equal to 0.41 rad, *J* equal to 0.41, *T* equal to 900 Pa and *OP* equal to 9000 Pa. In summary:

- The value of β used (0.41) is below the active stress state limit of 0.54, given by equation 54a. The passive limit for β is 0.15 rad.
- The Mohr-Coulomb yield function surface plot for this case shows that calculated *J*-values were outside of Mohr-Coulomb criterion limits. The value for *J*-input is set equal to 1.3. The active *J*-limit is 0.26 and the passive *J*-limit is 3.85.
- *T* takes a non-zero value as the granular material used was assumed to be cohesive. Moisture content of the sand was not indicated. This is consistent with the cone hopper without insert analysis above.
- A relatively large non-zero value of overpressure *OP* was used. This is reasonable due to the large scale silo installed above the cone hopper.

When compared to experimental data for a cone hopper without an insert, correlation was reduced.

Chapter 7.0 – Conclusions and Further Work

Chapter 7.1 Conclusions

This research project has developed stress analysis within silos and hoppers using the principal stress arc method. Data has been produced that contributes to the knowledge of stress distributions within granular materials. The research was specifically focused on the principal stress arc method, providing models for more complex geometries than previously have been available. The geometries include those which are currently in use in industry (Schulze 2008, McGee 2008). The principal stress arc method is a development of prior methods (Enstad 1975, Li 1994, Matchett 2004,2006a,2006b). The current principal stress arc method was developed using findings from research into the field of Photo-elasticity including use of Lamé-Maxwell equations (Maxwell 1853, Love 1927, Coker et al 1957, Frocht 1941, Durrance 1967, Zapletal 1970, Olsen 1982). The purpose of this assumption was to allow the incremental element walls to more closely follow the trajectories of principal stresses. An early version of the principal stress arc method (Matchett 2004) did not take account of curvature of the incremental element in the direction normal to the principal stress arc. The effect of this modification after Lamé-Maxwell can be seen in Figure 36 in Chapter 4.1.

National design codes for silos and hoppers are based on approximate techniques that assume vertical and horizontal directions of principal stresses, with constant horizontal stress across the silos (Nedderman 1992, Schulze 2008). The national standards used in industry are modified by use of empirical data and consultants are available to provide expert advice, although methods commonly employed by the industry can be proved to be conservative (Enstad 1975, Drescher et al 1995, Matchett 2004). According to the knowledge of the author there are no industrial standards that provide data for loading on inserts within hoppers. The findings from the research project can be used to combat common flow problems and provide new information on structural loading of silos and hoppers, including inserts used to promote flow.

Conclusions and Further Work

Various methods for analysis of stress distributions within silos and hoppers are available and are discussed in Chapter 2.0. The literature survey demonstrated the methods that are available to the silo and hopper designer, from continuum analysis type including the method of differential slices, to the relatively complex discrete element method. While the principal stress arc method is not without its limitations, other stress analysis methods also have features that limit their use. Chapter 2.7 summarizes research on the available methods with reasoned discussion on development of the current principal stress arc method.

- The Method of Differential Slices (Janssen 1895, Nedderman 1992) makes use of axes that do not coincide with the directions of principal stress, which are not known. The method also makes use of an empirical stress ratio for calculation of the second principal stress, and uses averaged stress values across the width of the silo or hopper.
- The Method of Characteristics (Sokolovskii 1965) is used for soil mechanics case studies, for example retaining walls. It is therefore not appropriate for complex geometries.
- The Radial Stress Field (Jenike 1961, Purutyan et al 2001) uses a variable orientation of principal stresses within the model – leading to great complexities. Jenike's work has been employed in industry to great effect, although his methods have been proved to be conservative.
- Motzkus' method (Motzkus 1974, Schulze 2006b) of insert load calculation made use of averaged stresses rather than two-dimensional calculations.
- Early Principal Stress Arc methods included Enstad (1975), who assumed a constant minor principal stress along the edge of a curved incremental slice. This has been demonstrated by Nedderman (1992) to be incorrect. Li (1994) also made use of an averaged principal stress along a curved surface. Matchett (2004) proposed a two-dimensional version of the principal stress arc method for the wedge hopper case. The method was subsequently used by Matchett (2004) to represent rotationally symmetric three-dimensional systems – silos with parallel-sided rat holes. Matchett (2004,2006a,2006b) did not take account of the angle resulting from precession of the incremental arc centre.

- Finite Element Methods (Haussler and Eibl 1984, Kamath and Puri 1999) are available. Experimental data is not available in sufficient quantity to verify Finite Element methods or other models (Malone and Xu 2008). This comment can be applied to the research project models. Recent FEM publications model the silo or hopper walls only, with loading from granular material applied as boundary conditions to the shell mesh (Vidal et al 2008, Sadowski and Rotter 2011). Alternative methods or assumptions are required to provide values for these boundary conditions. It is possible that the principal stress arc algorithms could be used for this purpose. A small amount of research work is available on three-dimensional models making use of an FE mesh to represent the granular material; in their work, Goodey et al (2006) used the case study of a square-section silo above a pyramidal hopper.

An alternative to continuum analysis methods, the Discrete Element Method (Kruggel-Emden et al 2008), is becoming viable as available computational power increases. This method uses individual particles as separate entities in the model and is growing in popularity. DEM is limited by computer programming power to compute the locations of thousands or even millions of particles (Goda and Ebert 2005). As with Finite Element Methods, the accuracy of results depend on appropriate definition of boundary conditions and interpretation of results.

Continuum and discrete analysis methods are limited by collection of experimental data. The literature survey highlighted that collection of experimental data has improved over recent years, with powder characterisation equipment allowing more detailed repeatable measurement of granular materials (Freeman 2010). This allows more accurate methods of stress calculation to become feasible. When compared to available experimental data, results produced by the new models were not always in agreement with experimental data.

One possible explanation for the lack of correlation within one of the three-dimensional cases is that the cone hopper geometry, without use of an insert, dictated that funnel flow would be produced (according to Jenike 1964, Schulze 2008). With an angle of internal friction ϕ of 36 degrees and wall friction angle ϕ_W of 22 degrees, Wojcik and Tejchman's cone hopper would need a half-angle α of less than

10 degrees to approach mass-flow. The half-angle is given as 45 degrees in Figure 45, which implies funnel flow for the given granular material within a cone hopper according to Jenike's design procedure. Nedderman (1992) indicated that use of the Coulomb failure model with the Radial Stress Field method did not fit well with empirical data for an emptying funnel flow hopper, and recommended use of the Conical Yield function for this application. Calculated results did not conform to the Conical Yield function – it is proposed that the constant *M* within this function may take a variable form, as shown in Figures 70 and 72, Chapters 5.6.6 and 5.6.7. Previous methods have employed the Conical Yield function and used a constant value of *M*.

The project aims were as follows:

A. To develop algorithms to predict stresses in hoppers and silos using principal stress arc geometry methods.

B. To implement these methods in various hopper configurations including cones, wedges and hoppers with inserts.

C. To compare resultant data with experimental data from the literature.

D. To use the models to develop new methods of design for hopper systems.

To achieve these aims, spreadsheet- and Microsoft QBasic computer language-based algorithms have been developed for parallel-sided silos, wedge hoppers, cones hoppers and cone hoppers with conical inserts and conical rat holes.

It is the opinion of the research team that these models are accurate. The following points support this claim:

- Self-checking was completed.
- Checking by other members of research team.
- Method has sound mathematical base of force balance equations.
- Comparison between spreadsheets and QBasic algorithms.

- Comparison to experimental data and previous versions of the principal stress arc method.
- Statistical testing completed.
- The authors who provided experimental data in the literature compared their findings to prior methods with varying degrees of success. In Chapter 4, Walker and Blanchard 1967 compared to Walker 1966; Tuzun and Nedderman 1985 compared to Janssen 1895/Walker 1966/Walters 1973; Drescher et al 1995 compared to Jenike 1964/Walker 1966/Enstad 1975.

In support of the above, within Chapters 4, 5 and 6, results produced by finite element analysis models (Yunming et al 2011, Wojcik and Tejchman 2008, Ding et al 2011) were used for validation purposes. Correlation between calculated results was demonstrated for some locations within the subject silos and hoppers. Correlation reduced towards the hopper apex. It is possible that the hopper apex induces unstable results due to the presence of a singularity at this location. Figure 41 in Chapter 4.4, Figure 49 in Chapter 5.4.1 and Figure 51 in Chapter 5.4.2 gave confidence to validation of the proposed principal stress arc method using FEA modelling.

The different approaches used in the finite element analyses included Drucker-Prager yield surfaces (Yunming et al 2011, Ding et al 2011) and a model described by a hypoplastic constitutive equation (Wojcik and Tejchman 2008). The Drucker-Prager yield surface provides limits that are approximations to the Mohr-Coulomb equivalent used by principal stress arc methods. Use of a hypoplastic material model is a departure from the assumption of Mohr-Coulomb failure surface. Rombach et al (2005) provide a comparison of results produced from finite element analyses using elastic-plastic and hypoplastic materials models. Correlation is demonstrated between the two methods. Wojcik and Tejchman's (2008) hypoplastic model makes the assumption of Coulomb friction between the granular material and vessel walls. For the above reasons it is proposed that the validation exercises were valid.

The assumption of a circular principal stress arc has not been consistent in this field of research, with previous authors considering other shapes (Janssen 1895, Walker 1966, Benink 1989). The limited evidence on this subject supports the assumption of a circular arc (Faure and Gendrin 1989, Sakaguchi et al 1993, Langston et al 1995, Kamath and Puri 1999, Berry et al 2000, McCue and Hill 2005, Matchett 2007), indicating that this geometry should allow development of models that imitate reality.

Limitations of the principal stress arc method include the assumptions of arc shape, lack of experimental data for verification and lack of consideration of dynamic forces. In addition to this, the three-dimensional models make use of rotational symmetry. This limits the use of current models to symmetrical shapes.

In conclusion, the wall stress data comparisons completed as part of this research project, with development of the models using further experimental data for validation, may be used for structural design of silos and hoppers. Loading to the vessel shell and inserts may be more accurately determined. To consider the extreme case, this could avoid failure of structures. The critical outlet dimensions calculated via the principal stress arc method may also be used to improve current industrial practice. Prior methods have been proved to be conservative through work on this research project.

Chapter 7.2 Specific summaries of case studies

Chapter 7.2.1 Two-dimensional parallel-sided silo and wedge hopper

The first case studies completed as part of the project were the two-dimensional parallel-sided silo and wedge hopper. The wedge hopper case was first proposed by Matchett (2004), although the model used did not take account of curvature in the direction normal to the principal stress arc. The current method with revision due to precession of the arc centres was published after work on this research project.

The case was an ideal one, where stresses in the third dimension were not considered in the analysis. The silo and wedge hopper were assumed to be ‘long’ in that friction or stresses in the direction normal to the page (Figure 32 in Chapter 4.1) were not considered in the force balance equations. In Chapter 4.4 validation exercises were successfully carried out, through comparison to previous principal stress arc models and via using calculated data from a finite element analysis of a wedge hopper (Yunming et al 2011). The Yunming et al validation was feasible due to similarities in material model used: the Mohr-Coulomb criterion used in the principal stress arc method assumes a rigid-plastic failure mode (Nedderman 1992). The comparison to previous principal stress arc models was successful: at shallow depths both old and new models demonstrated similar characteristics, while at greater depths the new models indicated variation in stress horizontally across the vessel. Experimental data indicates that horizontal stress variation is present in reality (Walter & Blanchard 1967).

In Chapter 4.6 calculated results from the principal stress arc method were compared to experimental data for wall normal stresses. In the two cases studies of two-dimensional silo and hopper, correlation between calculated and experimental data was displayed.

As noted in Chapter 4.6, stresses calculated by the principal stress arc method were compared to Schulze and Schwedes (1994) and Berry et al (2000). The comparison showed that the principal stress arc method produced values that were in reasonable agreement with the experimental data. In some cases the principal stress arc method improved on conservative critical outlet diameter estimates made by use of prior methods. Jenike's method is frequently used in industry (Jenike 1964, Schulze 2008). As part of this research project, calculated values were compared to data from the literature (Walker and Blanchard 1967, Tuzun and Nedderman 1985, Drescher et al 1995). The work is to be published (O'Neill et al 2012 [in preparation]).

Chapter 7.2.2 Three-dimensional parallel-sided silo and cone hopper

As a logical development, the three-dimensional silo and cone hopper analyses followed the two-dimensional method above. Matchett (2006a,2006b) considered silos with and without parallel-sided rat holes. As part of this research project Matchett et al (2007) analysed the cone hopper case. In these early versions of the principal stress arc method, the modifications after Lamé-Maxwell were not included and as such were considered approximations to the current method. The case study accounting for precession of arc centres was published after work as part of this research project.

The rotational symmetry provided by the silo and cone hopper is used to produce a model which allows calculation of stresses including those in the third dimension – azimuthal stress σ_θ . A three-dimensional force balance was completed. The analysis gives two differential equations in three unknown stresses. Hence not all stresses are specified by solution of the equations. As noted above experimental data is not available to verify all results provided by the model. There are no data available for azimuthal stress. Prior to the current principal stress arc method few authors have been in a position to comment on stresses in the third dimension although its presence has been acknowledged (Nedderman 1992, Johanson 1995, Johanson 2004, Matchett 2006a,2006b). Various relationships for azimuthal stresses to the other principal stresses have been proposed and are investigated in Chapter 5.6. To the author's knowledge this research project constitutes the most substantial comparison to experimental data in the field of azimuthal stress relationships. Equation 62 was used for the relationship to azimuthal stresses in the three-dimensional cases. This relationship improved correlation when compared to the alternative methods. As noted above correlation was poor when *J*-values were used within passive and active limits for silos and hoppers of dimensions conducive to funnel flow. There are few data available for other principal stresses within the granular material.

In Chapter 5.4 validation exercises were successfully carried out using Wojcik and Tejchman (2008) and Ding et al (2011) finite element model data. Comparisons were also made to previous principal stress arc models. Wojcik and Tejchman made use of a hypoplastic material model rather than the rigid-plastic assumption of the principal stress arc method. Ding et al used a Drucker-Prager material model, which provided a yield surface not unlike the Mohr-Coulomb equivalent. The validation exercise demonstrated correlation with both material models. In Chapter 5.6 stress distributions calculated by the principal stress arc method were successfully compared to data from the literature (Wojcik and Tejchman 2008, Rao and Ventaswarlu 1974, Walker and Blanchard 1967, Diniz and Nascimento 2006). To support the correlation shown in the analyses, statistical *t*-tests were carried out on the resultant data in Appendix Five. This work using three-dimensional silo and cone hopper geometries is to be published (O'Neill et al 2012 [in preparation]).

Chapter 7.2.3 Three-dimensional cone hopper with conical insert and rat hole

The conical insert and conical rat hole models were developed from the three-dimensional cone hopper model. This case has not been published prior to this research project. Matchett's (2006a,2006b) work covered parallel-sided silos with parallel-sided rat holes. The insert model proposed for this research project is limited by geometry as the insert wall coincides with the hopper wall at the theoretical hopper apex. The model can be used to provide loads on inserts, something which is lacking in current theoretical knowledge and national standards (Nedderman 1992, Schulze 2008).

Few data was available to allow comparison of this case (Wojcik and Tejchman 2008). A model validation exercise was carried out in Chapter 6.4 with partial success using data produced via finite element analysis (Wojcik and Tejchman 2008), for the conical insert case. Different material models were used in the two analyses: the assumptions of a Mohr-Coulomb yield surface and a model described by a hypoplastic constitutive equation. In Chapter 6.6 experimental data was successfully used for comparison between principal stress arc calculated values and data from the literature. No data was available for comparison of the rat hole model. Nedderman (1992) noted that the Coulomb model, used with the assumption of the Radial Stress Field, does not reliably predict the location of the rat hole in (dynamic) core flow. The model proposed by this research project assumes that static material forms an annulus around the central void of the conical rat hole, therefore wall friction at the void boundary is zero. Zero wall friction at this location was assumed by Matchett (2006a), in his work on vertical rat holes.

With the conical insert case, correlation to experimental data reduced when comparison was made between theoretical results with an insert and experimental data without an insert.

Chapter 7.3 Further work

During completion of this research project it became apparent that further work could be completed with three-dimensional shapes that do not make use of rotational symmetry. A key assumption of the principal stress arc method is the circular principal stress arc. This shape restricts the method to analysis of geometrical shapes that do have rotational symmetry, unless assumptions are made of the stress state in 'unswept' areas of the silo or hopper. To use a square-section silo or pyramidal hopper as an example, the circular arc geometry would not be able to model material adjacent to the four corners. A version of the method can be developed that does not make use of such symmetry.

Two possible modifications for a three-dimensional version of the principal stress arc method are as below.

- Application of the work by Jessop (1949) to stress distributions within silos and hoppers. This would be a departure from the current theory that azimuthal stress acts in a circular direction.
- Modify three-dimensional principal stress arc model to use incremental element instead of an annulus shape.

Other areas of possible further work include:

- Algorithms allowing variable bulk density as stresses increase. Comparisons with experimental data indicated that variable density may improve correlation.
- A varying *M*-value within the Conical Yield function. In addition to review of the validity of the Mohr-Coulomb criterion, the three-dimensional silo and cone hopper models were used to review the Conical Yield function. The model results did not correlate to a constant *M*-value. The Conical Yield function i.e. equation 68 can be reduced to a quadratic equation of the form $Z{\sigma_\theta}^2 + Y\sigma_\theta + X = 0$, where X and Y are functions of σ_R and σ_ε. Solution of this equation for the purpose of providing σ_θ-values did not consistently provide usable values for equation 68.

- Development of an insert model to cover more complex insert shapes, including the Inverted Cone type (McGee 2008).
- Development of an improved user interface so that the program can be widely used by researchers and industrialists.
- Further systematic investigation of discrepancies between predictions and experimental data and other numerical results, including finite element methods.

As noted throughout the project, the lack of detailed experimental data has limited validation of the proposed method and prior models created over the past 100 years.

Chapter 8.0 - Appendix One

References

References

1. Abadie, J., Carpentier, J., 1969. Generalization of the Wolfe Reduced Gradient Method to the Case of Nonlinear Constraints. In *Optimization*, R. Fletcher (ed.).

2. Abdullah, E.C., Geldart D., 1999. The use of bulk density measurements as flowability indicators. *Powder Technology*, **102** (2) pp. 151-165.

3. Ai, J. et al., 2011. Assessment of rolling resistance models in discrete element simulations. *Powder Technology*, **206 (**3) pp. 269-282.

4. Ajax Equipment. *Testimonials and Endorsements From Some of Our Customers*. Ajax Equipment Limited [internet]. Available from http://www.ajax.co.uk/testimonials.htm [cited 14.07.12].

5. Anand, A. et al., 2009. Predicting discharge dynamics of wet cohesive particles from a rectangular hopper using the discrete element method (DEM). *Chemical Engineering Science*, **64** (24) pp. 5268-5275.

6. Baker, K., 2005. *Optimization Modeling with Spreadsheets*. International Student Edition, Brooks/Cole.

7. Bates, L. *Powder Testing for Flow*. Ajax Equipment Limited [internet]. Available from: http://www.ajax.co.uk/papers.htm [cited 14.07.12].

8. Bates, L. *Storage and feeding of particulate solids*. Ajax Equipment Limited [internet]. Available from: http://www.ajax.co.uk/papers.htm [cited 14.07.12].

9. Bazaraa, M.S. et al., 1993. *Non-linear Programming: Theory and Algorithms*. John Wiley & Sons, 2nd ed.

10. Benink, E.J., 1989. A new theory for hopper stresses during discharge. *Bulk Solids Handling*, **9** (4) pp. 429-432.

References

11. Berry, R.J. et al., 2000. Measurement of critical cohesive arches in silos using laser ranging. Proceeding of *From Powder to Bulk,* IMechE, England, pp. 131-141.

12. Bierwisch, C. et al., 2009. Die filling optimization using three-dimensional discrete element modeling. *Powder Technology*, **196** (2) pp. 169-179.

13. BS EN 1991-4:2006 Eurocode 1 – *Actions on structures – Part 4: Silos and tanks.*

14. BS EN 1993-4-1:2007 Eurocode 3 – *Design of steel structures – Part 4-1: Silos.*

15. Carson, J.W., 2000. *Silo failures: case histories and lessons learned*. Jenike & Johanson, Inc. [internet]. Available from: http://www.jenike.com/TechPapers/ [cited 14.07.12].

16. Chen, J.F. et al., 1998. Statistical inference of unsymmetrical silo pressures from comprehensive wall strain measurements. *Thin-Walled Structures*, **31** (1) pp. 117-136.

17. Chen, M., Fan, S.S., 2002. Tolerance evaluation of minimum zone straightness using non-linear programming techniques: a spreadsheet approach. *Computers and Industrial Engineering*, **43** (1) pp. 437-453.

18. Cleary, P.W., Sawley, M.L., 2002. DEM modelling of industrial granular flows: 3D case studies and the effect of particle shape on hopper discharge. *Applied Mathematical Modelling*, **26** (2) pp. 89-111.

19. Coetzee, C.J., Els, D.N.J., 2009. Calibration of discrete element parameters and the modelling of silo discharge and bucket filling. *Computers and Electronics in Agriculture*, **65** (2) pp. 198-212.

References

20. Coker, E.G. et al., 1957. *A Treatise on Photo-Elasticity*. 2nd Ed. Amsterdam: Cambridge University Press.

21. Coulomb C.A., 1776. Essai sur une application des regles des maximis et minimis a quelques problemes de statique relatifs a l'architecture. *Memoires de l'Academie Royale pres Divers Savants*, **7** [in French].

22. Cundall, P.A., Strack, O.D.L., 1979. A discrete numerical model for granular assembles, Geotechnique **29** (1) pp. 47–65.

23. Deacon, J., 2009. *Student's t-test*. The University of Edinburgh - School of Biological Sciences [internet]. Available from http://www.biology.ed.ac.uk/research/groups/jdeacon/statistics/table1.html [cited 14.07.12].

24. DIN 1055-6:2005-03 *Actions on structures – Part 6: Design loads for buildings and loads in silo bins*.

25. Ding, S., et al., 2011. Development of normal pressure and frictional traction along the walls of a steep conical hopper during filling. *Thin-Walled Structures*, **49** (10) pp. 1246-1250.

26. Diniz, M.J., Nascimento, J.W.B., 2006. Analysis of pressures in vertical silo of masonry of bricks [Análise de pressões em silo vertical de alvenaria de tijolos]. Revista *Brasileira de Engenharia Agricola e Ambiental*, **10** (1) pp. 212-219 [in Portuguese].

27. Drescher, A. et al., 1995. Arching in hoppers: I. Arching theories and bulk material flow properties. *Powder Technology*, **84** (2) pp. 165-176.

28. Drucker, D.C., Prager, W., 1952. Soil mechanics and plastic analysis for limit design. *Quarterly of Applied Mechanics*, **10** (2) pp. 157-165.

References

29. Durrance, E.M., 1967. Photoelastic stress studies and their application to a mechanical analysis of the Tertiary Ring-Complex of Ardnamurchan, Argyllshire. *Proceedings of the Geologists' Association*, **78** (2) pp. 289-318.

30. Eastop T.D., McConkey A., 1993. *Applied Thermodynamics for Engineering Technologists*. 5th ed. Longman.

31. Einav, I., 2007. Breakage mechanics—Part II: Modelling granular materials. *Journal of the Mechanics and Physics of Solids*, **55** (6) pp. 1298-1320.

32. Enstad, G., 1975. On the theory of arching in mass flow hoppers. *Chemical Engineering Science*, **30** (10) pp. 1273-1283.

33. Faure, Y.H., Gendrin, P., 1989. Filtration of a granular medium by textiles. *Powders and Grains*. Biariez and Gourdes (eds.), Rotterdam: Balkema.

34. Freeman, R., 2007. Measuring the flow properties of consolidated, conditioned and aerated powders – a comparative study using a powder rheometer and a rotational shear cell. *Powder Technology*, **174** (1-2) pp. 25-33.

35. Freeman, R., 2010. *FT4 Powder Rheometer System*. Freeman Technology [internet]. Available from: http://www.freemantech.co.uk/en/ft4-system/ft4-powder-rheometer.html [cited 14.07.12].

36. Frenning, G., 2008. An efficient finite/discrete element procedure for simulating compression of 3D particle assemblies. *Computer Methods in Applied Mechanics and Engineering*, **197** (49-50) pp. 4266-4272.

37. Frocht, M.M., 1941. *Photoelasticity*. New York: John Wiley & Sons, Inc.

38. Fylstra, D. et al., 1998. Design and Use of the Microsoft Excel Solver. *Interfaces*, **28** (5) pp. 29-55.

References

39. Gallego, E. et al., 2011. A simplified analytical procedure for assessing the worst patch load location on circular steel silos with corrugated walls. *Engineering Structures,* **33** (6) pp. 1940-1954.

40. Galybin, A.N., Mukhamediev, Sh.A., 2004. Determination of elastic stresses from discrete data on stress orientations. *International Journal of Solids and Structures,* **41** pp. 5125-5142.

41. Gauss, C.F., 1809. *Theoria Motus Corporum Coelestium in sectionibus conicis solem ambientium* [in Latin].

42. Geldart, D., Williams, J.C., 1985. Flooding from hoppers: identifying powders likely to give problems. *Powder Technology,* **43** (2) pp. 181-183.

43. Geldart, D. et al., 2006. Characterization of powder flowability using measurement of angle of repose. *China Particuology,* **4** (3-4) pp. 104-107.

44. Goda, T.J., Ebert, F., 2005. Three-dimensional discrete element simulations in hoppers and silos. *Powder Technology*, **158** (1-3) pp. 58-68.

45. Goodey, R.J. et al., 2006. Predicted patterns of filling pressures in thin-walled square silos. *Engineering Structures*, **28** (1) pp. 109-119.

46. Haar, A., von Karman, T., 1909. Zur Theorie der Spannungzustande in Plastischen und Sandartingen Medien, *Nachr. Ges. Wiss. Gottingen Math-Phys.,* **K1** pp. 204-218 [in German].

47. Hancock, A.W., 1970. *PhD Thesis*. Cambridge.

48. Haussler, U., Eibl, J., 1984. Numerical investigations on discharging silos. *Journal of Engineering Mechanics Division*, ASCE, 110 (EM6) pp. 957-971.

49. Hearn, E.J., 2003. *Mechanics of Materials Volume 1: An Introduction to the Mechanics of Elastic and Plastic Deformation of Solids and Structural Materials*. 3rd Edition, Butterworth-Heinemann.

50. Janssen, H.A., 1895. Getreidedruck in Silozellen. *Ztg. Ver. dt. Ing*., **39** pp. 1045-1049 [in German].

51. Jenike, A.W., 1961. *Gravity Flow of Bulk Solids, Bull. No. 108*, Engng. Exp. Station, Univ. Utah, Salt Lake City.

52. Jenike, A.W., 1964. *Storage and Flow of Solids, Bull. No. 123*, Engng. Exp. Station, Univ. Utah, Salt Lake City.

53. Jenike, A.W., 1967. Quantitative design of mass flow bins. *Powder Technology*, **1** (4) pp. 237-244.

54. Jenike, A.W., 1987. A theory of flow of particulate solids in converging and diverging channels based on a conical yield function. *Powder Technology*, **50** (3) pp. 229-236.

55. Jessop, H.T., 1949. The Determination of the Separate Stresses in Three-dimensional Stress Investigations by the Frozen Stress Method. *Journal of Scientific Instruments*, **26** pp. 27-31.

56. Johanson, J., 1995. Predicting rathole stability in funnel-flow bins. *Proceedings of Partec 95 Conference, Nurnberg, Germany pp. 407–416.*

57. Johanson, K., 2004. Rathole stability analysis for aerated powder materials. *Powder Technology*, **141** (1-2) pp. 161-170.

58. Johanson, K. et al., 2005. Quantitative measurement of particle segregation mechanisms. *Powder Technology*, **159** (1) pp. 1-12.

References

59. Juan, A. et al., 2006. Establishing stress state of cylindrical metal silos using finite element method: comparison with ENV 1993. *Thin-Walled Structures,* **44** (11) pp. 1192–1200.

60. Kamath, S. et al., 1993. Flow properties of powders using four testers – measurement, comparison and assessment. *Powder Technology*, **76** (3) pp. 277-289.

61. Kamath, S., Puri, V.M., 1999. Finite element model development and validation for incipient flow analysis of cohesive powders from hopper bins. *Powder Technology*, **102** (2) pp. 184-193.

62. Karlsson, T. et al., 1998. Finite element simulation of granular material flow in plane silos with complicated geometry. *Powder Technology,* **99** (1) pp. 29-39.

63. Ketterhagen, W.R. et al., 2007. Granular segregation in discharging cylindrical hoppers: a discrete element and experimental study. *Chemical Engineering Science,* **62** (22) pp. 6423-6439.

64. Ketterhagen, W.R. et al., 2008. Modeling granular segregation in flow from quasi-three-dimensional, wedge-shaped hoppers. *Powder Technology*, **179** (3) pp. 126–143.

65. Ketterhagen, W.R. et al., 2009. Predicting the flow mode from hoppers using the discrete element method *Powder Technology*, **195** (1) pp. 1-10.

66. Khanam, J., Nanda, A., 2005. Flow of granules through cylindrical hopper. *Powder Technology*, **150** (1) pp. 30-35.

67. Kolymbas, D., 2000. *Introduction to Hypoplasticity (Introduction to Geotechnical Engineering & Tunnelling).* Rotterdam: Taylor & Francis.

68. Kruggel-Emden, H. et al., 2007. Review and extension of normal force models for the Discrete Element Method. *Powder Technology,* **171** (3) pp. 157-173.

69. Kruggel-Emden, H. et al., 2008. A study on the validity of the multi-sphere Discrete Element Method. *Powder Technology*, **188** (2) pp. 153-165.

70. Kruggel-Emden, H. et al., 2010. A study on adjusted contact force laws for accelerated large scale discrete element simulations. *Particuology*, **8** (2) pp. 161-175.

71. Kruyt, N.P., 1993. Results of Jenike's (1987) radial stress field theory for the flow of granular materials in conical hoppers: Flow regimes and flow factors. *Powder Technology*, **76** (1) pp. 109-112.

72. Landry, J.W. et al., 2004. Discrete element simulation of stress distribution in silos: crossover from two to three dimensions. *Powder Technology,* **139** (3) pp. 233-239.

73. Langston, P.A. et al., 1995. Discrete element simulation of granular flow in 2D and 3D hoppers: dependence on discharge rate and wall stress on particle interactions. *Chemical Engineering Science*, **50** (6) pp. 967-987.

74. Langston, P.A. et al., 2004. Distinct element modelling of non-spherical frictionless particle flow. *Chemical Engineering Science*, **59** (2) pp. 425-435.

75. Lasdon, L.S. et al., 1978. Design and Testing of a Generalized Reduced Gradient Code for Nonlinear Programming. *ACM Transactions on Mathematical Software*, **4** (1) pp. 34-50.

76. Li, H., 1994. Mechanics of arching in a moving bed standpipe with interstitial gas flow. *Powder Technology*, **78** (2) pp. 179-187.

References

77. Li, R.K.J. et al., 1998. Morphology and dynamic mechanical properties of glass beads filled low density polyethylene composites. *Journal of Materials Processing Technology*, **79** (1-3) pp. 59–65.

78. Li, J. et al., 2004. Flow of sphero-disc particles in rectangular hoppers – a DEM and experimental comparison in 3D. *Chemical Engineering Science*, **59** (24) pp. 5917-5929.

79. Li, Y. et al., 2009. DEM simulations and experiments of pebble flow with monosized spheres. *Powder Technology*, **193** (3) pp. 312-318.

80. Love, A.E.H., 1927. *A Treatise on the Mathematics of Elasticity*. 4th Ed, New York: Dover Publications.

81. Malone, K.F., Xu, B.H., 2008. Determination of contact parameters for discrete element method simulations of granular systems. *Particuology*, **6** (6) pp. 521-528.

82. Marinelli, J., Carson, J.W., 2001. *Solve solids flow problems in bins, hoppers and feeders*. Jenike & Johanson, Inc. [internet]. Available from: http://www.jenike.com/TechPapers/ [cited 14.07.12].

83. Martinez, M.A. et al., 2002. Simulation of axi-symmetric discharging in metallic silos. Analysis of the induced pressure distribution and comparison with different standards. *Engineering Structures*, **24** (12) pp. 1561-1574.

84. Matchett, A.J. et al., 2000. A reliable, vibrationally activated, mass-flow hopper system. *Powder to Bulk, International Conference of the IMechE, June 13–15, London.*

85. Matchett, A.J. et al., 2001. A vibrational hopper for reliable flow. *PARTEC2001 Conference, Nurnberg, March 2001.*

86. Matchett, A.J., 2004. A theoretical model of vibrationally induced flow in a conical hopper system. *Chemical Engineering Research and Design*, **82** (A1) pp. 85-98.

87. Matchett, A.J., 2006a. Rotated, circular arc models of stress in silos applied to core flow and vertical rat-holes. *Powder Technology*, **162** (2) pp. 87-89.

88. Matchett, A.J., 2006b. Stresses in a bulk solid in a cylindrical silo, including an analysis of rat-holes and an interpretation of rat-hole stability criteria. *Chemical Engineering Science*, **61** (6) pp. 2035-2047.

89. Matchett, A.J. et al., 2007. Analytical solutions to stress distribution problems in wedge and conical hoppers. *Proceedings of Enstimac 2007 Conference, Ecoles des Mines D'Albi, France.*

90. Matchett, A.J., 2007. The shape of the cohesive arch in hoppers and silos — Some theoretical considerations. *Powder Technology*, **171** (3) pp. 133–145.

91. Matchett, A.J. et al., 2008. Stress distributions in 2-dimensional, wedge hoppers with circular arc stress orientation — A co-ordinate-specific Lamé–Maxwell model. *Powder Technology,* **187** (3) pp. 298-306.

92. Matchett, A.J. et al., 2009. Stresses in bulk solids in wedge hoppers: A flexible formulation of the co-ordinate specific, Lamé–Maxwell equations for circular arc, principal stress systems. *Powder Technology*, **194** (3) pp. 166-180.

93. Materials Today (ed.), 2006 Bulk density measured in real time. *Materials Today*, **9** (6) p. 62.

94. Matsusaka, S. et al., 1995. Micro-feeding of fine powders using a capillary tube with ultrasonic vibration. *Advanced Powder Technology*, **6** (4) pp. 283–293.

References

95. Matsusaka S. et al., 1996, Micro-feeding of a fine powder using vibrating capillary tube. *Advanced Powder Technology,* **7** (2) pp. 141–151.

96. Maxwell, J.C., 1853. On the equilibrium of elastic solids. *Transactions of the Royal Society of Edinburgh*, **20** pp. 87-120.

97. McCue, S.W., Hill, J.M., 2005. Free surface problems for static Coulomb-Mohr granular solids. *Mathematics and Mechanics of Solids,* **10** (6) pp. 651-672.

98. McDowell, G.R. et al., 1996. The fractal crushing of granular materials. *Journal of the Mechanics and Physics of Solids,* **44** (12) pp. 2079-2102.

99. McGee, E. Insert Solutions. *The Chemical Engineer* magazine, issue 802 April 2008 pp. 38-39.

100. McGlinchey, D. (ed.), 2005. *Characterisation of Bulk Solids*. Oxford: Blackwell Publishing Ltd.

101. Mio, H. et al., 2009. Speed-up of computing time for numerical analysis of particle charging process by using discrete element method. *Chemical Engineering Science*, **64** (5) pp. 1019–1026.

102. Mohr, O., 1906. *Techiniche Mechanik*. Berlin: William Ernst und Sohn [in German].

103. Moreea, S.B.M., Nedderman, R.M., 1996. Exact stresses and velocity distributions in a cohesionless material discharging from a conical hopper. *Chemical Engineering Science*, **51 (**16) pp. 3931-3942.

104. Morton, K.W., Mayers, D.F., 1994. *Numerical solution of partial differential equations*. UK: Cambridge University Press.

105. Motzkus, U., 1974. *Belastung von Siloböden und Auslauftrichtern durch körnige Schüttgüter*. Dissertation TU Braunschweig [in German].

106. Muite, B.K. et al., 2004. Silo music and silo quake: granular flow-induced vibration. *Powder Technology,* **145** (3) pp. 190-202.

107. Nedderman, R.M., 1992. *Statics and Kinematics of Granular Material*. New York: Cambridge University Press.

108. O'Neill, J.C. et al., 2009. Stresses in bulk solids in cone hoppers: numerical solutions to the 3-dimensional stress distribution problem, using circular arc geometry. *Proceedings of Flexible Automation and Intelligent Manufacturing 2009 Conference, Teesside University, UK.*

109. O'Neill, J.C. et al., 2012. Stresses in bulk solids in cone hoppers: numerical solutions to the 3-dimensional stress distribution problem, using circular arc geometry with comparison to experimental data. *In preparation.*

110. Olsen, G.A., 1982. *Elements of Mechanics of Materials.* 4th ed. Englewood Cliffs, Prentice-Hall, Inc.

111. Ooi, J.Y. et al., 1996. Prediction of static wall pressures in coal silos. *Construction and Building Materials,* **10** (2) pp. 109-116.

112. Orband, J.L.R., Geldart, D., 1997. Direct measurement of powder cohesion using a torsional device. *Powder Technology*, **92** (1) pp.25-33.

113. Perry, G., 1993. *QBASIC by example*. USA: QUE.

114. Pitman, E.B., 1986. Stress and velocity fields in two- and three-dimensional hoppers. *Powder Technology,* **47** (3) pp. 219-231.

115. Puri, V.M., Ladipo, D.D., 1997. Computer controlled shear cell for measurement of flow properties of particulate materials. *Powder Technology*, **92** (2) pp. 135-146.

116. Purutyan, H. et al., 2001. *Solve solids handling problems by retroftting*. Jenike & Johanson, Inc. [internet]. Available from: http://www.jenike.com/TechPapers/ [cited 14.07.12].

117. Ramirez, A., et al., 2010. Pressure measurements in steel silos with eccentric hoppers. *Powder Technology*, **201** (1) pp. 7-20.

118. Rankine, W.J.M., 1857. On the stability of loose earth. *Philosophical Transactions of the Royal Society of London*, **147**.

119. Rao, V.L., Venkateswarlu, D., 1974. Static and dynamic wall pressures in experimental mass flow hoppers. *Powder Technology*, **10** (3) pp. 143-152.

120. Reimbert, M., Reimbert, A., 1976. *Silos: Theory and Practice*. Trans Tech Publications.

121. Rombach, G.A., et al., 2005. Modelling of granular flow in silos based on finite element method ANSYS vs. SILO. *Proceedings of Conference "Powder and Grains", Stuttgart, pp. 469-473.*

122. Rotter, R.M. et al., 2005. Flow pattern measurements in a full-scale silo containing iron ore. *Chemical Engineering Science*, **60** (11) pp. 3029-3041.

123. Rousseeuw, P. J., 1984. Least Median of Squares Regression. *Journal of the American Statistical Association*, **79** (388) pp. 871–880.

124. Sadowski, A.J., Rotter, J.M., 2011. Steel silos with different aspect ratios: I – Behaviour under concentric discharge. *Journal of Constructional Steel Research*, 67 (10) pp. 1537-1544.

References

125. Sakaguchi, H. et al., 1993. Plugging the flow of granular materials during the discharge from a silo. *International Journal of Modern Physics B*, **7** (9, 10) pp. 1949-1963.

126. Schulze, D., Schwedes, J., 1994. An examination of initial stresses in hoppers. *Chemical Engineering Science*, **49** (13) pp. 2047-2058.

127. Schulze, D., 2006a. *Flow Properties of Powders and Bulk Solids*. Dietmar Schulze [internet]. Available from: http://www.dietmar-schulze.de/grdle1.pdf [cited 14.07.12].

128. Schulze, D., 2006b. *Stresses in silos*. Dietmar Schulze [internet]. Available from: http://www.dietmar-schulze.de/fre.html [cited 14.07.12].

129. Schulze, D., 2008. *Powders and Bulk Solids: Behavior, Characterization, Storage and Flow*. New York: Springer-Verlag Berlin Heidelberg.

130. Schmidt, L. C., Wu, Y. H., 1989. Prediction of dynamic wall pressures on silos. *Int. J. Bulk Solid Handling*, **9** pp. 333-338.

131. Shier, R., 2004. *Statistics: 1.1 Paired t-tests*. Mathematics Learning Support Centre [internet]. Available from: http://mlsc.lboro.ac.uk/resources/statistics/Pairedttest.pdf [cited 14.07.12].

132. Shingareva, I., Lizarraga-Celaya, C., 2011. *Solving Nonlinear Partial Differential Equations with Maple and Mathematica*. New York: SpringerWein.

133. Smewing, J., 2002. Testing powder flow. *Focus on Powder Coatings*, **2002** (12) pp. 2-3.

134. Snider, D.M., 2007. Three fundamental granular flow experiments and CPFD predictions. *Powder Technology*, **176** (1) pp. 36-46.

135. Sokolovskii, V.V., 1965. *Statics of granular materials*. Oxford: Pergamon Press.

136. Song, C.Y., 2004. Effects of patch loads on structural behaviour of circular flat-bottomed steel silos. *Thin-Walled Structures*, **42** (11) pp. 1519-1542.

137. Stroud, K.A., 1996. *Further Engineering Mathematics*. 3rd ed. Palgrave.

138. Stroud, K.A., Booth, D.J., 2001. *Engineering Mathematics*. 5th ed. Palgrave Macmillan.

139. Strusch, J., Schwedes, J., 1994. The use of slice element methods for calculation of insert loads. *Bulk Solids Handling*, **14** (3) pp. 505-512.

140. Tardos, G., 1999. *Stresses in bins and hoppers*. Educational Resources for Particle Technology [internet]. Available from: http://www.erpt.org/retiredsite/992Q/tard-00.htm [cited 14.07.12].

141. Tatemoto, Y. et al., 2005. Numerical simulation of cohesive particle motion in vibrated fluidized bed. *Chemical Engineering Science*, **60** (18) pp. 5010-5021.

142. Tejchman, J., Klisinski, M., 2001. FE-studies on rapid flow of bulk solids in silos. *Granular Matter*, **3** (4) pp. 215-230.

143. Terzaghi, K., 1925. *Erdbaumechanik auf bodenphysikalischer Grundlage*. Franz Deuticke Vienna: Leipzig und Wein [in German].

144. To, K. et al., 2002. Flow and jam of granular materials in a two-dimensional hopper. *Physica A: Statistical Mechanics and its Applications*, **35** (1-2) pp. 174-180.

145. Tuzun, U., Nedderman, R.M., 1985. Gravity flow of granular materials around obstacles – II. *Chemical Engineering Science*, 40 (3) pp. 337-351.

146. Venkatramaiah, C., 2006. *Geotechnical Engineering*. Delhi: New Age International Pvt Ltd Publishers.

147. Vidal, P. et al., 2008. Finite element analysis under different boundary conditions of the filling of cylindrical steel silos having an eccentric hopper. *Journal of Constructional Steel Research*, **64** (4) pp. 480-492.

148. Walker, D.M., 1966. An approximate theory for pressures and arching in hoppers. *Chemical Engineering Science*, **21** (11) pp. 975-997.

149. Walker, D.M., Blanchard, M.H., 1967. Pressures in experimental coal hoppers. *Chemical Engineering Science*, **22** (12) pp. 1713-1745.

150. Walters, J., 1973. A theoretical analysis of stresses in axially-symmetric hoppers and bunkers. *Chemical Engineering Science*, **28** (3) pp. 779-789.

151. Wasilczuk, M., Rotta, G., 2008. Modeling lubricant flow between thrust-bearing pads. *Tribology International*, **41** (9-10) pp. 908-913.

152. CST Industries. *Weaver Conical Hopper Industrial Silo Reclaimers.* CST Industries, Inc [internet]. Available from: http://cstindustries.com/products/conical-hopper-reclaimers/ [cited 14.07.12].

153. Wojcik, M. et al., 2003. Numerical calculation of wall pressures and stresses in steel cylindrical silos with concentric and eccentric hoppers. *Particulate Science and Technology,* **21** (3) pp. 247-258.

154. Wojcik, M., Tejchman, J., 2008. Application of an Uncoupled ALE-formulation to Confined Granular Flow in Silos. *Proceedings of the 12th International Conference of International Association for Computer Methods and Advances in Geomechanics (IACMAG).*

155. Wojcik, M., Tejchman, J., 2009. Modeling of shear localization during confined granular flow in silos within non-local hypoplasticity. *Powder Technology,* **192** (3) pp.298-310.

156. Wolfe, P., 1963. Methods of Nonlinear Programming. In *Recent Advances in Mathematical Programming*, R.L. Graves and P. Wolfe (eds.).

157. Wong, A.C., 2000. Characterisation of the flowability of glass beads by bulk densities ratio. *Chemical Engineering Science*, 55 (18) pp. 3855-3859.

158. Wu, J. et al., 2009. Multi-scale study of particle flow in silos. *Advanced Powder Technology,* **20** (1) pp. 62-73.

159. Yunming, Y. et al., 2011. Numerical analysis of silo behavior using non-coaxial models. *Chemical Engineering Science,* **66** (8) pp. 1715-1727.

160. Zapletal, A., 1970. Generalized Lamé-Maxwell equations. *Acta Technica CSAV (Ceskoslovensk Akademie Ved),* **15** (1) pp. 60-64.

161. Zhao, Y., Teng, J.G., 2004. Buckling experiments on steel silo transition junctions II: Finite element modelling. *Journal of Constructional Steel Research,* **60** (12) pp. 1803-1823.

162. Zhu, H.P. et al., 2007. Discrete particle simulation of particulate systems: Theoretical developments. *Chemical Engineering Science*, **62** (13) pp. 3378-3396.

163. Zhu, H.P. et al., 2008. Discrete particle simulation of particulate systems: A review of major applications and findings. *Chemical Engineering Science*, **63** (23) 1 2008, pp. 5728-5770.

Chapter 9.0 – Appendix Two

Derivation of Equations

9.1 Article extracts

9.1.1 Extract from Janssen

The derivation of Janssen's (1895, also Nedderman 1992) equation is shown below, in support of Chapter 2.2.1.

Consider forces acting on a small element of width δx at depth x below surface (Figure 6). Forces acting are gravity, normal contact forces (σ_n) and shear forces (τ) at wall. Force balance on element δx in Figure 7:

$$\delta x A - (\sigma_x + \delta x)A - \tau \int \delta x + \rho g A \delta x = 0$$

$$\therefore \delta x - (\sigma_x + \delta x) - \frac{\tau}{A} \int \delta x + \rho g \delta x = 0$$

$$\therefore -\frac{d\sigma}{dx} - \frac{S}{A}\tau + \rho g = 0 \tag{A.1}$$

Assume $\tau = \mu\sigma_n$ (coefficient of friction multiplied by normal contact forces). If material is in a state of incipient failure:

$$K_A = \frac{1-\sin\phi}{1+\sin\phi} \text{ or } K_P = \frac{1+\sin\phi}{1-\sin\phi}$$

$$\therefore \frac{d\sigma}{dx} + \frac{SK\mu}{A}\sigma = \rho g$$

$$Let \beta = \frac{SK\mu}{A}$$

$$\therefore \frac{d\sigma}{dx} + \beta\sigma = \rho g$$

$$\frac{d\sigma}{dx} = \rho g - \beta\sigma$$

$$\frac{d\sigma}{\rho g - \beta\sigma} = dx \tag{A.2}$$

Use boundary conditions at $x = 0$, $\sigma = 0$ (surface stress);

Derivation of Equations

$$\int_0^\sigma \frac{d\sigma}{\rho g - \beta\sigma} = \int_0^x dx$$

$$\therefore -\frac{1}{\beta}\left[\ln(\rho g - \beta\sigma)\right]_0^\sigma = \left[x\right]_0^x$$

$$-\frac{1}{\beta}\left[\ln(\rho g - \beta\sigma) - \ln(\rho g - 0)\right] = x - 0$$

$$\ln\frac{\rho g - \beta\sigma}{\rho g} = -\beta x$$

$$\frac{\rho g - \beta\sigma}{\rho g} = e^{-\beta x}$$

$$\rho g - \beta\sigma = \rho g e^{-\beta x}$$

$$\beta\sigma = \rho g - \rho g e^{-\beta x}$$

$$\sigma = \frac{1}{\beta}\left(\rho g - \rho g e^{-\beta x}\right)$$

$$\therefore \sigma = \frac{\rho g}{\beta}\left(1 - e^{-\beta x}\right) \tag{A.3}$$

Equation A.3 is the solution to Janssen's analysis, shown as equation 4 in the main text. The solution can be used to prove that applying a load to the top surface of the granular material does not promote flow at large depths *x*. Use boundary conditions at $x = 0,\ \sigma = Q$ (stress at top surface);

$$\int_Q^\sigma \frac{d\sigma}{\rho g - \beta\sigma} = \int_0^x dx$$

$$\therefore -\frac{1}{\beta}\left[\ln(\rho g - \beta\sigma)\right]_Q^\sigma = \left[x\right]_0^x$$

$$-\frac{1}{\beta}\left[\ln(\rho g - \beta\sigma) - \ln(\rho g - \beta Q)\right] = x - 0$$

$$\ln\frac{\rho g - \beta\sigma}{\rho g - \beta Q} = -\beta x$$

$$\frac{\rho g - \beta\sigma}{\rho g - \beta Q} = e^{-\beta x}$$

$$\rho g - \beta\sigma = \left(\rho g - \beta Q\right)\rho g e^{-\beta x}$$

$$\beta\sigma = \rho g - \rho g e^{-\beta x} + \beta Q e^{-\beta x}$$

$$\sigma = \frac{\rho g}{\beta} - \frac{\rho g}{\beta}e^{-\beta x} + Q e^{-\beta x}$$

$$\therefore \sigma = \frac{\rho g}{\beta}\left(1 - e^{-\beta x}\right) + Q e^{-\beta x} \tag{A.4}$$

The new solution equation A.4 is represented graphically in Figure 8, demonstrating exponential growth of σ, with increasing depth x. Equation A.4 is equivalent to equation 5 in the main text.

9.1.2 Extract from Walters

Walters (1973) developed previous works to provide a theory for stress fields within converging hoppers. The derivation below represents and extract from Walters' paper in support of Chapter 2.2.1, where a force balance was performed to provide the initial differential equations.

$$\frac{\delta\bar{\sigma}_z}{\delta_z} + \frac{1}{A}\frac{dA}{dz}\bar{\sigma}_z + \frac{P}{A}(\tau_\omega + \sigma_\omega \tan\alpha) = \rho g \qquad \text{(A.5)}$$

Walters relates the mean vertical stress $\bar{\sigma}_z$ to vertical stress at the wall $(\sigma_z)_\omega$ by use of a distribution factor, D.

$$(\sigma_z)_\omega = D\bar{\sigma}_z \qquad \text{(A.6)}$$

$$D = \frac{\cos\eta\left(1+\sin^2\delta\right)\pm 2\left(\sin^2\delta - \sin^2\eta\right)^{0.5}}{\cos\eta(1+\sin^2\delta)\pm 2y\sin\delta} \qquad \text{(A.7)}$$

where $y = \frac{2}{3c}[1-(1-c)^{1.5}]$ and $c = (\tan\eta\,/\,\tan\delta)^2$

Derivation of Equations

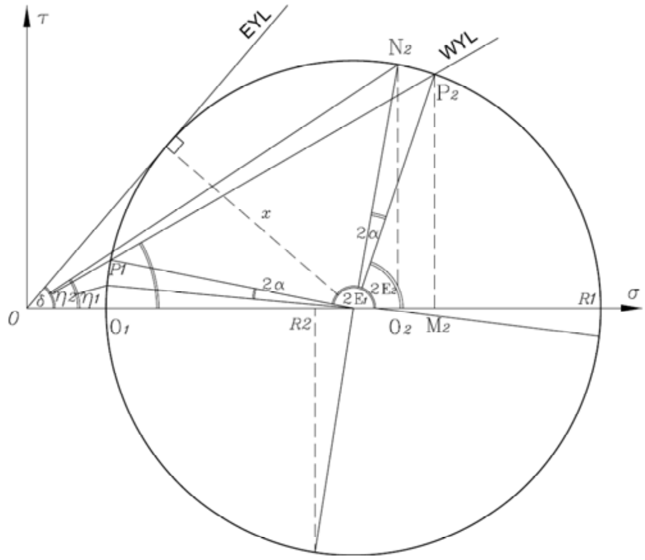

Figure A.1. Static and dynamic stresses at the wall (Walters 1973)

From the geometry of Figure A.1, Walters (1973) demonstrates the following relationships;

$2\varepsilon = \frac{\pi}{2} + \phi \pm \cos^{-1}(\sin\phi \,/\, \sin\delta)$ and $2\varepsilon + 2\alpha = \frac{\pi}{2} + \eta \pm \cos^{-1}(\sin\eta \,/\, \sin\delta)$

$$\tau_\omega = PM = x \sin 2\varepsilon$$

$$\sigma_\omega = OM = \frac{x}{\sin\delta} + x\cos 2\varepsilon$$

$$(\tau_{rz})_\omega = NQ = x\sin(2\varepsilon + 2\alpha)$$

$$(\sigma_z)_\omega = OR = \frac{x}{\sin\delta} - x\cos(2\varepsilon + 2\alpha)$$

$$\therefore (\tau_{rz})_\omega = E(\sigma_z)_\omega \qquad \text{(A.8)}$$

where $E = \frac{\sin\delta\sin(2\varepsilon+2\alpha)}{1-\sin\delta\cos(2\varepsilon+2\alpha)}$

and $(\tau_\omega + \sigma_\omega\tan\alpha) = \frac{\sin\delta\sin 2\varepsilon + \tan\alpha(1+\sin\delta\cos 2\varepsilon)}{1-\sin\delta\cos(2\varepsilon+2\alpha)}(\sigma_z)_\omega = (E + \tan\alpha)(\sigma_z)_\omega$

$$\therefore E = \frac{\sin\eta\cos^2\delta}{\cos\eta(1+\sin^2\delta) \pm 2(\sin^2\delta - \sin^2\eta)^{0.5}} \qquad \text{(A.9)}$$

and $\frac{d\bar{\sigma}_z}{dz} + \frac{4\bar{\sigma}_z}{d-2z\tan\alpha}[ED + \tan\alpha(D-1)] = \rho g$ (A.10)

Equation A.10 is equivalent to equation 7 in the main text. Walters then converts equation A.10 into dimensionless form as follows;

Let $\bar{S}_z = \bar{\sigma}_z/\rho g d$, $Z = z/d$ and $K = 2\left(\frac{ED}{\tan\alpha} + D - 1\right)$

$\therefore \frac{d\bar{S}_z}{dZ} + \frac{2K\tan\alpha\bar{S}_z}{1-2Z\tan\alpha} = 1$ (A.11)

This simplified differential equation can now be solved by integration between limits of $\bar{S}_{z,0}$ at $Z = Z_0$ and $\bar{S}_z$ at Z, relusting in equation A.12 (equation 8 in main text).

$\therefore \bar{S}_z = \frac{1-2Z\tan\alpha}{2\tan\alpha\,(K-1)}\left[1 - \left(\frac{1-2Z\tan\alpha}{1-2Z_0\tan\alpha}\right)^{K-1}\right] + \bar{S}_{z,0}\left(\frac{1-2Z\tan\alpha}{1-2Z_0\tan\alpha}\right)^{K}$ (A.12)

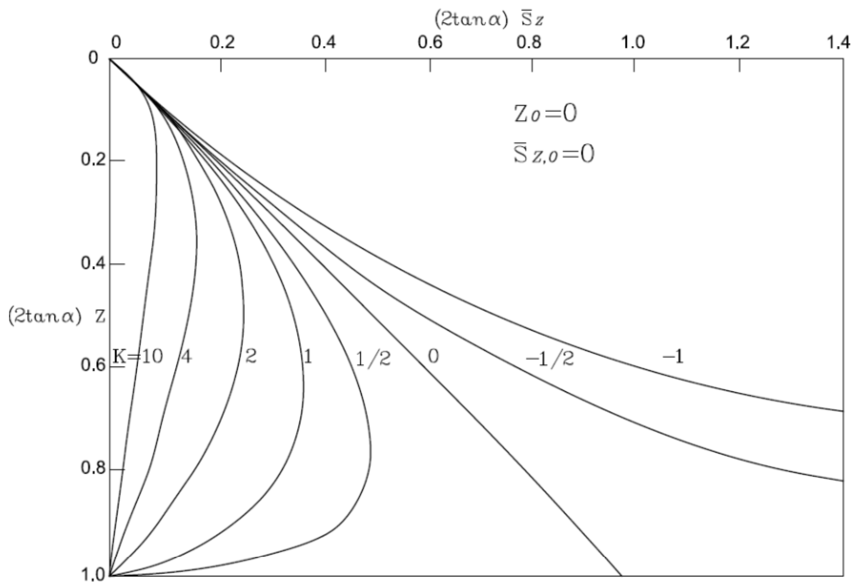

Figure A.2. Generalised vertical stress distribution for a hopper with no surcharge (Walters 1973)

In Figure A.2 Walters (1973) plots this solution for various valves of K. No surcharge is applied (note is the $\bar{S}_{z,0}$ vertical surcharge stress).

9.1.3 Extract from Enstad

Enstad (1975) published a theory for solution for stress fields within hoppers and silos. The derivation below represents an extract from the paper in support of Chapter 2.2.4, where principal stress arc methods were discussed. In the paper, Enstad states that the method is based on the assumptions shown in Figure 16a.

Considering the cross-section of the layer shown in Figure 16b, Enstad states that three forces are acting on the layer, the weight, the interaction with the powder above and below, and the reaction from the walls.

If a passive state of stress is considered,

$$r' = \frac{r \sin\theta}{\sin\left(\beta_p + \theta\right)}$$

The area of the cross-section of the layer will be given by,

$$\begin{aligned}\Delta A = {} & (r'+\Delta r')^2 \left(\beta_p + \theta\right) - (r'+\Delta r')^2 \sin\left(\beta_p + \theta\right)\cos\left(\beta_p + \theta\right) + \\ & (2r'+\Delta r')\sin\left(\beta_p + \theta\right)\Delta r \cos\theta - \left(r'^2 \left(\beta_p + \theta\right) - r'^2 \sin\left(\beta_p + \theta\right)\cos\left(\beta_p + \theta\right)\right)\end{aligned}$$

Neglecting second order terms of Δr, the area can be given as,

$$\Delta A = 2r\Delta r\left(\frac{\left(\beta_p + \theta\right)\sin\theta}{\sin^2\left(\beta_p + \theta\right)} + \frac{\sin\beta_p}{\sin\left(\beta_p + \theta\right)}\right)\sin\theta$$

The weight of the layer per unit length along the slot outlet will then be given by,

$$\Delta W = 2\gamma r\Delta r\left(\frac{\left(\beta_p + \theta\right)\sin\theta}{\sin^2\left(\beta_p + \theta\right)} + \frac{\sin\beta_p}{\sin\left(\beta_p + \theta\right)}\right)\sin\theta$$

Derivation of Equations

The powder on top of the layer will exert the downward stress $\sigma_2(r+\Delta r)$ on the layer. This results in the downward force,

$$F_2 + \Delta F_2 = 2(r + \Delta r)\sin\theta\sigma_2(r + \Delta r)$$

per unit length of the layer along the slot outlet. From the powder below, the layer will experience the upward force,

$$F_2 = 2r\sin\theta\sigma_2(r)$$

The net downward force will then be given by,

$$\Delta F_2 = 2\Delta r\left(\sigma_2 + r\frac{d\sigma_2}{dr}\right)\sin\theta = 2\Delta r\left(\sigma + r\frac{d\sigma}{dr}\right)\sin\theta(1-\sin\delta)$$

per unit length along the slot outlet.

The net lift from the walls will be given by,

$$\Delta F_1 = 2\left(\sigma_1\Delta r\cos\beta_p\sin(\beta_p + \theta) - \sigma_2\Delta r\sin\beta_p\cos(\beta_p + \theta)\right)$$

which can be simplified to,

$$\Delta F_1 = 2\Delta r\sigma\left(\sin\theta + \sin\delta\sin(2\beta_p + \theta)\right)$$

Neglecting accelerations,

$$\Delta W + \Delta F_2 = \Delta F_1$$

Letting $\Delta r \to 0$, this yields the differential equation A.13 or equation 14 in the main text,

$$r\frac{d\sigma}{dr} - X\sigma = -\gamma Yr \qquad \text{(A.13)}$$

where

$$X = \frac{\sin\delta}{1-\sin\delta}\left(1 + \frac{\sin(2\beta_p + \theta)}{\sin\theta}\right)$$

$$Y = \frac{\sin\theta(\beta_p + \theta) + \sin\beta_p \sin(\beta_p + \theta)}{(1-\sin\delta)\sin^2(\beta_p + \theta)}$$

The solution of the differential equation is given by equation A.14 or equation 15 in the main text,

$$\sigma(r) = \frac{\gamma Yr}{X-1} + \left(\sigma(R) - \frac{\gamma YR}{X-1}\right)\left(\frac{r}{R}\right)^x \qquad \text{(A.14)}$$

where $\sigma(R)$ is the mean stress at the transition between the hopper and vertical part of the silo. In Figure 17, Enstad plots the resulting equation for $\sigma_2(r)$.

9.2 Derivation of equation twenty nine

In Figure 32, Chapter 4.1, a two-dimensional wedge hopper has half angle to the vertical α_1 and α_2 respectively. A circular arc cuts the right-side wedge at distance *x* above the apex and has radius *R*, derived as follows.

Since $\dfrac{y}{\sin(\alpha_1 + \alpha_2)} = \dfrac{r}{\sin(\beta_1 + \gamma)}$ and $\dfrac{y}{\sin(\alpha_1 + \alpha_2 + \beta_1 + \beta_2)} = \dfrac{R}{\sin\gamma}$,

where $\gamma = 180 - \dfrac{\pi}{2} - \dfrac{\alpha_1 + \alpha_2 + \beta_1 + \beta_2}{2}$

$$\therefore R = y\frac{\sin\gamma}{\sin(\alpha_1+\alpha_2+\beta_1+\beta_2)}$$
$$= \frac{r\sin(\alpha_1+\alpha_2)\sin\gamma}{\sin(\alpha_1+\alpha_2+\beta_1+\beta_2)\sin(\beta_1+\gamma)}$$

where $r = \frac{x}{\cos\alpha_2}$

$$\therefore R = \frac{x\sin(\alpha_1+\alpha_2)\sin\gamma}{\cos\alpha_2\sin(\alpha_1+\alpha_2+\beta_1+\beta_2)\sin(\beta_1+\gamma)} \tag{A.15}$$

Let $\lambda = \alpha_1+\alpha_2+\beta_1+\beta_2$

$$\therefore R = x\frac{\sin(\alpha_1+\alpha_2)\sin\gamma}{\cos\alpha_2\sin\lambda\sin(\beta_1+\gamma)}$$
$$a_1 = \frac{\sin\gamma\sin(\alpha_1+\alpha_2)}{\sin\lambda\cos\alpha_2\sin(\gamma+\beta_1)}$$
$$R = a_1x \tag{A.16}$$

Equation A.16 is equivalent to equation 29 in the main text.

9.3 Derivation of equation forty

In Figure 36, Chapter 4.1, an incremental element cuts the right-hand side of the model geometry with vertical height δx, and at angle ε to the vertical with incremental angle $\delta\varepsilon$.

$$OMCD = O_1FE + OM$$
$$O_1FE = R(x+\delta x)$$
$$O - O_1 = \delta O = z - y$$
$$OM = \delta O\cos\varepsilon$$
$$\therefore R(x) + \delta w = R(x+\delta x) + \delta O\cos\varepsilon \tag{A.17}$$

Since $R(x) = a_1x$ and $R(x+\delta x) = a_1(x+\delta x) = a_1x + a_1\delta x$,

$$\therefore a_1 x + \delta w = a_1 x + a_1 \delta x + \delta O \cos \varepsilon$$

$$\therefore \delta w = a_1 \delta x + \delta O \cos \varepsilon = \left(a_1 + \frac{\delta O}{\delta x} \cos \varepsilon\right) \delta x \tag{A.18}$$

Since $\frac{z}{\sin \beta_2} = \frac{(r+\delta r)}{\sin(\alpha_2+\beta_2)}$ and $\frac{y}{\sin \beta_2} = \frac{r}{\sin(\alpha_2+\beta_2)}$

also $\cos \alpha_2 = \frac{x}{r} = \frac{x+\delta x}{r+\delta r}$

$\therefore x = r \cos \varepsilon$

and,

$$\delta x = \frac{x(r+\delta r)}{r} - x = \frac{xr + x\delta r}{r} - x = \frac{r^2 \cos \alpha_2}{r} + \frac{r \cos \alpha_2 \, \delta r}{r} - x$$

$$\therefore \delta x = \frac{r^2 \cos \alpha_2}{r} + \frac{r \cos \alpha_2 \, \delta r}{r} - r \cos \alpha_2 = \delta r \cos \alpha_2$$

$$\delta O = \frac{\sin \beta_2 (r+\delta r)}{\sin(\alpha_1+\beta_2)} - \frac{r \sin \beta_2}{\sin(\alpha_1+\beta_2)} = \frac{\sin \beta_2 (r+\delta r) - r \sin \beta_2}{\sin(\alpha_1+\beta_2)} = \frac{\delta r \sin \beta_2}{\sin(\alpha_1+\beta_2)}$$

Since $\delta r = \frac{\delta x}{\cos \alpha_2}$,

$\delta O = \frac{\delta x \sin \beta_2}{\cos \alpha_2 \sin(\alpha_1+\beta_2)}$ and $\frac{\delta O}{\delta x} = \frac{\sin \beta_2}{\cos \alpha_2 \sin(\alpha_1+\beta_2)} = a_2$

and,

$$\delta w = \left(a_1 + \frac{\sin \beta_2}{\cos \alpha_2 \sin(\alpha_1 + \beta_2)} \cos \varepsilon\right) \delta x$$

$$\therefore \left(\frac{\partial w}{\partial x}\right) = a_1 + a_2 \cos \varepsilon \tag{A.19}$$

The version of equation A.19 is used in Chapter 4.1 to allow calculation of the variable incremental element thickness for applications where angles α_1 and α_2 are identical. For unequal angle situations, the following equation replaces the equal angle case.

$OMCD = O_1FE + OM = R(x) + \delta w$

$O_1FE = R(x + \delta x)$

$O - O_1 = \delta O = z - y$

$OM = \delta O \cos(\varepsilon - \eta)$

$\frac{O_1}{\sin\beta_2} = \frac{R(x+\delta x)}{\sin(\alpha_2 - \eta_1)}$ and $\frac{O}{\sin\beta_2} = \frac{R(x)}{\sin(\alpha_2 - \eta_1)}$

$$\therefore \delta O = \frac{R(x+\delta x)\sin\beta_2}{\sin(\alpha_2-\eta_1)} - \frac{R(x)\sin\beta_2}{\sin(\alpha_2-\eta_1)} = \frac{R(\delta x)\sin\beta_2}{\sin(\alpha_2-\eta_1)} = \frac{a_1\delta x\sin\beta_2}{\sin(\alpha_2-\eta_1)} \tag{A.20}$$

Where η_1 can be found using O_x and O_z;

$O_z = x\tan\alpha_2 - R\sin(\alpha_2 + \beta_2)$

$O_x = x - R\cos(\alpha_2 + \beta_2)$

$\therefore \eta_1 = \tan^{-1}\frac{\tan\alpha_2 - a_1\sin(\alpha_2+\beta_2)}{1 - a_1\cos(\alpha_2+\beta_2)}$, since $R = a_1x$.

$R(x) + \delta w = R(x + \delta x) + \delta O\cos(\varepsilon - \eta_1)$

$a_1 + \delta w = a_1x + \delta x + \delta O\cos(\varepsilon - \eta_1)$

$\delta w = a_1\delta x + \delta O\cos(\varepsilon - \eta_1)$

$$\delta w = \left(a_1 + \frac{\delta O}{\delta x}\cos(\varepsilon - \eta_1)\right)\delta x$$

$$\therefore \left(\frac{\partial w}{\partial x}\right) = a_1 + a_2\cos(\varepsilon - \eta_1) \tag{A.21}$$

Equation A.21 is equivalent to equation 40 in the main text.

9.4 Force balance equations in R- and ε -directions for two-dimensional silo and wedge hopper cases

A force balance in two directions can be completed on the incremental element shown in Figure 33, Chapter 4.1.

Force balance in ε –direction;

$$\left[\sigma_\varepsilon R_2 \delta\psi\right]_\varepsilon \cos {}^{\delta\psi}\!/_2 - \left[\sigma_\varepsilon R_2 \delta\psi\right]_{\varepsilon+\delta\varepsilon} \cos\left(\delta\varepsilon + {}^{\delta\psi}\!/_2\right)$$
$$+\left[\sigma_R R \delta\varepsilon\right]_\varepsilon \sin {}^{\delta\varepsilon}\!/_2 - \left[\sigma_R\right]_{x+\delta x, \varepsilon+\delta\psi} \frac{(R+\delta w)\delta\varepsilon}{\cos\delta\xi}\sin\delta\xi \tag{A.22}$$
$$+R\delta\varepsilon\delta w \rho g \sin\varepsilon = 0$$

First line of equation A1 contains

$$R_2\delta\psi = \delta w \cos {}^{\delta\psi}\!/_2$$

Hence this becomes

$$\left[\sigma_\varepsilon \delta w\right]_\varepsilon \cos^2 {}^{\delta\psi}\!/_2 - \left[\sigma_\varepsilon \delta w\right]_{\varepsilon+\delta\varepsilon} \cos {}^{\delta\psi}\!/_2 \cos\left(\delta\varepsilon + {}^{\delta\psi}\!/_2\right)$$

Divide by δx and $\delta\varepsilon$, and in the limit as δx and $\delta\varepsilon$ tend to zero, this tends to the force balance component below. Note $\cos\delta\psi \Rightarrow 1$.

$$-\frac{\partial}{\partial\varepsilon}\left[\sigma_\varepsilon\left(\frac{\partial w}{\partial x}\right)\right]$$

The first term of the second line of equation A1 will disappear as the limits tend to zero. Non-zero terms below.

$$\begin{aligned}
-\left[\sigma_R\right]_{x+\delta x, \varepsilon+\delta\psi} \frac{(R+\delta w)\delta\varepsilon}{\cos\delta\xi}\sin\delta\xi &= -\delta\varepsilon \tan\delta\xi\left[\sigma_R + \frac{\partial\sigma_R}{\partial x}\delta\varepsilon + \frac{\partial\sigma_R}{\partial\varepsilon}\delta x\right](R+\delta w) \\
&= -\delta\varepsilon \tan\delta\xi\left[\sigma_R + \frac{\partial\sigma_R}{\partial x}\delta\varepsilon + \frac{\partial\sigma_R}{\partial\varepsilon}\delta x\right] \\
&\quad \left[R + a_1\delta x + \delta O\cos(\varepsilon-\eta)\right] \\
&= -\delta\varepsilon \tan\delta\xi\left[\sigma_R + \frac{\partial\sigma_R}{\partial x}\delta\varepsilon + \frac{\partial\sigma_R}{\partial\varepsilon}\delta x\right] \\
&\quad \left[\left(R + \frac{\partial R}{\partial x}\delta x\right) + a_2\cos(\varepsilon-\eta)\delta x\right]
\end{aligned}$$

(A.23)

Divide by δx and $\delta\varepsilon$. This gives one non-zero term in the limit:

$$-[\sigma_R]_{x+\delta x}\frac{\tan\delta\xi}{\delta x}\to -R\sigma_R\left(\frac{a_2\sin(\varepsilon-\eta)}{R}\right)=-\sigma_R a_2\sin(\varepsilon-\eta) \tag{A.24}$$

Hence

$$\begin{aligned}&-\frac{\partial}{\partial\varepsilon}\left[\sigma_\varepsilon\left(\frac{\partial w}{\partial x}\right)\right]+R\left(\frac{\partial w}{\partial x}\right)\rho g\sin\varepsilon-\sigma_R a_2\sin(\varepsilon-\eta)=0\\ &\frac{\partial F}{\partial\varepsilon}=R\left(\frac{\partial w}{\partial x}\right)\rho g\sin\varepsilon-\sigma_R a_2\sin(\varepsilon-\eta)\end{aligned} \tag{A.25}$$

Equation A.25 is equivalent to equation 51 in the main text.

Force balance in *R*-direction;

$$\begin{aligned}&-[\sigma_\varepsilon R_2\delta\psi]_\varepsilon\sin{}^{\delta\psi}\!/_2+[\sigma_\varepsilon R_2\delta\psi]_{\varepsilon+\delta\varepsilon}\sin\left(\delta\varepsilon+{}^{\delta\psi}\!/_2\right)\\ &+[\sigma_R R\delta\varepsilon]_x\cos{}^{\delta\varepsilon}\!/_2-[\sigma_R]_{x+\delta x,\varepsilon+\delta\varepsilon}\frac{(R+\delta w)\delta\varepsilon}{\cos\delta\xi}\cos\delta\xi\\ &-R\delta\varepsilon\delta w\rho g\cos\varepsilon=0\end{aligned} \tag{A.26}$$

First line of equation contains

$$R_2\delta\psi=\delta w\cos{}^{\delta\psi}\!/_2$$

Hence

$$-\left[\sigma_\varepsilon\delta w\cos{}^{\delta\psi}\!/_2\right]_\varepsilon\sin{}^{\delta\psi}\!/_2+\left[\sigma_\varepsilon\delta w\cos{}^{\delta\psi}\!/_2\right]_{\varepsilon+\delta\varepsilon}\sin\left(\delta\varepsilon+{}^{\delta\psi}\!/_2\right)$$

Divide by δx and $\delta\varepsilon$, and in the limit as δx and $\delta\varepsilon$ tend to zero, this tends to the force balance component below. Note $\cos\delta\psi\Rightarrow 1$, $\sin\delta\psi\Rightarrow\delta\psi$, and $\delta\psi\Rightarrow 0$.

$$\frac{-\left[\sigma_\varepsilon \frac{\partial w}{\partial x}\right]_\varepsilon \sin \delta\psi\!\big/_2 + \left[\sigma_\varepsilon \frac{\partial w}{\partial x}\right]_{\varepsilon+\delta\varepsilon} \sin\left(\delta\varepsilon + \delta\psi\!\big/_2\right)}{\delta\varepsilon}$$

$$\frac{-\left[\sigma_\varepsilon \frac{\partial w}{\partial x}\right]_\varepsilon \sin \delta\psi\!\big/_2 + \left[\sigma_\varepsilon \frac{\partial w}{\partial x}\right]_{\varepsilon+\delta\varepsilon} \left(\sin\delta\varepsilon \cos \delta\psi\!\big/_2 + \cos\delta\varepsilon \sin \delta\psi\!\big/_2\right)}{\delta\varepsilon}$$

$$\frac{-\left[\sigma_\varepsilon \frac{\partial w}{\partial x}\right]_\varepsilon \sin \delta\psi\!\big/_2 + \left[\sigma_\varepsilon \frac{\partial w}{\partial x}\right]_{\varepsilon+\delta\varepsilon} \sin\delta\varepsilon \cos \delta\psi\!\big/_2 + \left[\sigma_\varepsilon \frac{\partial w}{\partial x}\right]_{\varepsilon+\delta\varepsilon} \cos\delta\varepsilon \sin \delta\psi\!\big/_2}{\delta\varepsilon}$$

$$-\left\{\frac{\left[\sigma_\varepsilon \frac{\partial w}{\partial x}\right]_\varepsilon + \left[\sigma_\varepsilon \frac{\partial w}{\partial x}\right]_{\varepsilon+\delta\varepsilon}}{\delta\varepsilon}\right\} \sin \delta\psi\!\big/_2 + \left[\sigma_\varepsilon \frac{\partial w}{\partial x}\right]_{\varepsilon+\delta\varepsilon} \frac{\sin\delta\varepsilon}{\delta\varepsilon}$$

Since $\frac{\partial}{\partial\varepsilon}\left[\sigma_\varepsilon \frac{\partial w}{\partial x}\right] \sin \delta\psi\!\big/_2 \Rightarrow 0$ and $\frac{\sin\delta\varepsilon}{\delta\varepsilon} \Rightarrow 1$

$\therefore \left[\sigma_\varepsilon \frac{\partial w}{\partial x}\right]$ or F

First term of second line of equation A.26 will disappear as previous. Non-zero terms below.

$$\begin{aligned}
-\left[\sigma_R\right]_{x+\delta x,\varepsilon+\delta\psi} \frac{(R+\delta w)\delta\varepsilon}{\cos\delta\xi} \cos\delta\xi &= -\delta\varepsilon\left[\left[\sigma_R\right]_{x+\delta x} + \frac{\partial\sigma_R}{\partial x}\delta\psi\right]\begin{bmatrix} R + a_1\delta x \\ + \delta O \cos(\varepsilon-\eta) \end{bmatrix} \\
&= -\delta\varepsilon\left[\left[\sigma_R\right]_{x+\delta x} + \frac{\partial\sigma_R}{\partial x}\delta\psi\right]\begin{bmatrix} [R]_{x+\delta x} \\ + a_2 \cos(\varepsilon-\eta)\delta x \end{bmatrix} \\
&= -\delta\varepsilon\begin{bmatrix} \left[R\sigma_R\right]_{x+\delta x} + [R]_{x+\delta x} \frac{\partial\sigma_R}{\partial x}\delta\psi \\ + \left[\sigma_R\right]_{x+\delta x} a_2 \cos(\varepsilon-\eta)\delta x \\ + \frac{\partial\sigma_R}{\partial x}\delta\psi a_2 \cos(\varepsilon-\eta)\delta x \end{bmatrix}
\end{aligned}$$

(A.27)

Divide by δx and $\delta\varepsilon$. In the limit:

$$F-\frac{\partial}{\partial x}\left[R\sigma_R\right]-R\frac{\partial\sigma_R}{\partial\varepsilon}\frac{\partial\psi}{\partial x}-\sigma_R a_2\cos(\varepsilon-\eta)-R\left(\frac{\partial w}{\partial x}\right)\rho g\cos\varepsilon=0 \qquad \text{(A.28)}$$

Note the last term of equation A.6 tends to zero as it contains $\delta\psi$ and δx .

Force balance equations can now be found for the horizontal and vertical directions by combining terms from A.25 and A.28;

$$\frac{\partial F}{\partial\varepsilon}\sin\varepsilon-R\left(\frac{\partial w}{\partial x}\right)\rho g\sin^2\varepsilon+\sigma_R a_2\sin(\varepsilon-\eta)\sin\varepsilon+$$
$$F\cos\varepsilon-\frac{\partial}{\partial x}\left[R\sigma_R\cos\varepsilon\right]-R\frac{\partial\sigma_R}{\partial\varepsilon}\frac{\partial\psi}{\partial x}\cos\varepsilon-\sigma_R a_2\cos(\varepsilon-\eta)\cos\varepsilon-R\left(\frac{\partial w}{\partial x}\right)\rho g\cos^2\varepsilon=0$$
$$-\frac{\partial}{\partial x}\left[R\sigma_R\cos\varepsilon\right]+F\cos\varepsilon+\frac{\partial F}{\partial\varepsilon}\sin\varepsilon-\cos\varepsilon\left\{\sigma_R a_2\cos(\varepsilon-\eta)+R\frac{\partial\sigma_R}{\partial\varepsilon}\frac{\partial\psi}{\partial x}\right\}-$$
$$R\left(\frac{\partial w}{\partial x}\right)\rho g+\sigma_R a_2\sin(\varepsilon-\eta)\sin\varepsilon=0$$

$$-\frac{\partial}{\partial x}\left[R\sigma_R\cos\varepsilon\right]+\frac{\partial}{\partial\varepsilon}\left[\sigma_\varepsilon\left(\frac{\partial w}{\partial x}\right)\sin\varepsilon\right]-R\left(\frac{\partial w}{\partial x}\right)\rho g-\cos\varepsilon\left\{\begin{matrix}\sigma_R a_2\cos(\varepsilon-\eta)\\+R\dfrac{\partial\sigma_R}{\partial\varepsilon}\dfrac{\partial\psi}{\partial x}\end{matrix}\right\}.. \qquad \text{(A.29)}$$
$$+\sigma_R a_2\sin(\varepsilon-\eta)\sin\varepsilon=0$$

Equation A.29 is equivalent to equation 48 in the main text.

$$-\frac{\partial F}{\partial\varepsilon}\cos\varepsilon+R\left(\frac{\partial w}{\partial x}\right)\rho g\sin\varepsilon\cos\varepsilon-\sigma_R a_2\sin(\varepsilon-\eta)\cos\varepsilon+$$
$$F\sin\varepsilon-\frac{\partial}{\partial x}\left[R\sigma_R\sin\varepsilon\right]-R\frac{\partial\sigma_R}{\partial\varepsilon}\frac{\partial\psi}{\partial x}\sin\varepsilon-\sigma_R a_2\cos(\varepsilon-\eta)\sin\varepsilon-R\left(\frac{\partial w}{\partial x}\right)\rho g\cos\varepsilon\sin\varepsilon=0$$
$$-\frac{\partial}{\partial x}\left[R\sigma_R\sin\varepsilon\right]+F\sin\varepsilon-\frac{\partial F}{\partial\varepsilon}\cos\varepsilon-\sin\varepsilon\left\{\sigma_R a_2\cos(\varepsilon-\eta)+R\frac{\partial\sigma_R}{\partial\varepsilon}\frac{\partial\psi}{\partial x}\right\}-$$
$$\sigma_R a_2\sin(\varepsilon-\eta)\cos\varepsilon=0$$

$$-\frac{\partial}{\partial x}\left[R\sigma_R \sin\varepsilon\right]-\frac{\partial}{\partial\varepsilon}\left[\sigma_\varepsilon\left(\frac{\partial w}{\partial x}\right)\cos\varepsilon\right]-\sin\varepsilon\left\{\sigma_R a_2\cos(\varepsilon-\eta)+R\frac{\partial\sigma_R}{\partial\varepsilon}\frac{\partial\psi}{\partial x}\right\}$$
$$-\sigma_R a_2\sin(\varepsilon-\eta)\cos\varepsilon=0$$

(A.30)

Equation A.30 is equivalent to equation 49 in the main text. Using A.30:

$$\frac{\partial}{\partial x}\left[a_1 x\sigma_R\sin\varepsilon\right]=-\frac{\partial}{\partial\varepsilon}\left[F\cos\varepsilon\right]-\sin\varepsilon\left\{\sigma_R a_2\cos(\varepsilon-\eta)+R\frac{\partial\sigma_R}{\partial\varepsilon}\frac{\partial\psi}{\partial x}\right\}$$
$$-\sigma_R a_2\sin(\varepsilon-\eta)\cos\varepsilon$$
$$a_1\sin\varepsilon\left[x\frac{\partial\sigma_R}{\partial x}+\sigma_R\right]=F\sin\varepsilon-\cos\varepsilon\frac{\partial F}{\partial\varepsilon}-\sin\varepsilon\left\{\sigma_R a_2\cos(\varepsilon-\eta)+R\frac{\partial\sigma_R}{\partial\varepsilon}\frac{\partial\psi}{\partial x}\right\}$$
$$-\sigma_R a_2\sin(\varepsilon-\eta)\cos\varepsilon$$
$$R\sin\varepsilon\frac{\partial\sigma_R}{\partial x}=F\sin\varepsilon-\cos\varepsilon\frac{\partial F}{\partial\varepsilon}-\sin\varepsilon\left\{\sigma_R a_2\cos(\varepsilon-\eta)+R\frac{\partial\sigma_R}{\partial\varepsilon}\frac{\partial\psi}{\partial x}\right\}-$$
$$\sigma_R a_2\sin(\varepsilon-\eta)\cos\varepsilon-a_1\sigma_R\sin\varepsilon$$
$$\frac{\partial\sigma_R}{\partial x}=\frac{F}{R}-\frac{\cos\varepsilon}{R\sin\varepsilon}\frac{\partial F}{\partial\varepsilon}-\frac{1}{R}\left\{\sigma_R a_2\cos(\varepsilon-\eta)+R\frac{\partial\sigma_R}{\partial\varepsilon}\frac{\partial\psi}{\partial x}\right\}$$
$$-\frac{\sigma_R a_2\sin(\varepsilon-\eta)\cos\varepsilon}{R\sin\varepsilon}-\frac{a_1\sigma_R}{R}$$

(A.31)

Equation A.31 is equivalent to equation 50 in the main text. Using A.29:

$$-\frac{\partial}{\partial x}\left[a_1 x\sigma_R\cos\varepsilon\right]+\frac{\partial}{\partial\varepsilon}\left[F\sin\varepsilon\right]-R\left(\frac{\partial w}{\partial x}\right)\rho g-\cos\varepsilon\left\{\sigma_R a_2\cos(\varepsilon-\eta)+R\frac{\partial\sigma_R}{\partial\varepsilon}\frac{\partial\psi}{\partial x}\right\}$$
$$+\sigma_R a_2\sin(\varepsilon-\eta)\sin\varepsilon=0$$
$$-a_1\cos\varepsilon\left[x\frac{\partial\sigma_R}{\partial x}+\sigma_R\right]+\sin\varepsilon\frac{\partial F}{\partial\varepsilon}+F\cos\varepsilon-R\left(\frac{\partial w}{\partial x}\right)\rho g-$$
$$\cos\varepsilon\left\{\sigma_R a_2\cos(\varepsilon-\eta)+R\frac{\partial\sigma_R}{\partial\varepsilon}\frac{\partial\psi}{\partial x}\right\}+\sigma_R a_2\sin(\varepsilon-\eta)\sin\varepsilon=0$$
$$-R\cos\varepsilon\frac{\partial\sigma_R}{\partial x}-a_1\sigma_R\cos\varepsilon+\sin\varepsilon\frac{\partial F}{\partial\varepsilon}+F\cos\varepsilon-R\left(\frac{\partial w}{\partial x}\right)\rho g-$$
$$\cos\varepsilon\left\{\sigma_R a_2\cos(\varepsilon-\eta)+R\frac{\partial\sigma_R}{\partial\varepsilon}\frac{\partial\psi}{\partial x}\right\}+\sigma_R a_2\sin(\varepsilon-\eta)\sin\varepsilon=0$$

(A.32)

Substitute A.32 into A.31:

$$-R\cos\varepsilon\left[\begin{array}{l}\dfrac{F}{R}-\dfrac{\cos\varepsilon}{R\sin\varepsilon}\dfrac{\partial F}{\partial\varepsilon}-\dfrac{1}{R}\left\{\sigma_R a_2\cos(\varepsilon-\eta)+R\dfrac{\partial\sigma_R}{\partial\varepsilon}\dfrac{\partial\psi}{\partial x}\right\}-\\ \dfrac{\sigma_R a_2\sin(\varepsilon-\eta)\cos\varepsilon}{R\sin\varepsilon}-\dfrac{a_1\sigma_R}{R}\end{array}\right]-$$

$$a_1\sigma_R\cos\varepsilon+\sin\varepsilon\frac{\partial F}{\partial\varepsilon}+F\cos\varepsilon-R\left(\frac{\partial w}{\partial x}\right)\rho g-$$

$$\cos\varepsilon\left\{\sigma_R a_2\cos(\varepsilon-\eta)+R\frac{\partial\sigma_R}{\partial\varepsilon}\frac{\partial\psi}{\partial x}\right\}+\sigma_R a_2\sin(\varepsilon-\eta)\sin\varepsilon=0$$

$$-F\cos\varepsilon+\frac{\cos^2\varepsilon}{\sin\varepsilon}\frac{\partial F}{\partial\varepsilon}+\cos\varepsilon\left\{\sigma_R a_2\cos(\varepsilon-\eta)+R\frac{\partial\sigma_R}{\partial\varepsilon}\frac{\partial\psi}{\partial x}\right\}+\frac{\sigma_R a_2\sin(\varepsilon-\eta)\cos^2\varepsilon}{\sin\varepsilon}+$$

$$\cos\varepsilon a_1\sigma_R-a_1\sigma_R\cos\varepsilon+\sin\varepsilon\frac{\partial F}{\partial\varepsilon}+F\cos\varepsilon-R\left(\frac{\partial w}{\partial x}\right)\rho g-$$

$$\cos\varepsilon\left\{\sigma_R a_2\cos(\varepsilon-\eta)+R\frac{\partial\sigma_R}{\partial\varepsilon}\frac{\partial\psi}{\partial x}\right\}+\sigma_R a_2\sin(\varepsilon-\eta)\sin\varepsilon=0$$

$$\frac{\cos^2\varepsilon}{\sin\varepsilon}\frac{\partial F}{\partial\varepsilon}+\sin\varepsilon\frac{\partial F}{\partial\varepsilon}+\sigma_R a_2\sin(\varepsilon-\eta)\left(\frac{\cos^2\varepsilon}{\sin\varepsilon}+\sin\varepsilon\right)-R\left(\frac{\partial w}{\partial x}\right)\rho g=0$$

$$\frac{\partial F}{\partial\varepsilon}\left(\frac{\cos^2\varepsilon}{\sin\varepsilon}+\frac{\sin^2\varepsilon}{\sin\varepsilon}\right)+\sigma_R a_2\sin(\varepsilon-\eta)\left(\frac{\cos^2\varepsilon}{\sin\varepsilon}+\frac{\sin^2\varepsilon}{\sin\varepsilon}\right)-R\left(\frac{\partial w}{\partial x}\right)\rho g=0$$

$$\frac{\partial F}{\partial\varepsilon}=R\left(\frac{\partial w}{\partial x}\right)\rho g\sin\varepsilon-\sigma_R a_2\sin(\varepsilon-\eta)$$

(A.33)

Equation A.33 is equivalent to equation 51 in the main text.

9.5 Derivation of Mohr-Coulomb criterion

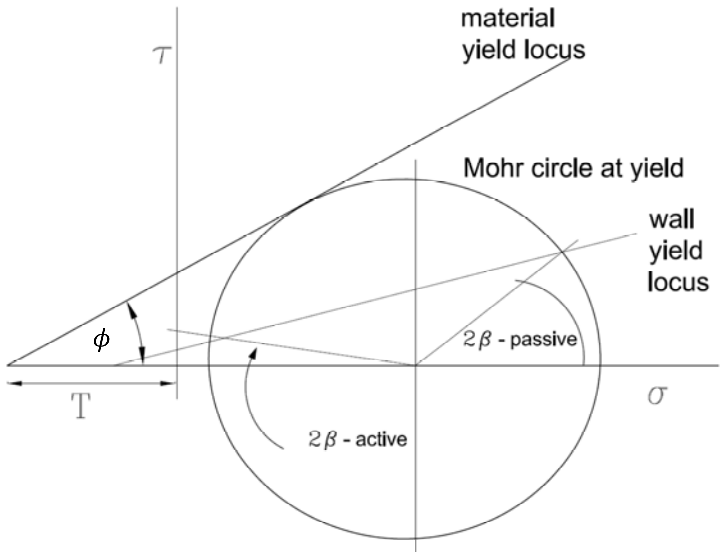

Figure A.3. Bulk material yield locus (Matchett 2006b)

Figure A.3 shows the linearized yield locus for a typical cohesive granular material. A relationship between σ_ε and σ_R can be derived from this as follows;

$$\tau = \sigma \tan\phi + c \tag{A.34}$$

where τ is shear stress, σ is normal stress, ϕ is angle of yield locus, and *c* is cohesion

Equation A.34 is equivalent to equation 20 in the main text.

Let $T = \dfrac{c}{\tan\phi}$, where T is the tensile intercept.

$$\therefore \tau = \tan\phi(\sigma + T)$$

A ratio of effective stresses can be assumed (Matchett 2006b), in the form of a *J*-value;

$$\frac{\sigma'_\varepsilon}{\sigma'_R} = J$$

$\sigma'_\varepsilon = \sigma_\varepsilon + T$ and $\sigma'_R = \sigma_R + T$

$$\therefore J = \frac{\sigma_\varepsilon + T}{\sigma_R + T}$$
$$J(\sigma_R + T) = \sigma_\varepsilon + T$$
$$\sigma_\varepsilon = J(\sigma_R + T) - T$$
$$\sigma_\varepsilon = J\sigma_R + JT - T$$
$$\therefore \sigma_\varepsilon = J\sigma_R + T(J-1) \qquad \text{(A.35)}$$

9.6 Force balance equations in R- and ε -directions for axially symmetric three-dimensional silo and cone hopper cases

A force balance can be completed on the incremental element shown in Figure 48, Chapter 5.1.

Force balance in vertical direction;

$$-[\sigma_\varepsilon R_2 \delta\psi 2\pi\bar{r}]_\varepsilon \cos{}^{\delta\psi}\!/_2 \sin\varepsilon + [\sigma_\varepsilon R_2 \delta\psi 2\pi\bar{r}]_{\varepsilon+\delta\varepsilon} \cos\left(\delta\varepsilon + {}^{\delta\psi}\!/_2\right)\sin\varepsilon$$
$$+[\sigma_R R\delta\varepsilon 2\pi\bar{r}]_x \sin{}^{\delta\varepsilon}\!/_2 \cos\varepsilon - [\sigma_R]_{x+\delta x,\varepsilon+\delta\psi}(R+\delta w)\delta\varepsilon 2\pi\bar{r}\cos(\varepsilon+\delta\xi)$$
$$-2\pi\bar{r}R\delta\varepsilon\delta w\rho g = 0 \qquad \text{(A.36)}$$

First line of equation contains,

$$R_2\delta\psi = \delta w \cos{}^{\delta\psi}\!/_2$$

Hence,

$$-[\sigma_\varepsilon \delta w\bar{r}]_\varepsilon 2\pi\cos^2{}^{\delta\psi}\!/_2 \sin\varepsilon + [\sigma_\varepsilon \delta w\bar{r}]_{\varepsilon+\delta\varepsilon} 2\pi\cos{}^{\delta\psi}\!/_2 \cos\left(\delta\varepsilon + {}^{\delta\psi}\!/_2\right)\sin\varepsilon$$

Divide by $\delta x\delta\varepsilon$ and 2π, and take limits:

$$\frac{\partial}{\partial\varepsilon}\left[\sigma_\varepsilon\left(\frac{\partial w}{\partial x}\right)\bar{r}\sin\varepsilon\right]$$

Derivation of Equations

The first two terms of second line of equation:

$$[\sigma_R R\delta\varepsilon 2\pi\bar{r}]_x \sin{}^{\delta\varepsilon}\!/_2 \cos\varepsilon - [\sigma_R]_{x+\delta x,\varepsilon+\delta\psi}(R+\delta w)\delta\varepsilon 2\pi\bar{r}\cos(\varepsilon+\delta\xi)$$

Divide by $\delta\varepsilon$ and 2π:

$$[\sigma_R R\bar{r}\cos\varepsilon]_x - ([R]_{x+\delta x} + a_2\cos(\varepsilon-\eta)\delta x)\{[\bar{r}\sigma_R]_{x+\delta x,\varepsilon+\delta\psi}\cos(\varepsilon+\delta\xi)\}$$

$$[\sigma_R R\bar{r}\cos\varepsilon]_x - ([R]_{x+\delta x} + a_2\cos(\varepsilon-\eta)\delta x)\left\{[\bar{r}\sigma_R]_{x+\delta x} + \frac{\partial}{\partial\varepsilon}(\bar{r}\sigma_R)\delta\psi\right\}\cos(\varepsilon+\delta\psi)$$

$$[\sigma_R R\bar{r}\cos\varepsilon]_x - \begin{pmatrix} [R]_{x+\delta x}[\bar{r}\sigma_R]_{x+\delta x} + [\bar{r}\sigma_R]_{x+\delta x}a_2\cos(\varepsilon-\eta)\delta x + \\ [R]_{x+\delta x}\frac{\partial}{\partial\varepsilon}(\bar{r}\sigma_R)\delta\psi + \\ a_2\cos(\varepsilon-\eta)\delta x\frac{\partial}{\partial\varepsilon}(\bar{r}\sigma_R)\delta\psi \end{pmatrix}\begin{pmatrix}\cos\varepsilon\cos\delta\psi - \\ \sin\varepsilon\sin\delta\psi\end{pmatrix}$$

$$[\sigma_R R\bar{r}\cos\varepsilon]_x - \begin{pmatrix} [R]_{x+\delta x}[\bar{r}\sigma_R]_{x+\delta x} + [\bar{r}\sigma_R]_{x+\delta x}a_2\cos(\varepsilon-\eta)\delta x + \\ [R]_{x+\delta x}\frac{\partial}{\partial\varepsilon}(\bar{r}\sigma_R)\delta\psi + a_2\cos(\varepsilon-\eta)\delta x\frac{\partial}{\partial\varepsilon}(\bar{r}\sigma_R)\delta\psi \end{pmatrix}(\cos\varepsilon - \delta\psi\sin\varepsilon)$$

$$[\sigma_R R\bar{r}\cos\varepsilon]_x - [R]_{x+\delta x}[\bar{r}\sigma_R]_{x+\delta x}\cos\varepsilon - [\bar{r}\sigma_R]_{x+\delta x}a_2\cos(\varepsilon-\eta)\delta x\cos\varepsilon -$$
$$[R]_{x+\delta x}\frac{\partial}{\partial\varepsilon}(\bar{r}\sigma_R)\delta\psi\cos\varepsilon + [R]_{x+\delta x}[\bar{r}\sigma_R]_{x+\delta x}\delta\psi\sin\varepsilon +$$
$$[\bar{r}\sigma_R]_{x+\delta x}a_2\cos(\varepsilon-\eta)\delta x\delta\psi\sin\varepsilon + [R]_{x+\delta x}\frac{\partial}{\partial\varepsilon}(\bar{r}\sigma_R)\delta\psi\delta\psi\sin\varepsilon$$
$$\therefore [\sigma_R R\bar{r}\cos\varepsilon]_x - [\sigma_R R\bar{r}\sigma_R\cos\varepsilon]_{x+\delta x} - [\bar{r}\sigma_R]_{x+\delta x}a_2\cos(\varepsilon-\eta)\delta x\cos\varepsilon -$$
$$[R]_{x+\delta x}\frac{\partial}{\partial\varepsilon}(\bar{r}\sigma_R)\delta\psi\cos\varepsilon + [R]_{x+\delta x}[\bar{r}\sigma_R]_{x+\delta x}\delta\psi\sin\varepsilon$$

Take limits:

$$-\frac{\partial}{\partial x}[R\bar{r}\sigma_R\cos\varepsilon] - \cos\varepsilon\left(\bar{r}\sigma_R a_2\cos(\varepsilon-\eta) + R\frac{\partial}{\partial\varepsilon}(\bar{r}\sigma_R)\frac{\partial\psi}{\partial x}\right) + R\bar{r}\sigma_R\sin\varepsilon\frac{\partial\psi}{\partial x}$$

Since,

$$R\frac{\partial}{\partial\varepsilon}\left(\bar{r}\sigma_R\right)\frac{\partial\psi}{\partial x}=R^2\frac{\partial}{\partial\varepsilon}\left(\sin\varepsilon\sigma_R\right)\frac{\partial\psi}{\partial x}$$

$$=R^2\left(\sigma_R\cos\varepsilon+\sin\varepsilon\frac{\partial\sigma_R}{\partial\varepsilon}\right)\frac{\partial\psi}{\partial x}$$

$$=R^2\sigma_R\cos\varepsilon\frac{\partial\psi}{\partial x}+R^2\sin\varepsilon\frac{\partial\sigma_R}{\partial\varepsilon}\frac{\partial\psi}{\partial x}$$

Hence,

$$-\frac{\partial}{\partial x}\left[R^2\sigma_R\cos\varepsilon\sin\varepsilon\right]-\cos\varepsilon\sin\varepsilon\left(R\sigma_R a_2\cos(\varepsilon-\eta)+R^2\frac{\partial\sigma_R}{\partial\varepsilon}\frac{\partial\psi}{\partial x}\right)$$
$$+R^2\sigma_R\frac{\partial\psi}{\partial x}(\sin^2\varepsilon-\cos^2\varepsilon)$$

Since,

$$\frac{\partial\psi}{\partial x}=\frac{a_2\sin(\varepsilon-\eta)}{R}$$

Hence,

$$-\frac{\partial}{\partial x}\left[R^2\sigma_R\cos\varepsilon\sin\varepsilon\right]-\cos\varepsilon\sin\varepsilon\left(R\sigma_R a_2\cos(\varepsilon-\eta)+R^2\frac{\partial\sigma_R}{\partial\varepsilon}\frac{\partial\psi}{\partial x}\right)$$
$$+Ra_2\sigma_R\sin(\varepsilon-\eta)(\sin^2\varepsilon-\cos^2\varepsilon)$$

Collecting terms:

$$\frac{\partial}{\partial x}\left[R^2\sigma_R\cos\varepsilon\sin\varepsilon\right]=\frac{\partial}{\partial\varepsilon}\left[RF\sin^2\varepsilon\right]-\cos\varepsilon\sin\varepsilon\left(R\sigma_R a_2\cos(\varepsilon-\eta)+R^2\frac{\partial\sigma_R}{\partial\varepsilon}\frac{\partial\psi}{\partial x}\right)$$
$$-Ra_2\sigma_R\sin(\varepsilon-\eta)\cos 2\varepsilon-R^2\left(\frac{\partial w}{\partial x}\right)\rho g\sin\varepsilon$$

(A.37)

Equation A.37 is equivalent to equation 58 in the main text.

Force balance in horizontal direction;

Derivation of Equations

$$\left[\sigma_\varepsilon R_2 \delta\psi \bar{r}\right]_\varepsilon \sin{}^{\delta\psi}\!/_{2} \cos\varepsilon - \left[\sigma_\varepsilon R_2 \delta\psi \bar{r}\right]_{\varepsilon+\delta\varepsilon} \sin\left(\delta\varepsilon + {}^{\delta\psi}\!/_{2}\right)\cos\varepsilon$$
$$+\left[\sigma_R R \delta\varepsilon \bar{r}\right]_x \cos{}^{\delta\varepsilon}\!/_{2} \sin\varepsilon - \left[\sigma_R\right]_{x+\delta x,\varepsilon+\delta\psi}\left(R+\delta w\right)\delta\varepsilon\bar{r}\sin\left(\varepsilon+\delta\xi\right) + R\delta\varepsilon\delta w\sigma_\theta = 0$$

(A.38)

First line of equation contains,

$$R_2\delta\psi = \delta w \cos{}^{\delta\psi}\!/_{2}$$

Hence,

$$\left[\sigma_\varepsilon \delta w \bar{r}\right]_\varepsilon \cos{}^{\delta\psi}\!/_{2} \sin{}^{\delta\psi}\!/_{2} \cos\varepsilon - \left[\sigma_\varepsilon \delta w \bar{r}\right]_{\varepsilon+\delta\varepsilon} \cos{}^{\delta\psi}\!/_{2} \sin\left(\delta\varepsilon + {}^{\delta\psi}\!/_{2}\right)\cos\varepsilon$$

Divide by $\delta x \delta\varepsilon$, and take limits:

$$\frac{\left[\sigma_\varepsilon \frac{\partial w}{\partial x}\bar{r}\right]_\varepsilon \sin{}^{\delta\psi}\!/_{2}\cos\varepsilon - \left[\sigma_\varepsilon \frac{\partial w}{\partial x}\bar{r}\right]_{\varepsilon+\delta\varepsilon}\sin\left(\delta\varepsilon + {}^{\delta\psi}\!/_{2}\right)\cos\varepsilon}{\delta\varepsilon}$$

$$\frac{\left[\sigma_\varepsilon \frac{\partial w}{\partial x}\bar{r}\right]_\varepsilon \sin{}^{\delta\psi}\!/_{2}\cos\varepsilon - \left[\sigma_\varepsilon \frac{\partial w}{\partial x}\bar{r}\right]_{\varepsilon+\delta\varepsilon}\left(\sin\delta\varepsilon\cos{}^{\delta\psi}\!/_{2} + \cos\delta\varepsilon\sin{}^{\delta\psi}\!/_{2}\right)\cos\varepsilon}{\delta\varepsilon}$$

$$\frac{\left[\sigma_\varepsilon \frac{\partial w}{\partial x}\bar{r}\right]_\varepsilon \sin{}^{\delta\psi}\!/_{2}\cos\varepsilon - \left[\sigma_\varepsilon \frac{\partial w}{\partial x}\bar{r}\right]_{\varepsilon+\delta\varepsilon}\sin\delta\varepsilon\cos{}^{\delta\psi}\!/_{2}\cos\varepsilon - \left[\sigma_\varepsilon \frac{\partial w}{\partial x}\bar{r}\right]_{\varepsilon+\delta\varepsilon}\cos\delta\varepsilon\sin{}^{\delta\psi}\!/_{2}\cos\varepsilon}{\delta\varepsilon}$$

$$\left\{\frac{\left[\sigma_\varepsilon \frac{\partial w}{\partial x}\bar{r}\right]_\varepsilon - \left[\sigma_\varepsilon \frac{\partial w}{\partial x}\bar{r}\right]_{\varepsilon+\delta\varepsilon}}{\delta\varepsilon}\right\}\sin{}^{\delta\psi}\!/_{2}\cos\varepsilon - \left[\sigma_\varepsilon \frac{\partial w}{\partial x}\bar{r}\right]_{\varepsilon+\delta\varepsilon}\frac{\sin\delta\varepsilon}{\delta\varepsilon}\cos\varepsilon$$

Since $\frac{\partial}{\partial\varepsilon}\left[\sigma_\varepsilon \frac{\partial w}{\partial x}\bar{r}\right]\sin{}^{\delta\psi}\!/_{2} \Rightarrow 0$ and $\frac{\sin\delta\varepsilon}{\delta\varepsilon} \Rightarrow 1$

Derivation of Equations

$$\therefore -\frac{\partial}{\partial \varepsilon}\left[\sigma_{\varepsilon}\left(\frac{\partial w}{\partial x}\right)\bar{r}\cos\varepsilon\right] \text{ or } -\frac{\partial}{\partial \varepsilon}\left[F\bar{r}\cos\varepsilon\right]$$

The first two terms of second line of equation:

$$\left[\sigma_R R\delta\varepsilon\bar{r}\right]_x \cos{}^{\delta\varepsilon}\!/_2 \sin\varepsilon - \left[\sigma_R\right]_{x+\delta x,\varepsilon+\delta\psi}\left(R+\delta w\right)\delta\varepsilon\bar{r}\sin\left(\varepsilon+\delta\xi\right)$$

Divide by $\delta\varepsilon$:

$$\left[\sigma_R R\bar{r}\sin\varepsilon\right]_x - \left(\left[R\right]_{x+\delta x} + a_2\cos\left(\varepsilon-\eta\right)\delta x\right)\left\{\left[\bar{r}\sigma_R\right]_{x+\delta x,\varepsilon+\delta\psi}\sin\left(\varepsilon+\delta\xi\right)\right\}$$

$$\left[\sigma_R R\bar{r}\sin\varepsilon\right]_x - \left(\left[R\right]_{x+\delta x} + a_2\cos\left(\varepsilon-\eta\right)\delta x\right)\left\{\left[\bar{r}\sigma_R\right]_{x+\delta x} + \frac{\partial}{\partial\varepsilon}\left(\bar{r}\sigma_R\right)\delta\psi\right\}\sin\left(\varepsilon+\delta\psi\right)$$

$$\left[\sigma_R R\bar{r}\sin\varepsilon\right]_x - \begin{pmatrix} \left[R\right]_{x+\delta x}\left[\bar{r}\sigma_R\right]_{x+\delta x} + \left[R\right]_{x+\delta x}\dfrac{\partial}{\partial\varepsilon}\left(\bar{r}\sigma_R\right)\delta\psi + \\ \left[\bar{r}\sigma_R\right]_{x+\delta x} a_2\cos\left(\varepsilon-\eta\right)\delta x + \\ a_2\cos\left(\varepsilon-\eta\right)\delta x\dfrac{\partial}{\partial\varepsilon}\left(\bar{r}\sigma_R\right)\delta\psi \end{pmatrix}\left(\sin\varepsilon\cos\delta\psi + \cos\varepsilon\sin\delta\psi\right)$$

$$\left[\sigma_R R\bar{r}\sin\varepsilon\right]_x - \begin{pmatrix} \left[R\right]_{x+\delta x}\left[\bar{r}\sigma_R\right]_{x+\delta x} + \left[R\right]_{x+\delta x}\dfrac{\partial}{\partial\varepsilon}\left(\bar{r}\sigma_R\right)\delta\psi + \\ \left[\bar{r}\sigma_R\right]_{x+\delta x} a_2\cos\left(\varepsilon-\eta\right)\delta x \end{pmatrix}\left(\sin\varepsilon + \delta\psi\cos\varepsilon\right)$$

$$\left[\sigma_R R\bar{r}\sin\varepsilon\right]_x - \left[R\bar{r}\sigma_R\right]_{x+\delta x}\sin\varepsilon - \left[R\right]_{x+\delta x}\frac{\partial}{\partial\varepsilon}\left(\bar{r}\sigma_R\right)\delta\psi\sin\varepsilon - \left[\bar{r}\sigma_R\right]_{x+\delta x}a_2\cos\left(\varepsilon-\eta\right)\delta x\sin\varepsilon -$$
$$\left[R\right]_{x+\delta x}\left[\bar{r}\sigma_R\right]_{x+\delta x}\delta\psi\cos\varepsilon - \left[R\right]_{x+\delta x}\frac{\partial}{\partial\varepsilon}\left(\bar{r}\sigma_R\right)\delta\psi\delta\psi\cos\varepsilon - \left[\bar{r}\sigma_R\right]_{x+\delta x}a_2\cos\left(\varepsilon-\eta\right)\delta x\delta\psi\cos\varepsilon$$

$$\therefore \left[\sigma_R R\bar{r}\sin\varepsilon\right]_x - \left[\sigma_R R\bar{r}\sin\varepsilon\right]_{x+\delta x} - \left[R\right]_{x+\delta x}\frac{\partial}{\partial\varepsilon}\left(\bar{r}\sigma_R\right)\delta\psi\sin\varepsilon - \left[\bar{r}\sigma_R\right]_{x+\delta x}a_2\cos\left(\varepsilon-\eta\right)\delta x\sin\varepsilon -$$
$$\left[\sigma_R R\bar{r}\right]_{x+\delta x}\delta\psi\cos\varepsilon$$

Divide by δx, and take limits:

$$-\frac{\partial}{\partial x}\left[\sigma_R R\bar{r}\sin\varepsilon\right] - R\frac{\partial}{\partial\varepsilon}\left(\bar{r}\sigma_R\right)\frac{\partial\psi}{\partial x}\sin\varepsilon - \bar{r}\sigma_R a_2\cos\left(\varepsilon-\eta\right)\sin\varepsilon - \sigma_R R\bar{r}\frac{\partial\psi}{\partial x}\cos\varepsilon$$

Since $\dfrac{\partial\psi}{\partial x} = \dfrac{a_2\sin\left(\varepsilon-\eta\right)}{R}$, and

$$R\frac{\partial}{\partial \varepsilon}(\bar{r}\sigma_R)\frac{\partial \psi}{\partial x}\sin\varepsilon = R^2\sigma_R\cos\varepsilon\sin\varepsilon\frac{\partial \psi}{\partial x} + R^2\sin^2\varepsilon\frac{\partial \sigma_R}{\partial \varepsilon}\frac{\partial \psi}{\partial x}$$

Hence:

$$-\frac{\partial}{\partial x}\left[\sigma_R R^2\sin^2\varepsilon\right] - R^2\sigma_R\cos\varepsilon\sin\varepsilon\frac{\partial \psi}{\partial x} - R^2\sin^2\varepsilon\frac{\partial \sigma_R}{\partial \varepsilon}\frac{\partial \psi}{\partial x} -$$
$$R\sigma_R a_2\cos(\varepsilon-\eta)\sin^2\varepsilon - R\sigma_R a_2\sin(\varepsilon-\eta)\cos\varepsilon\sin\varepsilon$$
$$\therefore -\frac{\partial}{\partial x}\left[\sigma_R R^2\sin^2\varepsilon\right] - 2R\sigma_R a_2\sin(\varepsilon-\eta)\cos\varepsilon\sin\varepsilon - R^2\sin^2\varepsilon\frac{\partial \sigma_R}{\partial \varepsilon}\frac{\partial \psi}{\partial x} -$$
$$R\sigma_R a_2\cos(\varepsilon-\eta)\sin^2\varepsilon$$

Collecting terms:

$$\therefore \frac{\partial}{\partial x}\left[R^2\sigma_R\sin^2\varepsilon\right] = -\frac{\partial}{\partial \varepsilon}\left[RF\cos\varepsilon\sin\varepsilon\right] - \sin^2\varepsilon\left(R\sigma_R a_2\cos(\varepsilon-\eta) + R^2\frac{\partial \sigma_R}{\partial \varepsilon}\frac{\partial \psi}{\partial x}\right)$$
$$- R\sigma_R a_2\sin(\varepsilon-\eta)\sin 2\varepsilon + R\left(\frac{\partial w}{\partial x}\right)\sigma_\theta \qquad \text{(A.39)}$$

Equation A.39 is equivalent to equation 59 in the main text.

Since $R = a_1 x$, and $F = \sigma_\varepsilon\left(\frac{\partial w}{\partial x}\right)$. For a symmetrical cone, $\eta = 0$.

Using A.37, since,

$$
\begin{aligned}
R\frac{\partial}{\partial\varepsilon}\left[F\sin^2\varepsilon\right] &= \frac{\partial}{\partial\varepsilon}\left[RF\frac{1-\cos 2\varepsilon}{2}\right] \\
&= \frac{\partial}{\partial\varepsilon}\left[\frac{RF}{2}-\frac{RF\cos 2\varepsilon}{2}\right] \\
&= \frac{R}{2}\frac{\partial}{\partial\varepsilon}\left[F - F\cos 2\varepsilon\right] \\
&= \frac{R}{2}\left(\frac{\partial F}{\partial\varepsilon}-\cos 2\varepsilon\frac{\partial F}{\partial\varepsilon}+F\sin 2\varepsilon\right) \\
&= R\left(\frac{\partial F}{\partial\varepsilon}\frac{1-\cos 2\varepsilon}{2}+\frac{F}{2}\sin 2\varepsilon\right) \\
&= 2RF\sin\varepsilon\cos\varepsilon + R\sin^2\varepsilon\frac{\partial F}{\partial\varepsilon}
\end{aligned}
$$

Hence,

$$
\frac{\partial}{\partial x}\left[R^2\sigma_R\cos\varepsilon\sin\varepsilon\right] = 2RF\sin\varepsilon\cos\varepsilon + R\sin^2\varepsilon\frac{\partial F}{\partial\varepsilon} - R\sigma_R a_2\cos^2\varepsilon\sin\varepsilon - R^2\cos\varepsilon\sin\varepsilon\frac{\partial\sigma_R}{\partial\varepsilon}\frac{\partial\psi}{\partial x} - Ra_2\sigma_R\sin\varepsilon\cos 2\varepsilon - R^2\left(\frac{\partial w}{\partial x}\right)\rho g\sin\varepsilon
$$

$$
\frac{\partial}{\partial x}\left[R^2\sigma_R\cos\varepsilon\sin\varepsilon\right] = 2RF\sin\varepsilon\cos\varepsilon + R\sin^2\varepsilon\frac{\partial F}{\partial\varepsilon} - R\sigma_R a_2\left(\cos^2\varepsilon\sin\varepsilon + \sin\varepsilon\cos 2\varepsilon\right) - R^2\cos\varepsilon\sin\varepsilon\frac{\partial\sigma_R}{\partial\varepsilon}\frac{\partial\psi}{\partial x} - R^2\left(\frac{\partial w}{\partial x}\right)\rho g\sin\varepsilon
$$

$$
\frac{\partial}{\partial x}\left[R^2\sigma_R\cos\varepsilon\sin\varepsilon\right] = 2RF\sin\varepsilon\cos\varepsilon + R\sin^2\varepsilon\frac{\partial F}{\partial\varepsilon} - R^2\cos\varepsilon\sin\varepsilon\frac{\partial\sigma_R}{\partial\varepsilon}\frac{\partial\psi}{\partial x} - R^2\left(\frac{\partial w}{\partial x}\right)\rho g\sin\varepsilon - R\sigma_R a_2\left(\cos^2\varepsilon\sin\varepsilon + \sin\varepsilon\cos^2\varepsilon - \sin\varepsilon\sin^2\varepsilon\right)
$$

$$
\therefore \frac{\partial}{\partial x}\left[R^2\sigma_R\right] = 2RF + R\frac{\sin\varepsilon}{\cos\varepsilon}\frac{\partial F}{\partial\varepsilon} - R\sigma_R a_2\left(2\cos\varepsilon - \frac{\sin^2\varepsilon}{\cos\varepsilon}\right) - R^2\frac{\partial\sigma_R}{\partial\varepsilon}\frac{\partial\psi}{\partial x} - \frac{R^2}{\cos\varepsilon}\left(\frac{\partial w}{\partial x}\right)\rho g
$$

(A.40)

Using A.38, since,

$$R\frac{\partial}{\partial\varepsilon}\left[F\cos\varepsilon\sin\varepsilon\right]=R\frac{\partial}{\partial\varepsilon}\left[F\frac{\sin 2\varepsilon}{2}\right]$$
$$=R\left(\frac{\sin 2\varepsilon}{2}\frac{\partial F}{\partial\varepsilon}+F\cos 2\varepsilon\right)$$
$$=RF\left(\cos^2\varepsilon-\sin^2\varepsilon\right)+R\sin\varepsilon\cos\varepsilon\frac{\partial F}{\partial\varepsilon}$$

Hence,

$$\frac{\partial}{\partial x}\left[R^2\sigma_R\sin^2\varepsilon\right]=-RF\left(\cos^2\varepsilon-\sin^2\varepsilon\right)-R\sin\varepsilon\cos\varepsilon\frac{\partial F}{\partial\varepsilon}-$$
$$R\sigma_R a_2\cos\varepsilon\sin^2\varepsilon-R^2\sin^2\varepsilon\frac{\partial\sigma_R}{\partial\varepsilon}\frac{\partial\psi}{\partial x}-R\sigma_R a_2\sin\varepsilon\sin 2\varepsilon+R\left(\frac{\partial w}{\partial x}\right)\sigma_\theta$$

$$\therefore\frac{\partial}{\partial x}\left[R^2\sigma_R\right]=-RF\frac{\cos 2\varepsilon}{\sin^2\varepsilon}-R\frac{\cos\varepsilon}{\sin\varepsilon}\frac{\partial F}{\partial\varepsilon}-$$
$$R\sigma_R a_2\frac{\left(\cos\varepsilon\sin^2\varepsilon+\sin\varepsilon\sin 2\varepsilon\right)}{\sin^2\varepsilon}-R^2\frac{\partial\sigma_R}{\partial\varepsilon}\frac{\partial\psi}{\partial x}+\frac{R}{\sin^2\varepsilon}\left(\frac{\partial w}{\partial x}\right)\sigma_\theta \qquad \text{(A.41)}$$

Substitute A.40 and A.41:

$$2RF+R\frac{\sin\varepsilon}{\cos\varepsilon}\frac{\partial F}{\partial\varepsilon}-R\sigma_R a_2\left(2\cos\varepsilon-\frac{\sin^2\varepsilon}{\cos\varepsilon}\right)-R^2\frac{\partial\sigma_R}{\partial\varepsilon}\frac{\partial\psi}{\partial x}-\frac{R^2}{\cos\varepsilon}\left(\frac{\partial w}{\partial x}\right)\rho g=$$
$$-RF\frac{\cos 2\varepsilon}{\sin^2\varepsilon}-R\frac{\cos\varepsilon}{\sin\varepsilon}\frac{\partial F}{\partial\varepsilon}-R\sigma_R a_2\frac{\left(\cos\varepsilon\sin^2\varepsilon+\sin\varepsilon\sin 2\varepsilon\right)}{\sin^2\varepsilon}-R^2\frac{\partial\sigma_R}{\partial\varepsilon}\frac{\partial\psi}{\partial x}+\frac{R}{\sin^2\varepsilon}\left(\frac{\partial w}{\partial x}\right)\sigma_\theta$$
$$\left(\tan\varepsilon+\frac{1}{\tan\varepsilon}\right)\frac{\partial F}{\partial\varepsilon}=-F\left(2+\frac{\cos^2\varepsilon-\sin^2\varepsilon}{\sin^2\varepsilon}\right)-\sigma_R a_2\frac{1}{\cos\varepsilon}+$$
$$\frac{R}{\cos\varepsilon}\left(\frac{\partial w}{\partial x}\right)\rho g+\frac{1}{\sin^2\varepsilon}\left(\frac{\partial w}{\partial x}\right)\sigma_\theta$$

$$\left(\frac{1}{\tan\varepsilon\cos^2\varepsilon}\right)\frac{\partial F}{\partial\varepsilon}=-F\left(2+\frac{\cos^2\varepsilon-\sin^2\varepsilon}{\sin^2\varepsilon}\right)-\sigma_R a_2\frac{1}{\cos\varepsilon}$$
$$+\frac{R}{\cos\varepsilon}\left(\frac{\partial w}{\partial x}\right)\rho g+\frac{1}{\sin^2\varepsilon}\left(\frac{\partial w}{\partial x}\right)\sigma_\theta$$
$$\left(\frac{1}{\tan\varepsilon}\right)\frac{\partial F}{\partial\varepsilon}=-F\left(\frac{2\sin^2\varepsilon}{\tan^2\varepsilon}+\frac{\cos^2\varepsilon-\sin^2\varepsilon}{\tan^2\varepsilon}\right)-\sigma_R a_2\cos\varepsilon$$
$$+R\left(\frac{\partial w}{\partial x}\right)\rho g\cos\varepsilon+\frac{1}{\tan^2\varepsilon}\left(\frac{\partial w}{\partial x}\right)\sigma_\theta$$
$$\left(\frac{1}{\tan\varepsilon}\right)\frac{\partial F}{\partial\varepsilon}=-F\left(\frac{2\sin^2\varepsilon+\cos^2\varepsilon-\sin^2\varepsilon}{\tan^2\varepsilon}\right)-\sigma_R a_2\cos\varepsilon$$
$$+R\left(\frac{\partial w}{\partial x}\right)\rho g\cos\varepsilon+\frac{1}{\tan^2\varepsilon}\left(\frac{\partial w}{\partial x}\right)\sigma_\theta$$
$$\therefore\frac{\partial F}{\partial\varepsilon}=\left(\frac{1}{\tan\varepsilon}\right)\left(-F+\left(\frac{\partial w}{\partial x}\right)\sigma_\theta\right)-\sigma_R a_2\sin\varepsilon$$
$$+R\left(\frac{\partial w}{\partial x}\right)\rho g\sin\varepsilon \qquad \text{(A.42)}$$

Equation A.42 is equivalent to equation 60 in the main text.

Substitute A.42 into A.41:

$$\frac{\partial}{\partial x}\left[R^2\sigma_R\right]=-RF\frac{\cos 2\varepsilon}{\sin^2\varepsilon}-R\frac{\cos\varepsilon}{\sin\varepsilon}\left[\begin{array}{l}\frac{-F}{\tan\varepsilon}+\left(\frac{\partial w}{\partial x}\right)\frac{\sigma_\theta}{\tan\varepsilon}-\sigma_R a_2\sin\varepsilon\\+R\left(\frac{\partial w}{\partial x}\right)\rho g\sin\varepsilon\end{array}\right]$$
$$-R\sigma_R a_2\frac{\left(\cos\varepsilon\sin^2\varepsilon+\sin\varepsilon\sin 2\varepsilon\right)}{\sin^2\varepsilon}-R^2\frac{\partial\sigma_R}{\partial\varepsilon}\frac{\partial\psi}{\partial x}+\frac{R}{\sin^2\varepsilon}\left(\frac{\partial w}{\partial x}\right)\sigma_\theta$$
$$\therefore\frac{\partial}{\partial x}\left[R^2\sigma_R\right]=RF\left(-\frac{\cos 2\varepsilon}{\sin^2\varepsilon}+\frac{\cos\varepsilon}{\sin\varepsilon\tan\varepsilon}\right)-\frac{R\cos\varepsilon}{\sin\varepsilon\tan\varepsilon}\left(\frac{\partial w}{\partial x}\right)\sigma_\theta-$$
$$R^2\left(\frac{\partial w}{\partial x}\right)\rho g\cos\varepsilon+R\sigma_R a_2\left(\cos\varepsilon-\frac{\left(\cos\varepsilon\sin^2\varepsilon+\sin\varepsilon\sin 2\varepsilon\right)}{\sin^2\varepsilon}\right)-R^2\frac{\partial\sigma_R}{\partial\varepsilon}\frac{\partial\psi}{\partial x}+\frac{R}{\sin^2\varepsilon}\left(\frac{\partial w}{\partial x}\right)\sigma_\theta$$
$$\therefore\frac{\partial}{\partial x}\left[R^2\sigma_R\right]=RF\left(\frac{-\cos^2\varepsilon+\sin^2\varepsilon+\cos^2\varepsilon}{\sin^2\varepsilon}\right)+R\left(\frac{\partial w}{\partial x}\right)\sigma_\theta\left(\frac{1}{\sin^2\varepsilon}-\frac{\cos^2\varepsilon}{\sin^2\varepsilon}\right)-$$
$$R^2\left(\frac{\partial w}{\partial x}\right)\rho g\cos\varepsilon+R\sigma_R a_2\left(\cos\varepsilon-\cos\varepsilon-2\cos\varepsilon\right)-R^2\frac{\partial\sigma_R}{\partial\varepsilon}\frac{\partial\psi}{\partial x}$$

$$\therefore \frac{\partial}{\partial x}\left[R^2\sigma_R\right] = RF - R^2\left(\frac{\partial w}{\partial x}\right)\rho g \cos\varepsilon - 2R\sigma_R a_2 \cos\varepsilon - Ra_2 \sin\varepsilon \frac{\partial \sigma_R}{\partial \varepsilon} + R\left(\frac{\partial w}{\partial x}\right)\sigma_\theta$$

(A.43)

Equation A.43 is equivalent to equation 61 in the main text.

9.7 Derivation of Haar-von Karman hypothesis from equation fifty nine

Equation 59 can be used to derive a relationship for azimuthal stress values.

$$\frac{\partial}{\partial x}\left[R^2\sigma_R \sin^2\varepsilon\right] = -\frac{\partial}{\partial \varepsilon}\left[RF\cos\varepsilon\sin\varepsilon\right] - \sin^2\varepsilon\left(R\sigma_R a_2 \cos(\varepsilon-\eta) + R^2\frac{\partial \sigma_R}{\partial \varepsilon}\frac{\partial \psi}{\partial x}\right)$$
$$- R\sigma_R a_2 \sin(\varepsilon-\eta)\sin 2\varepsilon + R\left(\frac{\partial w}{\partial x}\right)\sigma_\theta$$

(A.44)

Equation A.44 is equivalent to equation 59 in the main text.

Let $\varepsilon = 0$ and $\eta = 0$:

$$\therefore \frac{\partial}{\partial \varepsilon}\left[RF\cos\varepsilon\sin\varepsilon\right] = R\left(\frac{\partial w}{\partial x}\right)\sigma_\theta$$

Since $\frac{\partial}{\partial \varepsilon}\left[RF\cos\varepsilon\sin\varepsilon\right] = R\left[F\left(\cos^2\varepsilon - \sin^2\varepsilon\right) + \sin\varepsilon\cos\varepsilon\frac{\partial F}{\partial \varepsilon}\right]$,

When $\varepsilon = 0$, $R\left[F\left(\cos^2\varepsilon - \sin^2\varepsilon\right) + \sin\varepsilon\cos\varepsilon\frac{\partial F}{\partial \varepsilon}\right] = RF$

$$\therefore RF = R(a_1 + a_2)\sigma_\theta$$
$$F = (a_1 + a_2)\sigma_\theta$$
$$\sigma_\varepsilon(a_1 + a_2) = (a_1 + a_2)\sigma_\theta$$
$$\therefore \sigma_\varepsilon = \sigma_\theta \qquad \text{(A.45)}$$

Derivation of Equations

Equation A.45 is equivalent to equation 65 in the main text, which is in accordance with prior knowledge (Haar and von Karman 1909, Nedderman 1992).

9.8 Derivation of Lamé-Maxwell equations

9.8.1 Two-dimensional derivation for equations 16 and 17

Coker et al (1957) and Olsen (1982) give brief derivations of the Lamé-Maxwell equations of equilibrium (equations 16 and 17 in the main text, Chapter 3.1). In Figure A.4, element ABCO is an incremental element bounded by four principal stress trajectories. Principal stresses σ_1 and σ_2 act over stress trajectories s_1 and s_2. The principal stress trajectories have radii ρ_1 and ρ_2.

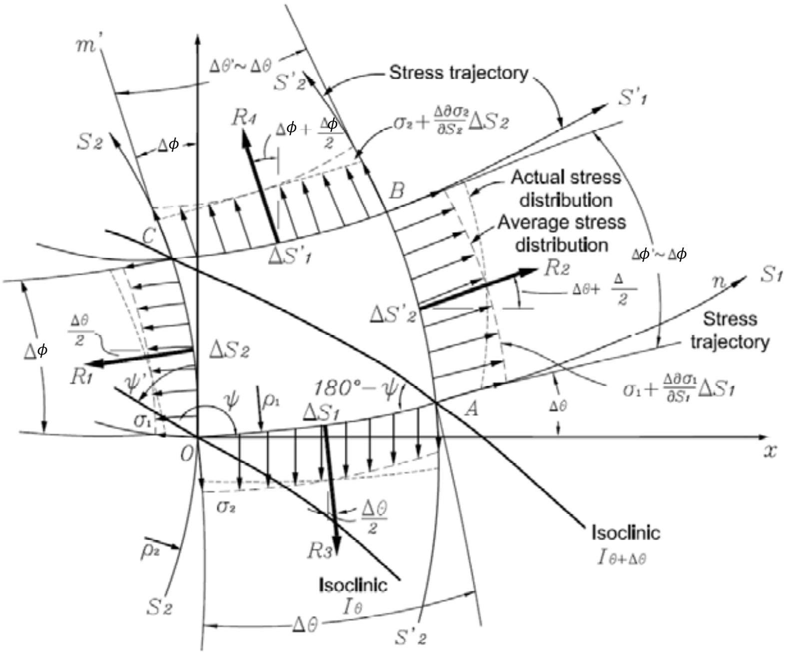

Figure A.4. Incremental element ABCO (Olsen 1982)

Equilibrium equation in *x*-direction;

$$-\sigma_1 \Delta s_2 \cos\frac{\Delta\phi}{2} + \left(\sigma_1 + \frac{\partial\sigma_1}{\partial s_1}\Delta s_1\right)\Delta s'_2 \cos\left(\Delta\theta + \frac{\Delta\phi}{2}\right)$$
$$+\sigma_2 \Delta s_1 \sin\frac{\Delta\theta}{2} - \left(\sigma_2 + \frac{\partial\sigma_2}{\partial s_2}\Delta s_2\right)\Delta s'_1 \sin\left(\Delta\phi + \frac{\Delta\theta}{2}\right) = 0$$

Since $\Delta s'_2 = \Delta s_2\left(1+\frac{\Delta s_1}{\rho_2}\right)$ and $\Delta s'_1 = \Delta s_1\left(1-\frac{\Delta s_2}{\rho_1}\right)$

$$\begin{aligned}
&-\sigma_1\Delta s_2\cos\frac{\Delta\phi}{2}+\left(\sigma_1+\frac{\partial\sigma_1}{\partial s_1}\Delta s_1\right)\Delta s_2\left(1+\frac{\Delta s_1}{\rho_2}\right)\cos\left(\Delta\theta+\frac{\Delta\phi}{2}\right)\\
&+\sigma_2\Delta s_1\sin\frac{\Delta\theta}{2}-\left(\sigma_2+\frac{\partial\sigma_2}{\partial s_2}\Delta s_2\right)\Delta s_1\left(1-\frac{\Delta s_2}{\rho_1}\right)\sin\left(\Delta\phi+\frac{\Delta\theta}{2}\right)=0
\end{aligned}\tag{A.46}$$

First line of equation A.46:

$$-\sigma_1\Delta s_2\cos\frac{\Delta\phi}{2}+\left(\sigma_1+\frac{\partial\sigma_1}{\partial s_1}\Delta s_1\right)\Delta s_2\left(1+\frac{\Delta s_1}{\rho_2}\right)\cos\left(\Delta\theta+\frac{\Delta\phi}{2}\right)$$

$$-\sigma_1\Delta s_2\cos\frac{\Delta\phi}{2}+\Delta s_2\cos\left(\Delta\theta+\frac{\Delta\phi}{2}\right)\left\{\sigma_1+\frac{\sigma_1\Delta s_1}{\rho_2}+\frac{\partial\sigma_1}{\partial s_1}\Delta s_1+\frac{\partial\sigma_1}{\partial s_1}\frac{\Delta s_1\Delta s_1}{\rho_2}\right\}$$

$$-\sigma_1\Delta s_2\cos\frac{\Delta\phi}{2}+\Delta s_2\cos\left(\frac{\Delta\phi}{2}\right)\left\{\sigma_1+\frac{\sigma_1\Delta s_1}{\rho_2}+\frac{\partial\sigma_1}{\partial s_1}\Delta s_1+\frac{\partial\sigma_1}{\partial s_1}\frac{\Delta s_1\Delta s_1}{\rho_2}\right\}$$

$$-\sigma_1\Delta s_2\cos\frac{\Delta\phi}{2}+\sigma_1\Delta s_2\cos\left(\frac{\Delta\phi}{2}\right)+\Delta s_2\cos\left(\frac{\Delta\phi}{2}\right)\left\{\frac{\sigma_1\Delta s_1}{\rho_2}+\frac{\partial\sigma_1}{\partial s_1}\Delta s_1\right\}$$

$$\therefore\ \frac{\sigma_1\Delta s_1\Delta s_2}{\rho_2}+\frac{\partial\sigma_1}{\partial s_1}\Delta s_1\Delta s_2$$

Second line of equation A.46:

$$\sigma_2\Delta s_1\sin\frac{\Delta\theta}{2}-\left(\sigma_2+\frac{\partial\sigma_2}{\partial s_2}\Delta s_2\right)\Delta s_1\left(1-\frac{\Delta s_2}{\rho_1}\right)\sin\left(\Delta\phi+\frac{\Delta\theta}{2}\right)$$

$$\sigma_2\Delta s_1\sin\frac{\Delta\theta}{2}-\Delta s_1\sin\left(\Delta\phi+\frac{\Delta\theta}{2}\right)\left\{\sigma_2-\frac{\sigma_2\Delta s_2}{\rho_1}+\frac{\partial\sigma_2}{\partial s_2}\Delta s_2-\frac{\partial\sigma_2}{\partial s_2}\frac{\Delta s_2\Delta s_2}{\rho_1}\right\}$$

$$\sigma_2\Delta s_1\sin\frac{\Delta\theta}{2}-\Delta s_1\sin\left(\Delta\phi+\frac{\Delta\theta}{2}\right)\sigma_2+\Delta s_1\sin\left(\Delta\phi+\frac{\Delta\theta}{2}\right)\frac{\sigma_2\Delta s_2}{\rho_1}-$$

$$\Delta s_1\sin\left(\Delta\phi+\frac{\Delta\theta}{2}\right)\frac{\partial\sigma_2}{\partial s_2}\Delta s_2+\Delta s_1\sin\left(\Delta\phi+\frac{\Delta\theta}{2}\right)\frac{\partial\sigma_2}{\partial s_2}\frac{\Delta s_2\Delta s_2}{\rho_1}$$

$$\therefore\ \sigma_2\Delta s_1\sin\frac{\Delta\theta}{2}-\Delta s_1\sigma_2\sin\left(\Delta\phi+\frac{\Delta\theta}{2}\right)$$

$$\sigma_2 \Delta s_1 \sin\frac{\Delta\theta}{2} - \Delta s_1 \sigma_2 \left(\sin\Delta\phi\cos\frac{\Delta\theta}{2} + \cos\Delta\phi\sin\frac{\Delta\theta}{2}\right)$$

$$\sigma_2 \Delta s_1 \sin\frac{\Delta\theta}{2} - \Delta s_1 \sigma_2 \sin\Delta\phi - \Delta s_1 \sigma_2 \sin\frac{\Delta\theta}{2}$$

$$\therefore -\Delta s_1 \sigma_2 \sin\Delta\phi$$

Hence:

$$\frac{\sigma_1 \Delta s_1 \Delta s_2}{\rho_2} + \frac{\partial\sigma_1}{\partial s_1}\Delta s_1 \Delta s_2 - \Delta s_1 \sigma_2 \Delta\phi = 0$$

Dividing by $\Delta s_1 \Delta s_2$:

$$\frac{\sigma_1}{\rho_2} + \frac{\partial\sigma_1}{\partial s_1} - \frac{\sigma_2 \Delta\phi}{\Delta s_2} = 0 \qquad \text{(A.47)}$$

Equation A.47 is equivalent to equation 16 in the main text.

Since $\Delta\phi = \dfrac{\Delta s_2}{\rho_2}$, $\therefore \dfrac{\sigma_1}{\rho_2} + \dfrac{\partial\sigma_1}{\partial s_1} - \dfrac{\sigma_2}{\rho_2} = \dfrac{\partial\sigma_1}{\partial s_1} + \dfrac{\sigma_1 - \sigma_2}{\rho_2} = 0$

Equilibrium equation in *y*-direction:

$$-\sigma_1 \Delta s_2 \sin\frac{\Delta\phi}{2} + \left(\sigma_1 + \frac{\partial\sigma_1}{\partial s_1}\Delta s_1\right)\Delta s'_2 \sin\left(\Delta\theta + \frac{\Delta\phi}{2}\right) -$$

$$\sigma_2 \Delta s_1 \cos\frac{\Delta\theta}{2} + \left(\sigma_2 + \frac{\partial\sigma_2}{\partial s_2}\Delta s_2\right)\Delta s'_1 \cos\left(\Delta\phi + \frac{\Delta\theta}{2}\right) = 0$$

Since $\Delta s'_2 = \Delta s_2\left(1 + \dfrac{\Delta s_1}{\rho_2}\right)$ and $\Delta s'_1 = \Delta s_1\left(1 - \dfrac{\Delta s_2}{\rho_1}\right)$

$$
\begin{aligned}
&-\sigma_1\Delta s_2 \sin\frac{\Delta\phi}{2}+\left(\sigma_1+\frac{\partial\sigma_1}{\partial s_1}\Delta s_1\right)\Delta s_2\left(1+\frac{\Delta s_1}{\rho_2}\right)\sin\left(\Delta\theta+\frac{\Delta\phi}{2}\right)-\\
&\sigma_2\Delta s_1 \cos\frac{\Delta\theta}{2}+\left(\sigma_2+\frac{\partial\sigma_2}{\partial s_2}\Delta s_2\right)\Delta s_1\left(1-\frac{\Delta s_2}{\rho_1}\right)\cos\left(\Delta\phi+\frac{\Delta\theta}{2}\right)=0
\end{aligned}
\tag{A.48}
$$

First line of equation A.48:

$$
\begin{aligned}
&-\sigma_1\Delta s_2 \sin\frac{\Delta\phi}{2}+\left(\sigma_1+\frac{\partial\sigma_1}{\partial s_1}\Delta s_1\right)\Delta s_2\left(1+\frac{\Delta s_1}{\rho_2}\right)\sin\left(\Delta\theta+\frac{\Delta\phi}{2}\right)\\
&-\sigma_1\Delta s_2 \sin\frac{\Delta\phi}{2}+\Delta s_2\sin\left(\Delta\theta+\frac{\Delta\phi}{2}\right)\left\{\sigma_1+\frac{\sigma_1\Delta s_1}{\rho_2}+\frac{\partial\sigma_1}{\partial s_1}\Delta s_1+\frac{\partial\sigma_1}{\partial s_1}\frac{\Delta s_1\Delta s_1}{\rho_2}\right\}
\end{aligned}
$$

$$
\begin{aligned}
&-\sigma_1\Delta s_2 \sin\frac{\Delta\phi}{2}+\left(\sigma_1+\frac{\partial\sigma_1}{\partial s_1}\Delta s_1\right)\Delta s_2\left(1+\frac{\Delta s_1}{\rho_2}\right)\sin\left(\Delta\theta+\frac{\Delta\phi}{2}\right)\\
&-\sigma_1\Delta s_2 \sin\frac{\Delta\phi}{2}+\Delta s_2\sin\left(\Delta\theta+\frac{\Delta\phi}{2}\right)\left\{\sigma_1+\frac{\sigma_1\Delta s_1}{\rho_2}+\frac{\partial\sigma_1}{\partial s_1}\Delta s_1+\frac{\partial\sigma_1}{\partial s_1}\frac{\Delta s_1\Delta s_1}{\rho_2}\right\}\\
&-\sigma_1\Delta s_2 \sin\frac{\Delta\phi}{2}+\sigma_1\Delta s_2\sin\left(\Delta\theta+\frac{\Delta\phi}{2}\right)+\frac{\sigma_1\Delta s_1\Delta s_2}{\rho_2}\sin\left(\Delta\theta+\frac{\Delta\phi}{2}\right)+\\
&\frac{\partial\sigma_1}{\partial s_1}\Delta s_1\Delta s_2\sin\left(\Delta\theta+\frac{\Delta\phi}{2}\right)+\frac{\partial\sigma_1}{\partial s_1}\frac{\Delta s_1\Delta s_1\Delta s_2}{\rho_2}\sin\left(\Delta\theta+\frac{\Delta\phi}{2}\right)\\
&\therefore -\sigma_1\Delta s_2 \sin\frac{\Delta\phi}{2}+\sigma_1\Delta s_2\sin\left(\Delta\theta+\frac{\Delta\phi}{2}\right)\\
&-\sigma_1\Delta s_2 \sin\frac{\Delta\phi}{2}+\sigma_1\Delta s_2\left(\sin\Delta\theta\cos\frac{\Delta\phi}{2}+\cos\Delta\theta\sin\frac{\Delta\phi}{2}\right)\\
&-\sigma_1\Delta s_2 \sin\frac{\Delta\phi}{2}+\sigma_1\Delta s_2\Delta\theta+\sigma_1\Delta s_2\ \frac{\Delta\phi}{2}\\
&\therefore \sigma_1\Delta s_2\Delta\theta
\end{aligned}
$$

Second line of equation A.48:

$$-\sigma_2\Delta s_1\cos\frac{\Delta\theta}{2}+\left(\sigma_2+\frac{\partial\sigma_2}{\partial s_2}\Delta s_2\right)\Delta s_1\left(1-\frac{\Delta s_2}{\rho_1}\right)\cos\left(\Delta\phi+\frac{\Delta\theta}{2}\right)$$
$$-\sigma_2\Delta s_1\cos\frac{\Delta\theta}{2}+\Delta s_1\cos\left(\Delta\phi+\frac{\Delta\theta}{2}\right)\left\{\sigma_2-\frac{\sigma_2\Delta s_2}{\rho_1}+\frac{\partial\sigma_2}{\partial s_2}\Delta s_2-\frac{\partial\sigma_2}{\partial s_2}\frac{\Delta s_2\Delta s_2}{\rho_1}\right\}$$
$$-\sigma_2\Delta s_1+\sigma_2\Delta s_1-\frac{\sigma_2\Delta s_1\Delta s_2}{\rho_1}+\frac{\partial\sigma_2}{\partial s_2}\Delta s_2\Delta s_1-\frac{\partial\sigma_2}{\partial s_2}\frac{\Delta s_1\Delta s_2\Delta s_2}{\rho_1}$$
$$\therefore -\frac{\sigma_2\Delta s_1\Delta s_2}{\rho_1}+\frac{\partial\sigma_2}{\partial s_2}\Delta s_2\Delta s_1$$

Hence:

$$-\frac{\sigma_2\Delta s_1\Delta s_2}{\rho_1}+\frac{\partial\sigma_2}{\partial s_2}\Delta s_2\Delta s_1+\sigma_1\Delta s_2\Delta\theta=0$$

Dividing by $\Delta s_1\Delta s_2$:

$$-\frac{\sigma_2}{\rho_1}+\frac{\partial\sigma_2}{\partial s_2}+\frac{\sigma_1\Delta\theta}{\Delta s_1}=0$$

Since $\Delta\theta=\dfrac{\Delta s_1}{\rho_1}$, $-\dfrac{\sigma_2}{\rho_1}+\dfrac{\partial\sigma_2}{\partial s_2}+\dfrac{\sigma_1}{\rho_1}=\dfrac{\partial\sigma_2}{\partial s_2}+\dfrac{\sigma_1-\sigma_2}{\rho_1}=0$ (A.49)

Equation A.49 is equivalent to equation 17 in the main text.

9.8.2 Three-dimensional derivation for equation 67

Love (1927, p. 91) gives special cases of Lamé-Maxwell stress equations applied to curvilinear coordinates. For a rotationally symmetric system:

$$h_1\frac{\partial\widehat{\alpha\alpha}}{\partial\alpha}+\frac{\widehat{\alpha\alpha}-\widehat{\beta\beta}}{\rho_{13}}-\frac{\widehat{\alpha\alpha}-\widehat{\gamma\gamma}}{\rho_{12}}+\rho F_\alpha=\rho f_\alpha \tag{A.50}$$

During private correspondence with the author, Professor Andrew Matchett proposed that equation A.50 would be equivalent to equation A.51 for a $(\theta - R(x) - \psi)$ coordinate system.

$$\frac{\partial \sigma_\theta}{\partial \theta} + \frac{\sigma_\theta - \sigma_R}{\rho_{\theta\psi}} - \frac{\sigma_\theta - \sigma_\varepsilon}{\rho_{\theta\varepsilon}} - \rho g_\theta = 0 \qquad \text{(A.51)}$$

Since $g_\theta = 0$, $\rho_{\theta\psi} = \rho_{\theta\varepsilon} = \infty$ and $\frac{\partial \sigma_\theta}{\partial \theta} = 0$, and dividing by $\rho_{\theta R}$,

$$\sigma_\theta = \sigma_R \left\{ \frac{1}{1 - \left(\frac{\rho_{\theta\psi}}{\rho_{\theta R}} \right)} \right\} - \sigma_\varepsilon \left\{ \frac{\left(\frac{\rho_{\theta\psi}}{\rho_{\theta R}} \right)}{1 - \left(\frac{\rho_{\theta\psi}}{\rho_{\theta R}} \right)} \right\} \qquad \text{(A.52)}$$

Let the ratio of radii be *k*,

$$\sigma_\theta = \sigma_R \left\{ \frac{1}{1-k} \right\} - \sigma_\varepsilon \left\{ \frac{k}{1-k} \right\} \qquad \text{(A.53)}$$

Equation A.53 is equivalent to equation 67 in the main text.

9.9 Force balance equations in R- and ε -directions for axially symmetric three-dimensional cone hopper with conical insert case

Figure 73, Chapter 6.1.1, shows the principal stress arc geometry. The void between hopper wall and insert has half angle α. A circular arc cuts the hopper right-hand side at a distance x above the apex with radius *R*, derived as follows.

Since $\dfrac{y}{\sin(\alpha + \alpha)} = \dfrac{r}{\sin(\beta + \gamma)}$ and $\dfrac{y}{\sin(\alpha + \alpha + \beta + \beta)} = \dfrac{R}{\sin \gamma}$,

where $\gamma = 180 - \dfrac{\pi}{2} - \dfrac{\alpha + \alpha + \beta + \beta}{2}$

$$\therefore R = y\frac{\sin\gamma}{\sin(\alpha+\alpha+\beta+\beta)}$$
$$= \frac{r\sin(\alpha+\alpha)\sin\gamma}{\sin(\alpha+\alpha+\beta+\beta)\sin(\beta+\gamma)}$$

where $r = \dfrac{x}{\cos(\Theta+\alpha)}$

$$\therefore R = \frac{x\sin(\alpha+\alpha)\sin\gamma}{\cos(\Theta+\alpha)\sin(\alpha+\alpha+\beta+\beta)\sin(\beta+\gamma)} \qquad \text{(A.54)}$$

Equation A.54 is equivalent to equation 71 in the main text.

Let $\lambda = \alpha+\alpha+\beta+\beta$

$$\therefore R = x\frac{\sin(\alpha+\alpha)\sin\gamma}{\cos(\Theta+\alpha)\sin\lambda\sin(\beta+\gamma)}$$
$$a_1 = \frac{\sin\gamma\sin(\alpha+\alpha)}{\sin\lambda\cos(\Theta+\alpha)\sin(\gamma+\beta)}$$
$$R = a_1 x$$

In Figure 73, an incremental element cuts the right-hand side of the model geometry with vertical height δx, and at angle ε to the vertical with incremental angle δε.

$$OCD = O_1FE + O_1J_1$$
$$= R(x) + \delta w$$
$$O_1FE = R(x+\delta x)$$
$$PTO_1 - PTO = \delta O$$
$$O_1J_1 = \delta O\cos(\varepsilon-\Theta)$$
$$\frac{PTO_1}{\sin\beta} = \frac{R(x+\delta x)}{\sin\alpha}$$

$$\frac{PTO}{\sin\beta} = \frac{R(x)}{\sin\alpha}$$
$$\therefore \delta O = \frac{R(x+\delta x)\sin\beta}{\sin\alpha} - \frac{R(x)\sin\beta}{\sin\alpha} = \frac{R(\delta x)\sin\beta}{\sin\alpha} = \frac{a_1\delta x\sin\beta}{\sin\alpha}$$

where Θ can be specified or found using *Ox* and *Oz*;

$$O_z = x\tan(\Theta+\alpha) - R\sin(\Theta+\alpha+\beta)$$
$$O_x = x - R\cos(\Theta+\alpha+\beta) \tag{A.55}$$

Equation A.55 is equivalent to equation 72 in the main text.

$$\therefore \Theta = \tan^{-1}\frac{x\tan(\Theta+\alpha) - R\sin(\Theta+\alpha+\beta)}{x - R\cos(\Theta+\alpha+\beta)}$$

since $R = a_1 x$, $\therefore \Theta = \tan^{-1}\dfrac{\tan(\Theta+\alpha) - a_1\sin(\Theta+\alpha+\beta)}{1 - a_1\cos(\Theta+\alpha+\beta)}$ (A.56)

Equation A.56 is equivalent to equation 73 in the main text.

$$OCD = O_1FE + O_1J_1$$
$$\therefore R(x) + \delta w = R(x+\delta x) + \delta O\cos(\varepsilon-\Theta)$$
$$a_1x + \delta w = a_1(x+\delta x) + \delta O\cos(\varepsilon-\Theta)$$
$$\delta w = a_1\delta x + \delta O\cos(\varepsilon-\Theta)$$
$$\frac{\delta O}{\delta x} = \frac{a_1\sin\beta}{\sin\alpha}$$
$$\therefore \delta w = \left(a_1 + \frac{\delta O}{\delta x}\cos(\varepsilon-\Theta)\right)\delta x \tag{A.57}$$

Equation A.57 is equivalent to equation 74 in the main text. From the main text equation 44 gives:

$$(R+\delta x)\sin\varepsilon = \delta O\sin\Theta + (R+\delta R)\sin(\varepsilon+\delta\psi) + soe \tag{A.58}$$

$$(R + a_1\delta x + \delta O\cos(\varepsilon-\Theta))\sin\varepsilon = \delta O\sin\Theta + (R+\delta R)(\sin\varepsilon + \delta\psi\cos\varepsilon) + soe$$

As δx and $\delta\varepsilon$ tend to zero,

$$(R + a_1\delta x + \delta O\cos(\varepsilon - \Theta))\sin\varepsilon = \delta O\sin\Theta + (R + \delta R)(\sin\varepsilon + \delta\psi\cos\varepsilon) + soe$$
$$R\delta\psi\cos\varepsilon = R\sin\varepsilon - a_1\delta x\sin\varepsilon + \delta O\cos(\varepsilon - \Theta)\sin\varepsilon - R\sin\varepsilon - \delta O\sin\Theta$$

$$\therefore \frac{\partial\psi}{\partial x} = \frac{a_2(\cos(\varepsilon - \Theta)\sin\varepsilon - \sin\Theta)}{a_1 x\cos\varepsilon} \qquad \text{(A.59)}$$

Equation A.59 is equivalent to equation 76 in the main text.

Therefore a force balance in vertical direction gives:

$$\begin{aligned}&-[\sigma_\varepsilon R_2\delta\psi 2\pi\bar{r}]_\varepsilon \cos{}^{\delta\psi}\!/_2 \sin\varepsilon + [\sigma_\varepsilon R_2\delta\psi 2\pi\bar{r}]_{\varepsilon+\delta\varepsilon}\cos\left(\delta\varepsilon + {}^{\delta\psi}\!/_2\right)\sin\varepsilon \\ &+ [\sigma_R R\delta\varepsilon 2\pi\bar{r}]_x \sin{}^{\delta\varepsilon}\!/_2 \cos\varepsilon - [\sigma_R]_{x+\delta x,\varepsilon+\delta\psi}(R + \delta w)\delta\varepsilon 2\pi\bar{r}\cos(\varepsilon + \delta\xi) \\ &- 2\pi\bar{r}R\delta\varepsilon\delta w\rho g = 0\end{aligned} \qquad \text{(A.60)}$$

First line of equation contains,

$$R_2\delta\psi = \delta w\cos{}^{\delta\psi}\!/_2$$

Hence,

$$-[\sigma_\varepsilon\delta w\bar{r}]_\varepsilon 2\pi\cos^2{}^{\delta\psi}\!/_2 \sin\varepsilon + [\sigma_\varepsilon\delta w\bar{r}]_{\varepsilon+\delta\varepsilon} 2\pi\cos{}^{\delta\psi}\!/_2 \cos\left(\delta\varepsilon + {}^{\delta\psi}\!/_2\right)\sin\varepsilon$$

Divide by $\delta x\delta\varepsilon$ and 2π, and take limits:

$$\frac{\partial}{\partial\varepsilon}\left[\sigma_\varepsilon\left(\frac{\partial w}{\partial x}\right)\bar{r}\sin\varepsilon\right]$$

The first two terms of second line of equation:

Derivation of Equations

$$\left[\sigma_R R\delta\varepsilon 2\pi\bar{r}\right]_x \sin{}^{\delta\varepsilon}\!/_{2}\cos\varepsilon-\left[\sigma_R\right]_{x+\delta x,\varepsilon+\delta\psi}(R+\delta w)\delta\varepsilon 2\pi\bar{r}\cos(\varepsilon+\delta\xi)$$

Divide by $\delta\varepsilon$ and 2π:

$$\left[\sigma_R R\bar{r}\cos\varepsilon\right]_x-\left([R]_{x+\delta x}+a_2\cos(\varepsilon-\theta)\delta x\right)\left\{\left[\bar{r}\sigma_R\right]_{x+\delta x,\varepsilon+\delta\psi}\cos(\varepsilon+\delta\xi)\right\}$$

$$\left[\sigma_R R\bar{r}\cos\varepsilon\right]_x-\left([R]_{x+\delta x}+a_2\cos(\varepsilon-\theta)\delta x\right)\left\{\left[\bar{r}\sigma_R\right]_{x+\delta x}+\frac{\partial}{\partial\varepsilon}(\bar{r}\sigma_R)\delta\psi\right\}\cos(\varepsilon+\delta\psi)$$

$$\left[\sigma_R R\bar{r}\cos\varepsilon\right]_x-\begin{pmatrix}[R]_{x+\delta x}\left[\bar{r}\sigma_R\right]_{x+\delta x}+\left[\bar{r}\sigma_R\right]_{x+\delta x}a_2\cos(\varepsilon-\theta)\delta x+\\ [R]_{x+\delta x}\dfrac{\partial}{\partial\varepsilon}(\bar{r}\sigma_R)\delta\psi+a_2\cos(\varepsilon-\theta)\delta x\dfrac{\partial}{\partial\varepsilon}(\bar{r}\sigma_R)\delta\psi\end{pmatrix}\begin{pmatrix}\cos\varepsilon\cos\delta\psi-\\ \sin\varepsilon\sin\delta\psi\end{pmatrix}$$

$$\left[\sigma_R R\bar{r}\cos\varepsilon\right]_x-\begin{pmatrix}[R]_{x+\delta x}\left[\bar{r}\sigma_R\right]_{x+\delta x}+\left[\bar{r}\sigma_R\right]_{x+\delta x}a_2\cos(\varepsilon-\theta)\delta x+\\ [R]_{x+\delta x}\dfrac{\partial}{\partial\varepsilon}(\bar{r}\sigma_R)\delta\psi+a_2\cos(\varepsilon-\theta)\delta x\dfrac{\partial}{\partial\varepsilon}(\bar{r}\sigma_R)\delta\psi\end{pmatrix}(\cos\varepsilon-\delta\psi\sin\varepsilon)$$

$$\left[\sigma_R R\bar{r}\cos\varepsilon\right]_x-[R]_{x+\delta x}\left[\bar{r}\sigma_R\right]_{x+\delta x}\cos\varepsilon-\left[\bar{r}\sigma_R\right]_{x+\delta x}a_2\cos(\varepsilon-\theta)\delta x\cos\varepsilon-$$

$$[R]_{x+\delta x}\frac{\partial}{\partial\varepsilon}(\bar{r}\sigma_R)\delta\psi\cos\varepsilon+[R]_{x+\delta x}\left[\bar{r}\sigma_R\right]_{x+\delta x}\delta\psi\sin\varepsilon+$$

$$\left[\bar{r}\sigma_R\right]_{x+\delta x}a_2\cos(\varepsilon-\theta)\delta x\delta\psi\sin\varepsilon+[R]_{x+\delta x}\frac{\partial}{\partial\varepsilon}(\bar{r}\sigma_R)\delta\psi\delta\psi\sin\varepsilon$$

$$\therefore\left[\sigma_R R\bar{r}\cos\varepsilon\right]_x-\left[\sigma_R R\bar{r}\sigma_R\cos\varepsilon\right]_{x+\delta x}-\left[\bar{r}\sigma_R\right]_{x+\delta x}a_2\cos(\varepsilon-\theta)\delta x\cos\varepsilon$$

$$-[R]_{x+\delta x}\frac{\partial}{\partial\varepsilon}(\bar{r}\sigma_R)\delta\psi\cos\varepsilon+[R]_{x+\delta x}\left[\bar{r}\sigma_R\right]_{x+\delta x}\delta\psi\sin\varepsilon$$

Take limits:

$$-\frac{\partial}{\partial x}\left[R\bar{r}\sigma_R\cos\varepsilon\right]-\cos\varepsilon\left(\bar{r}\sigma_R a_2\cos(\varepsilon-\Theta)+R\frac{\partial}{\partial\varepsilon}(\bar{r}\sigma_R)\frac{\partial\psi}{\partial x}\right)+R\bar{r}\sigma_R\sin\varepsilon\frac{\partial\psi}{\partial x}$$

Since,

$$\begin{aligned}R\frac{\partial}{\partial\varepsilon}(\bar{r}\sigma_R)\frac{\partial\psi}{\partial x}&=R\frac{\partial}{\partial\varepsilon}\left[(O_Z+R\sin\varepsilon)\sigma_R\right]\frac{\partial\psi}{\partial x}=R^2\frac{\partial}{\partial\varepsilon}\left[(\Omega+\sin\varepsilon)\sigma_R\right]\frac{\partial\psi}{\partial x}\\&=R^2\left(\sigma_R[1+\cos\varepsilon]+\sin\varepsilon\frac{\partial\sigma_R}{\partial\varepsilon}\right)\frac{\partial\psi}{\partial x}\\&=R^2\sigma_R(1+\cos\varepsilon)\frac{\partial\psi}{\partial x}+R^2\sin\varepsilon\frac{\partial\sigma_R}{\partial\varepsilon}\frac{\partial\psi}{\partial x}\end{aligned}$$

where $\Omega=\dfrac{\sin\beta\sin\Theta}{\sin\alpha}$ and $\bar{r}=O_Z+R\sin\varepsilon$

Hence,

$$-\frac{\partial}{\partial x}\left[R^2(\Omega+\sin\varepsilon)\sigma_R\cos\varepsilon\right]-\cos\varepsilon\begin{pmatrix}R(\Omega+\sin\varepsilon)\sigma_R a_2\cos(\varepsilon-\Theta)+\\ R^2\sigma_R(1+\cos\varepsilon)\frac{\partial\psi}{\partial x}+R^2\sin\varepsilon\frac{\partial\sigma_R}{\partial\varepsilon}\frac{\partial\psi}{\partial x}\end{pmatrix}+$$

$$R^2(\Omega+\sin\varepsilon)\sigma_R\sin\varepsilon\frac{\partial\psi}{\partial x}$$

Since,

$$\frac{\partial\psi}{\partial x}=\frac{a_2\sin(\varepsilon-\Theta)}{R}$$

Hence,

$$-\frac{\partial}{\partial x}\left[R^2(\Omega+\sin\varepsilon)\sigma_R\cos\varepsilon\right]-\cos\varepsilon\begin{pmatrix}R(\Omega+\sin\varepsilon)\sigma_R a_2\cos(\varepsilon-\Theta)+\\ R^2\sigma_R(1+\cos\varepsilon)\frac{a_2\sin(\varepsilon-\Theta)}{R}+\\ R^2\sin\varepsilon\frac{\partial\sigma_R}{\partial\varepsilon}\frac{a_2\sin(\varepsilon-\Theta)}{R}\end{pmatrix}+$$

$$R^2(\Omega+\sin\varepsilon)\sigma_R\sin\varepsilon\frac{a_2\sin(\varepsilon-\Theta)}{R}$$

$$-\frac{\partial}{\partial x}\left[R^2(\Omega+\sin\varepsilon)\sigma_R\cos\varepsilon\right]-\cos\varepsilon\begin{pmatrix}R(\Omega+\sin\varepsilon)\sigma_R a_2\cos(\varepsilon-\Theta)+\\ R\sigma_R(1+\cos\varepsilon)a_2\sin(\varepsilon-\Theta)+\\ Ra_2\sin(\varepsilon-\Theta)\sin\varepsilon\frac{\partial\sigma_R}{\partial\varepsilon}\end{pmatrix}+$$

$$R(\Omega+\sin\varepsilon)\sigma_R a_2\sin(\varepsilon-\Theta)\sin\varepsilon$$

Collecting terms:

$$\frac{\partial}{\partial x}\left[R^2(\Omega+\sin\varepsilon)\sigma_R\cos\varepsilon\right]=R\sigma_R a_2\sin(\varepsilon-\Theta)(\Omega\sin\varepsilon-\cos\varepsilon-\cos2\varepsilon)-$$

$$-\cos\varepsilon\left(R\sigma_R a_2(\Omega+\sin\varepsilon)\cos(\varepsilon-\Theta)-R^2\sin\varepsilon\frac{\partial\psi}{\partial x}\frac{\partial\sigma_R}{\partial\varepsilon}\right)$$

$$\frac{\partial}{\partial x}\left[R^2\sigma_R\cos\varepsilon\sin\varepsilon\right]=\frac{\partial}{\partial\varepsilon}\left[RF\sin^2\varepsilon\right]-\cos\varepsilon\sin\varepsilon\left(R\sigma_R a_2\cos(\varepsilon-\Theta)+R^2\frac{\partial\sigma_R}{\partial\varepsilon}\frac{\partial\psi}{\partial x}\right)$$
$$-Ra_2\sigma_R\sin(\varepsilon-\Theta)\cos 2\varepsilon-R^2\left(\frac{\partial w}{\partial x}\right)\rho g\sin\varepsilon$$

$$\frac{\partial}{\partial x}\left[R^2(\Omega+\sin\varepsilon)\sigma_R\cos\varepsilon\right]=\frac{\partial}{\partial\varepsilon}\left[F\sin\varepsilon(O_Z+R\sin\varepsilon)\right]+$$
$$R\sigma_R a_2\sin(\varepsilon-\Theta)(\Omega\sin\varepsilon-\cos\varepsilon-\cos 2\varepsilon)-R\left(\frac{\partial w}{\partial x}\right)\rho g(O_Z+R\sin\varepsilon) \quad \text{(A.61)}$$
$$-\cos\varepsilon\left(R\sigma_R a_2(\Omega+\sin\varepsilon)\cos(\varepsilon-\Theta)-R^2\sin\varepsilon\frac{\partial\psi}{\partial x}\frac{\partial\sigma_R}{\partial\varepsilon}\right)$$

Equation A.61 is equivalent to equation 77 in the main text.

Force balance in horizontal direction;

$$\left[\sigma_\varepsilon R_2\delta\psi\bar{r}\right]_\varepsilon\sin{}^{\delta\psi}\!/_2\cos\varepsilon-\left[\sigma_\varepsilon R_2\delta\psi\bar{r}\right]_{\varepsilon+\delta\varepsilon}\sin\left(\delta\varepsilon+{}^{\delta\psi}\!/_2\right)\cos\varepsilon$$
$$+\left[\sigma_R R\delta\varepsilon\bar{r}\right]_x\cos{}^{\delta\varepsilon}\!/_2\sin\varepsilon-\left[\sigma_R\right]_{x+\delta x,\varepsilon+\delta\psi}(R+\delta w)\delta\varepsilon\bar{r}\sin(\varepsilon+\delta\xi)+R\delta\varepsilon\delta w\sigma_\theta=0$$

(A.62)

First line of equation contains

$$R_2\delta\psi=\delta w\cos{}^{\delta\psi}\!/_2$$

Hence

$$\left[\sigma_\varepsilon\delta w\bar{r}\right]_\varepsilon\cos{}^{\delta\psi}\!/_2\sin{}^{\delta\psi}\!/_2\cos\varepsilon-\left[\sigma_\varepsilon\delta w\bar{r}\right]_{\varepsilon+\delta\varepsilon}\cos{}^{\delta\psi}\!/_2\sin\left(\delta\varepsilon+{}^{\delta\psi}\!/_2\right)\cos\varepsilon$$

Divide by $\delta x\delta\varepsilon$, and take limits:

$$\frac{\left[\sigma_\varepsilon \frac{\partial w}{\partial x}\bar{r}\right]_\varepsilon \sin \delta\psi/2 \cos\varepsilon - \left[\sigma_\varepsilon \frac{\partial w}{\partial x}\bar{r}\right]_{\varepsilon+\delta\varepsilon} \sin\left(\delta\varepsilon + \delta\psi/2\right)\cos\varepsilon}{\delta\varepsilon}$$

$$\frac{\left[\sigma_\varepsilon \frac{\partial w}{\partial x}\bar{r}\right]_\varepsilon \sin \delta\psi/2 \cos\varepsilon - \left[\sigma_\varepsilon \frac{\partial w}{\partial x}\bar{r}\right]_{\varepsilon+\delta\varepsilon} \left(\sin\delta\varepsilon \cos \delta\psi/2 + \cos\delta\varepsilon \sin \delta\psi/2\right)\cos\varepsilon}{\delta\varepsilon}$$

Since $\frac{\partial}{\partial\varepsilon}\left[\sigma_\varepsilon \frac{\partial w}{\partial x}\bar{r}\right]\sin \delta\psi/2 \Rightarrow 0$ and $\frac{\sin\delta\varepsilon}{\delta\varepsilon} \Rightarrow 1$

$$\frac{\left[\sigma_\varepsilon \frac{\partial w}{\partial x}\bar{r}\right]_\varepsilon \sin \delta\psi/2 \cos\varepsilon - \left[\sigma_\varepsilon \frac{\partial w}{\partial x}\bar{r}\right]_{\varepsilon+\delta\varepsilon} \sin\delta\varepsilon \cos \delta\psi/2 \cos\varepsilon - \left[\sigma_\varepsilon \frac{\partial w}{\partial x}\bar{r}\right]_{\varepsilon+\delta\varepsilon} \cos\delta\varepsilon \sin \delta\psi/2 \cos\varepsilon}{\delta\varepsilon}$$

$$\left\{\frac{\left[\sigma_\varepsilon \frac{\partial w}{\partial x}\bar{r}\right]_\varepsilon - \left[\sigma_\varepsilon \frac{\partial w}{\partial x}\bar{r}\right]_{\varepsilon+\delta\varepsilon}}{\delta\varepsilon}\right\}\sin \delta\psi/2 \cos\varepsilon - \left[\sigma_\varepsilon \frac{\partial w}{\partial x}\bar{r}\right]_{\varepsilon+\delta\varepsilon} \frac{\sin\delta\varepsilon}{\delta\varepsilon}\cos\varepsilon$$

$$\therefore -\frac{\partial}{\partial\varepsilon}\left[\sigma_\varepsilon\left(\frac{\partial w}{\partial x}\right)\bar{r}\cos\varepsilon\right] \text{ or } -\frac{\partial}{\partial\varepsilon}\left[F\bar{r}\cos\varepsilon\right]$$

The first two terms of second line of equation A.62:

$$\left[\sigma_R R\delta\varepsilon\bar{r}\right]_x \cos \delta\varepsilon/2 \sin\varepsilon - \left[\sigma_R\right]_{x+\delta x,\varepsilon+\delta\psi}\left(R+\delta w\right)\delta\varepsilon\bar{r}\sin\left(\varepsilon+\delta\xi\right)$$

Divide by $\delta\varepsilon$:

$$\left[\sigma_R R\bar{r}\sin\varepsilon\right]_x - \left(\left[R\right]_{x+\delta x} + a_2\cos\left(\varepsilon-\Theta\right)\delta x\right)\left\{\left[\bar{r}\sigma_R\right]_{x+\delta x,\varepsilon+\delta\psi}\sin\left(\varepsilon+\delta\xi\right)\right\}$$

$$\left[\sigma_R R\bar{r}\sin\varepsilon\right]_x - \left(\left[R\right]_{x+\delta x} + a_2\cos\left(\varepsilon-\Theta\right)\delta x\right)\left\{\left[\bar{r}\sigma_R\right]_{x+\delta x} + \frac{\partial}{\partial\varepsilon}\left(\bar{r}\sigma_R\right)\delta\psi\right\}\sin\left(\varepsilon+\delta\psi\right)$$

$$\left[\sigma_R R\bar{r}\sin\varepsilon\right]_x - \begin{pmatrix} \left[R\right]_{x+\delta x}\left[\bar{r}\sigma_R\right]_{x+\delta x} + \left[R\right]_{x+\delta x}\frac{\partial}{\partial\varepsilon}\left(\bar{r}\sigma_R\right)\delta\psi + \\ \left[\bar{r}\sigma_R\right]_{x+\delta x} a_2\cos\left(\varepsilon-\Theta\right)\delta x + \\ a_2\cos\left(\varepsilon-\Theta\right)\delta x\frac{\partial}{\partial\varepsilon}\left(\bar{r}\sigma_R\right)\delta\psi \end{pmatrix}\left(\sin\varepsilon\cos\delta\psi + \cos\varepsilon\sin\delta\psi\right)$$

Derivation of Equations

$$[\sigma_R R\bar{r}\sin\varepsilon]_x - \begin{pmatrix} [R]_{x+\delta x}[\bar{r}\sigma_R]_{x+\delta x} + [R]_{x+\delta x}\dfrac{\partial}{\partial\varepsilon}(\bar{r}\sigma_R)\delta\psi + \\ [\bar{r}\sigma_R]_{x+\delta x}a_2\cos(\varepsilon-\Theta)\delta x \end{pmatrix}(\sin\varepsilon + \delta\psi\cos\varepsilon)$$

$$[\sigma_R R\bar{r}\sin\varepsilon]_x - [R\bar{r}\sigma_R]_{x+\delta x}\sin\varepsilon - [R]_{x+\delta x}\frac{\partial}{\partial\varepsilon}(\bar{r}\sigma_R)\delta\psi\sin\varepsilon - [\bar{r}\sigma_R]_{x+\delta x}a_2\cos(\varepsilon-\Theta)\delta x\sin\varepsilon -$$

$$[R]_{x+\delta x}[\bar{r}\sigma_R]_{x+\delta x}\delta\psi\cos\varepsilon - [R]_{x+\delta x}\frac{\partial}{\partial\varepsilon}(\bar{r}\sigma_R)\delta\psi\delta\psi\cos\varepsilon - [\bar{r}\sigma_R]_{x+\delta x}a_2\cos(\varepsilon-\Theta)\delta x\delta\psi\cos\varepsilon$$

$$\therefore [\sigma_R R\bar{r}\sin\varepsilon]_x - [\sigma_R R\bar{r}\sin\varepsilon]_{x+\delta x} - [R]_{x+\delta x}\frac{\partial}{\partial\varepsilon}(\bar{r}\sigma_R)\delta\psi\sin\varepsilon - [\bar{r}\sigma_R]_{x+\delta x}a_2\cos(\varepsilon-\Theta)\delta x\sin\varepsilon -$$

$$[\sigma_R R\bar{r}]_{x+\delta x}\delta\psi\cos\varepsilon$$

Divide by δx, and take limits:

$$-\frac{\partial}{\partial x}[\sigma_R R\bar{r}\sin\varepsilon] - R\frac{\partial}{\partial\varepsilon}(\bar{r}\sigma_R)\frac{\partial\psi}{\partial x}\sin\varepsilon - \bar{r}\sigma_R a_2\cos(\varepsilon-\Theta)\sin\varepsilon - \sigma_R R\bar{r}\frac{\partial\psi}{\partial x}\cos\varepsilon$$

Since $\dfrac{\partial\psi}{\partial x} = \dfrac{a_2\sin(\varepsilon-\Theta)}{R}$, and

$$R\frac{\partial}{\partial\varepsilon}(\bar{r}\sigma_R)\frac{\partial\psi}{\partial x}\sin\varepsilon = R\frac{\partial}{\partial\varepsilon}[(O_Z + R\sin\varepsilon)\sigma_R]\frac{\partial\psi}{\partial x}\sin\varepsilon =$$

$$R^2\frac{\partial}{\partial\varepsilon}[(\Omega+\sin\varepsilon)\sigma_R]\frac{\partial\psi}{\partial x}\sin\varepsilon$$

$$= R^2\left(\sigma_R[1+\cos\varepsilon] + \sin\varepsilon\frac{\partial\sigma_R}{\partial\varepsilon}\right)\frac{\partial\psi}{\partial x}\sin\varepsilon$$

$$= R^2\sigma_R(\sin\varepsilon + \cos\varepsilon\sin\varepsilon)\frac{\partial\psi}{\partial x} + R^2\sin^2\varepsilon\frac{\partial\sigma_R}{\partial\varepsilon}\frac{\partial\psi}{\partial x}$$

where $\Omega = \dfrac{\sin\beta\sin\Theta}{\sin\alpha}$ and $\bar{r} = O_Z + R\sin\varepsilon$

Hence:

$$-\frac{\partial}{\partial x}\left[\sigma_R R^2(\Omega+\sin\varepsilon)\sin\varepsilon\right] - R^2\sigma_R(\sin\varepsilon+\cos\varepsilon\sin\varepsilon)\frac{\partial\psi}{\partial x} - R^2\sin^2\varepsilon\frac{\partial\sigma_R}{\partial\varepsilon}\frac{\partial\psi}{\partial x} -$$

$$(\Omega+\sin\varepsilon)R\sigma_R a_2\cos(\varepsilon-\Theta)\sin\varepsilon - \sigma_R R^2(\Omega+\sin\varepsilon)\frac{\partial\psi}{\partial x}\cos\varepsilon$$

$$-\frac{\partial}{\partial x}\left[\sigma_R R^2(\Omega+\sin\varepsilon)\sin\varepsilon\right]-R\sigma_R a_2\sin(\varepsilon-\Theta)(\sin\varepsilon+2\cos\varepsilon\sin\varepsilon+\Omega\cos\varepsilon)-$$
$$R^2\sin^2\varepsilon\frac{\partial\sigma_R}{\partial\varepsilon}\frac{\partial\psi}{\partial x}-(\Omega+\sin\varepsilon)R\sigma_R a_2\cos(\varepsilon-\Theta)\sin\varepsilon$$

Collecting terms:

$$\frac{\partial}{\partial x}\left[\sigma_R R^2(\Omega+\sin\varepsilon)\sin\varepsilon\right]=-\frac{\partial}{\partial\varepsilon}\left[RF(\Omega+\sin\varepsilon)\cos\varepsilon\right]-$$
$$R\sigma_R a_2\sin(\varepsilon-\Theta)(\sin\varepsilon+2\cos\varepsilon\sin\varepsilon+\Omega\cos\varepsilon)-R^2\sin^2\varepsilon\frac{\partial\sigma_R}{\partial\varepsilon}\frac{\partial\psi}{\partial x}- \qquad \text{(A.63)}$$
$$(\Omega+\sin\varepsilon)R\sigma_R a_2\cos(\varepsilon-\Theta)\sin\varepsilon+R\left(\frac{\partial w}{\partial x}\right)\sigma_\theta$$

Equation A.63 is equivalent to equation 78 in the main text.

Since $R=a_1x$, and $F=\sigma_\varepsilon\left(\frac{\partial w}{\partial x}\right)$

$$\frac{\partial}{\partial\varepsilon}\left[RF(\Omega+\sin\varepsilon)\cos\varepsilon\right]=R\frac{\partial}{\partial\varepsilon}\left[\Omega F\cos\varepsilon+F\cos\varepsilon\sin\varepsilon\right]=R\frac{\partial}{\partial\varepsilon}\left[\Omega F\cos\varepsilon+F\frac{\sin 2\varepsilon}{2}\right]$$
$$=R\left(\Omega\cos\varepsilon\frac{\partial F}{\partial\varepsilon}-\Omega F\sin\varepsilon+F\frac{\sin 2\varepsilon}{2}\frac{\partial F}{\partial\varepsilon}+F\cos 2\varepsilon\right)$$
$$=R\frac{\partial F}{\partial\varepsilon}\left(\Omega\cos\varepsilon+F\frac{\sin 2\varepsilon}{2}\right)+RF(\cos 2\varepsilon-\Omega\sin\varepsilon)$$

(A.64)

Hence,

$$\frac{\partial}{\partial x}\left[R^2(\Omega+\sin\varepsilon)\sigma_R\cos\varepsilon\right]=R\frac{\partial F}{\partial\varepsilon}\left(\Omega\cos\varepsilon+F\frac{\sin 2\varepsilon}{2}\right)+RF(F\cos 2\varepsilon-\Omega F\sin\varepsilon)+$$
$$R\sigma_R a_2\sin(\varepsilon-\Theta)(\Omega\sin\varepsilon-\cos\varepsilon-\cos 2\varepsilon)-R^2\left(\frac{\partial w}{\partial x}\right)\rho g(\Omega+\sin\varepsilon)$$
$$-\cos\varepsilon\left(R\sigma_R a_2(\Omega+\sin\varepsilon)\cos(\varepsilon-\Theta)-R^2\sin\varepsilon\frac{\partial\psi}{\partial x}\frac{\partial\sigma_R}{\partial\varepsilon}\right)$$

Derivation of Equations

$$\frac{\partial}{\partial x}\left[R^2\sigma_R\right]=\frac{R}{(\Omega+\sin\varepsilon)}\frac{\partial F}{\partial\varepsilon}\left(\Omega+F\frac{\sin 2\varepsilon}{2\cos\varepsilon}\right)+\frac{RF}{(\Omega+\sin\varepsilon)\cos\varepsilon}\left(\frac{\cos 2\varepsilon}{\cos\varepsilon}-\Omega\frac{\sin\varepsilon}{\cos\varepsilon}\right)+$$
$$\frac{R}{(\Omega+\sin\varepsilon)\cos\varepsilon}\sigma_R a_2\sin(\varepsilon-\Theta)(\Omega\sin\varepsilon-\cos\varepsilon-\cos 2\varepsilon)-\frac{R^2}{\cos\varepsilon}\left(\frac{\partial w}{\partial x}\right)\rho g$$
$$-R\sigma_R a_2\cos(\varepsilon-\Theta)-\frac{R^2\sin\varepsilon}{\Omega+\sin\varepsilon}\frac{\partial\psi}{\partial x}\frac{\partial\sigma_R}{\partial\varepsilon}$$

(A.65)

Using A.63, since,

$$\frac{\partial}{\partial\varepsilon}\left[RF(\Omega+\sin\varepsilon)\cos\varepsilon\right]=R\frac{\partial}{\partial\varepsilon}\left[\Omega F\cos\varepsilon+F\frac{\sin 2\varepsilon}{2}\right]$$
$$=R\left(\Omega\cos\varepsilon\frac{\partial F}{\partial\varepsilon}-\Omega F\sin\varepsilon+\frac{\sin 2\varepsilon}{2}\frac{\partial F}{\partial\varepsilon}+F\cos 2\varepsilon\right)$$
$$=R\frac{\partial F}{\partial\varepsilon}\left(\Omega\cos\varepsilon+\frac{\sin 2\varepsilon}{2}\right)+RF(\cos 2\varepsilon-\Omega\sin\varepsilon)$$

Hence,

$$\frac{\partial}{\partial x}\left[\sigma_R R^2(\Omega+\sin\varepsilon)\sin\varepsilon\right]=-R\frac{\partial F}{\partial\varepsilon}\left(\Omega\cos\varepsilon+\frac{\sin 2\varepsilon}{2}\right)-RF(\cos 2\varepsilon-\Omega\sin\varepsilon)-$$
$$R\sigma_R a_2\sin(\varepsilon-\Theta)(\sin\varepsilon+2\cos\varepsilon\sin\varepsilon+\Omega\cos\varepsilon)-R^2\sin^2\varepsilon\frac{\partial\sigma_R}{\partial\varepsilon}\frac{\partial\psi}{\partial x}-$$
$$(\Omega+\sin\varepsilon)R\sigma_R a_2\cos(\varepsilon-\Theta)\sin\varepsilon+R\left(\frac{\partial w}{\partial x}\right)\sigma_\theta$$

$$\frac{\partial}{\partial x}\left[\sigma_R R^2\right]=-\frac{R}{\Omega+\sin\varepsilon}\frac{\partial F}{\partial\varepsilon}\left(\Omega\frac{\cos\varepsilon}{\sin\varepsilon}+\frac{\sin 2\varepsilon}{2\sin\varepsilon}\right)-\frac{RF}{\Omega+\sin\varepsilon}\left(\frac{\cos 2\varepsilon}{\sin\varepsilon}-\Omega\right)-$$
$$\frac{R}{(\Omega+\sin\varepsilon)\sin\varepsilon}\sigma_R a_2\sin(\varepsilon-\Theta)(\sin\varepsilon+2\cos\varepsilon\sin\varepsilon+\Omega\cos\varepsilon)- \qquad \text{(A.66)}$$
$$\frac{R^2\sin\varepsilon}{\Omega+\sin\varepsilon}\frac{\partial\sigma_R}{\partial\varepsilon}\frac{\partial\psi}{\partial x}-R\sigma_R a_2\cos(\varepsilon-\Theta)+\frac{R}{(\Omega+\sin\varepsilon)\sin\varepsilon}\left(\frac{\partial w}{\partial x}\right)\sigma_\theta$$

Substitute A.64 and A.65:

$$\frac{R}{(\Omega+\sin\varepsilon)}\frac{\partial F}{\partial\varepsilon}\left(\Omega+F\frac{\sin 2\varepsilon}{2\cos\varepsilon}\right)+\frac{RF}{(\Omega+\sin\varepsilon)\cos\varepsilon}\left(\frac{\cos 2\varepsilon}{\cos\varepsilon}-\Omega\frac{\sin\varepsilon}{\cos\varepsilon}\right)+$$
$$\frac{R}{(\Omega+\sin\varepsilon)\cos\varepsilon}\sigma_R a_2\sin(\varepsilon-\Theta)(\Omega\sin\varepsilon-\cos\varepsilon-\cos 2\varepsilon)-\frac{R^2}{\cos\varepsilon}\left(\frac{\partial w}{\partial x}\right)\rho g$$
$$-R\sigma_R a_2\cos(\varepsilon-\Theta)-\frac{R^2\sin\varepsilon}{\Omega+\sin\varepsilon}\frac{\partial\psi}{\partial x}\frac{\partial\sigma_R}{\partial\varepsilon}=-\frac{R}{\Omega+\sin\varepsilon}\frac{\partial F}{\partial\varepsilon}\left(\Omega\frac{\cos\varepsilon}{\sin\varepsilon}+\frac{\sin 2\varepsilon}{2\sin\varepsilon}\right)$$
$$-\frac{RF}{\Omega+\sin\varepsilon}\left(\frac{\cos 2\varepsilon}{\sin\varepsilon}-\Omega\right)-\frac{R}{(\Omega+\sin\varepsilon)\sin\varepsilon}\sigma_R a_2\sin(\varepsilon-\Theta)\begin{pmatrix}\sin\varepsilon+2\cos\varepsilon\sin\varepsilon+\\ \Omega\cos\varepsilon\end{pmatrix}-$$
$$\frac{R^2\sin\varepsilon}{\Omega+\sin\varepsilon}\frac{\partial\sigma_R}{\partial\varepsilon}\frac{\partial\psi}{\partial x}-R\sigma_R a_2\cos(\varepsilon-\Theta)+\frac{R}{(\Omega+\sin\varepsilon)\sin\varepsilon}\left(\frac{\partial w}{\partial x}\right)\sigma_\theta$$

LH:

$$\frac{R}{(\Omega+\sin\varepsilon)}\frac{\partial F}{\partial\varepsilon}\left(\Omega+F\frac{\sin 2\varepsilon}{2\cos\varepsilon}\right)+\frac{R}{\Omega+\sin\varepsilon}\frac{\partial F}{\partial\varepsilon}\left(\Omega\frac{\cos\varepsilon}{\sin\varepsilon}+\frac{\sin 2\varepsilon}{2\sin\varepsilon}\right)$$

$$\frac{RF}{(\Omega+\sin\varepsilon)\cos\varepsilon}\left(\frac{\cos 2\varepsilon}{\cos\varepsilon}-\Omega\frac{\sin\varepsilon}{\cos\varepsilon}\right)+\frac{RF}{\Omega+\sin\varepsilon}\left(\frac{\cos 2\varepsilon}{\sin\varepsilon}-\Omega\right)$$
$$\frac{R}{(\Omega+\sin\varepsilon)\cos\varepsilon}\sigma_R a_2\sin(\varepsilon-\Theta)(\Omega\sin\varepsilon-\cos\varepsilon-\cos 2\varepsilon)+$$
$$\frac{R}{(\Omega+\sin\varepsilon)\sin\varepsilon}\sigma_R a_2\sin(\varepsilon-\Theta)(\sin\varepsilon+2\cos\varepsilon\sin\varepsilon+\Omega\cos\varepsilon)$$
$$-R\sigma_R a_2\cos(\varepsilon-\Theta)+R\sigma_R a_2\cos(\varepsilon-\Theta)$$
$$-\frac{R^2\sin\varepsilon}{\Omega+\sin\varepsilon}\frac{\partial\psi}{\partial x}\frac{\partial\sigma_R}{\partial\varepsilon}+\frac{R^2\sin\varepsilon}{\Omega+\sin\varepsilon}\frac{\partial\sigma_R}{\partial\varepsilon}\frac{\partial\psi}{\partial x}$$

RH:

$$\frac{R^2}{\cos\varepsilon}\left(\frac{\partial w}{\partial x}\right)\rho g$$

$$\frac{R}{(\Omega+\sin\varepsilon)\sin\varepsilon}\left(\frac{\partial w}{\partial x}\right)\sigma_\theta$$

Derivation of Equations

LH:

$$\frac{R}{(\Omega+\sin\varepsilon)}\frac{\partial F}{\partial\varepsilon}\left(\Omega+F\frac{\sin 2\varepsilon}{2\cos\varepsilon}\right)+\frac{R}{\Omega+\sin\varepsilon}\frac{\partial F}{\partial\varepsilon}\left(\Omega\frac{\cos\varepsilon}{\sin\varepsilon}+\frac{\sin 2\varepsilon}{2\sin\varepsilon}\right)$$

$$\frac{R}{(\Omega+\sin\varepsilon)}\frac{\partial F}{\partial\varepsilon}\left(\Omega+F\frac{\sin 2\varepsilon}{2\cos\varepsilon}+\Omega\frac{\cos\varepsilon}{\sin\varepsilon}+\frac{\sin 2\varepsilon}{2\sin\varepsilon}\right)$$

$$\frac{RF}{(\Omega+\sin\varepsilon)\cos\varepsilon}\left(\frac{\cos 2\varepsilon}{\cos\varepsilon}-\Omega\frac{\sin\varepsilon}{\cos\varepsilon}\right)+\frac{RF}{\Omega+\sin\varepsilon}\left(\frac{\cos 2\varepsilon}{\sin\varepsilon}-\Omega\right)$$

$$\frac{RF}{(\Omega+\sin\varepsilon)}\left(\frac{\cos 2\varepsilon}{\cos^2\varepsilon}-\Omega\frac{\sin\varepsilon}{\cos^2\varepsilon}+\frac{\cos 2\varepsilon}{\sin\varepsilon}-\Omega\right)$$

$$\frac{R}{(\Omega+\sin\varepsilon)\cos\varepsilon}\sigma_R a_2\sin(\varepsilon-\Theta)(\Omega\sin\varepsilon-\cos\varepsilon-\cos 2\varepsilon)+$$

$$\frac{R}{(\Omega+\sin\varepsilon)\sin\varepsilon}\sigma_R a_2\sin(\varepsilon-\Theta)(\sin\varepsilon+2\cos\varepsilon\sin\varepsilon+\Omega\cos\varepsilon)$$

$$\frac{R}{(\Omega+\sin\varepsilon)}\sigma_R a_2\sin(\varepsilon-\Theta)\left(\Omega\frac{\sin\varepsilon}{\cos\varepsilon}-1-\frac{\cos 2\varepsilon}{\cos\varepsilon}+1+2\cos\varepsilon+\Omega\frac{\cos\varepsilon}{\sin\varepsilon}\right)$$

Hence:

$$\frac{R}{(\Omega+\sin\varepsilon)}\frac{\partial F}{\partial\varepsilon}\left(\Omega+F\frac{\sin 2\varepsilon}{2\cos\varepsilon}+\Omega\frac{\cos\varepsilon}{\sin\varepsilon}+\frac{\sin 2\varepsilon}{2\sin\varepsilon}\right)+\frac{RF}{(\Omega+\sin\varepsilon)}\left(\begin{array}{l}\frac{\cos 2\varepsilon}{\cos^2\varepsilon}-\\ \Omega\frac{\sin\varepsilon}{\cos^2\varepsilon}+\frac{\cos 2\varepsilon}{\sin\varepsilon}-\Omega\end{array}\right)+$$

$$\frac{R}{(\Omega+\sin\varepsilon)}\sigma_R a_2\sin(\varepsilon-\Theta)\left(\Omega\frac{\sin\varepsilon}{\cos\varepsilon}-1-\frac{\cos 2\varepsilon}{\cos\varepsilon}+1+2\cos\varepsilon+\Omega\frac{\cos\varepsilon}{\sin\varepsilon}\right)=$$

$$\frac{R^2}{\cos\varepsilon}\left(\frac{\partial w}{\partial x}\right)\rho g+\frac{R}{(\Omega+\sin\varepsilon)\sin\varepsilon}\left(\frac{\partial w}{\partial x}\right)\sigma_\theta$$

$$\frac{\partial F}{\partial\varepsilon}\left(\Omega+F\frac{\sin 2\varepsilon}{2\cos\varepsilon}+\Omega\frac{\cos\varepsilon}{\sin\varepsilon}+\frac{\sin 2\varepsilon}{2\sin\varepsilon}\right)+F\left(\frac{\cos 2\varepsilon}{\cos^2\varepsilon}-\Omega\frac{\sin\varepsilon}{\cos^2\varepsilon}+\frac{\cos 2\varepsilon}{\sin\varepsilon}-\Omega\right)+$$

$$\sigma_R a_2\sin(\varepsilon-\Theta)\left(\Omega\frac{\sin\varepsilon}{\cos\varepsilon}-\frac{\cos 2\varepsilon}{\cos\varepsilon}+2\cos\varepsilon+\Omega\frac{\cos\varepsilon}{\sin\varepsilon}\right)=$$

$$\frac{R(\Omega+\sin\varepsilon)}{\cos\varepsilon}\left(\frac{\partial w}{\partial x}\right)\rho g+\frac{1}{\sin\varepsilon}\left(\frac{\partial w}{\partial x}\right)\sigma_\theta$$

$$\therefore \frac{\partial F}{\partial \varepsilon} = \frac{\left[\begin{array}{l} -F\left(\frac{\cos 2\varepsilon}{\cos^2 \varepsilon} - \Omega \frac{\sin \varepsilon}{\cos^2 \varepsilon} + \frac{\cos 2\varepsilon}{\sin \varepsilon} - \Omega\right) - \\ \sigma_R a_2 \sin(\varepsilon - \Theta)\left(\Omega \frac{\sin \varepsilon}{\cos \varepsilon} - \frac{\cos 2\varepsilon}{\cos \varepsilon} + 2\cos \varepsilon + \Omega \frac{\cos \varepsilon}{\sin \varepsilon}\right) + \\ \frac{R(\Omega + \sin \varepsilon)}{\cos \varepsilon}\left(\frac{\partial w}{\partial x}\right)\rho g + \frac{1}{\sin \varepsilon}\left(\frac{\partial w}{\partial x}\right)\sigma_\theta \end{array}\right]}{\left(\begin{array}{l} \Omega + F\frac{\sin 2\varepsilon}{2\cos \varepsilon} + \Omega \frac{\cos \varepsilon}{\sin \varepsilon} + \\ \frac{\sin 2\varepsilon}{2\sin \varepsilon} \end{array}\right)} \tag{A.67}$$

Equation A.67 is equivalent to equation 81 in the main text. Substitute A.67 into A.66:

$$\begin{aligned} \frac{\partial}{\partial x}\left[\sigma_R R^2\right] = & -G\left(\Omega \frac{\cos \varepsilon}{\sin \varepsilon} + \frac{\sin 2\varepsilon}{2\sin \varepsilon}\right) - \frac{RF}{\Omega + \sin \varepsilon}\left(\frac{\cos 2\varepsilon}{\sin \varepsilon} - \Omega\right) - \\ & \frac{R}{(\Omega + \sin \varepsilon)\sin \varepsilon}\sigma_R a_2 \sin(\varepsilon - \Theta)(\sin \varepsilon + 2\cos \varepsilon \sin \varepsilon + \Omega \cos \varepsilon) - \\ & \frac{R^2 \sin \varepsilon}{\Omega + \sin \varepsilon}\frac{\partial \sigma_R}{\partial \varepsilon}\frac{\partial \psi}{\partial x} - R\sigma_R a_2 \cos(\varepsilon - \Theta) + \frac{R}{(\Omega + \sin \varepsilon)\sin \varepsilon}\left(\frac{\partial w}{\partial x}\right)\sigma_\theta \end{aligned} \tag{A.68}$$

Equation A.68 is equivalent to equation 82 in the main text.

Where $$G = R\frac{\left[\begin{array}{l} -F\left(\frac{\cos 2\varepsilon}{\cos^2 \varepsilon} - \Omega \frac{\sin \varepsilon}{\cos^2 \varepsilon} + \frac{\cos 2\varepsilon}{\sin \varepsilon} - \Omega\right) - \\ \sigma_R a_2 \sin(\varepsilon - \Theta)\left(\Omega \frac{\sin \varepsilon}{\cos \varepsilon} - \frac{\cos 2\varepsilon}{\cos \varepsilon} + 2\cos \varepsilon + \Omega \frac{\cos \varepsilon}{\sin \varepsilon}\right) + \\ \frac{R(\Omega + \sin \varepsilon)}{\cos \varepsilon}\left(\frac{\partial w}{\partial x}\right)\rho g + \frac{1}{\sin \varepsilon}\left(\frac{\partial w}{\partial x}\right)\sigma_\theta \end{array}\right]}{\left(\Omega + F\frac{\sin 2\varepsilon}{2\cos \varepsilon} + \Omega \frac{\cos \varepsilon}{\sin \varepsilon} + \frac{\sin 2\varepsilon}{2\sin \varepsilon}\right)(\Omega + \sin \varepsilon)} \tag{A.69}$$

Equation A.69 is equivalent to equation 83 in the main text.

9.10 Force balance equations in R- and ε -directions for axially symmetric three-dimensional cone hopper with conical rat hole case

Figure 75, Chapter 6.1.2, shows the principal stress arc geometry. The static material between hopper wall and rat hole surface forms half angle α. A circular arc cuts the hopper right-hand side at a distance x above the apex with radius *R*, derived as follows.

Since $\dfrac{y}{\sin\alpha} = \dfrac{r}{\sin\gamma}$ and $\dfrac{y}{\sin(\alpha+\beta_2)} = \dfrac{R}{\sin\gamma}$,

where $\gamma = 180 - \dfrac{\pi}{2} - \dfrac{\alpha+\beta_2}{2}$

$$\therefore R = y\frac{\sin\gamma}{\sin(\alpha+\beta_2)}$$
$$= \frac{r\sin\alpha\sin\gamma}{\sin(\alpha+\beta_2)\sin\gamma}$$

where $r = \dfrac{x}{\cos(\Theta+\alpha)}$

$$\therefore R = \frac{x\sin\alpha}{\cos(\Theta+\alpha)\sin(\alpha+\beta_2)} \qquad \text{(A.70)}$$

Let $\lambda = \alpha + \beta_2$

$$\therefore R = x\frac{\sin\alpha}{\cos(\Theta+\alpha)\sin\lambda}$$
$$a_1 = \frac{\sin\alpha}{\sin\lambda\cos(\Theta+\alpha)}$$
$$R = a_1 x$$

In Figure 75 an incremental element cuts the right-hand side of the model geometry with vertical height δx, and at angle ε to the vertical with incremental angle δε.

$$OCD = O_1FE + O_1J_1$$
$$= R(x) + \delta w$$

$$O_1FE = R(x + \delta x)$$
$$PTO_1 - PTO = \delta O$$
$$O_1J_1 = \delta O \cos(\varepsilon - \Theta)$$
$$\frac{PTO_1}{\sin\beta} = \frac{R(x + \delta x)}{\sin\alpha}$$

$$\frac{PTO}{\sin\beta} = \frac{R(x)}{\sin\alpha}$$
$$\therefore \delta O = \frac{R(x + \delta x)\sin\beta_2}{\sin\alpha} - \frac{R(x)\sin\beta_2}{\sin\alpha} = \frac{R(\delta x)\sin\beta_2}{\sin\alpha} = \frac{a_1\delta x\sin\beta_2}{\sin\alpha}$$

where Θ can be specified or found using *Ox* and *Oz*;

$$O_z = x\tan(\Theta + \alpha) - R\sin(\Theta + \alpha + \beta_2)$$
$$O_x = x - R\cos(\Theta + \alpha + \beta_2)$$
$$\therefore \Theta = \tan^{-1}\frac{x\tan(\Theta + \alpha) - R\sin(\Theta + \alpha + \beta_2)}{x - R\cos(\Theta + \alpha + \beta_2)}$$

since $R = a_1 x$, $\therefore \Theta = \tan^{-1}\dfrac{\tan(\Theta + \alpha) - a_1\sin(\Theta + \alpha + \beta_2)}{1 - a_1\cos(\Theta + \alpha + \beta_2)}$

$$OCD = O_1FE + O_1J_1$$
$$\therefore R(x) + \delta w = R(x + \delta x) + \delta O\cos(\varepsilon - \Theta)$$
$$a_1x + \delta w = a_1(x + \delta x) + \delta O\cos(\varepsilon - \Theta)$$
$$\delta w = a_1\delta x + \delta O\cos(\varepsilon - \Theta)$$
$$\frac{\delta O}{\delta x} = \frac{a_1\sin\beta}{\sin\alpha}$$
$$\therefore \delta w = \left(a_1 + \frac{\delta O}{\delta x}\cos(\varepsilon - \Theta)\right)\delta x \qquad \text{(A.71)}$$

Equation A.71 is equivalent to equation 80 in the main text.

Chapter 10.0 - Appendix Three

Spreadsheet-based Numerical Solutions

Spreadsheet-based numerical solutions

In this chapter the spreadsheet-based mathematical models are described. These models were used to develop, and provide comparison to, the QBasic algorithms. The parallel-sided silo case will be used as an example and is described in detail below in Chapter 10.1. Differences between the parallel-sided silo case and subsequent case studies are explained in Chapters 10.2 to 10.6. Microsoft Excel 2007 spreadsheet files are included on the CD accompanying the research project thesis.

10.1 Spreadsheet-based model for two-dimensional parallel-sided silo case

The spreadsheet file name for this model is 'Excel 2D Silo LM.xlsx'. Starting at the surface of the material:

$$x = H$$
$$\sigma_R = 0$$

Where H is the height of the material in the silo, and the stress value σ_R is set to zero – assumed to be the open surface of the material. The σ_R-value at x equal to H can be set to a non-zero value to represent overpressure. The model has the capability of adjusting the boundary condition of zero to be located at the supposed location of cohesive arch.

Values for ε are split into increments, for example for fifty increments:

$$\delta\varepsilon = \frac{(\beta_1+\beta_2)}{50} \qquad \text{(A.72)}$$

At the silo left-hand wall, the value of σ_ε is calculated using the known stress relationship via equation A.35 (the equation of a linearized yield locus), which is derived in Appendix Two, Chapter 9.5.

$$\sigma_\varepsilon = J\sigma_R + (J-1)T \qquad \text{(A.35, Chapter 9.5)}$$

Equation A.35 can also be used as a boundary condition at the centre of the silo. The model has the capability to adjust to a central location for the Mohr-Coulomb criterion.

The spreadsheet is now used to calculate σ_ε at all subsequent points of ε for this value of x, with appropriate Euler numerical solution methods (forward step shown below). The Euler method can be modified to suit the position of equation A.35.

$$\sigma_\varepsilon = F \Big/ \left(\frac{\partial w}{\partial x}\right) \tag{A.73}$$

Equation 51, Chapter 4.2, is used to calculate $\left(\frac{\partial \sigma_\varepsilon}{\partial \varepsilon}\right)$ for each value of ε at x.

Equation 50 is used to calculate $\left(\frac{\partial \sigma_R}{\partial x}\right)$ for each value of ε. A backward step Euler method is used to calculate σ_R at the next point down through the silo:

$$(\sigma_R)_{x+\delta x} = (\sigma_R)_x - \left(\frac{\partial \sigma_R}{\partial x}\right)\delta x \tag{A.74}$$

The above is repeated for all values of ε, allowing the model to produce tabular and graphical results for stresses σ_ε and σ_R. For control of data input values for the model, values for β were chosen to suit limits approximated equation 54 in Chapter 4.5. Other values were chosen to suit a vertical wall silo set-up, including zero α-values.

The information presented below demonstrates use of the two-dimensional model spreadsheet. The spreadsheet can be used for comparison of the numerical stress solutions to the Mohr-Coulomb stress assumption method.

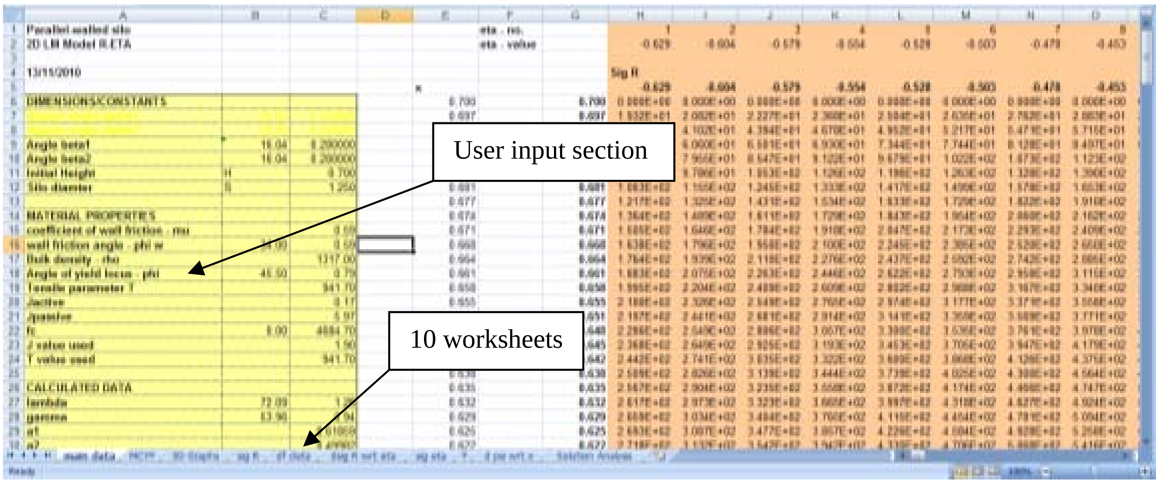

Figure A.5. Detail of user input section of 2-D parallel-sided silo spreadsheet

In the ‘main data’ worksheet shown in Figure A.5, the yellow shaded cells (A6:C35) allow user input of silo dimensional data and granular material properties.

DIMENSIONS/CONSTANTS		
Angle beta1	16.04	0.280000
Angle beta2	16.04	0.280000
Initial Height	H	0.700
Silo diameter	S	1.250

In the DIMENSIONS/CONSTANTS area of the ‘main data’ worksheet, variables including β-angle, initial height of the granular material fill *H*, silo diameter *S* and *k*-value are set.

Spreadsheet-based numerical solutions

MATERIAL PROPERTIES		
coefficient of wall friction - mu		0.59
wall friction angle - phi w	34.00	0.59
Bulk density - rho		1317.00
Angle of yield locus - phi	45.50	0.79
Tensile parameter T		941.70
Jactive		0.17
Jpassive		5.97
fc	0.00	4684.70
J value used		1.90
T value used		941.70

In the MATERIAL PROPERTIES area, the granular material properties are defined including wall friction angle ϕ_w, bulk density ρ, angle of yield locus/internal friction ϕ and tensile parameter T. The tensile parameter, failure criterion and limits for J-values are automatically calculated and displayed. The user should set the cells titled 'J value used' and 'T value used' to the required value.

CALCULATED DATA		
lambda	68.75	1.20
gamma	55.62	0.97
a1		0.00
a2		1.00
Radius R		2.66

In the CALCULATED DATA area λ, γ, a_1, a_2 and radius R are calculated and displayed automatically for information purposes and for use in spreadsheet calculations.

INCREMENTS		
Number of eta increments		50.00
deta		2.400E-02
dx		1.500E-02

In the INCREMENTS area, the number of eta increments can be input by the user; $\delta\varepsilon$ is then calculated. Increments in the x-direction are set by increasing the number of rows in the $\sigma_R/\sigma_\varepsilon$/etc calculation areas; from the number of x-increments δx is calculated.

To the right of the yellow-shaded user input section of this worksheet, different coloured areas of cells denote the calculation areas for σ_R, σ_ε, $\frac{\partial \sigma_R}{\partial x}$, and F; cells E1:HI201. Each of the values given in the different sections correspond to a different position within the silo, identified by x and ε coordinates running along the boundaries of the sections. Increments of x and ε are 200 and 50 respectively, but can be modified as required.

SIG R OPTION	**1**
SURFACE BOUNDARY CONDITION	1
ARCH BOUNDARY CONDITION	2
SIG ETA OPTION	**2**
LH WALL BOUNDARY CONDITION	1
CENTRE BOUNDARY CONDITION	2
MOHR COULOMB CRITERION	3

The green shaded cells (A38:B45 – visible in Figure A.6) allow the user to alter the location of boundary conditions and change relationships used for the three principal stresses. The SIG R OPTION locates the position of zero radial stress at either the upper or lower surface of the granular material. The SIG ETA OPTION moves the location of the Mohr-Coulomb relationship from the centreline of the silo/hopper to the left wall of the silo, or allows σ_ε-values to be calculated entirely from use of equation A.35. Directly below the green shaded cells, limits for β-values are shown in cells A53 and A54.

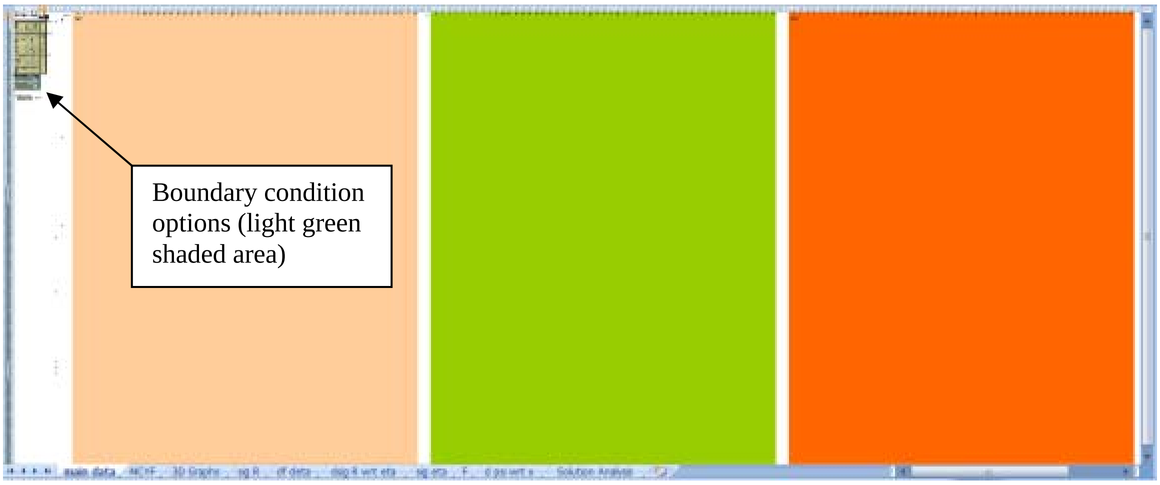

Figure A.6. Overview of parallel-sided silo spreadsheet

In Figure A.6, the screenshot has been zoomed out to allow most of the ‘main data’ worksheet to be in view – at this magnification no detail is apparent, so a section by section explanation will be undertaken in reverse order (from right to left).

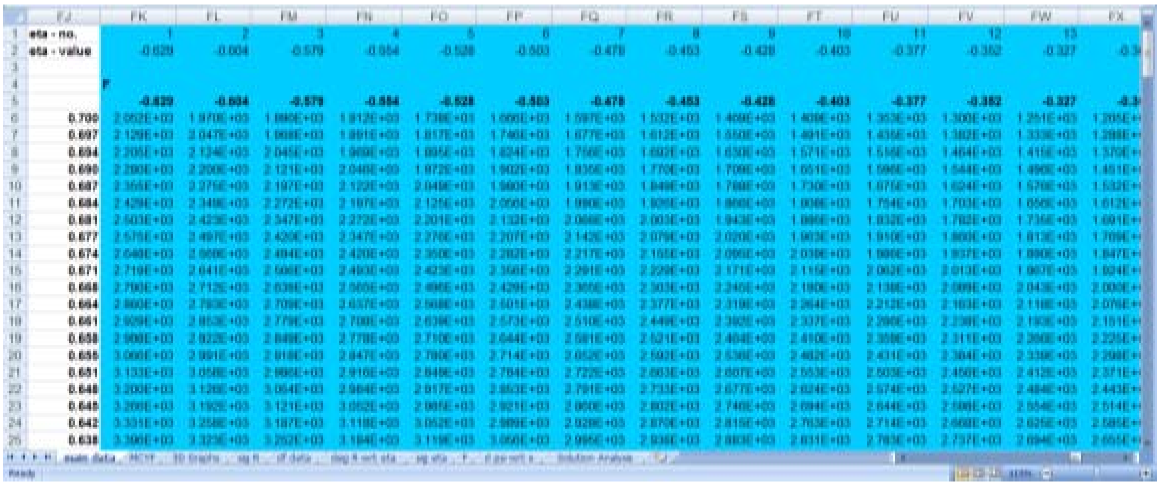

Figure A.7. Detail of *F* calculation area

The blue shaded area of the worksheet FJ1:HI201 shows values for *F* which, for the “left-hand wall” boundary condition model, are calculated via a forwards-step Euler numerical solution of the form shown below.

$$[F]_{\delta\varepsilon+\varepsilon} = [F]_{\delta\varepsilon} + \left[\frac{\partial F}{\partial \varepsilon}\right]_{\delta\varepsilon} \delta\varepsilon \qquad \text{(A.75)}$$

with initial condition $F = \sigma_\varepsilon \left(\frac{\partial w}{\partial x}\right)$ (A.76)

For the “centre” boundary condition model, the direction of the Euler method is adjusted to suit position within the silo; calculations left of the centre-line use a backwards-step method, while calculations to the right use forwards-step.

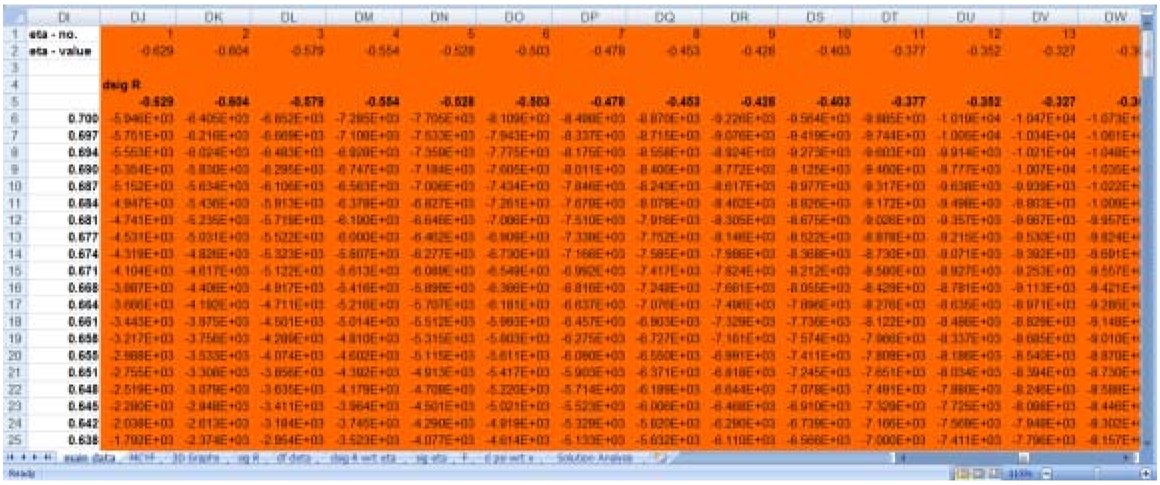

Figure A.8. Detail of $\frac{\partial \sigma_R}{\partial x}$ calculation area

The orange shaded area of the worksheet DI1:FH201 shows values for $\frac{\partial \sigma_R}{\partial x}$, calculated by use of the R-direction force balance.

Figure A.9. Detail of σ_ε calculation area

Spreadsheet-based numerical solutions

The green shaded area of the worksheet BH1:DG201 allows calculation of values for σ_ε. Here either the Mohr-Coulomb derived relationship given by equation A.35 can be used to give σ_ε from σ_R, or via $\sigma_\varepsilon = F \Big/ \left(\frac{\partial w}{\partial x}\right)$. In the latter case equation A.35 is used at a point within the silo to act as an initial condition. Depending on requirements, this boundary condition can be positioned either at the left-hand wall of the silo or at its centre.

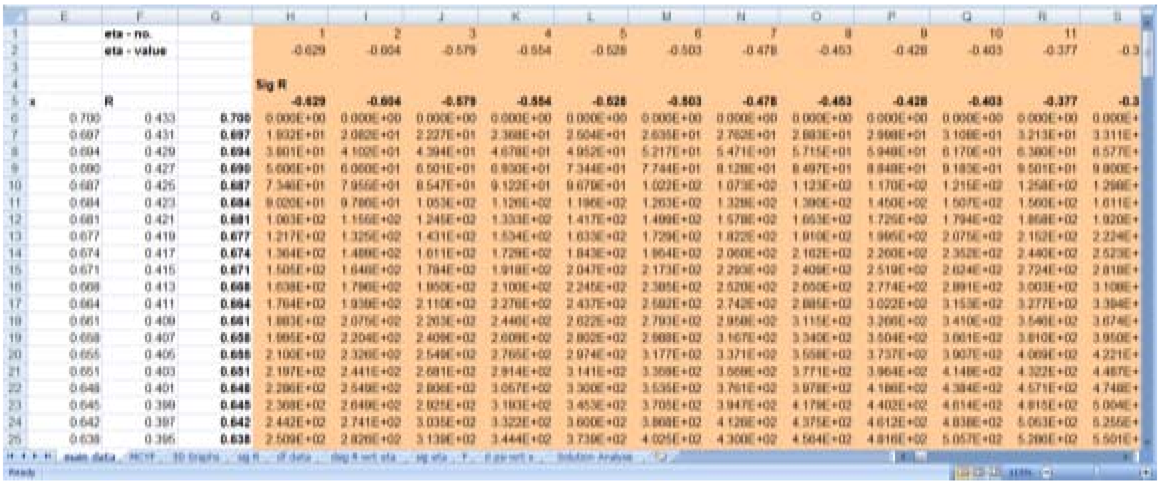

	E	F	G	H	I	J	K	L	M	N	O	P	Q	R	S
1		eta - no.		1	2	3	4	5	6	7	8	9	10	11	
2		eta - value		-0.629	-0.604	-0.579	-0.554	-0.528	-0.503	-0.478	-0.453	-0.428	-0.403	-0.377	-0.3
3															
4				Sig R											
5	x	R		-0.629	-0.604	-0.579	-0.554	-0.528	-0.503	-0.478	-0.453	-0.428	-0.403	-0.377	-0.3
6	0.700	0.433	0.700	0.000E+00	0.000E+00	0.000E+00	0.000E+00	0.000E+00	0.000E+00	0.000E+00	0.000E+00	0.000E+00	0.000E+00	0.000E+00	0.000E+
7	0.697	0.431	0.697	1.932E+01	2.082E+01	2.227E+01	2.368E+01	2.504E+01	2.635E+01	2.762E+01	2.883E+01	2.998E+01	3.108E+01	3.213E+01	3.311E+
8	0.694	0.429	0.694	3.801E+01	4.102E+01	4.394E+01	4.678E+01	4.952E+01	5.217E+01	5.471E+01	5.715E+01	5.948E+01	6.170E+01	6.380E+01	6.577E+
9	0.690	0.427	0.690	5.606E+01	6.060E+01	6.501E+01	6.930E+01	7.344E+01	7.744E+01	8.128E+01	8.497E+01	8.848E+01	9.183E+01	9.501E+01	9.800E+
10	0.687	0.425	0.687	7.346E+01	7.955E+01	8.547E+01	9.122E+01	9.678E+01	1.022E+02	1.073E+02	1.123E+02	1.170E+02	1.215E+02	1.258E+02	1.298E+
11	0.684	0.423	0.684	9.020E+01	9.780E+01	1.053E+02	1.126E+02	1.196E+02	1.263E+02	1.328E+02	1.390E+02	1.450E+02	1.507E+02	1.560E+02	1.611E+
12	0.681	0.421	0.681	1.063E+02	1.156E+02	1.246E+02	1.333E+02	1.417E+02	1.499E+02	1.578E+02	1.653E+02	1.725E+02	1.794E+02	1.858E+02	1.920E+
13	0.677	0.419	0.677	1.217E+02	1.325E+02	1.431E+02	1.534E+02	1.633E+02	1.729E+02	1.822E+02	1.910E+02	1.995E+02	2.075E+02	2.152E+02	2.224E+
14	0.674	0.417	0.674	1.364E+02	1.488E+02	1.611E+02	1.729E+02	1.843E+02	1.954E+02	2.060E+02	2.162E+02	2.260E+02	2.352E+02	2.440E+02	2.523E+
15	0.671	0.415	0.671	1.505E+02	1.648E+02	1.784E+02	1.918E+02	2.047E+02	2.173E+02	2.293E+02	2.409E+02	2.519E+02	2.624E+02	2.724E+02	2.818E+
16	0.668	0.413	0.668	1.638E+02	1.798E+02	1.950E+02	2.100E+02	2.245E+02	2.385E+02	2.520E+02	2.650E+02	2.774E+02	2.891E+02	3.003E+02	3.108E+
17	0.664	0.411	0.664	1.764E+02	1.938E+02	2.110E+02	2.276E+02	2.437E+02	2.592E+02	2.742E+02	2.885E+02	3.022E+02	3.153E+02	3.277E+02	3.394E+
18	0.661	0.409	0.661	1.883E+02	2.075E+02	2.263E+02	2.446E+02	2.622E+02	2.793E+02	2.958E+02	3.115E+02	3.266E+02	3.410E+02	3.546E+02	3.674E+
19	0.658	0.407	0.658	1.995E+02	2.204E+02	2.409E+02	2.609E+02	2.802E+02	2.988E+02	3.167E+02	3.340E+02	3.504E+02	3.661E+02	3.810E+02	3.950E+
20	0.655	0.405	0.655	2.100E+02	2.326E+02	2.548E+02	2.765E+02	2.974E+02	3.177E+02	3.371E+02	3.558E+02	3.737E+02	3.907E+02	4.069E+02	4.221E+
21	0.651	0.403	0.651	2.197E+02	2.441E+02	2.681E+02	2.914E+02	3.141E+02	3.358E+02	3.568E+02	3.771E+02	3.964E+02	4.148E+02	4.322E+02	4.487E+
22	0.648	0.401	0.648	2.286E+02	2.548E+02	2.806E+02	3.057E+02	3.300E+02	3.535E+02	3.761E+02	3.978E+02	4.186E+02	4.384E+02	4.571E+02	4.748E+
23	0.645	0.399	0.645	2.368E+02	2.649E+02	2.925E+02	3.193E+02	3.453E+02	3.705E+02	3.947E+02	4.179E+02	4.402E+02	4.614E+02	4.815E+02	5.004E+
24	0.642	0.397	0.642	2.442E+02	2.741E+02	3.035E+02	3.322E+02	3.600E+02	3.868E+02	4.126E+02	4.375E+02	4.612E+02	4.838E+02	5.053E+02	5.255E+
25	0.638	0.395	0.638	2.509E+02	2.826E+02	3.139E+02	3.444E+02	3.738E+02	4.025E+02	4.300E+02	4.564E+02	4.816E+02	5.057E+02	5.286E+02	5.501E+

Figure A.10. Detail of σ_R calculation area

The tan shaded area of the worksheet E1:BF201 shows values for σ_R, calculated by the backward step Euler numerical solution shown below. At the surface of the material within the silo (i.e. where x equals the initial height), the value of σ_R is set to zero to signify zero surface overpressure.

$$[\sigma_R]_{x-\delta x} = [\sigma_R]_x - \left[\frac{\partial \sigma_R}{\partial x}\right]_{\delta x} \delta x \qquad \text{(A.77)}$$

The model can be adjusted to select zero σ_R stress at the lower surface of the material (i.e. where x equals the proposed location of cohesive arch). A forward step Euler method is employed to calculate stresses up through the silo.

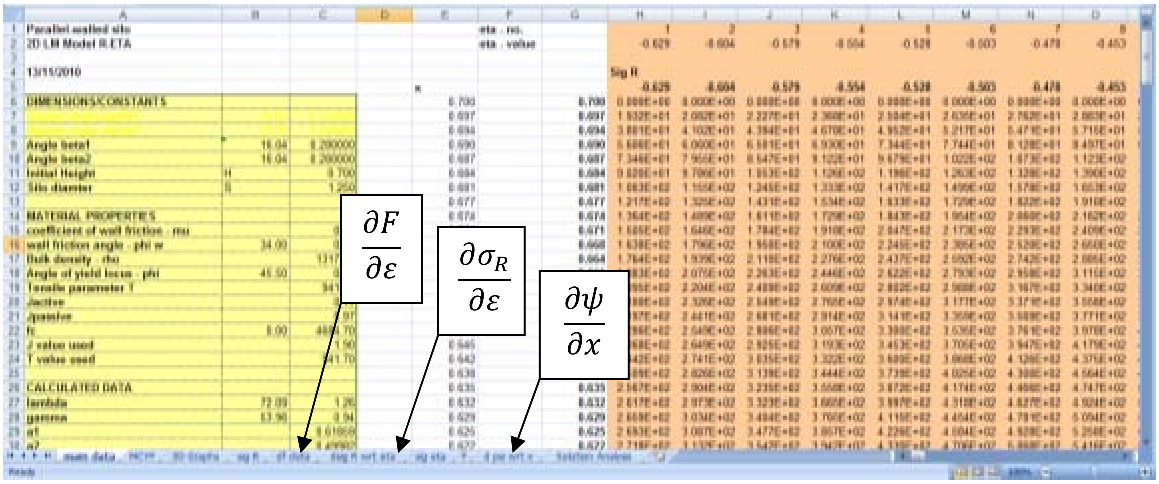

Figure A.11. Additional worksheets

The subsequent worksheets are used for calculation and analysis of the other variables necessary for the model.

- $\frac{\partial F}{\partial \varepsilon}$ is calculated by use of the ε-direction force balance (equation 51).
- $\frac{\partial \sigma_R}{\partial \varepsilon}$ is calculated by use of σ_R finite difference calculations.
- $\frac{\partial \psi}{\partial x}$ is calculated using equation 46.

Graphical displays include a two-dimensional surface plot of conformity to the Mohr-Coulomb Yield Function in Figure A.12, and various three-dimensional surface plots of stresses to allow analysis in Figure A.13. Coloured cells indicate that the stresses do not conform to the Mohr-Coulomb criterion i.e. Coulomb line (iii) in Figure 27 in Chapter 3.2.1.

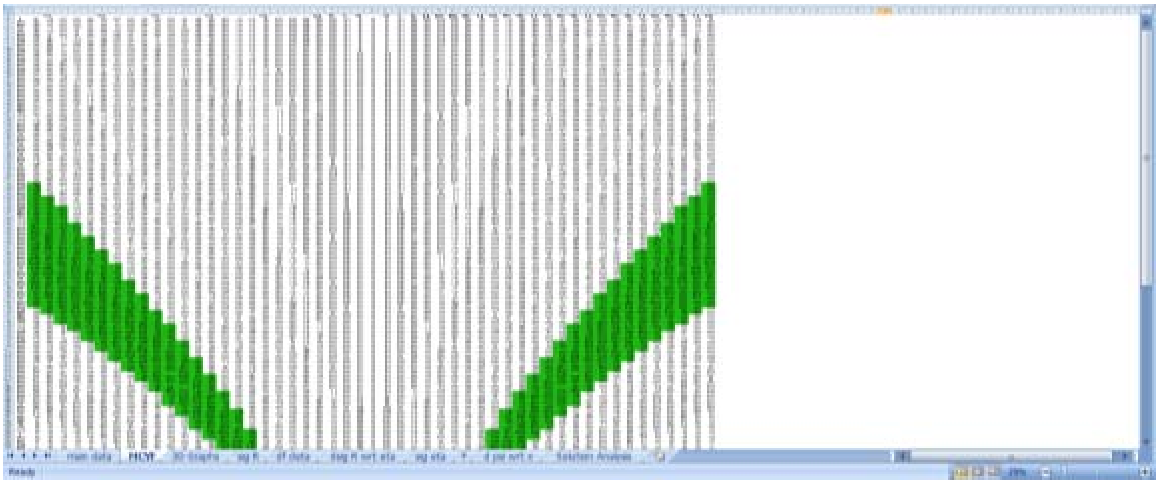

Figure A.12. Conformity to the Mohr-Coulomb Yield Function

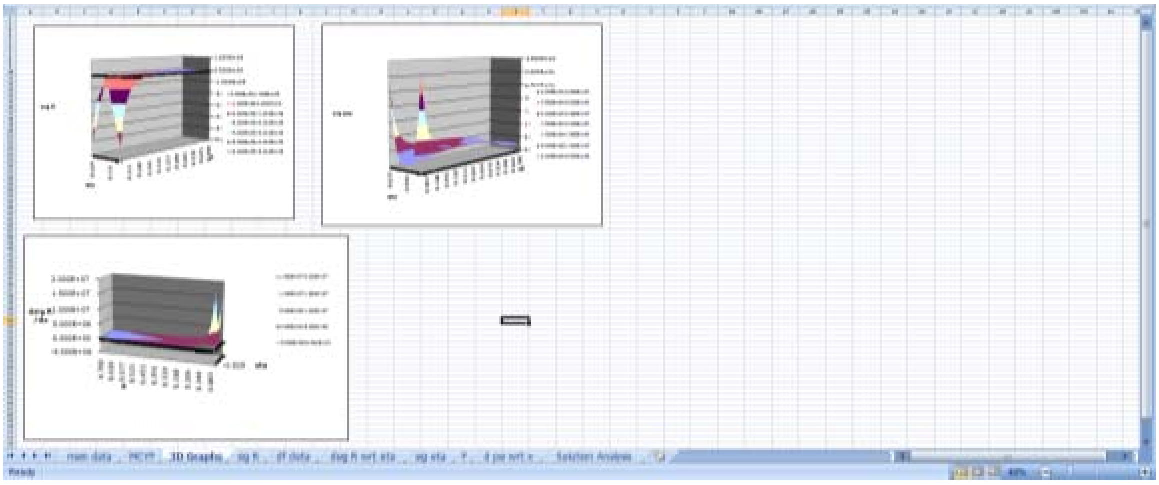

Figure A.13. 3-D surface plots of stress values

In the ‘least squares’ worksheet, cells F3:F5 represent calculated principal stress values at specific points within the silo, which have been resolved into wall stresses using equation 56. Cells G3:G5 represent manually inputted experimental data values. Cell M6 represents the sum of the squares of errors between cells F3:F5 and G3:G5. It is cell M6 that the Solver application attempts to reduce towards zero by modification of cells R11:R15, within the limits shown in cells R17:R21. Figure A.14 shows a screen shot of the parallel-sided silo spreadsheet used for comparison to experimental data.

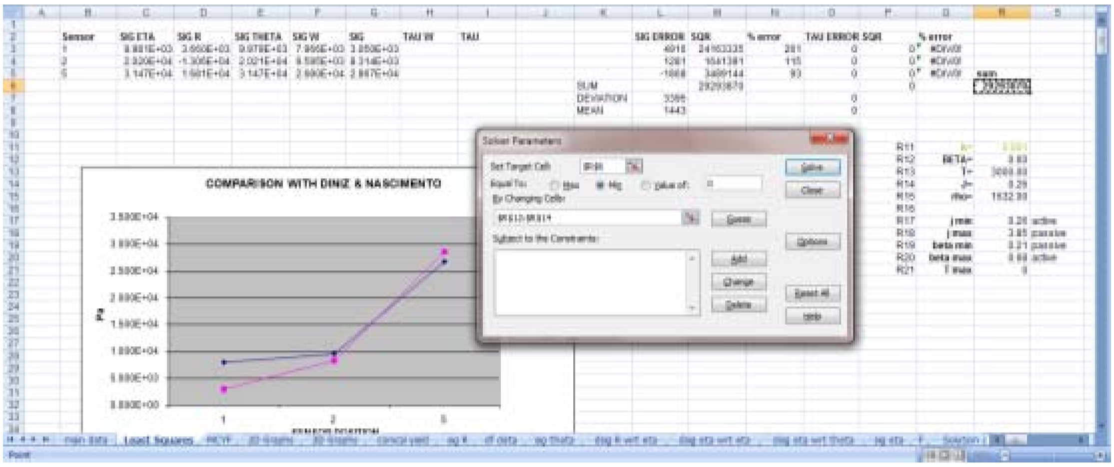

Figure A.14. Least squares worksheets with Solver dialogue box open

10.2 Spreadsheet-based model for two-dimensional wedge hopper case

The spreadsheet for the two-dimensional wedge-hopper case is similar to the two-dimensional parallel-sided silo case, with the main addition of use of non-zero α angles and a variable R-dimension. All other worksheets are similar to the parallel-sided silo case. The file name for this model is 'Excel 2D Unequal Wedge LM.xlsx'.

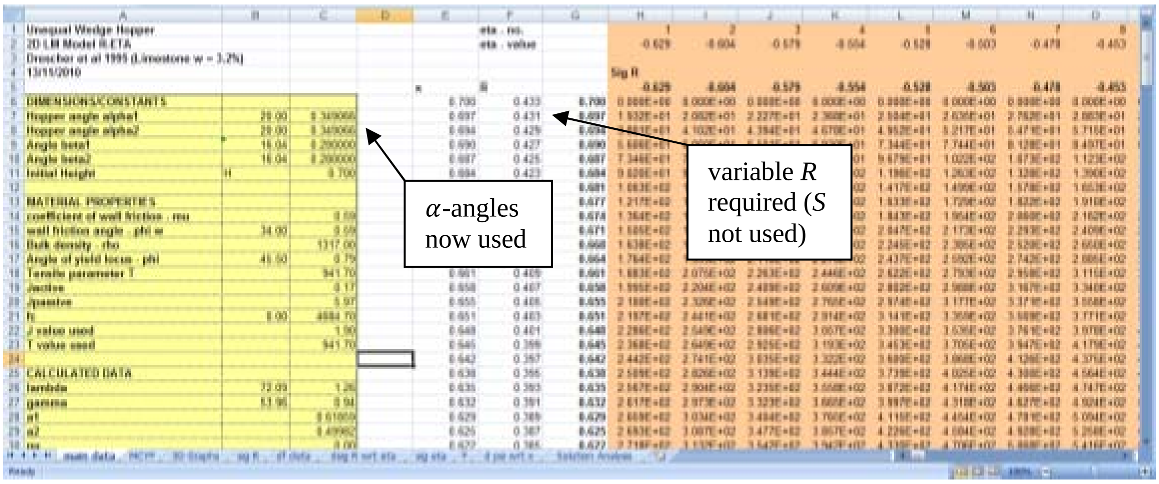

Figure A.15. User input section of 2-D wedge-hopper spreadsheet

The DIMENSIONS/CONSTANTS input section has been modified to include hopper half angles α and remove silo diameter S. Formulae across the spreadsheet have been modified to allow use of independent α_1, α_2, β_1, β_2 angles.

DIMENSIONS/CONSTANTS		
Hopper angle alpha1	20.00	0.349066
Hopper angle alpha2	20.00	0.349066
Angle beta1	16.04	0.280000
Angle beta2	16.04	0.280000
Initial Height	H	0.700

.

The MATERIAL PROPERTIES area remains identical to the parallel-sided silo case. The CALCULATED DATA section now has provision for a η-value in the event of independent α_1 and α_2 angles.

CALCULATED DATA		
lambda	72.09	1.26
gamma	53.96	0.94
a1		0.61859
a2		0.49982
nu		0.00

10.3 Spreadsheet-based model for three-dimensional parallel-sided silo case

The information presented below demonstrates use of the axially symmetric three-dimensional model spreadsheet. The file name for this model is ‘Excel 3D Silo LM.xlsx’.

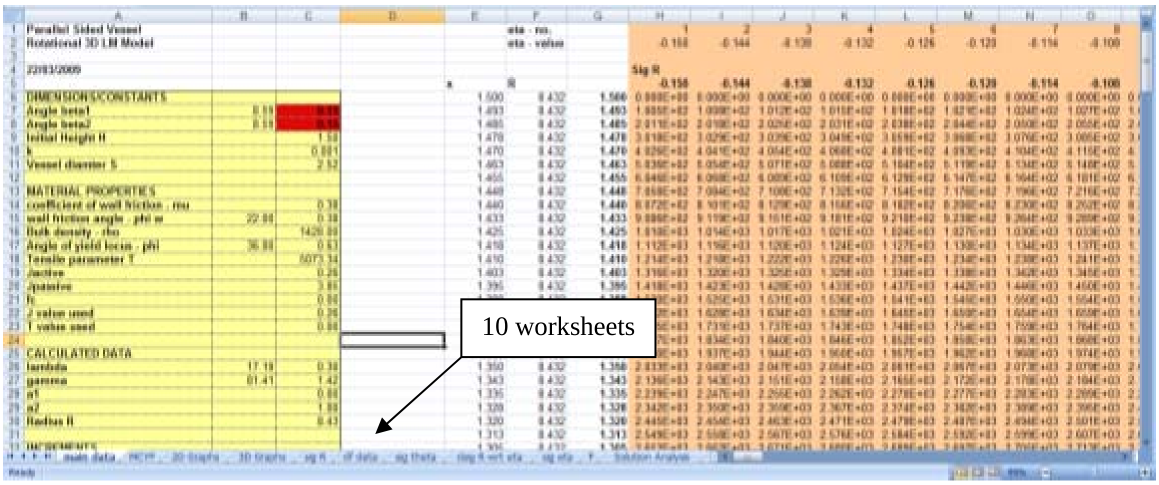

Figure A.16. Detail of user input section of 3-D parallel-sided silo spreadsheet

The three-dimensional version of the parallel-sided silo spreadsheet shares common features with the two-dimensional version described in Chapter 10.1. These features are listed below.

- The location of zero σ_R can be position at the material surface or at the proposed location of a cohesive arch.
- Fifty increments are used in the ε-direction.
- Two hundred increments are used in the x-direction.
- The ability to adjust the location of the Mohr-Coulomb criterion boundary condition.
- Zero alpha angles are used.
- A constant R-dimension is used.
- Two- and three-dimensional graphical displays of all stress values.

SIG R OPTION	**1**
SURFACE BOUNDARY CONDITION	1
ARCH BOUNDARY CONDITION	2
SIG ETA OPTION	**2**
LH WALL BOUNDARY CONDITION	1
CENTRE BOUNDARY CONDITION	2
MOHR COULOMB CRITERION	3
SIG THETA OPTION	**2**
HAAR VON KARMEN	1
SIG ETA / SIG R RELATIONSHIP	2

The three-dimensional version of the parallel-sided silo spreadsheet allows for calculation of azimuthal stress σ_θ using an additional worksheet containing equations 62 and 65 to 68. These equations relate the other two principal stresses to azimuthal stress values. The green shaded cells above (A37:B48) have been expanded to include the SIG THETA OPTION that allows the user a choice of relationships for calculation of σ_θ. Figure A.17 shows details of the σ_θ calculation area on the 'sig theta' worksheet.

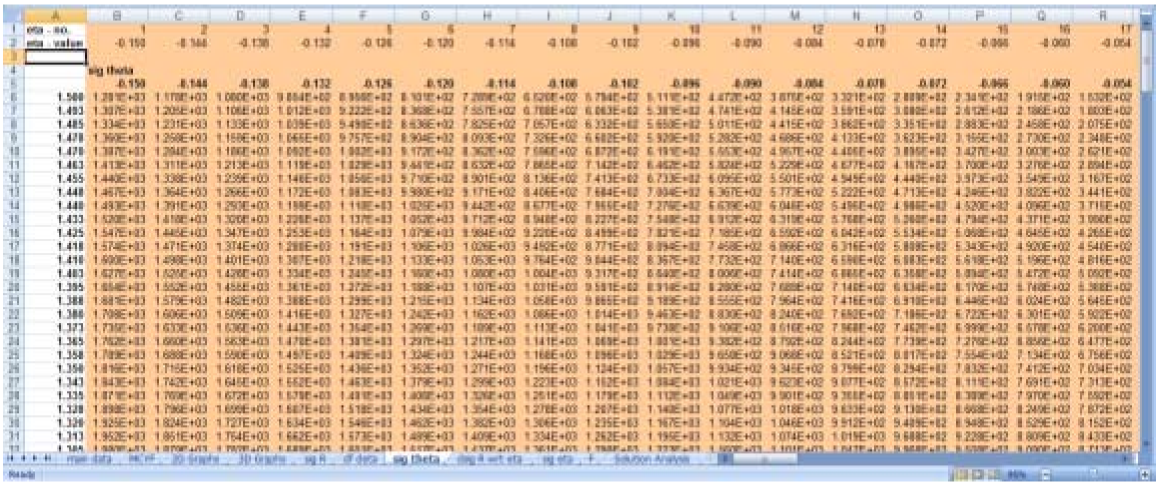

Figure A.17. Detail of σ_θ calculation area

The user input section is modified to allow input of a *k*-value, visible in Figure A.16 and in the table below, and to allow selection of azimuthal stress relationship.

DIMENSIONS/CONSTANTS		
Angle beta1	8.59	**0.15**
Angle beta2	8.59	**0.15**
Initial Height H		1.50
k		0.001
Vessel diameter S		2.52

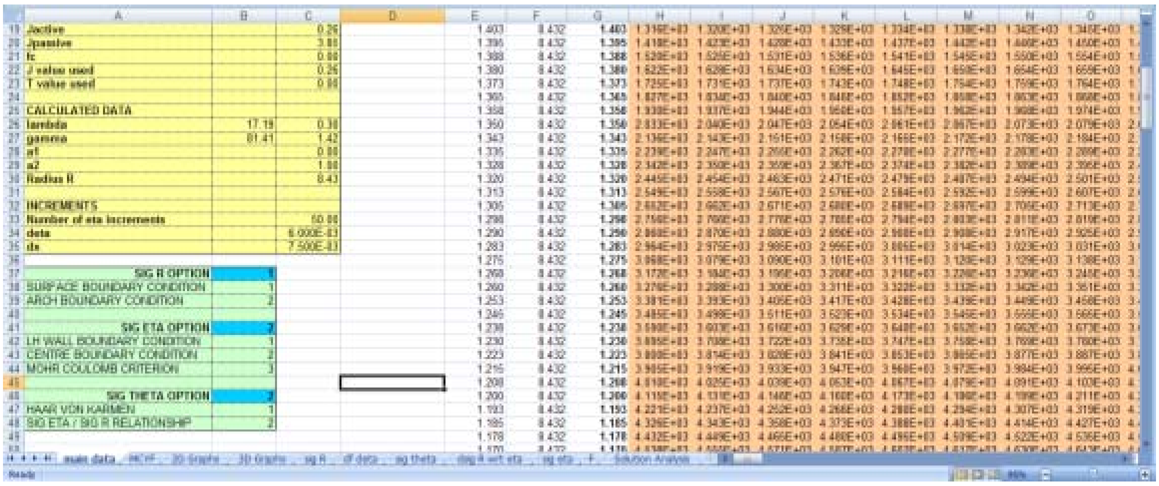

Figure A.18. Detail of user input section showing optional stress relationships

Figure A.18 demonstrates the optional stress relationships allowing choice of azimuthal stress relationship. In Figure A.19 stress values calculated using the spreadsheet and QBasic algorithms are compared to experimental data. A least squares method and the Excel Solver function is used to converge calculated results on empirical values. Findings are documented in Chapter 5.

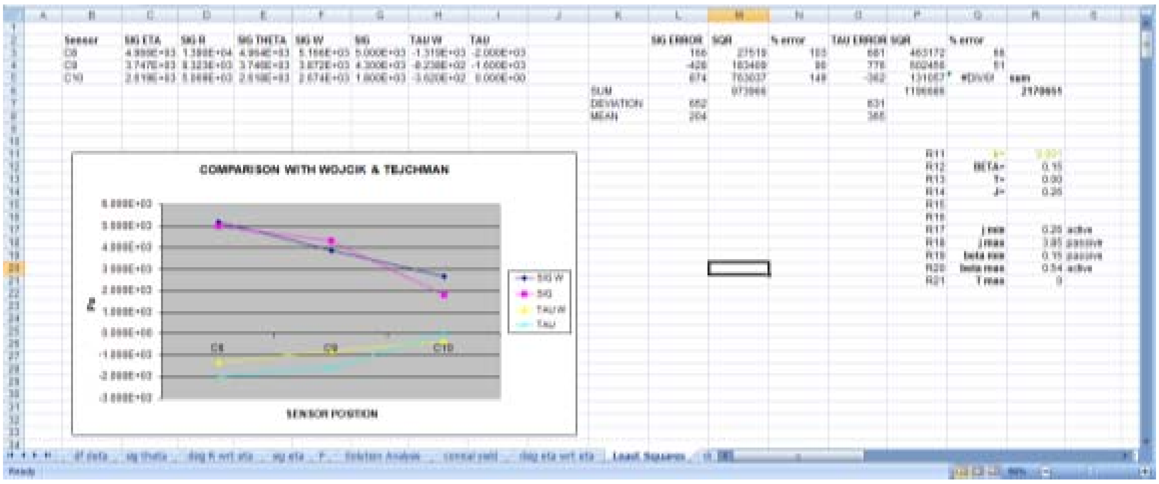

Figure A.19. Detail of least squares method calculation area

10.4 Spreadsheet-based model for three-dimensional cone-hopper case

As with their two-dimensional counterparts, the spreadsheet for the three-dimensional cone-hopper case is similar to the three-dimensional parallel-sided silo case in

Chapter 10.3, with the main addition of use of non-zero α angles and a variable R-dimension. All other worksheets are similar to the 3-D parallel-sided silo case. The file name for this model is 'Excel 3D Cone LM.xlsx'.

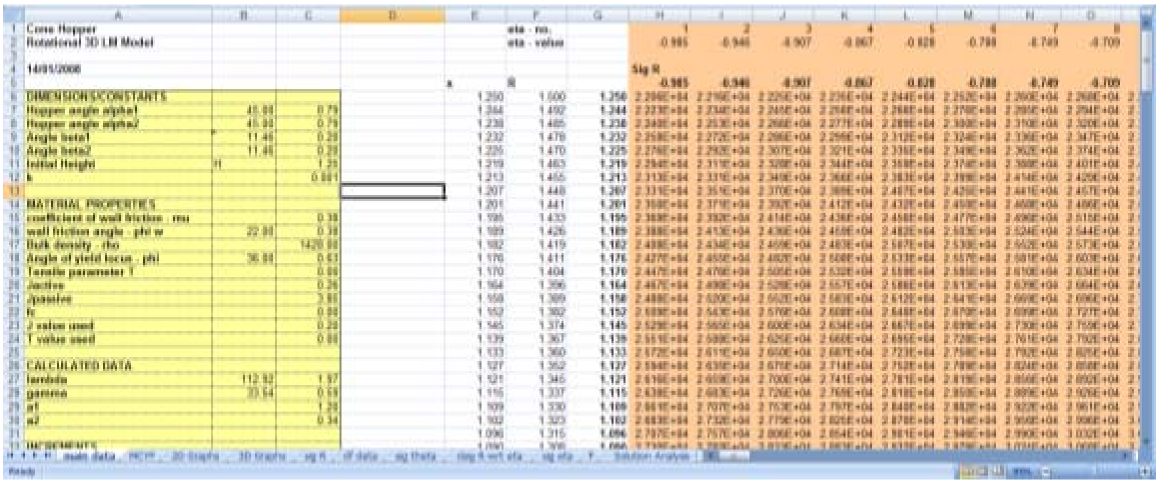

Figure A.20. Detail of user input section of 3-D cone-hopper spreadsheet

10.5 Spreadsheet-based model for three-dimensional cone-hopper with conical insert case

The spreadsheet for the three-dimensional cone hopper with conical insert is based on the equivalent cone model, without an insert. It can be seen in Figure A.21 that the insert angle Θ has been added. The file name for this model is 'Excel 3D Cone Insert LM.xlsx'.

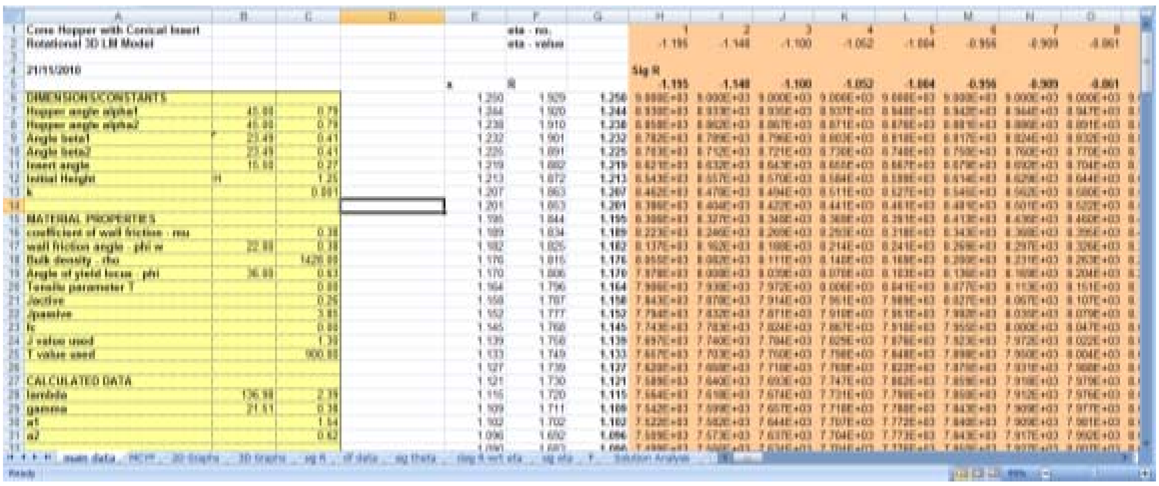

Figure A.21. Detail of user input section of 3-D cone-hopper with conical insert spreadsheet

10.6 Spreadsheet-based model for three-dimensional cone-hopper with conical rat hole case

The spreadsheet for the three-dimensional cone hopper with rat hole is based on the equivalent cone model, without an insert. It can be seen in Figure A.21 that the rat hole (void) Θ has been added. The file name for this model is ‘Excel 3D Cone rat hole LM.xlsx’.

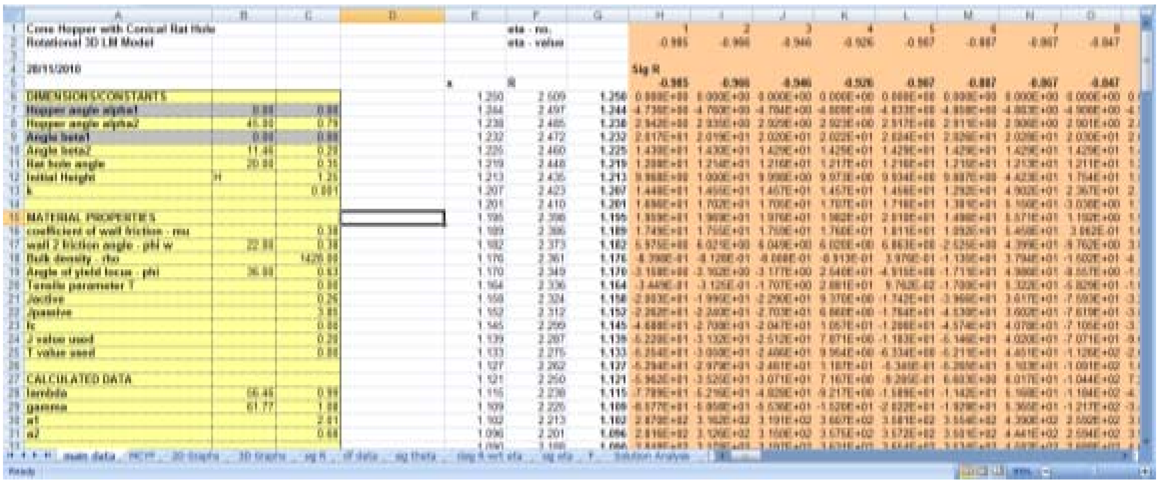

Figure A.22. Detail of user input section of 3-D cone-hopper with conical rat hole spreadsheet

Chapter 11.0 - Appendix Four

QBasic Algorithms/Programming

QBasic Algorithms/Programming

In this chapter the QBasic algorithms are introduced. The two-dimensional parallel-sided silo case is explained in detail in Chapter 11.1. Differences between the 2-D silo case and remaining case studies are explained in Chapters 11.2 to 11.6. Microsoft QB64 files are included on the CD accompanying the research project thesis.

11.1 QBasic algorithm for two-dimensional parallel-sided silo case

This algorithm follows the theory described in Chapters 4 and 10.1 for the two-dimensional parallel-sided silo case. User input is explained with the algorithm following in Chapter 11.1.2.

11.1.1 User input

When the QB64 interface opens with a blue screen, the algorithm can be accessed using the File menu. Select Open and choose the file with name ‘SILO_2D_LM.bas’. The programme text and title will now be visible. Choose Run then Start to execute the programme, or press function key F5.

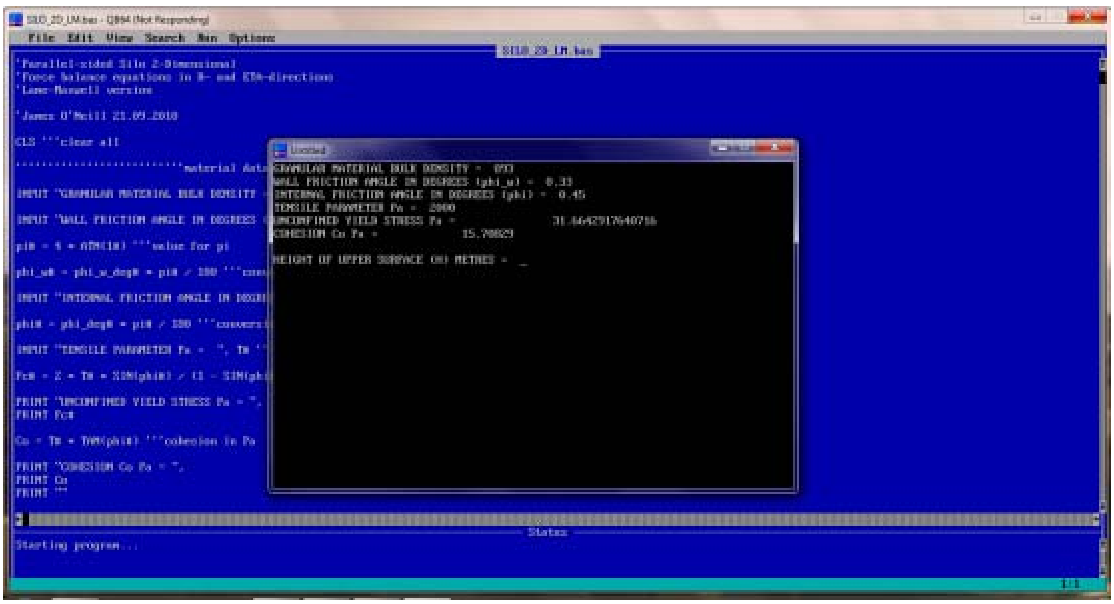

Figure A.23. QBasic algorithm screenshot

There will be a slight delay while the Execute file is created. The model will now request granular material data; a command prompt will ask for the materials bulk density ρ, as shown in Figure A.23 above, and subsequently the following data:

- Wall friction angle ϕ_w
- Internal friction angle ϕ
- Tensile parameter T

From the above data the algorithm will calculate and display unconfined yield stress σ_c and cohesive stress c as shown in Figure A.23.

The model will request dimensional data to define silo shape, including initial height of granular fill H, location of lower surface of material H_2 and silo diameter S. The lower surface may be the proposed location of the cohesive arch, or the transition between silo and hopper.

From the data inputted thus far, the model will display suggested limits for β and request a β-value to use in calculations. In a similar manner J-limits are shown and a J-value requested. This is visible in Figure A.24.

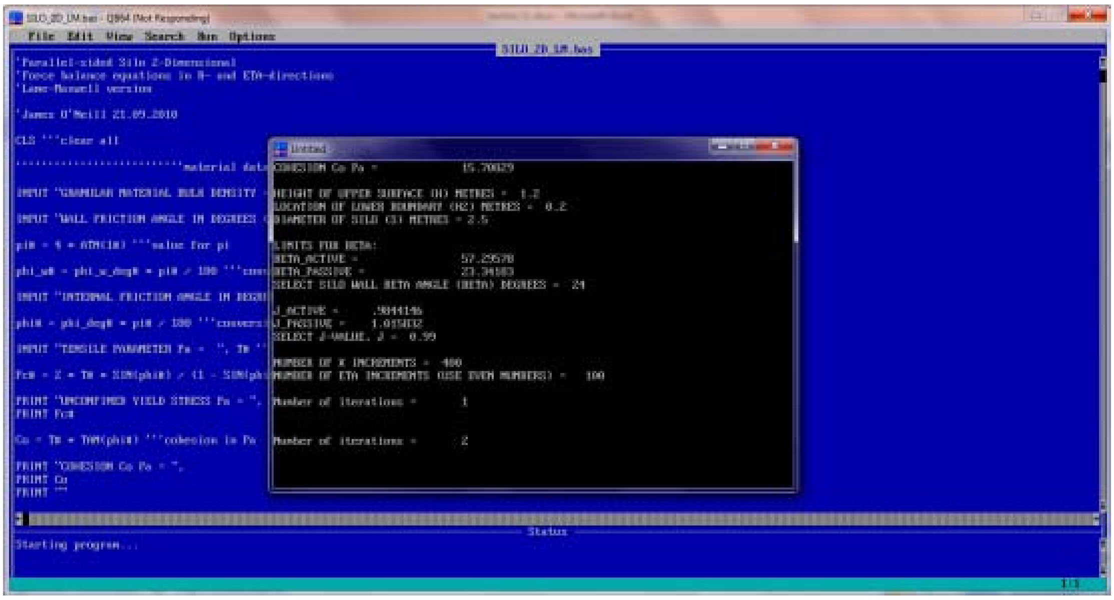

Figure A.24. QBasic algorithm screenshot

Number of x- and ε-increments are requested. Entry of this information will start the calculation of the stress distributions. The displayed number of iterations will increase as the programme cycles through the WHILE loop and is displayed on the command prompt screen. The WHILE loop is a Newton-Raphson type (Stroud 1996). When the model converges on a solution within 0.1 Pa of successive radial stress σ_R results, then it will stop and ask for any button to be pressed to close the command prompt and return to the blue interface screen. Data can be retrieved from the ‘qb64’ folder in the form of comma separated variable files. These CSV files can be imported into appropriate graphical display software.

11.1.2 Programme text

The QBasic program for two-dimensional parallel-sided silo case is shown below. The model file for this algorithm has file name ‘SILO_2D_LM.bas’. Explanations are provided adjacent to the program text.

```
'Parallel-sided Silo 2-Dimensional
'Force balance equations in R- and ETA-directions
'Lame-Maxwell version

'James O'Neill 21.09.2010

CLS '''clear all

''''''''''''''''''''''''material data input

INPUT "GRANULAR MATERIAL BULK DENSITY =  ", RHO# '''bulk density in kg/m3 (assumed to be constant)

INPUT "WALL FRICTION ANGLE IN DEGREES (phi_w) =  ", phi_w_deg# '''angle of wall friction in degrees

pi# = 4 * ATN(1#) '''value for pi

phi_w# = phi_w_deg# * pi# / 180 '''conversion to radians

INPUT "INTERNAL FRICTION ANGLE IN DEGREES (phi) =  ", phi_deg# '''angle of internal friction/yield locus in degrees
```

```
phi# = phi_deg# * pi# / 180 '''conversion to radians

INPUT "TENSILE PARAMETER Pa =  ", T# '''tensile intercept in Pa

Fc# = 2 * T# * SIN(phi#) / (1 - SIN(phi#)) '''unconfined yield stress in Pa

PRINT "UNCONFINED YIELD STRESS Pa = ",
PRINT Fc#

Co = T# * TAN(phi#) '''cohesion in Pa

PRINT "COHESION Co Pa = ",
PRINT Co
PRINT ""

''''''''''''''''''''''''''''silo and model geometry data input

INPUT "HEIGHT OF UPPER SURFACE (H) METRES =  ", H# '''upper surface height in metres

INPUT "LOCATION OF LOWER BOUNDARY (H2) METRES =  ", H2# '''choose location of lower boundary of model (e.g. cohesive arch across silo)

INPUT "DIAMETER OF SILO (S) METRES = ", S# '''choose diameter of silo

ALPHA# = 0 '''zero half angle for silo case

BETA_ACTIVE_CALC# = SIN(phi_w#) / SIN(phi#) + phi_w#

BETA_ACTIVE = (180 / pi#) '* ATN(BETA_ACTIVE_CALC# / (1 + (1 - BETA_ACTIVE_CALC# ^ 2) ^ 0.5)) '''active BETA-value to be shown on screen in degrees (no built in arcsin function)
PRINT ""
```

```
PRINT "LIMITS FOR BETA:"
PRINT "BETA_ACTIVE = ", BETA_ACTIVE

BETA_PASSIVE_CALC# = SIN(phi_w#) / SIN(phi#) - phi_w#

BETA_PASSIVE = (180 / pi#) * ATN(BETA_PASSIVE_CALC# / (1 + (1 - BETA_PASSIVE_CALC# ^ 2) ^ 0.5)) '''active BETA-value to be shown on screen in degrees (no built in arcsin function)
PRINT "BETA_PASSIVE = ", BETA_PASSIVE

INPUT "SELECT SILO WALL BETA ANGLE (BETA) DEGREES =  ", BETA_DEG# '''selection of angle between principal stress arc and wall normal in degrees

BETA# = BETA_DEG# * pi# / 180 '''conversion to radians

R# = S# / (SIN(BETA#) + SIN(BETA#)) '''R is constant within silos

LAMBDA# = (BETA# + BETA# + ALPHA# + ALPHA#) '''sum of ALPHA and BETA angles in radians

GAMMA# = pi# / 2 - LAMBDA# / 2 '''constant resulting from model geometry in radians

A1# = SIN(GAMMA#) * SIN(ALPHA# + ALPHA#) / (SIN(LAMBDA#) * COS(ALPHA#) * SIN(GAMMA# + BETA#)) '''constant resulting from model geometry in radians

A2# = ((1 - A1# * COS(ALPHA# + BETA#)) ^ 2 + (TAN(ALPHA#) - A1# * SIN(ALPHA# + BETA#)) ^ 2) ^ 0.5 '''constant resulting from model geometry in radians

NU# = 0 '''angle between lines of constant ETA between principal stress arcs is zero for silo case
```

```
J_ACTIVE = (1 - SIN(phi#)) / (1 + SIN(phi#)) '''active J-value to be shown on screen
PRINT ""
PRINT "J_ACTIVE = ", J_ACTIVE
J_PASSIVE = (1 + SIN(phi#)) / (1 - SIN(phi#)) '''passive J-value to be shown on screen
PRINT "J_PASSIVE = ", J_PASSIVE
INPUT "SELECT J-VALUE, J =  ", J# '''selection of J-value
PRINT ""
INPUT "NUMBER OF X INCREMENTS =  ", DELTA_X_INC# '''choose number of increments in X-direction (e.g. 200 down through silo)
INPUT "NUMBER OF ETA INCREMENTS (USE EVEN NUMBERS) =   ", DELTA_ETA_INC# '''choose number of increments in ETA-direction (e.g. 50 across silo)
o# = _ROUND((DELTA_ETA_INC# + 1) / 2) '''centre-line of silo (e.g. column 26 in a 51-column matrix)
DELTA_X# = (H# - H2#) / DELTA_X_INC# '''X-increment size
DELTA_ETA# = LAMBDA# / DELTA_ETA_INC# '''ETA-increment size
DIM X#(DELTA_X_INC# + 1, DELTA_ETA_INC# + 1) '''define and populate a matrix for X, from upper surface (H) to lower boundary (H2) using X-increment as step size
FOR B = 1 TO DELTA_ETA_INC# + 1
X#(1, B) = H#
FOR A = 2 TO DELTA_X_INC# + 1
X#(A, B) = X#(A - 1, B) - DELTA_X#
```

```
NEXT
NEXT
DIM ETA#(DELTA_X_INC# + 1, DELTA_ETA_INC# + 1) '''define and populate a matrix for ETA, from left-hand silo wall to right-hand wall using ETA-increment as step size
FOR C = 1 TO DELTA_X_INC# + 1
ETA#(C, 1) = -(ALPHA# + BETA#)
FOR D = 2 TO DELTA_ETA_INC# + 1
ETA#(C, D) = ETA#(C, D - 1) + DELTA_ETA#
NEXT
NEXT
DIM PW_WRTX#(DELTA_X_INC# + 1, DELTA_ETA_INC# + 1) '''define and populate a matrix for model variable PW_WRTX
FOR C = 1 TO DELTA_X_INC# + 1
FOR B = 1 TO DELTA_ETA_INC# + 1
PW_WRTX#(C, B) = A1# + A2# * COS(ETA#(C, B) - NU#)
NEXT
NEXT
DIM PPSI_WRTX#(DELTA_X_INC# + 1, DELTA_ETA_INC# + 1) '''define and populate a matrix for PPSI_WRTX
FOR B = 1 TO DELTA_ETA_INC# + 1
FOR C = 1 TO DELTA_X_INC# + 1
PPSI_WRTX#(C, B) = A2# * SIN(ETA#(C, B) - NU#) / R#
NEXT
NEXT
''''''''''''''''''''''''''dimension matrices using X- and ETA-increment information, to allow QBasic to reserve memory space
DIM PF_WRTETA#(DELTA_X_INC# + 1, DELTA_ETA_INC# + 1) '''PSIG_R_WRTX#(row, column)
```

```
127     DIM PSIG_R_WRTETA#(DELTA_X_INC# + 1, DELTA_ETA_INC# + 1)
128     DIM SIG_ETA#(DELTA_X_INC# + 1, DELTA_ETA_INC# + 1) '''arc stress
129     DIM F#(DELTA_X_INC# + 1, DELTA_ETA_INC# + 1)
130     FOR B = 1 TO DELTA_ETA_INC# + 1
131     FOR C = 1 TO DELTA_X_INC# + 1
132     F#(C, B) = -2600
133     NEXT
134     NEXT
135     DIM PSIG_R_WRTX#(DELTA_X_INC# + 1, DELTA_ETA_INC# + 1)
136     DIM SIG_R#(DELTA_X_INC# + 1, DELTA_ETA_INC# + 1) '''radial stress
137     FOR B = 1 TO DELTA_ETA_INC# + 1
138     FOR C = 1 TO DELTA_X_INC# + 1
139     SIG_R#(C, B) = 9600
140     NEXT
141     NEXT
142
143     ''''''''''''''''''''''''Newton-Raphson type WHILE loop used to allow model to
converge on solution (see line 342 for closing statement)
144
145     Y# = 0 '''calculation for variable Y given on line 333 as last entry in SIG-R
matrix
146
147     DIFF# = 1 '''calculation for variable DIFF given on line 330
148
149     Numberofiterations = 0 '''used to display number of iterations during cycles,
see line 336
150
151     WHILE (DIFF# >= 0.1) '''if difference between new and previous result is
greater than unity, the WHILE loop will continue to cycle
152
153     ''''''''''''''''''''''''''calculate PF_WRTETA matrix using ETA-direction force
balance equation
154
155     FOR B = 1 TO DELTA_ETA_INC# + 1
```

```
FOR C = 1 TO DELTA_X_INC# + 1
PF_WRTETA#(C, B) = R# * RHO# * 9.81 * PW_WRTX#(C, B) * SIN(ETA#(C, B)) - A2# * SIG_R#(C, B) * SIN(ETA#(C, B) - NU#) '''ETA-DIRECTION FORCE BALANCE
NEXT
NEXT

''''''''''''''''''''''''''calculate PSIG_R_WRTETA matrix using finite difference method (LH wall uses forward difference, RH wall backward difference, remainder central difference)

FOR C = 1 TO DELTA_X_INC# + 1
PSIG_R_WRTETA#(C, 1) = (SIG_R#(C, 2) - SIG_R#(C, 1)) / DELTA_ETA#
NEXT

FOR P = 2 TO DELTA_ETA_INC#
FOR C = 1 TO DELTA_X_INC# + 1
PSIG_R_WRTETA#(C, P) = (SIG_R#(C, P + 1) - SIG_R#(C, P - 1)) / (2 * DELTA_ETA#)
NEXT
NEXT

FOR C = 1 TO DELTA_X_INC# + 1
PSIG_R_WRTETA#(C, DELTA_ETA_INC# + 1) = (SIG_R#(C, DELTA_ETA_INC# + 1) - SIG_R#(C, DELTA_ETA_INC#)) / DELTA_ETA#
NEXT

''''''''''''''''''''''''''calculate SIG_ETA matrix using F/PW_WRTX with a central boundary condition of Mohr-Coulomb criterion SIG_ETA=J*SIG_R+(J-1)*T

FOR B = 1 TO DELTA_ETA_INC# + 1
FOR C = 1 TO DELTA_X_INC# + 1
SIG_ETA#(C, B) = F#(C, B) / PW_WRTX#(C, B)
NEXT
```

```
NEXT
FOR C = 1 TO DELTA_X_INC# + 1
SIG_ETA#(C, o#) = J# * SIG_R#(C, o#) + (J# - 1) * T#
NEXT

''''''''''''''''''''''''''calculate F matrix using forward and reverse Euler method from central boundary condition of PW_WRTX*SIG_ETA

FOR C = 1 TO DELTA_X_INC# + 1
F#(C, o#) = PW_WRTX#(C, o#) * SIG_ETA#(C, o#)
NEXT
FOR E = o# TO DELTA_ETA_INC#
FOR C = 1 TO DELTA_X_INC# + 1
F#(C, E + 1) = F#(C, E) + PF_WRTETA#(C, E) * DELTA_ETA#
NEXT
NEXT
FOR G = o# TO 2 STEP -1
FOR C = 1 TO DELTA_X_INC# + 1
F#(C, G - 1) = F#(C, G) - PF_WRTETA#(C, G) * DELTA_ETA#
NEXT
NEXT

''''''''''''''''''''''''''calculate PSIG_R_WRTX matrix using R-direction force balance equation

FOR B = 1 TO DELTA_ETA_INC# + 1
FOR C = 1 TO DELTA_X_INC# + 1
PSIG_R_WRTX#(C, B) = F#(C, B) / R# - (COS(ETA#(C, B)) / (R# * SIN(ETA#(C, B)))) * PF_WRTETA#(C, B) - (1 / R#) * (SIG_R#(C, B) * A2# * COS(ETA#(C, B) - NU#) + R# * PSIG_R_WRTETA#(C, B) * PPSI_WRTX#(C, B)) - SIG_R#(C, B) * A2# * SIN(ETA#(C, B) - NU#) * COS(ETA#(C, B)) / (R# * SIN(ETA#(C, B))) - A1# * SIG_R#(C, B) / R# '''R-DIRECTION FORCE BALANCE
NEXT
NEXT
```

```

''''''''''''''''''''''''''calculate SIG_R matrix using reverse Euler method from surface boundary condition of zero

FOR B = 1 TO DELTA_ETA_INC# + 1
SIG_R#(1, B) = 0 ''''silo upper surface
NEXT

FOR B = 1 TO DELTA_ETA_INC# + 1
FOR N = 1 TO DELTA_X_INC#
SIG_R#(N + 1, B) = SIG_R#(N, B) - DELTA_X# * PSIG_R_WRTX#(N, B)
NEXT
NEXT

''''''''''''''''''''''''''various outputs of model variable matrices for testing purposes, recorded in the following comma separated value files:
''ETA.csv
''X.csv
''PSIG_R_WRTX.csv
''F.csv
''SIG_R.csv
''SIG_ETA.csv
''PSIG_R_WRTETA.csv
''PF_WRTETA.csv
''PPSI_WRTX.csv
''PW_WRTX.csv

OPEN "SIG_R.CSV" FOR OUTPUT AS #1
FOR C = 1 TO DELTA_X_INC# + 1
FOR B = 1 TO DELTA_ETA_INC# + 1
WRITE #1, SIG_R#(C, B),
NEXT
WRITE #1, ""
NEXT
```

```
CLOSE #1

OPEN "X.CSV" FOR OUTPUT AS #2
FOR C = 1 TO DELTA_X_INC# + 1
FOR B = 1 TO DELTA_ETA_INC# + 1
WRITE #2, X#(C, B),
NEXT
WRITE #2, ""
NEXT
CLOSE #2

OPEN "ETA.CSV" FOR OUTPUT AS #3
FOR C = 1 TO DELTA_X_INC# + 1
FOR B = 1 TO DELTA_ETA_INC# + 1
WRITE #3, ETA#(C, B),
NEXT
WRITE #3, ""
NEXT
CLOSE #3

OPEN "PW_WRTX.CSV" FOR OUTPUT AS #4
FOR C = 1 TO DELTA_X_INC# + 1
FOR B = 1 TO DELTA_ETA_INC# + 1
WRITE #4, PW_WRTX#(C, B),
NEXT
WRITE #4, ""
NEXT
CLOSE #4

OPEN "SIG_ETA.CSV" FOR OUTPUT AS #5
FOR C = 1 TO DELTA_X_INC# + 1
FOR B = 1 TO DELTA_ETA_INC# + 1
WRITE #5, SIG_ETA#(C, B),
NEXT
```

```
WRITE #5, ""
NEXT
CLOSE #5

OPEN "PSIG_R_WRTX.CSV" FOR OUTPUT AS #6
FOR C = 1 TO DELTA_X_INC# + 1
FOR B = 1 TO DELTA_ETA_INC# + 1
WRITE #6, PSIG_R_WRTX#(C, B),
NEXT
WRITE #6, ""
NEXT
CLOSE #6

OPEN "F.CSV" FOR OUTPUT AS #7
FOR C = 1 TO DELTA_X_INC# + 1
FOR B = 1 TO DELTA_ETA_INC# + 1
WRITE #7, F#(C, B),
NEXT
WRITE #7, ""
NEXT
CLOSE #7

OPEN "PSIG_R_WRTETA.CSV" FOR OUTPUT AS #8
FOR C = 1 TO DELTA_X_INC# + 1
FOR B = 1 TO DELTA_ETA_INC# + 1
WRITE #8, PSIG_R_WRTETA#(C, B),
NEXT
WRITE #8, ""
NEXT
CLOSE #8

OPEN "PF_WRTETA.CSV" FOR OUTPUT AS #9
FOR C = 1 TO DELTA_X_INC# + 1
FOR B = 1 TO DELTA_ETA_INC# + 1
```

```
WRITE #9, PF_WRTETA#(C, B),
NEXT
WRITE #9, ""
NEXT
CLOSE #9

OPEN "PPSI_WRTX.CSV" FOR OUTPUT AS #10
FOR C = 1 TO DELTA_X_INC# + 1
FOR B = 1 TO DELTA_ETA_INC# + 1
WRITE #10, PPSI_WRTX#(C, B),
NEXT
WRITE #10, ""
NEXT
CLOSE #10

SUM# = 0
FOR B = 1 TO DELTA_ETA_INC# + 1
SUM# = SUM# + SIG_R#(DELTA_X_INC# + 1, B) '''sum final row of SIG_R array
NEXT
DIFF# = ABS(SUM# - Y#) '''compare succesive iterations
Y# = 0
FOR B = 1 TO DELTA_ETA_INC# + 1
Y# = Y# + SIG_R#(DELTA_X_INC# + 1, B)
NEXT

Numberofiterations = Numberofiterations + 1 '''display number of iterations
PRINT ""
PRINT "Number of iterations = ",
PRINT Numberofiterations
PRINT ""

IF Numberofiterations = 100 THEN DIFF# = 0.01

```

```
WEND
```

11.2 QBasic algorithm for two-dimensional wedge hopper case

The QBasic program for two-dimensional wedge hopper case is shown below. The algorithm follows the theory introduced in Chapter 4, with similarities to the two-dimensional parallel-sided silo case in Chapter 11.1, with the main addition of use of non-zero α- and a variable R-dimension. The file name for this model is 'Wedge_2D_LM_UN.bas'.

The '*hopper and model geometry data input'* section has been modified to include independent α- and β-angles and η-value, and remove silo diameter S. The '*material data input'* area remains identical to the parallel-sided silo case.

```
'Wedge hopper 2-Dimensional (unequal half-angle)
'Force balance equations in R- and ETA-directions
'Lame-Maxwell version

'James O'Neill 19.09.2010

CLS '''clear all

''''''''''''''''''''''material data input

INPUT "GRANULAR MATERIAL BULK DENSITY =  ", RHO# '''bulk density in kg/m3 (assumed to be constant)

INPUT "WALL FRICTION ANGLE IN DEGREES (phi_w) =  ", phi_w_deg# '''angle of wall friction in degrees

pi# = 4 * ATN(1#) '''value for pi

phi_w# = phi_w_deg# * pi# / 180 '''conversion to radians

INPUT "INTERNAL FRICTION ANGLE IN DEGREES (phi) =  ", phi_deg# '''angle of internal friction/yield locus in degrees
```

```

phi# = phi_deg# * pi# / 180 '''conversion to radians

INPUT "TENSILE PARAMETER Pa =  ", T# '''tensile intercept in Pa

Fc# = 2 * T# * SIN(phi#) / (1 - SIN(phi#)) '''unconfined yield stress in Pa

PRINT "UNCONFINED YIELD STRESS Pa = ",
PRINT Fc#

Co = T# * TAN(phi#) '''cohesion in Pa

PRINT "COHESION Co Pa = ",
PRINT Co
PRINT ""

'''''''''''''''''''hopper and model geometry data input

INPUT "HEIGHT OF UPPER SURFACE (H) METRES =  ", H# '''upper surface height in metres

INPUT "LOCATION OF LOWER BOUNDARY (H2) METRES =  ", H2# '''choose location of lower boundary of model (e.g. cohesive arch across hopper outlet), used to avoid singularity at hopper apex

INPUT "LH WALL HALF ANGLE (ALPHA1) DEGREES =  ", ALPHA1_DEG# '''LH hopper wall half angle in degrees

ALPHA1# = ALPHA1_DEG# * pi# / 180 '''conversion to radians

INPUT "RH WALL HALF ANGLE (ALPHA2) DEGREES =  ", ALPHA2_DEG# '''RH hopper wall half angle in degrees

ALPHA2# = ALPHA2_DEG# * pi# / 180 '''conversion to radians
```

```
BETA_ACTIVE_CALC# = SIN(phi_w#) / SIN(phi#) + phi_w#

BETA_ACTIVE = (180 / pi#) * ATN(BETA_ACTIVE_CALC# / (1 + (1 - BETA_ACTIVE_CALC# ^ 2) ^ 0.5)) '''active BETA-value to be shown on screen in degrees (no built in arcsin function)
PRINT ""
PRINT "LIMITS FOR BETA:"
PRINT "BETA_ACTIVE = ", BETA_ACTIVE

BETA_PASSIVE_CALC# = SIN(phi_w#) / SIN(phi#) - phi_w#

BETA_PASSIVE = (180 / pi#) * ATN(BETA_PASSIVE_CALC# / (1 + (1 - BETA_PASSIVE_CALC# ^ 2) ^ 0.5)) '''active BETA-value to be shown on screen in degrees (no built in arcsin function)
PRINT "BETA_PASSIVE = ", BETA_PASSIVE

INPUT "SELECT LH WALL BETA ANGLE (BETA1) DEGREES =  ", BETA1_DEG# '''selection of angle between principal stress arc and LH wall normal in degrees

BETA1# = BETA1_DEG# * pi# / 180 '''conversion to radians

INPUT "SELECT RH WALL BETA ANGLE (BETA2) DEGREES =  ", BETA2_DEG# '''selection of angle between principal stress arc and RH wall normal in degrees

BETA2# = BETA2_DEG# * pi# / 180 '''conversion to radians

LAMBDA# = (BETA1# + BETA2# + ALPHA1# + ALPHA2#) '''sum of ALPHA and BETA angles in radians

GAMMA# = pi# / 2 - LAMBDA# / 2 '''constant resulting from model geometry in radians
```

```
A1# = SIN(GAMMA#) * SIN(ALPHA1# + ALPHA2#) / (SIN(LAMBDA#) * COS(ALPHA2#) * SIN(GAMMA# + BETA1#)) '''constant resulting from model geometry in radians
A2# = ((1 - A1# * COS(ALPHA2# + BETA2#)) ^ 2 + (TAN(ALPHA2#) - A1# * SIN(ALPHA2# + BETA2#)) ^ 2) ^ 0.5 '''constant resulting from model geometry in radians
NU# = ATN((TAN(ALPHA2#) - A1# * SIN(ALPHA2# + BETA2#)) / (1 - A1# * COS(ALPHA2# + BETA2#))) ''''angle between lines of constant ETA between principal stress arcs
J_ACTIVE = (1 - SIN(phi#)) / (1 + SIN(phi#)) '''active J-value to be shown on screen
PRINT ""
PRINT "J_ACTIVE = ", J_ACTIVE
J_PASSIVE = (1 + SIN(phi#)) / (1 - SIN(phi#)) '''passive J-value to be shown on screen
PRINT "J_PASSIVE = ", J_PASSIVE
INPUT "SELECT J-VALUE, J =  ", J# '''selection of J-value
PRINT ""
INPUT "NUMBER OF X INCREMENTS =  ", DELTA_X_INC# '''choose number of increments in X-direction (e.g. 200 down through hopper)
INPUT "NUMBER OF ETA INCREMENTS (USE EVEN NUMBERS) =   ", DELTA_ETA_INC# '''choose number of increments in ETA-direction (e.g. 50 across hopper)
o# = _ROUND((DELTA_ETA_INC# + 1) / 2) '''centre-line ofhopper (e.g. column 26 in a 51-column matrix)
```

```
DELTA_X# = (H# - H2#) / DELTA_X_INC# '''X-increment size
DELTA_ETA# = LAMBDA# / DELTA_ETA_INC# '''ETA-increment size
DIM X#(DELTA_X_INC# + 1, DELTA_ETA_INC# + 1) '''define and populate a matrix for X, from upper surface (H) to lower boundary (H2) using X-increment as step size
FOR B = 1 TO DELTA_ETA_INC# + 1
X#(1, B) = H#
FOR A = 2 TO DELTA_X_INC# + 1
X#(A, B) = X#(A - 1, B) - DELTA_X#
NEXT
NEXT
DIM ETA#(DELTA_X_INC# + 1, DELTA_ETA_INC# + 1) '''define and populate a matrix for ETA, from left-hand hopper wall to right-hand wall using ETA-increment as step size
FOR C = 1 TO DELTA_X_INC# + 1
ETA#(C, 1) = -(ALPHA1# + BETA1#)
FOR D = 2 TO DELTA_ETA_INC# + 1
ETA#(C, D) = ETA#(C, D - 1) + DELTA_ETA#
NEXT
NEXT
DIM PW_WRTX#(DELTA_X_INC# + 1, DELTA_ETA_INC# + 1) '''define and populate a matrix for model variable PW_WRTX
FOR C = 1 TO DELTA_X_INC# + 1
FOR B = 1 TO DELTA_ETA_INC# + 1
PW_WRTX#(C, B) = A1# + A2# * COS(ETA#(C, B) - NU#)
NEXT
NEXT
```

```
DIM R#(DELTA_X_INC# + 1, DELTA_ETA_INC# + 1) '''define and populate a matrix for (lower) arc radius R
FOR C = 1 TO DELTA_X_INC# + 1
FOR B = 1 TO DELTA_ETA_INC# + 1
R#(C, B) = A1# * X#(C, B)
NEXT
NEXT

DIM PPSI_WRTX#(DELTA_X_INC# + 1, DELTA_ETA_INC# + 1) '''define and populate a matrix for PPSI_WRTX
FOR B = 1 TO DELTA_ETA_INC# + 1
FOR C = 1 TO DELTA_X_INC# + 1
PPSI_WRTX#(C, B) = A2# * SIN(ETA#(C, B) - NU#) / R#(C, B)
NEXT
NEXT

""""""""""""'dimension matrices using X- and ETA-increment information, to allow QBasic to reserve memory space

DIM PF_WRTETA#(DELTA_X_INC# + 1, DELTA_ETA_INC# + 1) '''PSIG_R_WRTX#(row, column)
DIM PSIG_R_WRTETA#(DELTA_X_INC# + 1, DELTA_ETA_INC# + 1)
DIM SIG_ETA#(DELTA_X_INC# + 1, DELTA_ETA_INC# + 1) '''arc stress
DIM F#(DELTA_X_INC# + 1, DELTA_ETA_INC# + 1)
FOR B = 1 TO DELTA_ETA_INC# + 1
FOR C = 1 TO DELTA_X_INC# + 1
F#(C, B) = -2600
NEXT
NEXT
DIM PSIG_R_WRTX#(DELTA_X_INC# + 1, DELTA_ETA_INC# + 1)
DIM SIG_R#(DELTA_X_INC# + 1, DELTA_ETA_INC# + 1) '''radial stress
FOR B = 1 TO DELTA_ETA_INC# + 1
FOR C = 1 TO DELTA_X_INC# + 1
SIG_R#(C, B) = 9600
```

```
153     NEXT
154     NEXT
155
156     ''''''''''''''''''''''''''Newton-Raphson type WHILE loop used to allow model to
converge on solution (see line 365 for closing statement)
157
158     Y# = 0 '''calculation for variable Y given on line 356 as last entry in SIG-R
matrix
159
160     DIFF# = 1 '''calculation for variable DIFF given on line 353
161
162     Numberofiterations = 0 '''used to display number of iterations during cycles,
see line 359
163
164     WHILE (DIFF# >= 0.1) '''if difference between new and previous result is
greater than unity, the WHILE loop will continue to cycle
165
166     '''''''''''''''''''''''''''calculate PF_WRTETA matrix using ETA-direction force
balance equation
167
168     FOR B = 1 TO DELTA_ETA_INC# + 1
169     FOR C = 1 TO DELTA_X_INC# + 1
170     PF_WRTETA#(C, B) = R#(C, B) * RHO# * 9.81 * PW_WRTX#(C, B) *
SIN(ETA#(C, B)) - A2# * SIG_R#(C, B) * SIN(ETA#(C, B) - NU#) '''ETA-
DIRECTION FORCE BALANCE
171     NEXT
172     NEXT
173
174     ''''''''''''''''''''''''''calculate PSIG_R_WRTETA matrix using finite difference
method (LH wall uses forward difference, RH wall backward difference, remainder
central difference)
175
176     FOR C = 1 TO DELTA_X_INC# + 1
177     PSIG_R_WRTETA#(C, 1) = (SIG_R#(C, 2) - SIG_R#(C, 1)) / DELTA_ETA#
```

```
NEXT

FOR P = 2 TO DELTA_ETA_INC#
FOR C = 1 TO DELTA_X_INC# + 1
PSIG_R_WRTETA#(C, P) = (SIG_R#(C, P + 1) - SIG_R#(C, P - 1)) / (2 * DELTA_ETA#)
NEXT
NEXT

FOR C = 1 TO DELTA_X_INC# + 1
PSIG_R_WRTETA#(C, DELTA_ETA_INC# + 1) = (SIG_R#(C, DELTA_ETA_INC# + 1) - SIG_R#(C, DELTA_ETA_INC#)) / DELTA_ETA#
NEXT

''''''''''''''''''''''''''calculate SIG_ETA matrix using F/PW_WRTX with a central boundary condition of Mohr-Coulomb criterion SIG_ETA=J*SIG_R+(J-1)*T

FOR B = 1 TO DELTA_ETA_INC# + 1
FOR C = 1 TO DELTA_X_INC# + 1
SIG_ETA#(C, B) = F#(C, B) / PW_WRTX#(C, B)
NEXT
NEXT
FOR C = 1 TO DELTA_X_INC# + 1
SIG_ETA#(C, o#) = J# * SIG_R#(C, o#) + (J# - 1) * T#
NEXT

''''''''''''''''''''''''''calculate F matrix using forward and reverse Euler method from central boundary condition of PW_WRTX*SIG_ETA

FOR C = 1 TO DELTA_X_INC# + 1
F#(C, o#) = PW_WRTX#(C, o#) * SIG_ETA#(C, o#)
NEXT
FOR E = o# TO DELTA_ETA_INC#
FOR C = 1 TO DELTA_X_INC# + 1
```

```
F#(C, E + 1) = F#(C, E) + PF_WRTETA#(C, E) * DELTA_ETA#
NEXT
NEXT
FOR G = o# TO 2 STEP -1
FOR C = 1 TO DELTA_X_INC# + 1
F#(C, G - 1) = F#(C, G) - PF_WRTETA#(C, G) * DELTA_ETA#
NEXT
NEXT

""""""""""""'calculate PSIG_R_WRTX matrix using R-direction force balance equation

FOR B = 1 TO DELTA_ETA_INC# + 1
FOR C = 1 TO DELTA_X_INC# + 1
PSIG_R_WRTX#(C, B) = F#(C, B) / R#(C, B) - (COS(ETA#(C, B)) / (R#(C, B) * SIN(ETA#(C, B)))) * PF_WRTETA#(C, B) - (1 / R#(C, B)) * (SIG_R#(C, B) * A2# * COS(ETA#(C, B) - NU#) + R#(C, B) * PSIG_R_WRTETA#(C, B) * PPSI_WRTX#(C, B)) - SIG_R#(C, B) * A2# * SIN(ETA#(C, B) - NU#) * COS(ETA#(C, B)) / (R#(C, B) * SIN(ETA#(C, B))) - A1# * SIG_R#(C, B) / R#(C, B) '''R-DIRECTION FORCE BALANCE
NEXT
NEXT

""""""""""""'calculate SIG_R matrix using reverse Euler method from surface boundary condition of zero

FOR B = 1 TO DELTA_ETA_INC# + 1
SIG_R#(1, B) = 0 "'''hopper upper surface
NEXT

FOR B = 1 TO DELTA_ETA_INC# + 1
FOR N = 1 TO DELTA_X_INC#
SIG_R#(N + 1, B) = SIG_R#(N, B) - DELTA_X# * PSIG_R_WRTX#(N, B)
NEXT
```

```
NEXT

''''''''''''''''''''''''''various outputs of model variable matrices for testing purposes, recorded in the following comma separated value files:
'''ETA.csv
'''X.csv
'''R.csv
'''PSIG_R_WRTX.csv
'''F.csv
'''SIG_R.csv
'''SIG_ETA.csv
'''PSIG_R_WRTETA.csv
'''PF_WRTETA.csv
'''PPSI_WRTX.csv
'''PW_WRTX.csv

OPEN "SIG_R.CSV" FOR OUTPUT AS #1
FOR C = 1 TO DELTA_X_INC# + 1
FOR B = 1 TO DELTA_ETA_INC# + 1
WRITE #1, SIG_R#(C, B),
NEXT
WRITE #1, ""
NEXT
CLOSE #1

OPEN "X.CSV" FOR OUTPUT AS #2
FOR C = 1 TO DELTA_X_INC# + 1
FOR B = 1 TO DELTA_ETA_INC# + 1
WRITE #2, X#(C, B),
NEXT
WRITE #2, ""
NEXT
CLOSE #2
```

```
OPEN "R.CSV" FOR OUTPUT AS #3
FOR C = 1 TO DELTA_X_INC# + 1
FOR B = 1 TO DELTA_ETA_INC# + 1
WRITE #3, R#(C, B),
NEXT
WRITE #3, ""
NEXT
CLOSE #3

OPEN "ETA.CSV" FOR OUTPUT AS #4
FOR C = 1 TO DELTA_X_INC# + 1
FOR B = 1 TO DELTA_ETA_INC# + 1
WRITE #4, ETA#(C, B),
NEXT
WRITE #4, ""
NEXT
CLOSE #4

OPEN "PW_WRTX.CSV" FOR OUTPUT AS #5
FOR C = 1 TO DELTA_X_INC# + 1
FOR B = 1 TO DELTA_ETA_INC# + 1
WRITE #5, PW_WRTX#(C, B),
NEXT
WRITE #5, ""
NEXT
CLOSE #5

OPEN "SIG_ETA.CSV" FOR OUTPUT AS #6
FOR C = 1 TO DELTA_X_INC# + 1
FOR B = 1 TO DELTA_ETA_INC# + 1
WRITE #6, SIG_ETA#(C, B),
NEXT
WRITE #6, ""
NEXT
```

```
CLOSE #6

OPEN "PSIG_R_WRTX.CSV" FOR OUTPUT AS #7
FOR C = 1 TO DELTA_X_INC# + 1
FOR B = 1 TO DELTA_ETA_INC# + 1
WRITE #7, PSIG_R_WRTX#(C, B),
NEXT
WRITE #7, ""
NEXT
CLOSE #7

OPEN "F.CSV" FOR OUTPUT AS #8
FOR C = 1 TO DELTA_X_INC# + 1
FOR B = 1 TO DELTA_ETA_INC# + 1
WRITE #8, F#(C, B),
NEXT
WRITE #8, ""
NEXT
CLOSE #8

OPEN "PSIG_R_WRTETA.CSV" FOR OUTPUT AS #9
FOR C = 1 TO DELTA_X_INC# + 1
FOR B = 1 TO DELTA_ETA_INC# + 1
WRITE #9, PSIG_R_WRTETA#(C, B),
NEXT
WRITE #9, ""
NEXT
CLOSE #9

OPEN "PF_WRTETA.CSV" FOR OUTPUT AS #10
FOR C = 1 TO DELTA_X_INC# + 1
FOR B = 1 TO DELTA_ETA_INC# + 1
WRITE #10, PF_WRTETA#(C, B),
NEXT
```

```
WRITE #10, ""
NEXT
CLOSE #10

OPEN "PPSI_WRTX.CSV" FOR OUTPUT AS #11
FOR C = 1 TO DELTA_X_INC# + 1
FOR B = 1 TO DELTA_ETA_INC# + 1
WRITE #11, PPSI_WRTX#(C, B),
NEXT
WRITE #11, ""
NEXT
CLOSE #11

SUM# = 0
FOR B = 1 TO DELTA_ETA_INC# + 1
SUM# = SUM# + SIG_R#(DELTA_X_INC# + 1, B) '''sum final row of SIG_R array
NEXT
DIFF# = ABS(SUM# - Y#) '''compare successive iterations
Y# = 0
FOR B = 1 TO DELTA_ETA_INC# + 1
Y# = Y# + SIG_R#(DELTA_X_INC# + 1, B)
NEXT

Numberofiterations = Numberofiterations + 1 '''count number of iterations
PRINT ""
PRINT "Number of iterations = ",
PRINT Numberofiterations
PRINT ""

IF Numberofiterations = 100 THEN DIFF# = 0.01

WEND
```

11.3 QBasic algorithm for three-dimensional parallel-sided silo case

The QBasic program for three-dimensional parallel-sided silo case is shown below. The model file for this algorithm has file name ‘SILO_3D_LM.bas’. The algorithm follows the theory introduced in Chapter 5, with similarities to the two-dimensional version described in Chapter 11.1. These common features are listed below.

- The location of zero σ_R can be position at the material surface or at the proposed location of a cohesive arch.
- A variable number of increments can be used in the ε-direction.
- A variable number of increments are used in the *x*-direction.
- The use of the Mohr-Coulomb criterion as boundary condition along the centre line of the silo.
- Zero alpha angles are used.
- A constant *R*-dimension is used.

The three-dimensional version of the parallel-sided silo case allows for calculation of azimuthal stress σ_θ making use of equation 62. The algorithm can be modified for use either alternative σ_θ relationships including equations 65 to 68 in Chapter 5.6.1. The ‘*silo and model geometry data input’* section is modified to allow input of a *k*-value.

```
'Parallel-sided Silo 3-Dimensional
'Force balance equations in R- and ETA-directions
'Lame-Maxwell version

'James O'Neill 10.10.2010

CLS '''clear all

''''''''''''''''''''material data input

INPUT "GRANULAR MATERIAL BULK DENSITY =  ", RHO# '''bulk density
in kg/m3 (assumed to be constant)
```

```
INPUT "WALL FRICTION ANGLE IN DEGREES (phi_w) =  ", phi_w_deg# '''angle of wall friction in degrees

pi# = 4 * ATN(1#) '''value for pi

phi_w# = phi_w_deg# * pi# / 180 '''conversion to radians

INPUT "INTERNAL FRICTION ANGLE IN DEGREES (phi) =  ", phi_deg# '''angle of internal friction/yield locus in degrees

phi# = phi_deg# * pi# / 180 '''conversion to radians

INPUT "TENSILE PARAMETER Pa (T) =  ", T# '''tensile intercept in Pa

Fc# = 2 * T# * SIN(phi#) / (1 - SIN(phi#)) '''unconfined yield stress in Pa

PRINT "UNCONFINED YIELD STRESS Pa = ",
PRINT Fc#

Co = T# * TAN(phi#) '''cohesion in Pa

PRINT "COHESION Co Pa = ",
PRINT Co
PRINT ""

'''''''''''''''''''''silo and model geometry data input

INPUT "HEIGHT OF UPPER SURFACE (H) METRES =  ", H# '''upper surface height in metres

INPUT "LOCATION OF LOWER BOUNDARY (H2) METRES =  ", H2# '''choose location of lower boundary of model (e.g. cohesive arch across silo outlet), used to avoid singularity
```

```
INPUT "SILO DIAMETER (S) METRES =  ", S# '''input silo diamter
ALPHA# = 0 '''zero half-angle for silos
BETA_CALC# = SIN(phi_w#) / SIN(phi#)
BETA_ACTIVE = (180 / pi#) * 0.5 * (ATN(BETA_CALC# / (1 - BETA_CALC# ^ 2) ^ 0.5) + phi_w#) '''active BETA-value to be shown on screen in degrees (no built in arcsin function)
PRINT ""
PRINT "LIMITS FOR BETA:"
PRINT "BETA_ACTIVE = ", BETA_ACTIVE
BETA_PASSIVE = (180 / pi#) * 0.5 * (ATN(BETA_CALC# / (1 - BETA_CALC# ^ 2) ^ 0.5) - phi_w#) '''passive BETA-value to be shown on screen in degrees (no built in arcsin function)
PRINT "BETA_PASSIVE = ", BETA_PASSIVE
INPUT "SELECT SILO WALL BETA ANGLE (BETA) DEGREES =  ", BETA_DEG# '''selection of angle between principal stress arc and wall normal in degrees
BETA# = BETA_DEG# * pi# / 180 '''conversion to radians
R# = S# / (SIN(BETA#) + SIN(BETA#)) '''calculate constant principal stress arc radius
LAMBDA# = (BETA# + BETA# + ALPHA# + ALPHA#) '''sum of ALPHA and BETA angles in radians
GAMMA# = pi# / 2 - LAMBDA# / 2 '''constant resulting from model geometry in radians
```

```
A1# = SIN(GAMMA#) * SIN(ALPHA# + ALPHA#) / (SIN(LAMBDA#) * COS(ALPHA#) * SIN(GAMMA# + BETA#)) '''constant resulting from model geometry in radians

A2# = ((1 - A1# * COS(ALPHA# + BETA#)) ^ 2 + (TAN(ALPHA#) - A1# * SIN(ALPHA# + BETA#)) ^ 2) ^ 0.5 '''constant resulting from model geometry in radians

NU# = 0 '''angle between lines of constant ETA between principal stress arcs is zero for silos

J_ACTIVE = (1 - SIN(phi#)) / (1 + SIN(phi#)) '''active J-value to be shown on screen
PRINT ""
PRINT "J_ACTIVE = ", J_ACTIVE

J_PASSIVE = (1 + SIN(phi#)) / (1 - SIN(phi#)) '''passive J-value to be shown on screen
PRINT "J_PASSIVE = ", J_PASSIVE

INPUT "SELECT J-VALUE, J =  ", J# '''selection of J-value

PRINT ""
INPUT "NUMBER OF X INCREMENTS =  ", DELTA_X_INC# '''choose number of increments in X-direction (e.g. 200 down through silo)

INPUT "NUMBER OF ETA INCREMENTS (USE EVEN NUMBERS) =   ", DELTA_ETA_INC# '''choose number of increments in ETA-direction (e.g. 50 across silo)

INPUT "SELECT k-VALUE, k =  ", k# '''selection of k-value

o# = _ROUND((DELTA_ETA_INC# + 1) / 2) '''centre-line of silo (e.g. column 26 in a 51-column matrix)
```

```
DELTA_X# = (H# - H2#) / DELTA_X_INC# '''X-increment size

DELTA_ETA# = LAMBDA# / DELTA_ETA_INC# '''ETA-increment size

DIM X#(DELTA_X_INC# + 1, DELTA_ETA_INC# + 1) '''define and populate a matrix for X, from upper surface (H) to lower boundary (H2) using X-increment as step size
FOR B = 1 TO DELTA_ETA_INC# + 1
X#(1, B) = H#
FOR A = 2 TO DELTA_X_INC# + 1
X#(A, B) = X#(A - 1, B) - DELTA_X#
NEXT
NEXT

DIM ETA#(DELTA_X_INC# + 1, DELTA_ETA_INC# + 1) '''define and populate a matrix for ETA, from left-hand silo wall to right-hand wall using ETA-increment as step size
FOR C = 1 TO DELTA_X_INC# + 1
ETA#(C, 1) = -(ALPHA# + BETA#)
FOR D = 2 TO DELTA_ETA_INC# + 1
ETA#(C, D) = ETA#(C, D - 1) + DELTA_ETA#
NEXT
NEXT

DIM PW_WRTX#(DELTA_X_INC# + 1, DELTA_ETA_INC# + 1) '''define and populate a matrix for model variable PW_WRTX
FOR C = 1 TO DELTA_X_INC# + 1
FOR B = 1 TO DELTA_ETA_INC# + 1
PW_WRTX#(C, B) = A1# + A2# * COS(ETA#(C, B) - NU#)
NEXT
NEXT
```

```
DIM PPSI_WRTX#(DELTA_X_INC# + 1, DELTA_ETA_INC# + 1) '''define and populate a matrix for PPSI_WRTX (not required in calculation method below)
FOR B = 1 TO DELTA_ETA_INC# + 1
FOR C = 1 TO DELTA_X_INC# + 1
PPSI_WRTX#(C, B) = A2# * SIN(ETA#(C, B) - NU#) / R#
NEXT
NEXT

'''''''''''''''''''''''''dimension arrays using X- and ETA-increment information, to allow QBasic to reserve memory space

DIM PF_WRTETA#(DELTA_X_INC# + 1, DELTA_ETA_INC# + 1) '''PSIG_R_WRTX#(row, column)
DIM PSIG_R_WRTETA#(DELTA_X_INC# + 1, DELTA_ETA_INC# + 1)
DIM SIG_ETA#(DELTA_X_INC# + 1, DELTA_ETA_INC# + 1) '''arc stress
DIM F#(DELTA_X_INC# + 1, DELTA_ETA_INC# + 1)
FOR B = 1 TO DELTA_ETA_INC# + 1
FOR C = 1 TO DELTA_X_INC# + 1
F#(C, B) = 1
NEXT
NEXT
DIM PSIG_R_WRTX#(DELTA_X_INC# + 1, DELTA_ETA_INC# + 1)
DIM SIG_R#(DELTA_X_INC# + 1, DELTA_ETA_INC# + 1) '''radial stress
FOR B = 1 TO DELTA_ETA_INC# + 1
FOR C = 1 TO DELTA_X_INC# + 1
SIG_R#(C, B) = 1
NEXT
NEXT
DIM SIG_THETA#(DELTA_X_INC# + 1, DELTA_ETA_INC# + 1) '''azimuthal stress
FOR B = 1 TO DELTA_ETA_INC# + 1
FOR C = 1 TO DELTA_X_INC# + 1
SIG_THETA#(C, B) = 1
NEXT
```

```
147     NEXT
148
149     ''''''''''''''''''''''''''Newton-Raphson type WHILE loop used to allow model to
converge on solution (see line 366 for closing statement)
150
151     Y# = 0 '''calculation for variable Y given on line 357 as last entry in SIG-R
matrix
152
153     DIFF# = 1 '''calculation for variable DIFF given on line 354
154
155     Numberofiterations = 0 '''used to display number of iterations during cycles,
see line 360
156
157     WHILE (DIFF# >= 1) '''if difference between new and previous result is
greater than unity, the WHILE loop will continue to cycle
158
159     '''''''''''''''''''''''''''calculate PF_WRTETA matrix using ETA-direction force
balance equation
160
161     FOR B = 1 TO DELTA_ETA_INC# + 1
162     FOR C = 1 TO DELTA_X_INC# + 1
163     PF_WRTETA#(C, B) = (1 / TAN(ETA#(C, B))) * (-F#(C, B) + PW_WRTX#(C,
B) * SIG_THETA#(C, B)) - SIG_R#(C, B) * A2# * SIN(ETA#(C, B)) + R# *
PW_WRTX#(C, B) * RHO# * 9.81 * SIN(ETA#(C, B)) '''ETA-DIRECTION FORCE
BALANCE
164     NEXT
165     NEXT
166
167     ''''''''''''''''''''''''''calculate PSIG_R_WRTETA matrix using finite difference
method (LH wall uses forward difference, RH wall backward difference, remainder
central difference)
168
169     FOR C = 1 TO DELTA_X_INC# + 1
170     PSIG_R_WRTETA#(C, 1) = (SIG_R#(C, 2) - SIG_R#(C, 1)) / DELTA_ETA#
```

```
NEXT
FOR P = 2 TO DELTA_ETA_INC#
FOR C = 1 TO DELTA_X_INC# + 1
PSIG_R_WRTETA#(C, P) = (SIG_R#(C, P + 1) - SIG_R#(C, P - 1)) / (2 * DELTA_ETA#)
NEXT
NEXT
FOR C = 1 TO DELTA_X_INC# + 1
PSIG_R_WRTETA#(C, DELTA_ETA_INC# + 1) = (SIG_R#(C, DELTA_ETA_INC# + 1) - SIG_R#(C, DELTA_ETA_INC#)) / DELTA_ETA#
NEXT
''''''''''''''''''''''''''calculate SIG_ETA matrix using F/PW_WRTX with a central boundary condition of Mohr-Coulomb criterion SIG_ETA=J*SIG_R+(J-1)*T
FOR B = 1 TO DELTA_ETA_INC# + 1
FOR C = 1 TO DELTA_X_INC# + 1
SIG_ETA#(C, B) = F#(C, B) / PW_WRTX#(C, B)
NEXT
NEXT
FOR C = 1 TO DELTA_X_INC# + 1
SIG_ETA#(C, o#) = J# * SIG_R#(C, o#) + (J# - 1) * T#
NEXT
''''''''''''''''''''''''''calculate F matrix using forward and reverse Euler method from central boundary condition of PW_WRTX*SIG_ETA
FOR C = 1 TO DELTA_X_INC# + 1
F#(C, o#) = PW_WRTX#(C, o#) * SIG_ETA#(C, o#)
NEXT
FOR E = o# TO DELTA_ETA_INC#
FOR C = 1 TO DELTA_X_INC# + 1
```

```
F#(C, E + 1) = F#(C, E) + PF_WRTETA#(C, E) * DELTA_ETA#
NEXT
NEXT
FOR G = o# TO 2 STEP -1
FOR C = 1 TO DELTA_X_INC# + 1
F#(C, G - 1) = F#(C, G) - PF_WRTETA#(C, G) * DELTA_ETA#
NEXT
NEXT

''''''''''''''''''''''''''calculate SIG_THETA matrix using k relationship

FOR B = 1 TO DELTA_ETA_INC# + 1
FOR C = 1 TO DELTA_X_INC# + 1
SIG_THETA#(C, B) = SIG_ETA#(C, B) + k# * SIN(ETA#(C, B)) * SIG_R#(C, B)
NEXT
NEXT

''''''''''''''''''''''''''calculate PSIG_R_WRTX matrix using R-direction force balance equation

FOR B = 1 TO DELTA_ETA_INC# + 1
FOR C = 1 TO DELTA_X_INC# + 1
PSIG_R_WRTX#(C, B) = (F#(C, B)) / R# - (PW_WRTX#(C, B)) * RHO# * 9.81 * COS(ETA#(C, B)) - (2 * SIG_R#(C, B) * A2# * COS(ETA#(C, B))) / R# - (A2# * SIN(ETA#(C, B)) * PSIG_R_WRTETA#(C, B)) / R# + (SIG_THETA#(C, B) * PW_WRTX#(C, B)) / R# - (2 * A1# * SIG_R#(C, B)) / R# '''R-DIRECTION FORCE BALANCE
NEXT
NEXT

''''''''''''''''''''''''''calculate SIG_R matrix using reverse Euler method from surface boundary condition of zero

```

```
FOR B = 1 TO DELTA_ETA_INC# + 1
SIG_R#(1, B) = 0 '''''silo upper surface
NEXT

FOR B = 1 TO DELTA_ETA_INC# + 1
FOR N = 1 TO DELTA_X_INC#
SIG_R#(N + 1, B) = SIG_R#(N, B) - DELTA_X# * PSIG_R_WRTX#(N, B)
NEXT
NEXT

'''''''''''''''''''various outputs of model variable matrices for testing purposes, recorded in the following comma separated value files:
'''ETA.csv
'''X.csv
'''PSIG_R_WRTX.csv
'''F.csv
'''SIG_R.csv
'''SIG_ETA.csv
'''PSIG_R_WRTETA.csv
'''PF_WRTETA.csv
'''PPSI_WRTX.csv
'''PW_WRTX.csv
'''SIG_THETA.csv

OPEN "SIG_R.CSV" FOR OUTPUT AS #1
FOR C = 1 TO DELTA_X_INC# + 1
FOR B = 1 TO DELTA_ETA_INC# + 1
WRITE #1, SIG_R#(C, B),
NEXT
WRITE #1, ""
NEXT
CLOSE #1

OPEN "X.CSV" FOR OUTPUT AS #2
```

```
FOR C = 1 TO DELTA_X_INC# + 1
FOR B = 1 TO DELTA_ETA_INC# + 1
WRITE #2, X#(C, B),
NEXT
WRITE #2, ""
NEXT
CLOSE #2
OPEN "ETA.CSV" FOR OUTPUT AS #3
FOR C = 1 TO DELTA_X_INC# + 1
FOR B = 1 TO DELTA_ETA_INC# + 1
WRITE #3, ETA#(C, B),
NEXT
WRITE #3, ""
NEXT
CLOSE #3
OPEN "PW_WRTX.CSV" FOR OUTPUT AS #4
FOR C = 1 TO DELTA_X_INC# + 1
FOR B = 1 TO DELTA_ETA_INC# + 1
WRITE #4, PW_WRTX#(C, B),
NEXT
WRITE #4, ""
NEXT
CLOSE #4
OPEN "SIG_ETA.CSV" FOR OUTPUT AS #5
FOR C = 1 TO DELTA_X_INC# + 1
FOR B = 1 TO DELTA_ETA_INC# + 1
WRITE #5, SIG_ETA#(C, B),
NEXT
WRITE #5, ""
NEXT
CLOSE #5
```

```

OPEN "PSIG_R_WRTX.CSV" FOR OUTPUT AS #6
FOR C = 1 TO DELTA_X_INC# + 1
FOR B = 1 TO DELTA_ETA_INC# + 1
WRITE #6, PSIG_R_WRTX#(C, B),
NEXT
WRITE #6, ""
NEXT
CLOSE #6

OPEN "F.CSV" FOR OUTPUT AS #7
FOR C = 1 TO DELTA_X_INC# + 1
FOR B = 1 TO DELTA_ETA_INC# + 1
WRITE #7, F#(C, B),
NEXT
WRITE #7, ""
NEXT
CLOSE #7

OPEN "PSIG_R_WRTETA.CSV" FOR OUTPUT AS #8
FOR C = 1 TO DELTA_X_INC# + 1
FOR B = 1 TO DELTA_ETA_INC# + 1
WRITE #8, PSIG_R_WRTETA#(C, B),
NEXT
WRITE #8, ""
NEXT
CLOSE #8

OPEN "PF_WRTETA.CSV" FOR OUTPUT AS #9
FOR C = 1 TO DELTA_X_INC# + 1
FOR B = 1 TO DELTA_ETA_INC# + 1
WRITE #9, PF_WRTETA#(C, B),
NEXT
WRITE #9, ""
```

```
NEXT
CLOSE #9

OPEN "PPSI_WRTX.CSV" FOR OUTPUT AS #10
FOR C = 1 TO DELTA_X_INC# + 1
FOR B = 1 TO DELTA_ETA_INC# + 1
WRITE #10, PPSI_WRTX#(C, B),
NEXT
WRITE #10, ""
NEXT
CLOSE #10

OPEN "SIG_THETA.CSV" FOR OUTPUT AS #11
FOR C = 1 TO DELTA_X_INC# + 1
FOR B = 1 TO DELTA_ETA_INC# + 1
WRITE #11, SIG_THETA#(C, B),
NEXT
WRITE #11, ""
NEXT
CLOSE #11

SUM# = 0
FOR B = 1 TO DELTA_ETA_INC# + 1
SUM# = SUM# + SIG_R#(DELTA_X_INC# + 1, B) '''sum final row of SIG_R arrary
NEXT
DIFF# = ABS(SUM# - Y#) '''compare successive iterations
Y# = 0
FOR B = 1 TO DELTA_ETA_INC# + 1
Y# = Y# + SIG_R#(DELTA_X_INC# + 1, B)
NEXT

Numberofiterations = Numberofiterations + 1 '''count number of iterations
PRINT ""
```

```
PRINT "Number of iterations = ",
PRINT Numberofiterations
PRINT ""

IF Numberofiterations = 100 THEN DIFF# = 0.01

WEND
```

11.4 QBasic algorithm for three-dimensional cone hopper case

The QBasic program for three-dimensional cone hopper case is shown below. The file name for this model is 'CONE_3D_LM.bas'. The algorithm for the cone-hopper case follows the theory introduced in Chapter 5 and is similar to the three-dimensional parallel-sided silo case in Chapter 11.3, with the addition of a single non-zero α angle and a variable R-dimension.

```
'Cone Hopper 3-Dimensional
'Force balance equations in R- and ETA-directions
'Lame-Maxwell version

'James O'Neill 10.10.2010

CLS '''clear all

''''''''''''''''''''''''material data input

INPUT "GRANULAR MATERIAL BULK DENSITY =  ", RHO# '''bulk density in kg/m3 (assumed to be constant)

INPUT "WALL FRICTION ANGLE IN DEGREES (phi_w) =  ", phi_w_deg# '''angle of wall friction in degrees

pi# = 4 * ATN(1#) '''value for pi

phi_w# = phi_w_deg# * pi# / 180 '''conversion to radians

INPUT "INTERNAL FRICTION ANGLE IN DEGREES (phi) =  ", phi_deg# '''angle of internal friction/yield locus in degrees

phi# = phi_deg# * pi# / 180 '''conversion to radians

INPUT "TENSILE PARAMETER Pa (T) =  ", T# '''tensile intercept in Pa
```

```
Fc# = 2 * T# * SIN(phi#) / (1 - SIN(phi#)) '''unconfined yield stress in Pa

PRINT "UNCONFINED YIELD STRESS Pa = ",
PRINT Fc#

Co = T# * TAN(phi#) '''cohesion in Pa

PRINT "COHESION Co Pa = ",
PRINT Co
PRINT ""

'''''''''''''''''''''''''''hopper and model geometry data input

INPUT "HEIGHT OF UPPER SURFACE (H) METRES =  ", H# '''upper surface height in metres

INPUT "LOCATION OF LOWER BOUNDARY (H2) METRES =  ", H2# '''choose location of lower boundary of model (e.g. cohesive arch across hopper outlet), used to avoid singularity at hopper apex

INPUT "HOPPER WALL HALF ANGLE (ALPHA) DEGREES =  ", ALPHA_DEG# '''hopper wall half angle in degrees

ALPHA# = ALPHA_DEG# * pi# / 180 '''conversion to radians

BETA_CALC# = SIN(phi_w#) / SIN(phi#)

BETA_ACTIVE = (180 / pi#) * 0.5 * (ATN(BETA_CALC# / (1 - BETA_CALC# ^ 2) ^ 0.5) + phi_w#) '''active BETA-value to be shown on screen in degrees (no built in arcsin function)
PRINT ""
PRINT "LIMITS FOR BETA:"
PRINT "BETA_ACTIVE = ", BETA_ACTIVE
```

```
BETA_PASSIVE = (180 / pi#) * 0.5 * (ATN(BETA_CALC# / (1 - BETA_CALC# ^ 2) ^ 0.5) - phi_w#) '''passive BETA-value to be shown on screen in degrees (no built in arcsin function)
PRINT "BETA_PASSIVE = ", BETA_PASSIVE

INPUT "SELECT HOPPER WALL BETA ANGLE (BETA) DEGREES =  ", BETA_DEG# '''selection of angle between principal stress arc and wall normal in degrees

BETA# = BETA_DEG# * pi# / 180 '''conversion to radians

LAMBDA# = (BETA# + BETA# + ALPHA# + ALPHA#) '''sum of ALPHA and BETA angles in radians

GAMMA# = pi# / 2 - LAMBDA# / 2 '''constant resulting from model geometry in radians

A1# = SIN(GAMMA#) * SIN(ALPHA# + ALPHA#) / (SIN(LAMBDA#) * COS(ALPHA#) * SIN(GAMMA# + BETA#)) '''constant resulting from model geometry in radians

A2# = ((1 - A1# * COS(ALPHA# + BETA#)) ^ 2 + (TAN(ALPHA#) - A1# * SIN(ALPHA# + BETA#)) ^ 2) ^ 0.5 '''constant resulting from model geometry in radians

NU# = 0 '''angle between lines of constant ETA between principal stress arcs is zero for equal angle hoppers

J_ACTIVE = (1 - SIN(phi#)) / (1 + SIN(phi#)) '''active J-value to be shown on screen
PRINT ""
PRINT "J_ACTIVE = ", J_ACTIVE

```

```
J_PASSIVE = (1 + SIN(phi#)) / (1 - SIN(phi#)) '''passive J-value to be shown on screen
PRINT "J_PASSIVE = ", J_PASSIVE

INPUT "SELECT J-VALUE, J =  ", J# '''selection of J-value

PRINT ""
INPUT "NUMBER OF X INCREMENTS =  ", DELTA_X_INC# '''choose number of increments in X-direction (e.g. 200 down through hopper)

INPUT "NUMBER OF ETA INCREMENTS (USE EVEN NUMBERS) =   ", DELTA_ETA_INC# '''choose number of increments in ETA-direction (e.g. 50 across hopper)

INPUT "SELECT k-VALUE, k =  ", k# '''selection of k-value

o# = _ROUND((DELTA_ETA_INC# + 1) / 2) '''centre-line of hopper (e.g. column 26 in a 51-column matrix)

DELTA_X# = (H# - H2#) / DELTA_X_INC# '''X-increment size

DELTA_ETA# = LAMBDA# / DELTA_ETA_INC# '''ETA-increment size

DIM X#(DELTA_X_INC# + 1, DELTA_ETA_INC# + 1) '''define and populate a matrix for X, from upper surface (H) to lower boundary (H2) using X-increment as step size
FOR B = 1 TO DELTA_ETA_INC# + 1
X#(1, B) = H#
FOR A = 2 TO DELTA_X_INC# + 1
X#(A, B) = X#(A - 1, B) - DELTA_X#
NEXT
NEXT
```

```
DIM ETA#(DELTA_X_INC# + 1, DELTA_ETA_INC# + 1) '''define and populate a matrix for ETA, from left-hand hopper wall to right-hand wall using ETA-increment as step size
FOR C = 1 TO DELTA_X_INC# + 1
ETA#(C, 1) = -(ALPHA# + BETA#)
FOR D = 2 TO DELTA_ETA_INC# + 1
ETA#(C, D) = ETA#(C, D - 1) + DELTA_ETA#
NEXT
NEXT

DIM PW_WRTX#(DELTA_X_INC# + 1, DELTA_ETA_INC# + 1) '''define and populate a matrix for model variable PW_WRTX
FOR C = 1 TO DELTA_X_INC# + 1
FOR B = 1 TO DELTA_ETA_INC# + 1
PW_WRTX#(C, B) = A1# + A2# * COS(ETA#(C, B) - NU#)
NEXT
NEXT

DIM R#(DELTA_X_INC# + 1, DELTA_ETA_INC# + 1) '''define and populate a matrix for (lower) arc radius R
FOR C = 1 TO DELTA_X_INC# + 1
FOR B = 1 TO DELTA_ETA_INC# + 1
R#(C, B) = A1# * X#(C, B)
NEXT
NEXT

DIM PPSI_WRTX#(DELTA_X_INC# + 1, DELTA_ETA_INC# + 1) '''define and populate a matrix for PPSI_WRTX (not required in calculation method below)
FOR B = 1 TO DELTA_ETA_INC# + 1
FOR C = 1 TO DELTA_X_INC# + 1
PPSI_WRTX#(C, B) = A2# * SIN(ETA#(C, B) - NU#) / R#(C, B)
NEXT
NEXT

```

```
129	''''''''''''''''''''dimension arrays using X- and ETA-increment information, to allow QBasic to reserve memory space
130
131	DIM PF_WRTETA#(DELTA_X_INC# + 1, DELTA_ETA_INC# + 1) '''PSIG_R_WRTX#(row, column)
132	DIM PSIG_R_WRTETA#(DELTA_X_INC# + 1, DELTA_ETA_INC# + 1)
133	DIM SIG_ETA#(DELTA_X_INC# + 1, DELTA_ETA_INC# + 1) '''arc stress
134	DIM F#(DELTA_X_INC# + 1, DELTA_ETA_INC# + 1)
135	FOR B = 1 TO DELTA_ETA_INC# + 1
136	FOR C = 1 TO DELTA_X_INC# + 1
137	F#(C, B) = 1
138	NEXT
139	NEXT
140	DIM PSIG_R_WRTX#(DELTA_X_INC# + 1, DELTA_ETA_INC# + 1)
141	DIM SIG_R#(DELTA_X_INC# + 1, DELTA_ETA_INC# + 1) '''radial stress
142	FOR B = 1 TO DELTA_ETA_INC# + 1
143	FOR C = 1 TO DELTA_X_INC# + 1
144	SIG_R#(C, B) = 1
145	NEXT
146	NEXT
147	DIM SIG_THETA#(DELTA_X_INC# + 1, DELTA_ETA_INC# + 1) '''azimuthal stress
148	FOR B = 1 TO DELTA_ETA_INC# + 1
149	FOR C = 1 TO DELTA_X_INC# + 1
150	SIG_THETA#(C, B) = 1
151	NEXT
152	NEXT
153
154	''''''''''''''''''''Newton-Raphson type WHILE loop used to allow model to converge on solution (see line 381 for closing statement)
155
156	Y# = 0 '''calculation for variable Y given on line 372 as last entry in SIG-R matrix
157
```

```
158     DIFF# = 2 '''calculation for variable DIFF given on line 369
159
160     Numberofiterations = 0 '''used to display number of iterations during cycles, see line 375
161
162     WHILE (DIFF# >= 1) '''if difference between new and previous result is greater than unity, the WHILE loop will continue to cycle
163
164     '''''''''''''''''''''''''''calculate PF_WRTETA matrix using ETA-direction force balance equation
165
166     FOR B = 1 TO DELTA_ETA_INC# + 1
167     FOR C = 1 TO DELTA_X_INC# + 1
168     PF_WRTETA#(C, B) = (1 / TAN(ETA#(C, B))) * (-F#(C, B) + PW_WRTX#(C, B) * SIG_THETA#(C, B)) - SIG_R#(C, B) * A2# * SIN(ETA#(C, B)) + R#(C, B) * PW_WRTX#(C, B) * RHO# * 9.81 * SIN(ETA#(C, B)) '''ETA-DIRECTION FORCE BALANCE
169     NEXT
170     NEXT
171
172     ''''''''''''''''''''''''''calculate PSIG_R_WRTETA matrix using finite difference method (LH wall uses forward difference, RH wall backward difference, remainder central difference)
173
174     FOR C = 1 TO DELTA_X_INC# + 1
175     PSIG_R_WRTETA#(C, 1) = (SIG_R#(C, 2) - SIG_R#(C, 1)) / DELTA_ETA#
176     NEXT
177
178     FOR P = 2 TO DELTA_ETA_INC#
179     FOR C = 1 TO DELTA_X_INC# + 1
180     PSIG_R_WRTETA#(C, P) = (SIG_R#(C, P + 1) - SIG_R#(C, P - 1)) / (2 * DELTA_ETA#)
181     NEXT
182     NEXT
```

```

FOR C = 1 TO DELTA_X_INC# + 1
PSIG_R_WRTETA#(C, DELTA_ETA_INC# + 1) = (SIG_R#(C, DELTA_ETA_INC# + 1) - SIG_R#(C, DELTA_ETA_INC#)) / DELTA_ETA#
NEXT

''''''''''''''''''''''''''calculate SIG_ETA matrix using F/PW_WRTX with a central boundary condition of Mohr-Coulomb criterion SIG_ETA=J*SIG_R+(J-1)*T

FOR B = 1 TO DELTA_ETA_INC# + 1
FOR C = 1 TO DELTA_X_INC# + 1
SIG_ETA#(C, B) = F#(C, B) / PW_WRTX#(C, B)
NEXT
NEXT
FOR C = 1 TO DELTA_X_INC# + 1
SIG_ETA#(C, o#) = J# * SIG_R#(C, o#) + (J# - 1) * T#
NEXT

''''''''''''''''''''''''''calculate F matrix using forward and reverse Euler method from central boundary condition of PW_WRTX*SIG_ETA

FOR C = 1 TO DELTA_X_INC# + 1
F#(C, o#) = PW_WRTX#(C, o#) * SIG_ETA#(C, o#)
NEXT
FOR E = o# TO DELTA_ETA_INC#
FOR C = 1 TO DELTA_X_INC# + 1
F#(C, E + 1) = F#(C, E) + PF_WRTETA#(C, E) * DELTA_ETA#
NEXT
NEXT
FOR G = o# TO 2 STEP -1
FOR C = 1 TO DELTA_X_INC# + 1
F#(C, G - 1) = F#(C, G) - PF_WRTETA#(C, G) * DELTA_ETA#
NEXT
NEXT
```

```
'''''''''''''calculate SIG_THETA matrix using k relationship

FOR B = 1 TO DELTA_ETA_INC# + 1
FOR C = 1 TO DELTA_X_INC# + 1
SIG_THETA#(C, B) = SIG_ETA#(C, B) + k# * SIN(ETA#(C, B)) * SIG_R#(C, B)
NEXT
NEXT

'''''''''''''calculate PSIG_R_WRTX matrix using R-direction force balance equation

FOR B = 1 TO DELTA_ETA_INC# + 1
FOR C = 1 TO DELTA_X_INC# + 1
PSIG_R_WRTX#(C, B) = (F#(C, B)) / R#(C, B) - (PW_WRTX#(C, B)) * RHO# * 9.81 * COS(ETA#(C, B)) - (2 * SIG_R#(C, B) * A2# * COS(ETA#(C, B))) / R#(C, B) - (A2# * SIN(ETA#(C, B)) * PSIG_R_WRTETA#(C, B)) / R#(C, B) + (SIG_THETA#(C, B) * PW_WRTX#(C, B)) / R#(C, B) - (2 * A1# * SIG_R#(C, B)) / R#(C, B) '''R-DIRECTION FORCE BALANCE
NEXT
NEXT

'''''''''''''calculate SIG_R matrix using reverse Euler method from surface boundary condition of zero

FOR B = 1 TO DELTA_ETA_INC# + 1
SIG_R#(1, B) = 0 '''''hopper upper surface
NEXT

FOR B = 1 TO DELTA_ETA_INC# + 1
FOR N = 1 TO DELTA_X_INC#
SIG_R#(N + 1, B) = SIG_R#(N, B) - DELTA_X# * PSIG_R_WRTX#(N, B)
NEXT
```

```
NEXT

''''''''''''''''''''''''''various outputs of model variable matrices for testing purposes, recorded in the following comma separated value files:
'''ETA.csv
'''X.csv
'''PSIG_R_WRTX.csv
'''F.csv
'''SIG_R.csv
'''SIG_ETA.csv
'''PSIG_R_WRTETA.csv
'''PF_WRTETA.csv
'''PPSI_WRTX.csv
'''PW_WRTX.csv
'''SIG_THETA.csv
'''R.csv

OPEN "SIG_R.CSV" FOR OUTPUT AS #1
FOR C = 1 TO DELTA_X_INC# + 1
FOR B = 1 TO DELTA_ETA_INC# + 1
WRITE #1, SIG_R#(C, B),
NEXT
WRITE #1, ""
NEXT
CLOSE #1

OPEN "X.CSV" FOR OUTPUT AS #2
FOR C = 1 TO DELTA_X_INC# + 1
FOR B = 1 TO DELTA_ETA_INC# + 1
WRITE #2, X#(C, B),
NEXT
WRITE #2, ""
NEXT
CLOSE #2
```

```
OPEN "ETA.CSV" FOR OUTPUT AS #3
FOR C = 1 TO DELTA_X_INC# + 1
FOR B = 1 TO DELTA_ETA_INC# + 1
WRITE #3, ETA#(C, B),
NEXT
WRITE #3, ""
NEXT
CLOSE #3

OPEN "PW_WRTX.CSV" FOR OUTPUT AS #4
FOR C = 1 TO DELTA_X_INC# + 1
FOR B = 1 TO DELTA_ETA_INC# + 1
WRITE #4, PW_WRTX#(C, B),
NEXT
WRITE #4, ""
NEXT
CLOSE #4

OPEN "SIG_ETA.CSV" FOR OUTPUT AS #5
FOR C = 1 TO DELTA_X_INC# + 1
FOR B = 1 TO DELTA_ETA_INC# + 1
WRITE #5, SIG_ETA#(C, B),
NEXT
WRITE #5, ""
NEXT
CLOSE #5

OPEN "PSIG_R_WRTX.CSV" FOR OUTPUT AS #6
FOR C = 1 TO DELTA_X_INC# + 1
FOR B = 1 TO DELTA_ETA_INC# + 1
WRITE #6, PSIG_R_WRTX#(C, B),
NEXT
WRITE #6, ""
```

```
NEXT
CLOSE #6

OPEN "F.CSV" FOR OUTPUT AS #7
FOR C = 1 TO DELTA_X_INC# + 1
FOR B = 1 TO DELTA_ETA_INC# + 1
WRITE #7, F#(C, B),
NEXT
WRITE #7, ""
NEXT
CLOSE #7

OPEN "PSIG_R_WRTETA.CSV" FOR OUTPUT AS #8
FOR C = 1 TO DELTA_X_INC# + 1
FOR B = 1 TO DELTA_ETA_INC# + 1
WRITE #8, PSIG_R_WRTETA#(C, B),
NEXT
WRITE #8, ""
NEXT
CLOSE #8

OPEN "PF_WRTETA.CSV" FOR OUTPUT AS #9
FOR C = 1 TO DELTA_X_INC# + 1
FOR B = 1 TO DELTA_ETA_INC# + 1
WRITE #9, PF_WRTETA#(C, B),
NEXT
WRITE #9, ""
NEXT
CLOSE #9

OPEN "PPSI_WRTX.CSV" FOR OUTPUT AS #10
FOR C = 1 TO DELTA_X_INC# + 1
FOR B = 1 TO DELTA_ETA_INC# + 1
WRITE #10, PPSI_WRTX#(C, B),
```

```
NEXT
WRITE #10, ""
NEXT
CLOSE #10
OPEN "SIG_THETA.CSV" FOR OUTPUT AS #11
FOR C = 1 TO DELTA_X_INC# + 1
FOR B = 1 TO DELTA_ETA_INC# + 1
WRITE #11, SIG_THETA#(C, B),
NEXT
WRITE #11, ""
NEXT
CLOSE #11
OPEN "R.CSV" FOR OUTPUT AS #12
FOR C = 1 TO DELTA_X_INC# + 1
FOR B = 1 TO DELTA_ETA_INC# + 1
WRITE #12, R#(C, B),
NEXT
WRITE #12, ""
NEXT
CLOSE #12
SUM# = 0
FOR B = 1 TO DELTA_ETA_INC# + 1
SUM# = SUM# + SIG_R#(DELTA_X_INC# + 1, B) '''sum final row of SIG_R arrary
NEXT
DIFF# = ABS(SUM# - Y#) '''compare successive iterations
Y# = 0
FOR B = 1 TO DELTA_ETA_INC# + 1
Y# = Y# + SIG_R#(DELTA_X_INC# + 1, B)
NEXT
```

```
Numberofiterations = Numberofiterations + 1 '''count number of iterations
PRINT ""
PRINT "Number of iterations = ",
PRINT Numberofiterations
PRINT ""

IF Numberofiterations = 100 THEN DIFF# = 0.01

WEND
```

11.5 QBasic algorithm for three-dimensional cone hopper with conical insert case

The QBasic program for the three-dimensional cone hopper with conical insert case is shown below. The file name for this model is 'CINSERT_3D_LM.bas'. The algorithm for the conical insert case follows the theory introduced in Chapter 6. The model is based on the cone hopper case with the addition of an insert angle Θ.

```
'Cone Hopper with conical insert 3-Dimensional
'Force balance equations in R- and ETA-directions
'Lame-Maxwell version

'James O'Neill 24.11.2010

CLS '''clear all

''''''''''''''''''''material data input

INPUT "GRANULAR MATERIAL BULK DENSITY =  ", RHO# '''bulk density in kg/m3 (assumed to be constant)

INPUT "WALL FRICTION ANGLE IN DEGREES (phi_w) =  ", phi_w_deg# '''angle of wall friction in degrees

pi# = 4 * ATN(1#) '''value for pi

phi_w# = phi_w_deg# * pi# / 180 '''conversion to radians

INPUT "INTERNAL FRICTION ANGLE IN DEGREES (phi) =  ", phi_deg# '''angle of internal friction/yield locus in degrees

phi# = phi_deg# * pi# / 180 '''conversion to radians

INPUT "TENSILE PARAMETER Pa (T) =  ", T# '''tensile intercept in Pa

```

```
Fc# = 2 * T# * SIN(phi#) / (1 - SIN(phi#)) '''unconfined yield stress in Pa

PRINT "UNCONFINED YIELD STRESS Pa = ",
PRINT Fc#

Co = T# * TAN(phi#) '''cohesion in Pa

PRINT "COHESION Co Pa = ",
PRINT Co
PRINT ""

'''''''''''''''''''''hopper and model geometry data input

INPUT "HEIGHT OF UPPER SURFACE (H) METRES =  ", H# '''upper surface height in metres

INPUT "LOCATION OF LOWER BOUNDARY (H2) METRES =  ", H2# '''choose location of lower boundary of model (e.g. cohesive arch across hopper outlet), used to avoid singularity at hopper apex

INPUT "HOPPER WALL HALF ANGLE (ALPHA) DEGREES =  ", ALPHA_DEG# '''hopper wall half angle in degrees

ALPHA# = ALPHA_DEG# * pi# / 180 '''conversion to radians

BETA_CALC# = SIN(phi_w#) / SIN(phi#)

BETA_ACTIVE = (180 / pi#) * 0.5 * (ATN(BETA_CALC# / (1 - BETA_CALC# ^ 2) ^ 0.5) + phi_w#) '''active BETA-value to be shown on screen in degrees (no built in arcsin function)
PRINT ""
PRINT "LIMITS FOR BETA:"
PRINT "BETA_ACTIVE = ", BETA_ACTIVE

```

```
BETA_PASSIVE = (180 / pi#) * 0.5 * (ATN(BETA_CALC# / (1 - BETA_CALC# ^ 2) ^ 0.5) - phi_w#) '''passive BETA-value to be shown on screen in degrees (no built in arcsin function)
PRINT "BETA_PASSIVE = ", BETA_PASSIVE

INPUT "SELECT HOPPER WALL BETA ANGLE (BETA) DEGREES =  ", BETA_DEG# '''selection of angle between principal stress arc and wall normal in degrees

BETA# = BETA_DEG# * pi# / 180 '''conversion to radians
PRINT ""
INPUT "SELECT INSERT HALF ANGLE (THETA) DEGREES = ", THETA_DEG# '''selection of conical insert half angle

THETA# = THETA_DEG# * pi# / 180 '''conversion to radians

LAMBDA# = (BETA# + BETA# + ALPHA# + ALPHA#) '''sum of ALPHA and BETA angles in radians

GAMMA# = pi# / 2 - LAMBDA# / 2 '''constant resulting from model geometry in radians

A1# = SIN(GAMMA#) * SIN(ALPHA# + ALPHA#) / (SIN(LAMBDA#) * COS(ALPHA# + THETA#) * SIN(GAMMA# + BETA#)) '''constant resulting from model geometry in radians

A2# = ((1 - A1# * COS(ALPHA# + BETA#)) ^ 2 + (TAN(ALPHA#) - A1# * SIN(ALPHA# + BETA#)) ^ 2) ^ 0.5 '''constant resulting from model geometry in radians

NU# = 0 '''angle between lines of constant ETA between principal stress arcs is zero for equal angle hoppers

```

```
J_ACTIVE = (1 - SIN(phi#)) / (1 + SIN(phi#)) '''active J-value to be shown on screen
PRINT ""
PRINT "J_ACTIVE = ", J_ACTIVE

J_PASSIVE = (1 + SIN(phi#)) / (1 - SIN(phi#)) '''passive J-value to be shown on screen
PRINT "J_PASSIVE = ", J_PASSIVE

INPUT "SELECT J-VALUE, J =  ", J# '''selection of J-value

PRINT ""
INPUT "NUMBER OF X INCREMENTS =  ", DELTA_X_INC# '''choose number of increments in X-direction (e.g. 200 down through hopper)

INPUT "NUMBER OF ETA INCREMENTS (USE EVEN NUMBERS) =   ", DELTA_ETA_INC# '''choose number of increments in ETA-direction (e.g. 50 across hopper)

INPUT "SELECT k-VALUE, k =  ", k# '''selection of k-value

o# = _ROUND((DELTA_ETA_INC# + 1) / 2) '''centre-line of hopper (e.g. column 26 in a 51-column matrix)

DELTA_X# = (H# - H2#) / DELTA_X_INC# '''X-increment size

DELTA_ETA# = LAMBDA# / DELTA_ETA_INC# '''ETA-increment size

DIM X#(DELTA_X_INC# + 1, DELTA_ETA_INC# + 1) '''define and populate a matrix for X, from upper surface (H) to lower boundary (H2) using X-increment as step size
FOR B = 1 TO DELTA_ETA_INC# + 1
X#(1, B) = H#
FOR A = 2 TO DELTA_X_INC# + 1
```

```
X#(A, B) = X#(A - 1, B) - DELTA_X#
NEXT
NEXT

DIM ETA#(DELTA_X_INC# + 1, DELTA_ETA_INC# + 1) '''define and populate a matrix for ETA, from left-hand hopper wall to right-hand wall using ETA-increment as step size
FOR C = 1 TO DELTA_X_INC# + 1
ETA#(C, 1) = -(ALPHA# + BETA#)
FOR D = 2 TO DELTA_ETA_INC# + 1
ETA#(C, D) = ETA#(C, D - 1) + DELTA_ETA#
NEXT
NEXT

DIM PW_WRTX#(DELTA_X_INC# + 1, DELTA_ETA_INC# + 1) '''define and populate a matrix for model variable PW_WRTX
FOR C = 1 TO DELTA_X_INC# + 1
FOR B = 1 TO DELTA_ETA_INC# + 1
PW_WRTX#(C, B) = A1# + A2# * COS(ETA#(C, B) - NU# + THETA#)
NEXT
NEXT

DIM R#(DELTA_X_INC# + 1, DELTA_ETA_INC# + 1) '''define and populate a matrix for (lower) arc radius R
FOR C = 1 TO DELTA_X_INC# + 1
FOR B = 1 TO DELTA_ETA_INC# + 1
R#(C, B) = A1# * X#(C, B)
NEXT
NEXT

DIM PPSI_WRTX#(DELTA_X_INC# + 1, DELTA_ETA_INC# + 1) '''define and populate a matrix for PPSI_WRTX (not required in calculation method below)
FOR B = 1 TO DELTA_ETA_INC# + 1
FOR C = 1 TO DELTA_X_INC# + 1
```

```
PPSI_WRTX#(C, B) = A2# * (COS(ETA#(C, B) - THETA#) * SIN(ETA#(C, B)) - SIN(THETA#)) / (R#(C, B) * COS(ETA#(C, B)))
NEXT
NEXT

''''''''''''''''''''''''''dimension arrays using X- and ETA-increment information, to allow QBasic to reserve memory space

DIM PF_WRTETA#(DELTA_X_INC# + 1, DELTA_ETA_INC# + 1) '''PSIG_R_WRTX#(row, column)
DIM PSIG_R_WRTETA#(DELTA_X_INC# + 1, DELTA_ETA_INC# + 1)
DIM SIG_ETA#(DELTA_X_INC# + 1, DELTA_ETA_INC# + 1) '''arc stress
DIM F#(DELTA_X_INC# + 1, DELTA_ETA_INC# + 1)
FOR B = 1 TO DELTA_ETA_INC# + 1
FOR C = 1 TO DELTA_X_INC# + 1
F#(C, B) = 1
NEXT
NEXT
DIM PSIG_R_WRTX#(DELTA_X_INC# + 1, DELTA_ETA_INC# + 1)
DIM SIG_R#(DELTA_X_INC# + 1, DELTA_ETA_INC# + 1) '''radial stress
FOR B = 1 TO DELTA_ETA_INC# + 1
FOR C = 1 TO DELTA_X_INC# + 1
SIG_R#(C, B) = 1
NEXT
NEXT
DIM SIG_THETA#(DELTA_X_INC# + 1, DELTA_ETA_INC# + 1) '''azimuthal stress
FOR B = 1 TO DELTA_ETA_INC# + 1
FOR C = 1 TO DELTA_X_INC# + 1
SIG_THETA#(C, B) = 1
NEXT
NEXT

```

```
158 ''''''''''''''''''Newton-Raphson type WHILE loop used to allow model to converge on solution (see line 381 for closing statement)
159
160 Y# = 0 '''calculation for variable Y given on line 372 as last entry in SIG-R matrix
161
162 DIFF# = 2 '''calculation for variable DIFF given on line 369
163
164 Numberofiterations = 0 '''used to display number of iterations during cycles, see line 375
165
166 WHILE (DIFF# >= 1) '''if difference between new and previous result is greater than unity, the WHILE loop will continue to cycle
167
168 ''''''''''''''''''''calculate PF_WRTETA matrix using ETA-direction force balance equation
169
170 FOR B = 1 TO DELTA_ETA_INC# + 1
171 FOR C = 1 TO DELTA_X_INC# + 1
172 PF_WRTETA#(C, B) = (-F#(C, B) * (COS(2 * ETA#(C, B)) / COS(ETA#(C, B)) ^ 2 - (SIN(ETA#(C, B)) / COS(ETA#(C, B)) ^ 2) * SIN(BETA#) * SIN(THETA#) / SIN(ALPHA#) + COS(2 * ETA#(C, B)) / SIN(ETA#(C, B)) - SIN(BETA#) * SIN(THETA#) / SIN(ALPHA#)) - SIG_R#(C, B) * A2# * SIN(ETA#(C, B) - THETA#) * ((SIN(ETA#(C, B)) / COS(ETA#(C, B))) * SIN(BETA#) * SIN(THETA#) / SIN(ALPHA#) - COS(2 * ETA#(C, B)) / COS(ETA#(C, B)) + 2 * COS(ETA#(C, B)) + (COS(ETA#(C, B)) / SIN(ETA#(C, B))) * SIN(BETA#) * SIN(THETA#) / SIN(ALPHA#)) + R#(C, B) * PW_WRTX#(C, B) * RHO# * 9.81 * (SIN(BETA#) * SIN(THETA#) / SIN(ALPHA#) + SIN(ETA#(C, B))) / COS(ETA#(C, B)) + PW_WRTX#(C, B) * SIG_THETA# / SIN(ETA#(C, B))) / (SIN(BETA#) * SIN(THETA#) / SIN(ALPHA#) + F#(C, B) * SIN(2 * ETA#(C, B)) / (2 * COS(ETA#(C, B))) + (COS(ETA#(C, B)) / SIN(ETA#(C, B))) * SIN(BETA#) * SIN(THETA#) / SIN(ALPHA#) + SIN(2 * ETA#(C, B)) / (2 * SIN(ETA#(C, B)))) '''ETA-DIRECTION FORCE BALANCE
173 NEXT
```

```
NEXT

''''''''''''''''''''''''''calculate PSIG_R_WRTETA matrix using finite difference method (LH wall uses forward difference, RH wall backward difference, remainder central difference)

FOR C = 1 TO DELTA_X_INC# + 1
PSIG_R_WRTETA#(C, 1) = (SIG_R#(C, 2) - SIG_R#(C, 1)) / DELTA_ETA#
NEXT

FOR P = 2 TO DELTA_ETA_INC#
FOR C = 1 TO DELTA_X_INC# + 1
PSIG_R_WRTETA#(C, P) = (SIG_R#(C, P + 1) - SIG_R#(C, P - 1)) / (2 * DELTA_ETA#)
NEXT
NEXT

FOR C = 1 TO DELTA_X_INC# + 1
PSIG_R_WRTETA#(C, DELTA_ETA_INC# + 1) = (SIG_R#(C, DELTA_ETA_INC# + 1) - SIG_R#(C, DELTA_ETA_INC#)) / DELTA_ETA#
NEXT

''''''''''''''''''''''''''calculate SIG_ETA matrix using F/PW_WRTX with a central boundary condition of Mohr-Coulomb criterion SIG_ETA=J*SIG_R+(J-1)*T

FOR B = 1 TO DELTA_ETA_INC# + 1
FOR C = 1 TO DELTA_X_INC# + 1
SIG_ETA#(C, B) = F#(C, B) / PW_WRTX#(C, B)
NEXT
NEXT
FOR C = 1 TO DELTA_X_INC# + 1
SIG_ETA#(C, o#) = J# * SIG_R#(C, o#) + (J# - 1) * T#
NEXT
```

```
''''''''''''''''''''calculate F matrix using forward and reverse Euler method from central boundary condition of PW_WRTX*SIG_ETA

FOR C = 1 TO DELTA_X_INC# + 1
F#(C, o#) = PW_WRTX#(C, o#) * SIG_ETA#(C, o#)
NEXT
FOR E = o# TO DELTA_ETA_INC#
FOR C = 1 TO DELTA_X_INC# + 1
F#(C, E + 1) = F#(C, E) + PF_WRTETA#(C, E) * DELTA_ETA#
NEXT
NEXT
FOR G = o# TO 2 STEP -1
FOR C = 1 TO DELTA_X_INC# + 1
F#(C, G - 1) = F#(C, G) - PF_WRTETA#(C, G) * DELTA_ETA#
NEXT
NEXT

''''''''''''''''''''calculate SIG_THETA matrix using k relationship

FOR B = 1 TO DELTA_ETA_INC# + 1
FOR C = 1 TO DELTA_X_INC# + 1
SIG_THETA#(C, B) = SIG_ETA#(C, B) + k# * SIN(ETA#(C, B)) * SIG_R#(C, B)
NEXT
NEXT

''''''''''''''''''''calculate PSIG_R_WRTX matrix using R-direction force balance equation

FOR B = 1 TO DELTA_ETA_INC# + 1
FOR C = 1 TO DELTA_X_INC# + 1
PSIG_R_WRTX#(C, B) = -((COS(ETA#(C, B)) / SIN(ETA#(C, B))) * SIN(BETA#) * SIN(THETA#) / SIN(ALPHA#) + SIN(2 * ETA#(C, B)) / (2 * SIN(ETA#(C, B)))) * (-F#(C, B) * (COS(2 * ETA#(C, B)) / COS(ETA#(C, B)) ^ 2 -
```

```
(SIN(ETA#(C, B)) / COS(ETA#(C, B)) ^ 2) * SIN(BETA#) * SIN(THETA#) /
SIN(ALPHA#) + COS(2 * ETA#(C, B)) / SIN(ETA#(C, B)) - SIN(BETA#) *
SIN(THETA#) / SIN(ALPHA#)) - SIG_R#(C, B) * A2# * SIN(ETA#(C, B) - THETA#)
* ((SIN(ETA#(C, B)) / COS(ETA#(C, B))) * SIN(BETA#) * SIN(THETA#) /
SIN(ALPHA#) - COS(2 * ETA#(C, B)) / COS(ETA#(C, B)) + 2 * COS(ETA#(C, B)) +
(COS(ETA#(C, B)) / SIN(ETA#(C, B))) * SIN(BETA#) * SIN(THETA#) /
SIN(ALPHA#)) + R#(C, B) * PW_WRTX#(C, B) * RHO# * 9.81 * (SIN(BETA#) *
SIN(THETA#) / SIN(ALPHA#) + SIN(ETA#(C, B))) / COS(ETA#(C, B)) +
PW_WRTX#(C, B) * SIG_THETA#(C, B) / SIN(ETA#(C, B))) / (R#(C, B) *
(SIN(BETA#) * SIN(THETA#) / SIN(ALPHA#) + F#(C, B) * SIN(2 * ETA#(C, B)) / (2
* COS(ETA#(C, B))) + (COS(ETA#(C, B)) / SIN(ETA#(C, B))) * SIN(BETA#) *
SIN(THETA#) / SIN(ALPHA#) + SIN(2 * ETA#(C, B)) / (2 * SIN(ETA#(C, B)))) *
(SIN(BETA#) * SIN(THETA#) / SIN(ALPHA#) + SIN(ETA#(C, B)))) - (F#(C, B) /
(R#(C, B) * (SIN(BETA#) * SIN(THETA#) / SIN(ALPHA#) + SIN(ETA#(C, B))))) *
(COS(2 * ETA#(C, B)) / SIN(ETA#(C, B)) - SIN(BETA#) * SIN(THETA#) /
SIN(ALPHA#)) - SIG_R#(C, B) * A2# * SIN(ETA#(C, B) - THETA#) * (SIN(ETA#(C,
B)) + 2 * COS(ETA#(C, B)) * SIN(ETA#(C, B)) + COS(ETA#(C, B)) * SIN(BETA#) *
SIN(THETA#) / SIN(ALPHA#)) / ((SIN(BETA#) * SIN(THETA#) / SIN(ALPHA#) +
SIN(ETA#(C, B))) * R#(C, B) * SIN(ETA#(C, B))) - SIN(ETA#(C, B)) *
PSIG_R_WRTETA#(C, B) * (A2# * (COS(ETA#(C, B) - THETA#) * SIN(ETA#(C, B))
- SIN(THETA#)) / (R#(C, B) * COS(ETA#(C, B)))) / (SIN(BETA#) * SIN(THETA#) /
SIN(ALPHA#) + SIN(ETA#(C, B))) - SIG_R#(C, B) * A2# * SIN(ETA#(C, B) -
THETA#) / R#(C, B) + PW_WRTX#(C, B) * SIG_THETA#(C, B) / ((SIN(BETA#) *
SIN(THETA#) / SIN(ALPHA#) + SIN(ETA#(C, B))) * R#(C, B) * SIN(ETA#(C, B))) -
A2# * 2 * SIG_R#(C, B) / R#(C, B) '''R-DIRECTION FORCE BALANCE
NEXT
NEXT

''''''''''''''''''''''calculate SIG_R matrix using reverse Euler method from surface
boundary condition of zero

FOR B = 1 TO DELTA_ETA_INC# + 1
SIG_R#(1, B) = 0 '''''hopper upper surface
NEXT
```

```

FOR B = 1 TO DELTA_ETA_INC# + 1
FOR N = 1 TO DELTA_X_INC#
SIG_R#(N + 1, B) = SIG_R#(N, B) - DELTA_X# * PSIG_R_WRTX#(N, B)
NEXT
NEXT

''''''''''''''''''''''''''various outputs of model variable matrices for testing purposes, recorded in the following comma separated value files:
''ETA.csv
''X.csv
''PSIG_R_WRTX.csv
''F.csv
''SIG_R.csv
''SIG_ETA.csv
''PSIG_R_WRTETA.csv
''PF_WRTETA.csv
''PPSI_WRTX.csv
''PW_WRTX.csv
''SIG_THETA.csv
''R.csv

OPEN "SIG_R.CSV" FOR OUTPUT AS #1
FOR C = 1 TO DELTA_X_INC# + 1
FOR B = 1 TO DELTA_ETA_INC# + 1
WRITE #1, SIG_R#(C, B),
NEXT
WRITE #1, ""
NEXT
CLOSE #1

OPEN "X.CSV" FOR OUTPUT AS #2
FOR C = 1 TO DELTA_X_INC# + 1
FOR B = 1 TO DELTA_ETA_INC# + 1
```

```
WRITE #2, X#(C, B),
NEXT
WRITE #2, ""
NEXT
CLOSE #2
OPEN "ETA.CSV" FOR OUTPUT AS #3
FOR C = 1 TO DELTA_X_INC# + 1
FOR B = 1 TO DELTA_ETA_INC# + 1
WRITE #3, ETA#(C, B),
NEXT
WRITE #3, ""
NEXT
CLOSE #3
OPEN "PW_WRTX.CSV" FOR OUTPUT AS #4
FOR C = 1 TO DELTA_X_INC# + 1
FOR B = 1 TO DELTA_ETA_INC# + 1
WRITE #4, PW_WRTX#(C, B),
NEXT
WRITE #4, ""
NEXT
CLOSE #4
OPEN "SIG_ETA.CSV" FOR OUTPUT AS #5
FOR C = 1 TO DELTA_X_INC# + 1
FOR B = 1 TO DELTA_ETA_INC# + 1
WRITE #5, SIG_ETA#(C, B),
NEXT
WRITE #5, ""
NEXT
CLOSE #5
OPEN "PSIG_R_WRTX.CSV" FOR OUTPUT AS #6
```

```
FOR C = 1 TO DELTA_X_INC# + 1
FOR B = 1 TO DELTA_ETA_INC# + 1
WRITE #6, PSIG_R_WRTX#(C, B),
NEXT
WRITE #6, ""
NEXT
CLOSE #6

OPEN "F.CSV" FOR OUTPUT AS #7
FOR C = 1 TO DELTA_X_INC# + 1
FOR B = 1 TO DELTA_ETA_INC# + 1
WRITE #7, F#(C, B),
NEXT
WRITE #7, ""
NEXT
CLOSE #7

OPEN "PSIG_R_WRTETA.CSV" FOR OUTPUT AS #8
FOR C = 1 TO DELTA_X_INC# + 1
FOR B = 1 TO DELTA_ETA_INC# + 1
WRITE #8, PSIG_R_WRTETA#(C, B),
NEXT
WRITE #8, ""
NEXT
CLOSE #8

OPEN "PF_WRTETA.CSV" FOR OUTPUT AS #9
FOR C = 1 TO DELTA_X_INC# + 1
FOR B = 1 TO DELTA_ETA_INC# + 1
WRITE #9, PF_WRTETA#(C, B),
NEXT
WRITE #9, ""
NEXT
CLOSE #9
```

```
OPEN "PPSI_WRTX.CSV" FOR OUTPUT AS #10
FOR C = 1 TO DELTA_X_INC# + 1
FOR B = 1 TO DELTA_ETA_INC# + 1
WRITE #10, PPSI_WRTX#(C, B),
NEXT
WRITE #10, ""
NEXT
CLOSE #10

OPEN "SIG_THETA.CSV" FOR OUTPUT AS #11
FOR C = 1 TO DELTA_X_INC# + 1
FOR B = 1 TO DELTA_ETA_INC# + 1
WRITE #11, SIG_THETA#(C, B),
NEXT
WRITE #11, ""
NEXT
CLOSE #11

OPEN "R.CSV" FOR OUTPUT AS #12
FOR C = 1 TO DELTA_X_INC# + 1
FOR B = 1 TO DELTA_ETA_INC# + 1
WRITE #12, R#(C, B),
NEXT
WRITE #12, ""
NEXT
CLOSE #12

SUM# = 0
FOR B = 1 TO DELTA_ETA_INC# + 1
SUM# = SUM# + SIG_R#(DELTA_X_INC# + 1, B) '''sum final row of SIG_R arrary
NEXT
DIFF# = ABS(SUM# - Y#) '''compare successive iterations
```

```
Y# = 0
FOR B = 1 TO DELTA_ETA_INC# + 1
Y# = Y# + SIG_R#(DELTA_X_INC# + 1, B)
NEXT
Numberofiterations = Numberofiterations + 1 '''count number of iterations
PRINT ""
PRINT "Number of iterations = ",
PRINT Numberofiterations
PRINT ""
IF Numberofiterations = 100 THEN DIFF# = 0.01
WEND
```

11.6 QBasic algorithm for three-dimensional cone hopper with conical rat hole case

The QBasic program for the three-dimensional cone hopper with conical rat hole case is shown below. The file name for this model is ‘CRATHOLE_3D_LM.bas’. The algorithm for the conical rat hole case follows the theory introduced in Chapter 6. The model is based on the cone hopper case with the addition of an rat hole angle Θ.

```
'Cone Hopper with conical rat hole 3-Dimensional
'Force balance equations in R- and ETA-directions
'Lame-Maxwell version

'James O'Neill 28.11.2010

CLS '''clear all

''''''''''''''''''''''''''material data input

INPUT "GRANULAR MATERIAL BULK DENSITY =  ", RHO# '''bulk density in kg/m3 (assumed to be constant)

INPUT "WALL FRICTION ANGLE IN DEGREES (phi_w) =  ", phi_w_deg# '''angle of wall friction in degrees

pi# = 4 * ATN(1#) '''value for pi

phi_w# = phi_w_deg# * pi# / 180 '''conversion to radians

INPUT "INTERNAL FRICTION ANGLE IN DEGREES (phi) =  ", phi_deg# '''angle of internal friction/yield locus in degrees

phi# = phi_deg# * pi# / 180 '''conversion to radians

INPUT "TENSILE PARAMETER Pa (T) =  ", T# '''tensile intercept in Pa
```

```

Fc# = 2 * T# * SIN(phi#) / (1 - SIN(phi#)) '''unconfined yield stress in Pa

PRINT "UNCONFINED YIELD STRESS Pa = ",
PRINT Fc#

Co = T# * TAN(phi#) '''cohesion in Pa

PRINT "COHESION Co Pa = ",
PRINT Co
PRINT ""

"""""""""'hopper and model geometry data input

INPUT "HEIGHT OF UPPER SURFACE (H) METRES =  ", H# '''upper surface height in metres

INPUT "LOCATION OF LOWER BOUNDARY (H2) METRES =  ", H2# '''choose location of lower boundary of model (e.g. cohesive arch across hopper outlet), used to avoid singularity at hopper apex

INPUT "HOPPER WALL HALF ANGLE (ALPHA2) DEGREES =  ", ALPHA_DEG# '''hopper wall half angle in degrees

ALPHA# = ALPHA_DEG# * pi# / 180 '''conversion to radians

BETA_CALC# = SIN(phi_w#) / SIN(phi#)

BETA_ACTIVE = (180 / pi#) * 0.5 * (ATN(BETA_CALC# / (1 - BETA_CALC# ^ 2) ^ 0.5) + phi_w#) '''active BETA-value to be shown on screen in degrees (no built in arcsin function)
PRINT ""
PRINT "LIMITS FOR BETA:"
PRINT "BETA_ACTIVE = ", BETA_ACTIVE
```

```
BETA_PASSIVE = (180 / pi#) * 0.5 * (ATN(BETA_CALC# / (1 - BETA_CALC# ^ 2) ^ 0.5) - phi_w#) '''passive BETA-value to be shown on screen in degrees (no built in arcsin function)
PRINT "BETA_PASSIVE = ", BETA_PASSIVE

INPUT "SELECT HOPPER WALL BETA ANGLE (BETA2) DEGREES =  ", BETA_DEG# '''selection of angle between principal stress arc and wall normal in degrees

BETA# = BETA_DEG# * pi# / 180 '''conversion to radians
PRINT ""
INPUT "SELECT RAT HOLE HALF ANGLE (THETA) DEGREES = ", THETA_DEG# '''selection of conical insert half angle

THETA# = THETA_DEG# * pi# / 180 '''conversion to radians

LAMBDA# = (BETA# + ALPHA#) '''sum of ALPHA and BETA angles in radians

GAMMA# = pi# / 2 - LAMBDA# / 2 '''constant resulting from model geometry in radians

A1# = SIN(ALPHA#) / (SIN(LAMBDA#) * COS(ALPHA# + THETA#)) '''constant resulting from model geometry in radians

A2# = ((1 - A1# * COS(ALPHA# + BETA#)) ^ 2 + (TAN(ALPHA#) - A1# * SIN(ALPHA# + BETA#)) ^ 2) ^ 0.5 '''constant resulting from model geometry in radians

NU# = 0 '''angle between lines of constant ETA between principal stress arcs is zero for equal angle hoppers
```

```
J_ACTIVE = (1 - SIN(phi#)) / (1 + SIN(phi#)) '''active J-value to be shown on screen
PRINT ""
PRINT "J_ACTIVE = ", J_ACTIVE

J_PASSIVE = (1 + SIN(phi#)) / (1 - SIN(phi#)) '''passive J-value to be shown on screen
PRINT "J_PASSIVE = ", J_PASSIVE

INPUT "SELECT J-VALUE, J =  ", J# '''selection of J-value

PRINT ""
INPUT "NUMBER OF X INCREMENTS =  ", DELTA_X_INC# '''choose number of increments in X-direction (e.g. 200 down through hopper)

INPUT "NUMBER OF ETA INCREMENTS (USE EVEN NUMBERS) =   ", DELTA_ETA_INC# '''choose number of increments in ETA-direction (e.g. 50 across hopper)

INPUT "SELECT k-VALUE, k =  ", k# '''selection of k-value

o# = _ROUND((DELTA_ETA_INC# + 1) / 2) '''centre-line of hopper (e.g. column 26 in a 51-column matrix)

DELTA_X# = (H# - H2#) / DELTA_X_INC# '''X-increment size

DELTA_ETA# = LAMBDA# / DELTA_ETA_INC# '''ETA-increment size

DIM X#(DELTA_X_INC# + 1, DELTA_ETA_INC# + 1) '''define and populate a matrix for X, from upper surface (H) to lower boundary (H2) using X-increment as step size
FOR B = 1 TO DELTA_ETA_INC# + 1
X#(1, B) = H#
FOR A = 2 TO DELTA_X_INC# + 1
```

```
X#(A, B) = X#(A - 1, B) - DELTA_X#
NEXT
NEXT
DIM ETA#(DELTA_X_INC# + 1, DELTA_ETA_INC# + 1) '''define and populate a matrix for ETA, from left-hand hopper wall to right-hand wall using ETA-increment as step size
FOR C = 1 TO DELTA_X_INC# + 1
ETA#(C, 1) = -(ALPHA# + BETA#)
FOR D = 2 TO DELTA_ETA_INC# + 1
ETA#(C, D) = ETA#(C, D - 1) + DELTA_ETA#
NEXT
NEXT
DIM PW_WRTX#(DELTA_X_INC# + 1, DELTA_ETA_INC# + 1) '''define and populate a matrix for model variable PW_WRTX
FOR C = 1 TO DELTA_X_INC# + 1
FOR B = 1 TO DELTA_ETA_INC# + 1
PW_WRTX#(C, B) = A1# + A2# * COS(ETA#(C, B) - NU# + THETA#)
NEXT
NEXT
DIM R#(DELTA_X_INC# + 1, DELTA_ETA_INC# + 1) '''define and populate a matrix for (lower) arc radius R
FOR C = 1 TO DELTA_X_INC# + 1
FOR B = 1 TO DELTA_ETA_INC# + 1
R#(C, B) = A1# * X#(C, B)
NEXT
NEXT
DIM PPSI_WRTX#(DELTA_X_INC# + 1, DELTA_ETA_INC# + 1) '''define and populate a matrix for PPSI_WRTX (not required in calculation method below)
FOR B = 1 TO DELTA_ETA_INC# + 1
FOR C = 1 TO DELTA_X_INC# + 1
```

```
PPSI_WRTX#(C, B) = A2# * (COS(ETA#(C, B) - THETA#) * SIN(ETA#(C, B)) - SIN(THETA#)) / (R#(C, B) * COS(ETA#(C, B)))
NEXT
NEXT

''''''''''''''''''''''''''dimension arrays using X- and ETA-increment information, to allow QBasic to reserve memory space

DIM PF_WRTETA#(DELTA_X_INC# + 1, DELTA_ETA_INC# + 1) '''PSIG_R_WRTX#(row, column)
DIM PSIG_R_WRTETA#(DELTA_X_INC# + 1, DELTA_ETA_INC# + 1)
DIM SIG_ETA#(DELTA_X_INC# + 1, DELTA_ETA_INC# + 1) '''arc stress
DIM F#(DELTA_X_INC# + 1, DELTA_ETA_INC# + 1)
FOR B = 1 TO DELTA_ETA_INC# + 1
FOR C = 1 TO DELTA_X_INC# + 1
F#(C, B) = 1
NEXT
NEXT
DIM PSIG_R_WRTX#(DELTA_X_INC# + 1, DELTA_ETA_INC# + 1)
DIM SIG_R#(DELTA_X_INC# + 1, DELTA_ETA_INC# + 1) '''radial stress
FOR B = 1 TO DELTA_ETA_INC# + 1
FOR C = 1 TO DELTA_X_INC# + 1
SIG_R#(C, B) = 1
NEXT
NEXT
DIM SIG_THETA#(DELTA_X_INC# + 1, DELTA_ETA_INC# + 1) '''azimuthal stress
FOR B = 1 TO DELTA_ETA_INC# + 1
FOR C = 1 TO DELTA_X_INC# + 1
SIG_THETA#(C, B) = 1
NEXT
NEXT

```

```
158 ''''''''''''''''''''Newton-Raphson type WHILE loop used to allow model to converge on solution (see line 381 for closing statement)
159
160 Y# = 0 '''calculation for variable Y given on line 372 as last entry in SIG-R matrix
161
162 DIFF# = 2 '''calculation for variable DIFF given on line 369
163
164 Numberofiterations = 0 '''used to display number of iterations during cycles, see line 375
165
166 WHILE (DIFF# >= 1) '''if difference between new and previous result is greater than unity, the WHILE loop will continue to cycle
167
168 ''''''''''''''''''''calculate PF_WRTETA matrix using ETA-direction force balance equation
169
170 FOR B = 1 TO DELTA_ETA_INC# + 1
171 FOR C = 1 TO DELTA_X_INC# + 1
172 PF_WRTETA#(C, B) = (-F#(C, B) * (COS(2 * ETA#(C, B)) / COS(ETA#(C, B)) ^ 2 - (SIN(ETA#(C, B)) / COS(ETA#(C, B)) ^ 2) * SIN(BETA#) * SIN(THETA#) / SIN(ALPHA#) + COS(2 * ETA#(C, B)) / SIN(ETA#(C, B)) - SIN(BETA#) * SIN(THETA#) / SIN(ALPHA#)) - SIG_R#(C, B) * A2# * SIN(ETA#(C, B) - THETA#) * ((SIN(ETA#(C, B)) / COS(ETA#(C, B))) * SIN(BETA#) * SIN(THETA#) / SIN(ALPHA#) - COS(2 * ETA#(C, B)) / COS(ETA#(C, B)) + 2 * COS(ETA#(C, B)) + (COS(ETA#(C, B)) / SIN(ETA#(C, B))) * SIN(BETA#) * SIN(THETA#) / SIN(ALPHA#)) + R#(C, B) * PW_WRTX#(C, B) * RHO# * 9.81 * (SIN(BETA#) * SIN(THETA#) / SIN(ALPHA#) + SIN(ETA#(C, B))) / COS(ETA#(C, B)) + PW_WRTX#(C, B) * SIG_THETA# / SIN(ETA#(C, B))) / (SIN(BETA#) * SIN(THETA#) / SIN(ALPHA#) + F#(C, B) * SIN(2 * ETA#(C, B)) / (2 * COS(ETA#(C, B))) + (COS(ETA#(C, B)) / SIN(ETA#(C, B))) * SIN(BETA#) * SIN(THETA#) / SIN(ALPHA#) + SIN(2 * ETA#(C, B)) / (2 * SIN(ETA#(C, B)))) '''ETA-DIRECTION FORCE BALANCE
173 NEXT
```

```
NEXT

""""""""""""'calculate PSIG_R_WRTETA matrix using finite difference method (LH wall uses forward difference, RH wall backward difference, remainder central difference)

FOR C = 1 TO DELTA_X_INC# + 1
PSIG_R_WRTETA#(C, 1) = (SIG_R#(C, 2) - SIG_R#(C, 1)) / DELTA_ETA#
NEXT

FOR P = 2 TO DELTA_ETA_INC#
FOR C = 1 TO DELTA_X_INC# + 1
PSIG_R_WRTETA#(C, P) = (SIG_R#(C, P + 1) - SIG_R#(C, P - 1)) / (2 * DELTA_ETA#)
NEXT
NEXT

FOR C = 1 TO DELTA_X_INC# + 1
PSIG_R_WRTETA#(C, DELTA_ETA_INC# + 1) = (SIG_R#(C, DELTA_ETA_INC# + 1) - SIG_R#(C, DELTA_ETA_INC#)) / DELTA_ETA#
NEXT

""""""""""""'calculate SIG_ETA matrix using F/PW_WRTX with a central boundary condition of Mohr-Coulomb criterion SIG_ETA=J*SIG_R+(J-1)*T

FOR B = 1 TO DELTA_ETA_INC# + 1
FOR C = 1 TO DELTA_X_INC# + 1
SIG_ETA#(C, B) = F#(C, B) / PW_WRTX#(C, B)
NEXT
NEXT
FOR C = 1 TO DELTA_X_INC# + 1
SIG_ETA#(C, o#) = J# * SIG_R#(C, o#) + (J# - 1) * T#
NEXT

```

```
"""""""""'calculate F matrix using forward and reverse Euler method from central boundary condition of PW_WRTX*SIG_ETA

FOR C = 1 TO DELTA_X_INC# + 1
F#(C, o#) = PW_WRTX#(C, o#) * SIG_ETA#(C, o#)
NEXT
FOR E = o# TO DELTA_ETA_INC#
FOR C = 1 TO DELTA_X_INC# + 1
F#(C, E + 1) = F#(C, E) + PF_WRTETA#(C, E) * DELTA_ETA#
NEXT
NEXT
FOR G = o# TO 2 STEP -1
FOR C = 1 TO DELTA_X_INC# + 1
F#(C, G - 1) = F#(C, G) - PF_WRTETA#(C, G) * DELTA_ETA#
NEXT
NEXT

"""""""""'calculate SIG_THETA matrix using k relationship

FOR B = 1 TO DELTA_ETA_INC# + 1
FOR C = 1 TO DELTA_X_INC# + 1
SIG_THETA#(C, B) = SIG_ETA#(C, B) + k# * SIN(ETA#(C, B)) * SIG_R#(C, B)
NEXT
NEXT

"""""""""'calculate PSIG_R_WRTX matrix using R-direction force balance equation

FOR B = 1 TO DELTA_ETA_INC# + 1
FOR C = 1 TO DELTA_X_INC# + 1
PSIG_R_WRTX#(C, B) = -((COS(ETA#(C, B)) / SIN(ETA#(C, B))) * SIN(BETA#) * SIN(THETA#) / SIN(ALPHA#) + SIN(2 * ETA#(C, B)) / (2 * SIN(ETA#(C, B)))) * (-F#(C, B) * (COS(2 * ETA#(C, B)) / COS(ETA#(C, B)) ^ 2 -
```

```
(SIN(ETA#(C, B)) / COS(ETA#(C, B)) ^ 2) * SIN(BETA#) * SIN(THETA#) /
SIN(ALPHA#) + COS(2 * ETA#(C, B)) / SIN(ETA#(C, B)) - SIN(BETA#) *
SIN(THETA#) / SIN(ALPHA#)) - SIG_R#(C, B) * A2# * SIN(ETA#(C, B) - THETA#)
* ((SIN(ETA#(C, B)) / COS(ETA#(C, B))) * SIN(BETA#) * SIN(THETA#) /
SIN(ALPHA#) - COS(2 * ETA#(C, B)) / COS(ETA#(C, B)) + 2 * COS(ETA#(C, B)) +
(COS(ETA#(C, B)) / SIN(ETA#(C, B))) * SIN(BETA#) * SIN(THETA#) /
SIN(ALPHA#)) + R#(C, B) * PW_WRTX#(C, B) * RHO# * 9.81 * (SIN(BETA#) *
SIN(THETA#) / SIN(ALPHA#) + SIN(ETA#(C, B))) / COS(ETA#(C, B)) +
PW_WRTX#(C, B) * SIG_THETA#(C, B) / SIN(ETA#(C, B))) / (R#(C, B) *
(SIN(BETA#) * SIN(THETA#) / SIN(ALPHA#) + F#(C, B) * SIN(2 * ETA#(C, B)) / (2
* COS(ETA#(C, B))) + (COS(ETA#(C, B)) / SIN(ETA#(C, B))) * SIN(BETA#) *
SIN(THETA#) / SIN(ALPHA#) + SIN(2 * ETA#(C, B)) / (2 * SIN(ETA#(C, B)))) *
(SIN(BETA#) * SIN(THETA#) / SIN(ALPHA#) + SIN(ETA#(C, B)))) - (F#(C, B) /
(R#(C, B) * (SIN(BETA#) * SIN(THETA#) / SIN(ALPHA#) + SIN(ETA#(C, B))))) *
(COS(2 * ETA#(C, B)) / SIN(ETA#(C, B)) - SIN(BETA#) * SIN(THETA#) /
SIN(ALPHA#)) - SIG_R#(C, B) * A2# * SIN(ETA#(C, B) - THETA#) * (SIN(ETA#(C,
B)) + 2 * COS(ETA#(C, B)) * SIN(ETA#(C, B)) + COS(ETA#(C, B)) * SIN(BETA#) *
SIN(THETA#) / SIN(ALPHA#)) / ((SIN(BETA#) * SIN(THETA#) / SIN(ALPHA#) +
SIN(ETA#(C, B))) * R#(C, B) * SIN(ETA#(C, B))) - SIN(ETA#(C, B)) *
PSIG_R_WRTETA#(C, B) * (A2# * (COS(ETA#(C, B) - THETA#) * SIN(ETA#(C, B))
- SIN(THETA#)) / (R#(C, B) * COS(ETA#(C, B)))) / (SIN(BETA#) * SIN(THETA#) /
SIN(ALPHA#) + SIN(ETA#(C, B))) - SIG_R#(C, B) * A2# * SIN(ETA#(C, B) -
THETA#) / R#(C, B) + PW_WRTX#(C, B) * SIG_THETA#(C, B) / ((SIN(BETA#) *
SIN(THETA#) / SIN(ALPHA#) + SIN(ETA#(C, B))) * R#(C, B) * SIN(ETA#(C, B))) -
A2# * 2 * SIG_R#(C, B) / R#(C, B) '''R-DIRECTION FORCE BALANCE
NEXT
NEXT

'''''''''''''''''''''calculate SIG_R matrix using reverse Euler method from surface
boundary condition of zero

FOR B = 1 TO DELTA_ETA_INC# + 1
SIG_R#(1, B) = 0 ''''hopper upper surface
NEXT
```

```
FOR B = 1 TO DELTA_ETA_INC# + 1
FOR N = 1 TO DELTA_X_INC#
SIG_R#(N + 1, B) = SIG_R#(N, B) - DELTA_X# * PSIG_R_WRTX#(N, B)
NEXT
NEXT

''''''''''''''''''''''''''various outputs of model variable matrices for testing purposes, recorded in the following comma separated value files:
'''ETA.csv
'''X.csv
'''PSIG_R_WRTX.csv
'''F.csv
'''SIG_R.csv
'''SIG_ETA.csv
'''PSIG_R_WRTETA.csv
'''PF_WRTETA.csv
'''PPSI_WRTX.csv
'''PW_WRTX.csv
'''SIG_THETA.csv
'''R.csv

OPEN "SIG_R.CSV" FOR OUTPUT AS #1
FOR C = 1 TO DELTA_X_INC# + 1
FOR B = 1 TO DELTA_ETA_INC# + 1
WRITE #1, SIG_R#(C, B),
NEXT
WRITE #1, ""
NEXT
CLOSE #1

OPEN "X.CSV" FOR OUTPUT AS #2
FOR C = 1 TO DELTA_X_INC# + 1
FOR B = 1 TO DELTA_ETA_INC# + 1
```

```
WRITE #2, X#(C, B),
NEXT
WRITE #2, ""
NEXT
CLOSE #2

OPEN "ETA.CSV" FOR OUTPUT AS #3
FOR C = 1 TO DELTA_X_INC# + 1
FOR B = 1 TO DELTA_ETA_INC# + 1
WRITE #3, ETA#(C, B),
NEXT
WRITE #3, ""
NEXT
CLOSE #3

OPEN "PW_WRTX.CSV" FOR OUTPUT AS #4
FOR C = 1 TO DELTA_X_INC# + 1
FOR B = 1 TO DELTA_ETA_INC# + 1
WRITE #4, PW_WRTX#(C, B),
NEXT
WRITE #4, ""
NEXT
CLOSE #4

OPEN "SIG_ETA.CSV" FOR OUTPUT AS #5
FOR C = 1 TO DELTA_X_INC# + 1
FOR B = 1 TO DELTA_ETA_INC# + 1
WRITE #5, SIG_ETA#(C, B),
NEXT
WRITE #5, ""
NEXT
CLOSE #5

OPEN "PSIG_R_WRTX.CSV" FOR OUTPUT AS #6
```

```
FOR C = 1 TO DELTA_X_INC# + 1
FOR B = 1 TO DELTA_ETA_INC# + 1
WRITE #6, PSIG_R_WRTX#(C, B),
NEXT
WRITE #6, ""
NEXT
CLOSE #6
OPEN "F.CSV" FOR OUTPUT AS #7
FOR C = 1 TO DELTA_X_INC# + 1
FOR B = 1 TO DELTA_ETA_INC# + 1
WRITE #7, F#(C, B),
NEXT
WRITE #7, ""
NEXT
CLOSE #7
OPEN "PSIG_R_WRTETA.CSV" FOR OUTPUT AS #8
FOR C = 1 TO DELTA_X_INC# + 1
FOR B = 1 TO DELTA_ETA_INC# + 1
WRITE #8, PSIG_R_WRTETA#(C, B),
NEXT
WRITE #8, ""
NEXT
CLOSE #8
OPEN "PF_WRTETA.CSV" FOR OUTPUT AS #9
FOR C = 1 TO DELTA_X_INC# + 1
FOR B = 1 TO DELTA_ETA_INC# + 1
WRITE #9, PF_WRTETA#(C, B),
NEXT
WRITE #9, ""
NEXT
CLOSE #9
```

```
OPEN "PPSI_WRTX.CSV" FOR OUTPUT AS #10
FOR C = 1 TO DELTA_X_INC# + 1
FOR B = 1 TO DELTA_ETA_INC# + 1
WRITE #10, PPSI_WRTX#(C, B),
NEXT
WRITE #10, ""
NEXT
CLOSE #10
OPEN "SIG_THETA.CSV" FOR OUTPUT AS #11
FOR C = 1 TO DELTA_X_INC# + 1
FOR B = 1 TO DELTA_ETA_INC# + 1
WRITE #11, SIG_THETA#(C, B),
NEXT
WRITE #11, ""
NEXT
CLOSE #11
OPEN "R.CSV" FOR OUTPUT AS #12
FOR C = 1 TO DELTA_X_INC# + 1
FOR B = 1 TO DELTA_ETA_INC# + 1
WRITE #12, R#(C, B),
NEXT
WRITE #12, ""
NEXT
CLOSE #12
SUM# = 0
FOR B = 1 TO DELTA_ETA_INC# + 1
SUM# = SUM# + SIG_R#(DELTA_X_INC# + 1, B) '''sum final row of SIG_R arrary
NEXT
DIFF# = ABS(SUM# - Y#) '''compare successive iterations
```

```
Y# = 0
FOR B = 1 TO DELTA_ETA_INC# + 1
Y# = Y# + SIG_R#(DELTA_X_INC# + 1, B)
NEXT

Numberofiterations = Numberofiterations + 1 '''count number of iterations
PRINT ""
PRINT "Number of iterations = ",
PRINT Numberofiterations
PRINT ""

IF Numberofiterations = 100 THEN DIFF# = 0.01

WEND
```

<u>Chapter 12.0 - Appendix Five</u>

<u>Use of statistical *t*-tests</u>

Use of stastical *t*-tests

It can be demonstrated that correlation between calculated values and experimental data improves by adjustment of model parameters, using a statistical hypothesis tests test (Shier 2004). Effect of adjustment of variables can be analysed using *t*-tests, and the probability of the null hypothesis acceptability can be estimated. The null hypothesis is that correlation is not improved by the methods employed within this publication. The alternative hypothesis is that correlation is improved.

Table A.1 shows differences between calculated values and experimental data from the Wojcik and Tejchman (2008) analysis, in Chapter 5.6.1 of the main text. Data for calculated wall stresses σ_W are given with J and β set equal to their initial active values, as per Table 3 in the main text, and compared to data for calculated wall stresses after implementation of the Solver program (reference Figure 57). It is the difference between initial and final stress values to which the *t*-test can be applied.

Sensor	$\sigma_{W_{INITIAL}}$	$\sigma_{W_{FINAL}}$	σ	$(\sigma_{W_{INITIAL}} - \sigma)$	$(\sigma_{W_{FINAL}} - \sigma)$	Δ
C8	7.286E+03	5.166E+03	5.000E+03	2.286E+03	0.166E+03	-2.120E+03
C9	6.082E+03	3.872E+03	4.300E+03	1.782E+03	-0.428E+03	-2.210E+03
C10	4.881E+03	2.674E+03	1.800E+03	3.081E+03	0.874E+03	-2.207E+03

Table A.1. Comparison of Wojcik and Tejchman silo data.

The data above has three degrees of freedom n; Δ has mean value $\bar{d}$ of -2.179 and a standard deviation S_d of 0.04174. This information can be used to calculate the *t*-statistic using equation C1.

$$t = \frac{\bar{d}}{SE(\bar{d})}, \text{ where } SE(\bar{d}) = \frac{S_d}{\sqrt{n}} \text{ (Shier 2004)} \tag{A.78}$$

This parameter is then used to provide a probability for the null hypothesis, via *t*-distribution tables (Deacon 2009). The distribution for t_{n-1} is used to for comparison with the calculated *t*-value of 90.43.

Probability for the null hypothesis being acceptable is found to be less than 0.001. Therefore the null hypothesis, implying correlation did not improve, can be rejected in favour of the alternative hypothesis (Shier 2004).

Table A.2 shows differences between calculated values and experimental data from the Walker and Blanchard (1967) 30-degree cone hopper analysis, in Chapter 5.6.4 of the main text. Data for calculated wall stresses σ_W are given with *J* and β set equal to their initial active values in Table 12, and compared to data for calculated wall stresses after adjustment of variables (reference Figure 66).

X	$\sigma_{W_{INITIAL}}$	$\sigma_{W_{FINAL}}$	σ	$(\sigma_{W_{INITIAL}} - \sigma)$	$(\sigma_{W_{FINAL}} - \sigma)$	$\boldsymbol{\Delta}$
0.6	2.022E+03	2.664E+03	8.274E+03	6.252E+03	5.610E+03	-0.642E+03
0.5	3.067E+03	3.902E+03	9.653E+03	6.586E+03	5.751E+03	-0.835E+03
0.4	4.924E+03	5.811E+03	11.030E+03	6.106E+03	5.219E+03	-0.887E+03
0.3	8.303E+03	8.661E+03	12.410E+03	4.107E+03	3.749E+03	-0.358E+03
0.2	12.740E+03	9.260E+03	13.790E+03	1.050E+03	4.530E+03	3.480E+03

Table A.2. Comparison of Walker and Blanchard 30-degree hopper data.

The above data has five degrees of freedom *n*; Δ has mean value $\bar{d}$ of 0.1516 and a standard deviation S_d of 2.1450. Use of equation C1 provides a value of *t* equal to 0.1581. When this is compared to the *t*-distribution for t_{n-1}, a high probability in favour of the null hypothesis is returned. This indicates that average correlation between experimental and calculated data was not improved by use of the Solver application.

By inspection of the data, it can be seen that the initial and final values do not follow a similar distribution. This type of hypothesis test is sensitive to differing variances and distributions between two groups of data (Deacon 2009). The initial and final values for σ_W at *X* equal to 0.2 vary by a relatively large amount when compared to stresses at increased heights. If the σ_W-values at *X* equal to 0.2 are not considered in the calculation for equation C1, then the *t*-statistic is increased to 5.684. Probability in favour of the null hypothesis is reduced to below 0.001. Therefore the null hypothesis is rejected in favour of the alternative hypothesis.

Chapter 13.0 - Appendix Six

Azimuthal Stress Relationships

In Chapter 5.6 equation 62 is used to provide a relationship for azimuthal stress σ_θ from other principal stresses σ_R and σ_ε. Equation 62 was selected as stress distributions produced gave correlation to experimental data. The following information explains the process by which equation 62 was selected for the case study of the three-dimensional parallel-sided silo, with experimental data provided by Wojcik and Tejchman (2008). The three-dimensional silo algorithm was modified to allow use of alternative equations to provide σ_θ-values. The spreadsheet files are included on the CD attachment to the thesis.

SIG R OPTION	**1**
SURFACE BOUNDARY CONDITION	1
ARCH BOUNDARY CONDITION	2
SIG ETA OPTION	**2**
LH WALL BOUNDARY CONDITION	1
CENTRE BOUNDARY CONDITION	2
MOHR COULOMB CRITERION	3
SIG THETA OPTION	**1**
HAAR VON KARMEN (EQ 65)	1
EQUATION 62	2
EQUATION 66	3
EQUATION 67	4

Use of equation 68, the Conical Yield Function, was evaluated in Figures 70 and 72, in Chapters 5.6.6 and 5.6.7 respectively.

13.1 Equation 62 correlation

For the Wojcik and Tejchman (2008) silo experimental data, the dimensions shown in Figure 52 and material data for the loose dry sand were input to the three-dimensional silo algorithm. Initial values were used as below.

- β = 0.54 rad
- J = 0.26

- T= 500 Pa
- OP = 0 Pa
- k = 1

Table 3, in Chapter 5.6.1, shows poor correlation of theoretical results to experimental data. The Excel Solver application was used to vary these values, providing the correlation demonstrated in Figure 57. Final values of model parameters are shown below.

- β = 0.15 rad
- J = 0.26
- T= 200 Pa
- OP = 0 Pa
- k = 0.001

Figure A.19, in Chapter 10.3, is a screen shot of the three-dimensional silo algorithm 'least squares' work sheet, during use of the Solver application. It can be seen that averaged σ_W-values overestimate experimental data σ by 8% and averaged τ-values underestimate experimental data τ by 37%.

13.2 Equation 65 correlation

Using identical initial values as shown in Chapter 13.1 above, the three-dimensional silo model was used with equation 65 and the Solver application in an attempt to provide correlation to experimental data.

Model parameters were varied to produce the values below. It can be seen in Figure A.25 that averaged σ_W-values overestimate experimental data σ by 9% and averaged τ-values underestimate experimental data τ by 40%.

- β = 0.15 rad
- J = 0.26
- T = 200 Pa

- OP = 0 Pa

Due to use of relatively small k-value in equation 62, stress distributions and final model parameters produced by use of equation 65 gave similar results.

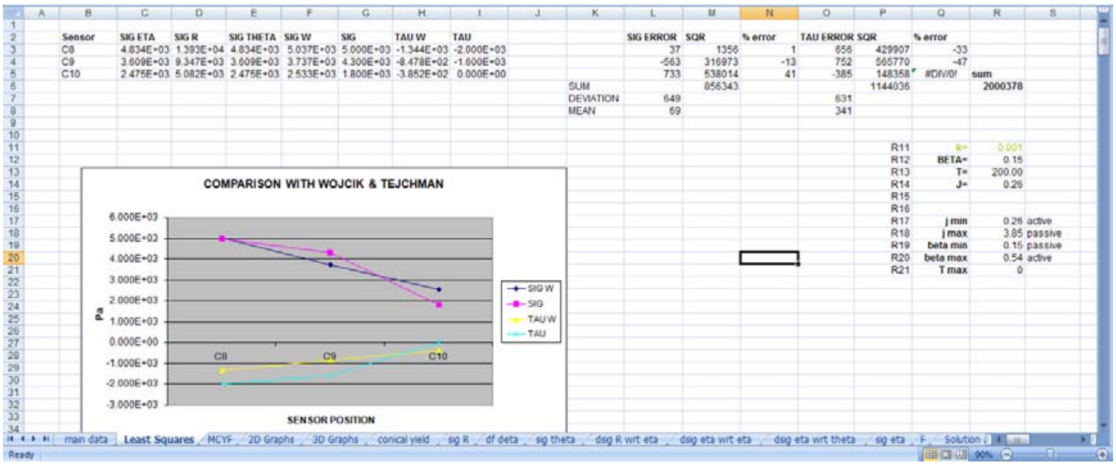

Figure A.25. Detail of ‘least squares’ work sheet using equation 65

13.3 Equation 66 correlation

Using identical initial values as shown in Chapter 13.1 above, the three-dimensional silo model was used with equation 66 and the Solver application.

Model parameters were varied to produce the values below. It can be seen in Figure A.26 that averaged σ_W-values overestimate experimental data by 12% and averaged τ-values underestimate experimental data by 20%.

- β = 0.2 rad
- J = 3.85
- T = 0 Pa
- OP = 0 Pa

Correlation appears to be demonstrated between theoretical and experimental values, however along the centre line of the silo (at $\varepsilon = 0$) values are unstable. This is discussed in Chapter 5.6.6.

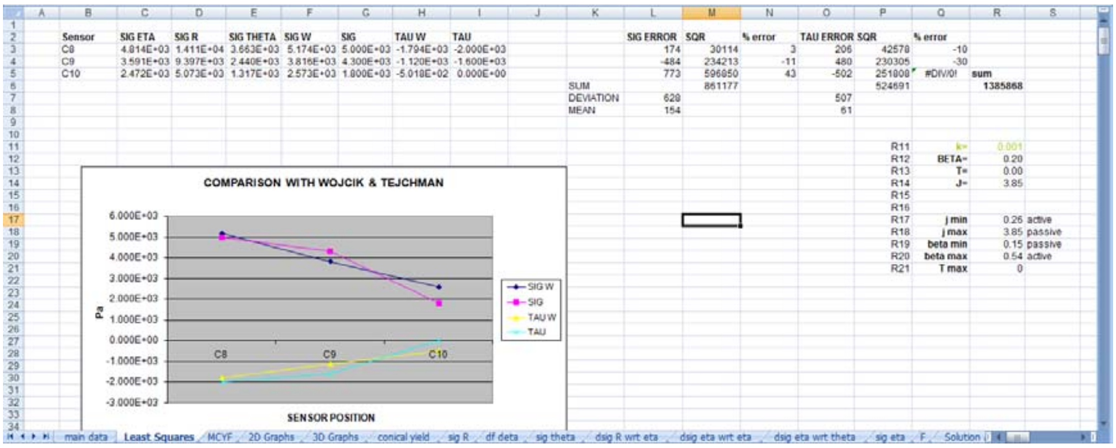

Figure A.26. Detail of 'least squares' work sheet using equation 66

13.4 Equation 67 correlation

Using identical initial values as shown in Chapter 13.1 above, the three-dimensional silo model was used with equation 67 and the Solver application.

Model parameters were varied to produce the values below. It can be seen in Figure A.27 that averaged σ_W-values overestimate experimental data by 181% and averaged τ-values underestimate experimental data by 109%.

- β = 0.15 rad
- J = 3.85
- T = 2000 Pa
- OP = 0 Pa

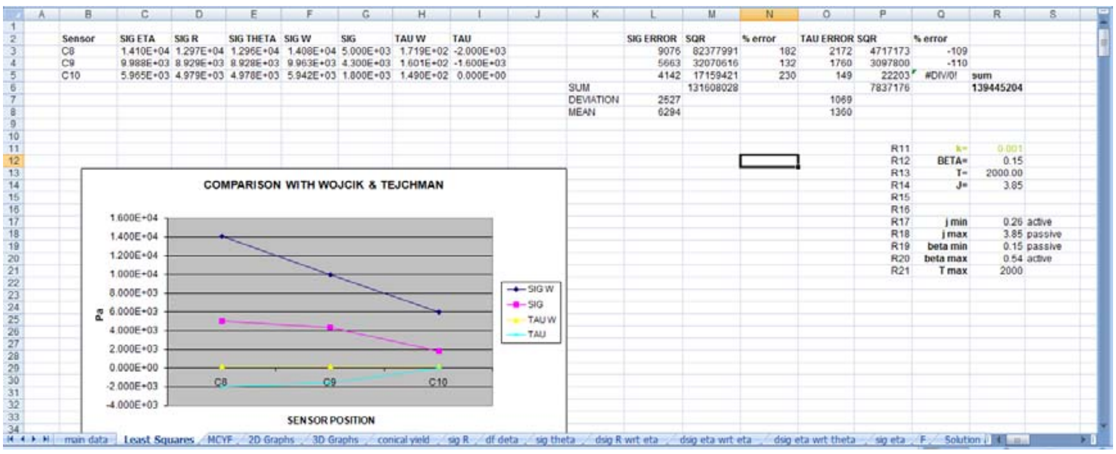

Figure A.27. Detail of 'least squares' work sheet using equation 67

Chapter 14.0 – Appendix Seven

Publications

Publications

14.1. Matchett, A.J., O'Neill, J.C., Shaw, A.P., 2007. Analytical solutions to stress distribution problems in wedge and conical hoppers. Proceedings of Enstimac 2007 Conference, Ecoles des Mines D'Albi, France.

14.2. Matchett, A.J., O'Neill, J.C., Shaw, A.P., 2008. Stress distributions in 2-dimensional, wedge hoppers with circular arc stress orientation — A co-ordinate-specific Lamé–Maxwell model. Powder Technology, **187** (3) pp. 298-306.

14.3. Matchett, A.J., O'Neill, J.C., Shaw, A.P., 2009. Stresses in bulk solids in wedge hoppers: A flexible formulation of the co-ordinate specific, Lamé–Maxwell equations for circular arc, principal stress systems. Powder Technology, **194** (3) pp. 166-180.

14.4. O'Neill, J.C., Matchett, A.J., Shaw, A.P., 2009. Stresses in bulk solids in cone hoppers: numerical solutions to the 3-dimensional stress distribution problem, using circular arc geometry. Proceedings of Flexible Automation and Intelligent Manufacturing 2009 Conference, Teesside University, UK.

ANALYTICAL SOLUTIONS TO STRESS DISTRIBUTION PROBLEMS IN WEDGE AND CONICAL HOPPERS

A.J.Matchett, J.O'Neill, A.P.Shaw
School of Science & Technology, University of Teesside, Middlesbrough TS1 3BA, England
Corresponding author: a.j.matchett@tees.ac.uk

Resumé:
La distribution des charges a été modelisé, pour les poudres en vrac dans un cône de distribution. Les equations utilisent l'orientation principale des charges, "circular arc".
Une solution analytique a été produite, basée sur l'hypothèse de "Haar-von Karman".
Les graphes de distributions des charges ont été produites et la dimension critique de la sortie a été calculée
Mots Cles: hopper, silo, bulk solids, stress distribution

INTRODUCTION

The calculation of stress distributions within bulk solids in hoppers and silos is a challenging task. In the continuum approach, for a given co-ordinate system, there are 6 independent components of the stress tensor, representing 6 unknowns. The general force balance equations for stable conditions or incipient flow may be stated as:

$$-\nabla.\tau + \rho\bar{g} = 0 \qquad (1)$$

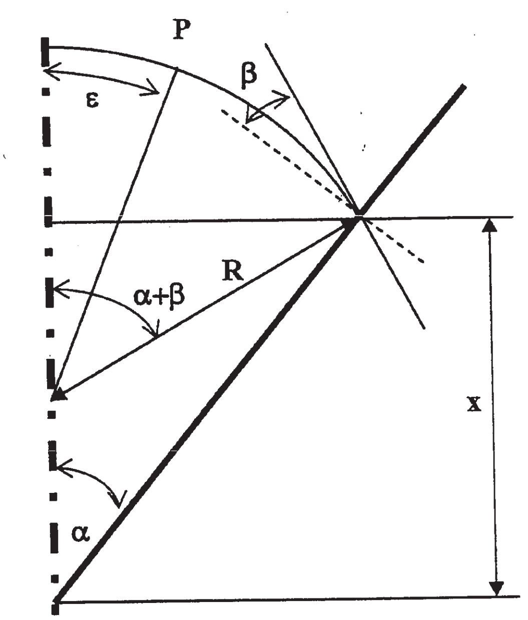

Figure 1: Principal stress orientation in a cone of half-angle α. The principal stress arc has radius R and makes angle β to the wall normal.

τ is the stress tensor and $\bar{g}$ is the vector acceleration due to gravity.

Equation 1 represents 3 force balance equations in an orthogonal co-ordinate system.

Therefore, extra information is required in order to obtain definite solutions. The problem has been discussed in depth by Nedderman[1] in his classic textbook.

CIRCULAR ARC GEOMETRY AND STRESS DISTRIBUTION

One way around the problems of stress analysis in bulk solids is to use a known, or assumed principal stress orientation. This approach was first used by Enstad[2] who proposed that principal stresses orientate in circular arcs, making a constant angle

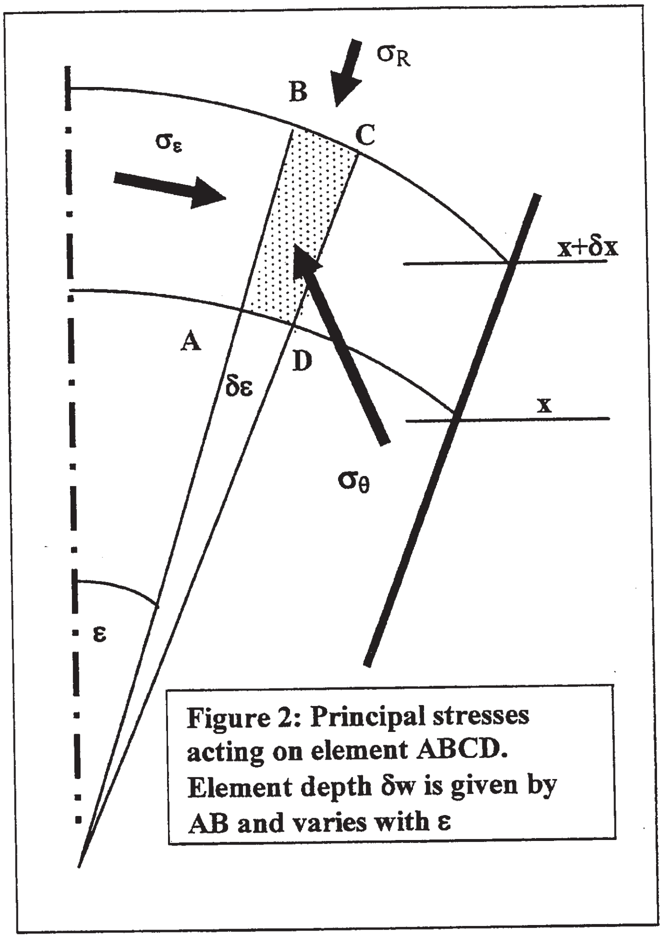

Figure 2: Principal stresses acting on element ABCD. Element depth δw is given by AB and varies with ε

with the vessel wall, controlled by wall friction. This greatly simplified stress analysis by working in principal stress space without shear stress terms in the resultant equations. Matchett[3][4] extended Enstad's approach into 2 dimensions in studies of ratholes.

For a cone, of half angle α, or a symmetrical 2-dimensional wedge, the situation is shown in Figure 1. Each principal stress arc of radius R, makes a constant angle to the wall normal, β. At its extremity the radius makes angle (α+β) with the vertical. A point P is specified by x, the height at which the arc cuts the wall, and ε, the angle of the arc radius to the vertical. Consider an incremental element δx–δε at x-ε: Figure 2.

Three principal stresses act in a rotationally symmetrical conical system:

σ_R: radial stress acting along R

σ_ε: stress acting along the principal stress arc

σ_θ: azimuthal stress acting rotationally about the cone centre-line(not present in a 2-D wedge)

Incremental element ABCD, Figure 2, has an element height δw=AB, which varies with ε in order to keep arc wall angle constant.

From the geometry of the system:

$$R = a_1 x : a_1 = \frac{\tan\alpha}{\sin(\alpha+\beta)} \quad (2)$$

$$\left(\frac{\partial w}{\partial x}\right) = a_1 + a_2 \cos\varepsilon : \quad (3)$$

$$a_2 = 1 - \cos(\alpha+\beta)$$

Consideration of the wall and material yield loci give limiting values of β[3][4]:

$$\beta_{passive} = 0.5\left(\arcsin\left(\frac{\sin\phi_w}{\sin\phi}\right) + \phi_w\right) \qquad (4)$$

$$\beta_{active} = 0.5\left(\arcsin\left(\frac{\sin\phi_w}{\sin\phi}\right) - \phi_w\right)$$

Horizontal and vertical force balances on the rotated element give[3][4]:

$$\frac{\partial}{\partial \varepsilon}\left[\bar{r}\left(\frac{\partial w}{\partial \varepsilon}\right)\sin\varepsilon\sigma_{\varepsilon}\right]-\frac{\partial}{\partial x}\left[\bar{r}R\cos\varepsilon\sigma_{R}\right]-\rho g\bar{r}R\left(\frac{\partial w}{\partial \varepsilon}\right)=0 \qquad (5)$$

$$-\frac{\partial}{\partial \varepsilon}\left[\bar{r}\cos\varepsilon\left(\frac{\partial w}{\partial \varepsilon}\right)\sigma_{\varepsilon}\right]-\frac{\partial}{\partial x}\left[R\bar{r}\sin\varepsilon\sigma_{R}\right]+R\left(\frac{\partial w}{\partial x}\right)\sigma_{\theta}=0 \qquad (6)$$

$\bar{r}$ is the radius of rotation of the element about the centre-line and:

$$\bar{r}=R\sin\varepsilon \qquad (7)$$

Simplification of equations 5-7 can be made by using the composite parameter:

$$F=\sigma_{\varepsilon}\left(\frac{\partial w}{\partial x}\right) \qquad (8)$$

$$\frac{\partial}{\partial x}\left[R^{2}\sigma_{R}\right]=2RF-\rho gR^{2}\left(\frac{\partial w}{\partial x}\right)\cos\varepsilon \qquad (9)$$

$$\frac{\partial F}{\partial \varepsilon}=\frac{\sigma_{\theta}}{\tan\varepsilon}\left(\frac{\partial w}{\partial x}\right)-\frac{F}{\tan\varepsilon}+\rho gR\left(\frac{\partial w}{\partial x}\right)\sin\varepsilon \qquad (10)$$

Equations 9 and 10 can be solved in a number of ways[3][4]. However, they are only 2 equations with 3 unknown stresses and a third equation is required.
The Haar-von Karman (HvK) hypothesis[1][5] provides a simplification that allows explicit analytical solutions. HvK proposes that the azimuthal stress, σ_θ, is a principal stress and is equal to the major or minor principal stress. In this situation:

$$\sigma_{\theta}=\sigma_{\varepsilon} \quad \therefore \frac{\partial F}{\partial \varepsilon}=\rho gR\left(\frac{\partial w}{\partial x}\right)\sin\varepsilon \qquad (11)$$

Equation 11 can be integrated with the boundary condition:

$$\varepsilon=A : F=F^{*} : \left(\frac{\partial w}{\partial x}\right)=W : \sigma_{R}=S=J\sigma_{\varepsilon}+(J-1)T : F^{*}=W\{J\sigma_{\varepsilon}+(J-1)T\} \qquad (12)$$

T is the tensile parameter from the linearised yield locus and J is the ratio of effective stresses: $J=(\sigma_{\varepsilon}+T)/(\sigma_{R}+T)$[3][4]. Thus, at ε=A, the state of stress is specified.

$$F=F^{*}+x\left[\left(\rho g a_{1}^{2}\right)(\cos A-\cos\varepsilon)+\left(\frac{\rho g a_{1}a_{2}}{2}\right)\left(\sin^{2}\varepsilon-\sin^{2}A\right)\right]$$

Therefore: $\quad F=F^{*}+xF' \qquad (13)$

$$F'=\left[\left(\rho g a_{1}^{2}\right)(\cos A-\cos\varepsilon)+\left(\frac{\rho g a_{1}a_{2}}{2}\right)\left(\sin^{2}\varepsilon-\sin^{2}A\right)\right]$$

Boundary condition ε=A would usually be taken at the wall(ε=α+β) or the arc apex(ε=0)
At ε=A, equation 9 becomes:

$$\frac{d}{dx}\left[R^{2}S\right]=2R\left(WJS+W(J-1)T\right)-\rho gR^{2}W\cos A \qquad (14)$$

Equation 14 rearranges to give a Walker/Enstad type of equation with solution:

$$S=-\frac{C_{2}}{C_{1}}+\frac{C_{3}}{(C_{1}-1)}x+(const2)x^{C_{1}} \qquad C_{1}=\frac{2WJ}{a_{1}}-2 \quad C_{2}=\frac{2W(J-1)T}{a_{1}} \quad C_{3}=\rho gW\cos A \qquad (15)$$

const2 is a constant of integration in x.
Equation 9 may then be written for the general case, in terms of F^*:

$$\frac{\partial}{\partial x}\left[x^2\sigma_R\right]=\frac{2x}{a_1}\left\{F^*+xF'\right\}-\left[\rho g\left(\frac{\partial w}{\partial x}\right)\cos\varepsilon\right]x^2$$

$$\frac{\partial}{\partial x}\left[x^2\sigma_R\right]=\left(\frac{2WJ}{a_1}\right)xS+\left(\frac{2W(J-1)T}{a_1}\right)x+x^2\left[\frac{2F'}{a_1}-\rho g\left(\frac{\partial w}{\partial x}\right)\cos\varepsilon\right] \quad (16)$$

Substituting for S from equation 15 and integrating with respect to x gives an explicit equation for σ_R:

$$\sigma_R=-\left(\frac{C_1}{C_2}\right)+\Theta x+(const2)x^{C_1}+\frac{(const3)}{x^2}$$

$$\Theta=\frac{\left[\frac{2F'}{a_1}+\frac{(C_1+2)C_3}{(C_1-1)}-\rho g\left(\frac{\partial w}{\partial x}\right)\cos\varepsilon\right]}{3} \quad (17)$$

const3 is a constant of integration in x.
Equations 13 and 16 completely describe the stress system for a rotationally symmetrical, Haar-von Karman conical stress system.
Equivalent equations for a 2-D wedge system may also be derived[7]. The equation for F is identical to equation 13, and:

$$\sigma_R=-\frac{C_2}{C_1}+\Theta x+(const2)x^{C_1}+\frac{(const3)}{x} \qquad C_1=\frac{WJ}{a_1}-1$$

$$\Theta=\frac{1}{2}\left[\frac{C_3(C_1+1)}{(C_1-1)}+\frac{F'}{a_1}-\rho g\left(\frac{\partial w}{\partial x}\right)\cos\varepsilon\right] \qquad C_2=W(J-1)T/a_1 \qquad C_3=W\rho g\cos A \quad (18)$$

PROPERTIES OF THE MODEL

The model is different from others in that it only assumes the state of stress on one line through the vessel, at ε=A. Stability must be checked at all other points in the model. The Mohr-Coulomb criteria states that:

$$J_{active}=\frac{1-\sin\phi}{1+\sin\phi}\leq J=\frac{\sigma_\varepsilon+T}{\sigma_R+T}\leq J_{passive}=\frac{1+\sin\phi}{1-\sin\phi} \quad (19)$$

Many solutions exist, dependent upon the chosen boundary conditions, but some contravene the stability criteria – equation 19.
Figure 3 shows passive and active stress simulations at ε=A, for conditions where const2 & const3 are determined at the upper surface, x=H, where H=3m, and depth (H-x) is plotted as a parameter. It was necessary to take A=wall for passive stress and A=0 for active stress from stability criteria. Stress variations across the cone are evident. At the wall, Walker/Enstad distributions are given, but stresses tend to infinity as x tends to zero away from the wall for both active and passive stress states at ε=A. This is quite inappropriate for prediction of the stable cohesive arch in passive stress.
A passive, stable, cohesive arch solution can be found by letting A=0, and determining const2 & const3 from upper and lower surfaces: $x=H_1 : \sigma_R=\sigma^*$ and $x=H_2 : \sigma_R=0$, respectively. The maximum stable arch is then the maximum value of H_2 at which the Mohr-Coulomb stability criterion is met. Figure 4 shows this solution for the same material/hopper as in Figure 3.

Figure 3: σ_R versus depth for material: ϕ=30°; T=3000 Pa
α=30°. Passive: J=3; β=21.5°. Active: J=0.33; β=7.5°

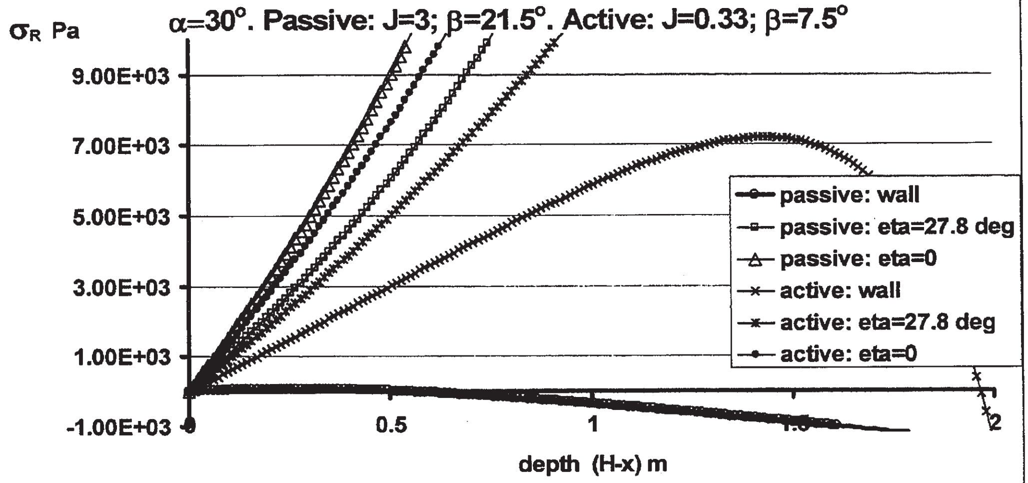

Figure 4a: σ_R in (H-x)-e space. A=0.
Material as in Figure 3. Stable arch solution

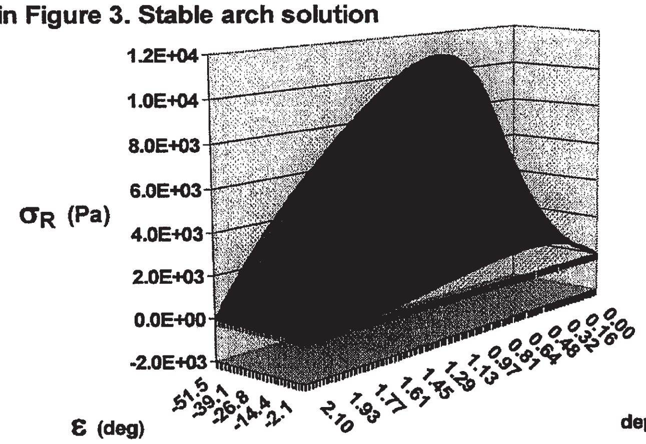

Figure 4b: σ_ε in (H-x)-e space.
See Figure 4a

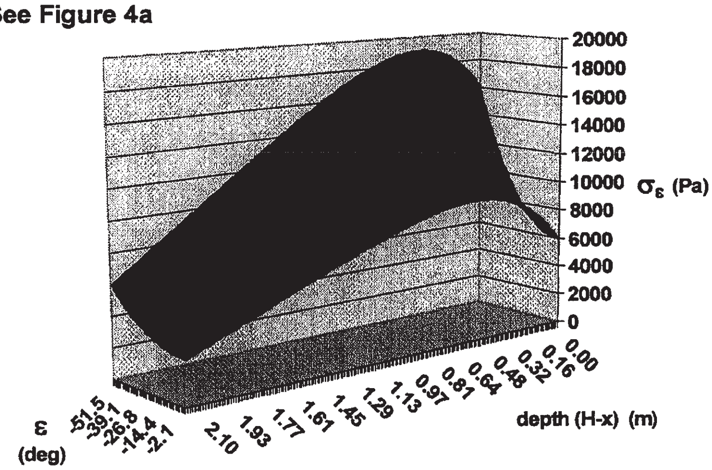

In order to ensure a stable surface (H_1=3m), a virtual passive surface stress condition has been imposed[7] and used to determine σ^*. This suggests problems with the circular arc approach at a free surface as mentioned by Nedderman of Enstad's model[1].
The minimum outlet for flow can be compared to Enstad and that for channel flow:
α=30°; β=21.5°; ϕ=30°; T=3000 Pa; H_1=3m; Minimum outlet:

Channel flow ($f_c/\rho g$)	0.306m
Enstad	0.732m
HvK circular arc model	0.491m

Thus, the present model predicts a stable arch between Enstad and the minimum value for channel flow.

DISCUSSION AND CONCLUSIONS

A 3-D stress distribution model has been derived using circular, stress arc geometry for bulk solids in a cone. While there are many approaches to solving the force balance equations that define the model, the Haar-von Karman hypothesis simplifies the equations to enable explicit analytical solutions. The system can model passive and active stress states, plus conditions in-between. Predicted stresses must be tested for stability by Mohr-Coulomb criteria, as the state of stress is only specified on a single line through the vessel, and many solutions are non-viable in this context.
Selection of appropriate boundary conditions allows prediction of the location of the stable cohesive arch and this prediction incorporates the stability criteria.
There is no direct evidence to support the HvK hypothesis, and this reflects our limited knowledge of stress distributions within hoppers. However, the HvK solution is just one possible set of solutions that can be achieved using the stress arc geometry approach.

REFERENCES

1. Nedderman, R.M., 1992, Statics and Kinematics of Granular Materials, Cambridge University Press
2. Enstad, G, 'On the theory of arching in mass flow hoppers', Chem.Eng.Sci., 1975, 30, 10, 1273-1283
3. Matchett A.J., 'Rotated, circular arc models of stress in silos applied to core-flow and vertical rat-holes', Powder Technology, 2005, ***162***, 87-99
4. Matchett A.J., 'Stresses in a bulk solid in a cylindrical silo, including an analysis of ratholes and an interpretation of rathole stability criteria', Chem.Eng.Sci, 2006, ***61***, 2035-2047
5. Haar A., von Karman T., 'Zur theorie der Spannungszustande in plastischen und sandartigen Medien', Nachr.Ges.Wiss.Gottingen, Math-Phys, 1909, K1, 204-218
6. Walker D.M., 'An approximate theory for pressure and arching in hoppers', Chem.Eng.Sci., 1966, 21, 975-997
7. Matchett A.J., 'Stresses in bulk solids in wedge hoppers: explicit, analytical solutions to the 2-dimensional stress distribution problem, using circular arc geometry', submitted for publication, Chem.Eng.Sci, 2006

Powder Technology 187 (2008) 298–306

Contents lists available at ScienceDirect

Powder Technology

journal homepage: www.elsevier.com/locate/powtec

Stress distributions in 2-dimensional, wedge hoppers with circular arc stress orientation — A co-ordinate-specific Lamé–Maxwell model

A.J. Matchett *, J.C. O'Neill, A.P. Shaw

School of Science & Technology, University of Teesside, Middlesbrough TS1 3BA, England

ARTICLE INFO

Article history:
Received 7 December 2007
Received in revised form 21 March 2008
Accepted 21 March 2008
Available online 4 April 2008

Keywords:
Hopper
Silo
Bulk solids
Powders
Stress
Arch
Cohesion

ABSTRACT

A 2-dimensional model of stress distribution in a wedge hopper has been developed. This is a co-ordinate-specific version of the Lamé–Maxwell equations in a space frame dictated by the assumption of circular arc, principal stress orientation.

A set of orthogonal, independent variables has been defined as x–ψ_o space. x is the vertical height of intersection of the circular principal stress arc with the wedge wall and the radius of the circular arc is proportional to x. ψ_o is the angle that the radius makes to the vertical at the lower arc in the system — lower boundary condition. The second principal stress follows ψ-lines through the vessel from ψ_o at the lower boundary, eventually passing through the vessel wall and leaving the system.

The model has been used to integrate the stress equations along lines of principal stress using numerical techniques. An analytical solution has been found at $\psi_o = 0$ of the same mathematical form as the Enstad/Walker/Walters equations.

The model can be used to predict the location of the stable, cohesive arch and to predict unviable stress states in terms of the Mohr–Coulomb yield criterion.

There is a requirement for experimental data of internal stress distributions within bulk solids in hoppers and silos to validate this and other models.

1. Introduction

The magnitude and orientation of stresses are the driving factors in gravity flow from hoppers and silos, and many other processes involving particles and bulk solids. Hence, an ability to estimate and model them is an important aspect of successful design and operation of such plant.

The modelling of the stress in hoppers and silos has a long history, dating back to the original paper of Janssen [1]. Further details are given in Nedderman's classic text [2].

Enstad [3] developed a unique approach to modelling by assuming that principal stresses aligned in circular arcs, making a constant angle with the vessel wall, controlled by wall friction. This method worked entirely in principal stress space and eliminated the need for shear terms in any force balance equations, greatly simplifying the mathematics of the resultant equations.

Matchett extended the Enstad approach to two dimensions, with rotational symmetry in order to describe the stability of ratholes [4,5], using the hopper specific R–ε co-ordinate system. These early papers were approximations in that they did not take account of curvature in the direction normal to the principal stress circular arc. However, recent analysis has shown the conclusions reached to be valid and consistent.

The present paper presents a rigorous 2-dimensional analysis of stress in a circular principal stress orientation after Enstad [3] and Matchett [4,5]. This gives a co-ordinate-specific version of the Lamé–Maxwell equations [6]. The equations can be integrated along the lines of principal stress, after Lamé–Maxwell.

2. The model geometry and co-ordinate systems

Consider a 2-dimensional wedge hopper with wall angles α_1 and α_2 — Fig. 1. A Cartesian co-ordinate system has its origin at the point of the wedge with axis X vertically, and Z horizontally. Thus a point P can be expressed in terms of $P(X,Z)$.

The system is one of plane stress — stresses in the third dimension are assumed to play no part in the analysis.

One of the two principal stresses acts in a circular arc orientation. An arc makes an angle β_1 to the normal of Wall 1 and β_2 to Wall 2 — Fig. 1. These angles are assumed to be constant throughout the vessel and are controlled by wall friction [2–4]:

$$\beta_{\text{passive}} = 0.5\left(\arcsin\left(\frac{\sin\phi_w}{\sin\phi}\right) + \phi_w\right)$$
$$\beta_{\text{active}} = 0.5\left(\arcsin\left(\frac{\sin\phi_w}{\sin\phi}\right) - \phi_w\right) \qquad (1)$$

* Corresponding author.
E-mail address: a.j.matchett@tees.ac.uk (A.J. Matchett).

0032-5910/$ – see front matter © 2008 Elsevier B.V. All rights reserved.
doi:10.1016/j.powtec.2008.03.013

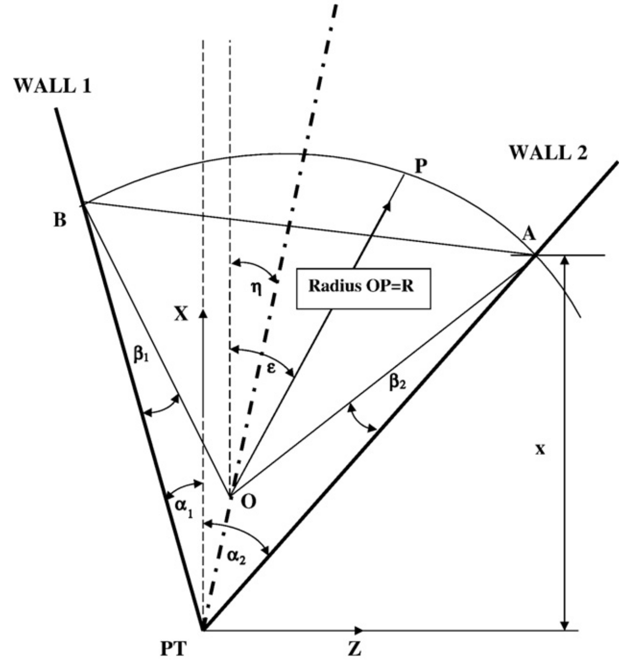

Fig. 1. General arrangement of the wedge hopper.

Subscripts passive and active denote the state of stress

ϕ is the angle of the yield locus
ϕ_w is the angle of wall friction

By definition, the second principal stress runs orthogonal to the circular arc throughout the wedge.

The validity of the circular arc principal stress orientation assumption has been discussed elsewhere, and will not be considered here in detail [2–5,7]. It is, at the very least, a viable, working assumption.

A circular arc co-ordinate system was proposed, specific to this stress system [4,5] — the R–ε or x–ε system. The point P may also be located by specifying the circular arc on which it resides, and the angle that the circular arc of radius R, through P, makes with the horizontal, ε, — Fig. 1. The location of the circular arc is specified by the vertical height, x, at which it cuts Wall 2. From the geometry of the system, it can be shown that:

$$\begin{aligned}
R &= a_1 x \\
a_1 &= \frac{\sin\gamma\sin(\alpha_1+\alpha_2)}{\sin\lambda\cos\alpha_2\sin(\gamma+\beta_1)} \\
\lambda &= \alpha_1+\beta_1+\alpha_2+\beta_2 \\
\gamma &= \frac{\pi}{2}-\frac{\lambda}{2}
\end{aligned} \tag{2}$$

Or for a symmetrical wedge with $\alpha_1=\alpha_2=\alpha : \beta_1=\beta_2=\beta$:

$$\begin{aligned}
R &= a_1 x \\
a_1 &= \frac{\tan\alpha}{\sin(\alpha+\beta)}
\end{aligned} \tag{2a}$$

In order to maintain the wall angles, the centre of each arc must progress through the wedge as x increases — along line O–O_1 in Fig. 2. Thus, for arc x, the arc centre, O, has co-ordinates O_X and O_Z in X–Z space, where:

$$\begin{aligned}
O_x &= x - R\cos(\alpha_2+\beta_2) \\
O_z &= x\tan\alpha_2 - R\sin(\alpha_2+\beta_2)
\end{aligned} \tag{3}$$

Point P in (X–Z) space can be related to its co-ordinates in (x–ε) space — Fig. 2

$$\begin{aligned}
X &= O_x + R\cos\varepsilon = x + R(\cos\varepsilon - \cos(\alpha_2+\beta_2)) = x\{1 + a_1(\cos\varepsilon - \cos(\alpha_2+\beta_2))\} \\
Z &= O_z + R\sin\varepsilon = x\tan\alpha_2 + R(\sin\varepsilon - \sin(\alpha_2+\beta_2)) = x\{\tan\alpha_2 + a_1(\sin\varepsilon - \sin(\alpha_2+\beta_2))\}
\end{aligned} \tag{4}$$

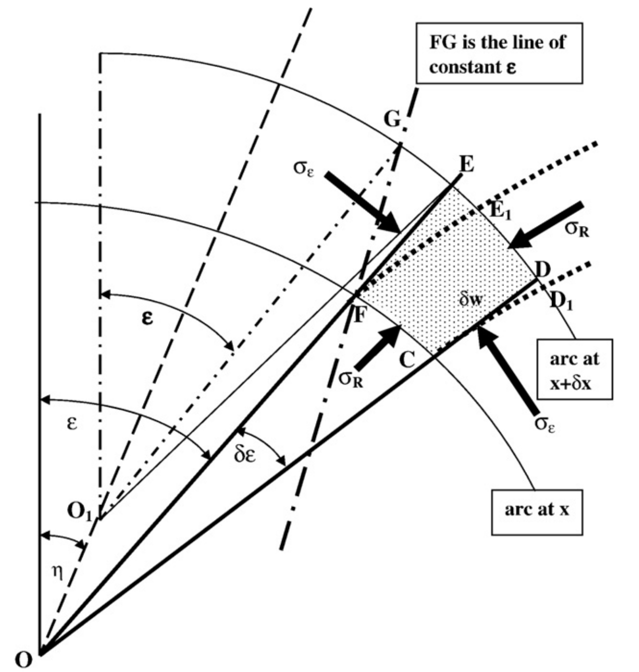

Fig. 2. The R–ε co-ordinate system and incremental element, along the principal stress trajectories.

The path of arc centre O makes an angle η with the vertical — Fig. 1. For a symmetrical wedge, $\eta=0$.

While x and ε are independent variables, they do not form an orthogonal, curvilinear, co-ordinate system. Fig. 2 shows an incremental element δx–$\delta\varepsilon$ coincident with the principal stress, circular arc orientations. Element CDEF shows an element of width $\delta\varepsilon$ at x, with element surfaces extended along the radius to $x+\delta x$ [4,5]. FG is the line of constant ε. Neither of these lines is orthogonal to the radius at $x+\delta x$. The trajectory of principal stress from x to $x+\delta x$ follows a curved path — element CD_1E_1F, where the stress trajectory and circular arc at $x+\delta x$ intersect at right-angles at D_1 & E_1.

The incremental element is shown in more detail in Fig. 3. Consider the principal stress trajectory in the direction of increasing x. At x this subtends an angle of ψ with the vertical. Whereas ε was an

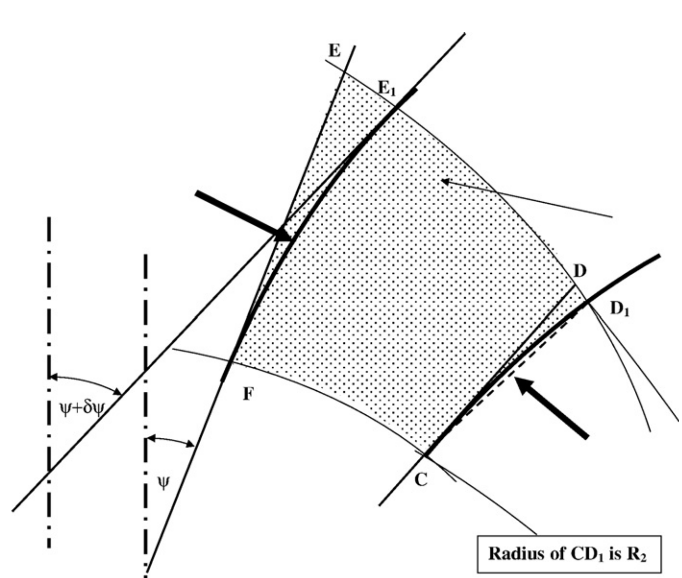

Fig. 3. Incremental element along the principal stress trajectories — derivation of the ψ line.

independent variable, the value of ψ is controlled by the circular arc orientation — ψ is not independent of x. Due to the curvature of the boundaries, the radius at $x+\delta x$ subtends an angle of $(\psi+\delta\psi)$ with the vertical. Linearised arc FE_1 makes angle $\delta\psi/2$ with radius OF.

The span of arc FE_1, δw, can be found — Fig. 4. Thus, the path of the radius at $x+\delta x$, from O to E_1, O–O_1–E_1, is resolved onto the radius at x — at angle ψ, with distance O–$O_1=\delta O$, then:

$$[R]_x + \delta w \cos(\delta\psi/2) = \delta O \cos(\psi - \eta) + [R]_{x+\delta x} \cos(\delta\psi)$$

Noting that:

$$\delta O^2 = \delta O_X^2 + \delta O_Z^2$$

and as $\delta\psi$ tends to zero, $\cos(\delta\psi)$ tends to 1, using Eq. (4) to find increments δO_X and δO_Z:

$$\begin{aligned}
&\left(\frac{\partial w}{\partial x}\right) = a_1 + a_2\cos(\psi-\eta)\\
&a_2 = \frac{\partial O}{\partial x} = \sqrt{\left(\frac{\delta O_x}{\delta x}\right)^2 + \left(\frac{\delta O_z}{\delta x}\right)^2}\\
&\therefore a_2 = \sqrt{\{1 - a_1\cos(\alpha_2+\beta_2)\}^2 + \{\tan\alpha_2 - a_1\sin(\alpha_2+\beta_2)\}^2}
\end{aligned} \tag{5}$$

and

$$\eta = \arctan\left(\frac{\delta O_z}{\delta O_x}\right) = \arctan\left\{\frac{\tan\alpha_2 - a_1\sin(\alpha_2+\beta_2)}{1 - a_1\cos(\alpha_2+\beta_2)}\right\} \tag{6}$$

In the limit, point E and E_1 will coincide. Thus, resolving onto the Z plane:

$$\delta O\sin(\psi-\eta) + [R\sin\psi]_{x+\delta x} = [R\sin\psi]_x + \delta w\sin(\psi + \delta\psi/2)$$

Hence:

$$\frac{\partial\psi}{\partial x} = \frac{a_2\sin(\psi-\eta)}{R} \tag{7}$$

Let arc FE_1 have a curvature R_2 through angle $\delta\psi$. Thus

$$R_2\delta\psi = \delta w$$

Therefore:

$$R_2 = \frac{\partial w}{\partial x}\Big/\frac{\partial\psi}{\partial x} \tag{8}$$

The trajectory of the second principal stress may be determined from Eq. (7). For a non-symmetrical wedge, ψ may be replaced by $\psi'=(\psi-\eta)$.

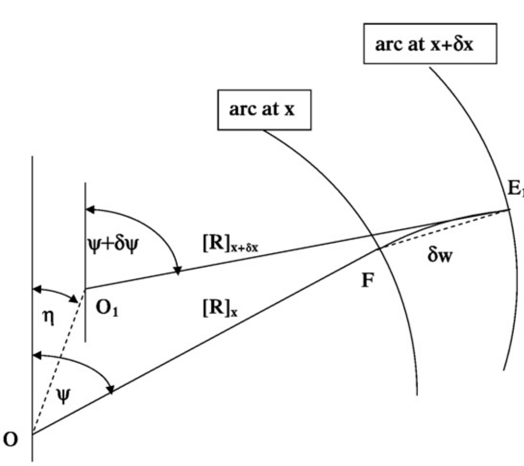

Fig. 4. Arc increment δw.

Thus for a symmetrical wedge:

$$\frac{\partial\psi}{\sin\psi} = \frac{a_2}{a_1}\frac{\partial x}{x}$$

hence:

$$\ln\left(\frac{\operatorname{cosec}\psi - \cot\psi}{\operatorname{cosec}\psi_o - \cot\psi_o}\right) = \left(\frac{a_2}{a_1}\right)\ln\left(\frac{x}{H}\right) \tag{9}$$

where the boundary condition is:

$$x = H \quad : \quad \psi = \psi_o$$

Eq. (9) shows that ψ is a function of x. This is the equation of the ψ-line. Hence x and ψ do not form a set of independent variables.

Unfortunately, it is not explicit in ψ or ψ_o.

Eq. (9) may be more conveniently written for differentiation as:

$$\ln(\operatorname{cosec}\psi - \cot\psi) - \ln(\operatorname{cosec}\psi_o - \cot\psi_o) = \left(\frac{a_2}{a_1}\right)\ln\left(\frac{x}{H}\right)$$

and noting that:

$$\frac{\partial}{\partial\psi}\ln(\operatorname{cosec}\psi - \cot\psi) = \operatorname{cosec}\psi$$

then:

$$\frac{\partial\psi}{\partial\psi_o} = \frac{\sin\psi}{\sin\psi_o} \tag{10}$$

It can be shown that x and ψ_o form a set of orthogonal, curvilinear, independent variables. Substitution of ψ for ε in Eq. (4) gives the equation of the ψ line in (X–Z) space. Thus:

$$\begin{aligned}
&\frac{\partial X}{\partial x} = [1 - a_1\cos(\alpha+\beta)] + a_1\left(\cos\psi - x\sin\psi\frac{\partial\psi}{\partial x}\right)\\
&\frac{\partial Z}{\partial x} = [\tan\alpha - a_1\sin(\alpha+\beta)] + a_1\left(\sin\psi + x\cos\psi\frac{\partial\psi}{\partial x}\right)\\
&\frac{\partial X}{\partial\psi_o} = -a_1 x\sin\psi\frac{\partial\psi}{\partial\psi_o}\\
&\frac{\partial Z}{\partial\psi_o} = a_1 x\cos\psi\frac{\partial\psi}{\partial\psi_o}
\end{aligned} \tag{11}$$

The unit base vector matrix can be formed [8,9]:

$$\begin{aligned}
&\begin{vmatrix} ex \\ e\psi_o \end{vmatrix} = \begin{vmatrix} \frac{1}{h_1}\frac{\partial X}{\partial x} & \frac{1}{h_1}\frac{\partial Z}{\partial x} \\ \frac{1}{h_2}\frac{\partial X}{\partial\psi_o} & \frac{1}{h_2}\frac{\partial Z}{\partial\psi_o} \end{vmatrix} \begin{vmatrix} eX \\ eZ \end{vmatrix}\\
&h_1^2 = \left(\frac{\partial X}{\partial x}\right)^2 + \left(\frac{\partial Z}{\partial x}\right)^2\\
&h_2^2 = \left(\frac{\partial X}{\partial\psi_o}\right)^2 + \left(\frac{\partial Z}{\partial\psi_o}\right)^2
\end{aligned} \tag{12}$$

where ex, $e\psi_o$, eX & eZ are unit vectors in the x, ψ_o, X and Z directions.

The transformation matrix in Eq. (12) is indicative of an orthogonal, curvilinear co-ordinate system. When the matrix is multiplied by its transpose, it gives the identity matrix — its inverse is equal to its transpose. This is characteristic of a set of curvilinear, orthogonal, independent variables [8,9].

Typical principal stress trajectories are shown in Fig. 5. The trajectories normal to the circular arc diverge as x increases — Eqs. (9) and (10).

3. Stress distributions

2-dimensional principal stress distributions along trajectories of principal stress are given by the well-known Lamé–Maxwell equations [6,8]:

$$\begin{aligned}
&\frac{\partial\sigma_1}{\partial s_1} + \frac{\sigma_1 - \sigma_2}{\rho_2} + \mathrm{grav1} = 0\\
&\frac{\partial\sigma_2}{\partial s_2} + \frac{\sigma_1 - \sigma_2}{\rho_1} + \mathrm{grav2} = 0
\end{aligned} \tag{13}$$

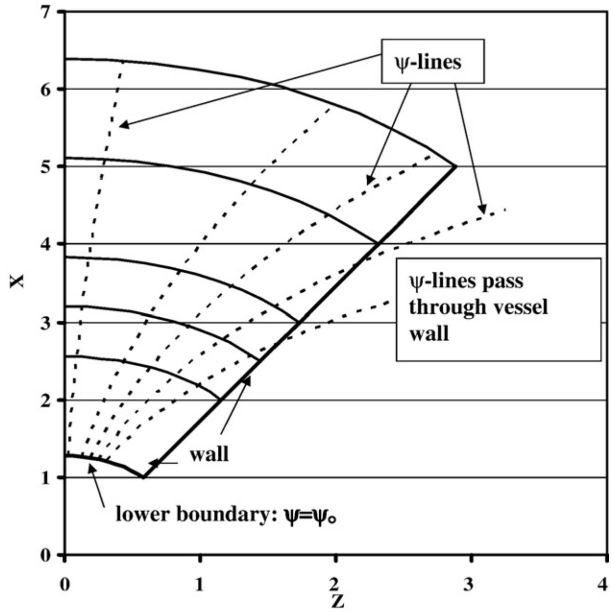

Fig. 5. Typical principal stress trajectories in a wedge hopper — not to scale.

where σ_1, σ_2 are principal stresses acting along trajectories s_1, s_2 respectively.

ρ_2, ρ_1 are the curvatures over which σ_1 and σ_2 act — ρ_2 is the curvature of trajectory s_2 grav1 and grav2 are the components of gravity.

An equivalent derivation can be performed upon incremental element CD_1E_1F in Figs. 1 and 2 in x–ψ_o space. Thus, incremental arc length CF is based upon an increment of ψ_o equal to $\delta\psi_o$. Therefore the actual arc length is $R\delta\psi$ which increases with x and:

$$\delta\psi = \frac{\partial\psi}{\partial\psi_o}\delta\psi_o$$

Thus, as x increases, not only does R increase, but $\delta\psi$ also increases — Fig. 5.

Principal stress σ_R acts upon surface CF, in the direction of R, and principal stress $\sigma\psi$ acts upon surface E_1F in the direction of ψ.

Table 1 gives the traction forces acting upon each side of incremental element CD_1E_1F.

Hence, static or incipient flow force balances in the R and ψ directions, with no inertial effects give:

$$\begin{aligned}&\left[\sigma_R R\left(\frac{\partial\psi}{\partial\psi_o}\right)\delta\psi_o\right]_x - \left[\sigma_R R\left(\frac{\partial\psi}{\partial\psi_o}\right)\delta\psi_o\right]_{x+\delta x}\cos\left(\frac{\partial\psi}{\partial x}\delta x\right)\\ &+\left[\sigma_\psi\delta w\right]_{\psi_o+\delta\psi_o}\sin\left(\frac{\partial\psi}{\partial\psi_o}\delta\psi_o\right)\\ &-R\left(\frac{\partial\psi}{\partial\psi_o}\right)\delta\psi_o\delta w\rho g\cos\psi = 0\end{aligned}$$

$$\begin{aligned}&\left[\sigma_\psi\delta w\right]_{\psi_o} - \left[\sigma_\psi\delta w\right]_{\psi_o+\delta\psi_o}\cos\left(\frac{\partial\psi}{\partial\psi_o}\delta\psi_o\right)\\ &-\left[\sigma_R R\left(\frac{\partial\psi}{\partial\psi_o}\right)\delta\psi_o\right]_{x+\delta x}\sin\left(\frac{\partial\psi}{\partial x}\delta x\right)\\ &+R\left(\frac{\partial\psi}{\partial\psi_o}\right)\delta\psi_o\delta w\rho g\sin\psi = 0\end{aligned}$$

In the limit, as δx and $\delta\psi_o$ tend to zero, the above equations become:

$$-\frac{\partial}{\partial x}\left[R\sigma_R\left(\frac{\partial\psi}{\partial\psi_o}\right)\right] + \sigma_\psi\left(\frac{\partial w}{\partial x}\right)\left(\frac{\partial\psi}{\partial\psi_o}\right) - R\left(\frac{\partial\psi}{\partial\psi_o}\right)\left(\frac{\partial w}{\partial x}\right)\rho g\cos\psi = 0 \quad (14)$$

$$-\frac{\partial}{\partial\psi_o}\left[\sigma_\psi\frac{\partial w}{\partial x}\right] - \sigma_R R\left(\frac{\partial\psi}{\partial\psi_o}\right)\left(\frac{\partial\psi}{\partial x}\right) + R\left(\frac{\partial\psi}{\partial\psi_o}\right)\left(\frac{\partial w}{\partial x}\right)\rho g\sin\psi = 0 \quad (15)$$

Table 1
Components of the force balance on incremental element CD_1E_1F — Figs. 2 & 3

Component	Area	Stress	Traction	Line of Action
				Angle to the vertical
Curve CF	$\left[R\frac{\delta\psi}{\partial\psi_o}\delta\psi_o\right]_x$	$[\sigma_R]_{x,\psi_o}$	$\left[\sigma_R R\frac{\partial\psi}{\partial\psi_o}\delta\psi_o\right]_x$	$[\psi+\delta\psi/2]_x$
Curve D_1E_1	$\left[R\frac{\delta\psi}{\partial\psi_o}\delta\psi_o\right]_{x+\delta x}$	$[\sigma_R]_{x+}\delta_x$	$\left[\sigma_R R\frac{\partial\psi}{\partial\psi_o}\delta\psi_o\right]_{x+\delta x}$	$[\psi+\delta\psi/2]_{x+\delta x}$
Curve E_1F	$[\delta w]_\psi$	$[\sigma_\psi]_\psi$	$[\sigma_\psi\delta w]_\psi$	$\pi/2-(\psi+\delta\psi/2)$
Curve CD_1	$[\delta w]_{\psi+\delta\psi}$	$[\sigma_\psi]_{\psi+\delta\psi}$	$[\sigma_\psi\delta w]_{\psi+\delta\psi}$	$\pi/2-(\psi+\delta\psi+\delta\psi/2)$
Gravity			$R\delta w\left(\frac{\partial\psi}{\partial\psi_o}\right)\rho g\delta\psi_o$	0

Eqs. (14) and (15) are co-ordinate-specific versions of the Lamé–Maxwell equations — Eq. (13). In fact, using the transformations shown in Table 2, Eqs. (14) and (15) become identical to Eq. (13): see Appendix.

The advantage of Eqs. (14) and (15) is that the principal stress orientation information is included in the equations.

Eqs. (14) and (15) may be integrated numerically with appropriate boundary conditions. In addition, Eq. (7) must also be integrated such that at a given value of x and ψ_o, ψ is also known — Fig. 5. These integrations have been implemented on Excel spreadsheets.

For a symmetrical wedge consider conditions at $\psi_o=0$, and assume that the state of stress is known along this line:

$$\psi_o = 0 \quad : \quad \sigma_R = S = J\sigma_\psi + (J-1)T \quad (16)$$

$\sigma_R=S$ at $\psi_o=0$ is the spine of the solution around which all other stress values are fixed.

J is a measure of the state of stress. For a linearised yield locus [4,5,7]:

$$\begin{aligned}&\tau = \sigma\tan\phi + c\\ &T = \frac{c}{\tan\phi}\\ &J_{\text{passive}} = \frac{1+\sin\phi}{1-\sin\phi}\\ &J_{\text{active}} = 1/J_{\text{passive}}\end{aligned}$$

ϕ is the internal angle of friction of the yield locus
c is the cohesion
T is the linearised tensile parameter
J is a measure of the state of stress, subscripts referring to the passive and active stress states, and to comply with the Mohr–Coulomb yield criterion:

$$J_{\text{passive}} \le J = \frac{\sigma_\psi + T}{\sigma_R + T} \le J_{\text{passive}}$$

Also, at some point in the vessel, the radial stress must be known:

$$\begin{aligned}&x = H_1 \quad : \quad \sigma_R = \sigma_R(\psi_o)\\ &x = H_1 \quad : \quad \psi = \psi_o\end{aligned} \quad (17)$$

Eqs. (14) and (15) may then be integrated, using Euler or Runge–Kutta for values of x between H_1 and H_2 ($H_2>H_1$).

Table 2
Comparisons of x–ψ_o equations — Eqs. (14) and (15)—with the Lame–Maxwell equations — Eq. (13)

Lame–Maxwell parameters	x–ψ_o parameters
σ_1	σ_R
σ_2	σ_ψ
δs_1	δw
δs_2	$R\delta\psi = R\left(\frac{\partial\psi}{\partial\psi_o}\right)\delta\psi_o$
ρ_1	$R_2 = \left(\frac{\partial w}{\partial x}\right)/\left(\frac{\partial\psi}{\partial x}\right)$
ρ_2	R
grav1	$\rho g\cos\psi$
grav2	$-\rho g\sin\psi$

Both of these approaches are helped by the presence of an analytical solution at $\psi_o=0$:

$$\psi_o=0\ :\ \psi=0\ :\ \frac{\partial\psi}{\partial\psi_o}=1\ :\ \frac{\partial\psi}{\partial x}=0$$
$$\psi_o=0\ :\ \sigma_R=S\ :\ \frac{\partial W}{\partial x}=W=(a_1+a_2)$$

Eq. (14) becomes:

$$\left(\frac{\partial\psi}{\partial\psi_o}\right)\frac{d}{dx}[RS]+RS\frac{\partial}{\partial x}\left(\frac{\partial\psi}{\partial\psi_o}\right)=\left(\frac{\partial\psi}{\partial\psi_o}\right)W\{JS+(J-1)T\}-\rho gRW\left(\frac{\partial\psi}{\partial\psi_o}\right) \tag{18}$$

Noting that:

$$\frac{\partial}{\partial x}\left(\frac{\partial\psi}{\partial\psi_o}\right)=\frac{\partial}{\partial\psi_o}\left(\frac{\partial\psi}{\partial x}\right)=\frac{a_2}{a_1}\left(\frac{\cos\psi}{x}\right)\left(\frac{\partial\psi}{\partial\psi_o}\right)$$

Then:

$$x\frac{dS}{dx}+S\left(1+\frac{a_2}{a_1}\right)=\frac{WJ}{a_1}S+\frac{W(J-1)T}{a_1}-\rho gWx \tag{19}$$

Eq. (19) has an analytical solution, with boundary condition:

$$x=H\ :\ S=S^*$$

$$\begin{aligned}
S&=-\frac{C_2}{C_1}+\left(\frac{C_3}{C_1-1}\right)x+(\mathrm{const})x^{C_1}\\
C_1&=\frac{WJ}{a_1}-1-\frac{a_2}{a_1}\\
C_2&=\frac{W(J-1)T}{a_1}\\
C_3&=\rho gW\\
(\mathrm{const})&=\frac{\left(S^*+\frac{C_2}{C_1}-\left(\frac{C_3}{C_1-1}\right)H\right)}{H^{C_1}}
\end{aligned} \tag{20}$$

Eq. (20) has the mathematical form as the Enstad/Walker/Walters equations of stress distribution [3,10,11].

The model can be applied in two ways:

1. Fixed stress mode: Fix the stress $\sigma_R=S$ at H_1 & H_2 (for $\psi_o=0$). J is adjusted to conform to the chosen boundary values within the Mohr–Coulomb limits.
2. Stress state mode: Fix stress $\sigma_R=S$ at $x=H_2$ and fix J — the state of stress (for $\psi_o=0$). Calculate the stress S at $x=H_1$ and put $\sigma_R=S$ at $x=H_1$ for all ψ_o.

The fixed stress mode can be used for modelling a stable cohesive arch. The stress state mode can be used to investigate a given value of J — for example the active stress state. Examples of both these are given below:

3.1. The cohesive arch

Values of H_1 and H_2 are fixed, $H_2>H_1$.

At $x=H_1$: $S=0$ and $\sigma_R=0$ for all ψ_o. This is the unconfined surface of the cohesive arch.

At $x=H_2$: $S=0$: at the bulk solids surface at $\psi_o=0$, the surface overpressure is zero. Other values may be chosen, as required. Thus

$$(\mathrm{const})=\frac{\left(\frac{C_2}{C_1}-\left(\frac{C_3}{C_1-1}\right)H_2\right)}{H_2^{C_1}} \tag{21}$$

The value of J is chosen in Eq. (20), such that the boundary values of S are given at $x=H_1$ as well as at $x=H_2$. On the spreadsheets this is done using the "solver" tool.

Eqs. (7), (14) and (15) are then integrated numerically.

The data presented is from a spreadsheet that has 80 increments in ψ_o and 200 increments in x.

Results from a typical simulation for a 30° wedge are shown in Fig. 6a–c)) and are conveniently plotted as surfaces in x–ψ_o space.

As ψ exceed $(\alpha+\beta)$ the ψ-line passes through the wall of the wedge and leaves the system — Fig. 5. Stresses have been put equal to zero beyond this point. The jagged edges of the stress surfaces are a result of this truncation.

The lower arch location (H_1) has been chosen arbitrarily. It must be checked for conformance to the Mohr–Coulomb yield criterion. This is done by the Mohr–Coulomb Yield Factor: MCYF:

$$\begin{aligned}
&J=\frac{\sigma_\psi+T}{\sigma_R+T}\\
&\mathrm{MCYF}=1\ \text{ if }\ J>J_{\mathrm{passive}}\\
&\mathrm{MCYF}=-1\ \text{ if }\ J<J_{\mathrm{active}}\\
&\mathrm{MCYF}=0\ \text{ if }\ J_{\mathrm{active}}\le J\le J_{\mathrm{passive}}\\
&\mathrm{MCYF}=-10\ \text{ if }\ \psi\ge(\alpha+\beta)
\end{aligned} \tag{22}$$

The last condition of Eq. (22) excludes data outside of the wall of the wedge.

Fig. 6c shows that the system invalidates Mohr–Coulomb yield in the region of the cohesive arch, at the wall.

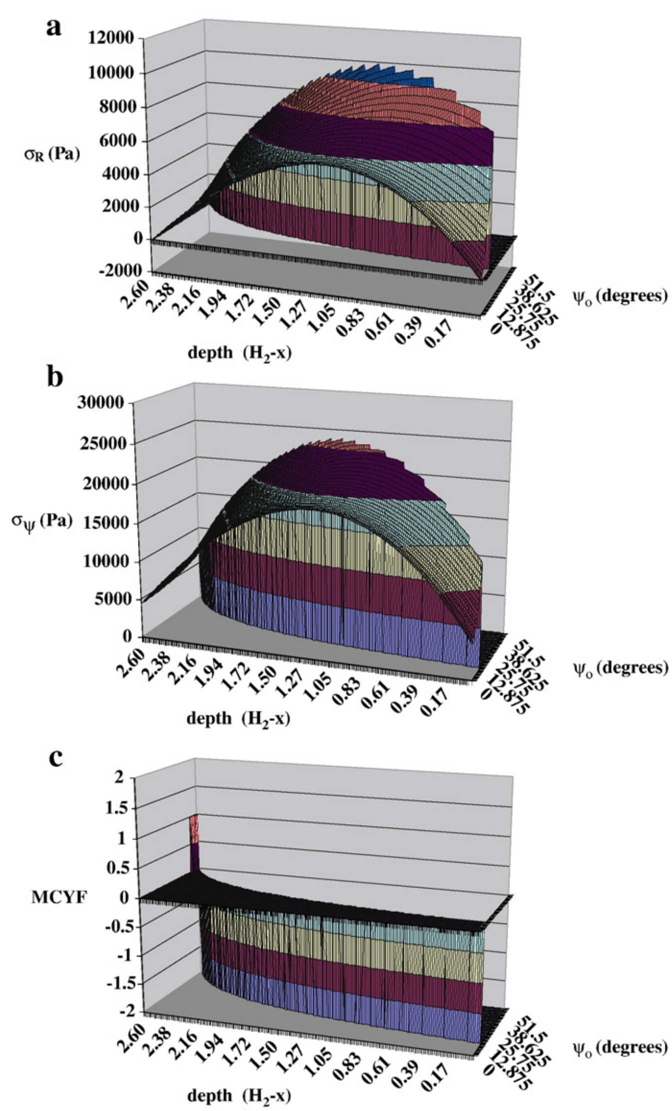

Fig. 6. Cohesive arch model in x–ψ_o space. a) σ_R. b) σ_ψ. c) MCYF. α=30°: β=21.5°: H_1=0.4 m: H_2=3 m (β calculated from Eq. (1) for passive stress). ρ=1000 kg/m^3: ϕ=30°: T=3000 Pa. J=2.510.

A similar calculation with H_1=0.35 (J=2.384) gives complete conformity to the Mohr–Coulomb criterion. This value was found by iteration to be the maximum value of H_1 that met Mohr–Coulomb conditions. Thus a stable arch may form when H_1<=0.35.

Therefore, the model may be used to calculate the location of the stable arch — maximum outlet for a stable arch/minimum outlet for flow, in a similar manner to Jenike's original model [2,12,13].

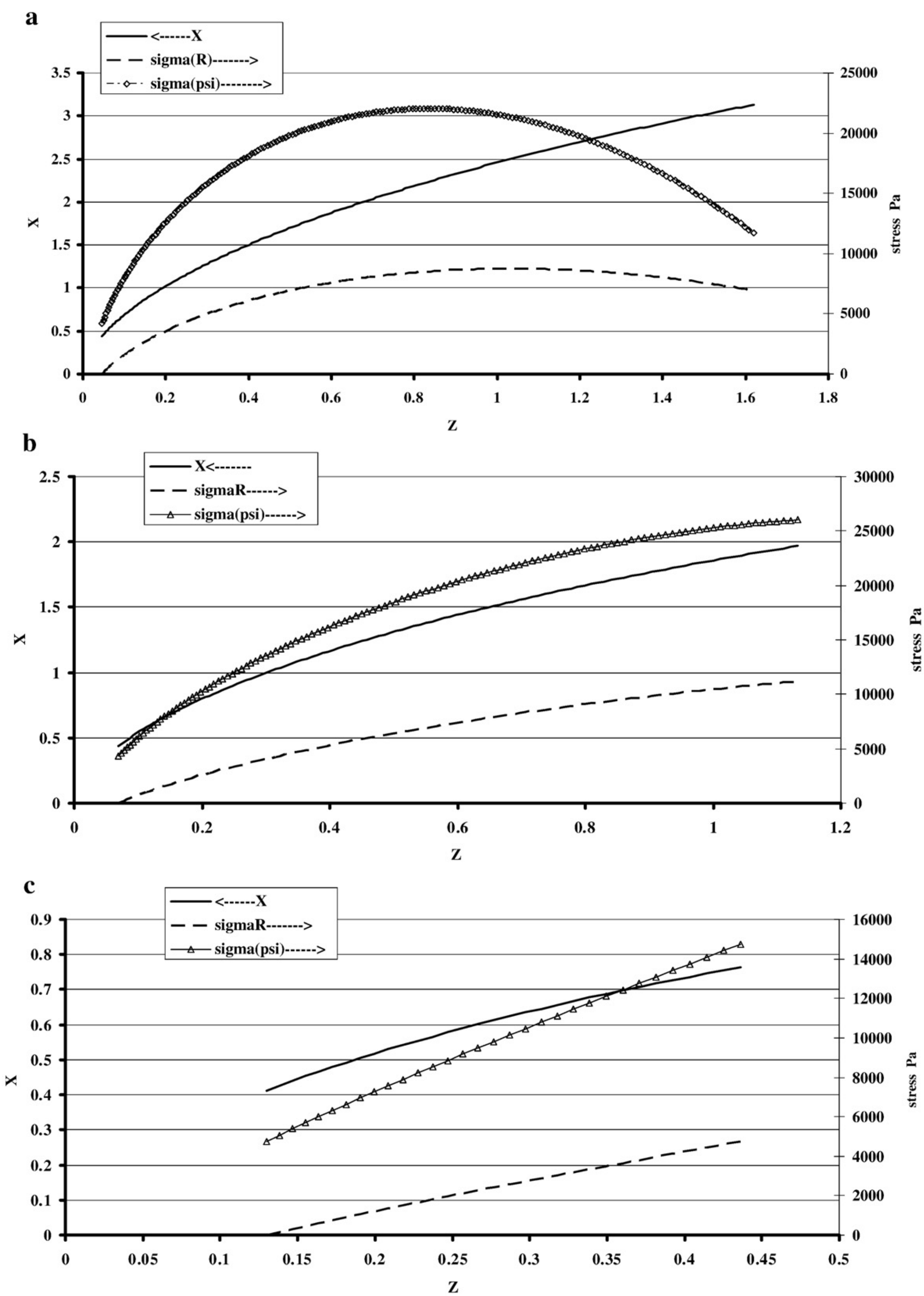

Fig. 7. Cartesian plots of data for conditions of the stable cohesive arch. a) ψ_o=10.3° b) ψ_o=15.45°. c) ψ_o=30.26°. α=30°: β=21.5°: H_1=0.35 m: H_2=3 m (β calculated from Eq. (1) for passive stress). ρ=1000 kg/m^3: ϕ=30°: T=3000 Pa. J=2.384.

It will be noted in Fig. 6a that the stress, σ_R, acting on the surface of the solids, at $x=H_2$ is not equal to zero — there is an overpressure. Nedderman noted this problem at the free surface of the Enstad approach in his text [2]. However, the surface stress is of the order of that imposed upon the circular arc by a levelled surface of material.

Fig. 6 show stress trends, but it is difficult to extract stress values from the graphs and the graphs are in x–ψ_o space rather than conventional Cartesian space. One method in which this may be overcome is to plot spatial and stress data in terms of horizontal co-ordinate Z. Examples are shown in Fig. 7a–c for the stable arch conditions ($H_1=0.35$) referred to above. These data are plotted at specific ψ_o values. The plot of X versus Z is the chi-line at the specified ψ_o value. Stresses may also be read from the right-hand axis. This enables a position in Cartesian space to be fixed and the stresses at that point to be determined.

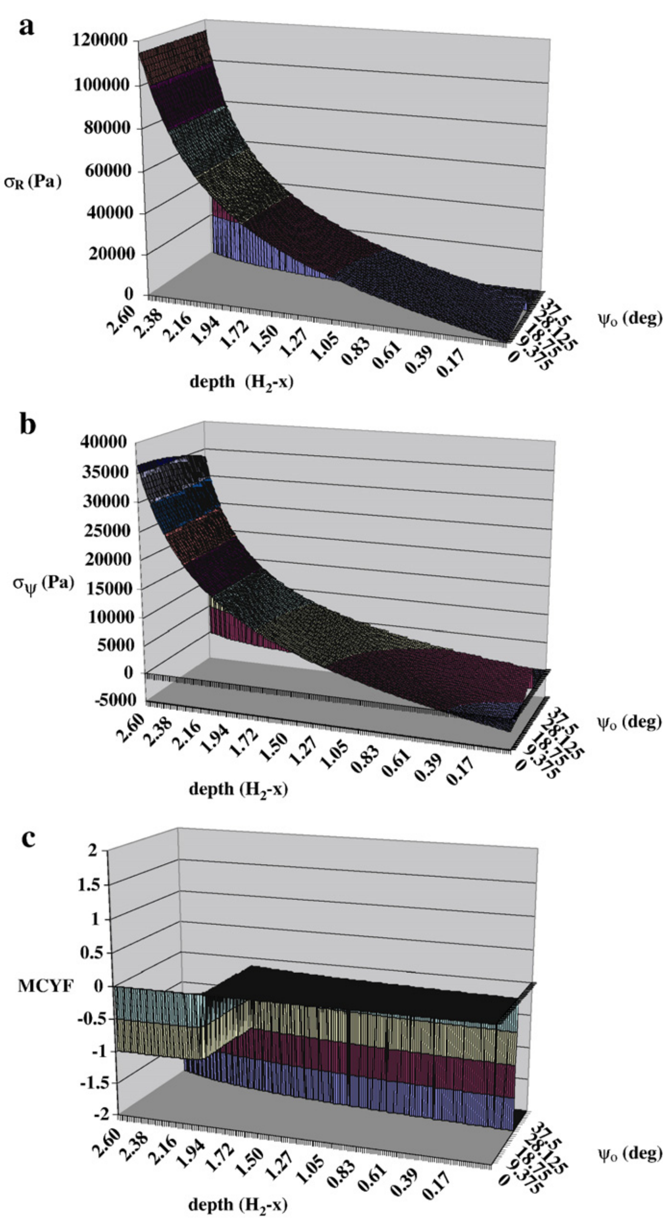

Fig. 8. Active stress state model in x–ψ_o space. a) σ_R. b) σ_ψ. c) MCYF. $\alpha=30°$: $\beta=7.5°$: $H_1=0.4$ m: $H_2=3$ m (β calculated from Eq. (1) for active stress). $\rho=1000$ kg/m^3: $\phi=30°$: $T=3000$ Pa. $J=0.3333$. Stress at $x=H_1$: $\sigma_R=1.148*10^5$ Pa.

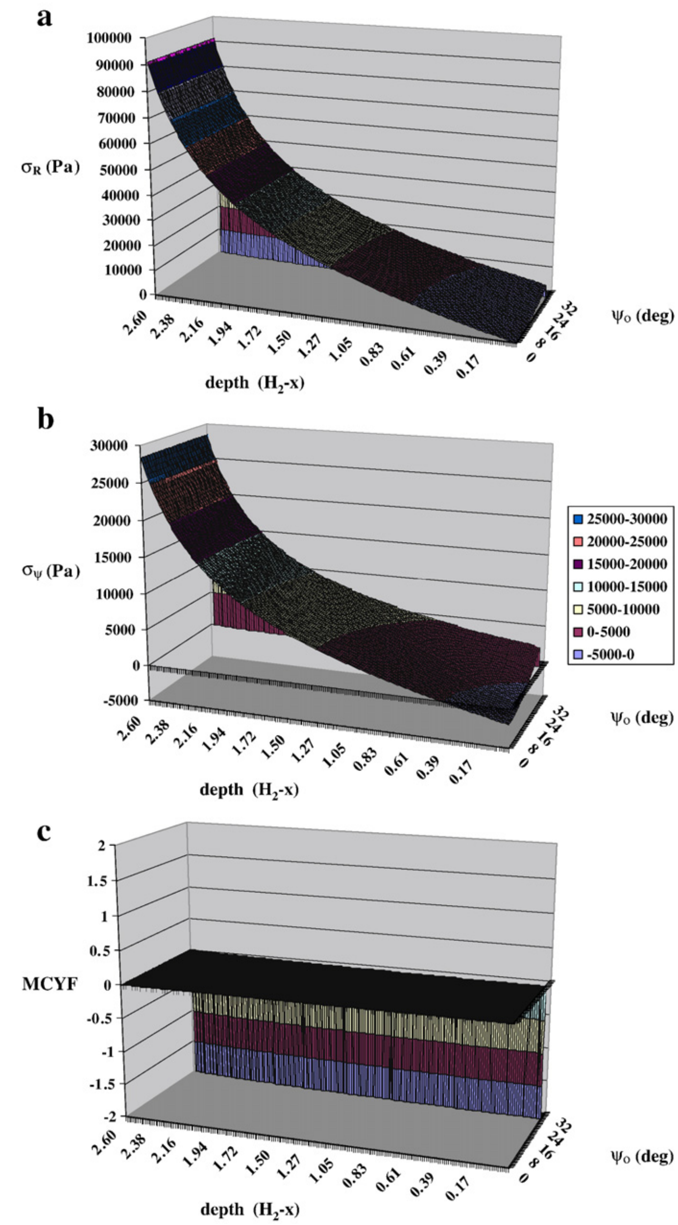

Fig. 9. Active stress state model in x–ψ_o space. a) σ_R. b) σ_ψ. c) MCYF. $\alpha=30°$: $\beta=2°$: $H_1=0.4$ m: $H_2=3$ m calculated from Eq. (1) for active stress). $\rho=1000$ kg/m^3: $\phi=30°$: $T=3000$ Pa. $J=0.3333$. Stress at $x=H_1$: $\sigma_R=91{,}212$ Pa.

3.2. The active stress state

Fig. 8a–c)) show the same hopper as in Fig. 6, but in a state of active stress.

$x=H_2$: $S=0$

$J=0.3333$

(const) is calculated using Eq. (21)

$$x=H_1\ :\ S=-\frac{C_2}{C_1}+\left(\frac{C_3}{C_1-1}\right)H_1+(\mathrm{const})H_1^{C_1} \tag{23}$$

$x=H_1$: $\sigma_R=S(H_1)$ for all ψ_o

Surface overpressure is again present on the upper surface, Fig. 7a. However, lateral stress variations are generally small.

The system contravenes the Mohr–Coulomb criterion in active stress towards the base of the hopper. β has been assigned its maximum value compatible with the active stress state for this calculation, as given by Eq. (1). If β is reduced, the offending region becomes smaller, until it disappears completely at β=2°. These conditions are shown in Fig. 9a–c)).

Alternatively, as J is increased from J_{active}, the region of non-compatibility with Mohr–Coulomb decreases, until it disappears at J=0.36, with S=1,087 * 10^5 Pa at x=0.4. However, this somewhat negates the concept of calculating stresses at a given stress state.

These observations suggest that the materials would plastically deform and stress orientations re-align until a compliant stress state was reached.

4. Discussion

The model of stress distributions within a circular arc principal stress orientation shows much, potentially useful information. The model is able to predict location of the stable cohesive arch, and to predict unviable stress situations according to the Mohr–Coulomb yield criterion. It is able to model conditions over a wide range of stress states from active to passive.

However, there are few experimental data on internal stress distributions within bulk solids to validate this, or other models, such as DEM or FEM.

The model follows principal stresses in x–ψ_o spaces and integrates along the ψ–lines — Eq. (9). However, ψ-lines pass through the walls of the wedge — Fig. 5. This makes implementation of the model difficult, other than in its present form. Limitations include:

- As x increases, the size of the incremental element increases due to both increase in arc radius, and reduction of the number of elements as ψ-lines pass through the walls of the system.
- Whilst it is relatively easy to implement boundary conditions at ψ_o=0, it would be far more difficult to impose wall boundary conditions, for example, as ψ changes with the increase in x.
- Likewise, it would be difficult to impose surface boundary conditions (x=H_2) and integrate down the wedge — new elements would appear down the length.

There are other ways of handling the above situations and we hope to present them in another paper [14].

5. Conclusions

A 2-dimensional model of stress distribution in a wedge hopper has been developed. This is a co-ordinate-specific version of the Lamé–Maxwell equations in a space frame dictated by the assumption of circular arc, principal stress orientation.

The model has been used to integrate the stress equations along lines of principal stress.

The model can be used to predict the location of the stable, cohesive arch and to predict unviable stress states in terms of the Mohr–Coulomb yield criterion.

6. Notation

a_1	Arc radius constant, $a_1 = \frac{\sin_\gamma \sin_{(\alpha_1+\alpha_2)}}{\sin_\lambda \cos_{\alpha_2} \sin_{(\gamma+\beta_1)}}$	[–]
a_2	Arc thickness constant, $a_2 = \sqrt{\{1 - a_1 \cos(\alpha_2+\beta_2)\}^2 + \{\tan\alpha_2 - a_1 \sin(\alpha_2+\beta_2)\}^2}$	[–]
(const)	Constant of integration	[Pa/m^{C_1}]
C_1	Constant in stress equations $C_1 = \frac{WJ}{a_1} - 1 - \frac{a_2}{a_1}$	[–]
C_2	Constant in stress equation $C_2 = W(J-1)T/a_1$	[Pa]
C_3	Constant in stress equation $C_3 = \rho g W$	[Pa/m]
c	Cohesion	[Pa]
ex, $e\psi_o$, eX, eZ	Unit vectors in x–ψ_o & X–Z space	[–]
g	Acceleration due to gravity	[m/s^2]
grav1, grav2	Components if gravity in directions s_1 & s_2	[Pa/m]
H	Value of x at for boundary condition in σ_R	[m]
H_1	Value of x for lower boundary conditions	[m]
H_2	Value of x at upper surface	[m]
h_1, h_2	Scaling factors for unit vector	[m]
J	Material ratio of effective stresses $J = \frac{\sigma_\varepsilon + T}{\sigma_R + T}$	[–]
MCYF	Mohr–Coulomb Yield Factor	[–]
O_x	Vertical co-ordinate of arc centre	[m]
O_z	Horizontal co-ordinate of arc centre	[m]
R	Principal stress arc radius	[m]
R_2	Local curvature of the ψ-line	[m]
S	Spinal value of σ_R: radial stress at ε=η	[Pa]
S^*	Boundary value of S	[Pa]
s_1, s_2	Principal stress directions in Lamé–Maxwell equation	[m]
T	Material tensile parameter — linearised yield locus	[Pa]
W	Value of $\partial w/\partial x$ at ε=η	[–]
x	Height of intersection of arc with Wall 2	[m]
X	Vertical co-ordinate	[m]
Z	Horizontal co-ordinate	[m]
α_1, α_2	Angle of wall to vertical	[rad]
β_1, β_2	Angle of arc to wall normal	[rad]
δw	Incremental element thickness	[m]
δO	Incremental change of arc centre O	[m]
$\delta\psi$	Increase in angle of orientation of stress — Fig. 4	[rad]
ε	Angular co-ordinate, angle between arc radius and vertical	[rad]
ϕ	Material angle of friction	[rad]
ϕ_w	Angle of wall friction	[rad]
γ	Angle γ=π/2−γ/2	[rad]
ψ	Angle of principal stress trajectory	[rad]
ψ_o	Value of ψ at x=H	[rad]
λ	Total span of arc λ=α_1+β_1+α_2+β_2	[rad]
η	Angle of precession of arc centre to vertical	[rad]
ρ	Bulk density	[kg/m^3]
ρ_1, ρ_2	Curvatures of principal stress space in the Lamé–Maxwell equations	[m]
$\sigma\psi$	Arc stress	[Pa]
σ_R	Radial stress	[Pa]
σ_1, σ_2	Principal stresses in the Lamé–Maxwell equations	[Pa]

Appendix A. Comparison of the force balance equations with the Lamé–Maxwell equations

Force balance Eqs. (14) and (15) can be transposed into the Lamé–Maxwell equations.

For the R-direction:

$$-\frac{\partial}{\partial x}\left[R\sigma_R\left(\frac{\partial\psi}{\partial\psi_o}\right)\right] + \sigma_\psi\left(\frac{\partial w}{\partial x}\right)\left(\frac{\partial\psi}{\partial\psi_o}\right) - R\left(\frac{\partial\psi}{\partial\psi_o}\right)\left(\frac{\partial w}{\partial x}\right)\rho g\cos\psi = 0$$

Expanding the differentials:

$$-\left(\frac{\partial\psi}{\partial\psi_o}\right)\frac{\partial}{\partial x}[R\sigma_R] - R\sigma_R\frac{\partial}{\partial x}\left(\frac{\partial\psi}{\partial\psi_o}\right) + \sigma_\psi\left(\frac{\partial w}{\partial x}\right)\left(\frac{\partial\psi}{\partial\psi_o}\right)$$
$$-R\left(\frac{\partial\psi}{\partial\psi_o}\right)\left(\frac{\partial w}{\partial x}\right)\rho g\cos\psi = 0$$

Divide by $\left(\frac{\partial\psi}{\partial\psi_o}\right)$ and note that from Eq. (10):

$$\frac{\partial}{\partial x}\left(\frac{\partial\psi}{\partial\psi_o}\right)/\left(\frac{\partial\psi}{\partial\psi_o}\right) = \frac{a_2\cos\psi}{R}$$

$$-R\frac{\partial\sigma_R}{\partial x} - (a_1 + a_2\cos\psi)\sigma_R + \sigma_\psi\left(\frac{\partial w}{\partial x}\right) - R\left(\frac{\partial w}{\partial x}\right)\rho g\cos\psi = 0$$

Divide by $\left(\frac{\partial w}{\partial x}\right) = (a_1 + a_2\cos\psi)$ gives:

$$\frac{\partial\sigma_R}{\partial w} + \frac{\sigma_R - \sigma_\psi}{R} + \rho g\cos\psi = 0 \qquad (24)$$

δw is clearly an increment along the principal stress trajectory, equivalent to δs_1 — Fig. 3. Hence, using the equivalences given in Table 2, Eq. (24) is a form of the first of the Lamé–Maxwell equations.

The force balance in the ψ direction can be given the same treatment:

$$-\frac{\partial}{\partial\psi_o}\left[\sigma_\psi\frac{\partial w}{\partial x}\right]-\sigma_R R\left(\frac{\partial\psi}{\partial\psi_o}\right)\left(\frac{\partial\psi}{\partial x}\right)+R\left(\frac{\partial\psi}{\partial\psi_o}\right)\left(\frac{\partial w}{\partial x}\right)\rho g\sin\psi=0$$

$$\sigma_\psi\frac{\partial}{\partial\psi_o}\left(\frac{\partial w}{\partial x}\right)+\left(\frac{\partial w}{\partial x}\right)\frac{\partial\sigma_\psi}{\partial\psi_o}=R\left(\frac{\partial\psi}{\partial\psi_o}\right)\left(\frac{\partial w}{\partial x}\right)\rho g\sin\psi-\sigma_R R\left(\frac{\partial\psi}{\partial\psi_o}\right)\left(\frac{\partial\psi}{\partial x}\right)$$

Divide by $\left(\frac{\partial\psi}{\partial\psi_o}\right)$ and apply the chain rule:

$$\frac{\partial\sigma_\psi}{\partial\psi}=R\rho g\sin\psi-R\sigma_R\frac{\left(\frac{\partial\psi}{\partial x}\right)}{\left(\frac{\partial w}{\partial x}\right)}-\sigma_\psi\frac{\frac{\partial}{\partial\psi}\left(\frac{\partial w}{\partial x}\right)}{\left(\frac{\partial w}{\partial x}\right)}$$

Now:

$$\frac{\partial\psi}{\partial x}=-\frac{\partial}{\partial\psi}\left(\frac{\partial w}{\partial x}\right)/R$$

From Eq. (8):

$$R_2=\left(\frac{\partial w}{\partial x}\right)/\left(\frac{\partial\psi}{\partial x}\right)$$

Hence:

$$\frac{\partial\sigma_\psi}{R\partial\psi}+\frac{\sigma_R-\sigma_\psi}{R_2}-\rho g\sin\psi=0 \tag{25}$$

Again, Eq. (25) is equivalent to the second Lamé–Maxwell equation using the equivalences in Table 2.

References

[1] H.A. Janssen, Versuche Uber Getreidedruck in Silozellen, Zeitschrift, Ver. Dtsch. Ing. 39 (1895) 1045–1049.
[2] R.M. Nedderman, Statics and Kinematics of Granular Materials, Cambridge University Press, 1992.
[3] G. Enstad, On the theory of arching in mass flow hoppers, Chem. Eng. Sci. 30 (10) (1975) 1273–1283.
[4] A.J. Matchett, Stresses in a bulk solid in a cylindrical silo, including an analysis of ratholes and an interpretation of rathole stability criteria, Chem. Eng. Sci 61 (2006) 2035–2047.
[5] A.J. Matchett, Rotated, circular arc models of stress in silos applied to core-flow and vertical rat-holes, Powder Technol. 162 (2006) 87–99.
[6] Gerner A. Olsen, Elements of Mechanics of Materials, Prentice–Hall, New Jersey, USA, 1982, p. 477.
[7] A.J. Matchett, The shape of the cohesive arch in hoppers and silos — some theoretical considerations, Powder Technol. 171 (3) (2007) 133–145.
[8] A.E.H. Love, A Treatise on the Mathematics of Elasticity, 4th Ed.Dover Publications, New York, 1927.
[9] Wikipedia, free encyclopedia, http://wikipedia.org/wiki/Curvilinear_Coordinates, 2007.
[10] D.M. Walker, An approximate theory for pressure and arching in hoppers, Chem. Eng. Sci. 21 (1966) 975–997.
[11] K. Walters, A theoretical analysis of stresses in silos with vertical walls, Chem. Eng. Sci. 28 (1973) 13–21.
[12] A.W. Jenike, Gravity flow of bulk solids, Utah Experimental Station, Bulletin, vol. 108, University of Utah, USA, 1961.
[13] A.W. Jenike, Flow and storage of solids, Utah Experimental Station, Bulletin, vol. 123, University of Utah, USA, 1967.
[14] A.J. Matchett, A.P. J.O'Neill, Shaw, Stresses in bulk solids in wedge hoppers: explicit, analytical solutions to the 2-dimensional stress distribution problem, using circular arc geometry, in preparation.

Powder Technology 194 (2009) 166–180

Contents lists available at ScienceDirect

Powder Technology

journal homepage: www.elsevier.com/locate/powtec

Stresses in bulk solids in wedge hoppers: A flexible formulation of the co-ordinate specific, Lame–Maxwell equations for circular arc, principal stress systems

A.J. Matchett *, J. O'Neill, A.P. Shaw

School of Science & Technology, University of Teesside, Middlesbrough, TS1 3BA, England, United Kingdom

ARTICLE INFO

Article history:
Received 17 December 2008
Received in revised form 24 March 2009
Accepted 8 April 2009
Available online 17 April 2009

Keywords:
Hopper
Silo
Bulk solids
Storage
Stress

ABSTRACT

A 2-D model of stress distribution within bulk solids, with circular arc principal stress orientation, in a wedge hopper was developed in a previous paper [Matchett, O'Neill, & Shaw, Stress distributions in 2-dimensional, wedge hoppers with circular arc stress orientation — a co-ordinate-specific Lamé–Maxwell model, Powder Technology, 187(2008) 298–306]. This model worked in an orthogonal, curvilinear co-ordinate system co-incident with the principal stress trajectories: $(x-\psi_o)$ space.

This paper presents an equivalent model in $(x-\varepsilon)$ space. This allows backward numerical integration of the force balance equations, enabling surface and wall boundary conditions to be modelled. This was not possible in the original model.

The equations are first-order, and boundary conditions can only be specified at single surfaces. Thus, if a stable, cohesive arch is proposed, the surface overpressure is determined by the model. Calculated overpressures have reasonable physical values.

The present model was integrated backwards from the surface downwards and it was found that the integration was very sensitive to the surface overpressure stresses.

Likewise, wall boundary conditions were specified with backwards integration in ε.

The minimum outlet for flow was calculated from the model and compared with the experimental data of Berry et al. Wall normal stresses in a wedge hopper from Schulze and Schwedes were also compared to model predictions. In both cases there was reasonable agreement between measurements and model predictions.

1. Introduction

Models of stress distribution in hoppers and silos form the basis of design algorithms and aid our understanding of bulk solid behaviour [1,2].

In a previous paper, the authors presented a model of 2-D stress distribution in a wedge hopper with the assumption of circular arc, principal stress orientation [3], after Enstad [4] and Matchett [5,6]. The general arrangement is shown in Fig. 1a), consisting of bulk material contained within a hopper with walls at angles α_1 and α_2 to the vertical. The bulk material resides between the upper and lower surfaces which give rise to boundary conditions in stress. The model was expressed in terms of orthogonal, curvilinear co-ordinates in $x-\psi_o$ space — Fig. 1b.

x is the vertical height of the circular arc, above the wedge apex (point PT) at the point of intersection with the wall. ψ is the angle that the radius through a point on the circular arc makes with the vertical. The principle stress σ_R follows the ψ-line, which is orthogonal to the circular arcs. σ_ψ acts along the path of the circular arc. — Fig. 1b). ψ_o is the value of ψ at the lower boundary and forms one co-ordinate in a 2-D curvilinear orthogonal system — Fig. 1b).

The following force balance equations were given:

$$-\frac{\partial}{\partial x}\left[R\sigma_R\left(\frac{\partial\psi}{\partial\psi_o}\right)\right]+\sigma_\psi\left(\frac{\partial w}{\partial x}\right)\left(\frac{\partial\psi}{\partial\psi_o}\right)-R\left(\frac{\partial\psi}{\partial\psi_o}\right)\left(\frac{\partial w}{\partial x}\right)\rho g\cos\psi=0 \quad (1)$$

$$-\frac{\partial}{\partial\psi_o}\left[\sigma_\psi\frac{\partial w}{\partial x}\right]-\sigma_R R\left(\frac{\partial\psi}{\partial\psi_o}\right)\left(\frac{\partial\psi}{\partial x}\right)+R\left(\frac{\partial\psi}{\partial\psi_o}\right)\left(\frac{\partial w}{\partial x}\right)\rho g\sin\psi=0 \quad (2)$$

The resultant force balance equations were shown to be co-ordinate specific forms of the Lamé–Maxwell equations [3,7].

The equations were integrated numerically along lines of principal stress and the model was used to predict the location of the stable, cohesive arch and investigate given states of stress along the hopper centre-line. Non-viable states of stress were identified by reference to the Mohr–Coulomb yield criterion.

* Corresponding author.
E-mail address: a.j.matchett@tees.ac.uk (A.J. Matchett).

0032-5910/$ – see front matter © 2009 Elsevier B.V. All rights reserved.
doi:10.1016/j.powtec.2009.04.002

Integration along the principal stress lines had several limitations:

i.) The ψ-lines, orthogonal to the circular arcs left the vessel through the wall as height increased — Fig. 1b). Thus, the number of elements across the wedge, in the numerical integration, decreased up the wedge.
ii.) Boundary conditions could only be imposed at $\psi_o = 0$, and at the bottom of the hopper.
iii.) Therefore, imposition of wall boundary conditions in stress was not possible.
iv.) Likewise, backward integration, from the top of the hopper downwards, was not possible.

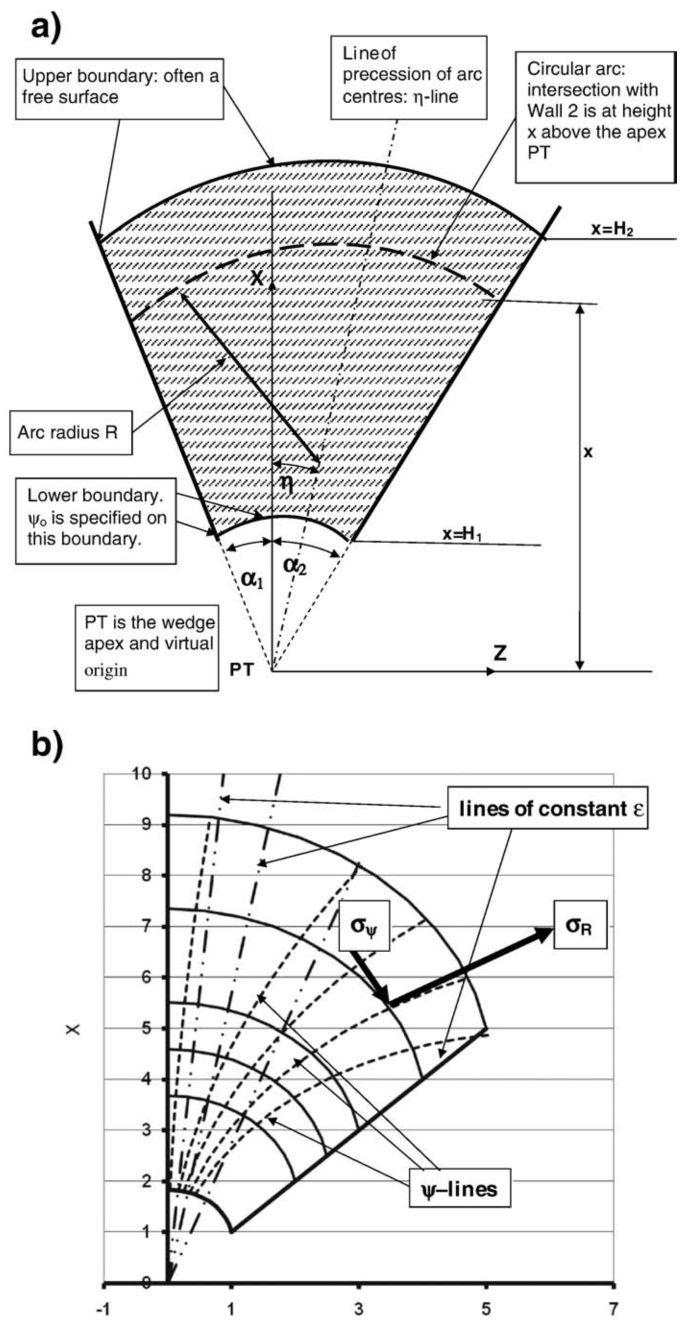

Fig. 1. a) General arrangement of the wedge hopper section. The hopper has angles α_1 and α_2. The bulk solid material is contained between a lower boundary and an upper boundary (shaded area on the figure). b) Representation of the circular arc and ψ-lines in wedge hopper. The lines are orthogonal and are the trajectories of the principal stresses [3]. σ_R follows the ψ-lines; σ_ψ follows the circular arcs.

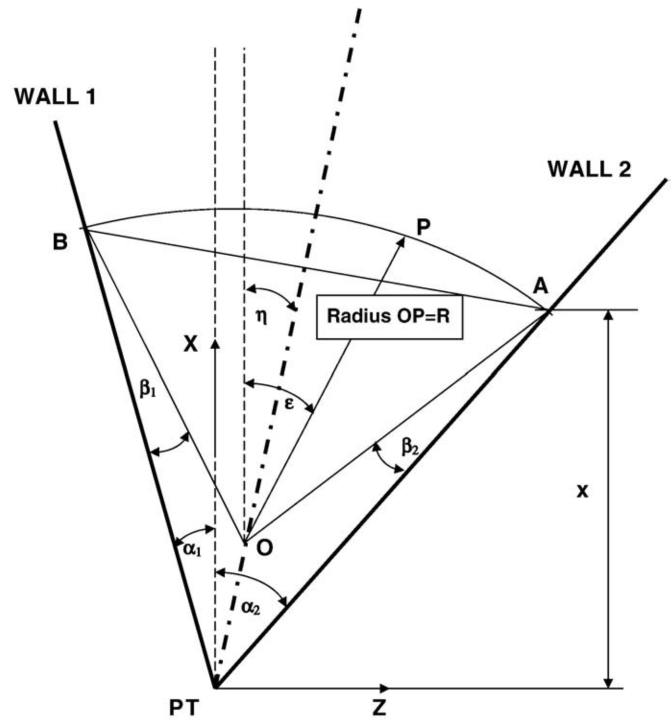

Fig. 2. The R–ε co-ordinate system in a wedge hopper.

Other models [5,6] worked in $x-\varepsilon$ space($R-\varepsilon$ co-ordinates). This co-ordinate system is not generally orthogonal, although locally R and ε are normal to each other. This co-ordinate system retains a constant number of elements across the circular arc and overcomes some of the limitations of the x–ψ_o system.

This paper presents a formulation of the circular arc, 2-D stress distribution problem for the wedge hopper in x–ε space. A range of solutions are presented and the calculated model outputs compared to experimental data for minimum outlet for flow and wall normal stresses.

2. R–ε (x–ε) co-ordinates

A wedge hopper has half angles α_1 and α_2. Principal stresses are assumed to orientate in circular arcs. Each arc makes angles β_1 and β_2 with walls 1 and 2 respectively — Fig. 2. Thus, one principal stress trajectory follows the circular arc and the second follows the ψ-line — Fig. 1b).

Plane stress is assumed and stresses in the third plane play no part in the analysis.

x is the vertical height at which the circular arc intersects wall 2. ε is the angle that the radius through a point makes with the vertical. Thus, point P, Fig. 2, can be uniquely expressed as $P(x, \varepsilon)$.

The maximum value of ε is $(\alpha_2+\beta_2)$ corresponding to the wall — Fig. 2.

The arc radius R is proportional to x:

$$
\begin{aligned}
&R = a_1 x \\
&a_1 = \frac{\sin\gamma\sin(\alpha_1+\alpha_2)}{\sin\lambda\cos\alpha_2\sin(\gamma+\beta_1)} \\
&\lambda = \alpha_1+\beta_1+\alpha_2+\beta_2 \\
&\gamma = \pi/2-\lambda/2
\end{aligned}
\tag{3}
$$

For a symmetrical hopper with $\alpha_1=\alpha_2=\alpha$ and $\beta_1=\beta_2=\beta$

$$a_1 = \frac{\tan\alpha}{\sin(\alpha+\beta)}$$

Cartesian co-ordinates (Z–X) are defined about the wedge apex with X in the vertical direction — Fig. 2.

The arc centre, O, has co-ordinates (O_x, O_z) in (X, Z) spaces, where:

$$O_x = x - R\cos(\alpha_2 + \beta_2)$$
$$O_z = x\tan\alpha_2 - R\sin(\alpha_2 + \beta_2)$$

Point P has coordinates in (X, Z) space of:

$$\begin{aligned} X &= O_x + R\cos\varepsilon = x + R(\cos\varepsilon - \cos(\alpha_2 + \beta_2)) \\ &= x\{1 + a_1(\cos\varepsilon - \cos(\alpha_2 + \beta_2))\} \\ Z &= O_z + R\sin\varepsilon = x\tan\alpha_2 + R(\sin\varepsilon - \sin(\alpha_2 + \beta_2)) \\ &= x\{\tan\alpha_2 + a_1(\sin\varepsilon - \sin(\alpha_2 + \beta_2))\} \end{aligned} \tag{4}$$

An incremental element between arcs at x and $x+\delta x$ is defined, of arcspan $\delta\varepsilon$ — Fig. 3. An incremental element can be created in a number of ways. Element $CDEF$ in Fig. 3 represents an element in which the radii at ε and $\varepsilon+\delta\varepsilon$ have been extended to cut the arc at $x+\delta x$. This ignores curvature normal to the circular arc and was the basis of the earlier models [5,6] which must be seen as approximations.

Fig. 4 shows radii at angle ε at x (OFE) and $x+\delta x$ (O_1HG). Line FG is a line of constant ε — it passes through (x, ε) and ($x+\delta x$, ε). Lines of constant ε radiate from the point of the wedge — Fig. 1. Thus, the (x, ε) system is not orthogonal [3].

An incremental element that is co-incident with the principal stress trajectories would be CD_1E_1F in Fig. 3, where lines at E_1 and D_1 are normal to the arc at $x+\delta x$.

The span of the arc between x and $x+\delta x$ has a length δw — curve FE_1 in Figs. 3 and 4. By resolution of the radius at $x+\delta x$ onto the radius at x, it can be generally shown that:

$$\frac{\partial w}{\partial x} = \frac{\partial O}{\partial x} + \frac{\partial R}{\partial x}\cos(\varepsilon - \eta) \tag{5}$$

where δO is the distance between arc centres from x to $x+\delta x$ and δR is the change in arc radius.

Eq. (5) is generic and can be applied to non-circular arcs and arcs in which α and β change with x.

For circular arcs with constant geometry:

$$\begin{aligned} \left(\frac{\partial w}{\partial x}\right) &= a_1 + a_2\cos(\varepsilon - \eta) \\ a_2 &= \frac{\partial O}{\partial x} = \sqrt{\left(\frac{\delta O_x}{\delta x}\right)^2 + \left(\frac{\delta O_z}{\delta x}\right)^2} \\ \therefore a_2 &= \sqrt{\{1 - a_1\cos(\alpha_2 + \beta_2)\}^2 + \{\tan\alpha_2 - a_1\sin(\alpha_2 + \beta_2)\}^2} \end{aligned} \tag{6}$$

The arc radius O moves along a line at angle η — Figs. 1a) and 2, where:

$$\eta = \arctan\left(\frac{\delta O_z}{\delta O_x}\right) = \arctan\left\{\frac{\tan\alpha_2 - a_1\sin(\alpha_2 + \beta_2)}{1 - a_1\cos(\alpha_2 + \beta_2)}\right\} \tag{7}$$

In a symmetrical wedge then $\eta = 0$.

Furthermore, points E_1 and D_1 are on ψ-lines. Thus, E_1 makes an angle of $\varepsilon+\delta\psi$ with the vertical, where $\delta\psi$ is the increase in slope of the radius between x and $x+\delta x$. Resolution of radii at x and $x+\delta x$ onto the Z-axis yields:

$$\begin{aligned} \frac{\partial\psi}{\partial x} &= \frac{a_2\{\cos(\varepsilon-\eta)\sin\varepsilon - \sin\eta\}}{a_1 x\cos\varepsilon} \\ &= \frac{a_2\{\cos(\varepsilon-\eta)\sin\varepsilon - \sin\eta\}}{R\cos\varepsilon} = \frac{a_2\sin(\varepsilon-\eta)}{R} \end{aligned} \tag{8}$$

For a symmetrical wedge, $\eta = 0$, and Eq. (5) becomes:

$$\frac{\partial\psi}{\partial x} = \frac{a_2\sin\varepsilon}{a_1 x} = \frac{a_2\sin\varepsilon}{R}$$

Principal stresses σ_R and σ_ε act radially and in the ε-direction, as shown in Fig. 3. σ_ε is the arc stress and acts over principal stress arc increment CD_1 and FE_1 and is equivalent to σ_ψ in x–ψ_o space [3]. σ_R is the radial stress relative to the (R–ε) co-ordinate system.

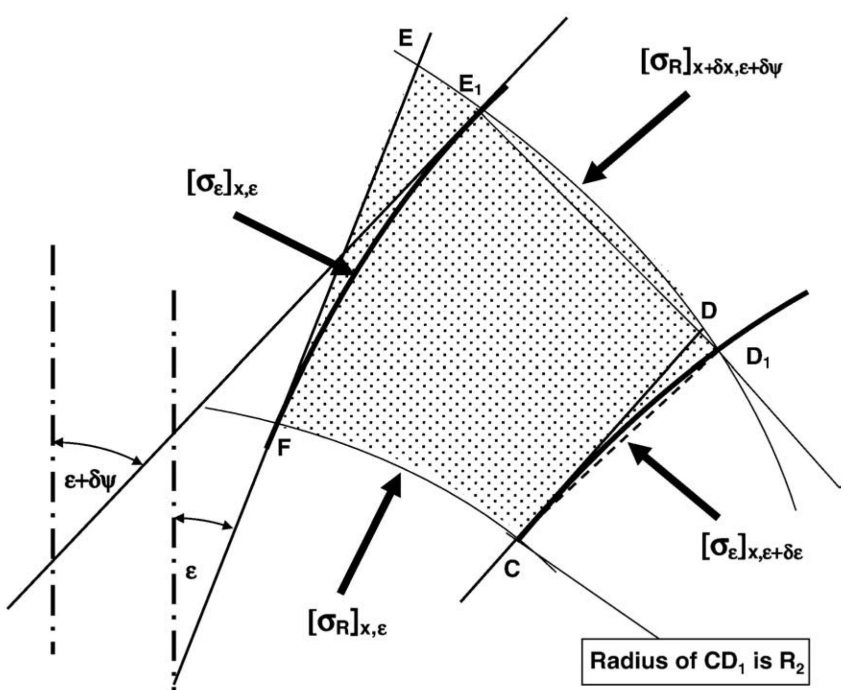

Fig. 3. Incremental element CD_1E_1F showing stresses acting on surfaces.

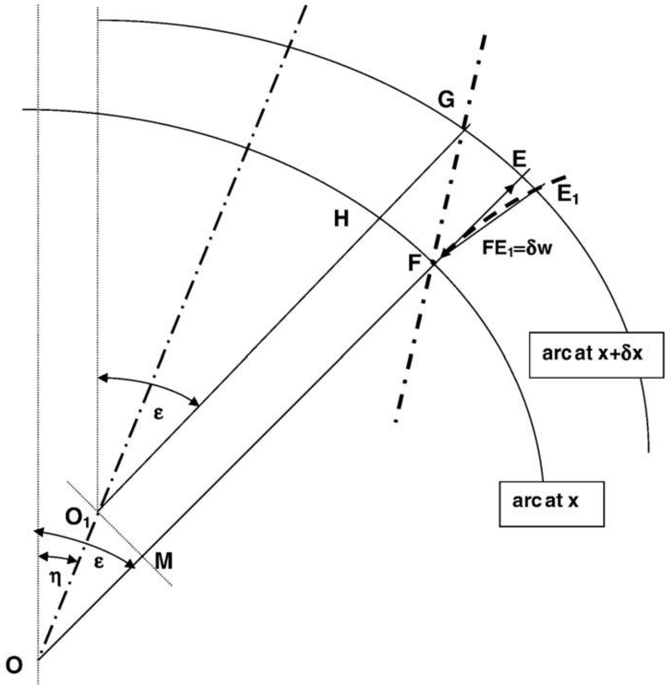

Fig. 4. Increment E_1F, showing step increment length δw. FG is the line of constant ε.

Due to the curvature of the ψ-line, the surface at D_1E_1 has $(x-\varepsilon)$ co-ordinates $(x+\delta x, \varepsilon+\delta\psi)$ — Fig. 3.

A force balance can be made over element CD_1E_1F, coincident with the principal stress trajectories, assuming stasis or incipient flow with no inertial terms. The tractions on each of the surfaces are shown in Table 1, after Olsen [7].

This yields radial and azimuthal forces balances, and it is convenient to express arc stress σ_ε as a composite function F:

$$F = \sigma_\varepsilon\left(\frac{\partial w}{\partial x}\right)$$
$$\frac{\partial}{\partial x}[R\sigma_R] = F - \rho g R\left(\frac{\partial w}{\partial x}\right)\cos\varepsilon - \left\{\sigma_R a_2 \cos(\varepsilon-\eta) + R\left(\frac{\partial \sigma_R}{\partial \varepsilon}\right)\left(\frac{\partial \psi}{\partial x}\right)\right\} \tag{9}$$

$$\frac{\partial F}{\partial \varepsilon} = \rho g R\left(\frac{\partial w}{\partial x}\right)\sin\varepsilon - \{a_2\sigma_R\sin(\varepsilon-\eta)\} \tag{10}$$

Eqs. (9) and (10) are general and are versions of the Lamé–Maxwell equations [7]. They are applicable to any system that may be treated as a continuum, in which the principal stresses orientate in smooth curves of known curvature. No assumptions are made about the nature of R. In this implementation of the equations, a circular arc principle stress orientation has been assumed with α and β assumed to be constant throughout the hopper.

There is an analytical solution at $\varepsilon=0$ identical to the $x-\psi_o$ model for a wedge at $\psi_o=0$ [3]:

$$\begin{aligned}&\varepsilon = 0\ :\ \sigma_R = S\ :\ \sigma_\varepsilon = JS + (J-1)T\\ &x = H\ :\ S = S^*\end{aligned} \tag{11}$$

$$\begin{aligned}
S &= -\frac{C_2}{C_1} + \left(\frac{C_3}{C_1-1}\right)x + (C_4)x^{C_1}\\
C_1 &= \frac{WJ}{a_1} - 1 - \frac{a_2}{a_1}\cos(-\eta)\\
C_2 &= \frac{W(J-1)T}{a_1}\\
C_3 &= \rho g W\\
(C_4) &= \frac{\left(S^* + \frac{C_2}{C_1} - \left(\frac{C_3}{C_1-1}\right)H\right)}{H^{C_1}}
\end{aligned} \tag{12}$$

Also, as in the $x-\psi_o$ model, for a stable, cohesive arch — Fig. 1a):

$$\begin{aligned}&x = H_1 : \sigma_R = 0 \text{ for all } \varepsilon \quad \text{lower boundary; cohesive arch surface}\\ &x = H_2 : S = S_2 \text{ for } \varepsilon = 0 \quad \text{upper surface; } S_2 = 0 \text{ for an open surface}\end{aligned} \tag{13}$$

Eqs. (11) and (12) assume a constant, linear relation between σ_R and σ_ε along the spine of the solution at $\varepsilon=0$. This relationship is based upon a linearised yield locus, in which the origin of the system is shifted from (0,0) in $(\sigma-\tau)$ space to $(-T,0)$.

T is a tensile stress factor, but is not the tensile strength of the material. $(-T)$ is the intercept of the linearised yield locus with the σ-axis.

The linearization is a simplification of a very complex physical system in which data are usually determined experimentally.

Yield conditions may then be expressed by the Mohr–Coulomb yield factor MCYF [3]:

$$\begin{aligned}
J &= \frac{\sigma_\varepsilon + T}{\sigma_R + T}\\
\mathrm{MCYF} &= 1 \ \text{ if } J > J_{\text{passive}}\\
\mathrm{MCYF} &= -1 \ \text{ if } J < J_{\text{active}}\\
\mathrm{MCYF} &= 0 \ \text{ if } J_{\text{active}} \le J \le J_{\text{passive}}
\end{aligned} \tag{14}$$

Eq. (14) is a ratio of effective stresses and follows from the approximation of a linearised yield locus [3,5,6]. It is the assumption of a constant effective stress ratio along the spine of the system [3]. There are numerous precedents for this approach [1,2,4].

The limiting location of the stable, cohesive arch is the maximum value of H_1 at which the Mohr–Coulomb criterion is met.

For example, Fig. 5 shows the limiting stable arch conditions for a typical system, from Fig. 7 in [3]. Fig. 5a and b show the stresses in $x-\varepsilon$ space, as in the original model [3].

The co-ordinate data can be transposed into Cartesian, Z–X co-ordinates using Eq. (4). The data, in triplet of (Z, X, stress) may then be

Table 1
Components of the force balance on incremental element CD_1E_1F — Fig. 3.

Component	Area	Stress	Traction	Line of action: Angle to the vertical
Curve CF	$R\delta\varepsilon$	$[\sigma_R]_x$	$[\sigma_R R\delta\varepsilon]_x$	$\varepsilon + \delta\varepsilon/2$
Curve D_1E_1	$(R+\delta w)\delta\varepsilon$	$[\sigma_R]_{x+\delta x,\varepsilon+\delta\psi} = \sigma_R + \frac{\partial\sigma_R}{\partial x}\delta x + \frac{\partial\sigma_R}{\partial\varepsilon}\delta\psi$	$[\sigma_R]_{x+\delta x,\varepsilon+\delta\psi}$	$\varepsilon + \delta\varepsilon/2 + \delta\psi$
Curve E_1F	$[\delta w]_\varepsilon$	$[\sigma_\varepsilon]_\varepsilon$	$[\sigma_\varepsilon\delta w]_\varepsilon$	$\pi/2 - (\varepsilon + \delta\psi/2)$
Curve CD_1	$[\delta w]_{\varepsilon+\delta\varepsilon}$	$[\sigma_\varepsilon]_{\varepsilon+\delta\varepsilon}$	$[\sigma_\varepsilon\delta w]_{\varepsilon+\delta\varepsilon}$	$\pi/2 - (\varepsilon + \delta\varepsilon + \delta\psi/2)$
Gravity			$R\delta\varepsilon\delta w\rho g$	0

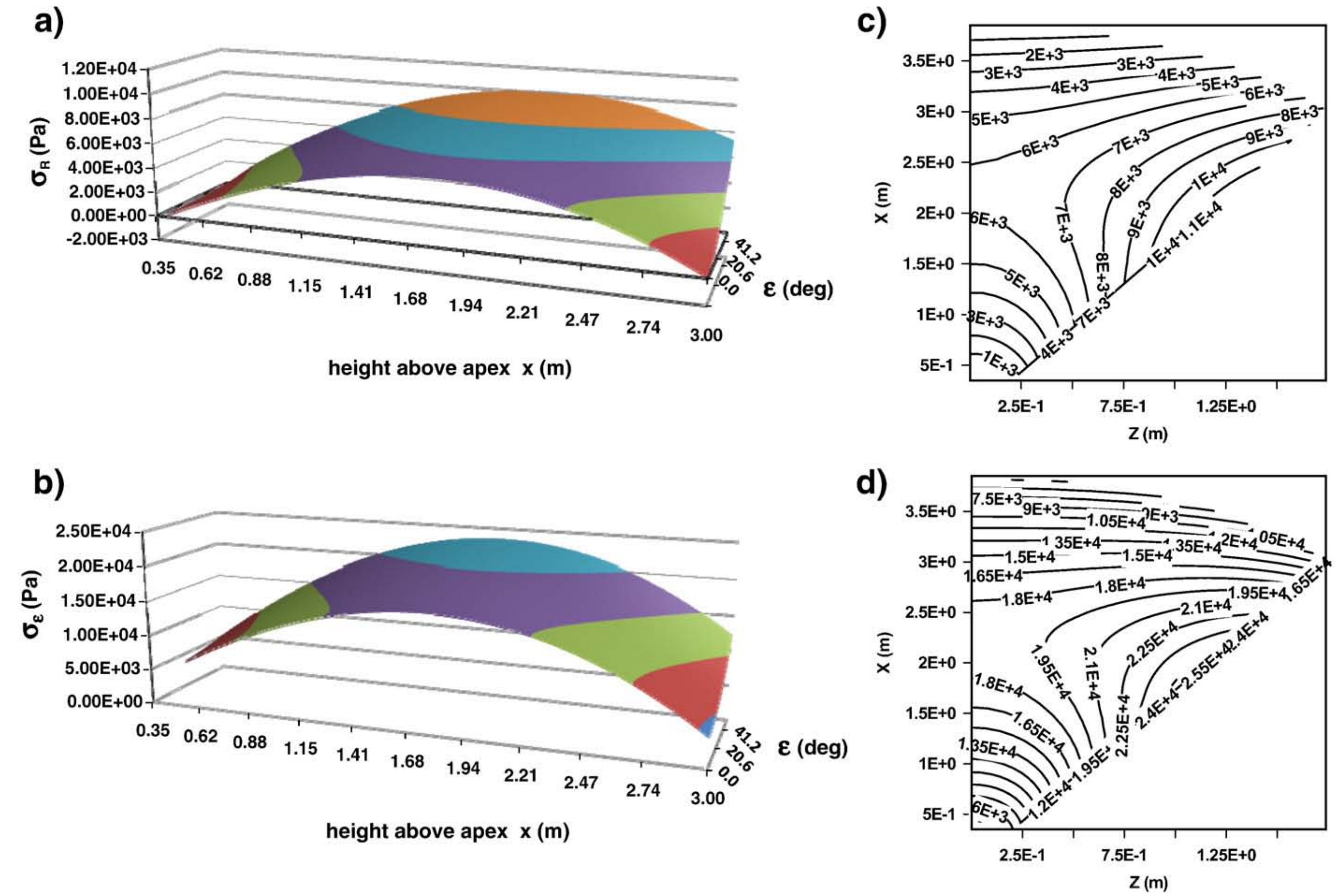

Fig. 5. Limiting stable arch conditions for a 30° symmetrical hopper. As in [3], Fig. 7. $\alpha=30°$: $\beta=21.5°$: $H_1=0.35$ m: $H_2=3$ m (β calculated for passive stress) $\rho=1000$ kg/m^3: $\phi=30°$: $T=3000$ Pa $J=2.384$. a) σ_R in x–ε space. b) σ_ε in x–ε space. c) σ_R in Z–X space: contour plot. d) σ_ε in Z–X space: contour plot.

plotted as contours and surfaces using appropriate data plotting packages. Fig. 5c and d show the data in Fig. 5a and b plotted in this form, using the inexpensive DPlot package [8].

3. Boundary conditions: backward integration; surface overpressure and wall boundary conditions

Eqs. (9) and (10) (and the original Lamé–Maxwell equations [7]) are first-order with respect to both x and ε — it is only possible to impose boundary conditions at single boundaries of x and ε. Therefore, when boundary conditions are imposed at a lower surface (stable, cohesive arch [3]) it is not possible to specify the conditions at the upper surface. It is possible to adjust surface stress at $\varepsilon=0$ ($\psi_o=0$) by variation of the J parameter [3], but the overpressure at all other values of ε is fixed by the model [3].

In many circumstances, the overpressure, P (Pa), in σ_R corresponded to the static vertical stress of a horizontal surface of material intersecting with the upper circular arc at $\varepsilon=0$:

$$P \approx \rho g R(1-\cos e) \tag{15}$$

For the hopper in Fig. 5, this corresponds to a maximum overpressure, at the wall, of 8200 Pa, equivalent to a depth of material of 0.83 m. This is a not unreasonable.

The x–ψ_o model only allowed forwards integration in x and ψ_o (or ε), and boundary conditions could only be imposed at $\psi_o=0$. The x–ε model allows backward integration in x and ε.

Surface boundary conditions may be imposed and the system integrated backwards towards the apex of the wedge. Fig. 6 shows the data for the hopper in Fig. 5, using backward integration with zero surface overpressure. Stresses in the region of the wall rapidly generate unrealistic, large, negative values — Fig. 6a. Fig. 6b and c show the effects of state of stress at $\varepsilon=0$ and overpressure on σ_R.

The backward integration was very sensitive to overpressure and numerical instability was sometimes experienced as x decreased. The equations were implemented on an Excel spreadsheet with 50 increments in ε and 200 increments in x. This was a relatively coarse approach, but was simple, flexible and gave stable solutions over a wide range of conditions. It also enabled some of the powerful, inbuilt functions of the spreadsheet to be used, for example graphical outputs and the use of "solver".

The instability had two causes:

i.) When σ_R took large negative values (Fig. 6a, b) and c), this lead to instability in the solution. Large, negative values of stress are physically unrealistic so any such solution would be rejected on these grounds.

ii.) Towards the wedge apex, as x decreased the step-length became large compared to the changes with respect to the spatial co-ordinate and this leads to instability at the relatively large step-length in the spreadsheet.

iii.) Much smaller step-lengths were possible using other forms of computation, such as QBasic, Visual or Matlab which overcame some of the limitations from ii) above. This allowed more flexible forms of data output, such as the data in triplets for Fig. 5c and d.

However, when the overpressures calculated from a forward integration were used in the backward integration then similar data were given.

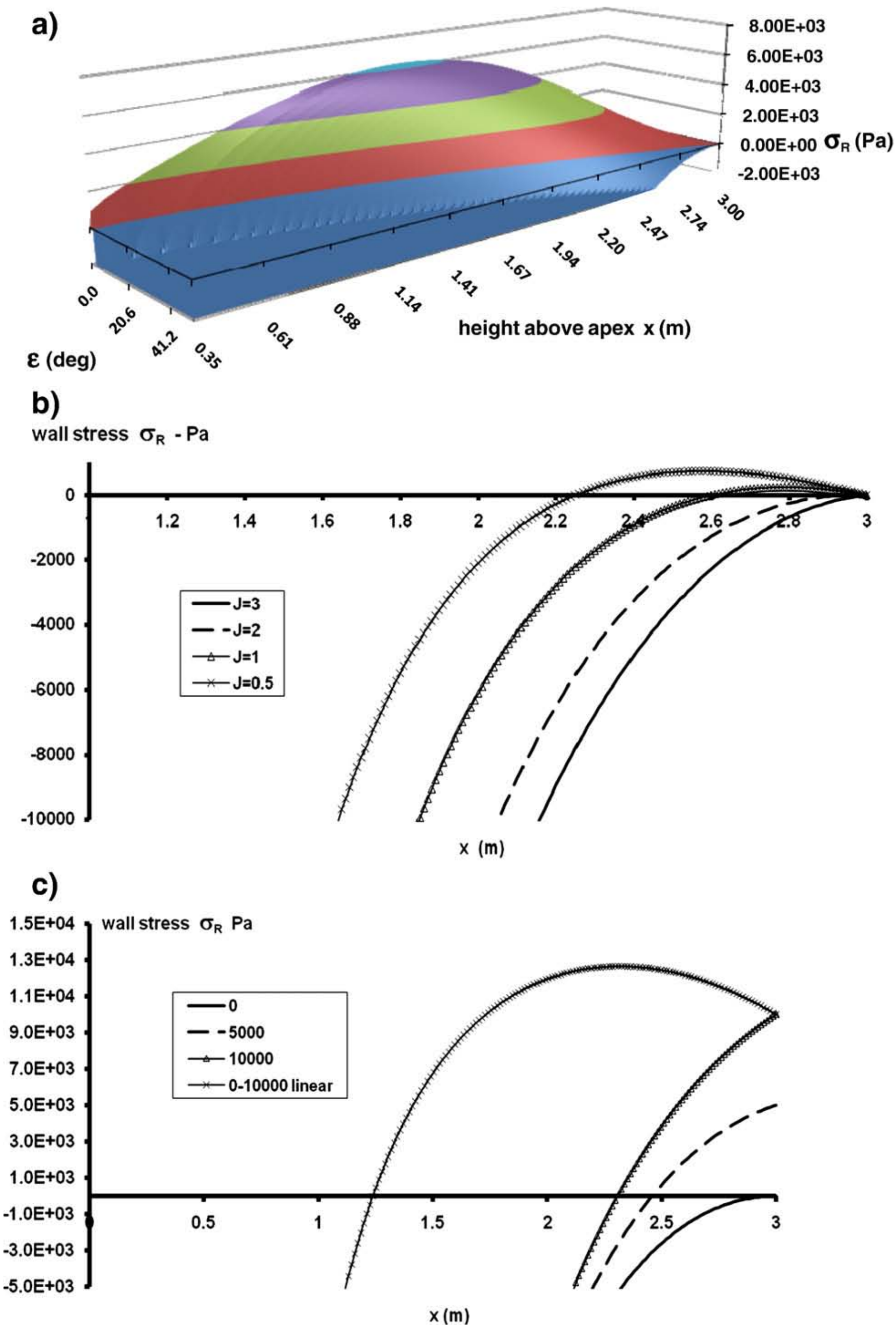

Fig. 6. Backward integration of the stress equations for the hopper and materials in Fig. 5. $\alpha = 30°$: $\beta = 21.5°$: $H_1 = 0.35$ m: $H_2 = 3$ m (β calculated for passive stress). $\rho = 1000$ kg/m^3: $\phi = 30°$: $T = 3000$ Pa. $J = 2.384$. a) σ_R in x–ε space — no overpressure. b) Effects of the state of stress at $\varepsilon = 0$ (J parameter) upon wall stress distribution. c) Effects of overpressure upon wall stress; $J = 2.384$.

Fig. 7 shows the data for the effects of surface overpressure with the active stress state at $\varepsilon = 0$ [3]. Stresses were very sensitive to the surface stress and also the surface stress distribution.

The x–ε implementation of the stress equations also enables boundary conditions in ε at the wall, with subsequent backward integration in ε of the form:

$$\varepsilon = (\alpha_2 + \beta_2) \ : \ \sigma_R = J_w \sigma_\varepsilon + (J_w - 1) T_w \tag{16}$$

where J_w and T_w and the values of linear stress parameters J and T at the wall.

This might seem like a good idea, particularly considering that Jenike's arch failure model depends upon failure of the potential arch at the vessel wall, resulting in mass flow [1,2]. However, Fig. 8a) shows large, positive stresses towards $\varepsilon = 0$. This implies that the wall boundary condition approach is unable to model the stable cohesive arch. Furthermore, there are issues of compliance with the Mohr–Coulomb yield criterion — Fig. 8c.

Generally, physically unrealistic outputs have been seen over a wide range of conditions using both surface and lower arch boundary conditions in x when wall boundary conditions have been used in ε. The imposition of a constant state of stress along the wall would therefore

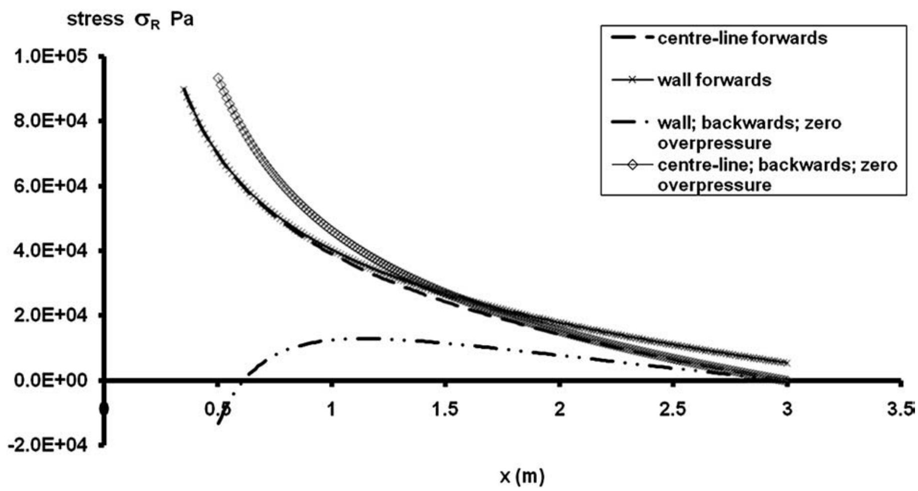

Fig. 7. Stress distributions for the active stress state at $\varepsilon=0$. $\alpha=30°$: $\beta=7.5°$: $H_1=0.35$ m: $H_2=3$ m (β calculated for active stress). $\rho=1000$ kg/m^3: $\phi=30°$: $T=3000$ Pa. $J=0.333$. Overpressure: $P=\rho gR\ (1-\cos\varepsilon)$ unless stated.

seem to be inappropriate in the application of this model. Generally, with wall boundary conditions, σ_R increases as ε decreases, whereas the reverse is true of centre boundary conditions — Fig. 5a) for example.

4. Properties of the model

The effects of the parameters within the model will now be shown, along with a comparison with other models.

The effect of bulk density is shown in Fig. 9, wherein an increase in bulk density leads to a general increase in stresses through the hopper, due to an increase in the body forces. This implementation of the model has assumed a constant bulk density throughout the hopper. This is usually considered adequate [1,2], but density variation (with compressive stress for example) could be incorporated into the solutions.

Increases in ϕ and T extend the area of the yield locus and decrease the radial stress σ_R — see Figs. 10 and 11. Fig. 10a) shows the variation of wall stresses down the wall of the wedge with T as parameter. Fig. 10b) shows stress variations across the hopper at the hopper mid-point. This is consistent with Fig. 5a) and b) with an increase in stresses towards the wall. This can be compared to Fig. 8a) with wall boundary conditions in ε, where σ_R decreases from the centre to the wall. This can explain the difficulty of the wall boundary condition implementation to meet the Mohr–Coulomb yield criterion within the model — Fig. 8c).

The effects on σ_ε are more complex causing increases over the upper part of the hopper.

The increase of ϕ has a similar effect upon stresses, causing a general decrease in σ_R and more complex changes in σ_ε. — Fig. 11.

These effects may be explained in terms of the model. An increase in ϕ and/or T is equivalent to an increase in friction and allows the material to support greater shear stresses — proportional to $(\sigma_\varepsilon-\sigma_R)$. Thus, for a given σ_R in the passive case, a greater value of σ_ε can be permitted. This implies that a greater proportion of the body force may be supported by arc stress, rather than radial stress.

Fig. 12 shows the effects of changing J along the spine of the solution at $\varepsilon=0$. The passive stress case ($\sigma_\varepsilon>\sigma_R$) gives a typical stress response with the stress passing through a maximum from the surface downwards. The active case shows a continuous increase in the stresses down the vessel.

The effect of an increase to wall angle β at constant hopper angle is to alter the arc radius — Eq. (3). This has a tendency to reduce stresses in the lower region of the hopper, but increase them in the top region. Fig. 13a) shows the effect upon stresses at the vessel wall. Fig. 13b) shows the transverse variations at the hopper mid-point expressed as stresses as a function of horizontal co-ordinate Z. The lower values of stress, suggested by Fig. 13a) are seen across the width of the hopper.

The maximum wall normal angle for a material at yield is given by the well-known equations [1,2,4]:

$$\beta_{\text{passive}} = 0.5\left(\phi_w + \arcsin\left(\frac{\sin\phi_w}{\sin\phi}\right)\right)$$
$$\beta_{\text{active}} = 0.5\left(\phi_w - \arcsin\left(\frac{\sin\phi_w}{\sin\phi}\right)\right) \tag{17}$$

Where the subscripts refer to the passive and active stress states.

Therefore, an increase in wall roughness will increase ϕ_w and therefore allow the system to sustain a greater value of β.

An increase in hopper angle α results in a general increase in stresses throughout the hopper — Fig. 14.

The wall normal stress, σ_w, may be calculated from the model data. Stress σ_ε acts at angle β to the wall normal. Therefore:

$$\sigma_w = \frac{(\sigma_\varepsilon+\sigma_R)}{2} + \frac{(\sigma_\varepsilon-\sigma_R)}{2}\cos 2\beta \tag{18}$$

The model may be compared to other models in terms of calculated wall normal stress. These comparisons have been made with boundary conditions at $\varepsilon=0$ in the circular arc model and upwards integration. Fig. 15a) and b) shows comparisons at 15° and 45° wall slopes. The models used for comparison include:

Nedderman's Janssen analysis extended to a wedge [2]
Enstad's original model [4]
Walker's model [10].

All the graphs have a similar shape, but the maximum value and its location along the wall varies from model to model.

Comparison of Fig. 15a) and b) with Fig. 14 show the same general increase in stresses with increase in hopper half-angle.

The present model can be seen to give predictions of wall normal stress within the range of values given by the other models. It was difficult to obtain equivalent data for the models due to their different bases and definitions. The circular arc model was applied assuming $J=J_{\text{passive}}$ and β had the maximum value for the passive stress state — Eq. (17). It would be possible to adjust these values to obtain a better fit to any of the other models — see the Discussion below.

5. Comparison of the model with experimental data

Unfortunately, there are no experimental data of internal stress distributions within the bulk solids in hoppers and silos to validate the model. The authors have argued previously that such data are essential, not just to the validation of these models, but others including FEM and DEM approaches [5,6,9] and such measurements are now viable with modern stress sensor technology.

However, there are two areas in which data are available:

i.) the measurement of wall normal stress
ii.) the measurement of the critical outlet dimension for flow.

Therefore, the circular arc principal stress models will be compared to the wall stress data [11] and used to calculate minimum outlets for flow and compared to the experimental data of Berry et al. [12,13].

6. Comparison of experimental wall normal stress data with model predictions

Many workers have measured wall stress data. However, most of the work has taken place in conical hopper sections rather than

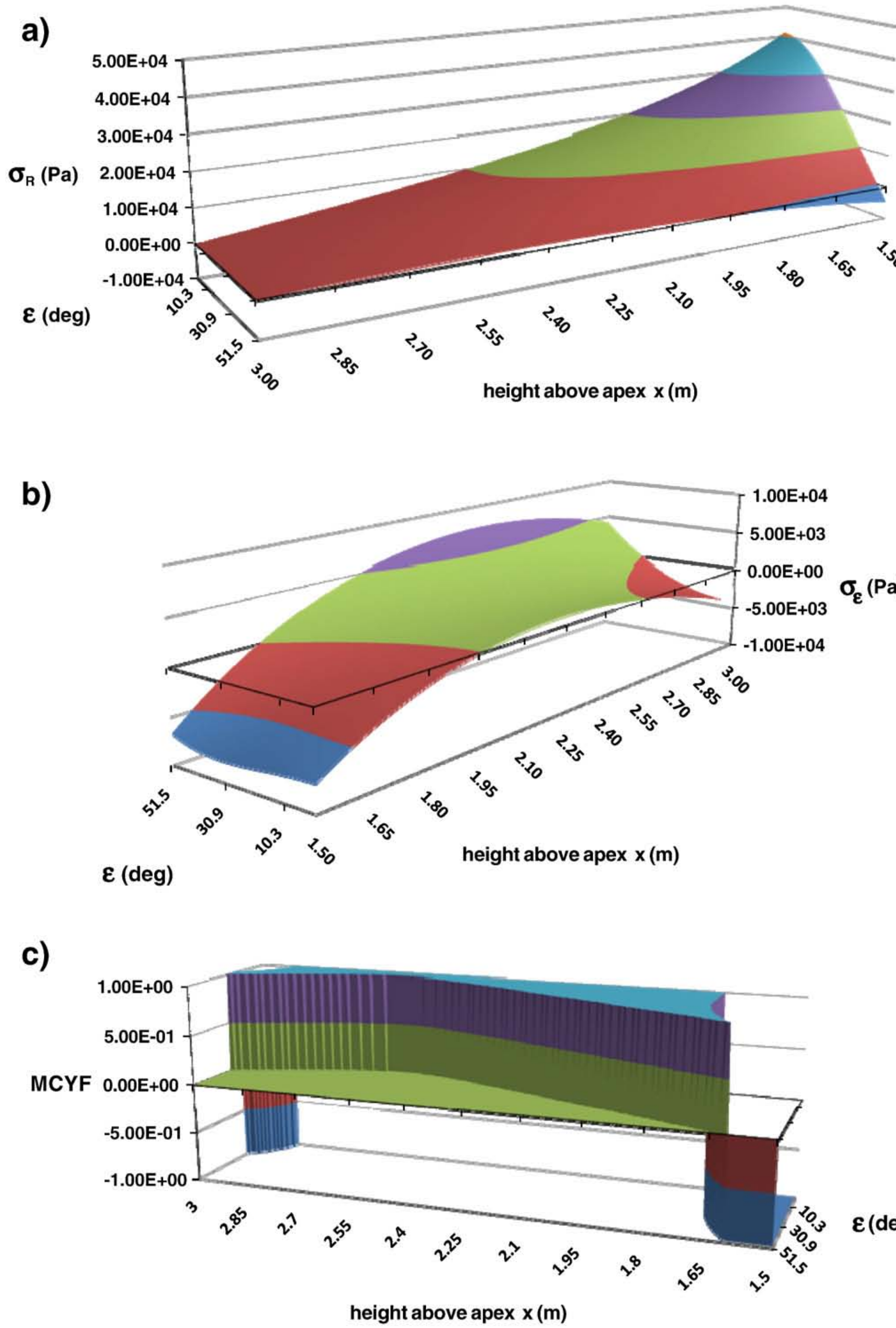

Fig. 8. Stress distributions for the hopper (Fig. 5) taking wall boundary conditions and integrating backwards. $\alpha = 30°$: $\beta = 21.5°$: $H_1 = 0.35$ m: $H_2 = 3$ m (β calculated for passive stress). $\rho = 1000$ kg/m^3: $\phi = 30°$: $T = 3000$ Pa. $J_w = 3$: $P = 0$. a) σ_R in x–ε space. b) σ_ε in x–ε space. c) MCYF in x–ε space.

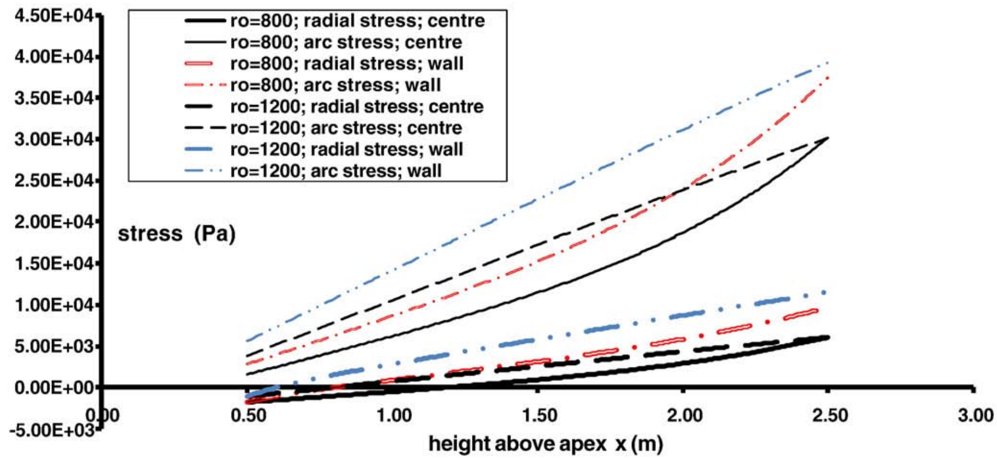

Fig. 9. The effects of bulk density upon stress distributions. $\alpha = 25°$: $\beta = 19.5°$: $H_1 = 0.5$ m: $H_2 = 2.5$ m (β calculated for passive stress) $\rho =$ parameter kg/m^3: $\phi = 35°$: $T = 3000$ Pa. $J = 3.69$(passive case): $P = 6000$.

wedges. Schulze and Schwedes [11] have provided some wall normal stress data for an experimental wedge hopper which will be used in this comparison [11].

Schulze and Schwedes [11] used limestone in a wedge hopper, outlet 100–300 mm, wall angle 10–40° with a 600 mm wide vertical section above. They measured wall stress at several points up the wedge.

Fig. 16 shows a comparison between model predictions and the experimental data presented in Fig. 2 of their paper [11]. The model was fitted to the data using a least-squares approach with J, β and P as

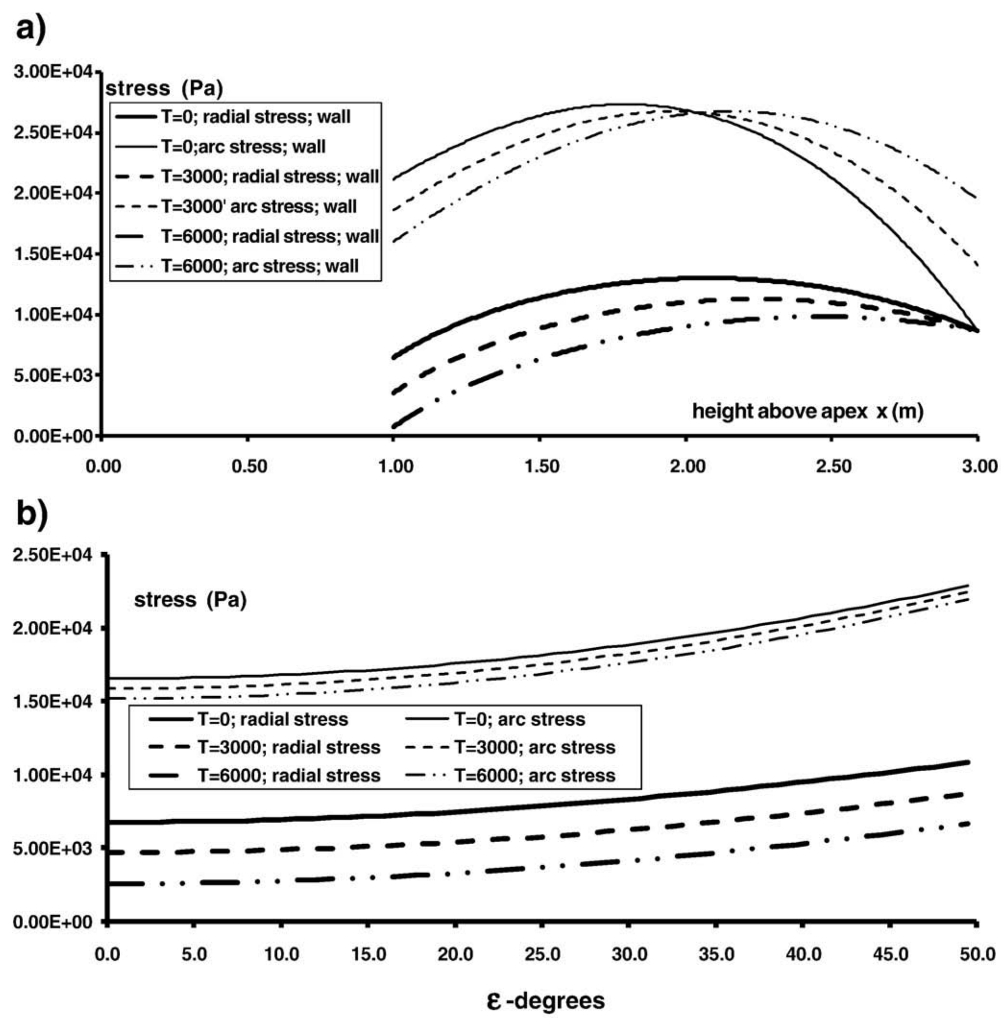

Fig. 10. The effects of tensile stress parameter T upon stress distribution. $\alpha = 30°$: $\beta = 24.5°$: $H_1 = 1$ m: $H_2 = 3$ m (β calculated for passive stress). $\rho = 1000$ kg/m^3: $\phi = 25°$: $T =$ parameter. $J = 2.464$(passive case): $P = 0$. a) Variation in stresses along the vessel wall. b) Transverse stress variations at the wedge mid-point.

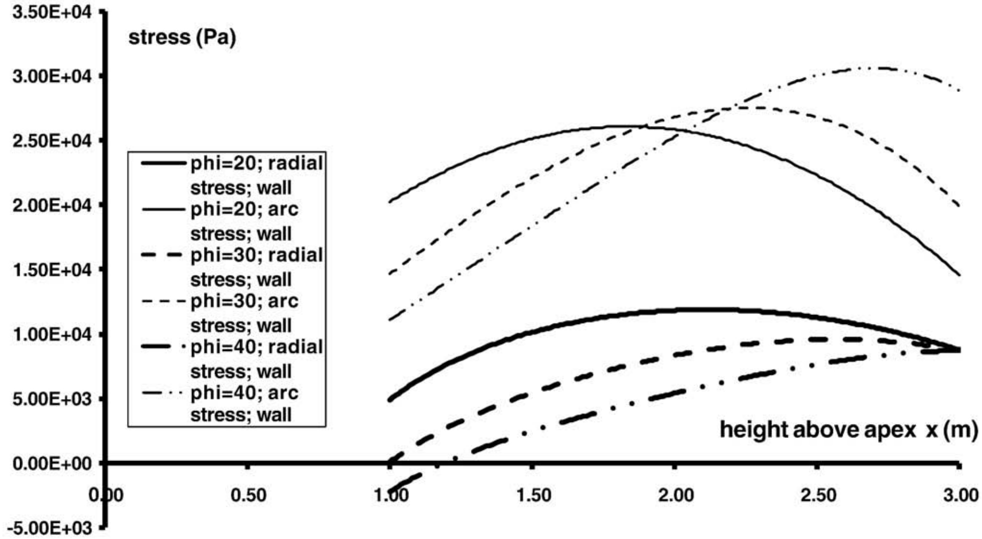

Fig. 11. The effect of angle of yield locus ϕ upon wall stresses. $\alpha=30°$: $\beta=24.5°$: $H_1=1$ m: $H_2=3$: β calculated for passive stress: function of ϕ: $\rho=1000$ kg/m^3: $\phi=$parameter: $T=4500$. $P=0$.

adjustable parameters: $J=3.51$: $\beta=35.7°$: $P=1126$ Pa. Excel "solver" was used to determine these values.

The results are in reasonable agreement, given the complexities of the experimental system. The confidence limits at the 0.05 level of the difference between the model and measured stress was $+/-260$ Pa, in data ranging from 3000–6000 Pa.

It is interesting to note that the model predicts that the material was tending to a passive state of stress at $\varepsilon=0$ ($\sigma_\varepsilon>\sigma_R$), as given by the J value, rather than the more usually assumed active state in the loading of a hopper. However, conditions at the base and the top of the hopper are difficult to assess.

It appears that the base of the hopper was not enclosed, but there was a gap between the bottom of the hopper and the conveyor beneath it. Likewise, the nature and extent of overpressure from the vertical section was not explicitly stated in the paper.

It is also interesting to note that Schulze and Schwedes[11] presented their stress data as a trend line rather than actual data points.

7. Comparison of minimum outlet dimensions with the data of Berry et al. [12,13]

Berry used a wedge hopper of variable geometry to determine the outlet dimension required for flow, for a number of materials over a range of wall slopes. He also measured the shape of the cohesive arch. He measured the minimum outlet for emptying of the vessel in two ways: "on filling", and "on emptying" [12,13]. He compared outlet dimensions with those predicted by Jenike [1], determined from a number of shear cell tests in the Jenike cell and the Walker annular cell.

Results are presented in Table 2, showing Berry's experimental data, his calculations of critical outlet according to Jenike and corresponding calculations using the circular arc model [3].

Several of Berry's yield loci were non-linear and the imposition of a linear yield locus, Eq. (11), was problematic. Two values were given from the circular arc model — a high value and a low value. The high value was based upon an estimate of ϕ and T from an average of the shear cell data over its experimental range. This is a "by eye" interpretation of the yield loci.

The low values used the Jenike value of fc given by Berry and an estimation of ϕ and T in the region of $\sigma=0$.

Data are presented graphically in Fig. 17a and b.

The lower values given by the circular arc model (based upon the Berry/Jenike's values of fc) are in reasonable agreement with the experimental values, with a tendency to underestimate the experimental values "at filling" and overestimate "at emptying".

The higher values of outlet are generally an overestimation and in the case of fly ash, quite a "healthy" overestimation: >300%.

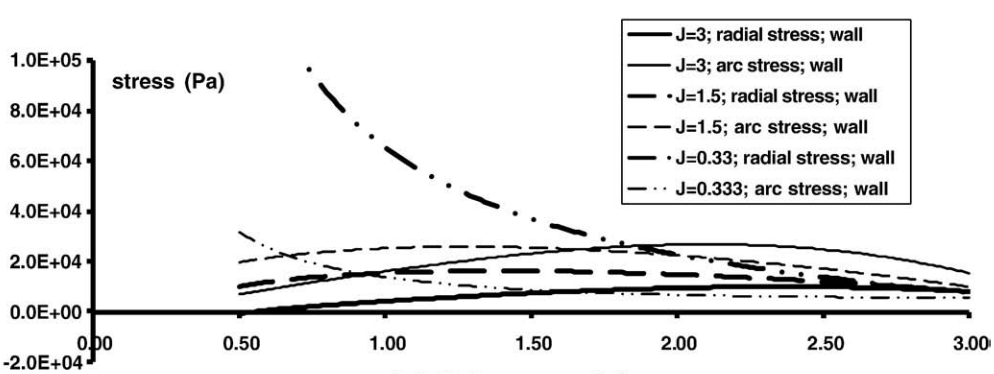

Fig. 12. The effect of state of stress parameter J upon stress distributions at the vessel wall. $\alpha=30°$: $\beta=21.5°$: $H_1=3$ m: $H_2=0.5$: $\rho=1000$ kg/m^3: $\phi=30°$: $T=3000$: $P=0$.

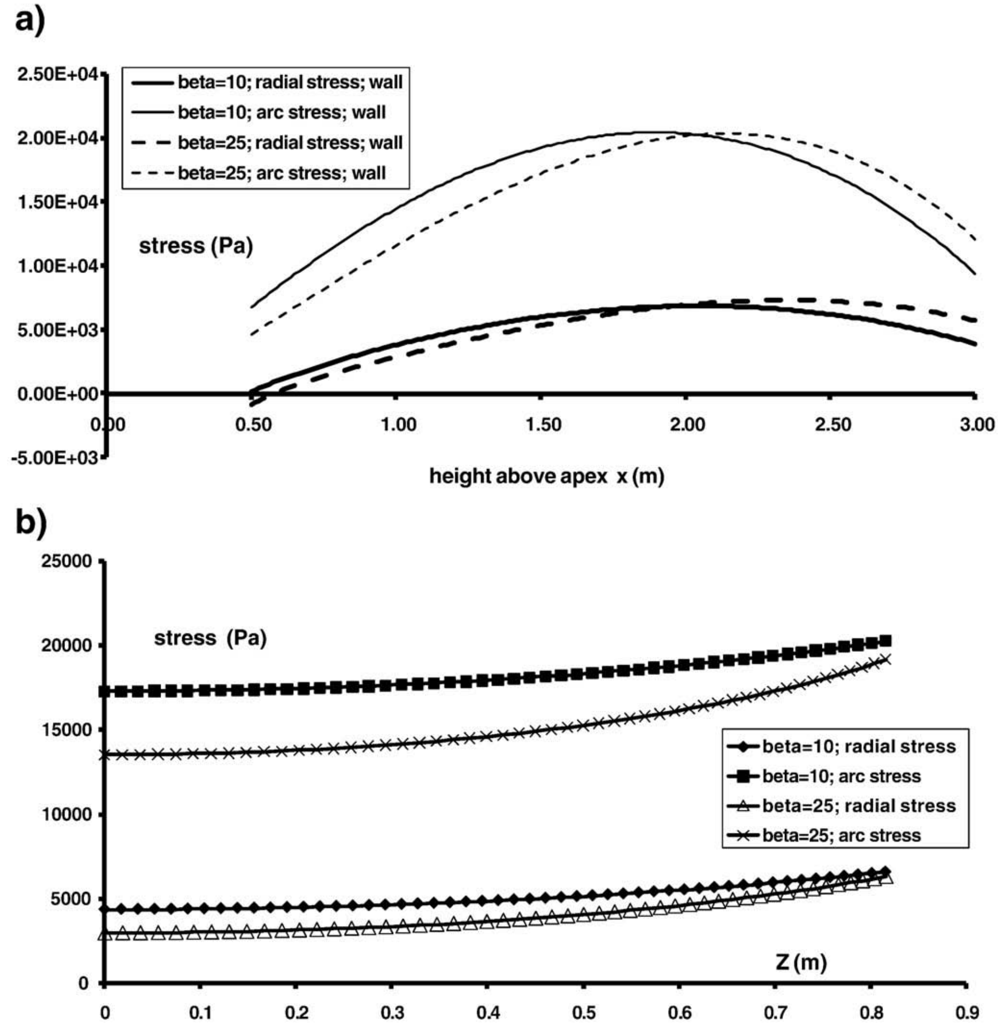

Fig. 13. The effect of wall normal angle, β, upon stress distribution. $\alpha=25°$: $\beta=$parameter: $H_1=0.5$ m: $H_2=3$ m. $\rho=900$ kg/m^3: $\phi=28°$: $T=3000$. $J=2.77$(passive case): $P=0$. a) variation in stresses at the wall with x. b) Transverse variation in stresses at the hopper mid-point, $x=1.75$.

The results for hydrated lime in the 45° hopper are not well-described by Berry's Jenike calculations, but the circular arc model gives reasonable values, compared to the experimental value. This hopper is beyond the range of mass-flow usually associated with the Jenike methodology.

Thus, there is evidence that the circular arc model can form the basis for the prediction of minimum outlets for flow.

However, the predicted values are critically dependent upon the value of fc chosen for the calculation. The values of fc generated by

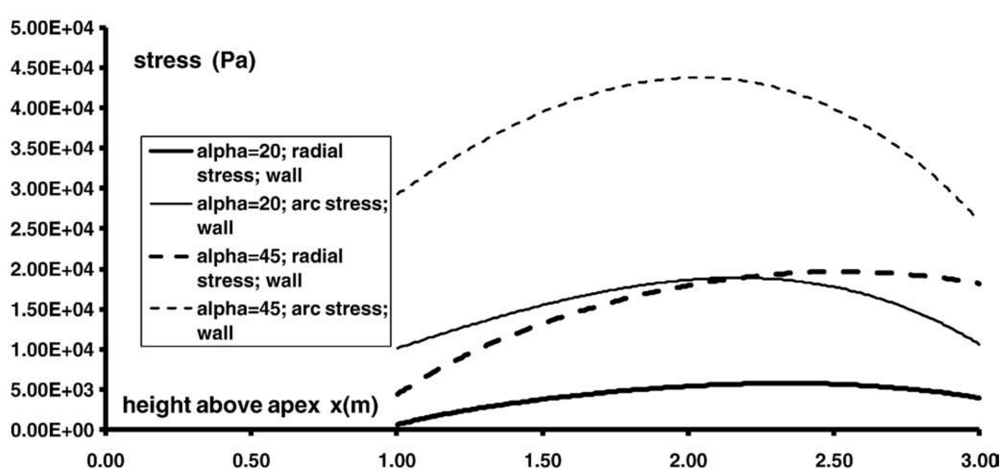

Fig. 14. The effect of hopper wall angle, α, upon stress distribution at the vessel wall. $\alpha=$parameter: $\beta=21.5°$: $H_1=1$ m: $H_2=3$ m. $\rho=900$ kg/m^3: $\phi=25°$: $T=3000$. $J=2.464$: $P=0$.

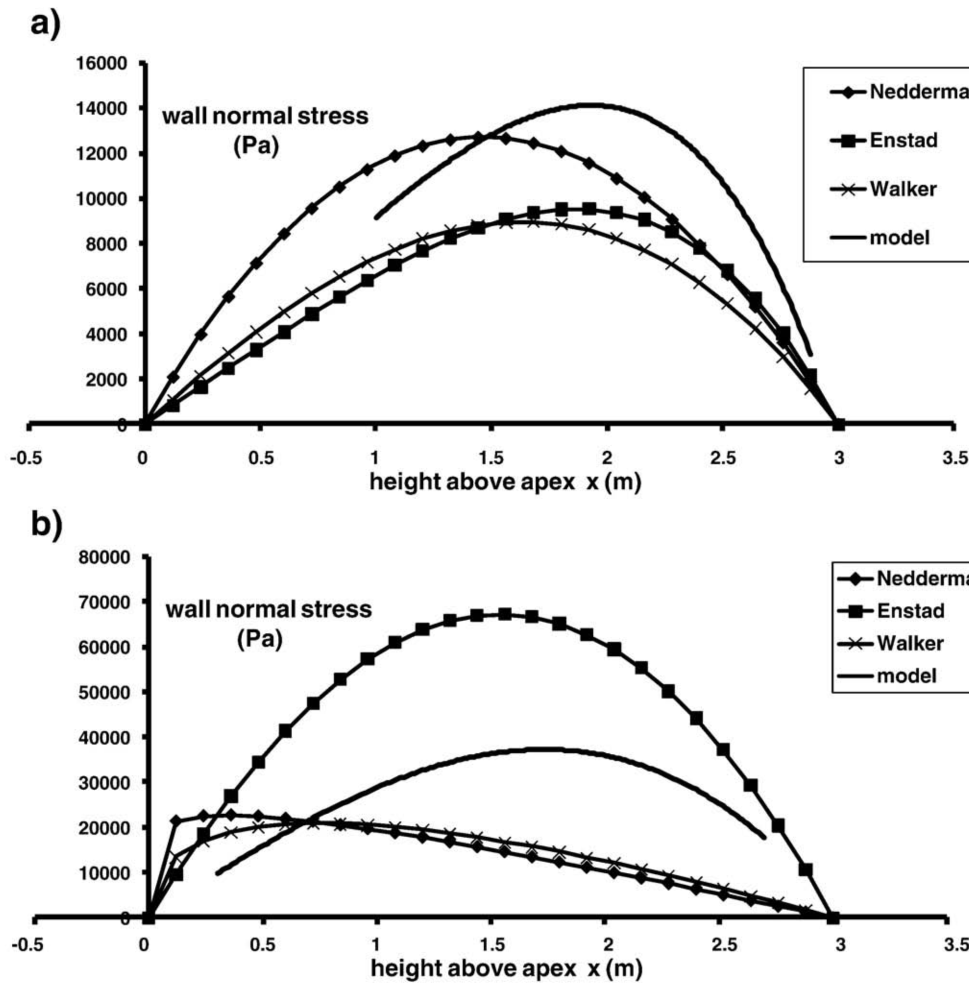

Fig. 15. Comparison of model predictions with other theories in terms of wall normal stress. Circular arc model parameters. $\beta=22.8$: $H_1=1$ m: $H_2=3$ m. $\rho=1000$ kg/m^3: $\phi=29°$: $T=0$. $J=2.88$(passive case): $P=0$. a) $\alpha=15°$. b) $\alpha=45°$.

classical Jenike methodology gave good agreement — Fig. 17a, b. Thus, there is a great deal more to successful hopper design than a simple flow/no flow model.

In several cases, however, the Jenike value of fc was much less than the minimum stresses used in the shear cell test (1000 Pa for Berry's Jenike cell and 400 Pa for the Walker cell), most notably with the fly ash — Table 2. In these cases, the Jenike values of fc were extrapolations beyond the range of measured data. However, these values of fc do give reasonable predictions, and the methodology has been tried and tested over many years.

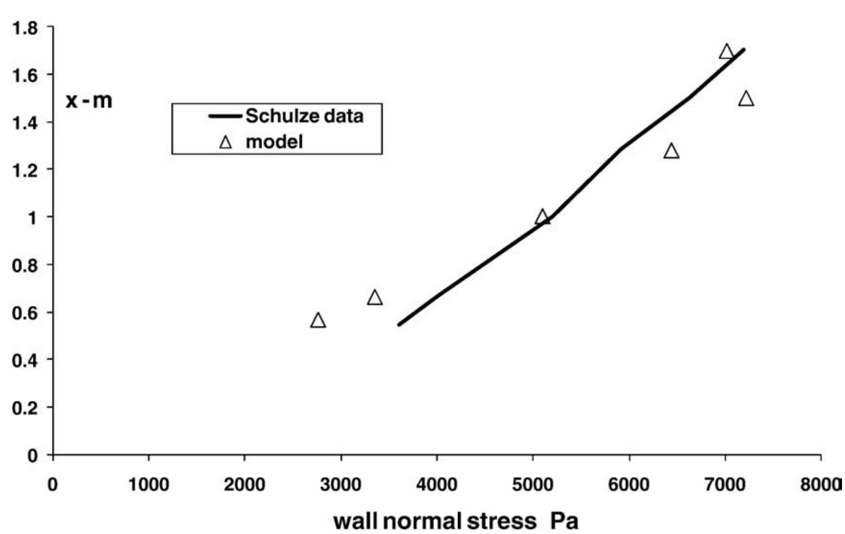

Fig. 16. Comparison of model predictions with the wall normal stress data of Schulze and Schwedes [11]. Model fitted to the data using a least squares method with J, β and P as parameters. Excel "solver" used. $\alpha=10°$: lower outlet width 200 mm: upper outlet width 600 mm. $J=3.51$: $\beta=35.7°$: $P=1126$ Pa. $\rho=1250$ kg/m^3: $\phi=38°$: $T=0$.

8. Discussion

The fundamental, force balance equations — Eqs. (9) and (10) will be considered separately from other assumptions used in order to obtain a mathematical/numerical solution.

The force balance equations are a form of the Lamé–Maxwell equations and are generally applicable to any continuum system with "smooth" paths for the principal stresses, from which curvatures can be calculated [7]. The equations can be applied to systems with principal stress orientations other than circular arc, such as parabolic or elliptical arc principal stress orientation. In these systems, R becomes a function of ε and x, not just of x — Eq. (3). The model may also be used with systems in which β is allowed to vary, and indeed α as well. These aspects of the equations will be a subject of future work, but α and β were assumed constant throughout the vessel in this paper.

The generalised force balance equations do not include material properties, other than bulk density for the body forces. The stresses in Eqs. (9) and (10) could be related to strain and/or rates of strain, as in the FEM approach. This is also a topic for further study.

The equations do not contain inertial terms — they are equilibrium/incipient flow equations. There are numerous precedents for this from Janssen to the present day [2]. The circular arc approach has limited application to flowing systems. It could not be used for fully developed flow, for example, as the stress systems would be quite different from the circular arc assumption inherent in the equations, and tend to "fluid-like" behaviour. However, the approach might be used in the initial stages of development of flow where "solids properties" still dominate, by use of residual inertia and/or appropriate flow rules.

As with many continuum models, the present model would require considerable modifications to handle discontinuities — stress discontinuities, development of shear plane and related phenomena.

Relatively simple mechanical properties have been used with the force balance equations in order to obtain 2-dimensional stress distributions, based upon the concept of the rigid-plastic solid. There are no elastic stresses within the solutions in the present paper.

The rigid-plastic solid within the present solutions has been approximated to a system with a linear yield locus. (−T) is the intercept of the yield locus with the σ-axis in $(\sigma-\tau)$ space. T is directly related to the more usual expression of cohesion c (Pa) [1,2]:

$$c = T \tan\phi \tag{19}$$

The yield locus would usually be determined experimentally [1,2,11,12], and it would be expected that c, T and ϕ would be determined from shear cell data, as in the estimation of the critical outlet for flow, using Berry et al's data: Fig. 17 [11,12].

Many attempts have been made to relate the yield locus, and specifically c and ϕ, to fundamental material properties with limited success. The current state of knowledge requires lab measurement.

The assumption of linearization is a reasonable approximation in many materials. However, problems were experienced with some of Berry's data which were highly non-linear as normal stress tended to zero. Even in such situations, it was possible to make reasonable estimates.

The solutions to the force balance equations depend upon an assumption of a relation between σ_R and σ_ε along a specified line in the system — the spine of the solution [3] — see Eqs. (11) and (16). The equations used in this paper are a cohesive extension of the assumption of a constant ratio of stresses, as seen in other models [2]. The stress relationship need not be linear and the model could incorporate other relationships. There is a rational basis for a linear relationship following the assumption of a linearised yield locus, and there is little information available to suggest that other relationships might be more appropriate.

Therefore, the model incorporates many simplifications with precedents dating back to Janssen [1,2]. One advantage of this

Table 2
Critical outlet dimension "at filling" from Berry' data [12,13] compared to Jenike and circular arc predictions.

Fly ash	Ref Run no.	Wall slope	Bulk density	Berry outlet at filling	Jenike outlet	Jenike fc	Critical slit width	Critical outlet dia.	Berry "at emptying" outlet (est.)
		Degrees	kg/m^3	m	m	Pa	m	m	m
	1	20	430	0.106	0.078	300	0.071	0.142	0.05
	2	30	430	0.098	0.081	299	0.071	0.142	0.03
	3	45	442	0.11	0.097	346	0.08	0.16	0.035
Hydrated	4	20	560	0.15	0.155	780	0.142	0.248	0.05
Lime	5	30	575	0.1	0.183	907	0.161	0.322	0.04
	6	45	663	0.12	0.4573	2454	0.298	0.435	0.05

Fly ash	Ref Run no.	Circular arc model outlet: High Phi	High T	High fc	High Min.outlet	Low Phi	Low T	Low fc	Low Min.outlet
		Degrees	Pa	Pa	m	Degrees	Pa	Pa	m
	1	55	176	1575	0.319	32	135	300	0.05
	2	55	176	1575	0.314	32	135	300	0.046
	3	55	176	1575	0.276	32	153.5	346	0.042
Hydrated	4	44.8	352	1680	0.216	44.8	164	780	0.104
Lime	5	44.8	352	1680	0.139	44.8	190	907	0.079
	6	44.8	352	1680	0.122	44.8	515	2454	0.191

Notes:
Critical outlets were calculated as the minimum outlet width for yield at the vessel wall.
High estimates for the circular arc model were taken from an overall average of shear cell yield loci data, whereas the low estimates were taken from Berry's estimate of fc and local value of ϕ determined in the region of zero normal stress.
Critical slit width and critical outlet diameter were calculated from the equations:

$$\text{width} = \frac{f_c}{\rho g}$$

$$\text{diameter} = \frac{2f_c}{\rho g}$$

fc values used were those of Jenike [1].
Critical outlet dimensions "at emptying" were generally smaller than those in Table 2, of the order of 30–50 mm: Figs. 8.1–8.9 of Berry's thesis [13].

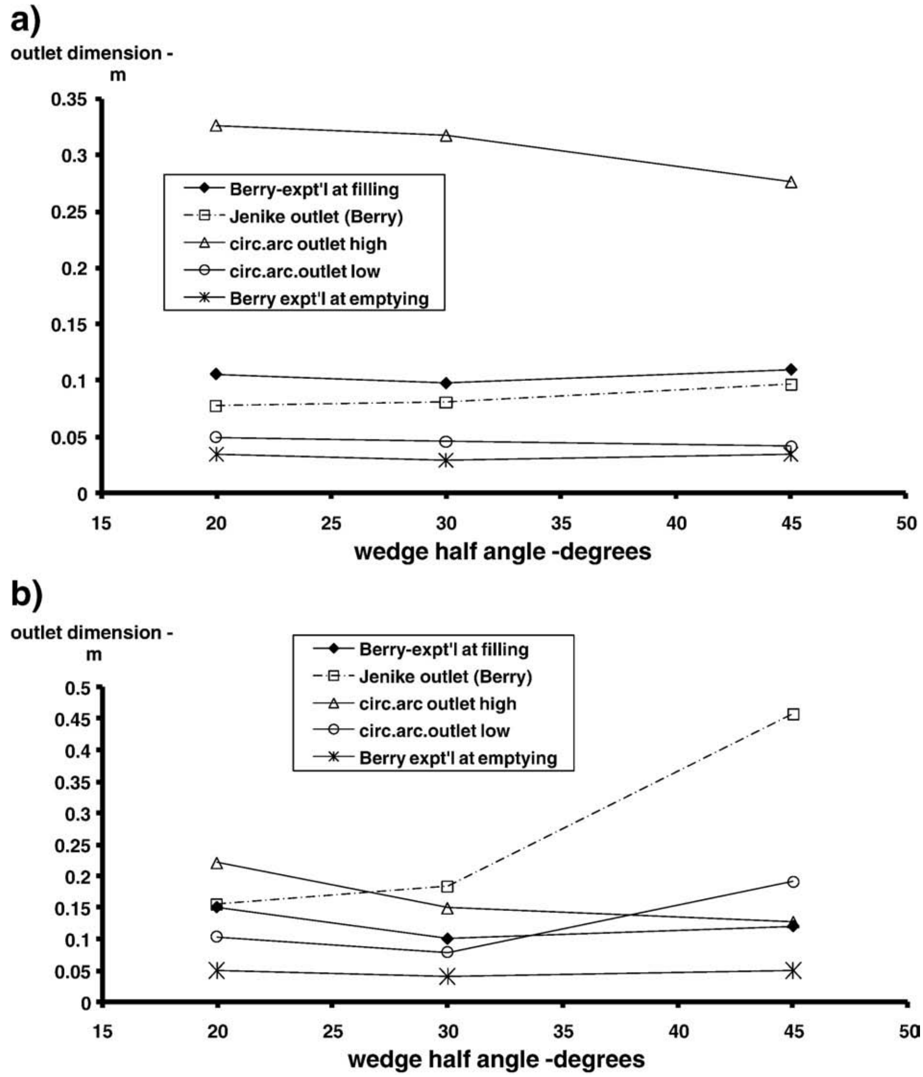

Fig. 17. Outlet dimensions for Berry's hopper — see Table 2 for details. a) fly ash. b) hydrated lime.

approach is that the model may be applied using standard data for bulk solid material characterisation: yield locus, and angle of wall friction. This has been demonstrated in Figs. 16 and 17.

However, the data required by the model is more extensive than the simpler, 1-dimensional analyses [2]. The input data can be divided into 3 groups:

1. Hopper geometry: hopper angles — α_1, α_2, upper surface H_2, lower surface H_1
2. Material properties: bulk density ρ, angle of friction ϕ, tensile stress parameter T, angle of wall friction ϕ_w
3. Stress specification data: angle to the wall normal β_1,β_2, stress state parameter J, overpressure P, wall boundary conditions or $\varepsilon=0$ boundary conditions in ε, upper or lower boundary conditions in x.

Data from 1 & 2 above are readily obtained and are usually quoted in papers.

Data in category 3 require some knowledge of internal stress distribution. This is not usually available, and the parameters P, J and β have been used as adjustable parameters with $\varepsilon=0$ boundary conditions in ε and lower boundary conditions in x to fit the model to experimental data — Figs. 16 and 17.

The stress parameters give the model great flexibility. Therefore, the model could be tuned to give good agreement with any of the 1-d models presented in Fig. 15, and it has also been fitted to the experimental wall normal stress data of Schulze and Schwedes [11] — Fig. 16.

Thus, the model can describe a range of experimental data to an acceptable level. However, perhaps this is not surprising given the number of parameters that may be adjusted. Therefore, the case for the model remains "not proved" until experimental data for internal stress distributions become available.

9. Conclusions

A 2-D model for stress distribution in $(x-\psi_o)$ space has been re-interpreted in $(x-\varepsilon)$ co-ordinates. This maintains the number of increments in numerical integration of the force balance equations and allows for backward integration with respect to both x and ε. It also enables wall boundary conditions to be considered.

The nature of the equations allows boundary conditions to be set at one boundary in x and one in ε only.

Backward integration from the surface to the apex has been shown to be very sensitive to surface conditions and the use of wall boundary conditions was problematic in terms of the Mohr–Coulomb yield criterion.

There are no data for internal stress distributions to validate and calibrate the model, but wall normal stress data of Schulze and Schwedes [11] has been modelled, and predicted outlet dimension for flow has been compared to the data Berry et al. [12] Both comparisons gave reasonable agreement between the model predictions and the experimental data.

Notation

Descriptive statistics for the variables (year-wise).

a_1	Arc radius constant, $a_1 = \frac{\sin\gamma \sin(\alpha_1 + \alpha_2)}{\sin\lambda \cos\alpha_2 \sin(\gamma + \beta_1)}$	[−]
a_2	Arc thickness constant, $a_2 = \sqrt{\{1 - a_1\cos(\alpha_2 + \beta_2)\}^2 + \{\tan\alpha_2 - a_1\sin(\alpha_2 + \beta_2)\}^2}$	[−]
C_1	Constant in stress equations $C_1 = \frac{WJ}{a_1} - 1 - \frac{a_2}{a_1}\cos(-\eta)$	[−]
C_2	Constant in stress equation $C_2 = W(J-1)T/a_1$	[Pa]
C_3	Constant in stress equation $C_3 = \rho g W$	[Pa/m]
(C_4)	Constant of integration	[Pa/m^{C_1}]c
c	Cohesion	[Pa]
F	composite arc stress parameter: $F = \sigma_\varepsilon\left(\frac{\partial w}{\partial x}\right)$	[Pa]
f	Function of x & ε	[−]
g	Acceleration due to gravity	[m/s^2]
H	Value of x at for boundary condition in σ_R	[m]
H_1	Value of x for lower boundary conditions	[m]
H_2	Value of x at upper surface	[m]
J	Material ratio of effective stresses $J = \frac{\sigma_\varepsilon + T}{\sigma_R + T}$	[−]
J_w	Value of J at the wall	[−]
MCYF	Mohr–Coulomb Yield Factor	[−]
O_x	Vertical co-ordinate of arc centre	[m]
O_z	Horizontal co-ordinate of arc centre	[m]
P	Surface overpressure	[Pa]
R	Principal stress arc radius	[m]
S	Spinal value of σ_R: radial stress at $\varepsilon = \eta$	[Pa]
S^*	Boundary value of S	[Pa]
T	Material tensile parameter — linearised yield locus	[Pa]
T_w	Value of T at the wall	[−]
W	Value of $\partial w/\partial x$ at $\varepsilon = \eta$	[−]
x	Height of intersection of arc with wall 2	[m]
X	Vertical co-ordinate	[m]
Z	Horizontal co-ordinate	[m]
α_1,α_2	Angle of wall to vertical	[rad]
β_1,β_2	Angle of arc to wall normal	[rad]
δw	Incremental element thickness	[m]
δO	Incremental change of arc centre O	[m]
$\delta\psi$	Increase in angle of orientation of stress — Fig. 4	[rad]
ε	Angular co-ordinate, angle between arc radius and vertical	[rad]
ϕ	Material angle of friction	[rad]
ϕ_w	Angle of wall friction	[rad]
γ	Angle $\gamma = \pi/2 - \lambda/2$	[rad]
ψ	Angle of principal stress trajectory	[rad]
ψ_o	Value of ψ at $x = H$	[rad]
λ	Total span of arc $\lambda = \alpha_1 + \beta_1 + \alpha_2 + \beta_2$	[rad]
η	Angle of precession of arc centre to vertical	[rad]
ρ	Bulk density	[kg/m^3]
σ_ε	Azimuthal, arc stress	[Pa]
σ_ψ	Arc stress in $(x-\psi_o)$ space	[Pa]
σ_R	Radial stress in $(x-\psi_o)$ space and $(x-\varepsilon)$ space	[Pa]
σ_w	Wall normal stress	[Pa]

References

[1] A.W. Jenike, Flow and storage of solids, Utah Experimental Station, Bulletin, vol. 123, University of Utah, USA, 1967.
[2] R.M. Nedderman, Statics and Kinematics of Granular Materials, Cambridge University Press, 1992.
[3] A.J. Matchett, J.C. O'Neill, A.P. Shaw, Stress distributions in 2- dimensional, wedge hoppers with circular arc stress orientation — a co-ordinate-specific Lamé–Maxwell model, Powder Technol. 187 (2008) 298–306.
[4] G. Enstad, On the theory of arching in mass flow hoppers, Chem. Eng. Sci. 30 (10) (1975) 1273–1283.
[5] A.J. Matchett, Stresses in a bulk solid in a cylindrical silo, including an analysis of ratholes and an interpretation of rathole stability criteria, Chem. Eng. Sci. 61 (2006) 2035–2047.
[6] A.J. Matchett, Rotated, circular arc models of stress in silos applied to core-flow and vertical rat-holes, Powder Technol. 162 (2006) 87–99.
[7] Gerner A. Olsen, Elements of Mechanics of Materials, Prentice-Hall, New Jersey, USA, 1982, p. 477.
[8] DPlot graph software for scientists & engineers, August 2008 www.dplot.com.
[9] A.J. Matchett, The shape of the cohesive arch in hoppers and silos — some theoretical considerations, Powder Technol. 171 (3) (2007) 133–145.
[10] D.M. Walker, An approximate theory for pressures and arching in hoppers, Chem. Eng. Sci. 21 (1966) 975–997.
[11] D. Schulze, J. Schwedes, An examination of initial stresses in hoppers, Chem. Eng. Sci. 49 (13) (1994) 2047–2058.
[12] R.J. Berry, A.H. Birks, M.S.A. Bradley, Measurement of critical cohesive arches in silos using laser ranging, from powder to bulk, IMechE, London, paper C566/039/2000, IMechE, London, UK, 13–15 June 2000, pp. 131–141, ISBN:1 86058 272 9.
[13] Berry, R.J., The measurement of cohesive arches in silos using the technique of laser ranging, Phd thesis, University of Greenwich, 2003

Stresses in bulk solids in cone hoppers: numerical solutions to the 3-dimensional stress distribution problem, using circular arc geometry

J.C. O'Neill*, A.J. Matchett, and A.P. Shaw

School of Science and Technology
University of Teesside
Middlesbrough, Tees Valley TS1 3BA, UK

ABSTRACT

In a previous paper, a 2-dimensional model of stress distribution within bulk solids, with circular arc principal stress orientation, in a wedge hopper was developed [1]. The model worked in an orthogonal, curvilinear co-ordinate system co-incident with the principal stress trajectories: ($x-\psi_0$) space. This paper presents a model with similar assumptions in 3-dimensional ($x-\varepsilon-\theta$) space. Stress distributions for cone hoppers with rotational symmetry are now the subject of analysis. Rotational symmetry is assumed through angle θ. Three principal stresses are defined ($\sigma_{R}.\ \sigma_{\varepsilon}$ and σ_{θ}). This is achieved via two static force balances on an incremental element, and assumption of a relationship between principal stresses. The numerical solution presented allows specification of arc stress along a given surface. As discussed in a previous paper [1], if a cohesive arch is specified, then stresses at the upper surface of the bulk solid are determined by the model. This calculated overpressure could be assumed to represent a horizontal material surface. Minimum flow outlet diameters from this model have been compared to available data.

1. INTRODUCTION

Granular materials, or 'bulk solids', can be defined as any material composed of many individual solid particles, irrespective of particle size [2]. Granular materials are used in a wide range of industries, including the medical, food, construction, chemical and manufacturing industries [3,4].

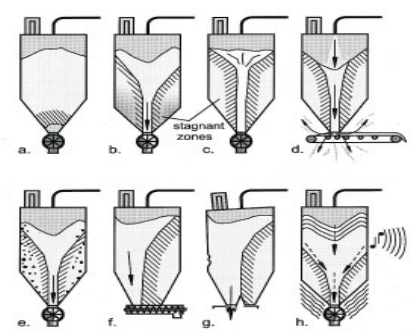

Figure 1: Possible problems during the operation of silos [5]

To allow processing of such materials, storage is required. Containers are often cylindrical, and can range in size from capacities measured in grams to thousands of tonnes [2]. At the base of the silo the container walls will converge to at least one small opening. This hopper section allows the flow of the granular material to be directed to the next stage of the process. In Figure 1, Schulze [5] describes some common problems encountered during flow of granular materials, including arching, funnel flow, rat-holing, flooding, segregation, eccentric flow and vibration.

Many of the problems indicated above are cause by poor design of the silo and hopper set-up. Knowledge of stress distributions within these granular materials is not only concerned with ensuring flow of material from hoppers: such knowledge is also required for mechanical design of the hopper silo walls [6,7,8,9]. A lack of consideration of internal stresses

* Corresponding author: Tel.: (0044) 7715824815; E-mail: james0neil@aol.com

can result in catastrophic failure [10].

The stress analysis model proposed in this paper seeks to predict distributions 3-dimensional cone hoppers. The expansion from earlier methods detailed in this paper will give a better understanding of the problem, improved design algorithms, ensuring reliable shell design and material flow. In previous papers [1,11,12,13] new models making use of circular arc geometry were presented. The works produced were based on a model developed originally used by Enstad [14]. Enstad's work calculated stresses in one direction only – in the vertical direction. Li [15] also made use of a model based on circular arc geometry. The models created for these papers initially provided force balance equations in two dimensions [11], and subsequently were expanded into three dimensions [12,13].

2. Model Geometry & Force Balance Equations

Model geometry has been defined in previous papers for two-dimensional hoppers [1,11] and three-dimensional hoppers/silos [12,13] with rotational symmetry. An important addition to two-dimensional models is the angle of rotational symmetry, whereby three-dimensional stress distributions can be observed. Matchett et al [1] and the current paper are developments from these prior works, and now take account of curvature normal to the circular arc after Lame-Maxwell [1,16].

The assumptions used in the new model are listed below. Incipient failure is assumed, therefore inertial terms are not included.

- Principal stresses act over successive sections circular arc sections of radius R [11].
- The arc under consideration cuts the wall at vertical height x from the vertex, and intersects the wall at distance r from the axis of rotation [11]; Figure 2.
- The incremental arc has a thickness of δ_w, which varies across the span of the arc with ε [11,12]; Figure 3.
- Positions within the vessel/hopper are located by height at which the arc cuts the vessel wall x, and arc angle ε [12]; Figure 2.
- In three-dimensional space there are three principal stresses acting: radial stress σ_R, arc stress σ_ε and azimuthal stress σ_θ [13]. Radial and arc stresses are orientated along circular paths of radius R. Azimuthal stresses act on the incremental element shown in Figure 3, and are orientated normal to the page.
- Rotational symmetry is assumed through azimuthal angle θ, shown in Figure 2 [12].

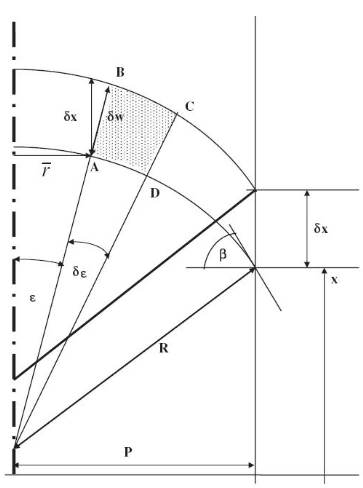

Figure 2: Model geometry [12]

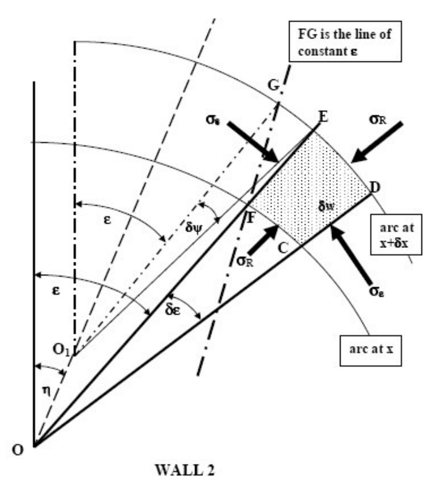

Figure 3: Circular arc incremental element [1]

Figure 2 [12] shows the principal stress arc geometry. The cone hopper has half angle to the vertical α_1 and α_2 respectively (for symmetrical systems $\alpha_1 = \alpha_2 = \alpha$); a circular arc cuts the right hand side wedge at a distance x above the apex with radius R. Point *A* has coordinates in *(X,Z)* space of:

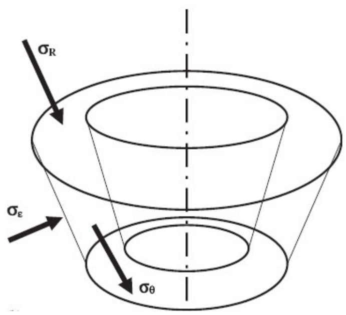

Figure 4: Stresses acting on the incremental element [12]

$$X = R\cos\varepsilon \tag{1}$$

$$Z = R\sin\varepsilon \tag{2}$$

If an incremental element is considered cutting the right-hand side with vertical height δx, and at an angle of ε to the vertical with incremental angle $\delta\varepsilon$ - see Figure 3 [1].

A detail of the incremental element is shown in Figure 3 [1]. Using the circular arc geometry initially set out by Matchett [11], a force balance on an incremental element can be completed. A sketch of the rotated incremental element is shown in Figure 4 [12].

3. Stress Distributions

The R-ε coordinate system is not orthogonal-curvilinear, as shown in Figure 3. The line of constant ε between the two arcs is *FG*. This must be considered when force balances are constructed. The centre point of the upper arc does not coincide with the centre point of the lower arc - the arc centre moves from point *O* to O_1.

Figure 3 [1] shows arc radii at angle ε for curves at x and $x + \delta x$. Lines O_1FE and *OMCD* are parallel, with distance *CD* equal to thickness δw. *M* is the normal projection from point O_1 onto line *OMCD*.

Therefore:

$$R = a_1 x \tag{3}$$

$$\left(\frac{\partial w}{\partial x}\right) = a_1 + a_2\cos\varepsilon \tag{4}$$

where

$$a_1 = \frac{\tan\alpha}{\sin(\alpha+\beta)} \quad \text{and} \quad a_2 = 1 - a_1\cos(\alpha+\beta)$$

A benefit of the circular arch approach results from defining an incremental element that is co-incident with the directions of principal stresses. Calculation of shear stress is therefore not required in the analysis. In Figure 3, principal stress σ_R acts on surfaces *CF* and *DE*. While *CD* and *EF* are normal to line *CF*, they are not normal to line *DE*, due to precession of the arc centre from *O* to O_1. The radius from O_1 normal to *DE* is at angle $(\varepsilon + \delta\psi)$ to the vertical. Therefore the surfaces on which σ_ε acts as a principal stress must be curved, as shown in Figure 3, and the incremental element upon which the force balance is based will be CD_1E_1F. σ_ε can be defined as a major principal stress acting upon the curved surface between $(R(x),\varepsilon)$ and $(R(x+\delta x),(\varepsilon+\delta\psi))$. From the system geometry:

$$R_2 = \frac{\partial w}{\partial x} \bigg/ \frac{\partial \psi}{\partial x} \tag{5}$$

and

$$\frac{\partial \psi}{\partial x} = \frac{a_2 \cos\varepsilon \sin\varepsilon}{a_1 x \cos\varepsilon} = \frac{a_2 \sin\varepsilon}{R} \tag{6}$$

Therefore

$$R_2 = \frac{R(a_1 + a_2 \cos\varepsilon)}{a_2 \sin\varepsilon} \tag{7}$$

For the cone hopper model, force balance equations are required to allow calculation of stresses, including those in the third dimension – azimuthal stress σ_θ. Three-dimensional force balances on the incremental element give equations in R - and ε -directions.

$$\frac{\partial F}{\partial \varepsilon} = \left(\frac{\left(\frac{\partial w}{\partial x}\right)\sigma_\theta - F}{\tan\varepsilon} \right) - \sigma_R a_2 \sin\varepsilon + R\left(\frac{\partial w}{\partial x}\right)\rho g \sin\varepsilon \tag{8}$$

$$\frac{\partial}{\partial x}\left[R^2 \sigma_R\right] = RF - R^2\left(\frac{\partial w}{\partial x}\right)\rho g \cos\varepsilon - 2R\sigma_R a_2 \cos\varepsilon - Ra_2 \sin\varepsilon \frac{\partial \sigma_R}{\partial \varepsilon} + R\left(\frac{\partial w}{\partial x}\right)\sigma_\theta \tag{9}$$

Azimuthal stresses are found via use of the Haar-von Karmen hypothesis [2], or by other relationships. These relationships can be assumed to follow the form of $\sigma_\theta = f(\sigma_\varepsilon, \sigma_R)$. Using equation 9, it can be shown that when ε is equal to zero, azimuthal stress is equal to arc stress. The relationship shown in equation 10 has been used for solutions demonstrated in this paper.

$$\sigma_\theta = \sigma_\varepsilon + k\varepsilon\sigma_R \tag{10}$$

3.1. COHESIVE ARCH MODELLING

Radial stress σ_R values are set at zero at a position chosen to represent a cohesive arch location. This location can be provided by on-site data or by estimation using Nedderman's equation 10.8.2 [2, p296]. Stresses at the top of the hopper are not fixed. Boundary conditions are obtained for arc stress σ_ε by use of the Mohr-Coulomb criterion. This Mohr-Coulomb relationship is used only to provide initial values – stress distributions throughout the model are system are specified by the model. Azimuthal stress σ_θ is obtained by a relationship with the other two principal stresses. After Matchett [12], azimuthal stress values can be calculated directly from equation 9. A boundary condition is needed, for example the relationship shown in equation 10.

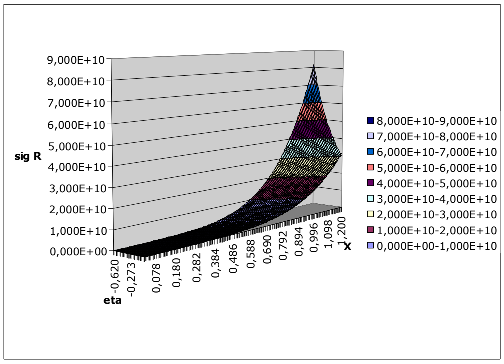

Figure 5a: $\sigma_R - x - \varepsilon$ for Cohesive Arch case

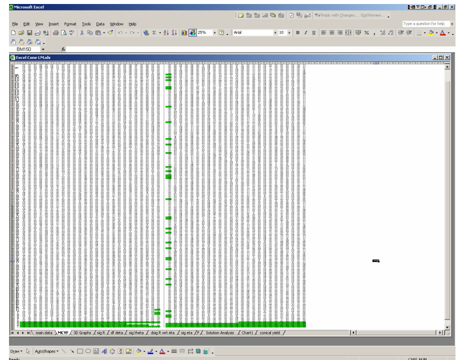

Figure 5b: MCYF for Cohesive Arch model case

In Figure 5a, σ_R values can be seen to increase from zero at the assumed location of cohesive arch. Radial stresses show a large overpressure at the material surface.

In the model used in this paper, it is assumed that a cohesive arch will be present when conformity to the Mohr-Coulomb criterion is demonstrated across the model. The initial height H of the material surface has been reduced - Figure 5b shows that the results conform to Mohr-Coulomb limits, with the exception of a small number of results (shaded cells at base of figure). Increase of the *k*-value further increases stability. From the hopper geometry given in Table 1, the results of these figures equate to a critical diameter of 0.05 metres. A smaller hopper outlet diameter than this critical dimension will be subject to arching. Nedderman's equation 10.8.2 gives the critical diameter as 1.22 metres.

3.2. Active Stress State Modelling

Radial stress σ_R values are set to zero at a position representing the surface of the granular material. Again the Mohr-Coulomb criterion is used to produce an initial value for arc stress σ_ε. Azimuthal stress σ_θ values are specified by the same relationship given by equation 10. Model values are not restricted, other than active stress state relationship along hopper centre-line.

In Figure 6a, σ_R values increase along the hopper centreline, towards the theoretical apex. This is in contravention to other models [14], where zero or negative stresses are assumed to indicate cohesive arching. It can be argued that if material within a hopper is stable, then stresses will increase to some positive value as per Janssen's equation [2]. In Figure 6b partial conformity to the Mohr-Coulomb is demonstrated.

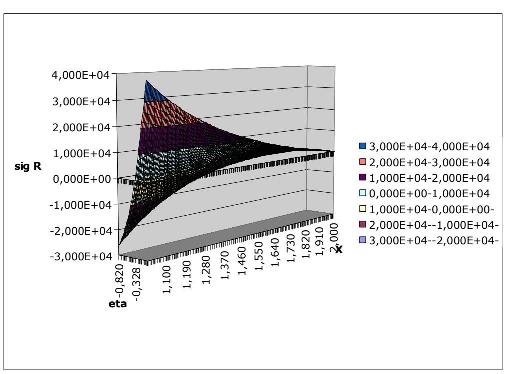

Figure 6a: $\sigma_R - x - \varepsilon$ for Active Stress case

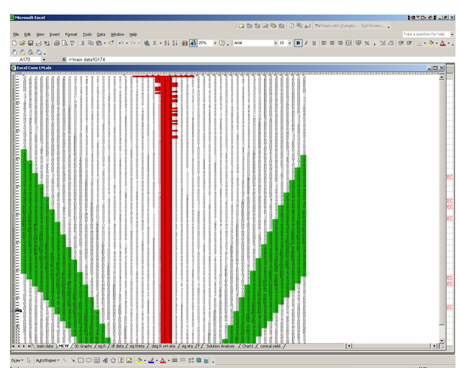

Figure 6b: MCYF for Active Stress case

If a passive stress case is used, with non-zero radial stress values at the hopper top surface, then a decrease in radial stress values is demonstrated. Use of non-zero values at this position represents material above the hopper – for example during a typical hopper and silo arrangement. Stress distributions produced can be favourably compared to results presented by Enstad [14].

4. DISCUSSION

Stress distributions within granular materials provide useful information for hopper and silo design. Cohesive arch location can be predicted and avoided. Active and passive stress cases can be modelled, and therefore stress situations unviable to the Mohr-Coulomb criterion can be determined. Azimuthal stresses within hoppers can now be modelled to a level not previously possible.

However, there are limitations of ($x-\varepsilon-\theta$) model. Boundary conditions may only be specified at one boundary in x and one in ε . This means that if stresses are fixed at the bottom of the hopper (for example a value of zero σ_R representing a cohesive arch), then the surface overpressure is specified by the model. Two possible solutions are by assuming a material surface affects results, at the transition from open surface to circular arc principal stress orientation, or by introducing elastic effects throughout the system between boundary conditions at either end of the model. Alternatively, if it is assumed that the hopper will be placed underneath a silo, then results can be compared to previous models [2,14,17], which demonstrate peak stress values at the transition from silo to hopper.

There is a lack of data for comparison with model results. At the time of writing it is not possible to verify the relationship proposed between principal stresses, as no experimental data are available on stress distributions. Some data are available for critical outlet widths [2]. When compared with model data substantial differences in predicted outlet sizes were present. Jenike's methods have been tested in industry; however some works [11] have indicated that an over-design may be present in the equation used. The geometry of the hopper should also be considered – a hopper of 1.2 metres in height and 2.1 metres in width, with a 1.22 metre outlet is unlikely to be susceptible to cohesive arching.

5. CONCLUSIONS

A three-dimensional model of stress distributions within cone hoppers has been presented, making use of rotational symmetry. The model provides radial, arc and azimuthal stress solutions through circular arc principal stress orientation. The information produced by the model can be used both for prediction of cohesive arch location and structural design of hoppers and silos.

The stress distributions produced have been compared to limited data. Model development would benefit from comparison to experimental data for verification of findings. Further work will include inserts and non-symmetrical hopper shapes.

Mathematical study of stress distributions within hoppers and silos is not a new discipline, however processing of granular materials in this way remains problematic [18].

REFERENCES

[1] *Matchett, A.J., O'Neill, J.C. and Shaw, A.P., 2008. Stress distributions in 2-dimensional, wedge hoppers with circular arc stress orientation – a coordinate-specific Lame-Maxwell model. Powder Technology,* ***187*** *(3) pp. 298-306.*

[2] *Nedderman, R.M., 1992. Statics and Kinematics of Granular Material. New York: Cambridge University Press.*

[3] *Ajax Equipment. Testimonials and Endorsements From Some of Our Customers. Ajax Equipment Limited [internet]. Available from http://www.ajax.co.uk/testimonials.htm [cited 03.08.08].*

[4] *McGlinchey, D. (ed.), 2005. Characterisation of Bulk Solids. Oxford: Blackwell Publishing Ltd.*

[5] *Schulze, D., 2008. Powders and Bulk Solids: Behavior, Characterization, Storage and Flow. New York: Springer-Verlag Berlin Heidelberg.*

[6] *Chen, J.F., Rotter, J.M., Ooi, J.Y., 1998. Statistical inference of unsymmetrical silo pressures from comprehensive wall strain measurements. Thin-Walled Structures **31** (1) pp. 117-136.*

[7] *Ooi, J.Y. et al, 1996. Prediction of static wall pressures in coal silos. Construction and Building Materials **10** (2) pp. 109-116.*

[8] *Song, C.Y., 2004. Effects of patch loads on structural behaviour of circular flat-bottomed steel silos. Thin-Walled Structures **42** (11) pp. 1519-1542.*

[9] *Zhao, Y. & Teng, J.G., 2004. Buckling experiments on steel silo transition junctions II: Finite element modelling. Journal of Constructional Steel Research **60** () pp. 1803-1823.*

[10] *Carson, J.W., 2000. Silo failures: case histories and lessons learned. Jenike & Johanson, Inc. [internet]. Available from: http://www.jenike.com/TechPapers/silo-failures.pdf [cited 03.08.08].*

[11] *Matchett, A.J., 2004. A theoretical model of vibrationally induced flow in a conical hopper system. Chemical Engineering Research and Design, **82** (A1) pp. 85-98.*

[12] *Matchett, A.J., 2006a. Rotated, circular arc models of stress in silos applied to core flow and vertical rat-holes. Powder Technology, **162** (2) pp. 87-89.*

[13] *Matchett, A.J., 2006b. Stresses in a bulk solid in a cylindrical silo, including an analysis of rat-holes and an interpretation of rat-hole stability criteria. Chemical Engineering Science, **61** (6) pp. 2035-2047.*

[14] *Enstad, G., 1975. On the theory of arching in mass flow hoppers. Chemical Engineering Science, **30** (10) pp. 1273-1283.*

[15] *Li, H., 1994. Mechanics of arching in a moving bed standpipe with interstitial gas flow. Powder Technology, **78** (2) pp. 179-187.*

[16] *Olsen, G.A., 1982. Elements of Mechanics of Materials. 4th Ed. Englewood Cliffs, Prentice-Hall. Inc.*

[17] *Walters, J., 1973. A theoretical analysis of stress in axially-symmetric hoppers and bunkers. Chemical Engineering Science, **28** (3) pp. 779-789*

[18] *McGee, E. Insert Solutions. The Chemical Engineer magazine, issue 802 April 2008 pp.38-39.*

NOTATION

a_1	arc radius constant	[-]
a_2	arc thickness constant	[-]
g	acceleration due to gravity	[m/s^2]
F	model variable, $F = \sigma_\varepsilon \left(\dfrac{\partial w}{\partial x}\right)$	[-]
H	value of x at for boundary condition in σ_R	[m]
J	material ratio of effective stresses $J = \dfrac{\sigma_\varepsilon + T}{\sigma_{R\varepsilon} + T}$	[-]
MCYF	Mohr-Coulomb Yield Factor	[-]
r	distance OA	[m]
$\bar{r}$	radius of rotation of incremental element	[m]
R	principal stress arc radius	[m]
R_2	upper arc radius	[m]
T	material tensile parameter – linearized yield locus	[Pa]
x	height of intersection of arc with Wall 2	[m]
X	vertical co-ordinate	[m]
Z	horizontal co-ordinate	[m]
α_1, α_2	angle of wall to vertical	[rad]
β_1, β_2	angle of arc to wall normal	[rad]

δw	incremental element thickness	[m]
δO	incremental change of arc centre O	[m]
$\delta\varepsilon$	increase in angle of orientation of stress – Figure 4	[rad]
$\delta\psi$	angle between 0_1G and 0_1E, due to progression of arc centres	[rad]
δx	incremental vertical height	[m]
ε	angular co-ordinate, angle between arc radius and vertical	[rad]
θ	azimuthal angle	[rad]
ρ	bulk density	[kg/m^3]
$\sigma\varepsilon$	arc stress	[Pa]
σ_R	radial stress	[Pa]
σ_θ	azimuthal stress	[Pa]

TABLE 1

	alpha	beta	Initial height	rho	phi	T	J	delta x	k
cohesive arch	30	5,5	1,2	1000	30	3000	3	0,006	3
active stress	30	17	2	1000	30	3000	0,33	0,005	1